2011 Synthesis and Processing Science Principal Investigators' Meeting

Hyatt Regency Crystal City, Arlington, Va.
September 18-21, 2011

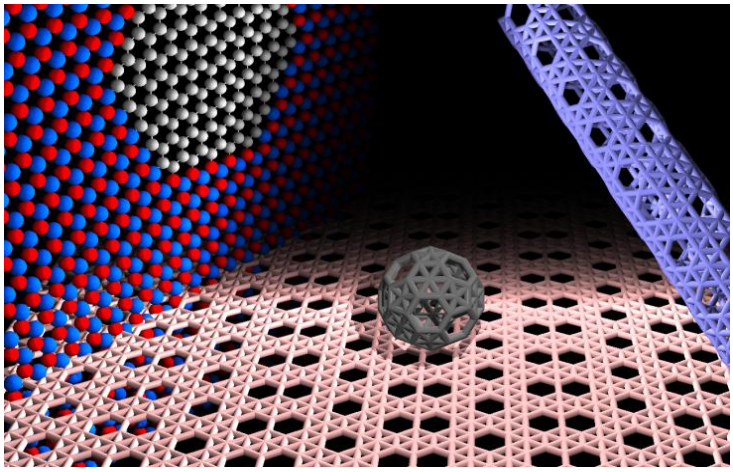

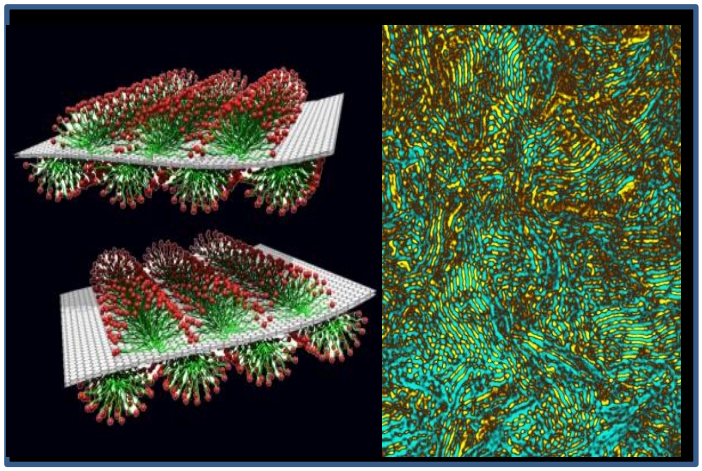

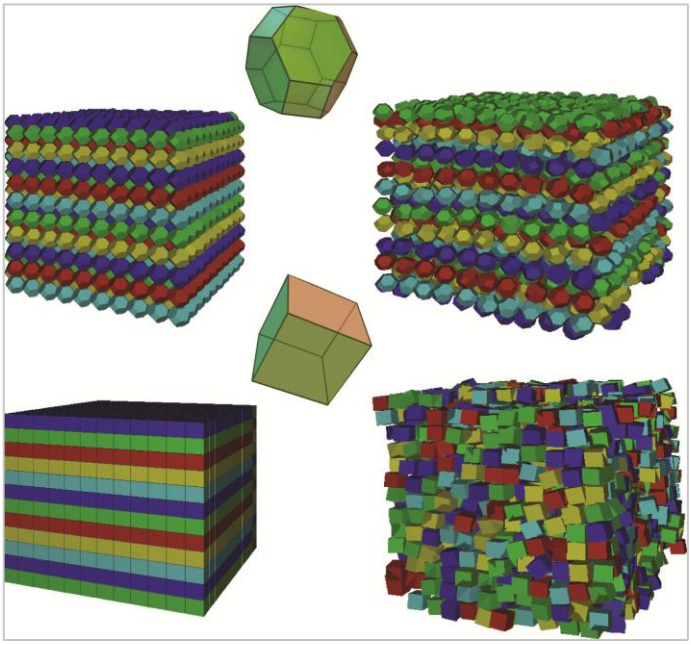

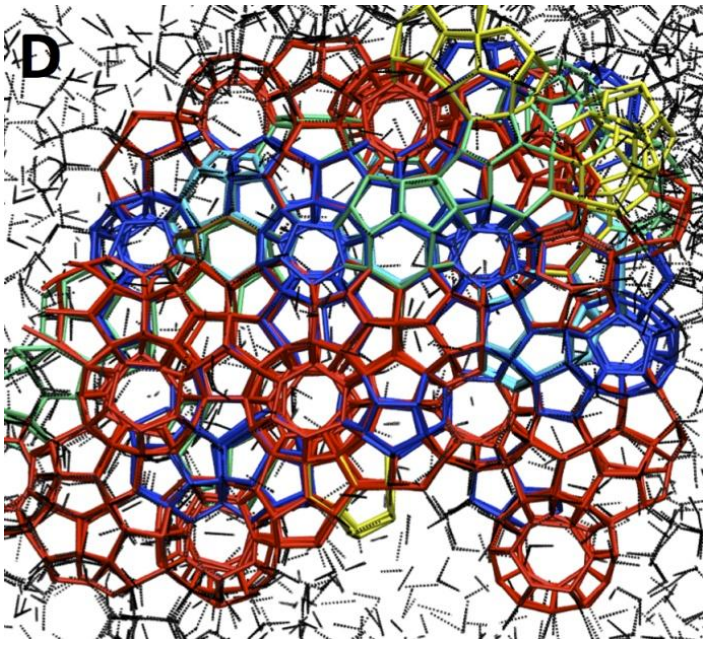

U.S. DEPARTMENT OF ENERGY | Office of Science

Office of Basic Energy Sciences
Materials Sciences and Engineering Division

1. Top Left: Computational analysis reveals variety of nanostructures of pure boron, from hollow fullerene-like to nanotubes, as well as boron rich combinations with other elements, notably white-graphene h-BN hybrids with C-graphene, of distinct electronic and optical properties to be found experimentally. *Nano Lett.* **11**, 3113 (2011) (Courtesy: Boris Yakobson, Rice University)

2. Top Right: A multiscale self-assembly approach is developed using functionalized graphene sheets as the nanoscale building block and surfactant as the molecular directing agent to form well controlled nanoporous metal oxide-graphene composites. . The whole structure self-assemble into 3D hexagonal or lamella or disordered architecture. *ACS Nano*, **4**, 1587 (2010). (Courtesy: Jun Liu, Pacific Northwest National Laboratory)

3. Bottom Left: Molecular simulation reveals novel plastic and liquid crystalline mesophases at intermediate volume fractions for assemblies of nano- and micro-scale space filling polyhedrons. Predictive guidelines correlating particle shape parameters with phase behavior are hence formulated. *Nature Materials*, **10,** 230 (2011). (Courtesy: Fernando Escobedo, Cornell University)

4. Bottom Right: Crystalline-like state with sI and sII domains formed during clathrate hydrate nucleation, providing insight into the nucleation mechanism as a function of driving force, which is a major outstanding challenge in hydrate science and engineering. *Science*, **326**, 1095 (2009) and *Journal of Physical Chemistry B*, **114,** 5775 (2010) (Courtesy: Carolyn Koh, Colorado School of Mines)

This document was produced under contract number DE-AC05-06OR23100 between the U.S. Department of Energy and Oak Ridge Associated Universities.

The research grants and contracts described in this document are supported by the U.S. DOE Office of Science, Office of Basic Energy Sciences, Materials Sciences and Engineering Division.

Table of Contents

Foreword

This abstract book comprises the scientific content of the 2011 Synthesis and Processing Science Principal Investigators' Meeting sponsored by the Materials Sciences and Engineering (MSE) Division in the Office of Science, Basic Energy Sciences (BES) of the U.S. Department of Energy (DOE). The meeting, held on September 18-21, 2011, at the Hyatt Regency Crystal City, Arlington, Virginia, is the third principal investigators' meeting on this topic and is one among a series of research theme-based principal investigators' meetings held by BES.

The purpose of this principal investigators' meeting is to bring together all of the researchers funded by BES-MSE in the Synthesis and Processing Science core research activity and in related programs so that they can get a firsthand look at the broad range of materials science research that is being supported in this important research area. The meeting will serve as a forum for the discussion of new results and research highlights, thus fostering a greater awareness of significant new advances in the field and the research of others in the program. The confidential and collegial meeting environment is intended to provide unique opportunities to develop new collaborations among PIs, and new ideas. In addition, the meeting affords BES program managers an opportunity to assess the state of the entire program at one time on a periodic basis, in order to chart future directions and identify new programmatic needs.

This year's meeting focuses on four topics within the Synthesis and Processing Science portfolio: Function-Driven Materials Design, Soft Materials and Soft-Hard Interfaces, Predictive Crystal Growth, and Large Scale Assembly. While this is one way of organizing and presenting the research within this broad portfolio, there are many other synergies that could be highlighted and will be considered at future meetings.

Let me take this opportunity to express my thanks to all the meeting attendees, especially the invited presenters, for their active participation and sharing their ideas and new research results. A special thanks is given to the selected invited speakers from the BES-MSE core research activities of Mechanical Behavior and Radiation Effects (Rishi Raj), and Physical Behavior of Materials (Duane Johnson) and the Energy Frontier Research Center at the Sandia National Laboratories (Michael Coltrin and George T. Wang), who graciously agreed to attend and share their perspectives. The dedicated efforts and invaluable advice of the meeting chairs, Jun Liu and Kristen Fichthorn, towards organizing this meeting are deeply appreciated. Finally, this meeting would not be possible without the logistical support from Teresa Crockett (BES-MSE) as well as Lee Ann Talley and Joreé O'Neal at Oak Ridge Institute for Science and Education (ORISE).

Bonnie Gersten
Program Manager, Synthesis and Processing Science
Materials Sciences and Engineering Division
Office of Basic Energy Sciences
U.S. Department of Energy

2011 DOE-BES-MSE Synthesis and Processing Science Principal Investigators' Meeting

The 2011 DOE-BES-MSE Principal Investigators' Meeting will focus on the coupling of experimental and theoretical approaches to address challenges in the Materials Synthesis and Processing Science Program. The meeting will emphasize the role of theoretical modeling and simulation in developing a fundamental understanding of the principles that govern the rational design of molecular and nanoscale building blocks, as well as their growth and assembly into complex structures and high-level architectures with desired functionality. The integration of theory and experiment offers the potential to address the following Grand Challenge problems for Basic Energy Sciences pursuant to Synthesis and Processing Science core research activities:

(1) *How do we control materials processes at the level of electrons?*
(2) *How do we design and perfect atom- and energy-efficient synthesis of revolutionary new forms of matter with tailored properties?*
(3) *How do remarkable properties of matter emerge from complex correlations of the atomic or electronic constituents, and how can we control these properties?*

New developments in theoretical methods, as well as in ultrafast *in situ* experimental characterization techniques, allow for unprecedented capabilities to probe the evolution of structures and morphologies from the atomic scale to the nanoscale and beyond. This opens new vistas for *new* materials design and direct experimental validation of theoretical predictions. Efforts to manipulate nucleation and growth kinetics, control interfacial phenomena during film growth, and achieve stepwise growth or multiscale assembly places particular emphasis on the intimate link between synthesis, *in situ* characterization, and modeling.

For this meeting, abstracts are organized within four sessions:

1. **(a) Function-Driven Materials Design:** Exploratory synthesis through advanced processing; **(b) Function-Driven Materials Design:** Exploratory caged materials; **and (c) Function-Driven Materials Design:** Use-inspired science

2. **Soft Materials and Soft-Hard Interfaces**

3. **Predictive Crystal Growth**

4. **Large Scale Assembly**

Each materials class presents its own challenges; however, several synthesis and processing science themes crosscut all materials systems. These include:

Crosscutting Questions

(1) **Synthesis Strategies for New Materials Discovery** – How to design synthesis

strategies for desired materials structures and functionalities? What theoretical advances are required to enable prediction of synthesis pathways for new classes of materials?

(2) **Theory Driven Synthesis** – What are the first-principles–based theoretical approaches to describe experimentally accessible materials? Can the understanding of materials design and growth mechanisms be used to predict the most thermodynamically plausible routes and techniques for synthesis?

(3) **Understanding Long-Range Correlation** – How do long-range interactions underpin the kinetics and thermodynamics of the growth of nanoscale and mesoscopic objects? How can one exploit these interactions?

(4) **Structure/Function Relation** – How do the properties of building blocks influence the performance of the whole material? What is the role of interfaces in driving the properties of nanocomposite materials? How to tailor a material's architecture to achieve certain desired properties?

(5) **In Situ Characterization Tools:** What novel *in situ* characterization techniques will enable experimental validation of theory and provide insight into molecular-level assembly processes?

Meeting sessions will be organized to address the following questions:

1. **Function-Driven Materials Design**: *Theoretical and experimental approaches to new material architecture and desired functionalities*

This session will address advances in experimental approaches and theoretical understanding of structure/property relationships in materials for energy utilization. The ultimate goal of this research direction involves starting from a desired functionality, predicting the required material architecture, and defining the synthetic pathway to achieve it. Developing molecular and nanoscale building blocks is the key step for realizing materials with unusual functionalities. The design of synthetic materials takes advantage of the dramatic difference in materials properties at the nanoscale compared to their behavior in the bulk. Resident properties of nanostructured materials tend to exhibit marked size and shape dependence, which provides the opportunity for fine-tuning their performance. However, the performance of materials assembled from nanoscale units depends not only on the properties of their nano-building blocks, but also on their overall architecture. The challenge is to gain a fundamental understanding of how emergent properties and functions are derived from an ensemble of materials and components, and how to design synthesis and assembly approaches to achieve desired structures and functionalities that are beneficial for meeting our energy needs.

2. **Soft Materials and Soft-Hard Interfaces**: *Polymer architectures through manipulation of interfacial interactions*

This session will focus on defining the design rules that influence polymer growth and structural transformations, and integrating soft matter with hard matter to create hybrid materials. Such materials hold the promise that tunable, multifunctional properties can be achieved through understanding interfacial interactions and developing associated processing strategies. Some examples include variable resistivity and tunable opto-electronic and mechanical properties of polymer/nanoparticle composites. To design

such composites requires understanding interactions in colloidal systems, phase formation and segregation in block copolymers, and interactions in nanoparticle/polymer systems. These are crucial in the quest to develop soft/hard/hybrid materials that can hierarchically organize into 3D architectures by self-assembly or through application of external stimuli. Controlling the topography of soft material surfaces is another processing challenge crucial to the development of nearly every functional thin-film polymer-hybrid structure.

3. **Predictive Crystal Growth**: *Universal laws for determining and controlling morphology and surface chemistry*

Crystalline structures and morphologies play a critical role in materials properties. This session will focus on the universal laws governing crystallization and crystal growth to address the synthesis and processing of large crystalline materials. A complex interplay of kinetic and thermodynamic effects determines the morphology and shape of a growing crystal. Many synthesis and processing techniques rely on processes far removed from equilibrium to push the system into thermodynamically less favored morphologies, which can be subsequently stabilized by functionalization. Progress in understanding the laws governing equilibrium and nonequilibrium crystal growth regimes will be reviewed. The questions addressed will include the possibility of predicting synthesis conditions for the formation of desired crystalline architectures, investigation of the factors governing diffusion and relaxation of atoms on a growing crystal surface, the processes by which adatom diffusion can be controlled by changing synthesis conditions, and the possibility of controlling structural evolution of the material during growth.

4. **Large Scale Assembly of Hybrid Materials**: *Mesoscopic and large assemblies beyond molecular and nanoscales*

Considerable emphasis has been placed on the synthesis of nanomaterials. This session will focus on the scalable synthesis of nanostructured materials and their assembly into large functional structures and architectures. Both top-down and bottom-up assembly approaches will be explored. In bottom-up approaches, the assembly of materials from nanoscale structures (e.g., nanoparticles, 2D flakes and sheets, and 1D nanowires and nanorods) often requires tailoring interactions between the building blocks by chemical functionalization. This approach calls for a thorough understanding of colloidal and interfacial forces governing assembly and growth. The top-down approach on the other hand offers additional means to guide materials synthesis and assembly through external fields. Progress in understanding the short- and long-range interactions responsible for the directed assembly of various architectures and the role of entropic effects in directing self-assembly and growth will be reviewed.

Summary: Overall, this meeting will endeavor to establish working relationships and collaborations among the principal investigators through the discovery and discussion of materials synthesis and processing challenges that crosscut materials classes with an emphasis on coupling theoretical and experimental approaches.

2011 Synthesis and Processing Science Principal Investigators' Meeting Agenda

Meeting Chairs: **Jun Liu and Kristen Fichthorn**
Pacific Northwest National Laboratory/ The Pennsylvania State University

Sunday, September 18, 2011

3:00 – 6:00 pm	Arrival and Registration
5:00 – 6:00 pm	Reception (No Host)
6:00 – 8:00 pm	***** Dinner on Your Own *****

Monday, September 19, 2011

7:30 – 8:30 am	***** Breakfast*****
8:30 – 9:00 am	*Introductory Remarks* **Arvind Kini** Team Leader, Materials Discovery, Design and Synthesis Team, Division of Materials Sciences and Engineering
9:00 – 9:20 am	**Bonnie Gersten** Program Manager, Synthesis and Processing Science Meeting Chairs: **Jun Liu and Kristen Fichthorn** Pacific Northwest National Laboratory/The Pennsylvania State University
Session 1a	**Function-Driven Materials Design:** Exploratory Synthesis Through Advanced Processing Chair: **Ivan Bozovic**, Brookhaven National Laboratory
9:20 – 9:40 am	**Duane Johnson (Invited),** Ames Laboratory *Defect-Mediated Materials Properties from Nanoparticle to Bulk Systems*
9:40 – 10:00 am	**Cedomir Petrovic**, Brookhaven National Laboratory *Exploratory (Bulk) Materials Synthesis and Characterization*
10:00 – 10:20 am	**Thomas Lograsso**, Ames Laboratory *Synthesis, Measurement, and Characterization of Magnetoelastic F-based Binary Alloys: Gap between Experimental Basis and Theoretical Predictions*
10:20 – 10:50 am	***** Break *****
Session 1a (continued)	**Function-Driven Materials Design:** Exploratory Synthesis Through Advanced Processing Chair: **I-Wei Chen**, University of Pennsylvania
10:50 – 11:10 am	**Pavel Zinin**, University of Hawaii *Synthesis of New Diamond-Like B-C Phases under High Pressure and Temperatures*
11:10 – 11:30 am	**Himanshu Jain**, Lehigh University *Laser Fabrication of Active Single-Crystal Architecture in Glass*

11:30 – 11:50 am	**Rishi Raj (Invited)**, University of Colorado at Boulder *Gargantuan Effects of Electrical Fields in the Processing of Ceramics at High Temperatures*
11:50 am – 12:15 pm	***Poster Introductions***
12:15 – 2:00 pm	***** Working Lunch/ Small Group Discussions *****
2:00 – 3:30 pm	***** Poster Session I *****
Session 2	**Soft Materials and Soft-Hard Interfaces** Chair: **James Runt**, The Pennsylvania State University
3:30 – 3:50 pm	**David Wang**, Colorado State University *Directed Assembly of Diblock Copolymer under Nano-Confinement*
3:50 – 4:10 pm	**Satish Kumar**, University of Minnesota *AC Electrohydrodynamic Instabilities in Thin Liquid Films: A Route to Hydrodynamic Self-Assembly of Topographical Patterns on Soft Materials*
4:10 – 4:30 pm	**Peter Green**, University of Michigan *Brush-Coated Nanoparticle Polymer Thin Films*
4:30 – 4:50 pm	**Michael Mackay**, University of Delaware *Nanoparticles Stabilize Thin Polymer Films: A Fundamental Study to Understand the Phenomenon*
4:50 – 5:20 pm	***** Break *****
5:20 – 5:40 pm	**Karl Mueller**, The Pennsylvania State University *Conduction Mechanisms and Structure of Ionomeric Single-Ion Conductors: Part 1: PEO-Based Polymer Systems*
5:40 – 6:00 pm	**Qiming Zhang**, The Pennsylvania State University *Giant Electrocaloric Effect at Room Temperature in Ferroelectric Polymers with Controlled Polar Nanostructures*
6:00 – 7:30 pm	***** Working Dinner and Meeting Discussions *****
7:30 – 8:30 pm	***** Poster Session I (Continues)*****

Tuesday, September 20, 2011

7:30 – 8:30 am	***** Breakfast*****
Session 3	**Predictive Crystal Growth** Chair: **Hanchen Huang**, University of Connecticut
8:30 – 8:50 am	**Pulickel M. Ajayan and Boris I. Yakobson**, Rice University *Boron Based Nanostructures: Stability and Synthetic Routes*
8:50 – 9:10 am	**David Geohegan**, Oak Ridge National Laboratory *Non-Equilibrium Synthesis of Nanostructured Materials: Real-Time Studies of the Growth Kinetics and Product Distribution of Graphene*
9:10 – 9:30 am	**Kristen Fichthorn**, The Pennsylvania State University *Multi-Scale Theory of the Growth and Assembly of Colloidal Nanoscale Materials*

9:30 – 9:50 am	**Peter Voorhees and Katsuyo Thornton***, Northwestern University and *University of Michigan *Four-Dimensional Analysis of the Evolution of Complex Dendritic Microstructures during Coarsening*
9:50 – 10:10 am	**Mathew Kramer**, Ames Laboratory *Predicting Phase Selection in Systems Driven Far from Equilibrium*
10:10 – 10:40 am	*****Break*****
Session 3 (Continued)	**Predictive Crystal Growth** Chair: **Gyula Eres,** Oak Ridge National Laboratory
10:40 – 11:00 am	**Stephen Garofalini**, Rutgers University *Atomistic Structure, Strength, and Kinetic Properties of Intergranular Films in Ceramics*
11:00 – 11:20 am	**Guangwen Zhou**, State University of New York–Binghamton *In Situ Visualization and Theoretical Modeling of Early-Stage Oxidation of Metal and Alloys*
11:20 – 11:40 am	**Francisco Zaera**, University of California–Riverside *Atomic Layer Deposition (ALD) of Metal and Metal Oxide Films: A Surface Science Study*
11:40 – 12:00 pm	**Stacey Bent**, Stanford University *Studies of Surface Reaction Mechanisms in Atomic Layer Deposition*
12:00 – 12:25 pm	***Poster Introductions***
12:25 – 2:00 pm	***** Working Lunch/ Small Group Discussions *****
2:00 – 3:30 pm	***** Poster Session II *****
Session 4	**Large Scale Assembly** Chair: **Michael Aziz**, Harvard University
3:30 – 3:50 pm	**George T. Wang (Invited)**, Sandia National Laboratories *III-Nitride Nanowires: From the Bottom-Up to the Top-Down*
3:50 – 4:10 pm	**Jason Fowlkes**, Oak Ridge National Laboratory *Design and Synthesis for Nanomaterials*
4:10 – 4:30 pm	**Salvatore Torquato**, Princeton University *Inverse Optimization Techniques for Targeted Self-Assembly*
4:30 – 4:50 pm	**Fernando A. Escobedo**, Cornell University *Mesoscopic Simulations of the Self-Assembly of Non-Spherical Colloids*
4:50 – 5:10 pm	**Itai Cohen**, Cornell University *Shear Induced Assembly of Anisotropic Colloidal Particles*
5:10 – 5:30 pm	**Eric Furst**, University of Delaware *Directed Self-Assembly of Nanodispersions*
5:30 – 5:50 pm	**Jun Liu**, Pacific Northwest National Laboratory *Molecularly Organized Nanostructural Materials*
5:50 – 7:30 pm	***** Working Dinner and Meeting Discussions *****
7:30 – 8:30 pm	***** Poster Session II (Continues) *****

Wednesday, September 21, 2011

7:30 – 8:30 am	***** Breakfast *****
Session 1b	**Function-Driven Materials Design:** Exploratory Caged Materials Chair: **Raymond Schaak**, The Pennsylvania State University
8:30 – 8:50 am	**Yves Chabal**, University of Texas at Dallas *Novel Theoretical and Experimental Approaches for Understanding and Optimizing Molecule-Sorbent Interactions in Metal Organic Framework Materials*
8:50 – 9:10 am	**Carolyn Koh**, Colorado School of Mines *Metastability of Clathrate Hydrates for Energy Storage*
9:10 – 9:30 am	**Angela Lueking**, The Pennsylvania State University *Hydrogen Caged in Carbon—Exploration of Novel Carbon-Hydrogen Interactions*
9:30 – 9:50 am	**George Nolas**, University of South Florida *A Fundamental Study of Inorganic Clathrates and Other Open-Framework Materials*
9:50 – 10:10 am	**Peter Pfeifer**, University of Missouri *Enhanced Hydrogen Storage in Boron-Doped Carbon Nanospaces*
10:10 – 10:30 am	***** Break *****
Session 1c	**Function-Driven Materials Design:** Use-Inspired Science Chair: **Michael Coltrin**, Sandia National Laboratory
10:30 – 10:50 am	**Chengdu Liang**, Oak Ridge National Laboratory *Solid Electrolyte and Solid Electrolyte Interface (SEI) on Nanostructured Cathode Materials*
10:50 – 11:10 am	**Prashant Kumta**, University of Pittsburgh *Fundamental Experimental and Theoretical Studies on a Novel Family of Oxide Catalyst Supports for Water Electrolysis*
11:10 – 11:30 am	**Meng Tao** and **Qiming Zhang**, University of Texas at Arlington *Doping Cuprous Oxide (Cu_2O) in Electrolyte Solution: Dopant Incorporation, Atomic Structures and Electrical Properties*
11:30 – 12:00 pm	*Remarks* **Kristen Fichthorn** and **Jun Liu**, Meeting Chairs **Bonnie Gersten**, Program Manager, Synthesis and Processing Science
12:00 pm	*****Lunch, Open Discussions and Adjourn***** (Optional box lunches available)

Session 1a

Function-Driven Materials Design: Exploratory Synthesis through Advanced Processing

Session Chairs: Ivan Bozovic, Brookhaven National Laboratory
I-Wei Chen, University of Pennsylvania

This page is intentionally blank.

SPEAKER
Duane D. Johnson, US/DOE Ames Laboratory, Iowa State University

TITLE
Defect-mediated materials properties from nanoparticle to bulk systems

ABSTRACT:
Examples of collaborative theoretical and experimental materials discovery and characterization involving critical defect-mediated materials properties in a variety of systems, from nanoparticle catalysis to surface chemistry to bulk mechanical behavior, and the origin of the behavior will be discussed. Particular emphasis will be placed on the critical cooperation between experiment and theory.

Exploratory (Bulk) Materials Synthesis and Characterization

Cedomir Petrovic

Condensed Matter Physics and Materials Science Department
Brookhaven National Laboratory, Upton NY 11973 USA
petrovic@bnl.gov

Program Scope

This program concentrates on design, discovery and characterization of new and advanced materials in condensed matter physics, with the aim to provide materials base for addressing electronic complexity in the energy related materials. Our research currently focuses on making model systems for studying of fundamentals of quantum criticality, unconventional low temperature superconductivity related to high T_c cuprate/iron based compounds and materials related to correlated electron thermoelectrics. Most often materials are made in the single crystal form since many observables of interest are tensor quantities and since this allows for the investigation of properties that are free of grain boundaries influence. New materials are prepared by the variety of crystal growth and materials synthesis methods: conventional arc melting and powder metallurgical techniques, solution methods, high temperature intermetallic, oxide, sulfide or salt fluxes, chemical vapor transport and deposition. Automated physical and structural characterization is the essential component of the lab. In order to optimize synthesis parameters, it is necessary to characterize structural and physical properties of materials. Quite often the same methods are used to probe and perturb crystal structure, transport, thermodynamic and magnetic properties, sometimes at extreme conditions of low temperatures and high magnetic fields. We gain access to NHMFL as well as to NSLS through a user proposal system. We are actively engaged in the constant buildup of our synthesis and characterization capabilities by custom designing and/or building of both materials synthesis and physical characterization tools. Extensive collaborations exist at BNL and externally. This program includes training of next generation of scientists. Students from neighboring universities (Stony Brook, Brown, Columbia, Johns Hopkins) are being or have been educated in arts and crafts of crystal growth, materials synthesis and characterization.

Recent progress

The concept of competing orders governs the behavior of many complex materials and in particular of heavy fermion and cuprate oxide superconductors [1]. Heavy fermios and cuprates have been investigated extensively due to putative unconventional pairing mechanism and proximity to an antiferromagnetic quantum critical point (QCP) [2,3]. Yet, some similarities such as heavy fermion electronic/magnetic low dimensionality and inhomogeneity have been advanced only in the recent years with the discovery of the "115" series of heavy fermion superconductors and their availability in the form suitable for application of certain experimental probes, such as neutron scattering. This program has developed large high quality single crystals of 115 heavy fermion superconductors with one of the lowest residual resistivities for any ternary compound, enabling many important experiments. $CeCoIn_5$ enters the Pauli-limited region close to H_{c2}. Many experiments point to a transition inside the superconducting mixed state for both field orientations. This transition, existing in a high-field, low-temperature region bordering H_{c2} has been considered as a candidate for a Fulde-Ferrell-Larkin-

Ovchinnikov (FFLO) state. High quality large single crystals made at EMSC enabled the observation of antiferromagnetic order (Q phase) for field perpendicular to the c axis on the high-field side of the transition [DOE pub. 2]. The magnetic wavevector is (q q 0.5), where q = 0.44 reciprocal lattice units. As the field is rotated towards the c axis, this order remains, however the magnetic moment disappears above 17º, indicating that the Q phase cannot be responsible for the anomalies seen with the field parallel to the c axis. The connection of the Q phase with possible FFLO-type order and its anisotropy is an open and interesting question.

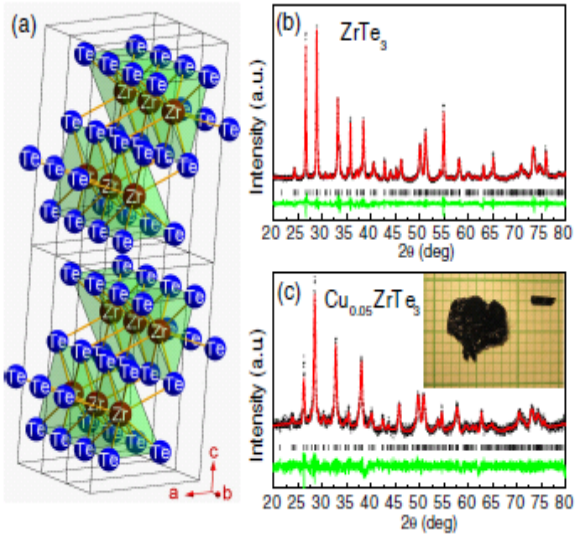

Figure 1: (a) The crystal structure of $ZrTe_3$. Crystallographic b axis runs along the shortest Zr-Zr distances and the c axis is along the vertical. (b,c) Comparison of the observed (crosses) and calculated (solid line) powder x-ray patterns of $ZrTe_3$ and $Cu_{0.05}ZrTe_3$. The bars (black) correspond to the Bragg reflections and the lowest solid line is the difference between the observed and the calculated patterns [DOE pub. 6].

Suppression of charge density wave (CDW) order brings about superconductivity in Cu_xTiSe_2 [4]. This is reminiscent of superconductivity in heavy fermion and the cuprate oxide phase diagram where the magnetic order is tuned by pressure (P) or doping to T→ 0. The superconducting mechanism in such electronic systems is likely to be mediated by the magnetic fluctuations [1]. Similarly, the domelike structure of T_c(P) and the pairing mechanism in Cu_xTiSe_2 is argued to stem from the type of quantum criticality related to fluctuations in CDW order [5,6], further supported by a domelike structure of T_c(P) [7] Chalcogenide superconductors represent a weak coupling side of the smectic order, akin to stripe order in cuprates. There is mounting evidence that in such systems CDW states transform into Fermi liquid through an intermediate phase. Therefore it is of interest to study the melting of CDW order parameter and possible nematic phases in a superconductor with a highly related and tunable two-dimensional electronic system. We have discovered bulk superconductivity and charge density wave (CDW) with superconducting T_c=3.8 K for Cu intercalated and 3.1 K for Ni intercalated (Fig. 1) quasi-two-dimensional crystals of $ZrTe_3$ [DOE pubs. 6-7]. The Cu,Ni intercalation results in the expansion of the unit cell orthogonal to the Zr-Zr metal chains and partial filling (Cu) or suppression of CDW energy gap (Ni). The dominant scattering mechanism in the normal state along the b axis is the electron–electron umklapp scattering.

The most favorable type of electronic structure for thermoelectric materials is the one that has a resonance in the density of states centered about 2-3 k_BT away from the Fermi energy. Kondo Insulators (KI) represent a close approximation of such an ideal case. In a KI, localized *f* or *d* states hybridize with conduction electron states leading to the formation of a small hybridization gap. The density of states just below and just above the hybridization gap becomes very large. The thermopower is very sensitive to variations in density of states in the vicinity of the Fermi level, hence very large absolute values of |S| > 100 μV/K can be expected and are reported in Kondo insulators. Thermoelectric properties of KI-like semiconductor $FeSb_2$ single crystals are very sensitive to the crystal growth parameters. We have shown that Metal Insulator transition (MIT) for electronic transport along the c - axis can be tuned by the synthesis procedure (Fig. 2). Crystals with MIT have greatly enhanced electrical conductivity while keeping the thermopower at a relatively high level. By this means, the thermoelectric power factor $S^2\sigma$ is

enhanced to a record high ~ 7800 $\mu WK^{-2}cm^{-1}$ at 28 K. We show that electrical conductivity differences are not caused by extrinsic impurities but are induced by subtle structural differences [8] (Fig. 3).

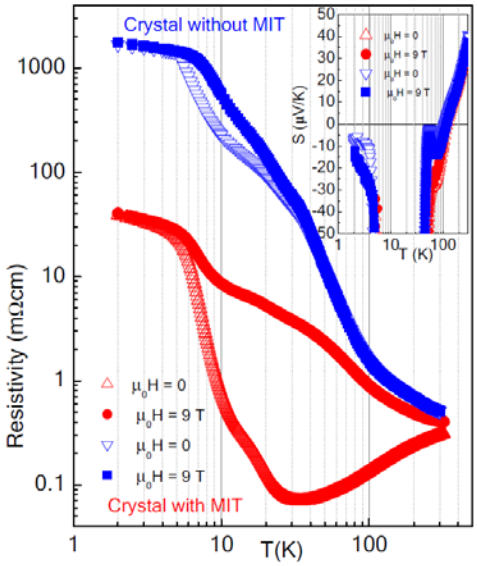

Figure 2: Resistivity along the high conductivity c-axis for crystals 1 and 2 as a function of temperature in zero magnetic field and in a field of 9 Tesla. Inset shows c-axis Seebeck coefficient of both single crystals in magnetic field of 0 T and 9 T below 8 K and above 40 K. Properties of crystals with MIT (without MIT) are shown by red (blue) color. The large S (several mV/K) is of purely electronic origin [8].

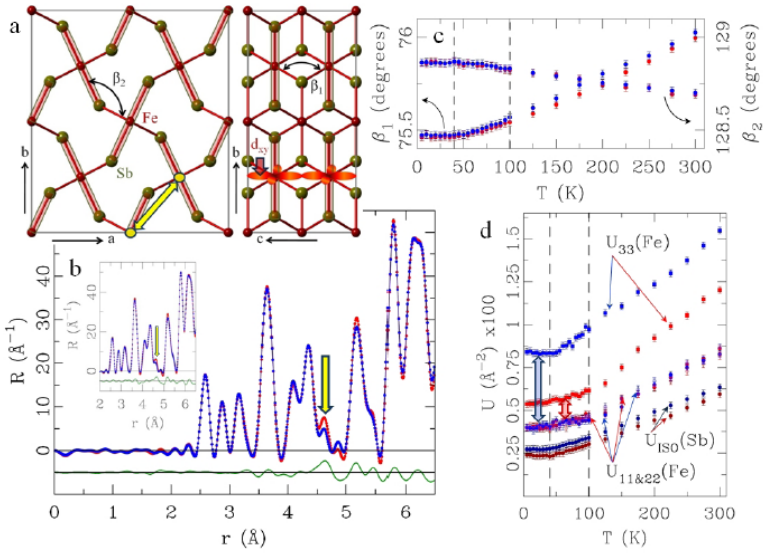

Figure 3: (a) 2x2x2 Pnnm unit cell of $FeSb_2$. Shaded rectangles denote short Fe-Sb distances within the $FeSb_6$ octahedra. Intrachain and interchain Fe-Sb-Fe angles are denoted as β_1 and β_2. Double arrow shows next near neighbour interchain Fe-Fe distance. (b) 10 K experimental RDF, R(r) for crystal 1 (red) and crystal 2 (blue). Feature in R(r) corresponding to the interchain Fe-Fe distance is marked by arrow. Inset shows the same at 100 K. (c) Temperature dependence of β_1 and β_2 (d) ADP factors for Fe (anisotropic) and Sb (isotropic). Dashed lines in (c) and (d) at 40 K and 100 K indicate temperatures of insulator-metal transition and change of the nature of the charge carriers, respectively [8].

Future Plan

We plan to pursue several interpenetrating exploratory synthesis and characterization paths building on our initial work and moving into following directions including:

1. Address the role of charge fluctuations in quantum criticality on the example of intercalated CDW (determine the phase diagram, putative dome with x or P, Fermi surface evolution and gap symmetry) and fluctuating valence heavy fermion superconductors such as $YbAlB_4$ (focus on substitution studies and synthesis of high quality crystals suitable for application of spectroscopic and high resolution structural probes). Explore other materials in this area.
2. Disorder in heavy fermion systems near QCP [9] where Griffiths phases (GP) are believed to play a key role. Since we can tune the disorder by the crystal growth procedure in several materials at the QCP, our goal would be to try to identify disorder related ground states such as cluster glass, magnetic or electronic GP which should exist between ordered phase and a paramagnetic heavy Fermi liquid. Interesting case is Pr^{3+} (J=4) since its ground state in crystalline electric fields carries quadrupole moments with orbital degeneracy. Therefore orbital (quadrupole) degrees of freedom could play a role in phases where Pr^{3+} is Kondo compensated.
3. Geometrically frustrated lattices with insulating magnetic ions contain strong fluctuations that prevent classical long range ordered states. They are excellent model systems for the study of exotic ordered states such as spin liquid. Concepts of rare earth intermetallic or Kondo frustrated systems are only emerging in the recent years. An exciting possibility would be to address the MIT on a Kondo frustrated lattice since this would be a QCP at T→ 0 with gapless charge

excitations (frustrated KI) [10]. The materials to explore include hybridizing rare earth compounds in structures with triangular networks.

4. We will explore some materials that show promise for good thermoelectrics. This includes the recently proposed topological mechanism of increasing ZT in the bulk nanostructured $Bi_{1-x}Sb_x$ alloys with the finite density of screw dislocations [11]. When both interface energy and supersaturation are low, the nucleation is heterogeneous and the growth is slow. In such conditions crystal growth mechanism is based on the screw dislocations. With the increase in temperature and decrease of concentration of soluble material the supersaturation decreases. Our synthesis tools offer large parameter space where the crystal growth conditions can be tuned.

References:

1. Report on of the Basic Energy Sciences, U.S. Department of Energy, Superconductivity, Washington, DC, 2006.
2. Qimiao Si and Frank Steglich, Science 329, 1161 (2010).
3. S. E. Sebastian et al., Proc. Nat. Ac.Sc. 107, 6175 (2010).
4. E. Morosan et al., Nature Phys. 2, 544 (2006).
5. H. Barath et al., Phys. Rev. Lett. 100, 106402 (2008).
6. K. Sun et al., Phys. Rev. B 78, 085124 (2008).
7. A. F. Kusmartseva et al., Phys. Rev. Lett. 103, 236401 (2009).
8. Q. Jie et al., submitted (2011).
9. Thomas Vojta, J. Low. Temp. Phys. 161, 299 (2010).
10. Piers Coleman and Andrey Nevidomskyy, J. Low Temp. Phys. 161, 182 (2010).
11. O. A. Tretiakov et al., Appl. Phys. Lett. 97, 073108 (2010).

DOE sponsored publications FY 09-11 resulting from work supported by this program*

1. *Evidence for electron-phonon interaction in $Fe_{1-x}M_xSb_2$ (M = Co, Cr) single crystals*
   N. Lazarevic, Z. V. Popovic, Rongwei Hu and C. Petrovic, Phys. Rev. B 81, 144302 (2010).
2. *Exploring the fragile antiferromagnetic superconducting phase in $CeCoIn_5$*
   E. Blackburn, P. Das, M. R. Eskildsen, E. M. Forgan, M. Laver, C. Niedermayer, C. Petrovic, and J. S. White, Phys. Rev. Lett 105, 187001 (2010).
3. *Universal heat conduction in the heavy-fermion superconductor $CeIrIn_5$: a line of nodes in the gap structure,* H. Shakirepour, M. A. Tanatar, C. Petrovic and Louis Taillefer, Phys. Rev. B 82, 184531 (2010).
4. *Evidence of phonon-charge-density waves coupling in $ErTe_3$*
   N. Lazarevic, Z. V. Popovic, Rongwei Hu and C. Petrovic, Phys. Rev. B 83, 024302 (2011).
5. *Absence of localized-spin magnetic scattering in the narrow-gap semiconductor $FeSb_2$*
   I. A. Zaliznyak, A. T. Savici, V. O. Garlea, Rongwei Hu and C. Petrovic
   Phys. Rev.B 83, 184414 (2011).
6. *Coexistence of charge density wave and bulk superconductivity in Cu_xZrTe_3*
   Xiangde Zhu, Hechang Lei and C. Petrovic, Phys. Rev. Lett. 106, 246404 (2011).
7. *Raising T_c in charge density wave superconductor $ZrTe_3$ by Ni intercalation*
   Hechang Lei, Xiangde Zhu and C. Petrovic, Europhys. Lett. 95, 17011 (2011).

* Selected out of 23 total publications and 12 supported by this program in FY 09-11 (by July 2011)

Novel Materials Preparation and Processing Methodologies

Synthesis, Measurement, and Characterization of Magnetoelastic Fe-based Binary Alloys:- Gap between Experimental Basis and Theoretical Predictions

Qingfeng Xing and Thomas A. Lograsso
Ames Laboratory, Ames IA 50014

Program Scope

The growth, control and modification of novel materials in single crystal and polycrystalline form, represent a national core competency that is essential for scientific advancement within and across traditional disciplinary boundaries, and are critical components of the Basic Energy Sciences' mission. In support of this mission, the Novel Materials Preparation and Processing Methodologies strengthen the materials synthesis efforts of the Ames Laboratory. The objective of Novel Materials is to quantify and control processing-structure-property relationships: the basic science of how chemical inhomogeneities and structural defects affect properties of highly responsive materials; advance the ability to synthesize and characterize high purity, high quality materials, primarily in single crystal form; develop unique capabilities and processing knowledge in the preparation, purification, and fabrication of metallic elements and alloys. Single crystals are often required to achieve scientific understanding of the origin of various phenomena, whether from intrinsic or extrinsic origins, to elucidate its properties as well as to evaluate a material's full functionality. Our research objectives are: 1) developing synthesis and processing capabilities that support rapid materials discovery using bulk combinatorial approaches, 2) identifying synthesis protocols for specific novel materials through the rapid development and modification of methods to prepare high quality well-characterized single crystals, and 3) utilizing solidification processing to access metastable states in controlled nanoscale architectures.

Recent Progress

One paragon of the scope is our work on magnetoelastic Fe-X (X = Ga, Ge, Si, Al, Mo) alloys. Fe-enriched Fe-Ga alloys offer an extraordinary combination of magnetoelasticity and mechanical properties and are rare-earth-free and environmentally green. Since the first publication of magnetostriction data on the Fe-Ga single crystals [1], we have focused in quantifying and controlling processing-structure-property relationships in the alloys. We experimentally clarified the phase dependence of the magnetostrictive behavior over a wide compositional range in the Fe-Ga alloy system. There are four magnetostriction-composition regimes (Fig. 1) [2, 3]. In regime I of disordered single phase A2 and regime III of well ordered single phase $D0_3$, the tetragonal magnetostriction constant, (3/2) λ_{100} increases with Ga content. In regime II, where an A2 + $D0_3$ phase mixture exists, and in regime IV, where $D0_3$ + secondary phases are present, (3/2) λ_{100} decreases with Ga content. The secondary phases small in size and $D0_3$ phase do not influence the distribution of the magnetic domains in the alloys, unless the secondary phases at higher Ga content are pronounced and large in size [4]. The relation between magnetic domains and the underlying microstructure is consistent with a more recent magnetic force microscopy study [5], which reveals that many reported maze magnetic domains in Fe-Ga alloys result from surface damage during metallographic preparation. In regime III, water-quenched alloys may contain a phase mixture of A2, B2, and $D0_3$, but this phase mixture shows higher (3/2) λ_{100} than the pure $D0_3$ obtained through slow cooling.

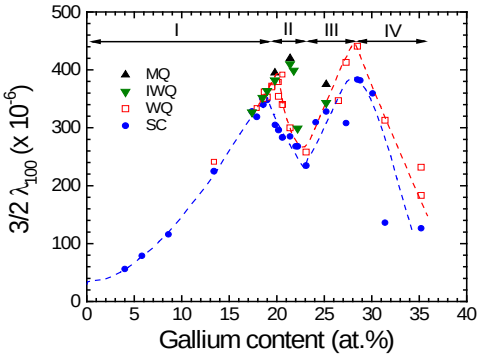

Fig. 1 Dependence of (3/2) λ_{100} on Ga content for Fe-Ga alloys [3]. SC: slow-cooling, WQ: RT water quench, IWQ: ice-water quench, MQ: metallic quench. The regimes I-IV are classified, based on phases, but the regime boundaries depend on sample thermal histories.

Many efforts have been made to model the magnetostrictive behaviors of the Fe-Ga alloys to answer the origin of the magnetostriction enhancement caused by Ga addition to body-centered cubic (bcc) α-Fe and to predict elements leading to further enhancements. The magnetoelastic behavior within a single phase region, such as the α-Fe solid solution, has not been adequately explained by any proposed model. For (3/2) λ_{100}, Clark *et al*. suggested that Ga-Ga pairs oriented along [100] directions within the bcc lattice to be the origin [6]. However, this hypothesis is in contrast to a recent EXAFS (extended x-ray absorption fine structure) study [7] in which the magnetostrictive atomic strain was found to be from Fe-Ga pairs, despite the presence of Ga-Ga pairs in the second coordination shell around Ga. Wu *et al.* [8] proposed an intrinsic model based on electronic spin-orbit coupling interactions. The model initially predicted wrong sign of $D0_3$ Fe-Ga [8] and was improved to yield computed (3/2) λ_{100} fitting perfectly with experimental values [9]. However, this model is limited only to certain discrete structural models which do not accurately account for a non-random solid solution, as evident from structural studies of the A2 phase [2]. In addition, there is an argument that the computed results based on this model do not occur in realistic disordered alloys [10]. On the other hand, an extrinsic model proposed by Khachaturyan and Viehland states the rearrangement under a magnetic field of structural domain variants within discrete heterogeneities is largely the source of the enhanced magnetostriction [11]. The domain variants are formed during a series of displacive phase transformations from $D0_3$ nanosized phases via Bain strain. However, this hypothesis lacks convincing support from the majority of Fe-Ga experimental results reported in literature event though it seems to be supported by some reports [12-15]. Furthermore, the change in (3/2) λ_{111} with Ga composition is rarely addressed in these existing models.

The essence of the extrinsic model is that the presence of short-range order (SRO), sometimes referred to as nano clusters or nano heterogeneity in literature, leads to the enhanced magnetostriction through a series of phase transformations. However, a synchrotron radiation study [16] and our laboratory x-ray diffraction work [3] reveal that SRO does not significantly affect the magnetostriction. We successfully used the rule of phase mixtures to estimate the effect of SRO [3]. SRO is solely a structural phenomenon, a precursor or first step in the pathway to long-range chemical ordering. The concurrent increase in magnetoelastic coupling with an increased tendency towards Ga chemical ordering with Ga addition does not imply a causal relationship. The observed nano precipitates [12-13] and maze magnetic domains on micron scale [14], supporting the extrinsic model, are proved to be from improper experimentation and data processing by other's [5] and our work.

We have employed differential EXAFS to extract atomic magnetostrictive strain in the Fe-X alloys to understand the origin of enhanced magnetostriction. As a first step, single crystal Fe was used as a gauge to evaluate the sensitivity and reliability of this method as well as to validate the current models. The (3/2) λ_{100} was determined to be 45 ppm by fitting the experimental differential Fe-K-edge spectra (Fig. 2) [17], consistent with the previously reported theoretical value calculated from a spin-orbit coupling theory as well as with the strain macroscopically measured with a strain gage on a single crystalline sample. This indicates spin-orbit coupling accounts for the origin of magnetostriction. Fe-Ga and Fe-Ge samples have been measured and the data analysis is underway.

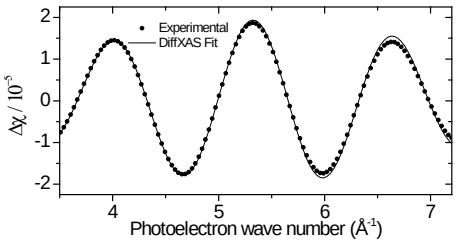

Fig. 2 Experimental differential EXAFS (DiffXAS) Fe-K-edge spectra (solid) and its theoretical fit (dotted).

We have also expanded the investigations to Fe-Ge [18] and Fe-Si [19], which have ordering processes similar to Fe-Ga system and Fe-Mo system which does not show ordering [20]. A magnetostriction constant is determined by magnetoelastic coupling factor and shear modulus for a material. The structural dependence of coupling factor offers insight of the magnetism. The tetragonal coupling factor $-b_1$ for a cubic crystal can be expressed as $-b_1 = 3/2\ \lambda_{100}\ (c_{11}-c_{12})$, where c_{11} and c_{12} are primary elastic constants. The coupling factors for various alloy systems are plotted in Fig. 3. In bcc phase (A2), all the alloys show

increasing coupling factor with X at.%. In $D0_3$ phase, the Fe-Ga and Fe-Al alloys show positive coupling factors but Fe-Ge and Fe-Si show negative coupling factors. Interestingly, Fe-Mo alloys display the largest coupling factor under a given X at.% for A2 phase. The comparison indicates the intrinsic origin of the enhanced magnetostriction.

In summary, we have gained from experimental work, a most fundamental basis of how the magnetoelasticity of Fe-X alloys is dependent on material structure (phase). All the experimental results are pointing to the intrinsic origin of magnetoelasticity in the Fe-X alloys. Currently there is a large gap between experimental results and theoretical predictions, as the realistic experimental facts are not completely taken into theoretical computations nor are the experimental results adequately explained.

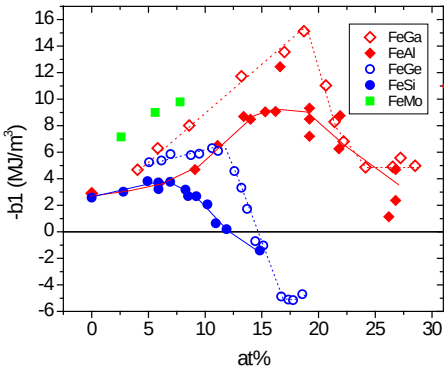

Fig. 3 A comparison of coupling factors, $-b_1$, among Fe-Ga, Fe-Al, Fe-Ge, Fe-Si, and Fe-Mo alloys.

Future Work

Zn is theoretically predicted as a good substitute for Ga for further enhancement of magnetostriction of Fe-12.5 at.% Ga due to change in the number of valence electrons [9] (see Fig. 4 for the calculated density of states), but this prediction lacks experimental verification. Magnetostriction of polycrystalline Fe-Zn alloys was reported [21], but has a larger uncertainty because of texture and porosity. Furthermore, it is in debate what equation can be used to derive two basic magnetostriction constants, (3/2) λ_{100} and (3/2) λ_{111} from magnetostriction measured from polycrystalline cubic materials [22]. Only materials in single crystal form can unambiguously deconvolute complex properties of materials and reveal fundamental properties. We will grow bcc Fe-Zn and Fe-Ga-Zn single crystals using the in-house 15 bar high pressure Bridgman furnace to overcome the high vapor pressure problem of Zn and measure the magnetoelasticity of the alloys. The results will complete the knowledge pool of Fe-X alloys and serve as a basis for future theoretical modeling work, no matter whether they are in agreement with or against the current prediction. The experimental work on Fe-X alloys is expected to ultimately propel theoretical modeling along a correct pathway to accurate predictions.

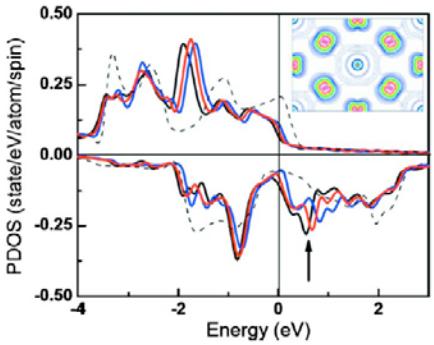

Fig. 4 The projected density of states for $d_{xz,yz}$ orbits of the Fe atoms nearest to Ga (or Zn) in Fe-12.5 at.% Ga (black lines), Fe-6.25 at.% Ga-6.25 at.% Zn (red/light gray lines), and Fe-12.5 at.% Zn (blue/dark gray lines). See Ref. [9] for details.

References

1. A. E. Clark, J. B. Restorff, M. Wun-Fogle, T. A. Lograsso, and D. L. Schlagel, IEEE Trans. Magn. **36**, 3238 (2000).
2. Q. Xing, Y. Du, R. J. McQueeney, and T. A. Lograsso, Acta Mater. **56**, 4536 (2008).
3. Q. Xing and T. A. Lograsso, Scripta Mater. **65**, 359 (2011).
4. Q. Xing and T. A. Lograsso, Appl. Phys. Lett. **93**, 182501 (2008).
5. C. Mudivarthi, S.-M. Na, R. Schaefer, M. Laver, M. Wuttig, and A. B. Flatau, J. Magn. Magn. Mater. **322**, 2023 (2010).
6. A. E. Clark, M. Wun-Fogle, J. B. Restorff, T. A. Lograsso, and J. R. Cullen, IEEE Trans. Magn. **37**, 2678 (2001).
7. M. P. Ruffoni, S. Pascarelli, R. Grössinger, R. Sato Turtelli, C. Bornio-Nunes, and R. F. Pettifer, Phys. Rev. Lett. **101**, 147202 (2008).

8. R. Wu R, Z. Yang, and J. Hong, J. Phys.: Condens. Matter. **15** S587 (2003).
9. Y. N. Zhang, J. X. Cao, and R. Q. Wu, Appl. Phys. Lett. **96**, 062508 (2010).
10. T. Khmelevska, S. Khmeleskyi, and P. Mohn, J. Appl. Phys. **103**, 073911 (2008).
11. A. G. Khachaturyan and D. Viehland, Metall. Mater. Trans. A **38A**, 2308 (2007); *ibid* 2317 (2007).
12. S. Bhattacharyya, J. R. Jinschek, A. Kachaturyan, H. Cao, J. F. Li, and D. Viehland, Phys. Rev. B **77**, 104107 (2008).
13. S. Bhattacharyya, J. R. Jinschek, J. F. Li, and D. Viehland, J. Alloy Cmpd. **501**, 1481 (2010).
14. F. Bai, H. Zhang, J. Li, and D. Viehland, Appl. Phys. Lett. **95**, 152511 (2009).
15. H. Cao, P. M. Gehring, C. P. Devreugd, J. A. Rodriguez-Rivera, J. Li, and D. Viehland, Phys. Rev. Lett. **102**, 127201 (2009), *ibid* Erratum: **102**, 119904 (2010).
16. Y. Du, M. Huang, S. Chang, D. L. Schlagel, T. A. Lograsso, and R. J. McQueeney, Phys. Rev. B **81**, 054432 (2010).
17. Q. Xing, T. A. Lograsso, M. P. Ruffoni, C. Azimonte, S. Pascarelli, and D. J. Miller, Appl. Phys. Lett. **97**, 072508 (2010).
18. G. Petculescu, J. B. LeBlanc, M. Wun-Fogle, J. B. Restorff, W. M. Yuhasz, T. A. Lograsso, and A. E. Clark, J. Appl. Phys. **105**, 07A932 (2009).
19. Q. Xing, D. Wu, and T. A. Lograsso, J. Appl. Phys. **107**, 09A911 (2010).
20. M. Huang, A. O. Mandru, G. Petculescu, A. E. Clark, M. Wun-Fogle, and T. A. Lograsso, J. Appl. Phys. **107**, 09A920 (2010).
21. R. P. Corson, S. Guruswamy, M. K. McCarter, and C. L. Lin, Int. J. Powder Metall. **45**, 45 (2009).
22. B. D. Cullity and C. D. Graham, Introduction to Magnetic Materials, 2nd Edition, IEEE Press, 2009, p. 254.

DOE Sponsored Publications on this topic during 2009-2011

Q. Xing and T. A. Lograsso, "Effect of cooling rate on magnetoelasticity and short-range order in Fe-Ga alloys", *Scripta Materialia*, **65**, 359-362 (2011).

G. Petculescu, K. L. Ledet, M. Huang, T. A. Lograsso, Y. N. Zhang, R. Q. Wu, M. Wun-Fogle, J. B. Restorff, A. E. Clark, and K. B. Hathaway, "Magnetostriction, elasticity, and $D0_3$ phase stability in Fe-Ga and Fe-Ga-Ge alloys", *Journal of Applied Phys*ics, **109** 07A904 (2011).

Q. Xing, T. A. Lograsso, M. P. Ruffoni, C. Azimonte, S. Pascarelli, and D. J. Miller, "Experimental exploration of the origin of magnetostriction in single crystalline iron", *Applied Physics Letters*, **97**, 072508 (2010).

Q. Xing, M. J. Kramer, D. Wu, and T. A. Lograsso, "Influence of surface oxidation on transmission electron microscopy characterization of Fe-Ga alloy", *Materials Characterization*, **61**, 598-602 (2010).

Q. Xing, D. Wu, and T. A. Lograsso, "Magnetoelasticity of Fe-Si Single Crystal", *Journal of Applied Phys*ics, **107**, 09A911 (2010).

M. Huang, A. O. Mandru, G. Petculescu, A. E. Clark, M. Wun-Fogle, and T. A. Lograsso, "Magnetostrictive and elastic properties of $Fe_{100-x}Mo_x$ ($2<x<12$) single crystals", *Journal of Applied Phys*ics, **107**, 09A920 (2010).

G. Petculescu, A. O. Mandru, W. M. Yuhasz, T. A. Lograsso, M. Wun-Fogle, J. B. Restorff, A. E. Clark, and K. B. Hathaway, "The effect of partial substitution of Ge for Ga on the elastic and magnetoelastic properties of Fe-Ga alloys", *Journal of Applied Phys*ics, **107**, 09A926 (2010).

Y. Du, Q. Xing, M. Wun-Fogle, J. B. Restorff, A. E. Clark, M. Huang, R. J. McQueeney, and T. A. Lograsso, "Determination of structural anisotropy of stress-annealed $Fe_{80.5}Ga_{19.5}$", *IEEE Transactions on Magnetics*, **45,** 0018-9464 (2009).

Q. Xing and T. A. Lograsso, "Phase identification of quenched Fe-25 at.% Ga", *Scripta Material*, **60**, 373-376 (2009).

G. Petculescu, J. B. LeBlanc, M. Wun-Fogle, J. B. Restorff, W. M. Yuhasz, T. A. Lograsso, and A. E. Clark, "Magnetoelastic coupling in $Fe_{100-x}Ge_x$ single crystals with $4<x<18$", *Journal of Applied Phys*ics, **105**, 07A932 (2009).

Synthesis of new Diamond-like B-C Phases Under High Pressure and Temperatures

Pavel Zinin, Li Chung Ming and Shiv Sharma
zinin@soest.hawaii.edu
Hawaii Institute of Geophysics and Planetology,
University of Hawaii, Honolulu, HI 96822

Program Scope

Novel B-C phases are predicted to be superhard, with hardness close to that of a cubic boron nitride (cBN), and may be conductors [1] or superconductors [2]. Superconductivity was found in boron-doped diamonds synthesized at high pressure (~9 GPa) and temperature (2,500–2,800 K) [3]. Theoretical simulations of pressure- and temperature-induced phase transition in the B-C system conducted by Lowther demonstrated that the incorporation of B atoms into a diamond structure does not lead to a drastic distortion of the cubic cell of the diamond [4]. Calculations of electron-phonon coupling performed for boron-doped diamond by Moussa and Cohen predicts stable diamond-like phases with high boron concentration and a maximum bulk T_c near 55 K for boron concentrations between 20% and 30% [5]. The aim of the research in this renewal proposal still remains the same as the original proposal: to synthesize a new class of *diamond-like* materials containing only boron and carbon, B-C, and study their properties.

Within the DOE project, we synthesized a novel cubic BC_3 (c-BC_3) phase under high pressure and high temperature (HPHT) conditions. Recently, we obtained direct experimental data on the synthesis of a c-BC_3 phase and the thorough characterization of this phase by x-ray diffraction, transmission electron microscopy, electron energy loss spectroscopy, and Raman scattering. It was found that diamond-like BC_2 coating can be deposited using chemical vapor deposition. The behavior of resistance of BC_2 layers is similar to that of semiconductors. Under the current DOE project, we successfully developed a new method for direct measurement of sound velocities (longitudinal and shear velocities) for opaque materials under high pressure in a diamond-anvil cell (DAC).

Recent Progress

Synthesis of the cubic BC_3

We synthesized a cubic BC_3 phase by a direct transformation from a graphitic phase at pressures above 40 GPa and a temperature around 2000 K in a laser-heated DAC. The x-ray pattern of the post-lasered c-BC_3 specimen recovered from 37 GPa shows a diffraction pattern characteristic of a cubic phase. All the graphite-like x-ray diffraction peaks were replaced by a completely new set of peaks. The new phase can be indexed by a cubic unit cell with lattice parameter, a_0 = 3.5866±0.0003 Å. The zero-pressure lattice parameter of the cubic phase obtained in this study is larger than that of diamond (i.e., a_0=3.5667 Å), which is consistent with the theoretical prediction [4].

X-ray results together with Raman measurements provide a strong indication that graphitic BC_3 (g-BC_3) has been transformed into another phase under high pressure and high temperature. However, by using only Raman scattering and x-ray data it is only possible to confirm that there is a new cubic phase; x-ray diffraction confirms the bulk crystal structure, and Raman scattering confirms that a phase transition occurred. The stoichiometry, nanostructure, chemical purity, and homogeneity of our c-BC_3 can only be unambiguously established by using transmission electron microscope (TEM) in conjunction with electron energy-loss spectroscopy (EELS) techniques.

Figure 1 shows a section of c-BC_3 removed by the Focus Ion Beam (FIB) instrument and thinned to electron transparency (~50 nm) for transmission electron microscopy measurements. A high resolution transmission electron microscope image of the c-BC_3 is shown in Fig. 2 and

demonstrates that the *c*-BC_3 is a single, uniform, nanocrystalline phase with a grain size of about 3-5 nm. The electron diffraction pattern of the nanocrystalline *c*-BC_3 measured from the thin section (insert in Fig. 2) shows the same diamond structure as revealed by the synchrotron x-ray diffraction. The three diffraction rings are consistent with the interplanar distances (111), (220), and (311), respectively, in the diamond structure.

EELS is especially suitable for obtaining local chemical composition and chemical bonding information in light element materials. The EELS spectrum of the *c*-BC_3 phase was collected with 0.1 eV/channel dispersion and 0.9 eV energy resolution. The B-K and C-K edge EELS spectra of the *c*-BC_3 phase are similar to those of BC_2N phases, and diamond and boron-containing diamond-like carbon (DLC) films (a-C:B). The B-K and C-K edge spectra are dominated by sp^3 bonding (1s $\rightarrow \sigma^*$ transition peaks) and show only weak, vestigial 1s $\rightarrow \pi^*$ transition peaks below the primary σ^* features. The EELS quantification of the elemental composition ratio was carried out on the *c*-BC_3 phase and yielded consistent compositions of B = 26.6 ± 3.4 at% and C = 73.4 ± 9.3 at%. Therefore, the composition of the phase is approximately BC_3 (B/C = 2.8 ± 0.7).

Elasticity and resistivity measurements of the BCx phases

This year, we found that a dense $BC_{1.8}$ layer could be deposited using low-pressure thermal chemical vapor deposition (CVD). Deposited BC_x film consisting of two layers with different concentrations of boron, $BC_{1.8}$ (BC_2) and $BC_{8.2}$, is shown in Fig. 3. Measurements of the elastic properties of the $BC_{1.8}$ layer revealed that the elastic moduli of the $BC_{1.8}$ layer are close to those of hard diamond-like materials and higher than those of TiC and SiC. The electrical properties of the $BC_{1.8}$ and $BC_{8.2}$ films were measured by a four-point probe system. Resistivity of most of the samples was found to be around $1\text{-}5\times10^{-5}$ Ω m, similar to that of graphite. Resistivity of several films appeared to be ($1.5\text{-}3.0\times10^{-7}$ Ω m) as low as that of iron (1.0×10^{-7} Ω m). The behaviour of resistance of $BC_{1.8\text{-}8.2}$ layers as a function of temperature is similar to that of semiconductors. This finding indicates that it is possible to obtain hard BCx phases at nearly ambient conditions with conductivity similar to that of graphite.

Laser Ultrasonics Measurements of Elasticity of Opaque Solids Under High Pressure

Under the current DOE project, we successfully developed a new method for direct measurement of sound velocities (longitudinal and shear velocities) for opaque materials under high pressure in a DAC. Laser opto-acoustics uses laser radiation for the excitation of the acoustic waves in opaque materials. The main obstacle to measuring sound velocity in a DAC is that the thickness of the sample cannot be measured directly because it decreases as pressure increases. In the configuration we propose, the sound wave is excited using a pump laser and detected by a probe laser separated from the pump laser by a distance *d* (Fig. 4). The time of flight, τ, of the sound wave from the point of excitation (point A, Fig. 4) to the point of detection (point D, Fig. 4) can be described by a simple equation $c^2\tau^2 = d^2 + 4h^2$, where *c* is sound velocity. The sound velocity and thickness *h* of the sample under pressure can then be obtained by fitting experimental data (τ, *d*) in a coordinates system.

In a preliminary study, we successfully demonstrated that by using laser ultrasonics (LU) in diamond anvil cells (LU-DACs) it is possible to reliably measure both *longitudinal and shear* velocities of an iron layer at pressures up to 23 GPa and fullerene molecules in DAC at pressures up to 30 GPa. We chose to use iron because it is a material in which acoustical waves are easily excited by a short laser pulse. Success in the acousto-optic detection of sound waves in iron under high pressure opens a way to study the elastic properties of other functional materials, such as superhard materials synthesized under HPHT conditions. A thin layer of iron can also be used as a transducer for opto-acoustical sound excitation and acousto-optical sound detection in DAC loaded with different non-transparent material. We later instituted an improved algorithm for the determination of shear wave velocity in iron under high pressure within the frame of an earlier proposed laser

ultrasonics technique. The modification allowed us to improve the accuracy of shear wave velocity determination. Statistical errors of the sample thickness and longitudinal and shear velocities measurements were found to be less than 2%.

Future Plans

We plan to continue our research in several directions: (a) conduct synthesis of BCx phases with B/C ratio higher that ¼; (b) conduct a comprehensive study of the elastic (LU-DAC technique and Brillouin scattering), electrical (under ambient and low temperatures), and vibrational properties of the novel BCx phases and films; (c) study a correlation between the B/C ratio and the elastic and electrical properties of the graphitic and dense BCx phases; and (d) measure the isothermal compressibility of the recently synthesized diamond-like BCx phases using synchrotron-based x-ray diffraction at the APS.

References

1. Xu, L.F., et al., Prediction of a three dimensional conductive superhard material: diamond-like BC(2). J. Phys. Chem. C, **114** (2010) 22688.
2. Moussa, J.E. and M.L. Cohen, Constraints on T-c for superconductivity in heavily boron-doped diamond. Physical Review B, **77** (2008) 8.
3. Ekimov, E.A., et al., Superconductivity in diamond. Nature, **428** (2004) 542.
4. Lowther, J.E., Potential super-hard phases and the stability of diamond-like boron-carbon structures. J. Phys. Condes. Matter., **17** 2005. 17(21): p. 3221-3229.
5. Liu, Z.Y., et al., Prediction of a sandwichlike conducting superhard boron carbide: First-principles calculations. Phys. Rev. B, 73 (2006) 4.

DOE Sponsored Publications in 2009-2011 from Current Grant

P. V. Zinin, L. C. Ming, S. K. Sharma, Y. Liu, S. M. Hong. "Ultraviolet Raman spectroscopy of the graphitic BCx phases". *Diam. Related Mater.* **18** (2009) 1123–1128.

P. Zinin, L. Ming, S. Sharma, V. Khabashesku, X. Liu, S. Hong, S. Endo. "Ultraviolet and near-infrared Raman spectroscopy of graphitic C_3N_4 phase". *Chem. Phys. Lett.*, **472** (2009) 69–73.

J. E. Lowther, P. V. Zinin, L. C. Ming, "Vibrational energies of graphene and hexagonal structured planar B-C complexes". *Phys. Rev. B,* **79**, (2009) 033401.

N. Chigarev, P. Zinin, D. Mounier, A. Bulou, L. C. Ming, T. Acosta, V. Gusev, "Analysis of ultrasonic echoes induced by pulsed laser action on iron film in a diamond anvil cell", *High Press. Res*. **30** (2010) 78.

P. V. Zinin, N. Chigarev, D. Mounier, A. Bulou, L. C. Ming, T. Acosta, V. Gusev, "Evaluation of elastic properties of iron in diamond anvil cell by laser ultrasonics technique", *J. Phys. Conf. Ser*. **215**, (2010) 012053.

X. R. Liu, P. V. Zinin, L. C. Ming, T. Acosta, S. K. Sharma, A. K. Misra, S. M. Hong, "Raman spectroscopy of melamine at high pressures", *J. Phys. Conf. Ser*. **215** (2010) 012045.

L. C. Ming, P. V. Zinin, X. R. Liu, Y. Nakamoto, R. Jia, "Synthesis of dense BC_x phases under high-pressure and high-temperature", *J. Phys. Conf. Ser*. **215** (2010) 012135.

N. Chigarev , P. Zinin, D. Mounier, A. Bulou, A. Zerr, L. C. Ming, V. Gusev, "Laser ultrasonic measurements in a diamond anvil cell on Fe and the KBr pressure medium", *J. Phys. Conf. Ser.* **278** (2011) 017012.

M. G. Beghi, A. G. Every, V. Prakapenka, P. V. Zinin, "Measurements of the elastic properties of solids by Brillouin spectroscopy", in T. Kundu (ed.), *Ultrasonic Nondestructive Evaluation: Engineering and Biological Material Characterization*, Taylor & Francis, N.Y., chapter 10, in press (2011).

Eleven DOE Sponsored Publications in 2007-2011 from Preceding Grant

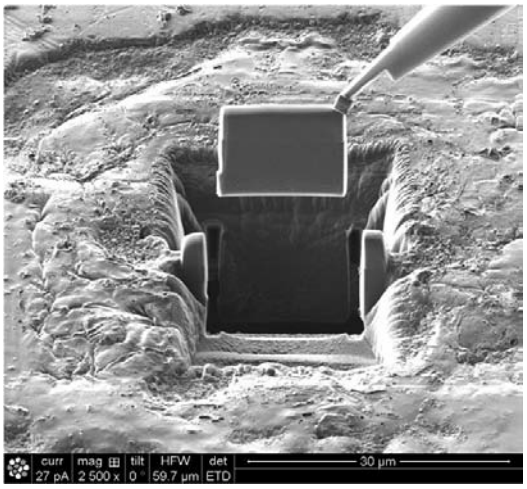

Fig. 1. Scanning electron microscope image of the small wedge of the *c*-BC_4 phase removed by FIB instrument.

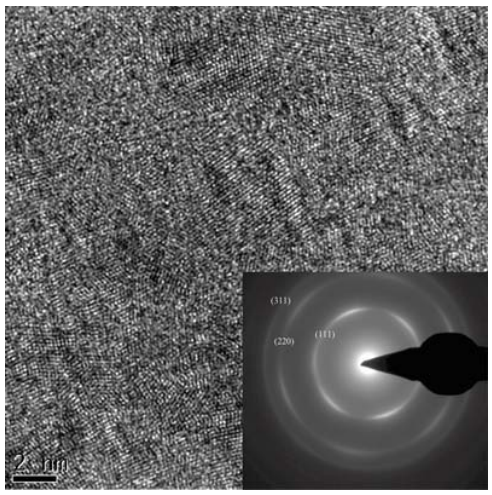

Fig. 2. High resolution TEM image of the *c*-BC_3 phase. Insert is a selected area in the electron diffraction pattern of an area of the nanocrystalline *c*-BC_3 phase. The three readily-distinguishable diffraction rings correspond to the (111), (220), and (311) reflections.

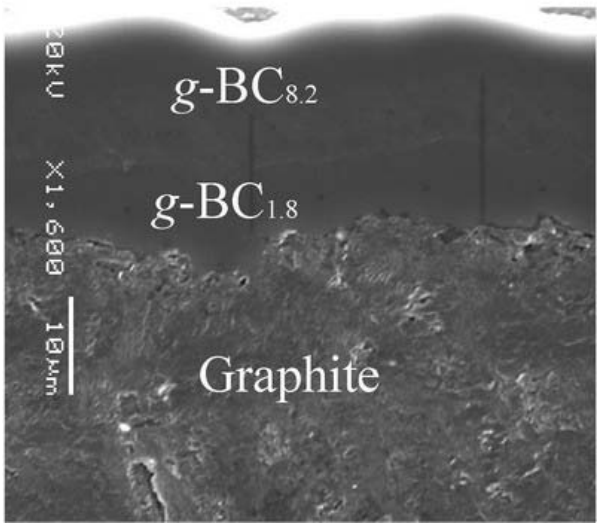

Fig. 3. SEM image of the *g*-BC_x film-deposited on a graphite substrate by the LPCVD method; the cross-section of the specimen shows two layers with different boron concentrations, *g*-$BC_{1.8}$ and *g*-$BC_{8.2}$.

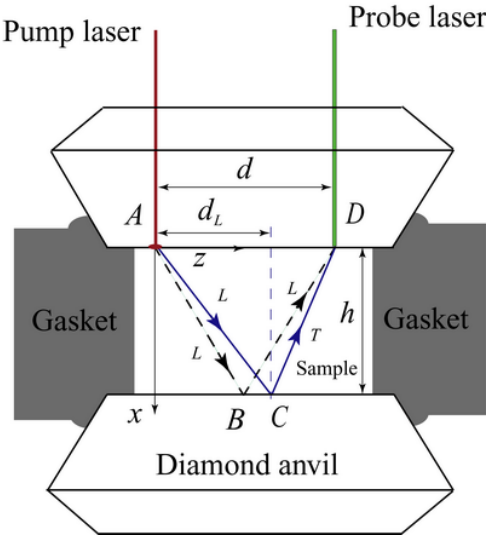

Fig. 4. Sketch of sound wave propagation in the DAC where *h* is the thickness of the layer, *d* is the distance between the pump and a probe laser beams, and *x* and *z* are Cartesian coordinates.

Laser Fabrication of Active Single-crystal Architecture in Glass

Project No. DE-SC0005010

PI: Himanshu Jain. Co-PI: Volkmar Dierolf. Research Associate: Pradyumna Gupta

Lehigh University, Bethlehem, PA 18015 USA

H.Jain@Lehigh.edu

Program Scope

There is a growing interest in the families of special glasses such as chalcogenides, fluoride and heavy metal oxide glasses for their unique combination of properties. For instance, chalcogenide glasses, by virtue of being made of heavier elements and weaker bonds than the oxide glasses, have low phonon energy and high polarizability that lead to high transmittance in the infrared region, higher refractive index, semiconductivity and an overall higher sensitivity to light [1]. These glasses have found applications in infrared optics, optical and electric data storage, photonic integrated circuits etc.

Several applications such as data storage and integrated optics depend on the ability to create and modify optically or electrically active elements on chalcogenide glasses. In this respect, laser direct-write method is a simple but powerful technique that promises spatial selectivity and a high level of control on the morphology, crystallinity and orientation of active features. Recently, it has been successfully demonstrated by fabricating active ferroelectric single crystal architecture in a model oxide glass. This project attempts to extend the same basic concepts to chalcogenide glasses, which respond significantly differently to laser irradiation than oxides. Thus far we have demonstrated the formation of such structures using laser direct-write method, and identified laser and sample parameters that affect the formation of crystalline features. Our current understanding of laser crystallization of oxide glasses suggests that photoinduced thermal effects are the primary driver of crystallization. However, results on chalcogenide glasses indicate contribution of other photostructural changes such as photo-expansion/contraction and field induced atomic movement in the transformation of glass into crystal. A fundamental understanding of these photo-effects on crystallization is a special aspect of chalcogenide glasses, which is a part of this study.

Recent Progress

Identification of suitable glass compositions

Since there was no previous observation of direct laser writing of single crystal on a chalcogenide glass, our first task was to demonstrate the proof of concept for this class of materials. To this effect and for developing a scientific understanding, we followed four criteria for selecting chalcogenide glass compositions, which are based on past experience with oxide systems. A suitable composition should satisfy the following conditions: (1) it forms glass easily, (2) the glass devitrifies into only one crystalline phase, (3) the crystalline phase is ferroelectric and (4) it has sufficient strength for handling. Compositions in the Ge-Sb-S-I system have been found to satisfy these conditions and their laser crystallization was expected to form just the SbSI ferroelectric crystal phase [2]. Since SbSI is a well-known chalcogenide ferroelectric, its general characteristics have been reported in literature to help understand its interactions with laser. Two glass compositions in the Ge-Sb-S-I system have been identified: $10GeS_2.90SbSI$ (Ge10) and $20GeS_2.80SbSI$ (Ge20). In addition to satisfying above requirements for laser crystallization, these compositions also offer the possibility of controling the crystallization kinetics e.g. the increase in the amount of GeS_2 should slow the crystallization

process as it increases both the glass transition and the crystallization temperatures. The samples were prepared by the conventional melt-quench method. Also microwave heating was explored, which offered advantage of lower vapor pressures and safer operation.

Formation of chalcogenide ferroelectric single crystal

The previously developed laser writing set up was optimized for the selected chalcogenide glasses, which have a much smaller band gap than the oxide glasses. Fig. 1 shows a laser-written crystal line created using this arrangement. Images in the inset show Kikuchi diffraction patterns from different parts of the line using Electron Backscattered Diffraction (EBSD). Same pattern from all parts of the line indicate the single crystal nature of the line. The inset on the right also shows X-ray diffraction (XRD) pattern from a different sample that was laser-crystallized on the surface. XRD pattern from this sample shows excellent match with the standard powder diffraction pattern of SbSI, confirming the formation of single phase upon laser-crystallization.

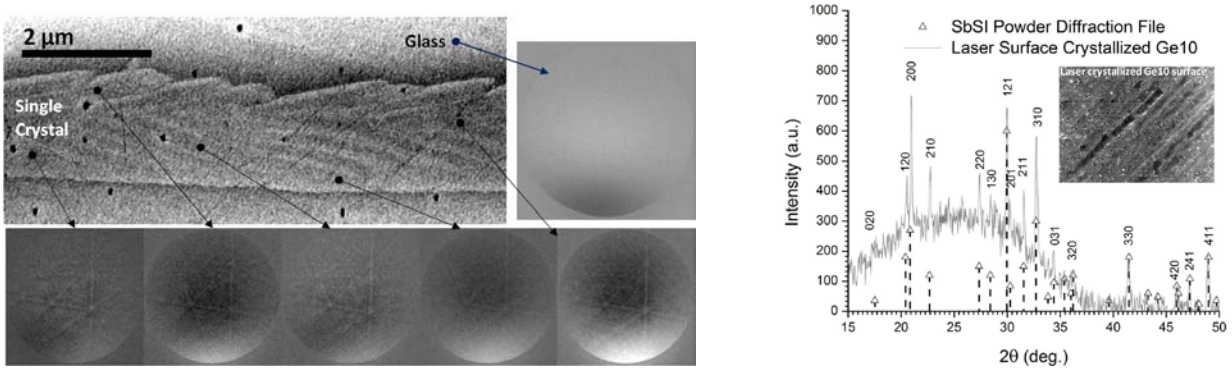

Figure 1. Scanning electron micrograph of the crystal line created using laser. Electron backscattered diffraction from different spots along the line and glass are shown. The right side compares X-ray diffraction pattern from laser crystallized surface of Ge10 sample and standard powder diffraction file of SbSI crystalline phase.

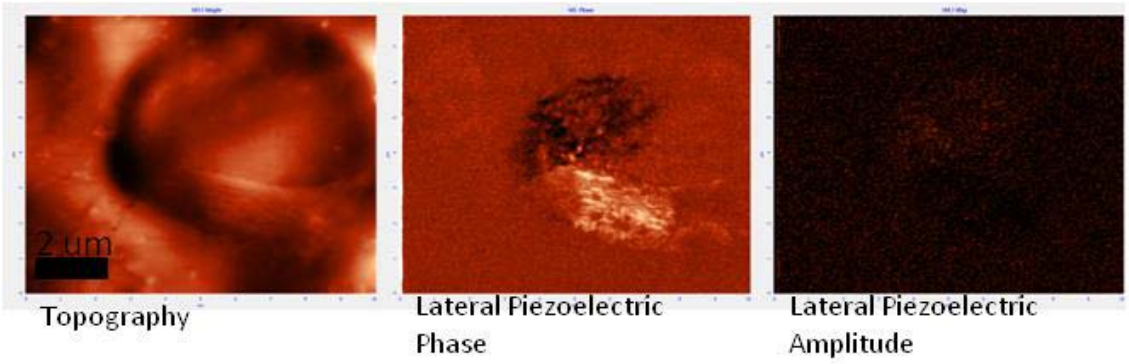

Figure 2. Topography and lateral piezoresponse maps of a crystalline spot made on the Ge10 chalcogenide sample.

Piezoresponse force microscopy has been used to make a direct observation of the ferroelectric functionality of the crystalline features. Fig. 2 shows the topographic image and piezoelectric response maps in lateral

direction for a crystalline spot made on Ge10 glass. The excellent contrast on the piezoelectric phase-image indicates piezoelectric functionality of the crystallites. However, the amplitude-image does not show good contrast. Optimization of sample preparation and instrument parameters is underway to obtain better contrast and clarify this difference.

Mechanism of laser-crystallization

Initially, laser induced heating was assumed to be the main driver of crystallization in the present chalcogenide system as it was show to be for oxide glasses. However, a comparison of irradiated regions in the two systems hints significantly different mechanisms for the two kinds of systems. As shown schematically in Fig. 3, the laser irradiation forms single crystal below the surface of the prototypic $LaBGeO_5$ glass [3]. A gradual narrowing of the profile of the cross-section of crystal from top to bottom agrees with the decreasing intensity of light as it passes through glass. On the other hand, in the present chalcogenide glass the crystal forms in a depressed region while both sides of the irradiated region are raised. The depth of the crystal seems to correspond to the penetration depth of laser light, which is much larger in rare earth doped oxide glass than in chalcogenide glasses.

The complex profile of the glass region around the crystal line in Fig. 3 (right) suggests that laser induced phenomena, other than just the increase in temperature, affect the crystallization process in chalcogenides. Photoinduced effects such as photoplasticity, atomic migration and photoexpansion are pronounced in chalcogenides but essentially absent in oxide glasses and therefore appear to affect the crystallization of the former.

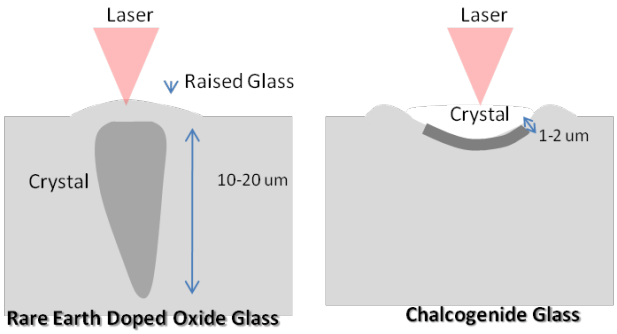

Figure 3. Schematic diagram of the cross-section of laser induced single crystal formed in oxide glasses vs. chalcogenide glasses.

Future Plans

The laser-crystallization of Ge10 sample has been sensitive to the position of laser focal point with respect sample surface. Indeed surface quality of the samples has a large effect on the crystallization process as an uneven surface can change the focus depth of the laser light. We will evaluate the impact of this processing parameter with experiments on carefully prepared flat samples. This may require the development of a method for polishing chalcogenide glass that is much softer than typical oxides.

As mentioned in the last section, photoinduced effects (besides photothermal) appear to impact the laser-crystallization behavior of chalcogenide glasses. Therefore, a better understanding of relevant

photoinduced phenomena will be necessary to identify major driving forces that determine morphology and orientation of laser formed crystals.

In-situ Raman spectroscopy has been recently shown to be a potentially effective tool for monitoring the crystallization stages of Ge10 composition where the excitation laser was used both as the pump and the probe [4]. We plan to pursue this method of structural characterization using two independent lasers, one to probe the structure and anothe to cause photostructural changes. The use of separate probe and excitation laser would avoid fluorescence from the sample and allow changing laser parameters independently, which can be crucial for optimizing the Raman output and studying the effects of excitation laser parameter such as power, focal spot size etc. on crystallization.

Micro-Raman and piezoresponse force microscopy (PFM) are being developed for characterizing the orientation, crystallinity, ferroelectric response and domain structure of laser-written micro and nano structures. Micro-Raman of chalcogenide glasses is expected to be somewhat challenging since the defect states of chalcogenide glass can result in the absorption of light of even sub bandgap energy if it is sufficiently intense. This type of excitation beam may cause photostructural changes as well.

PFM is a scanning probe microscopy technique that offers nanometer resolution, and has been useful in characterizing the state of laser crystallized features on oxide glasses. We plan to develop and use it on our samples. However, as shown in Fig. 2, its application to chalcogenide glasses faces challenges from the relatively poor surface quality of glasses. Weaker bonds in chalcogenide glasses lead to low chemical and environmental resistance and therefore, these glasses develop electrically dead layer easily. Other than sample parameters, the properties of probe tip such as stiffness, coating etc. affect the response. We will attempt to optimize the sample and PFM parameters and obtain quantifiable information on the piezoresponse and domain structure of laser-written features.

References

1. A. Zakery, and S. R. Elliott, "*Optical properties and applications of chalcogenide glasses: a review*," J. Non-Cryst. Solids, 330 (1-3), 1-12 (2003).
2. E.I. Gerzanich, V.A. Lyakhovitskaya, V.M. Fridkin, B.A. Popovkin, in *Current Topics in Materials science,* E. Kaldis, ed. (North-Holland, Amsterdam 10, 55–190, 1982).
3. P. Gupta, H. Jain, D. B. Williams, T. Honma, Y. Benino, and T. Komatsu, "*Creation of Ferroelectric, Single-Crystal Architecture in $Sm_{0.5}La_{0.5}BGeO_5$ Glass*," J. Am. Ceram. Soc. 91(1), 110-114 (2008).
4. Lihua Ding, Jing Ren, Himanshu Jain, Donghui Zhao, Guang Yang, Guorong Chen, "*Self-Reversible Photodarkening of the Mixed GeS2–SbSI Glasses*," J. Am. Ceram. Soc., 94(6), 1657–1660 (2011).

DoE Sponsored Publications in Past 1 Year from Current Grant

1. Pradyumna Gupta, Adam Stone, Nathaniel Woodward, Volkmar Dierolf, Himanshu Jain, "Laser fabrication of semiconducting ferroelectric single crystal SbSI features on chalcohalide glass," Optical Materials Express, In press.

Gargantuan Effects of Electrical Fields in the Processing of Ceramics at High Temperatures

Rishi Raj
Department of Mechanical Engieering
University of Colorado at Boulder
Boulder, CO 80309
www.rishirajboulder.com

September 19, 2011
Arlington, VA

Speaking generally, processing means the assembling of atoms and molecules into structures that, as a whole, have certain properties. The pathway and the rate at which this assembly occurs depends not only upon the intrinsic interactions between species, but also on externally imposed driving forces. These driving forces, or process parameters, can be chemical, mechanical and electrical, or combinations of them. Seemingly disparate examples, will often fit into this general picture. In deformation processing, such as superplastic shaping of ceramics, the driving force has a mechanical nature. In sintering, the capillary force, also in essence a mechanical force, is the driver. Dispersion of colloidal suspensions is achieved by controlling the pH, which affects the chemical and electrical state of charged molecules (the Debye layer) on the surface of particles in the suspension. The rheology of these emulsions depends on pH since the pH greatly affects the forces between particles. In nature, the healing of bones, a biochemical process, is known to be influenced by mechanical loading and electrical fields. The way trees grow is influenced by the wind, which exerts stress on their limbs. In summary, it would not be out of place, to investigate the fundamental coupling between electro-chemical-mechanical forces in the processing of inorganic materials.

This BES sponsored research effort at the University of Colorado seeks to understand the fundamental tenets of the electro-chemico-mechanical coupling in the deformation and sintering of ceramics at high temperatures. We seek to show unequivocally that electrical fields influence the rates of deformation and sintering in ceramics, to rigorously quantify this effect, and then to enunciate the fundamental, molecular mechanisms that link these forces in synergistic ways to strongly influence the outcome of these processes. The work seeks to add the "electrical field" dimension to the well-established, current understanding of sintering and deformation of ceramics, where the driving force is prescribed in terms of how the mechanical stress affects the chemical potential of charged species at interfaces, and the kinetics of mass transport by solid-state diffusion. These governing equations have been incorporated into full analysis of the flow field of mass-transport, which has given us the grand relationship for the sintering and deformation rate in terms of the applied stress, temperature, and the microstructure.

In order to clarify the role of electrical field in sintering and deformation, our experiments are conducted by applying the field by means of a pair of electrodes to the specimens, leaving the other parameters, such as the furnace temperature, and the applied stress unaffected so that each can be controlled independently of the other parameters, to elicit how they separately influence the process.

The experimental work has unearthed two remarkable findings: **(a)** The application of an electrical field above a specific threshold produces an unexpectedly high rate of sintering and deformation, whereby a process that nominally requires several hours is completed within a few seconds,

at temperatures that are hundreds of degrees below the usual sintering temperature. **(b)** The threshold value of this electrical field is coupled to the applied stress, falling further as the applied stress is increased. We have called this process flash-sintering.

Other observations that reflect on the underlying mechanism of this discovery are that the direction of the applied electrical field does not influence the process, the magnitude of the effect is sensitive to the grain size, and nearly all ceramics with some degree of ionic character exhibit the flash effect.

The experimental observations in our laboratory have led us to formulate a simple hypothesis for flash sintering (and deformation). The concept is that the electrical field can, under certain circumstance, induce a diffusion avalanche by nucleating a cascade of defects. These defects are visualized as Frenkel pairs, that is, a vacancy and an interstitial, bearing opposite charges, produced by the displacement of the atom species from its lattice site under the influence of an applied electrical field. The migration of these charges to different interfacial sites under the bias of the applied stress, produces rapid sintering and deformation. The electrical field does work on the system by extracting the charge from the vacancies and interstitials and transporting the charge through the external circuit.

While the work is specifically related to the role of electrical fields on sintering and deformation processing, the larger perspective of the coupling between chemical, electrical and mechanical forces is always in our minds. We seek to develop a unifying theory based upon basic thermodynamic and kinetic principles that can have a general significance. For example, the following questions are being pursued: **(a)** How is the difference in the total Gibbs free energy between the starting and the end state of the process, partitioned into chemical, mechanical and electrical contributions? **(b)** To what extent can the activation barrier for the movement of charged defects be influenced by the electrical fields? **(c)** How does space charge (the Debye layer) at interfaces, which is often present in inorganic systems constituted from molecules that have at least some degree of polar (ionic) nature, interact with the applied field to influence interfacial energy and kinetics?

A couple of references from our recent work:

•M. Cologna, B. Rashkova, and R. Raj, "Flash Sintering of Nanograin Zirconia in < 5 s at 850 degrees C", Journal of the American Ceramic Society, vol. 93, no. 11, pp. 3556-3559 (2010).

•Raj, R., J. C. S. Francis and M. Cologna, “Influence of Externally Imposed and Internally Generated Electrical Fields on Grain Growth, Diffusional Creep, Sintering and Related Phenomena,” Journal of the American Ceramic Society, vol. 94[7], 1941-1965 (2011).

This page is intentionally blank.

Poster Session I

This page is intentionally blank.

Depolarized Light Scattering from Plasmonic Structures

George Chumanov
gchumak@clemson.edu
Department of Chemistry
Clemson University, Clemson, SC 29634

Program Scope

Nanoscale materials attract considerable interest because of their unusual properties and potential for practical applications. Most of the activity in this field is focused on the synthesis of homogeneous nanoparticles from metals, metal oxides, semiconductors, and polymers. It is well recognized that properties of nanoparticles can be further enhanced if they are made as hybrid structures. This research is concerned with the synthesis, characterization, and application of plasmonic Ag nanoparticles (NPs) and structures. One of the emphases is on asymmetric hybrid nanoparticles (AHN). These are composed of a metal plasmonic core with other layers and particles on their surface. The layers and particles are places on the surface in an asymmetric fashion. These structures exhibit new properties that arise from the interactions between the core and the layers thereby rendering the development of AHNs fundamentally and practically important.

Plasmonic NPs exhibit unique optical properties arising from the excitation of the collective oscillations of the conduction electrons. Plasmon resonances can be tuned across the visible spectral range by varying the particle size, shape, and dielectric environment. Their excitation in Ag NPs represents the most efficient mechanism by which light interacts with matter. Because of this efficiency, tunability, and photochemical robustness, plasmonic AHNs are ideal for applications involving interaction with light. We design structures for novel optical applications.

Recent Progress

Irradiation of Ag NPs with light results in the excitation of plasmon resonances. Plasmon resonances can "enhance" many optical phenomena such as Raman scattering fluorescence, infrared absorption, second harmonic generation, and Rayleigh scattering, mainly via a strong evanescent field associated with the oscillating electrons. Ag NPs with the diameter of ca. 100 nm have a Rayleigh scattering cross section six times larger than their geometric cross section, thereby making them attractive for optical labeling. Importantly, Ag NPs can efficiently depolarize scattered light thereby providing a novel imaging platform. The scattered light is called depolarized when it has a significant component with the polarization perpendicular to that of the incident light. By exciting Ag NPs with linearly polarized light and analyzing them through a crossed polarizer, one can selectively measure depolarized light on a dark background resulting in a high contrast imaging.

It is expected that plasmonic AHNs can exhibit intense depolarized scattering due to their inherent asymmetric structure. The depolarized light scattering from plasmonic particles is expected to be a complex function of the excitation wavelength and the particle's shape and size. Recognizing the importance of the fundamental understanding of this phenomenon, we initiated comprehensive systematic studies of the depolarized

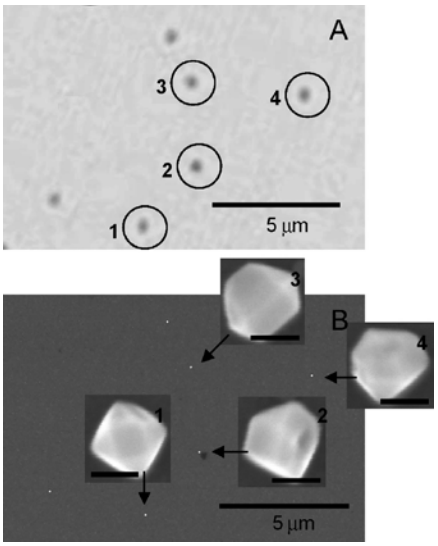

Fig. 1. (A) Bright-field optical microscopy image of ca. 80 nm Ag NPs and (B) corresponding electron microscopy image. Small scale bars are 50 nm.

light scattering from plasmonic structures. As a first part of these studies we have completed the depolarized scattering spectroscopy of individual Ag NPs of different shapes and sizes. We have characterized eight different single particles and relate the spectroscopic data to the shape and size of the particles. One of the most challenging aspects of this study was establishing the correlation between incident polarization and the orientation of the particles. Because the particle size is below the diffraction limit, electron microscopy was employed to determine the shape and the orientation of Ag NPs. The same particles were then further 'aligned' for spectroscopic interrogation. This approach is presented in **Fig. 1**, where panel A presents a bright field optical microscopy image aligned with the electron microscopy image of the same particles (panel B). Each particle was excited with linearly polarized white light, and the polarization vector was rotated in 10□ increments through the entire 360□circle. The image of an individual particle was sent through a cross-polarizer (analyzer) into a multichannel spectrometer for measuring scattering spectra. Note that both the excitation polarizer and analyzer were rotated simultaneously always maintaining their cross polarized orientation.

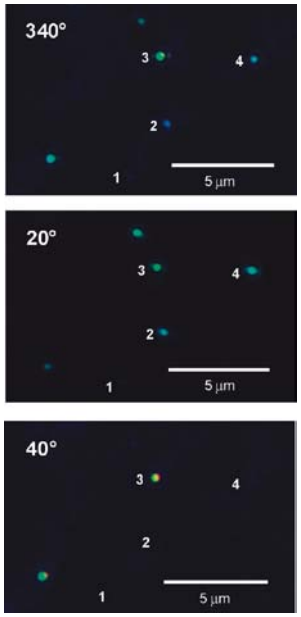

Fig. 2. Depolarized optical microscopy image of ca. 80 nm Ag NPs at 340° 20°, and 40° incident polarization angles.

As the excitation polarization angle was rotated, the individual particle appeared brighter and dimmer reflecting the complex behavior of the depolarized scattering (**Fig. 2**). Data from each individual particle were summarized as shown **Fig. 3**, where the upper panel presents depolarized scattering spectra and the other two panels correspond to the scattering intensity at different polarizations also overlayed with the actual particle. As can be clearly seen, the depolarized scattering intensity strongly depends upon polarization with the strongest scattering occurring when the incident polarization is oriented between major and minor axes of the particles. Note, that only asymmetric particles exhibited strong depolarized scattering. From the analysis of the data, a mechanism for the depolarized light scattering from plasmonic particles was elaborated. This mechanism is discussed in details in the published paper. In essence, the depolarized light scattering from asymmetric plasmonic NPs originates from the interference of the two dephased induced polarizability components (alone major and minor axes of the particle). The two components should have an overlapping frequency region and their simultaneous excitation requires the incident polarization vector to be in the direction in between the two exes. When the two

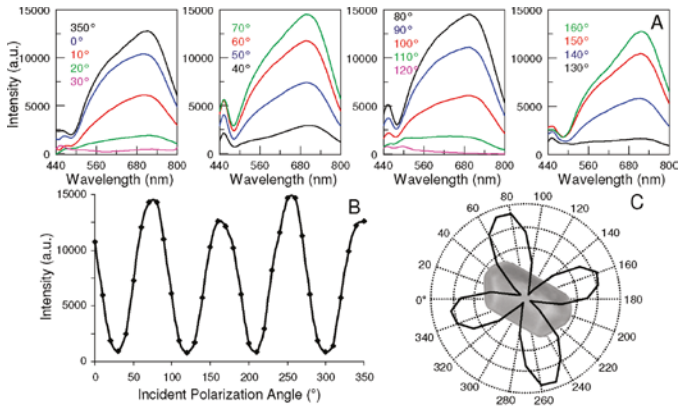

Fig.3. (A) Depolarized scattering spectra from NP 8 with different incident polarization angles. (B) X-Y plot and (C) radar plot of the depolarized scattering maximum intensity from NP 8 as a function of the incident polarization angle.

polarization components oscillate out-of-phase due to the fundamental dispersion relationship near a resonance, they produce field that is orthogonal to the incident field.

The fundamental understanding of the depolarized light scattering from plasmonic NPs will facilitate the development of new type of optical labels and many new applications.

Future Plans

Near-future work will proceed along two venues. First, we will continue the ongoing fundamental studies of the depolarized light scattering from plasmonic structures. The next phase will include clusters such as dimers, trimers, and tetramers of plasmonic particles (**Fig. 7**) as well as Ag NPs with asymmetrically positioned dielectric caps. The clusters in this figure were synthesized by the self assembly followed by overcoating with a thin layer of sol-gel silica for stability purposes. We will measure depolarization spectral maps for each type of clusters and overlay them with clusters' shape. The ultimate goal of this work is to be able a rational design of plasmonic structures with optimized depolarized light scattering properties for practical applications. We are also currently working and continue to pursue the synthesis of core/multi-shell plasmonic structures with the goal of making fluorescence labels with long Stokes shifts. The basic idea here is to utilize plasmon coupling between thin metal shells separated by dielectric layers impregnated with organic fluorophores for the efficient energy transfer from the fluorophore with the highest exited state to the fluorophore with the lowers one.

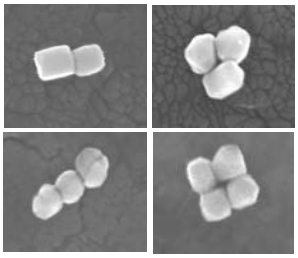

Fig. 7

Publications in the Last Two Years

1. C. F. Huebner, V. Tsyalkovsky, R. R. Roeder, P. Rungta, A. Childress, G. Chumanov, S. H. Foulger "Enhancing the electroluminescent performance of colloidally-based MEH-PPV organic light emitting devices with silver nanoparticles" Submitted 2011.
2. J. C. Heckel, G. Chumanov "Depolarized Light Scattering From Single Silver Nanoparticles" *J. Phys. Chem. C*, **115**, 7261–7269 (2011).
3. K. S. Iyer, B. Zdyrko, S. Malynych, G. Chumanov, I. Luzinov "Reversible submergence of nanoparticles into ultrathin block copolymer films" *Soft Matter.*, , 7, 2538-2542 (2011).

4. S. Z. Malynych, A. Tokarev, S. Hudson, G. Chumanov, J. Ballato K. G. Kornev "Magneto-controlled illumination with opto-fluidics" *J. Mag. Mag. Matter.*, 322(14), 1894-1897 (2010).
5. M. K. Kinnan, G. Chumanov "Plasmon Coupling in Two-Dimensional Arrays of Silver Nanoparticles: II. Effect of the Particle Size and Interparticle Distance" *J. Phys. Chem. C* , **114**, 7496-7501 (2010).
6. J. Henson, J. C. Heckel, E. Dimakis, J. Abell, A. Bhattacharyya, G. Chumanov, T. D. Moustakas, R. Paiella, "Plasmon Enhanced Light Emission from InGaN Quantum Wells via Coupling to Chemically Synthesized Silver Nanoparticles" *App. Phys. Lett.*, **95**, 151109 (2009).

Metal Oxide Core Shell Nanostructures as Building Blocks for Efficient Light Emission

James A. Dorman and Jane P. Chang
jpchang@seas.ucla.edu
Department of Chemical and Biomolecular Engineering
UCLA, Los Angeles, CA 90095

Program Scope

The objective of this research is to synthesize core-shell nano-structured metal oxide materials and investigate their structural, electronic and optical properties to understand the microscopic pathways governing the energy conversion process, thereby controlling and improving their efficiency.

Recent Progress

(1) Re-Y_2O_3 core-shell nano-particles for improved luminescent lifetime

To assess the effect of a Y_2O_3 shell on the luminescent lifetime, the distance between the Er^{3+} ion and the surface hydroxyl sites were increased through the addition of an Y_2O_3 shell, with a thickness ranging from 3-12 nm. As a baseline comparison, the lifetimes of the $^4S_{3/2} - {}^4I_{15/2}$ radiative transition (565 nm) from the Er^{3+}:Y_2O_3 (1 mol %) NPs were 122 and 76 μs at 77 and 298 K, respectively (Figure 1). The overall measured lifetime gradually increases with increasing Y_2O_3 shell thickness at both temperatures. As the Y_2O_3 shell thickness reached 8 nm, the lifetime was improved by 42 % at 77 K and 53 % at 298 K. As expected, the passive shell layer decreased the amount of energy transferred to the hydroxyl groups proportional to the thickness of the shell at both temperatures. As the Y_2O_3 shell thickness increased up to 12 nm, a decrease in the lifetime from its peak value was observed. However, at 77 K, the decrease was minimal, while at 298 K, the decrease reduced the lifetime nearly to the level of the baseline (without shell). This is because the lifetime feature of the $^4S_{3/2} - {}^4I_{15/2}$ state was governed by not only radiative processes but also non-radiative relaxation pathways such as phonon vibrations. The multiphonon relaxation played a significant role in luminescence quenching at 298 K with the 12 nm shell. It is believed that the lifetimes were reduced due to thermal vibrations of the thick poly-crystalline shell layer that was deposited around the core.

Due to the cooperative energy transfer observed with photoluminescence, it was important to elucidate the spatial effect of Yb^{3+}, a sensitizer, on the luminescent lifetimes. The Er^{3+},Yb^{3+}:Y_2O_3 core had an emission lifetime of 140 μs and 90 μs at 77 K and 298 K, respectively, representing a 14 % and 18 % increase, with respect to that of the Er^{3+}:Y_2O_3 NPs. The Er^{3+},Yb^{3+}:Y_2O_3|Y_2O_3 NPs layer showed a comparable increase to that of the Er^{3+}:Y_2O_3|Y_2O_3 NPs. Lifetimes of both sensitized systems are slightly longer than the Er^{3+}:Y_2O_3 NPs due to the energy transfer between the Er^{3+}-Yb^{3+} ion pairs. To assess the energy transfer from Yb^{3+} in the shell into Er^{3+} in the core, shells with two concentrations of Yb^{3+} (20 mol % and 100 mol %) were prepared. A maximum lifetime increase of 32 % was measured from the Er^{3+}:Y_2O_3|Yb_2O_3 NPs at 77 K. The lifetimes were improved due to increased energy transfer between the Yb^{3+}-Er^{3+} ion pairs proportional to the shell Yb^{3+} concentration. Overall, the addition of the Yb^{3+} doped shell layer increased lifetimes by preventing quenching cause by surface hydroxyl groups

and producing a favorable energy transfer due to the spatial control of the active ions, Er^{3+}, and the sensitizer ions, Yb^{3+}, within the core-shell structure.

Additionally, the energy transfer can be quantified through the upconversion luminescence. Focusing on the $^4S_{3/2}$ energy level, the upconversion intensity vs. pump power relationship is probed for five core shell NPs to determine the statistical photon requirement (*n*). The average photon requirements for the different structures were extracted from the slope of the line plotted in Figure 2. The Er^{3+} doped core had a photon requirement of 2.16, slightly higher than the theoretical requirement of 2 photons, suggesting that some energy was lost to phonons due to the excited state absorption (ESA) upconversion. The addition of a passive Y_2O_3 shell or an active Yb_2O_3 shell on the Er^{3+}:Y_2O_3 core reduced n to 1.65 and 1.43, respectively. Comparably, co-doping the core with Yb^{3+} (4 mol %) and subsequently adding a passive Y_2O_3 shell achieved an *n* value of 1.81 and 1.50, respectively, slightly higher than that when an active shell was employed. The decrease in the statistical photons required for upconversion was an additional confirmation of increased energy transfer from Yb^{3+} to Er^{3+} ions. Positioning the Yb^{3+} ions in the shell resulted in a higher proportion of the sensitizer-emitter pairs that were within the critical energy transfer distance predicted by the Förster-Dexter theory, as opposed to the co-doped system where the ions were randomly distributed within the core.

(2) Re-$LaPO_4$ core-shell nano-particles for white light generation

The synthesis of RE^{3+} doped $LaPO_4$ core-shell nanowires (NW) were carried out in order to produce a single white light source. Using a combination of trivalent Tb, Dy, and Eu ions, multiple shells of doped $LaPO_4$ were deposited around RE^{3+}:$LaPO_4$ NWs. Using the information gathered from the Y_2O_3:Er^{3+} system, it was decided that the mutli-shell method would produce the largest increase in luminescence efficiency while limiting any energy transfer that may occur between the dopant ions. The excitation spectra showed that multiple excitation wavelengths can be used to excite all three ions concurrently. Additional excitation bands centered at 340 nm are possible with the incorporation of Ce^{3+} as a sensitizer, due to the $^2F_{5/2}$-5D energy transition, depending on the efficiency of energy transfer between ions. The normalized emission spectra of the RE^{3+}:$LaPO_4$ NWs are shown in Figure 3. Combining the three spectra results in a theoretical emission spectrum which covers the full visible range, and has the potential to emit white light if the intensities are engineered correctly.

The dopant concentrations were fixed at 5 mol % Eu^{3+} and Dy^{3+}, 2 mol % Tb^{3+}, and 10 mol % Ce^{3+} (when incorporated) for the various core-shell structure, in order to study the spatial effects on luminescence. The following series of multi-shell NWs were synthesized in order to study the effect of dopant position and sensitizer on the quality of light: Tb|Dy|Eu; Eu|Dy|Tb; Ce,Tb|Dy|Eu; Tb|Ce,Dy|Eu; Eu|Ce,Dy|Tb; and Eu|Dy|Ce,Tb and compared to the reference Ce^{3+},Tb^{3+},Dy^{3+},Eu^{3+}:$LaPO_4$ NWs. The emission spectra were collected for the NWs as the excitation wavelength was increased successively to determine the optimum excitation wavelength for white light emission. All samples resulted in emission spectra within the accepted range of white light generation based on the converted CIE color coordinates. The white light obtained varied between warm and cool white depending on the layering architecture, allowing for the utilization into a wide range of applications.

The emission lifetimes were chosen as an alternative figure of merit in order to quantify the optimal structure for application in white light LEDs. Typically, the excitation energies range between 300-365 nm, ideal for the next generation LEDs due to the low production costs. Lifetimes were collected for the three key raditative transitions, $^5D_0$-$^7F_2$ (Eu^{3+}), $^5D_4$-$^7F_5$ (Tb^{3+}) and $^4F_{9/2}$-$^6H_{15/2}$ (Dy^{3+}), for each RE ion observed in the emitted white light spectra. The doped multi-shell structures were compared to RE^{3+}:$LaPO_4$ NWs to assess the lifetime improvement. The multi-ion-doped core structure showed a decrease in emission lifetimes for all transitions, indicating the high RE^{3+} concentration in the NWs causes parasitic energy transfer between the dopant ions, reducing the total luminescence. Spatially distributing the RE ions within the core-shell structure resulted in emission lifetimes at or above the baseline reference for both Tb^{3+} and Eu^{3+} confirming the results from the Er^{3+}:Y_2O_3 NP system. However, the luminescent response of the Dy^{3+} dopant was dependent on the position of the Ce^{3+} dopant, suggesting a cooperative energy transfer between the two ions. The highest overall increase in the lifetimes was obtained with the Eu|Ce,Dy|Tb, using a 365 nm excitation source, yielding 3.2 ms, 0.9 ms, and 4.3 ms for the three key transitions, respectively. The measured lifetimes represented improvements of 16%, 31%, and 36% for the three key transitions when compared to $LaPO_4$ NWs doped with each constituent RE ion, respectively.

A high quality emission scan was collected for the Eu|Ce,Dy|Tb NPs to quantify the exact CIE color coordinates. The luminescence spectrum, shown in Figure 4, covers the full visible range similar to the normalized spectra shown in Figure 3. The observed transitions are labeled with an additional peak at 530 nm resulting from the Ce^{3+} emission. Converting the spectrum into the color coordinates, the data from this multi-shelled NP was at a coordinate of (0.35, 0.35), near the very center of the white light region of the CIE chart, as shown in the inset of Figure 4. Using the spatially controlled RE doped core-shell architecture, we were able to increase the overall quantum efficiency while controlling the emission spectra of the nanostructures. It is important to quantify the overall conversion efficiency of the nanostructures when paired with a LED excitation source.

Future Plans

Further experiments are under way to study the distance at which energy can transfer between RE ions during upconversion emission. Er^{3+} and Yb^{3+} will be separated within the core-shell structure by confining the Yb ions in the shell which will be a set distance from the Er ions through the use of a Y_2O_3 spacer shell. The NPs will be excited with either a 980 nm laser diode, which excites both ions, or a 915 nm laser diode, to excite the Yb ions only, allowing for the extraction of energy transfer coefficients. Additionally, the co-doped $LaPO_4$ phosphors will be studied using a variable wavelength excitation source with an integrating sphere assembly in order to extract exact quantum yields instead of using the relative increase in lifetimes.

DOE Sponsored Publications in 2009-2011 from Current Grant

1. J.A. Dorman, J.H. Choi, G. Kuzmanich and J. P. Chang, "High Quality White-Light Using Core-Shell RE^{3+}:$LaPO_4$ (RE= Eu, Tb, Dy, Ce) Nanophosphors", In preparation.
2. J.A. Dorman, J.H. Choi, G. Kuzmanich and J. P. Chang, "Estimating Er^{3+} Luminescence Lifetimes by Correlating the Judd-Ofelt Parameters to the EXAFS Crystal Modeling", In preparation.
3. J.A. Dorman, J.H. Choi, G. Kuzmanich and J. P. Chang, "Using a Controlled Core-Shell Rare-Earth Ion Doped Y_2O_3 Nano-Architecture to Increase Luminescence Efficiency", submitted

4. J. A. Dorman, Y. Mao, J. Bargar and J. P. Chang, "In Situ X-ray Diffraction and Absorption Studies of the Growth and Phase Transformation of Yttrium Hydroxide Nanotubes to Their Oxide Counterparts", Journal of Physical Chemistry C. 2010, 114 (41), 17422-17427

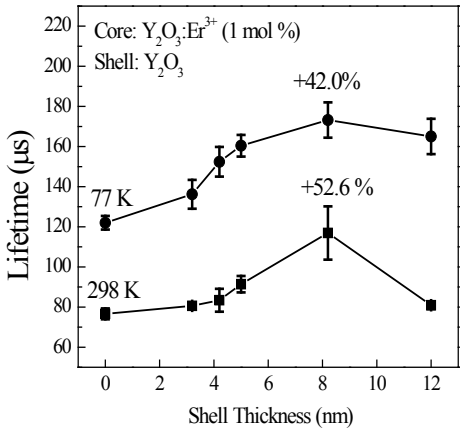

Figure 1: The measured lifetimes for 77 K and 298 K are shown as a function of the shell thickness. The maximum lifetime is measured after an 8 nm Y_2O_3 shell was deposited.

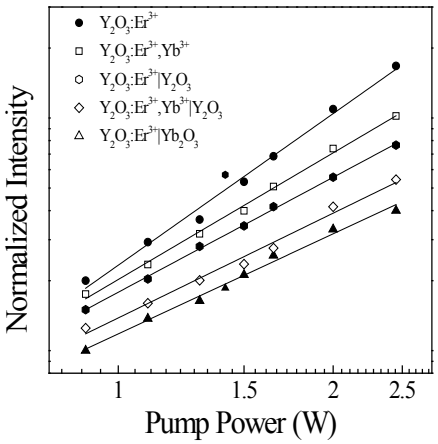

Figure 2: Log-log plot of the pump power dependence, from which the average photon requirement was determined. Intensities for each sample were normalized to that measured at the lowest powers, 0.9 W, and was offset for clarity.

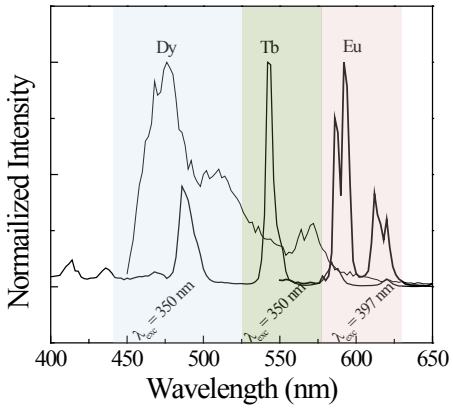

Figure 3: The normalized emission spectra are shown for the RE^{3+}:$LaPO_4$ nanowires. When combined, the three ions cover the full visible spectrum, ideal for white light emission.

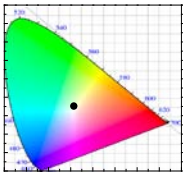

Figure 4: The detailed emission spectrum is shown covering the visible spectrum for the multi-shell multi-ion-doped NP. The inset shows the color quality of the Eu|Ce, Dy|Tb sample using a λ_{exc} of 365 nm (●).

Synthesis of ZTO Nanowires and Physical Deposition of Quantum Dots

Jiajun Chen, Qilin Dai, Liyou Lu, Jinke Tang, and Wenyong Wang*
Department of Physics and Astronomy
University of Wyoming, Laramie, WY 82071
*Email: wwang5@uwyo.edu

Program Scope

In this project we investigate quantum dot (QD) sensitized photovoltaic structures based on Zn_2SnO_4 (ZTO) nanowires. Published work on nanowire solar devices has mainly focused on binary oxide nanowires [1,2]. Compared with simple binary materials, ternary metal oxides such as Zn_2SnO_4 offer certain advantages. For example, optimizing their band alignment with respect to the electrochemical potentials of the redox couples can reduce back electron transfer and create a large photovoltage that is one of the major factors affecting the efficiencies of DSSCs [3,4]. We also inspect non-solution based synthesis and deposition of QDs on nanowires. Conventional solution-based QD synthesis methods involve linker molecules and ligands exchange, which have certain disadvantages. For example, linker molecules present transport barriers for photo-generated electrons, and ligand exchange processing is challenging for certain types of QDs. In this project we study physical methods such as pulsed laser deposition (PLD) of QDs on nanowires, which can avoid the use of ligand molecules and could possibly lead to solar cells with better performance.

Recent Progress

ZTO nanowires have been successfully synthesized in this research using a chemical vapor deposition (CVD) method [5]. The synthesis was performed in a 1-inch CVD system under vacuum. For ZTO nanowires, Zn foil and SnO powder were used as the source materials and Si wafers coated with Au were used as the substrates. The growth temperature was around 900 ºC. Figure 1(A) is a Field Emission Scanning Electron Microscope (FESEM) image of a single ZTO nanowire. The diameters of the nanowires were ~ 80 nm, and the lengths were close to 100 μm. The ZTO nanowires exhibit a stacking structure of rhombohedral crystals [6]. Figure 1(B) is a High Resolution Transmission Electron Microscopy (HRTEM) image, showing the crystalline structure and the $[1\bar{1}1]$ growth direction. Figure 2 shows the X-ray diffraction (XRD) patterns that verified the composition and crystal structure of the ZTO nanowires. Figure 3 shows detailed TEM examination of the ZTO nanowire's rhombohedral structure.

Quantum dots coating on nanowires was achieved using a modified pulsed laser deposition method. A Nd:YAG laser with a wavelength of 266 nm, pulse repetition rate of 10 Hz, and pulse energy of 95 mJ was used for the experiment. The deposition was carried out in a vacuum chamber under a pressure of 10^{-4} torr, which has a fused quartz window for the UV laser beam to pass through. The laser beam went through a lens with a focus length of 30 cm located in a proper position outside the chamber such that the laser energy could focus on the target positioned inside the chamber. The target was a CdSe bulk piece purchased from Alfa Aesar. The substrate was ZTO nanowires grown on a Si wafer. The distance between the plume from the target and the substrate is 6 cm.

Figure 4 shows the TEM images of CdSe QDs coated on the ZTO nanowire surface. From Fig. 4(A) and 4(C), it is obvious that the QDs are homogeneously distributed on the ZTO nanowire with a high coverage. The QDs are assembled uniformly around the nanowires as shown in Fig. 4(B), which is a magnified image of a region in Fig. 4(A). Fig. 4(D), which shows the high magnification image of a region in 4(C), reveals more information on the interface between the nanowire and QDs. It can be seen from Fig. 4(D) that the size of the QDs is about 5 nm, which should have strong absorption at wavelength of ~ 580 nm. The QDs are strongly bonded to the surface of the nanowire, suggesting that the QDs were grown *in situ* on the nanowire surface. This unique type of structure has several advantages compared to solution-based chemical methods for QD synthesis and deposition on nanowires for solar cell applications. First, the interface between the nanowire and QDs is clean and direct, without any organic ligands or linker molecules, which is unachievable in a chemical deposition process. Linker molecules and organic ligands from solution-based methods make the QD assembly on nanowire surfaces unstable, compete with QDs in light absorption, and, most importantly, create transport barriers for photo-generated electrons, thus decreasing the incident photon to electron conversion efficiency. Second, this physical deposition method is relatively fast compared to chemical approaches that require a much longer processing time for ligand exchange. Third, this method is more environment friendly since it avoids the use of toxic and dangerous chemicals. In summary, we have successful synthesized ZTO nanowires and developed a simple physical vapor deposition method based on pulsed laser deposition to directly assemble QDs on nanowires without involving any linker molecules or organic ligands. Such methods could possibly lead to nanostructure-based photovoltaic devices with improved performance.

Future Plans

Photovoltaic cells based on ternary metal oxide nanowires and physically deposited QDs are promising structures, and we will continue our investigation on this important subject. For nanowire synthesis, we will fine-tune the growth parameters including gas ratio, pressure, temperature, etc. to achieve a better fabrication control and nanowire yield. We will also study the low temperature growth of nanowires directly on transparent conducting oxides using Bi or other suitable catalysts. We will continue to explore PLD deposition of QDs on nanowires. Deposition parameters like the laser power, pulse rate, deposition time, deposition temperature and pressure will be adjusted to achieve better controlled QD growth. We will also explore wet methods like PLD in liquid, where the target and substrates are both placed in water or other liquid media during PLD. Such methods have been shown to be effective in producing uniform distribution of QDs on wires. The types of liquid media will be chosen in order to minimize the oxidation of the QDs and potentially reduce the tendency for the nanowires to bundle at the upper ends. We will also fabricate prototype PV cells using ZTO nanowires and PLD assembled CdSe QDs, and characterize device performance and investigate carrier transport mechanism in these structures.

References

1. M. Gratzel, "Solar energy conversion by dye-sensitized photovoltaic cells", Inorg. Chem. 44, 6841 (2005).
2. M. Law, L. E. Greene, J. C. Johnson, R. Saykally, and P. Yang, "Nanowire dye-sensitized solar cells", Nature Materials, 4, 455 (2005).
3. S. Y. Huang, G. Schlichthorl, A. J. Nozik, M. Gra1tzel, and A. J. Frank, "Charge Recombination in Dye-Sensitized Nanocrystalline TiO2 Solar Cells", J. Phys. Chem. B, 101, 2576 (1997).
4. G. Schlichthorl, S. Y. Huang, J. Sprague, and A. J. Frank, "Band Edge Movement and Recombination Kinetics in Dye-Sensitized Nanocrystalline TiO2 Solar Cells: A Study by Intensity Modulated Photovoltage Spectroscopy", J. Phys. Chem. B, 101, 8141 (1997).
5. Y. Xia et al., "One-dimensional nanostructures : synthesis, characterization, and application", Adv. Mater. 15, 353 (2003).
6. Y. Yang, X. Sun, B. Tay, J. Wang, Z. Dong, and H. Fan, "Twinned Zn2TiO4 Spinel Nanowires Using ZnO Nanowires as a Template", Adv. Mater. 19, 1839 (2007).

DOE Sponsored Publications in 2010-2011 from Current Grant

1. "Synthesis and Characterization of ZTO nanowires", Jiajun Chen, Liyou Lu, and Wenyong Wang, manuscript under preparation.
2. "Pulsed Laser Deposition of Quantum Dots on ZTO Nanowires for Photovoltaic Applications", Qilin Dai, Jiajun Chen, Liyou Lu, Wenyong Wang, and Jinke Tang, manuscript under preparation.

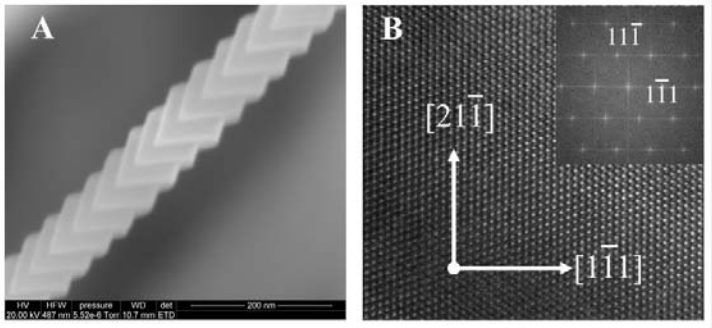

Fig. 1. (A) FESEM images of a ZTO nanowires. (B) TEM image of a ZTO nanowire showing the lattice structure and growth direction.

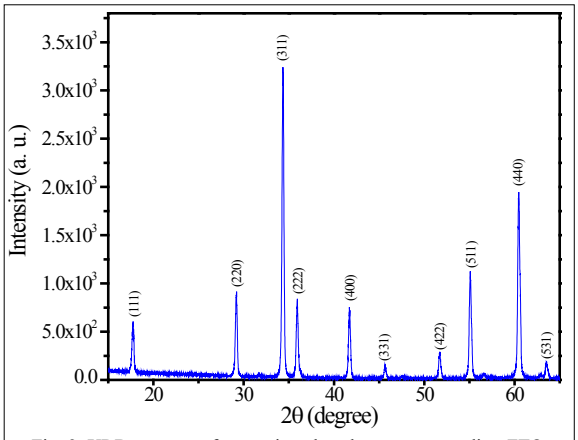

Fig. 2. XRD patterns of nanowires that show corresponding ZTO diffraction peaks.

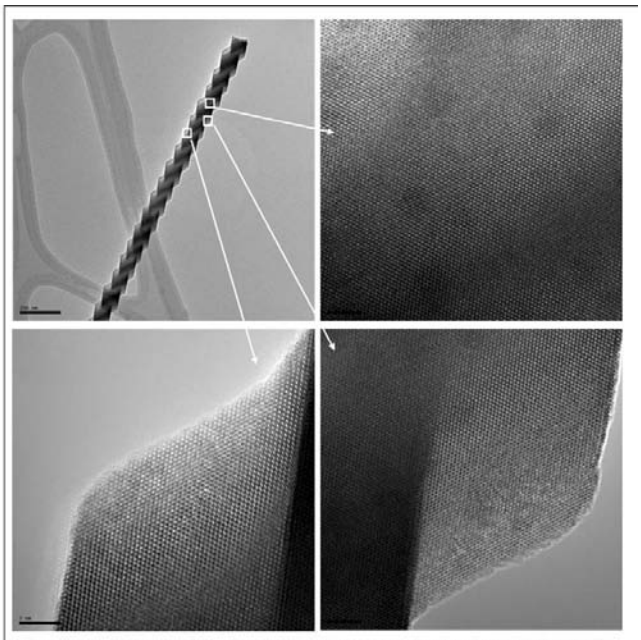

Fig. 3. TEM examination of ZTO nanowire's rhombohedral structure.

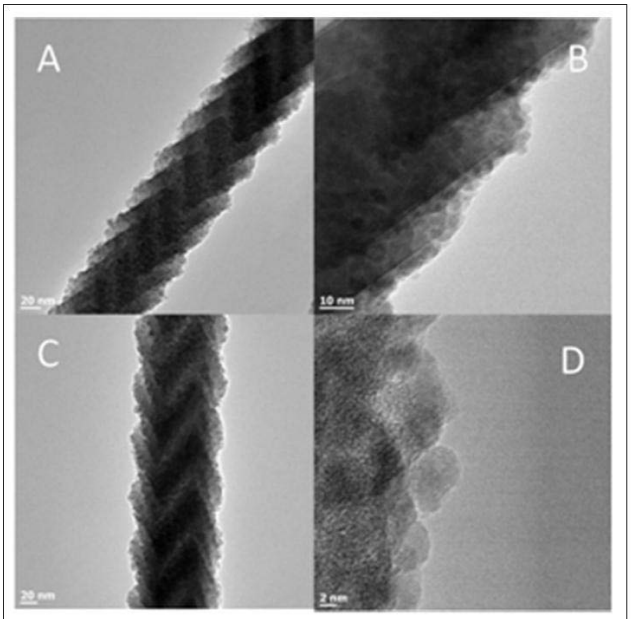

Fig. 4. TEM examination of PLD deposited QDs on ZTO nanowires.

Synthesis and Engineering of Submonolayer Type-II Quantum Dots to Enhance Material Properties of Wide Bandgap Semiconductors

Maria Tamargo,[1] Igor Kuskovsky,[2] Gertrude Neumark,[3] Carlos Meriles,[4] and Cevdet Noyan[3]
mtamargo@ccny.cuny.edu
1) Department of Chemistry, The City College of New York
2) Department of Physics, Queen College of CUNY
3) Department of Applied Physics, Columbia university
4) Department of Physics, The City College of New York

Program Scope:

Nanomaterials, whose properties are determined and controlled by their nanometer scale size, are revolutionizing materials technology and finding their way into a wide range of aspplications, including efficiency solar cells, miniature light emitters, bio-sensors and room-temperature infrared detectors. Semiconductor nanostructures such as quantum dots (QD), quantum wires and quantum wells (QW) are among the building blocks of these materials. Here, we extend our recent findings involving a type of nanostructure material that we refer to as sub-monolayer type-II QDs [1] and explore their potential to enhance materials properties into new regimes.

Type-II nanostructures are those in which the bands are staggered: that is, the material with the lower potential energy for electrons has the higher potential energy for holes, or alternatively, the material with lower potential for holes has the higher potential for electrons. Thus, electrons and holes are separated spatially. This spatial separation gives rise to relatively long carrier lifetimes and to a dependence of photoemission and photocurrents on the intensity of excitation, as well as on the external electric and magnetic fields.

We have extended the synthesis and controlled growth of sub-monolayer type-II nanostructures for the development of materials properties that may be of interest in novel technological applications. In particular, we have explored ways to engineer the band structure of the materials in order to achieve enhanced doping of difficult to dope materials and enhanced spectral response. These enhanced properties may have a profound impact on future technology, including solar cells and spintronics.

Recent Results:

Properties of ZnSe/ZnMgSe type II QD structures

Type-II ZnTe/ZnSe quantum dots (QDs) are particularly interesting because of their relatively large valence band (VB) and conduction band (CB) offsets [2]. Furthermore, II-VI wide band gap semiconductors, such as ZnSe, have long been difficult to dope p-type. Previously, high net acceptor concentrations (6×10^{18} cm^{-3}) was achieved for ZnSe by migration enhanced molecular beam epitaxy (ME-MBE), incorporating N within ZnTe nanoclusters embedded in the ZnSe, while keeping relatively low overall content of Te [3]. Unfortunately, this material exhibits rather low free hole concentrations, most likely due to the localization of the holes in the VB wells resulting from the large VB discontinuity between ZnTe and ZnSe. To modify the band structure and reduce the localization of the holes a series of samples was grown with Mg added to the ZnTe QDs. We have shown that the ZnMgTe QDs have a smaller VB offset, thus reducing the hole confinement.

High-resolution X-ray diffraction (HRXRD) measurements for the ZnSe:(Mg,Te) samples were performed on the X20A beamline at the National Synchrotron Light Source (NSLS) at Brookhaven National Lab (BNL). The symmetric scans made for peak positions corresponding to the (004) orientation is shown in Figures 1 (top) The (004) peaks are observed at about 66.05°, and correspond to the GaAs substrate. The SL(0) peak is caused by the addition of Bragg reflections from multilayer components of

the ZnSe:(Te,Mg) structure. Subsidiary satellite peaks appear symmetrically surrounding the zero order peaks, with spacing determined by the periodicity of the multilayers. Analysis of the peaks by fitting the spectra using commercially available Bede RADS software requires that we assume the formation of a ZnMgTe containing layer with an average thickness of 0.4 Å, to account for the QD layers. Excellent agreement between the simulation and experiment was observed. The simulation results showed that the average thicknesses of the ZnMgTe QD layers and ZnSe barriers are about 0.85 Å and 36.20 Å, respectively. Also, the data shows that Te is mainly confined inside the ZnMgTe QD layers, and there is a small amount of Te diffusion (~1.6%) inside the barrier. There is approximately 32% Mg inside the ZnMgTe layer. We have also used TEM to further elucidate the detailed crystalline structure of the QD layers. The origin of the additional sets of superlattice peaks (subsidiary peaks) can be explained by the presence of small, unintentional temperature oscillations of the Te source, which have since been corrected. In reciprocal space map, shown in the bottom of Figure 1, the diffuse scattered intensity is correlated in 'stripes' parallel to the q_x axis at the same positions as the coherent superlattice maxima, indicating a vertical correlation of the QDs.

Excitation dependent photoluminescence has also been performed on these samples. The results confirmed formation of type-II QDs. The detailed analysis of the data, using the information on Mg concentration obtained from HRXRD was being performed. The 325 nm line of a He-Cd laser was used as the excitation source. The excitation intensity was varied by using a set of neutral density filters (NDFs). The PL spectrum for this sample is shown in inset of Figure 2 (we show the spectrum obtained with $0.1I_{max}$, where I_{max} is the maximum excitation intensity in our set up). The spectrum consists of two bands at 2.34 eV (low energy peak) and 2.4 eV (high energy peak), respectively. Figure 2 shows peak positions of the high and low energy bands for various excitation intensities.

The low energy peak shows a blue shift of about 24 meV, while the high energy peak shows a blue shift of about 50 meV over four orders of increasing excitation intensity. Such a shift is a hallmark of type-II heterostructures, and appears because of the formation of a triangular-shaped quantum well around the QDs due to built-in electric field originating from the spatially separated photo-generated carriers. Finally, we were able, for the first time, to perform **Hall Effect measurements** in these samples. This suggests that the holes are more weakly bound than in the ZnSe/ZnTe QDs, without Mg in the dots. More detailed electrical measurements are being carried out.

Growth of ZnCdSe/ZnTe Type II QDs

Intermediate band solar cells (IBSCs) have been proposed to be substantially more efficient than conventional solar cells. IBSCs rely on multi-photon absorption with an assistance of an intermediate band in the mid-gap region of the semiconductor material used for the solar cell fabrication. In this regard, type-II quantum dots (QDs) are thought to be one of the best means to fabricate IBSCs. The staggered band alignment of type-II semiconductor heterostructures results in the spatial separation of photo-generated electrons and holes, suppressing both radiative and the Auger recombinations, making the carrier extraction process more efficient in a photovoltaic device. The band gap of the ideal IBSC host material is predicted to be between ~ 1.9 and 2.4 eV, making the $Zn_{1-x}Cd_xSe$ alloy an excellent candidate for the IBSC host material.

We have fabricated ZnTe/$Zn_{1-x}Cd_xSe$ QD multilayer structures on InP substrates, with $Zn_{1-x}Cd_xSe$ barriers layers lattice matched to InP. Initial undoped samples seem to be of high quality as indicated by sharp and streaky reflection high energy electron diffraction (RHEED) pattern throughout the growth. The narrow near-band-edge emission at ~ 2.2 eV and weak deep level emission at ~ 1.76 eV seen in the low temperature photoluminescence (PL) studies indicate the same. The PL emission from such a structure is found to be a broad band, probably due to the large size distribution of the QDs and the excitation intensity dependent PL shows a typical type-II behavior, as illustrated in Figure 3. The optical absorption and photoelectric response of doped samples, as well as the high resolution x-ray diffraction measurements, will also be reported.

Magneto-PL measurements

Spectroscopy in the presence of magnetic fields provides insight into the shape and size of the QDs. The applied magnetic field deforms the electron and hole wave-functions and causes a Zeeman splitting of the electronic levels. In general, the exciton energy, and thus the observed PL peaks, shift to higher energies (diamagnetic shift) [3]. When the magnetic field is relatively weak, perturbation theory predicts a quadratic field dependence of the exciton energy, whereas under a relatively strong field such dependence becomes linear. For type-II quantum dots in the cylindrical (plate) geometry additional features arise because of the spatial separation of the electrons and holes. In sufficiently strong magnetic field applied perpendicular to the plane of the nano-islands, the ground state of the electron wavefunction, having rotational symmetry, will accommodate a non-zero angular momentum making the electron-hole recombination forbidden. This manifests itself in oscillations of the ground state transition energy of the excitons (the so-called optical AB effect) [4], and as a result, on the luminescence properties of the nanostructures. Using the PL oscillation with energy or its intensity one can directly extract the in-plane size of the dots. We have successfully performed these studies for ZnTe/ZnSe QDs [5, 6]. The presence of AB oscillations will directly prove the existence of type-II QDs (or core shell 1-D system), since only closed electron (hole) orbits will give the effect. knowing the field B_1 one can estimate the electronic orbit radius, and then back to the size of the QDs using theory developed by us previously [7]. Since we can detect the field very precisely, and it scales as square root with the orbit radius, this allows for highly sensitive measurements of the QD lateral size, and its correlation with Te flux used during the growth.

Figures 4 (a) and (b) show the results for two samples studied. For sample A2996 (low Te flux) we observe the oscillation at about 2.1 T, which corresponds to electronic radius R_e (A2996) ≈ 17.7 nm, whereas for sample A3005 we get R_e (A3005) ≈ 18.2 nm.

References:

[1] Y. Gong, W. MacDonald, G. F. Neumark, M. C. Tamargo, I. L. Kuskovsky, *Phys. Rev. B* **77**, 155314 (2008).

[2] F. Malonga, D. Bertho, C. Jouanin, J. M. Jancu, *Phys. Rev. B* **52**, 5124 (1995).

[3] S. N. Walck and T. L. Reinecke, "Exciton diamagnetic shift in semiconductor nanostructures," Phys. Rev. B **57**, 9088-9096 (1998).

[4] A. B. Kalameitsev, V. M. Kovalev and A. O. Govorov, "Magnetoexcitons in type-II quantum dots," JETP Lett. **68**, 669 - 672 (1998).

[5] I. L. Kuskovsky, W. MacDonald, A. O. Govorov, L. Muroukh, X. Wei, M. C. Tamargo, M. Tadic and F. M. Peeters, "Optical Aharonov-Bohm effect in stacked type-II quantum dots," Phys. Rev. B **76** 035342 (2007).

[6] I. R. Sellers, V. R. Whitesides, I. L. Kuskovsky, A. O. Govorov and B. D. McCombe, "Aharanov-Bohm excitons at elevated temperatures in type-II ZnTe/ZnSe quantum dots," Phys. Rev. Lett. **100**, 136405-1-4 (2008).

[7] J. Costa e Silva, A. Chaves, J. A. K. Freire, V. N. Freire and G. A. Farias, "Theoretical investigation of excitons in type-I and type-II $Si/Si_{1-x}Ge_x$ quantum wires," Phys. Rev. B **74**, 085317-1-6 (2006).

DOE Sponsored Publications in 2010-2011

Qiang Zhang, Aidong Shen, Igor L. Kuskovsky, and Maria C. Tamargo, "Role of magnesium in band gap engineering of sub-monolayer type-II ZnTe quantum dots embedded in ZnSe" J. Appl. Phys. (2011) DOI:10.1063/1.3611418

Bidisha Roy, Aidong Shen, Maria C. Tamargo, and Igor L. Kuskovsky, “Effects of Varying MBE Growth Conditions on Layered Zn-Se-Te Structures” J. Elect. Mat., **40**, 1775 (2011) DOI: 10.1007/s11664-011-1690-1

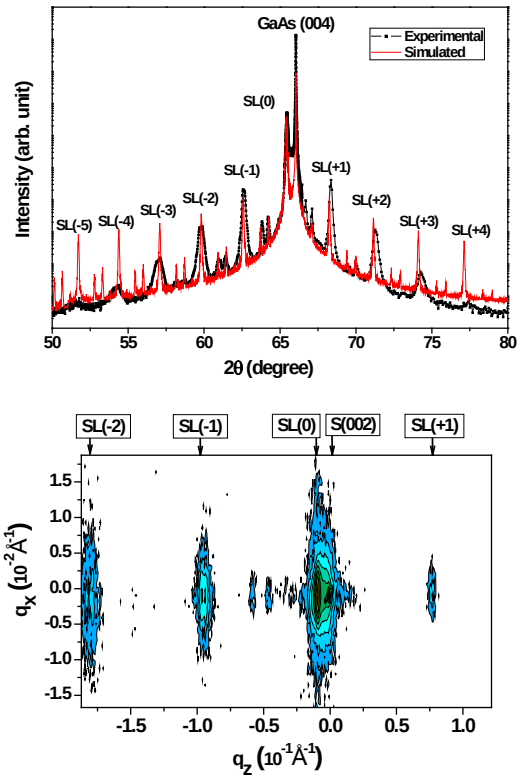

FIGURE 1 **top:** The experimental and simulated ω-2θ curves for (004) reflection for ZnMgTe/ZnSe type II QD structure. **Bottom:** The reciprocal space map for (002) reflection of the same structure.

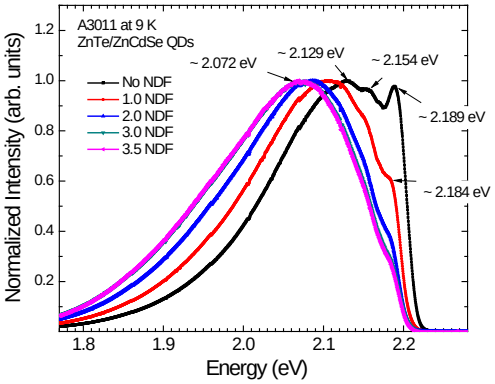

FIGURE 3 Excitation intensity dependent high and low energy peak positions for a ZnTe/ZnCdSe type II QD structure

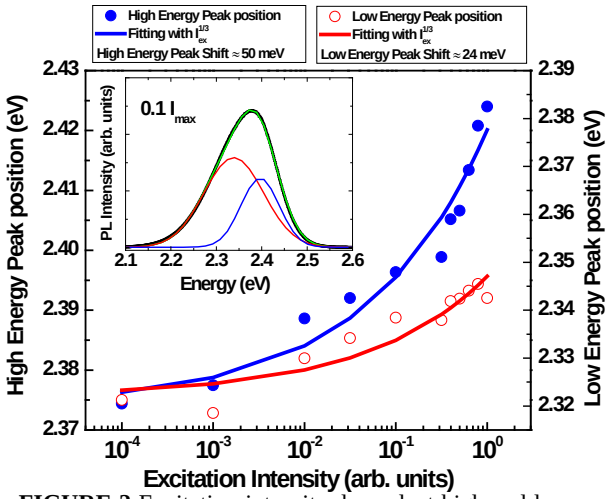

FIGURE 2 Excitation intensity dependent high and low energy peak positions (inset shows that the photoluminescence spectrum for 0.1Imax consists of two bands at 2.34 eV and 2.4 eV) for a ZnMgTe/ZnSe type II QD structure.

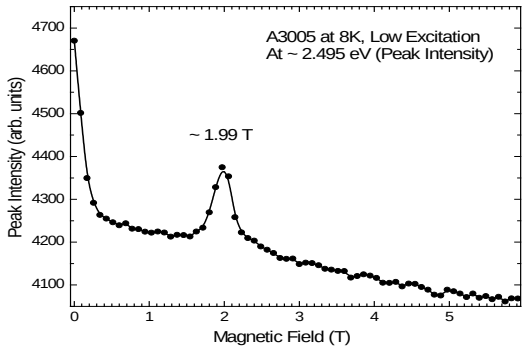

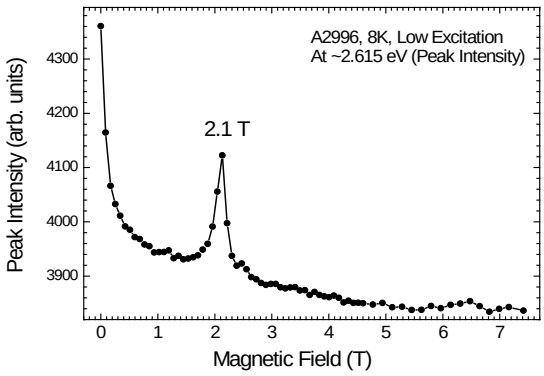

FIGURE 4 Oscillation of the PL peak intensity as a function of the magnetic field for two ZnTe type-II QD samples, indicative of the QD nature of the features.

Plasmonic Nanostructures Integrated with Semiconductor Light Emitting Materials for Enhanced Efficiency and Functionality

R. Paiella* and T. D. Moustakas
Department of Electrical Engineering and Photonics Center, Boston University, Boston, MA 02215
** Phone: 617-353-8883, Fax: 617-353-1283, Email: rpaiella@bu.edu*

1. Program Scope

This project is focused on the development and characterization of novel plasmonic nanostructures integrated with semiconductor photonic materials, and designed to engineer their radiative properties for enhanced efficiency and functionality. The specific materials platform employed is the family of nitride semiconductors InGaN and AlGaN, whose energy bandgap can be tuned across the visible and ultraviolet spectrum by varying the alloy composition. Consequently, these materials are technologically important for a wide range of optoelectronic device applications, including LEDs for solid-state lighting.

The key idea behind this research is the ability of plasmonic excitations to increase the spontaneous emission rate of nearby light emitters, by virtue of their highly confined electromagnetic fields and large densities of optical modes [1]. As a result, metallic nanostructures can be used to enhance the luminescence yield of light-emitting materials, provided that their geometry allows for efficient scattering of the excited plasmonic modes into radiation. Similar structures can also be designed to simultaneously control the far-field properties of the radiated light, including their degree of collimation, direction of propagation, and polarization state. In our work, we have used this basic idea to demonstrate strongly enhanced near-green light emission from InGaN/GaN quantum wells (QWs), using localized surface plasmon resonances (LSPRs) – and more recently lattice surface modes (LSMs) – supported by periodic arrays of Ag nanoparticles (NPs). More complex structures, involving coupled metallic films and NP arrays, have also been developed and investigated, which provide additional degrees of freedom for the near- and far-field control of semiconductor light emitters.

2. Recent Progress

<u>Localized surface plasmon resonances in non-diffracting Ag nanoparticle arrays</u>

Several square-periodic arrays of Ag nanocylinders were fabricated using electron-beam lithography on the top surface of InGaN/GaN multiple-QW samples grown by molecular beam epitaxy. A schematic cross-sectional view of the resulting device geometry is shown in Fig. 1(a). To ensure strong coupling between the QW excitons and the array plasmonic excitations, no additional cap layer was grown over the QWs, which therefore lie within the near field of the NPs. The QWs emission spectrum is centered around 495 nm, near the green spectral region which is particularly important from a technological standpoint due to the lack of efficient LEDs emitting at these wavelengths.

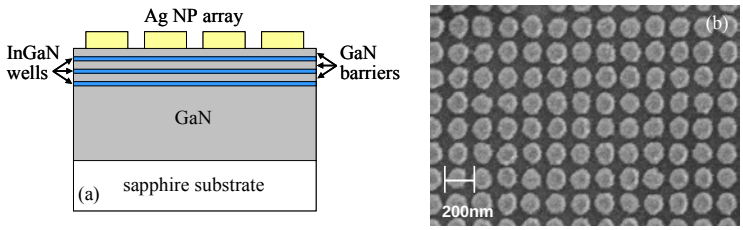

Fig. 1. (a) Schematic cross-sectional view of a NP-coated QW sample (not drawn to scale). (b) SEM image of a square-periodic array of Ag NPs fabricated by electron-beam lithography on GaN.

In Fig. 1(b) we show an SEM image of a representative NP array. Initially, the array period was kept below the wavelength of the emitted light in the semiconductor substrate, so that no diffractive coupling among the NPs could be excited and the array response is dominated by the NPs LSPRs, possibly

modified via near-field interactions [2]. To demonstrate plasmon-enhanced QW light emission, cw and time-resolved photoluminescence (PL) measurements were carried out using arrays of different geometrical parameters, i.e., different NP diameter D, NP height H, and array period P [3].

Representative results are shown in Fig. 2, for an array with D =120 nm, H =55 nm, and P =160 nm. In Fig. 2(a) we show two PL spectra measured from an uncoated region of the QW sample (blue line) and from the region underneath the array (red line). Proximity to the NPs clearly results in a substantial increase in PL peak intensity, by a factor of about 2.8 in this case. In Fig. 2(b) the blue and red lines are the measured time-resolved PL signals from the uncoated QWs and from underneath an identical array, respectively. A pronounced decrease in the exciton recombination lifetime is observed in going from the bare QWs to the array-coated region, from 123 to 74 ps based on the fitting curves shown in the figure.

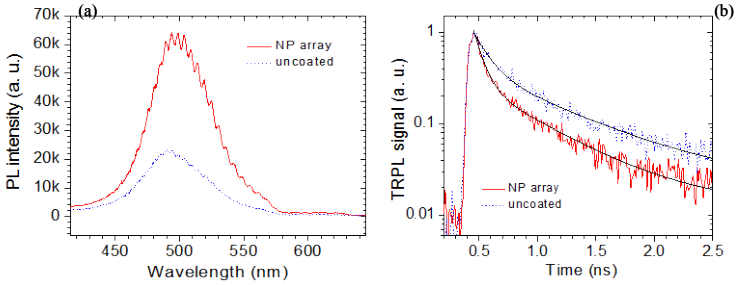

Fig. 2. PL spectra (a) and time-resolved PL (TRPL) signals (b) measured from an uncoated region of the QW sample under study (blue lines) and from the region underneath a Ag NP array (red lines).

These observations are in full agreement with a picture of plasmon-enhanced light emission. Due to the spatial proximity and relatively close spectral match between the QW excitons and the NP plasmonic excitations, efficient recombination via LSPR emission occurs in the sample region below the array, and the PL decay lifetime is correspondingly shortened. As a result, fewer carriers are "wasted" through nonradiative recombination processes and the internal quantum efficiency is enhanced. A sufficiently large fraction of the emitted LSPRs are then scattered by the NPs into radiation, leading to an overall increase in PL intensity.

The measured PL-intensity enhancement factors were also found to exhibit a strong dependence on the NP dimensions [3], underscoring the importance of geometrical tuning to optimize the various tradeoffs associated with this application. In particular, as the NP diameter D is increased the array plasmonic resonance red-shifts away from the QW emission wavelength, and therefore the exciton/LSPR resonant coupling decreases. At the same time, larger NPs feature larger plasmonic scattering efficiency, so that more and more of the excited LSPRs can be scattered into radiation as opposed to being absorbed in the metal. An optimum value of D therefore exists, which in the present case was found to be about 120 nm. Furthermore, the use of taller NPs was shown to provide a more favorable tradeoff between the aforementioned requirements of strong exciton/LSPR coupling and efficient LSPR scattering, consistent with the predictions of a previous study carried out under this grant [4]. In fact, a monotonic increase in PL-intensity enhancement with increasing NP height H (up to about 3.2 for H =100 nm) was observed.

Lattice surface modes in diffracting Ag nanoparticle arrays

We have also demonstrated plasmon-enhanced light emission using arrays with periods P comparable to or larger than the QW emission wavelength in the semiconductor λ_{em} [5], where strong diffraction of the emitted light can occur. In particular, when $P \approx \lambda_{em}$ some of the first-order diffracted light radiates at grazing angles (i.e., in the plane of the array). As a result, large plasmonic oscillations can be excited in each NP by the in-phase addition of the incident light and the light diffracted by all the other NPs in the array. This phenomenon produces a strong LSM resonance of mixed plasmonic and photonic character

[6], which can be expected to be particularly favorable in the context of enhanced light emission due to its large scattering efficiency and extended nature across the plane of the QWs.

Experimental results supporting this expectation are shown in Fig. 3(a), where the red lines are the PL spectra measured with four arrays of equal NP height H (55 nm) and equal nearest-neighbor spacing S (40 nm), but different periods P in the range of 200 to 340 nm. The blue lines are simultaneously measured emission spectra from nearby uncoated regions of the same sample. As shown in the figure, the plasmon-enhanced PL intensity is largest when the array period is about 240 nm, close to the QW emission wavelength in the semiconductor (about 225 nm, based on an estimated refractive index of 2.2). The corresponding increase in peak emission relative to the uncoated-QW case is 4.8×, which is significantly larger than the enhancement values measured with the non-diffracting arrays of the previous section.

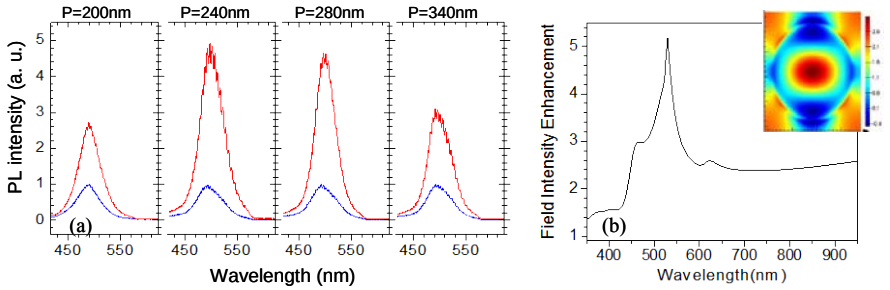

Fig. 3. (a) PL spectra measured with NP arrays of different period P (red lines) and from nearby uncoated QWs (blue lines). (b) Average field-intensity enhancement and (inset) electric-field distribution produced by the P=240-nm array in the plane of the QWs.

The key role played by LSMs in the arrays of Fig. 3(a) was confirmed via numerical simulations based on the finite-difference time-domain (FDTD) method. In particular, we found that the electric-field-intensity enhancement produced by the NPs in the plane of the QWs is dominated by a strong peak at the LSM resonance wavelength [e.g., about 500 nm in free space for P = 240 nm, as shown in Fig. 3(b)]. At this wavelength, the electric-field distribution in the same plane also features a complex pattern indicative of strong diffraction coupling among the NPs [e.g., see inset of Fig. 3(b), where one unit cell of the array, centered about a NP, is shown]. The particularly large PL intensities obtained with these arrays are mostly due to this strong field-intensity enhancement highly delocalized across the plane of the QWs.

Hybrid plasmonic resonances in coupled Ag thin-film/nanoparticle-array systems

More recently, we have also investigated the design and fabrication of the coupled thin-film/NP-array geometry shown schematically in Fig. 4(a), which consists of a nanoscale Ag layer and a square-periodic array of Ag nanocylinders separated by a thin dielectric (ZnS) film. Light emission in the near-field of this geometry involves the excitation of propagating surface plasmon polaritons (SPPs) on the surfaces of the Ag film, which are then diffractively scattered into radiation by the NP array. An important advantage of this approach is that it combines the uniform area coverage of continuous films with the efficient plasmonic scattering of NPs. Furthermore, it provides a large design parameter space that can be exploited to enable novel functionalities such as beam collimation and steering.

The plasmonic excitations of these complex nanostructures include propagating SPPs associated with even and odd charge-density waves in the Ag film, LSPRs of the NP array, and hybrid modes involving a superposition of SPPs and LSPRs [7]. To illustrate, the solid lines in Fig. 4(b) are the plasmonic dispersion curves of a specific coupled thin-film/NP-array geometry (computed via FDTD simulations), showing a clear anticrossing between propagating and localized modes indicative of strong coupling. These dispersion curves can be experimentally mapped by measuring the normal-incidence transmission spectra of otherwise identical systems with varying array period P, and plotting the energy of the measured transmission minima versus array wavevector $2\pi/P$. The results of these measurements for the

geometry of Fig. 4(b) are shown by the symbols in the same figure. The relative good agreement with the theoretical dispersion curves illustrates our ability to properly design and fabricate these systems.

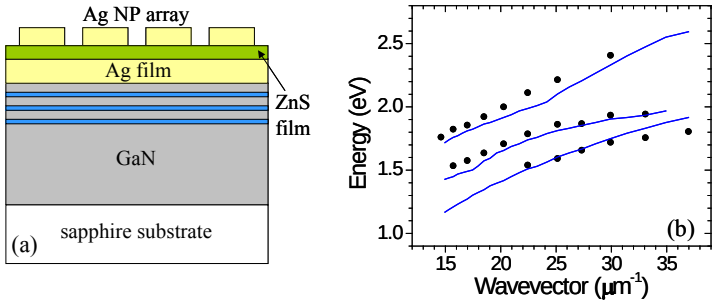

Fig. 3. (a) Schematic cross-sectional view of a coupled Ag thin-film/NP-array system. (b) Calculated plasmonic dispersion curves (solid lines) and measured resonance energies (symbols) of the geometry of (a) with 25-nm Ag-film thickness, 75-nm ZnS-film thickness, 30-nm NP height, and 100-nm NP diameter.

3. Future Plans

Future activities will focus on the use of similar plasmonic nanostructures to engineer the far-field properties of nitride-based light-emitting samples. For example, the coupled thin-film/NP-array systems just described will be used to demonstrate plasmon-enhanced PL and simultaneously beam collimation. More complex arrays, involving asymmetric unit cells, will also be designed and fabricated to enable unidirectional beam steering, a novel functionality for LED active materials with potentially significant applications in the area of smart lighting. Furthermore, we will continue ongoing efforts to integrate plasmonic nanostructures within (as opposed to on top of) the light-emitting materials using epitaxial overgrowth, which will allow us to demonstrate similar plasmonic effects, including plasmon-enhanced electroluminescence, with more realistic LED device geometries.

4. References

[1] W. L. Barnes, J. Mod. Opt. **45**, 661 (1998).

[2] C. L. Haynes, A. D. McFarland, L. L. Zhao, R. P. Van Duyne, G. C. Schatz, L. Gunnarsson, J. Prikulis, B. Kasemo, and M. Käll, *J. Phys. Chem. B* **107**, 7337 (2003).

[3] J. Henson, E. Dimakis, J. DiMaria, R. Li, S. Minissale, L. Dal Negro, T. D. Moustakas, and R. Paiella, Opt. Express **18**, 21322 (2010).

[4] J. Henson, J. DiMaria, and R. Paiella, J. Appl. Phys. **106**, 093111 (2009).

[5] J. Henson, J. DiMaria, E. Dimakis, T. D. Moustakas, and R. Paiella, in preparation.

[6] E. M. Hicks, S. S. Zou, G. Schatz, K. Spears, R. Van Duyne, L. Gunnarsson, T. Rindzevicius, B. Kasemo, and M. Käll, Nano Lett. **5**, 1065 (2005).

[7] Y. Chu and K. B. Crozier, Opt. Lett. **34**, 244 (2009).

5. Publications related to this project over the last two years

J. Henson, J. DiMaria, and R. Paiella, "Influence of nanoparticle height on plasmonic resonance wavelength and electromagnetic field enhancement in two-dimensional arrays," J. Appl. Phys. **106**, 093111 (2009).

J. Henson, J. C. Heckel, E. Dimakis, J. Abell, A. Bhattacharyya, G. Chumanov, T. D. Moustakas, and R. Paiella, "Plasmon enhanced light emission from InGaN quantum wells via coupling to chemically synthesized silver nanoparticles," Appl. Phys. Lett. **95**, 151109 (2009).

J. Henson, E. Dimakis, J. DiMaria, R. Li, S. Minissale, L. Dal Negro, T. D. Moustakas, and R. Paiella, "Enhanced near-green light emission from InGaN quantum wells by use of tunable plasmonic resonances in silver nanoparticle arrays," Opt. Express **18**, 21322 (2010).

R. Paiella, J. Henson, J. DiMaria, E. Dimakis, R. Li, S. Minissale, L. Dal Negro, and T. D. Moustakas, "Plasmon-enhanced near-green light emission from InGaN/GaN quantum wells," to be published in ECS Transactions **16**, Sept 2011.

Heteroepitaxial science of polar, semipolar and nonpolar (In)GaN

B. Leung, C. Yerino, Y. Zhang, and J. Han[1]
Department of Electrical Engineering, Yale University, New Haven, CT
Michael E. Coltrin
Sandia National Laboratories, Albuquerque, NM

Program Scope

Over the past two decades III-N heteroepitaxy has been carried out in largely an empirical manner. This program aims to establish a scientific and coherent model over a diverse range of heteroepitaxial phenomena occurred in III-N growth, from nucleation to coalescence, on a variety of crystallographic planes. A novel technique, differential selective area growth (Δ-SAG), is proposed as an accurate yet flexible method to monitor and record growth kinetics that determine the microstructural and morphological qualities. We also plan to demonstrate an active and effective control of the dynamic process of heteroepitaxy through the use of intrinsic and extrinsic morphactants, designed to alter the anisotropy of growth kinetics, to create new dimensions and a new paradigm in heteroepitaxial control that is at the heart of contemporary production of solid-state lighting devices.

Recent Progress

A. Mapping out kinetic Wulff plots for GaN MOCVD growth

This work represents a comprehensive attempt to correlate the heteroepitaxial dynamics in experiments with fundamental principles in crystal growth using the kinetic Wulff plot (or *v*-plot). We take into account the drastic asymmetry between the Ga-polar and the N-polar "hemispheres" that we have determined in the construction of the 3D *v*-plot and demonstrate that the comprehensive *v*-plot provides crucial insights to unlock the complex heteroepitaxial dynamics. . We have identified cusp points (local minima along all the directions) at (0001), {10$\underline{1}$1}, {11$\underline{2}$0}, {10$\underline{1}$0}, and (000$\underline{1}$). We have also included the measured saddle points determined by the concave growth fronts in the inner ring of a designed SAG mask pattern. Given the different bonding configurations and atomic arrangements of each plane, it should be no surprise that the growth rates along different directions, and consequently the 3D *v*-plot, depend strongly on the local stoichiometry of the reactants during growth. *These 3D v-plots can be considered "finger prints" of a particular growth condition or procedure (e.g., flow modulation, co-doping, etc.) that can provide insights (with platform-insensitive generality) to a wide range of observed effects during heteroepitaxy.*

B. Application of kinetic Wulff plot to heteroepitaxial growth

The minima (cusps, corresponding to the slowest-growing planes) on a 3D *v*-plot determine the shape evolution of a convex growth front, a phenomenon known for more than a century. Convex growth is typically encountered during the nucleation stage of growth, with the formation of islands bound by cusp planes (Fig 2, for example). The present work sheds light on less-understood coalescence stage, in which the majority of growth collision-fronts possess a concave nature, along either the in-plane or the out-of-plane directions with respect to the film growth plane [Fig. 1 (b) and (c)]. The concave growth fronts are formed when neighboring islands, grains, or domains (with convex facets) come into contact.

The following procedure, illustrated in Fig 1, can be applied to deduce the needed information regarding the *concave* growth between two coalescing facets: (i) in the 3D *v*-plot, plot the two surface-normal vectors that are associated with the two coalescing facets, (ii) slice the 3D *v*-plot with a plane

[1] jung.han@yale.edu

defined by the two vectors in (i) and obtain contour *P* at the intersection of the 3D *v*-plot with the slicing plane, (iii) find the *maxima* between the two vectors' ends on the 2D *v*-plot contour *P* of the sliced 3D *v*-plot, which are responsible for the *concave* growth between the two surface-normal orientations, (iv) at the maxima, slice the 3D *v*-plot with planes that are *orthogonal* to the 2D contour *P* and pass the origin of the 3D *v*-plot. The intersections of the 3D *v*-plot with the slicing planes give 2D *v*-plot contours *Q*, and (v) find the nearby *minima* on the 2D *v*-plot contours *Q*, which are the *saddle* points on the 3D *v*-plot defining the emerging fast-growing facets between the coalescing facets. If only one such fast-growing facet is found between the two coalescing facets, the concave growth front will be continuously *curved* (not faceted) [Fig. 1(c)] until it is completely filled. But if two or more fast-growing facets are available within the angular span, the coalescence will proceed with facetted planes defined by the two fast-growing planes. *This procedure represents a first rigorous methodology in correlating 3D v-plot with heteroepitaxial dynamics.*

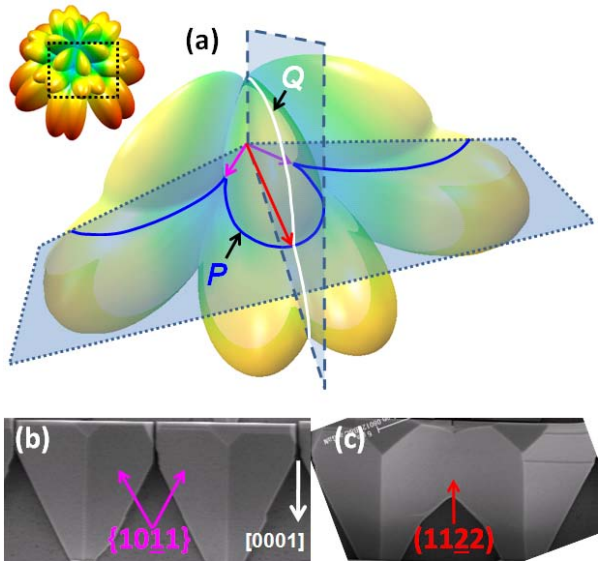

Fig. 1 (a) A magnified portion (marked out by the dotted square) of the kinetic Wulff plot and a schematic presentation of the procedure in determining the emerging facet (11$\underline{2}$2) during the coalescence of two {10$\underline{1}$1} facets. SEM images of two neighboring *a*-plane GaN SAG mesas right before (b) and during the coalescence (c). The two {10$\underline{1}$1} facets before the coalescence and the (11$\underline{2}$2) emerging between the two {10$\underline{1}$1} facets are marked out.

C. Modeling and Simulation of Morphology Evolution

A unique component in this program is the coupling between experimental study and modeled computation of crystal growth. One of us (MC at SNL) is developing modeling and simulation tools to help understand the GaN facet-dependent growth kinetics and morphology evolution observed in our Delta-SAG experiments. To date he has developed a crystal growth simulation code, illustrated in Figures . The model can handle an arbitrary number of crystal facets, and takes as input an initial geometry and growth velocities of each facet.

The initial model is limited to growth of convex crystal shapes ("outward growth"), which is simpler than the more complex geometric evolution seen in concave growth, which has been a focus in much of our experimental work. We are currently working on a new computational capability to model the evolution of arbitrary convex or concave geometries using a "level-set" numerical approach.

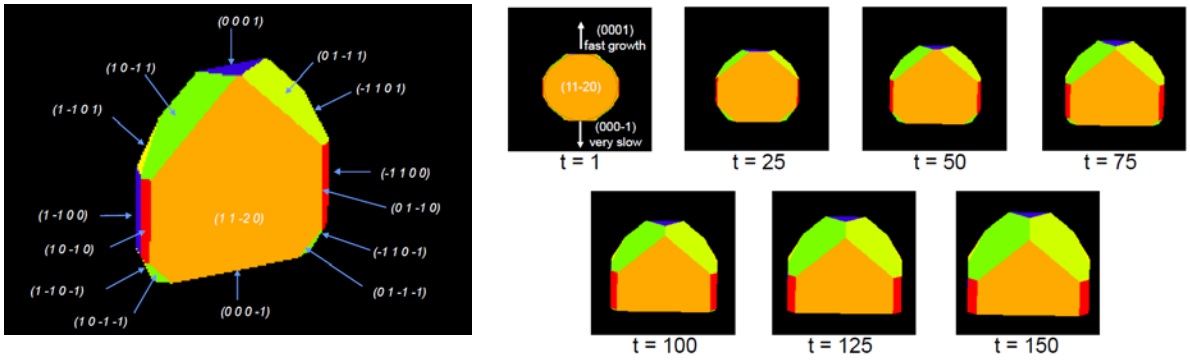

Fig. 2 (Left) the facets identified as minimums on the v-plot that bound a non-polar, a-plane SAG island. (Right) Simulation of

the shape evolution of SAG growth from a circular opening on non-polar a-plane using v-plot information complied experimentally.

D. Orientation-controlled heteroepitaxy - defect reduction and semipolar LED

Semipolar and nonpolar LEDs have been aggressively pursued worldwide since 2000. Very promising results in LDs and LEDs, in some cases superior to their c-plane counterparts, have been demonstrated on bulk, HVPE-grown substrates. However, these developmental efforts and the great potentials of semipolar and nonpolar orientations are bottlenecked by the very limited quantity of HVPE wafers. Heteroepitaxy of semipolar and nonpolar GaN on sapphire, be it planar or with epitaxial lateral overgrowth (ELO), suffers from a high density of stacking faults. In the past two years we have developed an orientation-controlled epitaxy (OCE) procedure in selectively growing c-plane GaN obliquely from the sidewall of trench-etched r-plane substrates (the elongated block within the trapezoids with the growth direction [0001] labeled with an arrow in Fig 3a), to produce stacking-fault free semipolar GaN upon coalescence (Fig 3a, the top surface) on sapphire substrates that can be mass-

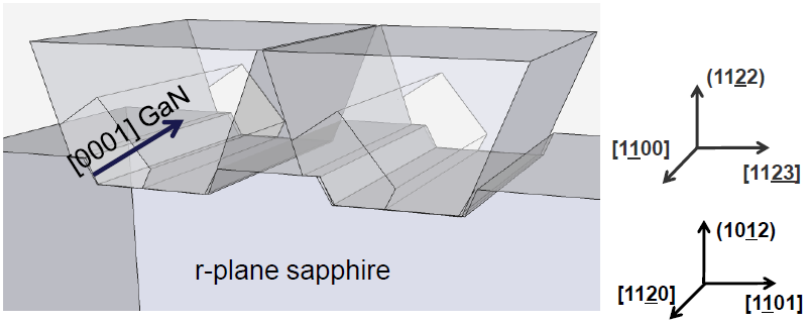

Fig 3a. 3D schematic drawing illustrating the selective, inclined growth of c-GaN off the side wall of trench-etched r-plane sapphire to produce semipolar (11$\bar{2}$2) GaN with very low defect densities.

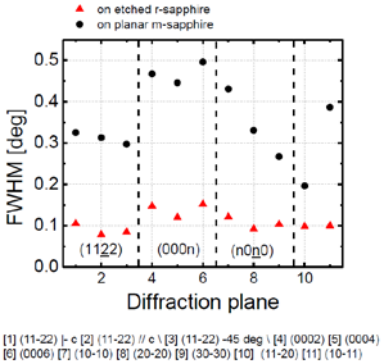

[1] (11-22) |- c [2] (11-22) // c \ [3] (11-22) -45 deg \ [4] (0002) [5] (0004) [6] (0006) [7] (10-10) [8] (20-20) [9] (30-30) [10] (11-20) [11] (10-11)

Fig 3b. FWHM of rocking curves over 11 diffraction planes for OCE-grown (red) and conventional (black) (11$\bar{2}$2) GaN.

manufactured. Using x-ray diffraction rocking curves over a broad range of diffraction planes (Fig 3b), we have confirmed that the microstructural quality of the (11$\bar{2}$2) GaN on *r*-sapphire is comparable to those used in conventional c-plane LEDs. The measured defect densities are below $10^4 cm^{-1}$ and in the mid $10^8 cm^{-2}$ for stacking faults and dislocations, respectively, the lowest values reported for heteroepitaxial semipolar GaN to the best of our knowledge.

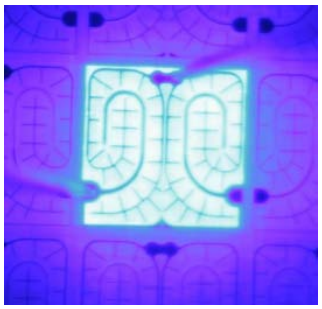

Fig 4a. Image of a (1122) LED on OCE template.

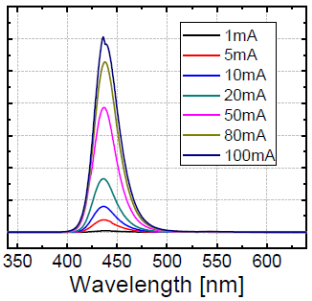

Fig 4b. LED spectrum under different injection current levels.

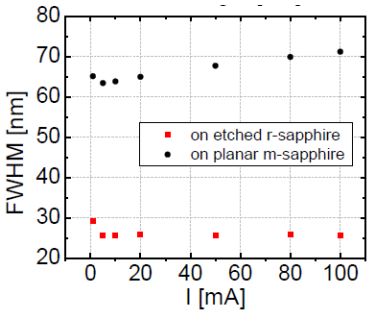

Fig 4c. Comparison of EL peak width for OCE (red) and conventional (black) semipolar LEDs.

We have attempted LEDs on such templates using the standard c-plane growth conditions (Fig 4a). Preliminary result reveals that EL spectrum shows a single-peak emission (Fig 4b), with a much reduced linewidth (~25 nm, Fig 4c) as compared to semipolar LEDs on planar wafer (~70 nm, Fig 4c), characteristically similar to LEDs fabricated on HVPE bulk wafers. We believe that our work at Yale has laid a unique foundation warranting a serious and in-depth effort in uncovering the potential of semipolar LEDs.

Future Plans

- Nanoscale selective area growth (Nano-SAG): we will extend the study of selective area growth into nanoscale by employing nanolithography to explore III-nitride SAG in the spatial scale of 50nm to 500 nm. As the lateral dimension of epitaxy becomes comparable and less than the layer thickness, we expect enhanced interactions between structural defects and surfaces, and between facets and the edge of nanomasks. We will apply SEM and TEM to derive kinetic and thermodynamic information.
- Wulff study of InGaN: The ability to prepare InGaN active regions in a non-planar and nano-tailored fashion will provide unprecedented opportunities in defect reduction, polarization control, heteroepitaxial stress relaxation, and a new way to manage the incorporation of Indium in InGaN. Facet-dependence and spatial variation of Indium incorporation will be mapped out to produce a deterministic guide for the OMVPE growth of InGaN.
- Modeling of Morphology Evolution: We are currently working on a new computational capability to model the evolution of arbitrary convex or concave geometries using a "level-set" numerical approach. This will be an important step toward understanding the continual dynamics in island formation and coalescence in heteroepitaxy.

DOE Sponsored Publications in 2009-2011 from Current Grant

- Q. Sun and J Han, *Heteroepitaxy of Nonpolar and Semipolar GaN*, to appear as a book chapter in Springer Series "Advances in GaN and ZnO-based Thin Film, Bulk and Nanostructured Materials and Devices", edited by S. J. Pearton (2011). (Study and application of kinetic Wulff plot is supported by this award, DOE DE-SC0001134; growth of non-polar and semipolar GaN and devices were supported by DOE DE-FC26-07NT43227.) **(Invited)**
- Q. Sun, et al., *Understanding and Controlling Heteroepitaxy with the Kinetic Wulff plot: a case study with GaN*, in press, J. Appl. Phys. (2011) (solely supported by this award, DOE DE-SC0001134)
- C. Yerino, et al., *Morphactant effect in MOCVD growth of GaN*, submitted to J. Crystal Growth (2011) (solely supported by this award, DOE DE-SC0001134)
- B. Leung, et al., *Design of heteroepitaxial growth of nonpolar and semipolar GaN by the kinetic Wulff plot,* submitted to Semicond. Sci. Technol. (2011) (solely supported by this award, DOE DE-SC0001134) **(Invited)**
- B. Leung, et al., *Growth evolution and microstructural characterization of semipolar (11-22) GaN selectively grown on etched r-plane sapphire,* submitted to J. Crystal Growth (2011) (The shaping and orientation control during patterned heteroepitaxy work is supported by this award, DOE DE-SC0001134; material characterizations were supported by DOE DE-FC26-07NT43227.)
- B. Leung, et al., *Optical emission characteristics of semipolar InGaN light emitting diodes by planar and orientation controlled heteroepitaxy*, submitted to Semicond. Sci. Technol. (2011) (The shaping and orientation control during patterned heteroepitaxy work is supported by this award, DOE DE-SC0001134; device fabrication and characterizations were supported by DOE DE-FC26-07NT43227.)
- C. Yerino, et al., Shape Transformation of Nanoporous GaN by Annealing: From Buried Cavities to Nanomembranes, Appl. Phys. Lett. 98, 251910 (2011) (solely supported by this award, DOE DE-SC0001134)
- C. Yerino, et al., GaN Kinetic Wulff Plot: Trends, Principles, and Applications, **Keynote Talk** at International Workshop on Nitride Semiconductors (IWN2010), Tampa, Florida, October 2010. (solely supported by this award, DOE DE-SC0001134)

Solid-State Lighting Science Energy Frontier Research Center

Michael E. Coltrin, Co-Director
mecoltr@sandia.gov
Sandia National Laboratories, Albuquerque, NM 87185

The overarching theme of our EFRC is the *exploration of energy conversion in tailored photonic structures*, a theme that is at the heart of solid-state lighting and other energy technologies, and a theme of major scientific interest as discovery-class research. We have organized the EFRC into three scientific Thrusts. Within each Thrust are specific research projects, which we refer to as "Challenges."

Our first scientific Thrust is: **"Competing Energy Conversion Routes in Light-Emitting InGaN."** In this Thrust, we are studying wide-bandgap materials and the complex interplay between their defect and luminescent properties. The first Challenge within this Thrust is "Point Defects in InGaN: Microscopic Origin and Influence on Luminescence," in which we seek to understand the relationship between specific material defects, their dependence on various synthesis conditions, and the production or suppression of InGaN luminescence. The second Challenge is "Radiative and Non-Radiative Processes in the High-Carrier-Density Regime," where we seek to understand radiative efficiency, which is due to the competition between radiative pathways and undesirable non-radiative pathways that produce heat instead of light. For InGaN materials, there is a complex array of potential non-radiative processes that presently limit the radiative efficiency but are very poorly understood.

Our second scientific Thrust is **"Beyond Spontaneous Emission."** In this Thrust, we are studying energy conversion routes in subwavelength photonic structures in which electromagnetic fields are stronger or more localized, and photonic densities of states can be more exquisitely controlled, than in structures typical of current solid-state-lighting technology. Such extreme conditions are scientifically interesting in their own right, as vehicles for the science of coherent, many-body phenomena. And, as new energy conversion routes are explored, entirely new solid-state-lighting materials structures may arise from their understanding. The first Challenge area is "Strongly Coupled Exciton-Photon Systems," in which we are exploring strong coupling between excitons and photons in optical microcavities containing active wide-bandgap GaN-based materials. The second Challenge is "Surface Plasmonic Intermediaries to Exciton-Photon Interactions," in which we are exploring the possibility that surface plasmons, with their strong confinement and greatly enhanced local electromagnetic fields, might someday be useful as intermediaries in the energy conversion process from excitons to free-space photons.

Our third scientific Thrust is **"Beyond 2D."** In this Thrust, we study energy conversion routes in 1D and 0D nanostructures that go beyond the conventional 2D planar heterostructures typical of solid-state lighting technology. These nanostructures are scientifically interesting in their own right, as vehicles for the science of the very small, and for studying how energy quantization and conversion are influenced by dimensionality and proximity to surfaces and interfaces. Also, because of fundamental differences in how lower dimensional structures are synthesized and how they accommodate lattice mismatch and strain, these structures allow study of defect-mediated energy conversion routes different from those occurring in traditional 2D heterostructures. The first technical Challenge in this Thrust is "Nanowires: Synthesis and Properties of Radial Heterostructures," in which we explore the relationship between the synthesis and resulting composition and microstructure of 1D nanowires, with an emphasis on developing the ability to tailor the densities of particular kinds of point and extended defects. The second Challenge is "Nanodots: Nonlinear Luminescence Dynamics," in which conversion of charged carriers into photons can be extremely efficient, but is also strongly influenced by particle size, microstructure, surface functionalization, and chemical environment.

Throughout this EFRC, our emphasis is on fundamental science enabled by integrated, interdisciplinary capabilities: linking state-of-the-art nano-materials design, synthesis and characterization; linking theory and experiment; and linking scientific understanding of isolated phenomena studied in model systems with empirical observations that are found in relevant technology platforms. Advances in nano-fabrication and nano-characterization enable such explorations in unusual nanostructure compositions and instantiations, and under experimental conditions specifically tailored to expose particular energy conversion processes. Building on our strengths in tool creation and allied technologies, we also place an emphasis on research tools (synthesis, characterization, and modeling) that both draw upon science and can be used to enable scientific investigations.

**The Solid-State Lighting Science Energy Frontier Research Center is supported by the U.S. Department of Energy Office of Basic Energy Sciences. Sandia National Laboratories is a multi-program laboratory managed and operated by Sandia Corporation, a wholly owned subsidiary of Lockheed Martin Corporation, for the U.S. Department of Energy's National Nuclear Security Administration under contract DE-AC04-94AL85000.

Publications in Peer-Reviewed Journals (First 2 years of operation)

Carmele, A.; Richter, M.; Chow, Weng W.; and Knorr, A. ANTIBUNCHING OF THERMAL RADIATION BY A ROOM-TEMPERATURE PHONON BATH: A NUMERICALLY SOLVABLE MODEL FOR A STRONGLY INTERACTING LIGHT-MATTER-RESERVOIR SYSTEM, *Phys. Rev. Lett.*, **104**, 156801 (2010). [10.1103/PhysRevLett.104.156801]

Lyo, S. Ken ENERGY TRANSFER FROM AN ELECTRON-HOLE PLASMA LAYER TO A QUANTUM WELL IN SEMICONDUCTOR STRUCTURES, *Phys. Rev. B*, **81**, 115303 (2010). [10.1103/PhysRevB.81.115303]

Schubert, Martin F.; and Schubert, E. Fred EFFECT OF HETEROINTERFACE POLARIZATION CHARGES AND WELL WIDTH UPON CAPTURE AND DWELL TIME FOR ELECTRONS AND HOLES ABOVE GAINN/GAN QUANTUM WELLS, *Appl. Phys. Lett.*, **96**, 131102 (2010). [10.1063/1.3373610]

Tsao, Jeffrey Y.; and Waide, P. THE WORLD'S APPETITE FOR LIGHT: EMPIRICAL DATA AND TRENDS SPANNING THREE CENTURIES AND SIX CONTINENTS, *Leukos*, (2010). [none]

Zhu, D.; Noemaun, A. N.; Schubert, Martin F.; Cho, J.; Schubert, E. Fred; Crawford, Mary H.; and Koleske, Daniel D. ENHANCED ELECTRON CAPTURE AND SYMMETRIZED CARRIER DISTRIBUTION IN GAINN LIGHT-EMITTING DIODES HAVING TAILORED BARRIER DOPING, *Appl. Phys. Lett.*, **96**, 121110 (2010). [10.1063/1.3371812]

Chow, Weng W.; Crawford, Mary H.; Tsao, Jeffrey Y.; and Kneissl, Michael INTERNAL EFFICIENCY OF INGAN LIGHT-EMITTING DIODES: BEYOND A QUASIEQUILIBRIUM MODEL, *Appl. Phys. Lett.*, **97**, 121105 (2010). [10.1063/1.3490232]

Dai, Qi; Shan, Qifeng; Wang, Jing; Chhajed, Sameer; Cho, Jaehee; Schubert, E. Fred; Crawford, Mary H.; Koleske, Daniel D.; Kim, Min-Ho; and Park, Yongjo CARRIER RECOMBINATION MECHANISMS AND EFFICIENCY DROOP IN GAINN/GAN LIGHT-EMITTING DIODES, *Appl. Phys. Lett.*, **97**, 133507 (2010). [10.1063/1.3493654]

Chhajed, Sameer; Cho, Jaehee; Schubert, E. Fred; Kim, Jong Kyu; Koleske, Daniel D.; and Crawford, Mary H. TEMPERATURE-DEPENDENT LIGHT-OUTPUT CHARACTERISTICS OF GAINN LIGHT-EMITTING DIODES WITH DIFFERENT DISLOCATION DENSITIES, *Status Solidi A*, **208**, 947 (2011). [10.1002/pssa.201026668]

Dai, Qi; Shan, Qifeng; Cho, Jaehee; Schubert, E. Fred; Crawford, Mary H.; Koleske, Daniel D.; Kim, Min-Ho; and Park, Yongjo ON THE SYMMETRY OF EFFICIENCY-VERSUS-CARRIER-CONCENTRATION CURVES IN GAINN/GAN LIGHT-EMITTING DIODES AND RELATION TO DROOP-CAUSING MECHANISMS, *Appl. Phys. Lett.*, **98**, 033506 (2011). [10.1063/1.3544584]

Armstrong, Andrew; Crawford, Mary H.; and Koleske, Daniel D. QUANTITATIVE AND DEPTH-RESOLVED INVESTIGATION OF DEEP-LEVEL DEFECTS IN INGAN/GAN HETEROSTRUCTURES, *J. Electron. Mater.*, **40**, 369 (2011). [10.1007/s11664-010-1453-4]

Subramania, Ganesh; Lee, Yun-Ju; and Fischer, Arthur J. SILICON-BASED NEAR-VISIBLE LOGPILE PHOTONIC CRYSTAL, *Adv. Mater. (Weinheim, Ger.)*, **22**, 4180 (2010). [10.1002/adma.201001965]

Miao, Xiaoyu; Brener, Igal; and Luk, Ting Shan NANOCOMPOSITE PLASMONIC FLUORESCENCE EMITTERS WITH CORE/SHELL CONFIGURATIONS, *J. Opt. Soc. Am. B*, **27**, 1561 (2010). [10.1364/JOSAB.27.001561]

Kabuss, Julia; Carmele, A.; Richter, M.; Chow, Weng W.; and Knorr, A. INDUCTIVE EQUATION OF MOTION APPROACH FOR A SEMICONDUCTOR QD-QED: COHERENCE INDUCED CONTROL OF PHOTON STATISTICS, *Phys. Stat. Solidi B*, **248**, 872 (2011). [DOI: 10.1002/pssb.201000851

Passmore, Brian S.; Adams, David C.; Ribaudo, Troy; Wasserman, Daniel; Lyon, Stephen; Chow, Weng W.; and Shaner, Eric A. OBSERVATION OF RABI SPLITTING FROM SURFACE-PLASMON COUPLED CONDUCTION-STATE TRANSITIONS IN ELECTRICALLY-EXCITED INAS QUANTUM DOTS, *Nano Lett.*, **11**, 338 (2011). [10.1021/nl102412h]

Shelton, David J.; Brener, Igal; Ginn, James C.; Sinclair, Michael B.; Peters, David W.; Coffey, Kevin R.; and Boreman, Glenn D. STRONG COUPLING BETWEEN NANOSCALE METAMATERIALS AND PHONONS, *Nano Lett.*,, (2011). [10.1021/nl200689z]

Tsao, Jeffrey Y.; Saunders, Harry D.; Creighton, J. Randall; Coltrin, Michael E.; and Simmons, Jerry A. SOLID-STATE LIGHTING: AN ENERGY ECONOMICS PERSPECTIVE, *J. Phys. D*, **43**, 354001 (2010). [10.1088/0022-3727/43/35/354001]

Haitz, Roland; and Tsao, Jeffrey Y. 'THE CASE' TEN YEARS AFTER AND FUTURE PROSPECTS, *Phys. Status Solidi A*, **208**, 17 (2011). [10.1002/pssa.201190000]

Baird, Lee; Ong, Cp. P.; Cole, R. Adam; Haegel, Nancy M.; Talin, A. Alec; Li, Qiming; and Wang, George T. TRANSPORT IMAGING FOR CONTACT-FREE MEASUREMENTS OF MINORITY CARRIER DIFFUSION IN GAN, GAN/ALGAN, AND GAN/INGAN CORE-SHELL NANOWIRES, *Appl. Phys. Lett.*, **98**, 132104 (2011). [10.1063/1.3573832]

Huang, Jianyu; Zheng, He; Mao, S X; Li, Qiming; and Wang, George T. IN SITU NANOMECHANICS OF GAN NANOWIRES, *Nano Lett.*, (2011). [10.1021/nl200002x]

Li, Qiming; and Wang, George T. STRAIN INFLUENCED INDIUM COMPOSITION DISTRIBUTION IN GAN/INGAN CORE-SHELL NANOWIRES, *Appl. Phys. Lett.*, **97**, 181107 (2010). [10.1063/1.3513345]

Forbes, Tori Z.; Nyman, May; Rodriguez, Mark A.; and Navrotsky, Alex THE ENERGETICS OF LANTHANUM TANTALATE MATERIALS, *J. Solid State Chem.*, **183**, 2516 (2010). [10.1016/j.jssc.2010.08.024]

SYNTHESIS, CHARACTERIZATION, AND INVESTIGATION OF CHARGE SEPARATION AND RECOMBINATION IN CARBON NANOTUBE-QUANTUM DOT NANOSCALE HETEROSTRUCTURES

Xiaohui Peng, Matthew Y. Sfeir, James A. Misewich, and Stanislaus S. Wong
Email: sswong@notes.cc.sunysb.edu
Condensed Matter Physics and Materials Sciences Department
Brookhaven National Laboratory
Upton, NY 11973

Preferred program session topic: I. Function driven materials design.

1. Program Scope

Since their discovery in 1991, carbon nanotubes (CNT)[1] have been the focus of intense interest and potential for significant technological impact that has already been demonstrated, including a demonstration of the world's smallest complementary transistors and a demonstration, from one of the Principal Investigators (PIs), of the world's smallest electrically controllable light source.[2] However, many challenges remain in the synthesis and characterization of the carbon nanotube materials family. Outstanding fundamental chemistry challenges include an enhancement of BNL's synthetic chemistry knowledge that would lead to better-defined control over the nature of carbon nanotubes. Ideally we would like higher purity materials, functionalized nanotubes, control of chirality and electronic structure of nanotubes, and an ability to organize these materials into functional assemblies. In addition, fundamental physical problems include the development of a better understanding of the connection between structure and electronic states. This includes the development of an understanding of excitonic effects, which are expected to be large in quasi 1-d materials. Other challenges include a complete understanding of the emerging optoelectric properties of carbon nanotubes. Since the recently discovered electroluminescence in carbon nanotubes is a physically distinctive method of producing light when compared with conventional semiconductor diode sources (e.g., the nanotube has no impurity doping profile and therefore no depletion field), progress in our fundamental understanding of this process has potential for application in diverse technological areas such as efficient lighting or for photovoltaic applications. Of particular interest are the optoelectronic properties of novel nanotube-quantum dot (CNT-QD) heterostructures, which have been synthesized by one of the PIs.[3, 4] This CNT-QD system combines a 1d system (CNT) with a 0d system (QD) in a new heterostructure in an attempt to combine the attractive charge transport and optical properties of each subsystem to produce a mixed dimensional hybrid with potential for efficient conversion of photons to separated electron and hole pairs for application in solar energy cells. The science of low-dimensional systems has advanced greatly in recent years. However, understanding and controlling the coupling of two low d systems with different dimensionality, especially at molecularly-defined interfaces, presents a new challenge that this research will address.

2. Recent Progress

The unique electronic structure and optical properties of double-walled carbon nanotubes (DWNTs) have rendered them as a key focus material of research in recent

years. However, the incorporation of DWNTs with quantum dots (QDs) into nanoscale composites via a covalent chemical approach as well as the optical properties of the composites has rarely been explored. In particular, we have been interested in this model system as to whether nanomaterial heterostructures can provide efficient pathways for charge separation relative to loss mechanisms such as recombination.

In this specific work,[5] the synthesis of DWNT-CdSe quantum dot (QD) heterostructures using a conventional covalent protocol has been demonstrated. CdSe QDs with terminal amino groups (i.e. using aminoethanethiol, AET) have been conjugated onto the surfaces of oxidized DWNTs by the formation of amide bonds. Moreover, the presence of charge transfer between CdSe quantum dots and DWNTs can account for the disappearance of trapped emission bands and the observation of excitonic luminescence (Figures 1 and 2), as illustrated in steady-state luminescence measurements and images, indicating that the trapped charges were transferred to DWNTs in the DWNT-CdSe QD heterostructure. Hence, we can conclude that chemical conjugation of DWNTs with CdSe plays a significant role in affecting the surface-state emission of the QDs. Importantly, we should note that the interpretation of our results may have been complicated by the presence of multiwalled carbon nanotubes (MWNTs) in our DWNT samples, although the extraneous presence of MWNTs should not influence the validity of our results, as the optical phenomena observed appear to be fundamentally dependent upon and intrinsically coupled to not only the nature of the QD and chemical linkers themselves but also the presence of a nanotube motif itself, as opposed to the actual type of nanotube studied. Thus, while additional experimental and theoretical studies on the effect of chemical functionalization on the properties of DWNTs are still needed, the experimental evidence presented herein suggests that DWNT-QD heterostructures exhibit potential for incorporation into devices such as photovoltaic cells, especially considering the observation of effective charge separation between CdSe and DWNTs.

Recent Progress on Other Projects

Correlating Titania Morphology and Chemical Composition with Dye Sensitized Solar Cell Performance

We have investigated[6] the use of various morphologies, including nanoparticles, nanowires, and sea-urchins of TiO_2 as the semiconducting material used as components of dye-sensitized solar cells (DSSCs). Analysis of the solar cells under AM 1.5 solar irradiation reveals the superior performance of nanoparticles, by comparison with two readily available commercial nanoparticle materials, within the DSSC architecture. The sub-structural morphology of films of these nanostructured materials has been directly characterized using SEM and indirectly probed using dye desorption. Furthermore, the surfaces of these nanomaterials were studied using TEM in order to visualize their structure, prior to their application within DSSCs. Surface areas of the materials have been quantitatively analyzed by collecting BET adsorption and desorption data. Additional investigation using open circuit voltage decay measurements reveals the efficiency of electron conduction through each TiO_2 material. Moreover, the utilization of various chemically distinctive titanate materials within the DSSCs has also been investigated, demonstrating the deficiencies of using these particular chemical compositions within traditional DSSCs.

3. Future Plans

The prototype 0d-1d material we choose to investigate consists of a carbon nanotube with an attached semiconductor quantum dot. There are a number of research tasks that must be performed to determine the potential for efficient charge separation in this heterojunction material. We must learn to rationally synthesize such 0d-1d heterostructures with control over important heterostructure design parameters such as: chemical composition, size, and shape of the nanoscale components, QD-CNT separation, and density of QD functionalization on CNTs. We need to determine the structure, both physical and electronic, of our samples. We will measure the optoelectronic properties of our samples. Finally, the physical structure, electronic structure, and optoelectronic properties must be correlated and used to develop a model for overall system behavior to feedback for heterostructure parameter tuning. Again, a challenge in unraveling the nature of nanomaterials is to make sense of the large diversity of structures generated in even the best syntheses. The importance of a robust synthesis cannot be minimized. For instance, terahertz spectroscopy[7] has been used to determine that the conductivity of nanocrystal hybrid nanostructures, created by growing nanocrystals *in situ* onto acid-modified CNTs (including DWNTs) by solvothermal methods, can be substantially reduced by the presence of electron trapping at surface defect sites, formed during the synthesis process.

The observed unique optical properties of CNT-CdSe composites, due to charge transfer between CNTs and CdSe, appear to be more intrinsically correlated with the surface properties of the actual CdSe QDs as well as the nature of the chemical linkers as opposed to the CNTs themselves. Specifically, we are interested in studying the charge-carrier dynamics within the CNT-QD heterostructures by engineering the properties of QDs and of their surface ligands (i.e. of different linker lengths, numbers, degree of hardness, and functional terminations).

4. References

1. Iijima, S.; Ichihashi, T., Single-shell carbon nanotubes of 1-nm diameter. *Nature* **1993,** 363, 603-604.
2. Misewich, J. A.; Martel, R.; Avouris, P.; Tsang, J. C.; Heinze, S.; Tersoff, J., Electrically Induced Optical Emission from a Single Carbon Nanotube FET. *Science* **2003,** 300, 783-786.
3. Banerjee, S.; Wong, S. S., Synthesis and Characterization of Carbon Nanotube-Nanocrystal Heterostructures. *Nano Lett.* **2002,** 2, (3), 195-200.
4. Peng, X. H.; Chen, J. Y.; Misewich, J. A.; Wong, S. S., Carbon nanotube-nanocrystal heterostructures. *Chemical Society Reviews* **2009,** 38, (4), 1076-1098.
5. Peng, X.; Sfeir, M. Y.; Zhang, F.; Misewich, J. A. a.; Wong, S. S., Covalent Synthesis and Optical Characterization of Double-walled Carbon Nanotube-Nanocrystal Heterostructures. *J. Phys. Chem. C* **2010,** 114, (19), 8766-8773.
6. Santulli, A. C.; Koenigsmann, C.; Tiano, A. L.; DeRosa, D.; Wong, S. S., Correlating Titania Morphology and Chemical Composition with Dye Sensitized Solar Cell Performance. *Nanotechnology* **2011,** 22, (24), 245402/1-13.

7. Jung, G. B.; Myung, Y.; Cho, Y. J.; Sohn, Y. J.; Jang, D. M.; Kim, H. S.; Lee, C.-W.; Park, J., Tetrahertz spectroscopy of nanocrystal-carbon nanotube and -graphene oxide hybrid nanostructures. *J. Phys. Chem. C* **2010,** 114, 11258-11265.

5. Selected DOE-sponsored Publications in 2010-2011 from Current Grant.

- Christopher Koenigsmann, Alexander C. Santulli, Kuanping Gong, Miomir Vukmirovic, Wei-ping Zhou, Eli Sutter, Stanislaus S. Wong, and Radoslav R. Adzic, "Enhanced Electrocatalytic Performance of Processed, Ultrathin, Supported Pd~Pt Core~Shell Nanowire Catalysts", *J. Am. Chem. Soc*., **133(25)**, 9783-9795 (2011).
- Christopher Koenigsmann and Stanislaus S. Wong, "One-Dimensional Noble Metal Electrocatalysts: A New Structural Paradigm for Direct Methanol Fuel Cells", invited Perspective article, *Energy & Environmental Sciences* (cover), **4(4)**, 1161 – 1176 (2011).
- Tae-Jin Park, Andrey A. Levchenko, Hongjun Zhou, Stanislaus S. Wong, and Alexandra Navrotsky, "Shape-dependent surface energetics of nanocrystalline TiO_2", *J. Mater. Chem.*, **20(39)**, 8639-8645 (2010).
- C. Koenigsmann, Wei-ping Zhou, Radoslav R. Adzic, Eli Sutter, and Stanislaus S. Wong, "Size-dependent enhancement of electrocatalytic performance in relatively defect-free, processed ultrathin platinum nanowires", *Nano Letters*, **10(8)**, 2806-2811 (2010).
- X. Peng, Matthew Y. Sfeir, Fen Zhang, James A. Misewich, and Stanislaus S. Wong, "Covalent Synthesis and Optical Characterization of Double-walled Carbon Nanotube-Nanocrystal Heterostructures", *J. Phys. Chem. C*, **114(19)**, 8766-8773 (2010).

An additional 16 sponsored publications in 2010-2011 from current grant.

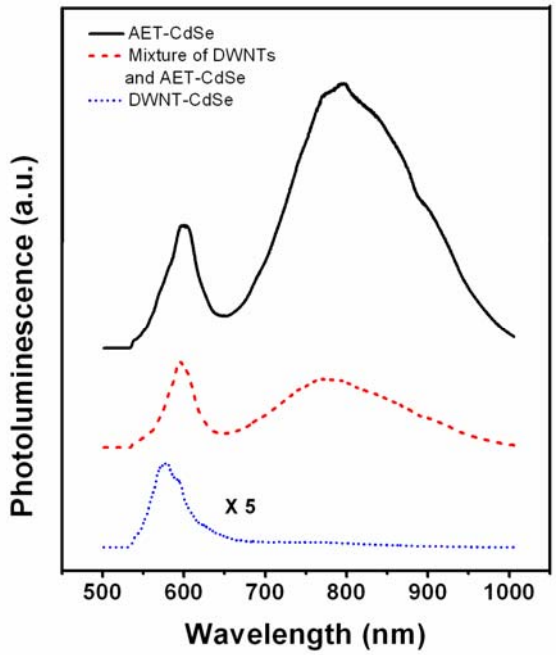

Figure 1. Steady-state photoluminescence spectra of DWNT-CdSe QD heterostructures, a physical mixture of DWNTs and AET-CdSe QDs, and AET-CdSe QDs.

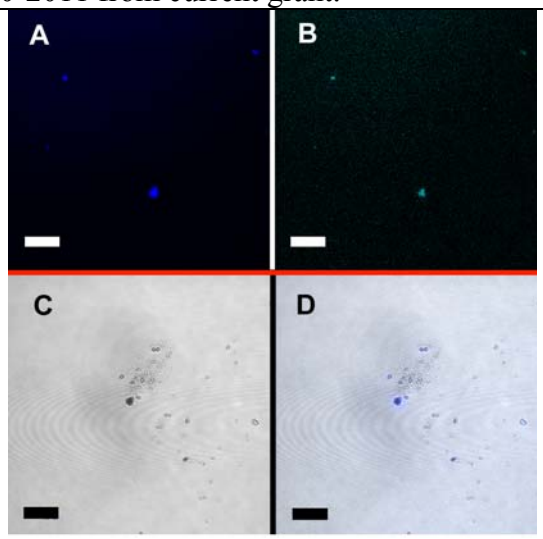

Figure 2. Confocal scanning fluorescence microscopy images of AET-CdSe QDs collected at ca. 600 nm (A) and ca. 800 nm (B). (C) Bright field image of DWNT-CdSe QD heterostructures. (D) Composite, merged image for the DWNT-CdSe QD heterostructure, including (C) and the corresponding fluorescence images collected at both ca. 600 nm and ca. 800 nm. Scale bars are 10 μm.

Novel Materials Preparation and Processing Methodologies I

Synthesis and characterization of RFeAsO based single crystals at ambient pressures

R. W. McCallum and T. A. Lograsso
Ames Laboratory, Ames IA 50014

Program Scope

The growth, control and modification of novel materials in single crystal and polycrystalline form, represent a national core competency that is essential for scientific advancement within and across traditional disciplinary boundaries, and are critical components of the Basic Energy Sciences' mission. In support of this mission, the Novel Materials Preparation and Processing Methodologies strengthen the materials synthesis efforts of the Ames Laboratory. The objective of Novel Materials is to quantify and control processing-structure-property relationships: the basic science of how chemical inhomogeneities and structural defects affect properties of highly responsive materials; advance the ability to synthesize and characterize high purity, high quality materials, primarily in single crystal form; develop unique capabilities and processing knowledge in the preparation, purification, and fabrication of metallic elements and alloys. Single crystals are often required to achieve scientific understanding of the origin of various phenomena, whether from intrinsic or extrinsic origins, to elucidate its properties as well as to evaluate a material's full functionality. Our research objectives are: 1) developing synthesis and processing capabilities that support rapid materials discovery using bulk combinatorial approaches, 2) identifying synthesis protocols for specific novel materials through the rapid development and modification of methods to prepare high quality well-characterized single crystals, and 3) utilizing solidification processing to access metastable states in controlled nanoscale architectures.

Recent Progress

The discovery of high transition temperature (T_c) superconductivity with structural units of (FeAs) layers has attracted extensive attention in the scientific community. Like the cuprates, this series of materials share a common structural feature, in this case the (FeAs) layers. However, in these materials, the planes may be separated by either oxide layers, such as $RO_{1-x}F_x$ in $RFeAsO_{1-x}F_x$ (R = light rare earth element), or metallic layers, such as AE metal in $AE_{1-x}K_xFe_2As_2$ (AE = Ca, Sr, or Ba) and Li in LiFeAs, offering the opportunity to study superconductivity in both oxides and intermetallics in closely related compounds. The preparation of polycrystalline $RFeAsO_{1-x}F_x$ has been plagued by high levels of irreproducibility characterized by large run-to-run variations in phase purity and superconducting fraction. As a result, the research direction the scientific community took was driven by the ability and availability of those material systems where single phase and more importantly single crystalline samples could be synthesized such as the $AE_{1-x}K_xFe_2As_2$ (AE = Ca, Sr, or Ba) and LiFeAs systems.

After the initial report of superconductivity with T_c~26 K in $LaFeAsO_{1-x}F_x$ [1], the maximum superconducting transition temperature for this class of materials was quickly raised to ~ 55 K by replacing La with other rare earth elements [2] or applying an external pressure. [3] Shortly after, superconductivity with T_c up to 38 K was observed in doped AFe_2As_2 ("122") compounds [4], which share the same structural unit of FeAs layers with *R*FeAsO ("1111") system. Although the 1111 system was discovered earlier and manifests a higher T_c, the focus of the scientific community shifted toward the 122 systems because (1) sizeable high quality single crystals of 122 system have been successfully produced by many groups and both electron and hole doping can be systematically manipulated and (2) the growth of large single crystals of the 1111 compound proved difficult so that the largest crystals were still in submillimeter size despite tremendous efforts.[5-7] We have found that NaAs is an effective solvent for *R*FeAsO (R=La, Ce, Pr, Nd, Sm, Gd) and consequently succeeded in growing a high yield of sizeable high quality single crystals by the flux method under ambient pressure [8] as shown in Figure 1. We have been able to reproducibly grow millimeter-sized single crystals of LaFeAsO, $LaFeAsO_{1-x}F_x$, and $LaFe_{1-x}Co_xAsO$ using NaAs as flux under ambient pressure with typical dimensions of 3 × 4 × 0.05-0.3 mm^3. Single crystal neutron diffraction and magnetization measurements confirm that the structural phase

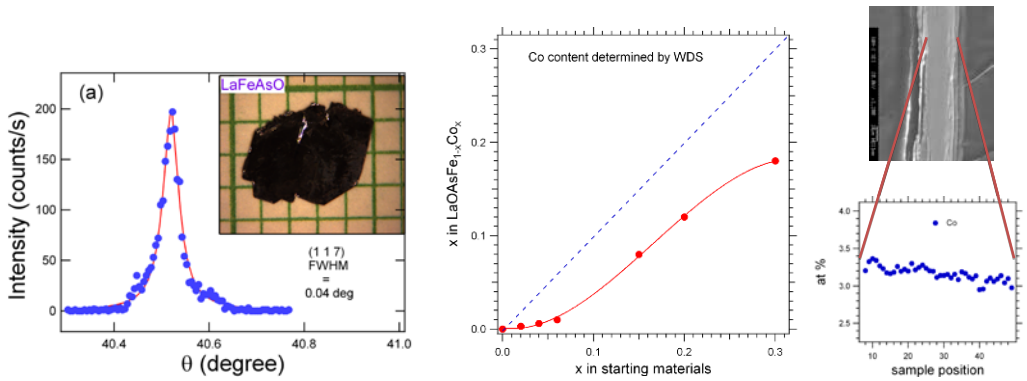

Fig. 1 Rocking curve through the (117) reflection of the LaFeAsO single crystal (left). Co content in $LaFe_{1-x}Co_xAsO$ as a function of initial Co additions (center), and, Co variation through thickness indicating coring segregation during solution growth (right).

transition (T_s = 153 K) magnetic order at T_{SDW} ~ 140 K, consistent with previous reports on polycrystalline samples.[9-11] The availability of these high quality crystals has resulted detailed magnetic, structural and transport measurements.[12-15] This synthesis protocol has since been adopted by other groups.[see 15-21]

We extended the use of NaAs flux to the doped compounds $LaFe_{1-x}Co_xAsO$ and $LaFeAsO_{1-x}F_x$ by partially replacing Fe with Co and NaAs with NaF, respectively. A number of single crystals with various doping contents were grown. Chemical analysis of cleaved surfaces using wavelength dispersive analysis (WDS) confirms the doping element has entered into the lattice. Co doping could be controlled through adjustment of the starting composition as shown in Fig. 1; however, F doping was found to be more erratic and without correlation with the amount of NaF additions. As with the parent compound, chemical analysis indicated ~0.2% (atomic) of Ta in all of our doped crystals. Composition profiles through the thickness of the plate crystal indicated Co variations (Fig. 1), resulting from coring segregation from solidification over a temperature range and is consistent with substitution of Fe with Co over a large range of composition.

In addition to the compositional variation and incorporated Ta in the crystals, second phases are a common defect in solution crystal growth. RFeAsO was found to also incorporate magnetic second phase inclusions. [22] Fig. 2 shows the temperature dependence of specific heat of three different pieces of NdFeAsO single crystals grown from the same batch. Only the low temperature range is displayed to highlight the difference around 12 K. The anomaly at 6 K comes from the magnetic order of Nd ions, which has been confirmed by neutron scattering. [13] While a well defined lambda anomaly was observed in one crystal, the magnitude of the lambda anomaly varied with other crystals and in some cases was barely observable. The ordering of Fe and Nd moments was studied with neutron single crystal diffraction and all crystals

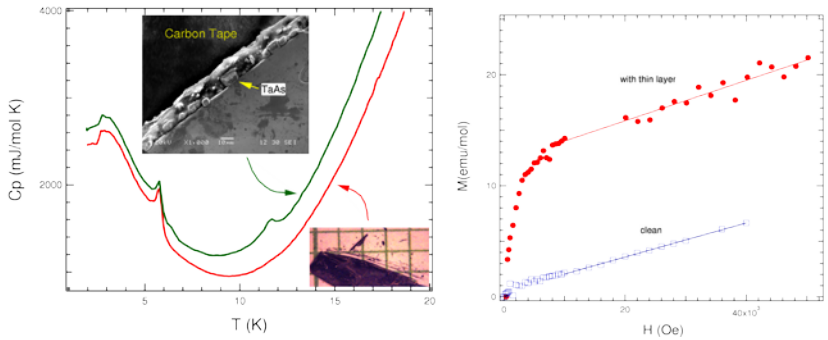

Fig. 2 The temperature dependence of specific heat (left) and magnetization-field (right) with field parallel to c-axis for NdFeAsO crystals before and after mechanically removing the edges. Upper inset shows a SEM picture of NdFeAsO single crystal illustrating the residual on the crystal edge. Lower inset demonstrates how the residue on the edges were removed mechanically with a surgical blade.

examined show the same ordering temperatures.[14] The temperature dependence of electrical resistivity did not show any observable difference around 12 K. These data suggests that the lambda anomaly observed at 12 K is due to impurities. Among all starting materials and other possible impurities, NdAs has been reported to order antiferromagnetically at 12 K and therefore is suspect. Electron microscopy confirmed the presence of impurity phases in a 10 μm thick layer observed on the edges of NdFeAsO crystals. This thin layer contains multiple phases consisting of TaAs which were surrounded by very fine particles. The rough surface of the thin layer makes it difficult to accurately determine the composition of the fine particles. Instead, we suspect that magnetic impurities might be the source of the 12 K signatures. We therefore mechanically removed the thin layer with the aid of a surgical blade (see the lower inset of Fig. 2) and measured the magnetization and specific heat of single crystal. As shown in Fig. 2, after removing the edges, no anomaly was observed around 12 K in the temperature dependence of specific heat. This confirms that NdAs impurities are contained within the thin layer adhered to the edges of NdFeAsO single crystals.

Future Work

During the next phase of this work we will focus on two objectives: 1) modify the growth protocol for enhanced control of dopants and 2) development of protocols for other Fe-based superconducting systems. For the first objective a fairly robust protocol for the growth of Co-doped superconducting compositions has been developed but more work is needed to mitigate non-uniformity of Co-dopants. We will investigate the use of isothermal growth to eliminate coring segregation during crystal growth. The variation of Co-content broadens the transition(s) and leads to inconclusive statement on the coexistence of superconductivity and magnetism. Taking advantage of the volatility of the components, controlled evaporative mass losses will be used to control the supersaturation of the solution. The natural thermal gradients with the growth furnace are sufficient to allow "cool" spots where vapor can condense resulting in a gentle transport of As from the solution melt to containment walls. Initial attempts have indicated that crystal growth occurs at the solid/liquid interface and large crystals are feasible. Additional experiments will be conducted to adjust growth rate through imposed temperature gradients as a means to control mass transfer rates. We will extend this approach to F-doped compositions where controlled doping is still a question.

Development of protocols for other Fe-based superconducting systems including $Ba_{1-x}K_xFe_2As_2$ and $BaFe_2(As_{1-x}P_x)_2$ we plan on developing the modified liquid encapsulant technique using a Sn-melt to seal the volatile K and As in the growth system starting from the melting point of Sn at 232 ºC. An additional goal is that of growing a series of large $Ba_{1-x}K_xFe_2As_2$ and $BaFe_2(As_{1-x}P_x)_2$ single crystals by the modified the liquid encapsulant technique. For $Ba_{1-x}K_xFe_2As_2$ single crystals, we aim to grow one freestanding single crystal with a mass of ~1 g, which can be used for neutron scattering measurements without alignment to gain a better understanding of the doping evolution of Fermi surface and resonance mode in $Ba_{1-x}K_xFe_2As_2$ system with varying K content. For $BaFe_2(As_{1-x}P_x)_2$ single crystals, we propose combining Sn-melt sealing and capillary shaping techniques to prepare crystals in the mm size.

References

1. Y. Kamihara, T. Watanabe, M. Hirano, and H. Hosono, J. Am. Chem. Soc.**130**, 3296 (2008).
2. Z. Ren, W. Lu, J. Yang, W. Yi , X-L. Shen, C. Zheng, G-C.Che, X-L. Dong, L-L. Sun, F. Zhou, and Z-X. Zhao**,** Chin. Phys. Lett. **25,** 2215-2216 (2008).
3. H. Takahashi, K. Igawa, K. Arii, Y. Kamihara, M. Hirano, and Hideo Hosono, Nature, **453,** 376-378 (2008).
4. M. Rotter, M. Pangerl, M. Tegel, and D. Johrendt, Angewandte Chemie International Edition, **47,** 7949 (2008).
5. A. Jesche, C. Krellner, M. de Souza, M. Lang, and C. Geibel, New J. Phys., 11 103050 (2009).
6. C. Martin, M. E. Tillman, H. Kim, M. A. Tanatar, S. K. Kim, A. Kreyssig, R. T. Gordon, M. D. Vannette, S. Nandi, V. G. Kogan, S. L. Bud'ko, P. C. Canfield, A. I. Goldman, and R. Prozorov, Phys. Rev. Lett. 102, 247002 (2009).
7. L. Fang, P. Cheng, Y. Jia, X. Zhu, H. Luo, G. Mu, C. Gu, and H.-H. Wen, J. Cryst. Growth 311, 358 (2009).
8. J.-Q. Yan, S. Nandi, J. L. Zarestky, W. Tian, A. Kreyssig, B. Jensen, A. Kracher, K. W. Dennis, R. J. McQueeney, A. I. Goldman, R. W. McCallum, and T. A. Lograsso, Appl. Phys. Lett., **95**, 222504(2009).

9. C. de la Cruz1, Q. Huang, J. W. Lynn, J. Li, W. Ratcliff II, J. L. Zarestky, H. A. Mook, G. F. Chen, J. L. Luo, N. L. Wang, and P. Dai, Nature, **453**, 899 (2008).
10. T. Nomura, S. W. Kim, Y. Kamihara, M. Hirano, P. V. Sushko, K. Kato, M. Takata, A. L. Shluger, H Hosono, Supercond. Sci. Technol., **21,** 125028 (2008).
11. M. A. McGuire, A. D. Christianson, A. S. Sefat, B. C. Sales, M. D. Lumsden, R. Jin, E. A. Payzant, and D. Mandrus, Phys. Rev. B **78,** 094517 (2008).
12. A. Ricci, N. Poccia, B. Joseph, L. Barba, G. Arrighetti, G. Ciasca, J.Q. Yan, R.W. McCallum, T.A. Lograsso, N.D. Zhigadlo, J. Karpinski, and A. Bianconi, Physical Review B, **82**, 144507 (2010).
13. W. Tian, W. Ratcliff, M.G. Kim, J.Q. Yan, P.A. Kienzle, Q. Huang, B. Jensen, K.W. Dennis, R.W. McCallum, T.A. Lograsso, R.J. McQueeney, A.I. Goldman, J.W. Lynn, and A. Kreyssig, Physical Review B, **82**, 060514 (2010).
14. H.F. Li, W. Tian, J.Q. Yan, J.L. Zarestky, R.W. McCallum, T.A. Lograsso, and D. Vaknin, Physical Review B, **82**, 064409 (2010).
15. C. Liu, Y. Lee, A.D. Palczewski, J.Q. Yan, T. Kondo, B.N. Harmon, R.W. McCallum, T.A. Lograsso and A. Kaminski, Physical Review B, **82**, 075135 (2010).
16. Z.G. Chen, R.H. Yuan, T. Dong, and N.L. Wang, Physical Review B, **81**, 100502 (2010).
17. T. Dong, Z.G. Chen, R.H. Yuan, B.F. Hu, B. Cheng, and N.L. Wang, Physical Review B, **82**, 054522 (2010).
18. S. Kitagawa, Y. Nakai, T. Iye, K. Ishida, Y. Kamihara, M. Hirano, and H. Hosono, Physical Review B, **81**, 212502 (2010).
19. Y.K. Luo, Y.K. Li, S.A. Jiang, J.H. Dai, G.H. Cao, and Z.A. Xu, Physical Review B, **81**, 134422 (2010).
20. F. Nitsche, A. Jesche, E. Hieckmann, T. Doert, and M. Ruck, Physical Review B, 82, 134514 (2010).
21. X.D. Zhou, C. Ye, P. Cai, X.F. Wang, X.H. Chen, and Y.Y. Wang, Physical Review Letters, **106**, 087001 (2011).
22. J.-Q. Yan, Q. Xing, B. Jensen, H. Xu, K. W. Dennis, R. W. McCallum, and T. A. Lograsso, Phys. Rev. B, **84**, 012501 (2011).

DOE Sponsored Publications on this topic

R.W. McCallum, J.Q. Yan, G.E. Rustan, E.D. Mun, Y. Singh, S. Das, R. Nath, S.L. Bud'ko, K.W. Dennis, D.C. Johnston, P.C. Canfield, M.J. Kramer, A. Kreyssig, T.A. Lograsso, and A.I. Goldman, "In Situ High Energy X-Ray Synchrotron Diffraction Study of the Synthesis and Stoichiometry of LaFeAsO and $LaFeAsO_{1-X}F_y$," *Journal of Applied Physics*, **105**, 123912 (2009).

J.Q. Yan, S. Nandi, J.L. Zarestky, W. Tian, A. Kreyssig, B. Jensen, A. Kracher, K.W. Dennis, R.J. McQueeney, A.I. Goldman, R.W. McCallum, and T.A. Lograsso, "Flux Growth at Ambient Pressure of Millimeter-Sized Single Crystals of LaFeAsO, $LaFeAsO_{1-x}F_x$, and $LaFe_{1-x}Co_xAsO$," *Applied Physics Letters*, **95**, 222504 (2009).

C. Liu, Y. Lee, A.D. Palczewski, J.Q. Yan, T. Kondo, B.N. Harmon, R.W. McCallum, T.A. Lograsso, and A. Kaminski, "Surface-Driven Electronic Structure in LaFeAsO Studied by Angle-Resolved Photoemission Spectroscopy," *Physical Review B*, **82**, 075135 (2010).

N. Ni, A. Thaler, J.Q. Yan, A. Kracher, E. Colombier, S.L. Bud'ko, and P.C. Canfield, "Temperature Versus Doping Phase Diagrams for $Ba(Fe_{1-x}\ Tm_x)_2As_2$(Tm=Ni,Cu,Cu/Co) Single Crystals," *Physical Review B*, **82**, 024519 (2010).

A. Ricci, N. Poccia, B. Joseph, L. Barba, G. Arrighetti, G. Ciasca, J.Q. Yan, R.W. McCallum, T.A. Lograsso, N.D. Zhigadlo, J. Karpinski, and A. Bianconi, "Structural Phase Transition and Superlattice Misfit Strain of RFeAsO (R=La, Pr, Nd, Sm)," *Physical Review B*, **82**, 144507 (2010).

A. Thaler, N. Ni, A. Kracher, J.Q. Yan, S.L. Bud'ko, and P.C. Canfield, "Physical and Magnetic Properties of $Ba(Fe_{1-x}\ Ru_x)_2As_2$ Single Crystals," *Physical Review B*, **82**, 014534 (2010).

W. Tian, W. Ratcliff, M.G. Kim, J.Q. Yan, P.A. Kienzle, Q. Huang, B. Jensen, K.W. Dennis, R.W. McCallum, T.A. Lograsso, R.J. McQueeney, A.I. Goldman, J.W. Lynn, and A. Kreyssig, "Interplay of Fe and Nd Magnetism in NdFeAsO Single Crystals," *Physical Review B*, **82**, 060514 (2010).

J.Q. Yan, B. Jensen, K.W. Dennis, R.W. McCallum, and T.A. Lograsso, "Flux Requirements for the Growth of RFeAsO (R=Rare Earth) Superconductors," *Applied Physics Letters*, **98**, 072504 (2011).

J.-Q. Yan, Q. Xing, B. Jensen, H. Xu, K. W. Dennis, R. W. McCallum, and T. A. Lograsso, "Contamination by Magnetic Starting Materials in Flux Grown Single Crystals of RFeAsO (R = Rare Earth)," *Physical Review B*, **84**, 012501 (2011).

Chemical Routes to Intermetallic, Carbide, and Chalcogenide Nanomaterials

Raymond E. Schaak
res20@psu.edu
Department of Chemistry and Materials Research Institute
The Pennsylvania State University, University Park, PA 16802

Program Scope

As applications continue to demand increasingly complex nanoscale materials, the complexity of the synthetic capabilities that generate them must also continue to expand. Chemical routes can produce some of the highest-quality and most complex nanostructures, but they have limitations in scope, materials generality, sample purity, scale, and precise control over subtle (yet important) structural and compositional features. This project uses superconducting materials, along with other energy-relevant materials systems including magnetic nanostructures and catalysts for solar cells and alternative fuel systems, as a platform for expanding the capabilities of chemical routes to nanoscale materials and for understanding how these capabilities influence structure and properties. Specifically, we seek to:

- Use tools developed for the chemical synthesis of nanoparticles as a platform for the synthesis and discovery of new and non-equilibrium phases in intermetallic and chalcogenide systems that are relevant to superconductivity, magnetism, and catalysis.
- Expand the capabilities of colloidal nanoparticle synthesis into non-traditional and chemically-challenging systems of relevance to superconductivity, magnetism, and catalysis, including metal carbides, metal borides, and intermetallic and chalcogenide systems containing early transition metals and post-transition metals for which solution chemistry syntheses are not straightforward.
- Develop chemical routes for fine-tuning composition and structure in complex materials systems where subtle changes directly influence properties, including magnetic metal carbide solid solutions and superconducting iron-based chalcogenides.
- Increase the scale of materials that can be generated using chemical synthesis routes, including larger multi-gram sample sizes and larger mm-size single crystals.
- Establish a new biological approach for the separation and purification of mixed-phase colloidal nanomaterials in order to generate samples free of adventitious impurities.

Recent Progress

We have made significant progress on all of the areas highlighted above, as can be seen from the publication list. This report will focus primarily on our most recent efforts in the synthesis, mechanistic understanding, chemical manipulation, and properties of metal chalcogenide nanostructures, as well as a brief overview of recent results involving low-temperature routes to novel nanostructured carbon, boron-substituted carbon, and metal carbide nanostructures.

Inspired by the discovery of superconductivity in several families of iron-based systems, including FeSe and related iron chalcogenides,[1] we studied the formation of PbO-type FeSe using solution chemistry synthesis techniques and discovered that colloidal nanosheets of FeSe,

FeTe, and Fe(Se,Te) could be generated. Unfortunately, the nanosheets were not superconducting, and we sought to investigate the influence of composition, morphology, and nanosheet thickness on their properties. We learned that while colloidal Fe-Se nanomaterials often form as impure and multi-phase samples, reacting them with trioctylphosphine leaches selenium in a controllable manner, allowing us to effectively "purify" multi-phase samples and fine-tune composition. This chemistry, which also works for many other metal chalcogenide systems and can be carried out under conditions that facilitate morphological retention, is chemically self-limiting and can be used for precise post-synthesis phase targeting and composition tunability, which could be especially important for the FeSe system.[2]

In order to investigate the influence of morphology and nanosheet thickness on the properties, we shifted to a different chalcogenide system – the narrow bandgap semiconductors GeSe, GeS, SnSe, and SnS that are of interest as possible light absorption layers in solution-processed solar cells[3] – because the chemistry associated with this system would allow us to better understand, at a mechanistic level, the factors that influence morphological tunability. We disovered that, like FeSe, all of these layered IV-VI semiconductor systems formed colloidal nanosheets. Interestingly, we learned how to simultaneously control lateral uniformity and nanosheet thickness in the SnSe system via a "grow-out" then "grow-up" layer-by-layer assembly pathway: pre-formed SnSe nanoparticle seeds agglomerate in two dimensions to form square-shaped nanosheets, then attachment of additional nanoparticles to the template nanosheet surfaces increases their thickness. The nanosheet thickness can be tuned by precursor concentration, since vertical growth continues only as long as the seed nanoparticles are present in solution. These colloidal nanosheets can be drop-cast as highly oriented films with optical bandgaps near 1 eV, and they exhibit impressive photocurrents that make them potentially attractive for solution-processed solar cells.

In addition to understanding how to chemically control composition and morphology in metal chalcogenide systems, we were also interested in using unconventional synthetic tools (such as low-temperature solution chemistry routes typically used for colloidal nanoparticle synthesis) to explore the formation of new chalcogenide phases. Through our investigations, we were able to synthesize isolatable bulk quantities of wurtzite-type MnSe, which is a metastable phase that is the elusive tetrahedrally-bonded end member of the $Zn_{1-x}Mn_xSe$ solid solution and is of interest for fundamental studies of magnetic semiconducting systems.[4] (Bulk MnSe adopts the octahedrally-coordinated rocksalt structure.) Wurtzite-type MnSe nanoparticles were found to have an optical bandgap of approx. 3.5 eV and are antiferromagnetic with $T_N = 64$ K.

In addition to the metal chalcogenide systems mentioned above, we have been working on novel nanostructured carbon-based materials. This work grew out of our initial work aimed at producing carbide and boride superconductors using low-temperature solution-mediated routes. Several years ago we synthesized crystalline nickel borocarbide nanoparticles using a direct solution route with no post-synthesis annealing.[5] Follow-up investigations indicated that related colloidal (metastable) Ni_3C nanoparticles, which are spherical and morphologically uniform, thermally decompose to form uniform graphite-encapsulated nickel particles. Acid leaching of the nickel yields monodisperse 20-nm hollow nanospheres of graphitic carbon, and these hollow carbon nanoshells (C-shells) serve as high surface area supports for anchoring Pt nanoparticles. The resulting "Pt/C-shell" materials are highly active catalysts for the oxygen reduction reaction,

showing apparent Pt mass activities that are more than twice that of comparable commercial and control catalysts. The colloidal Ni_3C nanoparticle precursors could also be modified to produce Ni_3C_{1-x} nanoparticles with tunable carbon content, and interrogation of the magnetic properties of this metal carbide solid solution allowed us to experimentally bridge prior (controversial) studies of the synthesis and properties of hexagonal Ni_3C nanoparticles vs. nanoparticles of hexagonal close packed Ni.[6] Finally, by incorporating boron in the Ni_3C precursor (e.g. $Ni_3C_{1-x}B_x$), we found that thermal decomposition and acid etching produced hollow nanostructures of boron-substituted carbon with high surface area, with maximum processing temperatures of < 500 ºC.

Future Plans

Building off of our recent results on SnSe and related systems, we are beginning to expand into solar cell materials, where our unique synthetic capabilities and mechanistic insights have the potential to lead to new nanostructured materials for improved solar cells. We have begun integrating our materials into solar cells. We continue to study the FeSe system with the goal of identifying the influence that novel chemical synthesis and manipulation techniques have on the properties, and our current efforts are aimed at chemically manipulating the Fe stoichiometry (to complement our recent report involving the manipulation of Se composition). As side projects, we continue to look for new materials via unconventional platforms for exploratory synthesis, as well as learn how to grow mm-scale single crystals of intermetallics at low temperatures using beaker chemistry techniques. Finally, we are approaching the problem of nanomaterials purity – the issue that most chemically-synthesized nanomaterials are interently impure and often multi-phase – by developing a new nanoparticle separation platform that exploits the specific surface recognition capabilities of combinatorially-identified proteins and peptide sequences. This is imperative for generating phase-pure samples for accurate determination of materials properties, including for superconducting and magnetic systems.

References

1. M.K. Wu, F.C. Hsu, K.W. Yeh, T.W. Huang, J.Y. Luo, M.J. Wang, H.H. Chang, T.K. Chen, S.M. Rao, B.H. Mik, C.L. Chen, Y.L. Huang, C.T. Ke, P.M. Wu, A.M. Chang, C.T. Wu, T.P. Perng, *Physica C* **2009**, *469*, 340-349.
2. (a) A.J. Williams, T.M. McQueen, R.J. Cava, *Solid State Commun.* **2009**, *149*, 1507-1509. (b) T.M. McQueen, Q. Huang, V. Ksenofontov, C. Felser, Q. Xu, H. Zandbergen, Y.S. Hor, J. Allred, A.J. Williams, D. Qu, J. Checkelsky, N.P. Ong, R.J. Cava, *Phys. Rev. B* **2009**, *79*, 014522.
3. P.D. Antunez, J.J. Buckley, R.L. Brutchey, *Nanoscale* **2011**, *3*, 2399-2411.
4. J.K. Furdyna, *J. Appl. Phys.* **1988**, *64*, R29-R64.
5. Z.L. Schaefer, X. Ke, P. Schiffer, R.E. Schaak, *J. Phys. Chem. C* **2008**, *112*, 19846-19851.
6. (a) Y. Goto, K. Taniguchi, T. Omata, S. Otsuka, B. Ohashi, S. Ueda, H. Yoshikawa, Y. Yamashita, H. Oohashi, K. Kobayashi, *Chem. Mater.* **2008**, *20*, 4156-4160. (b) L. He, *J. Magn. Magn. Mater.* **2010**, *322*, 1991-1993.

Publications (2009 – 2011, from this DOE grant)

1. N.L. Henderson, M.D. Straesser, P.D. Sabato, R.E. Schaak, "Toward Green Metallurgy: Low-Temperature Solution Synthesis of Bulk-Scale Intermetallic Compounds in Edible Plant and Seed Oils," *Green Chem.* **2009**, *11*, 974-978.
2. Q. Liu, H. Yan, J.C. Bauer, N.L. Henderson, D.W. Goodman, J.D. Batteas, R.E. Schaak, "Synthesis of CuPt Nanorod Catalysts with Tunable Lengths," *J. Am. Chem. Soc.* **2009**, *131*, 5720-5721.
3. T.H. Phan, R.E. Schaak, "Polyol Synthesis of Palladium Hydride: Bulk Powders vs. Nanocrystals," *Chem. Commun.* **2009**, 3026-3028.
4. K.N. Avery, J.E. Schaak, R.E. Schaak, "M13 Bacteriophage as a Biological Scaffold for Magnetically-Recoverable Metal Nanowire Catalysts: Combining Specific and Non-Specific Interactions to Design Multi-Functional Nanocomposites," *Chem. Mater.* **2009**, *21*, 2176-2178. [Featured in ***Chemical & Engineering News***]
5. J.F. Bondi, K.D. Oyler, N.H. Chou, X. Ke, P.E. Schiffer, R.E. Schaak, "Chemical Synthesis of Manganese Nanoparticles," *J. Am. Chem. Soc.* **2009**, *131*, 9144-9145.
6. K.D. Oyler, X. Ke, I.T. Sines, P.E. Schiffer, R.E. Schaak, "Chemical Synthesis of Lamellar FeSe, FeTe, and Fe(Se,Te) Nanocrystals," *Chem. Mater.* **2009**, *21*, 3655-3661.
7. N.H. Chou, K.D. Oyler, N.E. Motl, R.E. Schaak, "Colloidal Synthesis of Germanium Nanocrystals Using Room-Temperature Benchtop Chemistry," *Chem. Mater.* **2009**, *21*, 4105-4107.
8. Z.L. Schaefer, D.D. Vaughn, R.E. Schaak, "Solution Chemistry Synthesis, Morphology Studies, and Optical Properties of Five Distinct Nanocrystalline Au-Zn Intermetallic Compounds," *J. Alloys Compounds*, **2010**, *490*, 98-102.
9. I.T. Sines, R. Misra, P. Schiffer, R.E. Schaak, "Colloidal Synthesis of Non-Equilibrium Wurtzite-Type MnSe," *Angew. Chem. Int. Ed.* **2010**, 49, 4638-4640. **[Featured on the inside cover of the 27th issue of *Angew. Chem. Int. Ed.*, June 21, 2010]**
10. J.F. Bondi, R. Misra, X. Ke, I.T. Sines, P. Schiffer, R.E. Schaak, "Optimized Synthesis and Magnetic Properties of Intermetallic Au_3Fe_{1-x}, Au_3Ni_{1-x}, and Au_3Co_{1-x} Nanoparticles," *Chem. Mater.* **2010**, *22*, 3988-3994.
11. M.E. Anderson, S.S.N. Bharadwaja, R.E. Schaak, "Modified Polyol Synthesis of Bulk-Scale Nanostructured Bismuth Antimony Telluride," *J. Mater. Chem.* **2010**, *20*, 8362-8367.
12. Z.L. Schaefer, M.L. Gross, M.A. Hickner, R.E. Schaak, "Uniform Hollow Carbon Shells: Nanostructured Graphitic Supports for Improved Oxygen-Reduction Catalysis," *Angew. Chem. Int. Ed.* **2010**, 49, 7045-7048. **[Designated as a "hot paper" by the editors of *Angew. Chem. Int. Ed.*]**
13. D.D. Vaughn II, R.E. Schaak, "Colloidal Synthesis of Air-Stable Crystalline Germanium Nanoparticles with Tunable Sizes and Shapes," *Chem. Mater.* **2010**, *22*, 6103-6108.
14. D.D. Vaughn II, R.E. Schaak, "Single Crystal Colloidal Nanosheets of GeS and GeSe," *J. Am. Chem. Soc.* **2010**, *132*, 15170-15172.
15. I.T. Sines, R.E. Schaak, "Phase-Selective Chemical Extraction of Selenium and Sulfur from Nanoscale Metal Chalcogenides: A General Strategy for Synthesis, Purification, and Phase Targeting," *J. Am. Chem. Soc.* **2011**, *133*, 1294-1297.
16. Z. Luo, Y. Vasquez, J.F. Bondi, R.E. Schaak, "Pawley and Rietveld refinements using electron diffraction from $L1_2$-type intermetallic Au_3Fe_{1-x} nanocrystals during their *in-situ* order-disorder transition," *Ultramicroscopy* **2011**, in press.
17. Z.L. Schaefer, K.M. Weeber, R. Misra, P. Schiffer, R.E. Schaak, "Bridging hcp-Ni and Ni_3C via a Ni_3C_{1-x} Solid Solution: Tunable Composition and Magnetism in Colloidal Nickel Carbide Nanoparticles," *Chem. Mater.* **2011**, *23*, 2475-2480.
18. J.F. Bondi, R.E. Schaak, "Solution Chemistry Synthesis of Intermetallic Gold-Lithium Nanoparticles," *Eur. J. Inorg. Chem.* **2011**, in press.

Superconductors in Confined Geometries

Zhili Xiao
zxiao@niu.edu
Department of Physics, Northern Illinois University, DeKalb, Illinois 60115

Program Scope

As the size of a superconductor is reduced to a length scale comparable to the superconducting coherence length or magnetic penetration depth, the wave functions of its charge carriers - Cooper pairs or the distribution of the penetrated magnetic field will be strongly modified. Therefore, nanoscale superconductors are expected to exhibit properties different from their bulk counterparts. Superconductors in confined geometries provide unique platforms to investigate and to discover novel superconducting phenomena. It is also of practical importance in defining the size limit of a superconductor with regards to potential applications in electronic circuits.

One of the grand challenges in current research on nanoscale superconductors is to fabricate samples with desired geometries. We have been developing methods to synthesize superconducting nanostructures of various types and exploring their physical properties. For example, we developed a novel conversion approach to achieve superconducting $NbSe_2$ and NbN nanowires from non-superconducting $NbSe_3$ nanostructure precursors which could form easily due to their extremely anisotropic crystalline structure [1-3]. We also successfully grew nanowires and nanoribbons of high temperature (high-T_c) superconductors ($Bi_2Sr_2CaCu_2O_8$). This new class of free-standing superconducting nanowires and nanoribbons are stable in atmosphere and enable the exploration of superconducting properties and potential applications of individual nanostructures which can be as-prepared or modified with focused-ion-beam (FIB) milling [4].

Recent Progress

One-dimensional (1D) superconducting nanowires with diameters comparable to the superconducting coherence length have been a subject of intensive research in recent years due to their intriguing properties and novel potential applications. They have been the research subject of thermal and quantum phase slip phenomena which induce dissipation at temperatures near and away from the superconducting critical temperature, respectively. They are also highly desirable in future electronic nanodevices because nanowires of zero-resistance are ideal interconnects since they can circumvent the damaging heat produced by energy dissipation in a normal nano-conductor whose high resistance is inversely proportional to its cross-section area. Pursuing research on superconducting nanowires will provide fundamental understanding which will benefit nanoscale superconductivity and nanodevices.

When a 1D superconducting nanowire is multiply connected, i.e. it forms a 1D superconducting loop, the circulation of normal electrons and Cooper pairs in the presence of a magnetic field can produce the Aharonov-Bohm [5] and the Little-Parks [6,7] effects, respectively. These effects offer sensitive probes of proposed incoherent Cooper pairing in the pseudogap [8] and insulating phases [7] competing with superconductivity in copper oxide and conventional superconductors, of the relative contribution of individual bands in two-band superconductors [9] and of the interplay of superconductivity and magnetism in hybrid structures [10]. For small enough nanoscale loops, the Little-Parks depression of the transition temperature extends to $T = 0$ K, inducing a field-driven quantum phase transition to a metallic or insulating phase [11]. Aharanov-Bohm and Little-Parks effects in a 1D loop system are mediated by the orbital magnetic flux of the applied magnetic field.

However, it is extremely challenging to investigate the transport properties of individual 1D superconducting loops since standard four-probe measurements require electrical contacts which can smear out the electrical signal of the loop. We overcame this obstacle by studying an array of 1D

superconducting loops. Networks of 1D superconducting nanowires were successfully achieved through two nanofabrication approaches: i) focused-ion-beam (FIB) milling of a superconducting film and ii) deposition of the desired superconducting material onto a nanoporous substrate.

Left panel of Fig.1 shows a scanning electron microscopy (SEM) image of a superconducting niobium (Nb) nanowire network fabricated by FIB milling of a Nb film (60 nm thick) deposited onto silicon substrates with 200 nm thick oxide layers via DC magnetron sputtering. A triangular array of holes with diameter $d \approx 50$ nm and lattice spacing of $D = 150$ nm was fabricated into a Nb film of thickness 60 nm through FIB milling (FEI Nova 600, 30 KeV Ga^+, 10-20 nm beam diameter). The confining hole geometry makes the width of the sections between neighboring holes comparable to the superconducting coherence length, i.e. the superconducting section surrounding each hole forms a 1D loop. As demonstrated by the data presented in the right panel of Fig.1, we did observe the Little-Parks effect which presents itself as an oscillatory dependence of the critical temperature T_c on the applied magnetic field H. Such a nanowire network provides us a unique platform not only to explore properties of a 1D superconducting loop but also the coupling between them. As the field is tipped off perpendicular, the Little-Parks oscillations change character with a continuously increasing period. The periods of the transition temperature oscillations follow a relation of $H_{1\theta} = H_{1\perp}/\cos\theta$, where $H_{1\theta}$ and $H_{1\perp}$ are the oscillation periods at a field angle θ and in perpendicular field direction, respectively. This indicates that the Little-Parks oscillations in a tilted field respond only to the perpendicular component of the applied field.

Since the superconducting coherence is temperature dependence and shrinks quickly as the temperature decreases, the width of the superconducting sections between holes needs to be a few nanometers in order to observe Little-Parks effect at low temperatures. Due to the limitation of the beam size, however, FIB milling or electron-beam lithography patterning has difficulties in achieving a nanostructure with feature sizes smaller than 50 nm. Recently, we developed a new method to achieve a network of superconducting nanowires with widths smaller than 10 nm. They were fabricated by depositing the desired superconducting materials onto commercially available porous membranes (e.g. Anodisc 13 from Whatman Company). A typical SEM image of such a superconducting network is given in the left panel of Fig.2: the width of the superconducting nanowires is about 7-9 nm which is comparable to the zero-temperature superconducting coherence length of the deposited material (MoGe). That is, Little-Parks effect is expected to appear at any experimentally accessible temperatures. In fact, superconducting confinement effect can be clearly identified in the non-monotonic increase of the sample resistance with increasing magnetic field, as shown in the right panel of Fig.2.

Though this new fabrication method was developed to achieve ultrasmall superconducting nanowires to study new phenomena in confined superconductors, it can provide a versatile approach to obtain nanowire networks of other functional materials to take advantage of single nanowires while eliminating their nanofabrication obstacles. In fact, we utilized this method to fabricate networks of ultrasmall palladium (Pd) nanowires as high-performance hydrogen sensing elements and achieved hydrogen sensors with speed and sensitivity better than those based on single Pd nanowires fabricated with costly lithography methods. That work led to a publication in *Nano Letters* (item#4 in the publication list).

Future Plans

We plan to carry out the following experiments in the near future:

(i). *Networks of superconducting nanowires formed on home-made nonporous substrates:* Though the commercial nanoporous substrates were able to produce networks of nanowires with a width of a few nanometers, the area enclosed by the loop varies, leading to the period of the Little-Parks oscillation not being well defined. We are developing synthesis approaches to grow

nanoporous substrates with improved uniformity of the loop area and better order of the distribution of the loop.

(ii). *Nanowires and nanoribbons of* $YBa_2Cu_3O_{7-x}$ *high-T_c superconductor:* Synthesis of high-Tc superconducting nanowires and nanoribbons is one of the foci of this research project. We successfully grew nanowires and nanoribbons of $Bi_2Sr_2CaCu_2O_8$ (BSCCO-2212) which is extremely anisotropic and behaves as a 2-dimensional (2D) system. We are fabricating nanostructures of another representative high-T_c superconductor - $YBa_2Cu_3O_{7-x}$ which is much less anisotropic. We will explore properties of the as-prepared samples and those patterned with FIB milling.

(iii).*Superconductors at the Anderson limit*: More than 50 years ago Anderson [12] predicted a destabilization of superconductivity in confined superconductors with sizes at which the energy level spacing becomes equal to the superconducting energy gap. This criterion has been experimentally verified in many elemental superconductors (e.g. Al, Sn and In) through tuning the grain size in thin films by controlling the deposition conditions, e.g. quenching on liquid nitrogen cooled substrates. However, the thin film approach will not work for compound superconductors such as MgB_2 and $YBa_2Cu_3O_{7-x}$ which form only at 700 °C or higher. We are developing a ball-milling approach which enables us to fabricate these compound superconductors with sizes down to a few nanometers and to explore new properties in superconductors with sizes at or close to the Anderson limit.

References

[1]. Y. S. Hor et al., *Nano Letters* **5,** 397 (2005).

[2]. Y. S. Hor et al., *Applied Physics Letters* **87**, article # 142506 (2005).

[3]. U. Patel et al., *Physical Review B* **80**, article # 147003 (2009).

[4]. S. Avci et al., *Applied Physics Letters* **97**, article # 042511 (2010).

[5]. W. -R. Lee and H. -S. Sim, *Physical Review Letters* **104**, article # 196802 (2010).

[6]. B. Pannetier et al., *Physical Review Letters* **53**, 1845 (1984).

[7]. M. D. Stewart, Jr., et al. *Science* **318**, 1273 (2007).

[8]. F. Carillo et al., *Physical Review B* **81,** article # 054505 (2010).

[9]. Yu. S. Erin et al., *Low Temperature Physics* **34**, 891 (2008).

[10]. A. V. Samokhvalov et al., *Physical Review B* **79**, article # 174502 (2009); A. Yu. Aladyshkin et al., *ibid* **75**, 184519 (2007); D. S. Golubovic et al, *ibid* **68**, 172503 (2003).

[11]. Y. Liu et al, *Science* **294**, 2332 (2001); I. Sternfeld et al, *Physica C* **468**, 337 (2008).

[12]. P. W. Anderson, *J. Phys. Chem. Solids* **11**, 26 (1959).

DOE Sponsored Publications over the Past Two Years

1. *Studying single nanocrystals under high pressure using an x-ray nanoprobe*, Lin Wang, Yang Ding, Umesh Patel, Wenge Yang, Zhili Xiao, Zhonghou Cai, Wendy L. Mao, and Ho-kwang Mao, *Review Scientific Instruments* **82**, article # 043903 (2011).
2. *Transparent conducting films from $NbSe_3$ nanowires*, Sukanta De, Conor S Boland, Paul J. King, Sophie Sorel, Mustafa Lotya, U. Patel, Z. L. Xiao, and Jonathan N Coleman, *Nanotechnology* **22**, article # 285202 (2011).
3. *Conversion of carbon dioxide to few-layer graphene*, Amartya Chakrabarti, Jun Lu, Jennifer C. Skrabutenas, Tao Xu, Zhili Xiao, John A. Maguire, and Narayan S. Hosmane, *Journal of Materials Chemistry* **83**, 2087 (2011)

4. *Hydrogen gas sensing with networks of ultra-small palladium nanowires formed on filtration membranes*, X. Q. Zeng, M. L. Latimer, Z. L. Xiao, S. Panuganti, U. Welp, W. K. Kwok, T. Xu, *Nano Letters* **11,** 262 (2011).
5. *Low-temperature synthesis of superconducting nanocrystalline MgB_2*, Jun Lu, Zhili Xiao, Qiyin Lin, Helmut Claus, and Zhigang Zak Fang, *Journal of Nanomaterials* **2010**, article # 191058 (2010).
6. *Matching effect and dynamic phases of vortex matter in $Bi_2Sr_2CaCu_2O_8$ nanoribbon with a periodic array of holes*, S. Avci, Z. L. Xiao, J. Hua, A. Imre, R. Divan, J. Pearson, U. Welp, W. K. Kwok, and G. W. Crabtree, *Applied Physics Letters* **97**, article # 042511 (2010).
7. *Evaluating free flux flow in low-pinning molybdenum-germanium superconducting films*, M. L. Liang, M. N. Kunchur, J. Hua, and Z. L. Xiao, *Physical Review B* **82**, article # 064502 (2010).

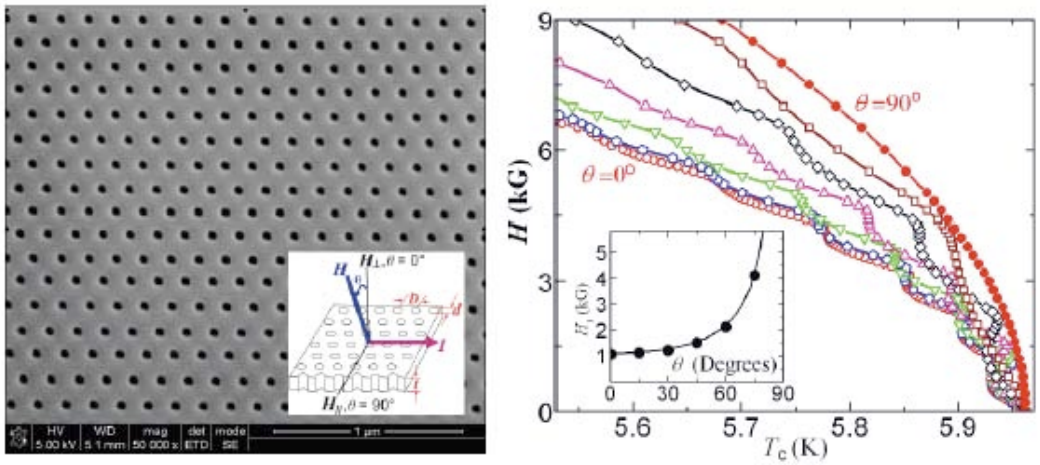

Fig.1. Left panel: Top-view scanning electron microscopy (SEM) micrograph of a Nb superconducting nanowire network of 60 nm thick fabricated by FIB milling of a continuous film. The inset shows definitions of the magnetic field direction θ, film thickness t, and lattice constant D. Right panel: Critical temperature – magnetic field (T_c-H) relation obtained at angles between 0° and 90° with an interval of 15°. Its inset gives the angular dependence of the oscillation period H_1.

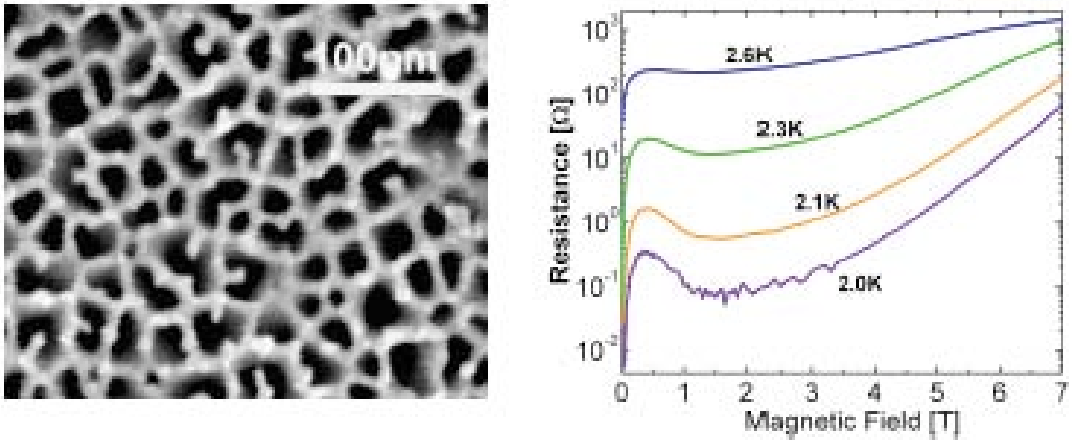

Fig.2. Left panel: Top-view SEM micrograph of a MoGe superconducting nanowire network of 10 nm thick. Right panel: Magnetoresistance of this sample at various temperatures.

Molecular Beam Epitaxy and Nano-structuring of Perovskite Oxide Materials toward understanding of Strongly Correlated Systems

Ivan Bozovic
bozovic@bnl.gov
Department of Condensed Matter Physics and Materials Science
Brookhaven National Laboratory P. O. Box 5000 Upton NY 11973-5000

Program Scope

The mechanism of high-temperature superconductivity (HTS) is one of the most important problems in Condensed Matter Physics. Some basic questions - the dimensionality, the spin and the charge of free carriers, the nature of superconducting transition, the effective interaction that causes electron pairing - are still open.

In many cases, the large scatter in experimental results can be traced back to materials science problems: HTS compounds and other complex oxides are by definition complex and have rich phase diagrams with many stable phases; for this and other reasons the samples tend to be chemically inhomogeneous. This is particularly true for HTS thin films, most of which contain secondary-phase precipitates. In the last decade, most experimental breakthroughs in HTS physics were triggered by advances in the synthesis of single crystals in either bulk or thin film form.

Using a unique molecular beam epitaxy (MBE) system, designed for atomic-layer-by-layer ('digital') sythesis, we grow single-crystal films of various complex oxides (cuprates, nickelates, bismuthates, etc.), as well as multilayers and superlattices with atomically perfect interfaces. From these, we manufacture tunnel junctions, field-effect devices, and HTS nano-structures. We use these unique samples for novel in-house exeriments which have already brought in several important results including the demonstrations of phase-separation of HTS and anti-ferromagnetic states on an atomic scale, Giant Proximity Effect, HTS in a single CuO_2 layer, and the field-effect driven (de)localization of electron pairs, as well as the discoveries of colossal photo-induced expansion and high-T_c interface superconductivity.

We have also established extensive collaborations worldwide. The oxide MBE group at BNL has emerged as the preeminent source of the highest-quality single-crystal HTS thin films and multilayer hetero-structures engineered down to a single atomic layer that are enabling breakthrough research of few dozen groups at national laboratories and leading universities in US as well as in Europe and Asia.

These experiments, our own and collaborative, are hoped to provide clear-cut answers to at least some of the above questions, which would significantly impact research on HTS and more broadly on strongly-correlated materials.

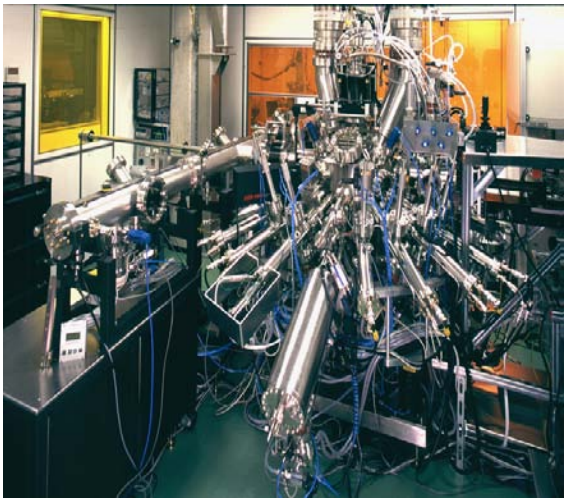

Fig. 1. The growth chamber of the oxide MBE system at BNL is equipped with 16 metal atom sources, a pure ozone source (providing high oxidation power in high vacuum), a scanning quartz-crystal rate monitor (QCM), a 16-channel atomic absorption spectroscopy system, a scanning RHEED system, and a time-of-flight ion scattering and recoil spectroscopy (TOF-ISARS) system.

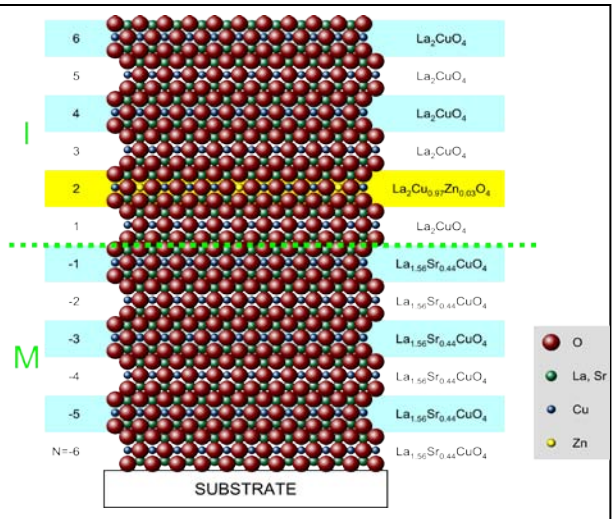

Fig. 2. Schematics of δ-doping using ALL-MBE in a 6 unit cells thick LSCO-LCO bilayer. The green dashed line indicates the position of nominal geometrical LSCO-LCO interface in-between the layers N = -1 and N = 1. By virtue of digital layer-by-layer synthesis, one can dope the selected layer(s) with Zn, which substitutes for Cu. In this figure, the N = 2 CuO_2 plane (the second above the interface) contains some Zn dopant atoms.

Recent Progress

High-Temperature Superconductivity in a Single Copper-Oxygen Plane. Some of the HTS cuprate materials are extremely anisotropic; this raises the question of how thin can a cuprate layer be and still retain HTS. To answer this question experimentally, we have used a new approach, interface superconductivity formed in LSCO-LCO bilayers, and a new method of profiling the superconducting properties with atomic resolution based on the so-called

δ-doping technique which amounts to placing the dopant atoms in a single atomic layer. Fig. 2 shows the schematic of such δ-doping, achieved by replacing a small amount (3%) of Cu by Zn, in an LSCO-LCO heterostructure. Zinc doping suppresses superconductivity very efficiently: T_c is reduced in $La_{1.85}Sr_{0.15}Cu_{0.97}Zn_{0.03}O_4$ by about a factor of 2 compared to $La_{1.85}Sr_{0.15}CuO_4$. The atomic-layer-by-layer synthesis method allows us to dope just a single, predetermined CuO_2 layer with Zn. Thus we can perform "δ-doping tomography" and compare a series of samples in which we vary systematically - in increments of 0.5 unit cells - the position of CuO_2 layer δ-doped by Zn.

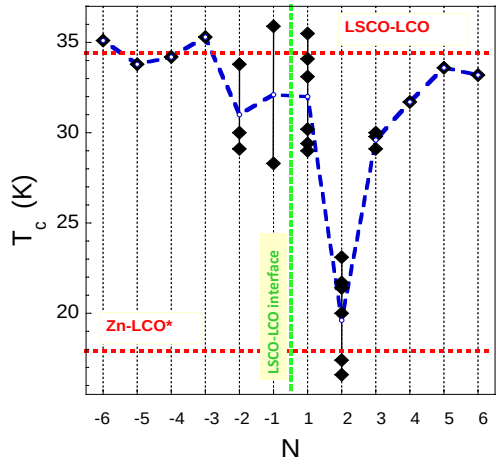

Fig. 3. Zn δ-doping reduces T_c dramatically only when Zn is placed in the second CuO_2 plane above the interface.

We prepared a set of LSCO-LCO bilayers, with each LSCO or LCO layer exactly 3 unit cells thick, so that each bilayer film contains 12 CuO_2 planes (Fig. 2). Apart from few undoped control samples, in every bilayer one CuO_2 plane is doped with 3% Zn. The position of the Zn-doped CuO_2 layer is varied systematically from the CuO_2 plane closest to the $LaSrAlO_4$ substrate (N = -6) to the one nearest to the free film surface (N = 6). We studied the superconducting transport properties of these films by measuring the temperature-dependent dc resistance $R(T)$ between 4.2 to 300 K. Most of the $R(T)$ curves almost coincided, and showed $T_c = 32 \pm 4$ K; this spread is similar to what we observe in single-phase films. However, one $R(T)$ curve, for the N = 2 sample, shows a much lower $T_c \approx 18$ K. In Fig. 3, we show the measured T_c as a function of the position (N = -6, -5,…-1, 1, 2, …, 6) of the CuO_2 plane doped with Zn. A pronounced depression of T_c, roughly by a factor of 2, occurs when the Zn dopant atoms are placed in the N = 2 layer, i.e., in the second CuO_2 plane above the LSCO-LCO interface. where $T_c = 18 \pm 3$ K. Measurements of the magnetic penetration depth $\lambda(T)$ by mutual inductance technique showed the same N-dependence. We conclude that this particular *single CuO_2 layer* is responsible for the interface superconductivity with $T_c = 32 \pm 4$ K.

Superconducting field-effect transistor: the nature of S-I transition. The cleanest approach to tune the density of mobile charge carriers is by applying an external electric field, like it is done in a field-effect transistor (FET). However, the Thomas-Fermi screening length in optimally doped LSCO is much shorter ($\lambda_{TF} = 6\pm2$ Å) than in a typical semiconductor. Thus, in order to dope the topmost CuO_2 layer at the surface of La_2CuO_4 (LCO) to the optimum level ($x = 0.15$, which corresponds to the areal carrier density of about 10^{18} m^{-2}) one needs the electric field strength exceeding 10^{10} V/m - and even then already the second CuO_2 layer below the surface would be doped only to a level of say $x \sim 0.05$ and hence probably not superconducting at all. This underlines the two main technical difficulties. First, one needs a layer that is extremely thin yet continuous and perfect enough to sustain HTS undiminished. Second, one needs a way to generate a huge electric field, far above the breakdown limit of any known dielectric. For these reasons, fabrication of a HTS FET has been a long-standing challenge.

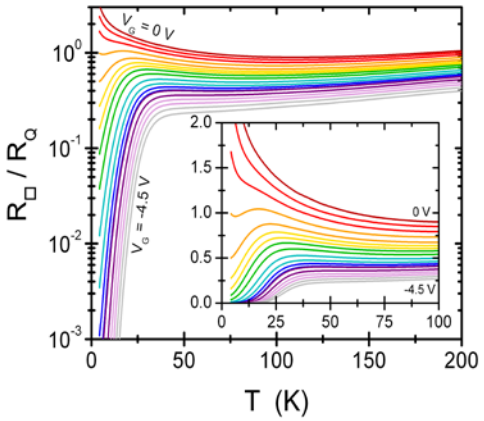

Fig. 4. Temperature dependence of resistance on log and linear (inset) scales. The gate voltage, and hence carrier density, is fixed for each curve and ranges from 0 V to -4.5 V in 0.25 V steps.

We achieved a breakthrough by leveraging on two recent technical advances. One is the capability of ALL-MBE to synthesize ultrathin - 1, 1.5 and 2 unit cells thick - films of $La_{2-x}Sr_xCuO_4$ (LSCO). The other is that in electrolyte-based supercapacitors huge electric fields (> 10^{10} V/m) have been attained inside the Helmholtz double layers; the induced surface charge density reaches 10^{18}-10^{19} m^{-2}. In our study, we fabricated lithographically a range of devices of well defined geometry, for accurate measurements of resistivity and magnetic susceptibility. Fig. 4 shows $R(T)$ curves of one such device for various values of the applied gate voltage V_{gate}. Large shifts are observed both in the normal state resistivity and in T_c. In this and other samples, we see shifts in x by up to ±0.035, and shifts in T_c by as much as 30 K. In some initially underdoped samples, these data span the superconductor-insulator (S-I) transition in a broad range, with dozens of curves on both sides; an example is shown in Fig. 4. Such data enable a meaningful scaling analysis; in Fig. 5, we have inverted the same $R_{\square}(T,x)$ matrix, scaling the abscisa as $u = |x-x_c|\, T^{-1/\nu z}$, with $\nu z = 1.5$. Over a hundred curves have collapsed to one, with the critical values $x_c \approx 0.06$ and $R_c = 6.45 \pm 0.10$ kΩ. The collapse is excellent up to 15-20 K; the exponent is identical on both sides of the transition. This is consistent with a continuous 2D S-I quantum phase transition (QPT), where quantum critical behavior extends up to about 0.5 T_c^{max}.

Our experimental results are consistent with the predictions of the bosonic theory in its simplest (self-dual) form. In particular, $R_c = R_Q \equiv h/(2e)^2$ seems very telling; the simplest explanation is that pairs exist on both sides of the *S-I* QPT, i.e., that the transition is driven by quantum *phase* fluctuations. This physical picture requires the existence of a Bose glass of localized Cooper pairs, and of freely moving vortices, on the insulating side of the QPT. Apart from revealing the nature of the *S-I* phase transition, the significance of this result is in that it indicates the existence, between *I* and *S* phases, of a strange new condensed state of matter, a *Bose metal*, which defies the basic tenet that all metals are Fermi Liquids.

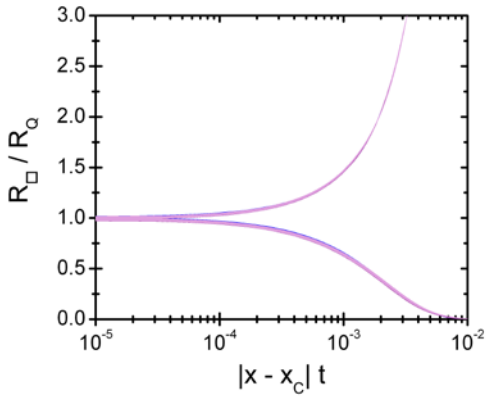

Fig. 5. Scaling of the same $R_\square(x,T)/R_Q$ data with respect to a single variable $u = |x\text{-}x_c|*t$, with $t = T^{-2/3}$.

Future Plans

We will use electrolyte-based HTS devices to further explore the nature of the *S-I* quantum phase transition in underdoped cuprates and the *S-M* transition in overdoped cuprates. We plan to (i) study the scaling of dynamic conductance with the applied electric field, which should provide a second constraint on the critical exponents ν and z and allow for their separate determination, (ii) extend the measurements to lower T, (iii) apply strong magnetic fields and (iv) repeat some of the experiments on few other cuprate superconductors, to check whether the observed behavior is common and perhaps universal.

Next, we are investigating systematically the effects of reduced dimensionality and confined geometries on HTS. We will synthesize atomically smooth films of optimally doped LSCO, BSCCO, or DBCO and lithographically fabricate nanowires, nanorings, nanodots, etc. We will measure the transport properties of these devices in order to determine the critical temperature T_c, the critical current density j_c, etc. One goal is to test the role of hypothetical dynamic charge stripes *vis-à-vis* the HTS state; if we find undiminished T_c in nanowires (and perhaps even in nanodots), this would imply that stripes are either absent or do not matter much in these samples. In HTS nanorings, we will measure transport in magnetic field and try to observe the Bohm-Aharonov oscillations, and in particular to study their temperature dependence, hoping to determine whether pairing indeed occurs well above T_c as postulated in some theories of HTS.

DOE-BES Workshop on Superconductivity has identified as one of the Priority Research Directions the search for new and improved artificial superconductors using MBE and atomic-layer engineering. One idea that we are pursuing is to artificially reduce the dimensionality of doped $BaBiO_3$ from 3D to 2D. Almost all known superconductors with $T_c > 20$ K – cuprates, pnictides, MgB_2, ZrNCl, etc., - have layered structures and are very anisotropic. The only exception is $Ba_{0.6}K_{0.4}BiO_3$, which is cubic and isotropic, and yet has $T_c = 30$ K. The question is what would happen if one could make its 2D analogue. Using ALL-MBE, we are able to alternate $BaBiO_3$ layers with layers of $BaLaO_3$. Fig. 6 shows the attempted structure, $Ba_3Bi_2LaO_{9-\delta}$, which was indeed confirmed both by XRD and high-resolution transmission electron microscopy (HRTEM). The films are highly crystalline and atomically smooth, but not superconducting, even though they are metallic; at low temperature, the temperature dependence changes sign suggesting weak localization or possibly a charge-density wave formation. Nevertheless, this is one of rare examples of successful digital synthesis of a novel, artificial meta-material. We plan to investigate this further by exploring different levels of doping with La, varying epitaxial strain by the choice of substrate, as well as photo-doping, and electrolyte-based field effect.

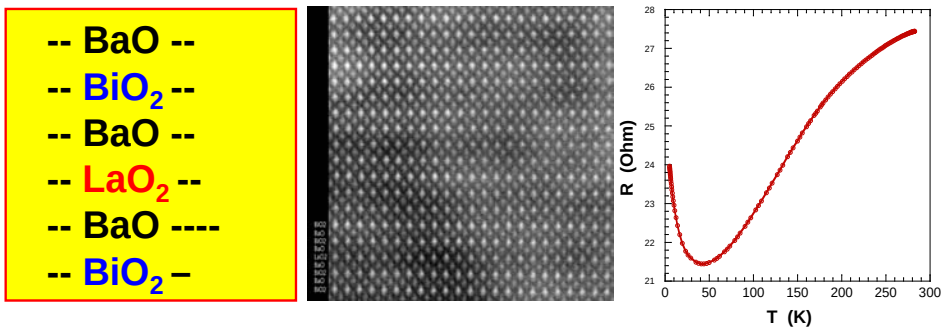

Fig. 6. Digital synthesis of a novel metamaterial. (a) The attempted layered structure, $Ba_3Bi_2LaO_9$. (b) The cross-section HRTEM (S. Pennycook, ORNL) of an actual BLBO film. (c) The measured resistance of a BLBO film. ($R = 25\ \Omega$ corresponds to $\rho \approx 500\ \mu\Omega$cm.)

DOE Sponsored research papers in 2009-20011 from Current Grant

1. A. T. Bollinger, G. Dubuis, J. Yoon, D. Pavuna, J. Misewich & I. Bozovic, "Superconductor–insulator transition in $La_{2-x}Sr_xCuO_4$ at the pair quantum resistance", ***Nature*** 472, 458 (2011).

2. L. S. Bilbro, R. Valdés Aguilar, G. Logvenov, O. Pelleg, I. Bozovic and N. P. Armitage, Temporal correlations of superconductivity above the transition temperature in $La_{2-x}Sr_xCuO_4$ probed by terahertz spectroscopy", ***Nature Physics*** 7, 298-302 (2011).

3. E. Morenzoni, B. M. Wojek, A. Suter, T. Prokscha, G. Logvenov & I. Bozovic, "The Meissner effect in a strongly underdoped cuprate above its critical temperature", ***Nature Communications*** 2, 272 (2011).

4. A. Suter, E. Morenzoni, T. Prokscha, B. M. Wojek, H. Luetkens, G. Nieuwenhuys, A. Gozar, G. Logvenov and I. Bozovic, "Two-Dimensional Magnetic and Superconducting Phases in Metal-Insulator $La_{2-x}Sr_xCuO_4$ Superlattices Measured by Muon-Spin Rotation", ***Phys. Rev. Letters*** 106, 237003 (2011).

5. M. Beyer, M. Beck, D. Stadter, H. Schafer, V. V. Kabanov, G. Logvenov, I. Bozovic, G. Koren, and J. Demsar1 Photoinduced melting of superconductivity in the high-T_c superconductor $La_{2-x}Sr_xCuO_4$ probed by time-resolved optical and THz techniques", Phys. Rev. B (2011) in press.

6. G. Dubuis, A. T. Bollinger, D. Pavuna and I. Božović, "Electric Field Effect on Superconductivity in $La_{2-x}Sr_xCuO_4$", J. Appl. Phys. (2011) in press

7. J. Pereiro, A. Petrovic, C. Panagopoulos and I. Božović, "Interface superconductivity: History, development and prospects", Physics Express 1, published online (2011).

8. I. Sochnikov, A. Shaulov, Y. Yeshurun, G. Logvenov and I. Bozovic, "Large oscillations of the magnetoresistance in nanopatterned high-temperature superconducting films", ***Nature Nanotechnology*** 5, 516-9 (2010).

9. H. Zhou, Y. Yacoby, R. Pindak, V. Butko, G. Logvenov and I. Bozovic, "Anomalous Expansion of the Copper-Apical Oxygen Distance in Superconducting $La_2CuO_4 - La_{1.55}Sr_{0.45}CuO_4$ Bilayers", ***Proc. Nat. Acad. Sci.*** 107, 8103-8107 (2010).

10. G. Logvenov, A. Gozar, V. Y. Butko, A. T. Bollinger, N. Bozovic, Z. Radovic and I. Bozovic, "Comprehensive study of high-T_c interface superconductivity", J. Chem. Phys. Solids **71**, 1098–1104 (2010).

11. J. A. Clayhold, O. Pelleg, D. W. Rench, B. M. Kerns, M. D. Schroer, D. C. Ingram, A. T. Bollinger, G. Logvenov and I. Bozovic, "Constraints on Models of Electrical Transport in Optimally Doped $La_{2-x}Sr_xCuO_4$ from Measurements of Radiation-Induced Defect Resistance", Journal of Superconductivity and Novel Magnetism 23, 339-342 (2010).

12. I. Sochnikov, A. Shaulov, Y. Yeshurun, G. Logvenov and I. Bozovic, "Oscillatory magnetoresistance in nanopatterned superconducting $La_{1.84}Sr_{0.16}CuO_4$ films", Phys. Rev. B 82, 094513 (2010)

13. G. Logvenov, A. Gozar and I. Bozovic, "High-temperature superconductivity in a single copper-oxygen plane", ***Science*** 326, 699–702 (2009).

14. S. Smadici, J. C. T. Lee, S. Wang, P. Abbamonte, A. Gozar, G. Logvenov, C. Deville Cavellin and I. Bozovic, "Superconducting Transition at 38 K in Insulating-Overdoped La_2CuO_4-$La_{1.64}Sr_{0.36}CuO_4$ Superlattices: Evidence for Interface Electronic Redistribution from Resonant Soft X-Ray Scattering", ***Phys. Rev. Lett.*** 102, 107004 (2009).

15. V. Butko, G. Logvenov, N. Bozovic, Z. Radovic and I. Bozovic, "Madelung Strain in Cuprate Superconductors – A Route to Enhancement of the Critical Temperature", ***Advanced Materials*** 21, 3644-3688 (2009).

16. J. A. Clayhold, O. Pelleg, A. T. Bollinger, G. Logvenov, B. M. Kerns, M. D. Schroer, D. W. Rench and I. Bozovic, "Statistical Characterization and Process Control for Improved Growth of $La_{2-x}Sr_xCuO_4$ Films", Journal of Superconductivity and Novel Magnetism 22, 797–804 (2009).

17. I. Božović, G. Logvenov, A. Gozar, A. Bollinger, O. Pelleg, Z. Radović and N. Božović, "Nano-structured films of cuprate superconductors and other complex oxides: MBE synthesis, characterization, and engineered properties", (Invited Keynote paper) Proc. ICCE-17, ed. by D. Hui, 2009.

18. S. V. Dordevic, L. W. Kohlman, L. C. Tung, Y.-J. Wang, A. Gozar, G. Logvenov and I. Bozovic, "Absence of magnetic field induced effects in the mid-infrared transmission of $La_{2-x}Sr_xCuO_4$ thin films", Phys. Rev. B 79, 134503 (2009).

19. I. Bozovic, A. Gozar, G. Logvenov, A. Bollinger, N. Bozovic and Zoran Radovic, "Insights in high-temperature superconductivity from the study of films and heterostructures synthesized by molecular beam epitaxy", Journal of Superconductivity and Novel Magnetism 22, 223-7 (2009).

In all of the above papers DOE funding under the DOE grant MA-509-MACA was explicitly acknowledged.

In this period, we also had one patent issued: I. Bozovic, G. Logvenov and A. M. Gozar, "High Temperature Interfacial Superconductivity", US Patent 2009/0137398, May 28, 2009.

Structure-property relationships at polar/nonpolar perovskite interfaces

S.A. Chambers (PI)[a], L. Qiao[a], T.C. Droubay[a], T.C. Kaspar[a], M.E. Engelhard[a], M.E. Bowden[a], V. Shutthanandan[a], P. Sushko,[b] T. Feng[c], H. D. Lee[c], T. Gustafsson[c], E. Garfunkel[c], A.B. Shah[d], J.-M. Zuo[d] and Q.M. Ramasse[e]

[a]Pacific Northwest National Laboratory, Richland, WA [b]University College, London, UK
[c]Rutgers University, Piscataway, NJ, [d]University of Illinois at Urbana-Champaign
[e]SuperSTEM Laboratory, STFC Daresbury, UK

I. Program scope

This program focuses on the growth and properties of doped transition metal and complex oxides prepared as epitaxial films. Our approach is to combine state-of-the-art epitaxial film growth techniques (plasma assisted molecular beam epitaxy (MBE) and off-axis pulsed laser deposition (PLD)) with definitive materials characterization and functional properties measurements, and the most advanced theoretical methods. Our interests include structural, compositional, magnetic, electronic, optical, and photochemical properties. Here we present our recent work on interfaces between the polar perovskites $LaAlO_3$ and $LaCrO_3$, and the nonpolar perovskite $SrTiO_3$. Of particular interest here are the relationships between composition and electronic properties at the interface.

II. Recent Progress

Complex oxides exhibit an exceedingly rich array of properties as a result of the electronic and magnetic degrees of freedom that can be built into the different sites in the lattice by the choice of metal cation. This richness has been exploited and built upon by preparing crystalline interfaces of dissimilar perovskites (general formula ABO_3). One of the most interesting and widely investigated systems of this kind is the $LaAlO_3/SrTiO_3(001)$ (LAO/STO) heterojunction. Despite the fact that both materials are wide-gap band insulators in the bulk, their interface can exhibit electronic conductivity,[1,2] and ultra-low temperature superconductivity,[3,4] above a critical thickness of 4 unit cells (u.c.), when prepared under certain rather specific conditions. These results have been widely interpreted as being due to an electronic reconstruction (or charge transfer) resulting from the polarity mismatch between LAO and STO, giving rise to a two-dimensional electron gas on the STO side of the interface.[5] This charge transfer is thought to eliminate the interface dipole, which if not removed by some means, would cause the electrostatic potential within the film to diverge. Most researchers tend to think of this interface in the most simplified way, as if it were atomically abrupt and defect free. Doing so allows simple models to be made and tested. Although a few papers have reported experimental results indicating that some degree of cation mixing occurs at the interface,[6-10] most investigators tend to ignore this phenomenon with regard to its effect on the electronic structure and model the interface in the most idealized terms.[11]

We have taken a different tack. Our approach has been to make a concerted effort to determine the extents of intermixing for the four metal cations, with the goal of elucidating how the various diffusion profiles affect electronic properties. We have used multiple techniques to study LAO/STO interfaces prepared by PLD in our laboratory,[12-14] and in the laboratories of others.[15] In summary, we have found that: (i) PLD–grown LAO is not necessarily stoichiometric, but exhibits a La:Al atom ratio which depends on plume angle,[16] (ii) the extent of intermixing of *A*-site cations (La and Sr) is greater than that for *B*-site cations (Al and Ti), as summarized in Fig. 1, paving the way for net donor (La) doping in the STO, (iii) the built-in potential within the LAO is much smaller than expected based on the simple polar catastrophe model of the LAO/STO interface, a result also independently found for MBE-grown LAO/STO,[17] (iv) the STO near the

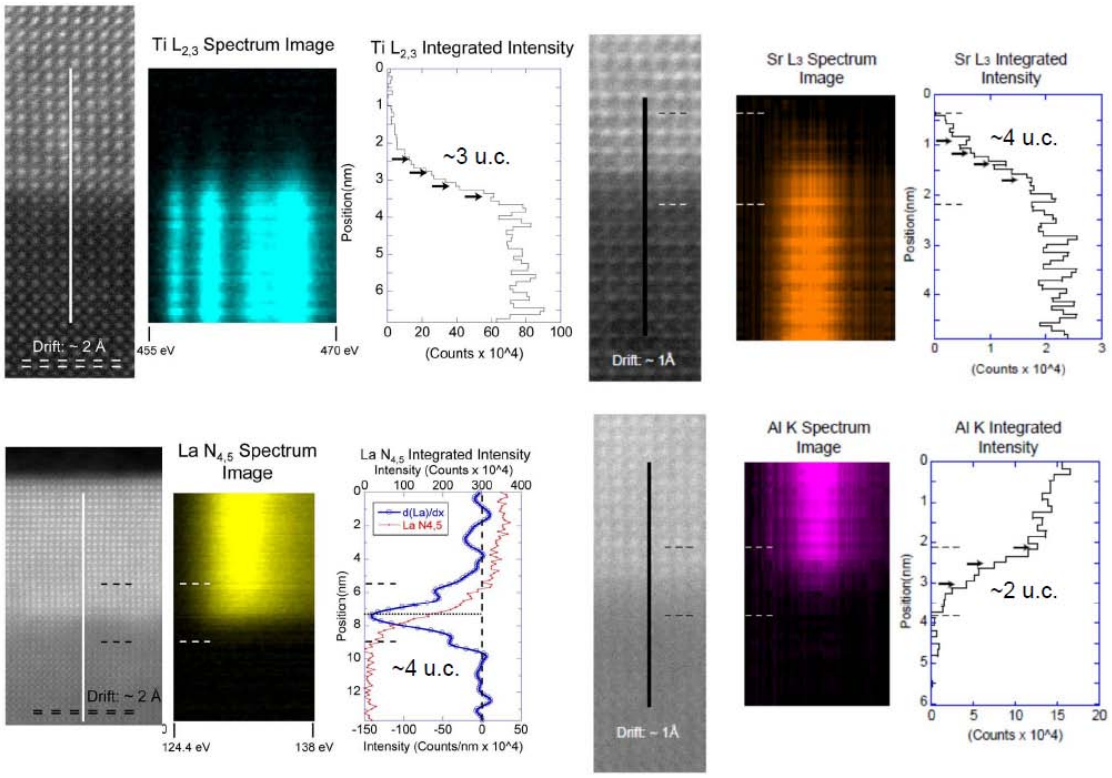

Fig. 1 Scanning transmission electron microcopy (STEM) and Ti $L_{2,3}$, Sr L_3, La $N_{4,5}$ and Al K-edge electron energy loss spectroscopy (EELS) images for 25 u.c. LAO/STO(001). The La diffuses into the STO to a depth of at least 4 u.c. whereas the Al, Sr, and Ti diffuse across the interface to a depth of 2, 4, and 3 u.c., respectively. Taken from ref. 15.

interface is in a nearly flat-band state, and does not exhibit the sharp downward band bending required to confine itinerant electrons to the interface, and, (v) the measured valence band offsets (VBO) are much smaller than predicted based on an idealized (i.e. abrupt and perfect) interface structure. We have also done extensive theoretical modeling of the interface.[15] The total electronic energies of ~65,000 different atom configurations were calculated using classical potentials and compared to that for the abrupt interface. We found that 49% of these configurations are energetically more stable than the idealized interface. The dipole is zero in 8% of all configurations, and among the most stable 10% of the configurations modeled, 29% have no dipole. Moreover, density functional and hybrid functional calculations on select intermixed and abrupt configurations corroborate the classical calculations. Additionally, the small experimental value of the VBO is accurately predicted only when intermixing is modeled. These results led us to argue that intermixing is a non-negligible perturbation to the interface electronic structure, and that interface conductivity may be better explained by intermixing and unintentional La doping of the underlying STO than by an electronic reconstruction.[15,18]

Electronic reconstruction leading to interface conductivity apparently does not occur for the $LaCrO_3$ (LCO)/STO(001) interface either, as recently shown using specimens grown by MBE in our laboratory.[19,20] LCO is an insulator with an optical gap of 3.3 e V,[21] for which the experimental electronic properties are well described using density functional theory (DFT) with a Hubbard *U* of zero.[22] Although LCO is orthorhombic in the bulk,[23] the pseudocubic lattice parameter for LCO is 3.885 Å, resulting in an excellent lattice match to STO (3.905 Å). Stoichiometric LCO grows in a layer-by-layer fashion on STO(001). The resulting films are coherently strained to the substrate for thicknesses of at least 50 nm. Preliminary STEM and

energy-dispersive x-ray analysis, along with high-resolution Rutherford backscattering (HRRBS), indicate that the interface is not atomically abrupt. Thus, unintentional doping in either the STO or the LCO may give rise to conductivity. Moreover, if the electronic reconstruction model is correct, this interface should be conductive above some critical thickness for the same reasons that LAO/STO should be conductive. Additionally, the band alignment, as determined by HRXPS, is conducive to electron confinement in the STO, should conductivity occur. These results are shown in Fig. 2. The valence band offset (VBO) is 2.45(6) eV. The top of the valence band (VB) is majority Cr 3*d* t_{2g}, and the spacing between the leading edge of this feature and that for the majority O 2*p* derived portion of the VB at deeper binding energy is 1.7(1) eV. Thus, the *dd* (Cr 3*d* t_{2g} → e_g) gap is ~3.3 – 1.7 = ~1.6. The conduction band offset (CBO) is then estimated as the VBO plus the Cr 3*d* t_{2g} → e_g gap minus the STO band gap, giving 0.8 eV. The band alignment is thus staggered (a type II heterostructure), as depicted in Fig. 2. The electric fields within the STO and LCO were determined by modeling the core-level peak widths for thin-film (5 u.c.) heterojunctions. No field was detected in the STO, and a field of ~200 meV per u.c. was detected in the LCO. This electronic structure is conducive to confining any itinerant electrons to the STO side of the interface, but dispersion into the STO may occur because of lack of sharp downward band bending within the STO.

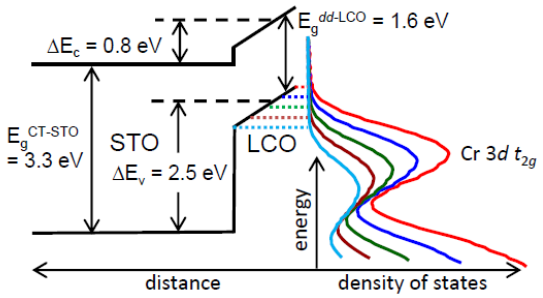

Fig. 2 Energy level diagram illustrating the band offsets and potential gradients extracted from XPS data for 5 u.c. LCO/STO(001). The five dotted lines in the LCO represent valence band maxima for each of the u.c. and connect to the associated VB DOS (right).

A built-in potential of ~200 meV per u.c. within the LCO is adequate to trigger an electronic reconstruction within a 5 u.c. film. Yet, the interface is completely insulating for 5 and 26 u.c. films. Our DFT calculations show that these results can be understood in terms of charge redistribution within the Cr 3*d* t_{2g} derived portion of the LCO valence band, which in turn strongly screens the electric field within the LCO and mitigates the polarity mismatch. This phenomenon, not previously considered, adds another level of complexity to the issue of conductivity at polar/nonpolar perovskite interfaces. At the same time, this physics is potentially important for optimizing the electronic structure of polar/nonpolar interfaces by judiciously selecting a combination of non-reducible and reducible cations at the *B* site.

III. Future Plans

Our future goals focus more on enhancing the conductivity of the polar perovskite itself, rather than investigating anomalous interface conductivity. To this end, we plan to investigate the detailed electronic and optical properties of $ATiO_{3-x}N_x$ and $Sr_xLa_{1-x}BO_3$ (*B* = Cr or Fe) grown on STO(001) and $(LaAlO_3)_{0.3}(Sr_2AlTaO_6)_{0.7}$(001) (LSAT) by MBE. $Sr_xLa_{1-x}BO_3$ will be prepared as both random alloys and ordered superlattices of the form $(SrBO_3)_m$/ $(LaBO_3)_n$ and the properties will be compared. Of particular interest is the extent to which the optical gap can be red-shifted into the visible by doping, and the associated enhancement of visible-light photochemical activity.

---

[1] A. Ohtomo and H. Y. Hwang, Nature **427**, 423 (2004).
[2] S. Thiel, G. Hammerl, A. Schmehl, C. W. Schneider, and J. Mannhart, Science **313**, 1942 (2006).
[3] N. Reyren, S. Thiel, A. D. Caviglia, L. F. Kourkoutis, G. Hammerl, C. Richter, C. W. Schneider, K. T., A.-S. Ruetschi, D. Jaccard, M. Gabay, D. A. Muller, J.-M. Triscone, and J. Mannhart, Science **317**, 1196 (2007).

[4] N. Reyren, S. Gariglio, A. D. Caviglia, D. Jaccard, T. Schneider, and J. M. Triscone, Appl. Phys. Lett. **94**, 112506 (2009).
[5] J. Mannhart and D. G. Schlom, Science **327**, 1607 (2010).
[6] N. Nakagawa, H. Y. Hwang, and D. A. Muller, Nat. Mat. **5**, 204 (2006).
[7] P. R. Willmott, S. A. Pauli, R. Herger, C. M. Schleputz, D. Martoccia, B. D. Patterson, B. Delley, R. Clarke, D. Kumah, C. Cionca, and Y. Yacoby, Phys. Rev. Lett. **99**, 155502 (2007).
[8] A. S. Kalabukhov, Y. A. Boikov, I. T. Serenkov, V. I. Sakharov, V. N. Popok, R. Gunnarsson, J. Borjesson, N. Ljustina, E. Olsson, D. Winkler, and T. Claeson, Phys. Rev. Lett. **103**, 146101 (2009).
[9] C. L. Jia, S. B. Mi, M. Faley, U. Poppe, J. Schubert, and K. Urban, Phys. Rev. B **79**, 081405 (2009).
[10] Y. Yamamoto, C. Bell, Y. Hikita, H. Y. Hwang, H. Nakamura, T. Kimura, and Y. Wakabayashi, Phys. Rev. Lett. **107**, 036104 (2011).
[11] R. Pentcheva and W. E. Pickett, J. Phys: Cond. Mat. **22**, 043001 (2010).
[12] L. Qiao, T. C. Droubay, T. Varga, M. E. Bowden, V. Shutthanandan, Z. Zhu, T. C. Kaspar, and S. A. Chambers, Phys. Rev. B **83**, 085408 (2011).
[13] L. Qiao, T. C. Droubay, V. Shutthanandan, Z. Zhu, P. V. Sushko, and S. A. Chambers, J. Phys.: Condens. Matter **22**, 312201 (2010).
[14] L. Qiao, T. C. Droubay, T. C. Kaspar, P. V. Sushko, and S. A. Chambers, Surf. Sci., in press (2011).
[15] S. A. Chambers, M. H. Engelhard, V. Shutthanandan, Z. Zhu, T. C. Droubay, L. Qiao, P. V. Sushko, T. Feng, H. D. Lee, T. Gustafsson, E. Garfunkel, A. B. Shah, J.-M. Zuo, and Q. M. Ramasse, Surf. Sci. Rep. **65**, 317 (2010).
[16] T. C. Droubay, L. Qiao, T. C. Kaspar, M. H. Engelhard, V. Shutthanandan, and S. A. Chambers, Appl. Phys. Lett. **97**, 124105 (2010).
[17] Y. Segal, J. H. Ngai, J. W. Reiner, F. J. Walker, and C. H. Ahn, Phys. Rev. B **80**, 241107(R) (2009).
[18] S. A. Chambers, Surf. Sci. **605**, 1133 (2011).
[19] L. Qiao, T. C. Droubay, M. E. Bowden, V. Shutthanandan, T. C. Kaspar, and S. A. Chambers, Appl. Phys. Lett., in press (2011).
[20] S. A. Chambers, L. Qiao, T. C. Droubay, T. C. Kaspar, B. Arey, and P. V. Sushko, submitted (2011).
[21] T. Arima, Y. Tokura, and J. B. Torrance, Phys. Rev. B **48**, 17006 (1993).
[22] K. P. Ong, P. Blaha, and P. Wu, Phys. Rev. B **77**, 073102 (2008).
[23] J. Yang, Acta Crystallogr., Sect. B: Struct. Sci **64**, 281 (2008).

IV. Sponsored Publications in 2010-2011

1. S.A. Chambers, "Epitaxial Growth and Properties of Doped Transition Metal and Complex Oxide Films", Advanced Materials **22**, 219 (2010).
2. T.C. Droubay, L. Qiao, T.C. Kaspar, M.H. Engelhard, V. Shutthanandan, S.A. Chambers, "Non-stoichiometric Material Transfer in the Pulsed Laser Deposition of $LaAlO_3$" Appl. Phys. Lett. **97,** 124105 (2010).
3. S.A. Chambers, M.H. Engelhard, V. Shutthanandan, Z. Zhu, T.C. Droubay, L. Qiao, P.V. Sushko, T. Feng, H. D. Lee, T. Gustafsson, E. Garfunkel, A. Shah, J. –M. Zuo, "Instability, Intermixing and Electronic Structure at the $LaAlO_3/SrTiO_3$(001) Interface", Surf. Sci. Rep. **65**, 317 (2010).
4. L. Qiao, T. C. Droubay, V. Shutthanandan, Z. Zhu, P. V. Sushko, S. A. Chambers, "Thermodynamic Instability at the Stoichiometric $LaAlO_3/SrTiO_3$ interface", J. Physics: Cond. Mat. **22**, 312201 (2010).
5. L. Qiao, T. C. Droubay, T. Varga, M. E. Bowden, V. Shutthanandan, Z. Zhu, T. C. Kaspar, S. A. Chambers, "Epitaxial growth, structure and intermixing at the $LaAlO_3/SrTiO_3$ interface as the film stoichiometry is varied", Phys. Rev. **B 83**, 085408 (2011).
6. S.A. Chambers, "Understanding the Mechanism of Conductivity at the $LaAlO_3/SrTiO_3$(001) Interface", invited Prospective for Surf. Sci. **605**, 1133 (2011).
7. L. Qiao, T. C. Droubay, T. C. Kaspar, P. V. Sushko, S. A. Chambers, "Cation mixing, band offsets and electric fields at the $LaAlO_3/SrTiO_3$(001) heterojunction with variable La:Al atom ratio", Surf. Sci., in press (2011).
8. L. Qiao, T.C. Droubay, M.E. Bowden, V.Shutthanandan, T.C. Kaspar, S. A. Chambers, "$LaCrO_3$ heteroepitaxy on $SrTiO_3$(001) by molecular beam epitaxy", App. Phys. Lett., in press (2011), and http://arxiv.org/abs/1105.4290.

Magnetic and electronic properties of doped oxide semiconductors

S.A. Chambers (PI)[a], T.C. Kaspar[a], T.C. Droubay[a], S.J.S. McCloy[a], J.V. Ryan[a], A. Ney[b], T. Kammermeier[b], K. Ollefs[b], S. Ye[b], V. Ney[b], F. Wilhelm[c], A. Rogalev[c], C.A. Johnson[d], K.R. Kittilstved[d], D.R. Gamelin[d], D.C. Look[e]

[a]Pacific Northwest National Laboratory, Richland, WA [b]Universität Duisburg-Essen, Duisburg, Germany [c]European Synchrotron Radiation Facility, Grenoble, France [d]University of Washington, Seattle, WA [e]Wright State University, Dayton, OH

I. Program Scope

This program focuses on the growth and properties of doped transition metal and complex oxides prepared as epitaxial films. Our approach is to combine state-of-the-art epitaxial film growth techniques (plasma assisted molecular beam epitaxy (MBE) and off-axis pulsed laser deposition (PLD)) with definitive materials characterization and functional properties measurements, and the most advanced theoretical methods. Our interests include structural, compositional, magnetic, electronic, optical, and photochemical properties. Doped ZnO is of particular interest, and has been widely studied for its potentially promising magnetic and electronic properties. Our approach is to deposit high quality epitaxial doped ZnO thin films by off-axis PLD, and thoroughly characterize them with both conventional materials characterization techniques and a suite of x-ray absorption spectroscopy (XAS) techniques. Structure-property relationships can then be elucidated.

II. Recent Progress

As a wide-bandgap, transparent semiconducting oxide, ZnO has been widely studied for a variety of electrical and optical applications. With the prediction of room temperature ferromagnetism in *p*-type Mn:ZnO by Dietl *et al*.[1] and in *n*-type Co:ZnO by Sato *et al*.,[2] a considerable effort was undertaken to identify transition-metal-doped ZnO which exhibited ferromagnetism at and above room temperature, in the hopes of developing a ferromagnetic dilute magnetic semiconductor (DMS) for use in potential spintronic devices. A review of the recent literature, however, demonstrates the disparate claims and ensuing controversy resulting from this field of investigation.[3,4]

We have grown both Mn:ZnO and Co:ZnO by off-axis PLD. We have shown by high-resolution x-ray diffraction (XRD), x-ray absorption near edge spectroscopy (XANES) and extended x-ray absorption fine structure (EXAFS), and high resolution transmission electron microscopy (TEM) that Co:ZnO exhibits exceedingly high structural quality. X-ray linear dichroism (XLD), an atom-specific spectroscopy which is highly sensitive to the local structural environment of the absorbing atom, combined with multiple scattering simulations, reveals that > 95% of the Co dopants are located at Zn sites. These high quality, thoroughly characterized samples were measured with sensitive magnetic techniques such as low temperature superconducting quantum interference device (SQUID) and x-ray magnetic circular dichroism (XMCD), and shown conclusively to be completely paramagnetic, with no ferromagnetic ordering, down to 2 K. Moreover, co-doping with Al, which results in degenerate *n*-type conductivity, was not found to induce ferromagnetism.

Although *n*-Co:ZnO is not a high-T_c DMS as originally predicted, our collaboration with the group of Professor Daniel Gamelin at the University of Washington (UW) has shown that Co:ZnO is an excellent model system for investigating dopant activation in a wide-gap semiconductor. This process is of considerable interest for solar photocatalysis. If doping can create new optical excitations in the visible region of the solar spectrum that lead to electrical conductivity, the material can in principle be used to

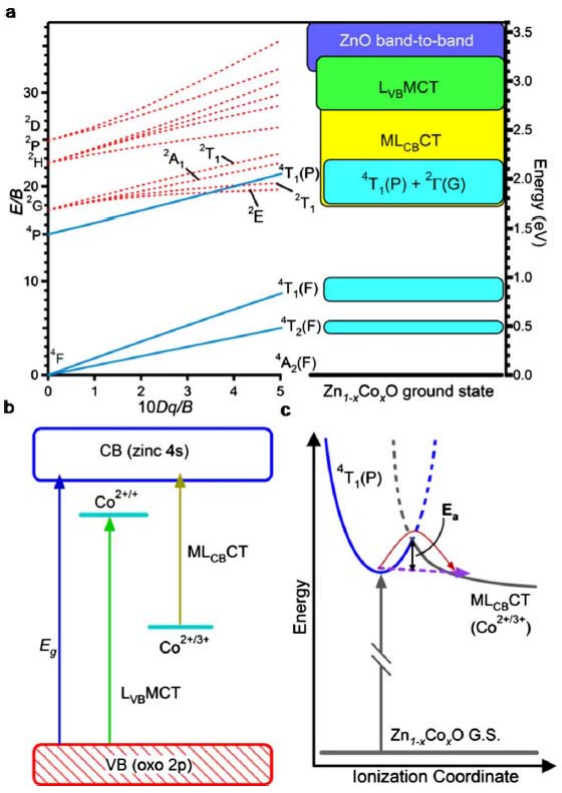

Fig. 1. Co^{2+} *d-d* excited transitions in Co:ZnO, as determined by photoconductivity and electronic absorption measurements.

harvest visible light to drive surface catalytic redox processes (photoelectrochemistry). This investigation employed photoconductivity (PC) transport measurements. The temperature dependence of electrical conductivity resulting from the photogenerated $^4T_1(P)$ Co *d-d* excitation at ~2.0 eV was investigated and found to result in spontaneous ionization at 27K, despite the localized nature of the excitation. An additional thermally assisted ionization process was found to occur at high temperatures that augments the *d-d* photoconductivity (Fig. 1). Moreover, it was found that the quantum efficiency for this process increases with decreasing Co concentration and increasing temperature. The former result is ascribed to the dependence of the conduction-band-edge potential on Co concentration.

We have also investigated Mn:ZnO by combining off-axis PLD with several atom-specific XAS techniques, TEM, secondary ion mass spectrometry (SIMS), vibrating sample magnetometry (VSM), and electrical transport to show that structurally-excellent Mn:ZnO grown in 10 mTorr of either N_2 or N_2O is: (i) not *p*-type, (ii) completely paramagnetic, and (iii) not characterized by a uniform Mn distribution. To the best of our knowledge, no group has succeeded in doping ZnO *p*-type in a stable, reproducibly way. So, not surprisingly, our Mn:ZnO films grown in N_2 and N_2O were highly resistive and paramagnetic, despite exhibiting N concentrations of up to ~10^{21} atoms/cm^3. Presumably, the holes from N were compensated by unintentional donors, as others have concluded. Mn K-shell XANES revealed that Mn is present as Mn(II), and EXAFS established that Mn substitutes for Zn in the lattice. Mn L-edge XMCD showed that the Mn is paramagnetic from ambient temperature down to 5K. However, the dependence of the Mn L-edge XMCD (normalized to the corresponding XANES) on magnetic field strength for all but the most dilute specimens was weaker than expected based on Monte Carlo simulations of a random distribution of Mn dopants, as seen in Fig. 2. This result indicates that Mn substitutes for Zn in a correlated fashion, presumably because of a total energy stabilization resulting from closer mutual proximity of the dopants.

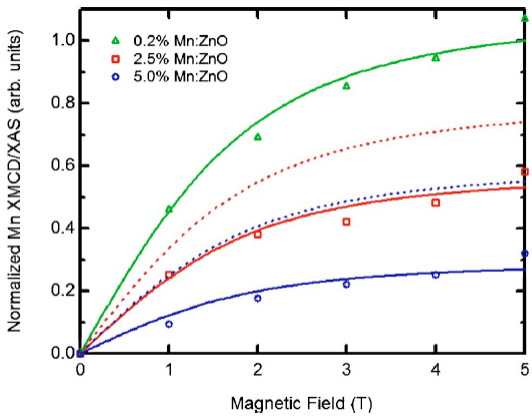

Fig. 2. Normalized Mn XMCD vs. magnetic field for Mn:ZnO films (symbols), and expected magnetization (lines).

These structurally excellent Mn:ZnO epitaxial films have also proved to be very useful for gaining fundamental insight into the electronic properties of model dilute magnetic II-VI oxides. Similar to Co:ZnO, PC measurements carried out by our collaborators at UW

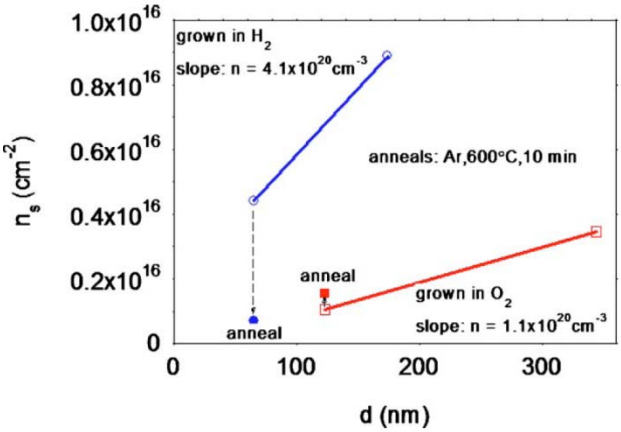

Fig. 3. Comparison of sheet carrier concentration n vs. film thickness d for Ga:ZnO grown in H_2 and O_2 (open symbols), and change in carrier concentration after annealing at 600°C in Ar.

reveal electronic conductivity initiated by a Mn-derived *d-d* transition at ~2.2 eV, a phenomenon generally not seen in other TM^{2+}-doped non-oxide II-VI semiconductors. Additionally, optical magnetic circular dichroism (MCD) measurements yield definitive insight into the *sp-d* exchange interaction between Mn and the ZnO band structure, an important defining property for candidate DMS materials. It was found that excitonic Zeeman splitting at the band edge in lightly doped films was inverted in sign and an order of magnitude larger compared to that for undoped ZnO. Thus, Mn:ZnO is similar to other magnetically doped II-VI semiconductors in that the Zeeman splitting is dominated by a strong *sp-d* exchange interaction.

ZnO is also a very attractive oxide semiconductor for use in technologies requiring optical transparency and high electrical conductivity. These include electrodes for flat- panel displays and photovoltaic cells, low-emissivity windows, window defrosters, and *n*-type layers in light-emitting and laser diodes. We have investigated *n*-type doping with H, and co-doping with H and Ga. We were the first group to report the results of growing ZnO in an H_2 ambient,[5,6] which revealed a new shallow donor state not previously observed. This donor state exhibited more thermal stability than what had previously been achieved by post-growth annealing in H_2, and was ascribed to interstitial H doping. Although the H concentration was not sufficiently high to determine lattice location by nuclear reaction analysis (NRA) and channeling, these results were consistent with H occupying O sites. As shown in Fig. 3, doping with Ga *and* growing in H_2 resulted in higher carrier concentrations and lower resistivities than deposition of Ga:ZnO in O_2 and post-growth annealing in Ar. Detailed SIMS measurements, along with advanced modeling of the transport data by our collaborator Prof. David Look, revealed that, contrary to the results of pure ZnO deposition in H_2, when Ga:ZnO is deposited in H_2 the H does not incorporate as a donor, but rather facilitates higher extents of Ga incorporation at Zn sites.

III. Future Plans

Our future plans are focused on maximizing electrical conductivity in ZnO. Our approach is to seek to understand and control the physics of transport in ZnO, paying close attention to the key parameters which ultimately determine the conductivity. The important physical quantities that must be controlled are the donor and acceptor concentrations, N_D and N_A, respectively. N_D is closely related to the donor dopant concentration, which can be measured with SIMS. N_A is harder to determine because no acceptor dopant is deliberately introduced into *n*-ZnO. The most likely acceptor is the Zn vacancy (V_{Zn}), and, in the case of Ga-doped ZnO, the $Ga_{Zn}V_{Zn}$ complex is also a possibility. In collaboration with Prof. David Look of Wright State University and other investigators, we will explore ways to detect and gain control over these undesirable acceptor defects. Our role at PNNL will be the PLD growth of ultrahigh quality ZnO, and characterization by HRXRD, RBS and SIMS. Prof. Look and his group will carry out temperature-dependent Hall effect and photoluminescence measurements, as well as modelling the transport data to extract N_D and N_A. Other collaborators, under Prof. Look's direction, will carry out XAS, positron annihilation, and theoretical modelling. By carrying out this suite of measurements and calculations for

films grown under different conditions, we will be able to *rationally* modify the growth process *in an informed way*, and in so doing, maximize conductivity.

---

[1]T. Dietl, H. Ohno, F. Matsukura, J. Cibert and D. Ferrand, Science **287** (2000).
[2]K. Sato and H. Katayama-Yoshida, Semicond. Sci. Technol. **17** (2002).
[3]S. A. Chambers, Surface Science Reports **61** 345 (2006).
[4]S. A. Chambers, Advanced Materials **22** 219 (2010).
[5]Y. J. Li, T. C. Kaspar, T. C. Droubay, Z. Zhu, V. Shutthanandan, P. Nachimuthu and S. A. Chambers, Applied Physics Letters **92** 152105 (2008).
[6]Y. J. Li, T. C. Kaspar, T. C. Droubay, A. G. Joly, P. Nachimuthu, Z. Zhu, V. Shutthanandan and S. A. Chambers, Journal of Applied Physics **104** 053711 (2008).

IV. Selected Sponsored Publications in 2010-2011

1. D.C. Look, T.C. Droubay, J.S. McCloy, Z. Zhu, and S.A. Chambers. "Ga-doped ZnO grown by pulsed laser deposition in H_2: The roles of Ga and H." *J. Vac. Sci. Technol. A* **29** 03A102 (2011).
2. C.A. Johnson, K.R. Kittilstved, T.C. Kaspar, T.C. Droubay, S.A. Chambers, G.M. Salley, and D.R. Gamelin. "Mid-gap electronic states in $Zn_{1-x}Mn_xO$." *Physical Review B* **82**, 115202 (2010).
3. A. Ney, V. Ney, S. Ye, K. Ollefs, T. Kammermeier, T.C. Kaspar, S.A. Chambers, F. Wilhelm, and A. Rogalev. "Magnetism of Co doped ZnO with Al codoping: Carrier-induced mechanisms versus extrinsic origins." *Physical Review B Rapid Communications* **82**, 041202(R) (2010).
4. C.A. Johnson, T.C. Kaspar, S.A. Chambers, G.M. Salley, and D.R. Gamelin. "Sub-band-gap photoconductivity in Co^{2+}-doped ZnO." *Physical Review B* **81**, 125206 (2010).
5. J.S. McCloy, J.V. Ryan, T. Droubay, T.C. Kaspar, S. Chambers, D.C. Look. "Magnetotransport properties of high quality Co:ZnO and Mn:ZnO single crystal pulsed laser deposition films: Pitfalls associated with magnetotransport on high resistivity materials." *Review of Scientific Instruments* **81** 063902 (2010).
6. V. Ney, S.Ye, T.Kammermeier, K.Ollefs, A.Ney, T.C.Kaspar, S.A.Chambers, F.Wilhelm, A.Rogalev. "Tuning the magnetic properties of $Zn_{1-x}Co_xO$ films." *Journal of Magnetism and Magnetic Materials* **322** 1232 (2010).
7. Ney, T. Kammermeier, K. Ollefs, S. Ye, V. Ney, T.C. Kaspar, S.A. Chambers, F. Wilhelm, A. Rogalev. "Anisotropic paramagnetism of Co-doped ZnO epitaxial films." *Physical Review B* **81** 054420 (2010).
8. A. Ney, M. Opel, T.C. Kaspar, V. Ney, S. Ye, K. Ollefs, T. Kammermeier, S. Bauer, K.-W. Nielsen, S.T.B. Goennenwein, M.H. Engelhard, S. Zhou, K. Potzger, J. Simon, W. Mader, S.M. Heald, J.C. Cezar, F. Wilhelm, A. Rogalev, R. Gross, S.A. Chambers. "Advanced spectroscopic synchrotron techniques to unravel the intrinsic properties of dilute magnetic oxides: the case of Co:ZnO." *New Journal of Physics* **12** 013020 (2010). Chosen as a Research Highlight, *Nature Materials* **9** 182 (2010).
9. T.C. Kaspar, T. Droubay, S.A. Chambers, and P.S. Bagus. "Spectroscopic Evidence for Ag(III) in Highly Oxidized Silver Films by X-ray Photoelectron Spectroscopy." *Journal of Physical Chemistry C* **114** 21562 (2010). *Research chosen for cover art.*
10. T.C. Kaspar, T.C. Droubay, S.A. Chambers. "Atomic oxygen flux determined by mixed-phase Ag/Ag_2O deposition." *Thin Solid Films* **519** 635 (2010).

Digital Synthesis: A Pathway to New Materials at Interfaces of Complex Oxides

Anand Bhattacharya
anand@anl.gov
Materials Science Division & Center for Nanoscale Materials
Argonne National Laboratory, Argonne, IL 60439

(i) Program Scope

The complex oxides host many fascinating and diverse collective states of condensed matter, with spin, charge and lattice degrees of freedom all playing their part. In our program, we seek to create, characterize, understand and manipulate novel states of condensed matter at interfaces of complex oxides using digital synthesis. Digital synthesis is a technique where ordered, undoped layers are stacked in integer sequences, and all charge transfer or doping takes place at atomically sharp interfaces, without the disorder that is associated with the usual chemical doping strategies. The richness of observed phenomena in the complex oxides, which have also presented some of the greatest challenges to our understanding, are due to the strongly interacting degrees of freedom in the materials. Surfaces and interfaces between complex oxides provide a unique environment for these degrees of freedom to 'reconstruct' and create new systems with properties that are qualitatively different from their bulk constituents. In this sense, they provide a pathway for discovering new materials. More specifically, we seek to discover and explore novel states of condensed matter with attributes such as tunability of collective states with strain, octahedral tilts, external fields and currents. These include multiferroic single-phase materials and heterostructures, superconductivity at interfaces between materials that may not be superconducting themselves, spin-polarized two-dimensional electron gases, and materials where strong spin-orbit coupling is the determinant property of the material. We seek to explore properties of materials that are known to have interesting phases, such as the manganites and cuprates, where the effects of disorder have been engineered away by digital synthesis. We create these materials systems using state-of-the-art, ozone-assisted oxide Molecular Beam Epitaxy (MBE) at the Center for Nanoscale Materials (CNM) at Argonne, and characterize them using the major DOE facilities for neutron and photon scattering, and at the new DOE Nanoscale Science Research Centers.

(ii) Recent Progress (since 2009):

Since 2009, we have made progress in three key directions: *(a)* Creating cation-ordered analogs of known manganite materials, including lower dimensional analogs, and studying the effects of cation ordering on collective properties. *(b)* Controlling octahedral tilts in multilayers of perovskite manganites and nickelates, using a parameter other than epitaxial strain. *(c)* Understanding how interfaces influence electronic and magnetic properties. Below we list some recent work that we are building upon, with the goal of tailoring novel properties in superlattices and heterostructures using our digital synthesis approach.

- *Enhanced Neel Temperatures in Digital LSMO:* We studied superlattices of $(LaMnO_3)_m/(SrMnO_3)_{2m}$ for m = 1 and 2 and also random alloys of the same composition. These superlattices are ordered analogues of the composition $La_{1/3}Sr_{2/3}MnO_3$, an antiferromagnetic insulator. We show that chemical ordering creates an enhancement of the

Neel temperature by >70 K. Our initial work showed signatures in transport of enhanced ordering temperatures (published in *Applied Physics Letters* in 2007.) Our recent work (published in *Nature Materials* **8**, 892 (2009)) includes measurements of the temperature dependence of the antiferromagnetic order, and corresponding changes in the *c*-axis lattice parameters, via neutron (HFIR) and x-ray (APS) scattering. The work establishes a definitive link between these two, and also demonstrates that there is a strong *in-plane* modulation in the lattice for the random alloy that is far less pronounced in the superlattice.

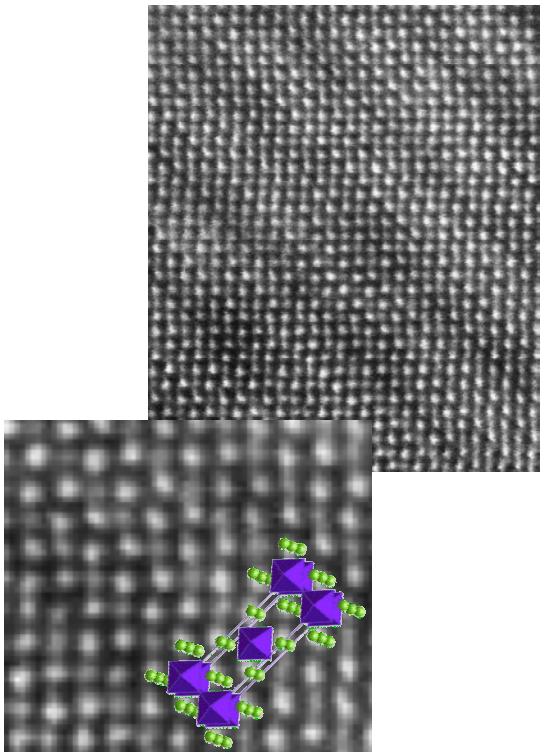

Fig.1. Scanning transmission electron microscopy image of $La_{2-x}Sr_xMnO_4$ grown with oxide MBE at Argonne. Cation-ordered samples of this two dimensional manganite have been studied to understand how the the effects of dimensionality and disorder may be disentangled in this class of materials [*Appl. Phys. Lett.* **98**, 072505 (2011)].

- *Disentangling effects of dimensionality and disorder in manganites*: We studied cation ordered analogs of $La_{2-x}Sr_xMnO_4$. This has a spin glass phase at low T instead of being a usual ferromagnet as in the 3D perovskite analogs, and we wanted to see if ordering the cations would create a 2-D ferromagnet. We have synthesized and characterized ordered analogs of this material. We discovered that cation ordering created a novel magnetic anisotropy and reduced the resistivity by over an order of magnitude at T< 100K. However, we did not observe any long range ferromagnetic order. (*Applied Physics Letters*, 2011).
- *Correlating structure and electronic properties at ($LaMnO_3$)/($SrMnO_3$) interfaces*: $LaMnO_3$ (Mn^{3+}) is a Jahn-Teller/Mott Hubbard insulator with an A-type (layered) antiferromagnetic (AF) ground state, while $SrMnO_3$ (Mn^{4+}) is a correlated insulator and a G-type (cubic) AF. The interfaces between these materials show properties related to mixed $3^+/4^+$ valence. Using STEM (scanning transmission electron microscopy) and EELS (electron energy loss spectroscopy) (with Amish Shah and Jim Zuo, UIUC) we studied the correlation between structure and electronic properties with atomic resolution in ($LaMnO_3$)/($SrMnO_3$) superlattices. (*Phys. Rev. B* 2010).

- Using high resolution x-ray diffraction at the Advanced Photon Source, we quantified the dependence of octahedral tilts on epitaxial strain in $LaNiO_3$ thin films grown with oxide MBE at Argonne. We followed this with a study of how these tilts in $LaNiO_3$ are affected when they are incorporated into superlattices with $SrMnO_3$. This work demonstrates a pathway to tune octahedral tilts with a control parameter other than epitaxial strain. (*Phys. Rev. B* 2010; *Phys. Rev B*. 2011).

- **(iii) Future Plans**

(a) Using our digital synthesis technique, we can create materials where the cation disorder associated with usual chemical doping strategies is nearly absent. As we have observed in our recent work with the manganites, this may have profound effects on long-range magnetic order. In our proposed research, we plan to extend these ideas to superconducting perovskites to better understand the role of cation disorder in their properties, particularly how this relates to competing order parameters, and how it might impact transition temperatures. *(b)* Interfaces may also allow the control of collective states. In this regard, we will explore how collective states such as superconductivity and magnetism, and phase transitions such as metal-insulator transitions may be controlled with electric fields and electric currents, an area of research we refer to as 'Mottronics'. *(c)* Lastly, we propose to create and study a new class of oxides where spin-orbit interactions coupled with Mott correlations and frustrated spin degrees of freedom may lead to novel states, including superconductivity, and exotic conducting states that may appear at surfaces or in the bulk. In these materials, there may be strong coupling of the momentum and spin of charge carriers leading to new phenomena, which may have relevance for spintronics. An understanding of these materials and their underlying physics may lead to entirely new concepts where the interface or surface 'is the material'[1] and provides the desired functionalities.

Synthesis Cluster: Synthesis of novel materials with single atomic layer control forms the basis for our research program. We are planning to create an oxide 'synthesis cluster' at the Material Science Division at Argonne for oxide thin films and heterostructures, with capabilities that will be in some ways complementary to those we currently use at the Center for Nanoscale Materials. The complex oxides are diverse in their chemical makeup, and not all can be created with the same techniques. For example, thin dielectrics grown with MBE can sometimes be leaky, and refractory elements such as Ru and Ir cannot be evaporated easily from Knudsen cells in an MBE system. Volatile elements such as Bi and K are probably not very compatible with elements that evaporate at much higher temperature, as they may vaporize from the walls and contaminate films of the more refractory metals. To address these issues, we seek to create a cluster of compact deposition tools that will each have a unique capability (volatiles, reactive sputtering, pulsed laser deposition etc.), where samples can be readily transferred between them under ultra–high vacuum conditions. This will enable us to create a broader range of heterostructures where the constituent materials are grown using techniques optimal to each material, while preventing interfacial contamination. At the first stage of this cluster, we are in the process of acquiring a compact state of the art oxide-MBE system, which we shall interface with a reactive oxide sputtering system. We anticipate that this stage will be operational by end of 2011/ early 2012.

(iv) Publications resulting from work supported by DOE BES from 2009-2011:

1. "Control of octahedral rotations in $LaNiO_3/SrMnO_3$ superlattices", S. J. May, C. R. Smith, J. –W. Kim, E. Karapetrova, A. Bhattacharya, P. J. Ryan, *Phys. Rev.* B **83**, 153411 (2011).
2. "Cation-ordering Effects in the Single layered Manganite $La_{2/3}Sr_{4/3}MnO_4$", B. B. Nelson-Cheeseman, A. B. Shah, T. S. Santos, S. D. Bader., J.-M. Zuo and A. Bhattacharya, *Appl. Phys. Lett*. **98**, 072505 (2011).

3. “Practical Spatial Resolution of Electron Energy Loss Spectroscopy in Aberration Corrected Scanning Transmission Electron Microscopy”, A.B. Shah, Q.M. Ramasse, J.G. Wen, A. Bhattacharya and J.M. Zuo, *Micron*, (2011) (in press) doi:10.1016/j.micron.2010.12.008
4. “Presence and spatial distribution of interfacial electronic states in $LaMnO_3$-$SrMnO_3$ superlattices”, A. B. Shah, Q. M. Ramasse, S. J. May, J. Kavich, J. G. Wen, X. Zhai, J. N. Eckstein, J. Freeland, A. Bhattacharya and J. M. Zuo, *Phys. Rev.* B **82**, 115112 (2010).
5. “Quantifying octahedral rotations in strained perovskite oxide films”, S. J. May, J.-W. Kim, J. M. Rondinelli, E. Karapetrova, N. A. Spaldin, A. Bhattacharya and P.J. Ryan, *Phys. Rev.* B **82**, 014110 (2010).
6. "DNA Sensing Using Nanocrystalline Surface-Enhanced Al_2O_3 Nanopore Sensors", B. M. Venkatesan, A. B. Shah, J. M. Zuo, and R. Bashir, *Advanced Functional Materials* **20**, 1266 (2010).
7. “Probing Interfacial Electronic Structures in Atomic Layer LaMnO3 and SrTiO3 Superlattices”, Amish B. Shah, Quentin M. Ramasse, Xiaofang Zhai, Jian Guo Wen, Steve J. May, Ivan Petrov, Anand Bhattacharya, Peter Abbamonte, James N. Eckstein, Jian-Min Zuo, *Advanced Materials* **22**, 1156 (2010).
8. "Instability, intermixing and electronic structure at the epitaxial $LaAlO_3/SrTiO_3(001)$ heterojunction," S. A. Chambers, M. H. Engelhard, V. Shutthanandan, Z. Zhu, T. C. Droubay, L. Qiao, P. V. Sushko, T. Feng, H. D. Lee, T. Gustafsson, E. Garfunkel, A. B. Shah, J. M. Zuo, and Q. M. Ramasse, *Surface Science Reports* **65**, 317-352 (2010).
9. “New Optical Absorption bands in Atomic Layer Superlatices” X. Zhai, C. S. Mohapatra, A. B. Shah, J.-M. Zuo and J. N. Eckstein, *Advanced Materials* **22**, 1136 (2010).
10. "Enhanced ordering temperatures in antiferromagnetic manganite superlattices", S. J. May, P. J. Ryan, J. L. Robertson, J.-W. Kim, T. S. Santos, S. G. E. te Velthuis, E. Karapetrova, J. L. Zarestky, J. N. Eckstein, S. D. Bader, and A. Bhattacharya, *Nature Materials* **8**, 892 (2009).
11. “Tuning between the metallic antiferromagnetic and ferromagnetic phases of $La_{1-x}Sr_xMnO_3$ near x=0.5 by digital synthesis”, T. S. Santos, S. J. May, J. L. Robertson and A. Bhattacharya, *Phys. Rev*. B **80**, 155114 (2009).
12. “Onset of metallic behavior in strained $(LaNiO_3)_n/(SrMnO_3)_2$ superlattices”, S. J. May, T. S. Santos and A. Bhattacharya, *Phys. Rev.* B **79**, 115127 (2009).

Development and Understanding of Multifunctional Nanostructured Magnetoelectric and Spintronic Materials

R.S. Katiyar, M. Gomez, G. Morell, L. Fonseca, W. Otano^, O. Perales[+], M.S. Tomar[+], Y. Ishikawa, R. Palai, R. Thomas, A. Kumar, J. Velev, V. Makrov

rkatiyar@uprrp.edu

(University of Puerto Rico, Rio Piedras, Mayaguez[+], Cayey^)

Program Scope

Magnetoelectric (ME) multiferroics and spintronics combine standard microelectronics with spin-dependent effects that arise from interactions between electrons and magnetic field. The spin dependent phenomena become challenging at the nonoscale where new physical effects emerge affecting the spin injection, transport, and switching times. CMOS compatible *Multifunctional Material*s to meet the near future demand of miniaturization of Si based technology and for the next generation technology beyond Si are the goals of this project. Such a technology has been following Moore's law during last 4 decades (i.e. the number of transistors per integrated circuit (IC) doubles roughly every 24 months).[1] For this advancement, however, the fundamental science and understanding is needed to develop high-k gate oxides (for 22 nm node technology and beyond), ME multiferroics, and dilute magnetic semiconductors (DMS). Such materials have the potential to form the basis of a new generation of energy efficient nanoscale electronic devices that are fast responding, have low power consumption and high integration density. In the present grant, the researchers are actively involved in the synthesis and characterization of various *functional oxides and silicides* to accomplish this goal.

Recent Progress

We designed and optimized a few ME multiferroic and dilute magnetic semiconductor nanostructures for energy efficient electronics applications, such as NVRAM, sensors and actuators, spin valves, data storage systems, due to high speed, low power consumption, radiation hard, and low costs. Many of these applications need a stack of thin film nanostructures (superlattices and heterostructures) and therefore, major part of our efforts in this period focused on demonstrating the feasibility of fabricating and characterizing thin film heterostructures. Some of the materials screened so far showed multifunctional properties, especially for the above spintronics and/or ME applications.

Magnetoelectric Multiferroics and High-K Dielectrics

- Mono-domain single crystals and thin films of multiferroic $BiFeO_3$ (BFO) were systematically studied using micro-Raman spectroscopy for better understanding of magnon-phonon coupling and dynamics of phase transition and phase diagram[2-4]. A weak magnon-phonon coupling has been observed in BFO thin films at magnetic phase transition temperature. Thin films showed the presence of a non-cubic β- and γ-phases at high temperature. We also discovered two new spin reorientation transitions at lower temperatures, namely at 140K and 200K in single phase multiferroic BFO. Moreover, considerable enhancement in the ferroelectric properties was observed at room temperature in $Bi(Fe_{0.95}Cr_{0.05})O_3$ compared to BFO.Multiferroic BFO thin film and high-*k* DSO insulating buffer were fabricated gives rise to a memory window of 1.7 V. The magnitude of the memory window demonstrates that BFO has potential in FET FeRAM applications. As a lead free ferroelectric, $Bi_{3.25}Nd_{0.75}Ti_3O_{12}$ with Pr ~20.0 μC/cm^2, E_c ~ 62kV/cm, ε_r ~ 400 and tanδ ~ 0.04 were successfully synthesized with clockwise CV hysteresis and a memory window of about 0.7V.
- Composite bilayers and superlattices (nano-capacitor) were fabricated utilizing ferroelectric $PbZr_{0.52}Ti_{0.48}O_3$(PZT) and half-metallic oxide $La_{0.67}Sr_{0.33}MnO_3$(LSMO) with different stacking periodicity. High remnant polarization (12-54μC/cm^2), dielectric constant (400-1700), and well saturated magnetization were observed showing giant frequency-dependent dielectric anomaly in the

vicinity of the ferromagnetic-phase transition. Magnetic control of ferroelectric interface was also observed in bilayers[5]. As the field H is increased, the hysteresis loop broadens (becomes lossy) and then disappears at ca. H=0.34T and ambient temperatures (**Fig. 1**), the process was reversible. This phenomena was explained due to collapse of colossal magneto-resistance of LSMO with suitable H, causing short circuiting of the PZT polarization due to high electric field across it.

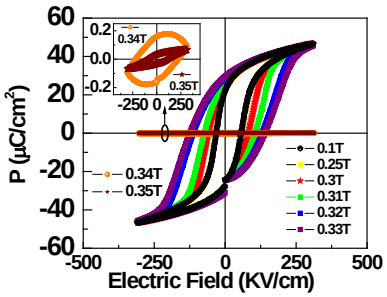

Fig. 1 *A significant magnetic field dependence is observed in the hysteretic loss near the critical field of H =.0.34 T, which is shown more clearly in the insert.*

- Novel $PbZr_{0.42}Ti_{0.38}Fe_{0.13}W_{0.07}O_3$ compound[6] was discovered showing enormous ME effect: switching not from +Pr to –Pr with applied magnetic field, H, but from Pr to zero with applied H of merely 0.5 Tesla. MMIS device structures of Pt/PZTFWx/$SrTiO_3$/Si (111) are fabricated showed well behaved and saturated C(V) hysteresis with 3-4 V memory windows (**Fig. 2**), suggesting good candidates for multiferroic RAMs.

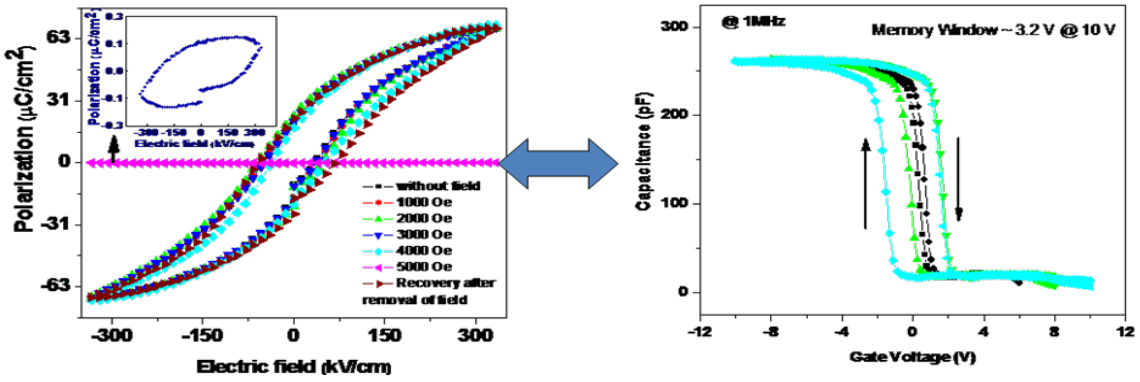

Fig. 2 *Electric Polarization in 80%PZT/20%PFW switching to zero under H=0.5T due to magnetoelectric coupling. Its integration with 6 nm high k-dielectric $SrTiO_3$ coated p-Si (111) for NVRAM device, showing a window ~ 3.2 V for memory applications*

- The PLD grown $LaGdO_3$ (LGO) high-k dielectric thin films showed effective dielectric constant (*k*) ~21.6 ± 1.7, flatband voltage ~10^{12} $eV^{-1}cm^{-2}$, conduction (ΔEc 2.73±0.12eV) and valence (ΔEv 1.86±0.12eV) band offset. Long n-channel LGO metal-oxide-semiconductor field effect transistors (MOSFET) with 7.5μm channel length and a channel width of 15 μm were fabricated and electrically characterized.

Dilute Magnetic semiconductors for spintronics applications

- ZnO based dilute magnetic semiconductors (DMS) for the novel magneto electronic devices were screened with various doping levels. The ZnCuO films showed nearly single crystalline phase (< 3% Cu doping)[7] with **ferromagnetic behavior** (M_s ~ 0.76 μ_B/Cu) that reduced on further increase in Cu doping. The high-T_c ferromagnetic property in Co-doped ZnO (ZCO), mediated by donor impurity band was tested by the controlled introduction of shallow donors (Al) in the $Zn_{0.9-x}Co_{0.1}O:Al_x$ (x = 0.005 and 0.01) thin films. The **saturation magnetization** for the 10% Co-doped ZnO was 4emu/cc at 300 K that reduced (~ 0.8 emu/cc) due to Al co-doping and the resistivity dropped abruptly, from ~ 10^3 Ω-cm for the ZCO film to 0.033 and 0.02 Ωcm for the 0.5% and 1.0% Al doped ZCO samples respectively **(Fig. 3)**. The optical band gap in the Mn-doped (1-10%) ZnO was found to increase (3.27 eV to 3.41 eV) due to Mn doping. We synthesized Antimony (Sb 3% and 5%) doped *p*-type ZnO films that exhibited **high hole concentration** of 6.25×10^{18} cm^{-3}, mobility of 57.44 cm^2/Vs, and low resistivity (Ωcm 0.017) in the 5% Sb-doped ZnO thin film[8].

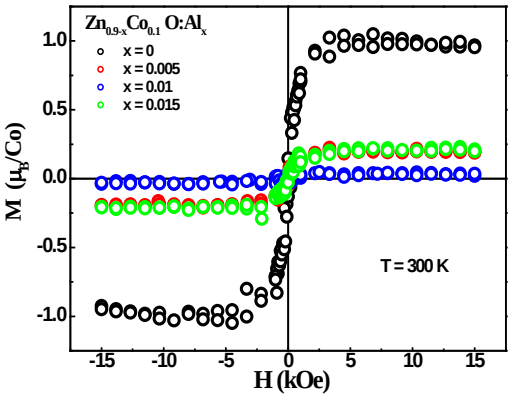

Fig. 3 *Room temperature ferromagnetism in 10% Co doped ZnO that decreased with Al co-doping*

- **(**$In_{1-x}Fe_x)_2O_3$ nanocrystalline samples with x=(0.0,0.05,0.10,0.15,0.20, and 0.25) were synthesized by a gel combustion method. The dc magnetization studies, as a function of temperature and field, indicate that the samples are ferromagnetic with Curie temperature (T_C) well above the room temperature.
- Delafossite p-type $CuFeO_2$ semiconductor was synthesized by a modified solid state reaction technique that shows reasonably good "turn-on field" which is the macroscopic field needed to get an emission current of 9 nA, was calculated as 5.72 V/m. Anharmonic phonon – phonon interaction was observed in delafossite $CuAlO_2$ thin films grown.

Theoretical Calculations for novel spintronics and multiferroics

- First-principles methods based on density-functional theory (DFT) in the local density approximation (LDA) were employed to study the ZnO/MgO interfaces. The band structure analysis at the ZnO/MgO heterostructure indicates that the charge carriers are not confined in the ZnO/MgO interface. The calculated density of states also shows that this heterostructure is not exhibiting any magnetic property. A partial substitution of Zn by some transition mental (TM) at the ZnO/MgO interface is made to investigate the electronic and magnetic properties on the Zn(TM)O/MgO (TM= Cu, Co, Fe, Mn, Cr). The hybrid DFT calculation with the HF exchange + GGA gives rise to a band gap of 3.15 eV in ZnO and 5.8 eV in MgO, in good agreement with the experimental values. The self-consistent field calculations at the ZnO/MgO interface with one Zn substituted by Co in the super cell showed the present of spin-polarized 2DEG at the interface. Studies on TM:ZnO/MgO heterostructure with and without hybrid functional are being carried out to elucidate the influence of TM substitution in the electronic and magnetic properties of the material.
- Theoretical work was also carried out on various aspects of spin-dependent tunneling and *tunneling magnetoresistance* (TMR) in magnetic tunnel junctions (MTJs) and predicted a number of important physical phenomena. Co/$SrTiO_3$/Co junctions with bcc Co(001) electrodes we predicted a very large TMR effect and explained the experimentally observed negative spin polarization.

- *Ferroelectric tunnel junction* FTJs, demonstrated that the interface structure and bonding and electronic properties of the barrier are sensitive to the polarization orientation. We have proposed a concept of *multiferroic tunnel junction* (MFTJ) in which two ferromagnetic electrodes are separated by ferroelectric barrier. In a MFTJ the tunneling conductance is controlled by *both* the magnetization orientation of the electrodes *and* the ferroelectric polarization of the barrier. Due to the co-existence of the TMR and TER effects such a MFTJ can function as a four-state nonvolatile memory device. As an example, we have studied electron and spin transport in $SrRuO_3/BaTiO_3/SrRuO_3$ *multiferroic tunnel junction* (MFTJs) based on density-functional calculations and predicted sizeable changes in the tunneling conductance with polarization orientation of the $BaTiO_3$ barrier and magnetization orientation $SrTiO_3$ electrodes.

Future Plans

As presented in the last Section, we have researched a number of materials during last three years and have indeed discovered some new and novel materials that may have potential in developing tetsbed devices for the energy efficient nanoscale electronics that are fast responding, have low power consumption, and are in the miniature form. However, the grand challenges for magnetoelectrics and spintronics applications, is the lack of proper understanding and precise control of properties of nanostructures including growth, phase purity, defects, size effects, cluster formations, orientation, and crystallinity. Our research plan for the next three years is, therefore, to develop better understanding of the materials properties and processes and determine their suitabilities for various proposed testbed nanostructures. The challenges are also in finding a room temperature multiferroic materials with appreciable ME coupling. The final part of the proposal considers the integration of the above materials for the standard silicon based applications. Challenges lie in finding a proper high-k dielectric to act as perfect buffer layer and gate-oxide to allow multifunctional materials integration within the CMOS process flow. Theoretical models will be developed for the understanding of the science of functional nanostructures. Challenges lie in tailoring the properties of the materials based on theoretical understanding to find novel materials and nanostructures with device level characteristics.

References

1. 1. G. E. Moore. Electronics Magazine **38**, No. 8, April 19, (1965).
2. Polarized Raman scattering of multiferroic $BiFeO_3$ single domain crystal and thin films, R. Palai, H. S. Schmid, and R. S. Katiyar, *17th IEEE International Symposium on the Applications of Ferroelectrics (ISAF)*, **2**, 10.1109/ISAF.2008.4693780 (2008)
3. Raman spectroscopy of single-domain multiferroic $BiFeO_3$, R. Palai, H. Schmid, J. F. Scott, and R. S. Katiyar, *Phy. Rev. B*, **81**, 064110 (2010)
4. Phonon spectroscopy near phase transition temperatures in multiferroic $BiFeO_3$ epitaxial thin films, R. Palai, J. F. Scott, and R. S. Katiyar, *Phy. Rev. B*, **81**, 024115 (2010)
5. Magnetic effects on dielectric and polarization behavior of multiferroic heterostructures, S. Dussan, Ashok Kumar, J. F. Scott, and R. S. Katiyar, *App. Phys. Lett.*, **96**, 072904 (2010)
6. Magnetic control of large room-temperature polarization**,** Ashok Kumar, G. L. Sharma, R.S. Katiyar, R. Pirc, R. Blinc, and J. F. Scott, *Journal of Physics: Condensed Matter*, **21**, 382204, (2009)
7. Microstructural and ferromagnetic properties of $Zn_{1-x}Cu_xO$ thin films, K. Samanta, P. Bhattacharya, and R. S. Katiyar, *J. Appl. Phys.* **105**, 113929, (2009)
8. Raman scattering studies of p-type Sb-doped ZnO thin films, K. Samanta, P. Bhattacharya, and R. S. Katiyar, *J. App. Phys.*, **108**, 113501 (2010)

DOE-EPSCoR Publications (2008-2011) for the Current *Grant #DE-FG02-08ER46526*

During the above period researchers of this project had published 74 articles in refereed scientific journals and conference proceedings.

$Ca_3Mn_2O_7$ and $Ca_3Ti_2O_7$—An Example of Multiferroic Matter by Design

Craig J. Fennie
fennie@cornell.edu
School of Applied and Engineering Physics
Cornell University, Ithaca, NY 14850

David A. Muller
david.a.muller@cornell.edu
School of Applied and Engineering Physics
Cornell University, Ithaca, NY 14850

Peter Schiffer
pes12@psu.edu
Department of Physics
Penn State University, University Park, PA 16802

Darrell G. Schlom
schlom@cornell.edu
Department of Materials Science and Engineering
Cornell University, Ithaca, NY 14850

I. Program Scope

Our SISGR objective is to create a ferromagnetic ferroelectric that can be deterministically switched between symmetry equivalent states using an electric field. The electric-field switching of a magnetization between 180° symmetry equivalent states has not been demonstrated in any material. The required coupling between ferroelectric and ferromagnetic domains allowing such switching is a missing feature in most multiferroics and is key to advancing the field both scientifically and technologically. Starting at the level of electrons and atoms our goal is to rationally design complex oxide heterostructures and interface-materials with this targeted emergent behavior. This is not a matter of simply optimizing material parameters, but rather begins with understanding a mechanism to control the interplay between the diverse microscopic degrees of freedom prevalent in complex oxides in order to achieve this desired behavior, and ends with the design of new material realizations. These realizations are in turn created with atomic-layer precision, structurally assessed to see that they are the intended realization, and finally their relevant properties are measured. In this program we will develop the scientific ideas necessary to apply this design paradigm to the creation of multiferroics with unprecedented coupling between ferroelectric and magnetic order parameters, i.e., strongly-coupled magnetic-ferroelectrics.

II. Recent Progress

Recently using first-principles theory our SISGR demonstrated that the strong coupling of octahedron rotations (a type of lattice distortion that is ubiquitous in complex crystalline materials) to magnetic properties provides an opportunity to achieve our SISGR goal: to create new ferromagnetic ferroelectrics that can be deterministically switched between symmetry equivalent states using an electric field. Our theory work shows for the first time how octahedron rotations simultaneously induce and thereby naturally couple ferroelectricity, magnetoelectricity and ferromagnetism, a breakthrough in the field of multiferroics.[1] This work, published in *Physical Review Letters*, has been highlighted in a Physical Review *Physics Viewpoint*[2] and a *Nature Materials News & Views*.[3]

This new mechanism, referred to as "hybrid improper ferroelectricity," is quite general. It involves any material in which a polarization is induced by a complex distortion pattern involving more than one octahedral rotation mode. It is a generalization of the mechanism found to give rise to improper ferroelectricity in $(SrTiO_3)_1/(PbTiO_3)_1$ superlattices in which single unit-cell-thick layers of the perovskites $SrTiO_3$ and $PbTiO_3$ are alternated.[4] First principles calculations identified two materials-specific embodiments involving known phases. One is $Ca_3Ti_2O_7$, in which two coupled octahedral rotation modes are predicted to give rise to a

polarization of magnitude 20 μC/cm^2.[1] The second is $Ca_3Mn_2O_7$ in which the two coupled octahedral rotation modes not only give rise to a polarization, this time of magnitude 5 μC/cm^2, but also induce weak ferromagnetism.[1] Further, our first-principles calculations have calculated the energetically favored switching path and predict that under 1.5% biaxial compression that an electric field will switch both the polarization and the magnetization deterministically by 180°!

Having used theory to identify phases with the desired multiferroic behavior, our SISGR has been actively pursuing their synthesis and characterization. $Ca_3Ti_2O_7$ and $Ca_3Mn_2O_7$ are both are $n = 2$ members of the Ruddlesden-Popper homologous series of phases.[5-7] Their crystal structure and the octahedral rotations involved are shown in Fig. 1.[2] To test the aforementioned predictions we are growing and measuring relevant properties of epitaxial $Ca_3Ti_2O_7$ and $Ca_3Mn_2O_7$ thin films. We have succeeded in the growth of both phases by reactive molecular-beam epitaxy using a shuttered growth technique, where the shuttering is used to deposit the constituent monolayers in the same order as the layering along the *c*-axis of these highly layered phases. Both are phase pure by x-ray diffraction, as is evident from the θ-2θ x-ray diffraction scan shown in Fig. 2. The phase purity and crystallinity of the films was monitored during growth by reflection high-energy electron diffraction and after growth by four-circle x-ray diffraction (XRD). XRD reveals (Fig. 2) that the $Ca_3Mn_2O_7$ films are single phase and epitaxial with (001) $Ca_3Mn_2O_7$ || (110) $YAlO_3$. The out-of-plane lattice spacing is c=1.94±0.01 nm, as expected for the targeted $Ca_3Mn_2O_7$ phase. Scanning transmission electron microscopy (Fig. 3)

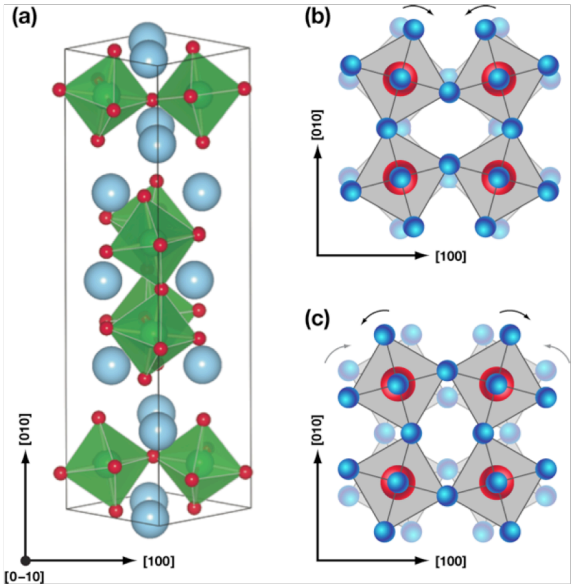

Fig. 1. (a) Crystal structure of $Ca_3Ti_2O_7$ and $Ca_3Mn_2O_7$. Both are $n = 2$ $A_{n+1}B_nO_{3n+1}$ Ruddlesden-Popper phases. The *A*-site cations Ca^{2+} are the large blue spheres and the *B*-site ions (Ti^{4+} and Mn^{4+}) lie at the center of the oxygen coordination polyhedra (octahedra). (b) Top view showing the octahedral rotation mode (*R*) and (c) octahedral tilt mode (*T*) in $Ca_3Mn_2O_7$. The *R* and *T* modes combine to induce a polarization. (from Ref. 2)

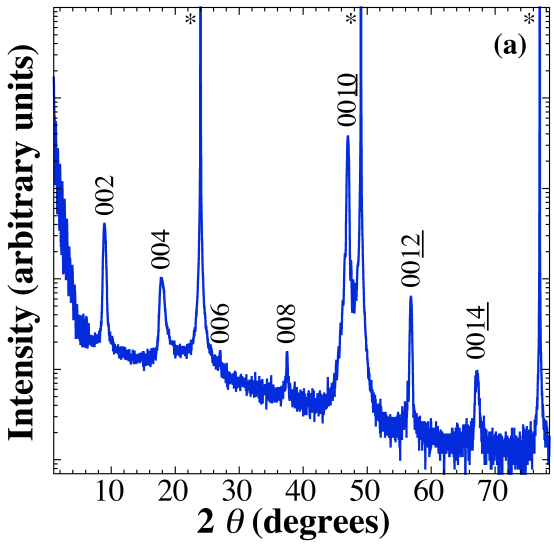

Fig. 2. θ-2θ x-ray diffraction scan of a 30 nm thick epitaxial (001)-oriented $Ca_3Mn_2O_7$ film grown on a (110) $YAlO_3$ substrate.

reveals that the films have the desired structure, but contain vertically-running double-SrO layers (Ruddlesden-Popper faults) in addition to those that run horizontally. Such defects are commonly seen in bulk[8-11] as well as thin-film[12] Ruddlesden-Popper materials. Measurements of magnetization as a function of temperature (Fig. 4) show a Néel transition temperature of T_N = 120 K, similar to bulk $Ca_3Mn_2O_7$. Measurements of the ferroelectric properties of $Ca_3Mn_2O_7$ and $Ca_3Ti_2O_7$ by second harmonic generation, ultraviolet Raman, and polarization vs. electric field measurements are in progress.

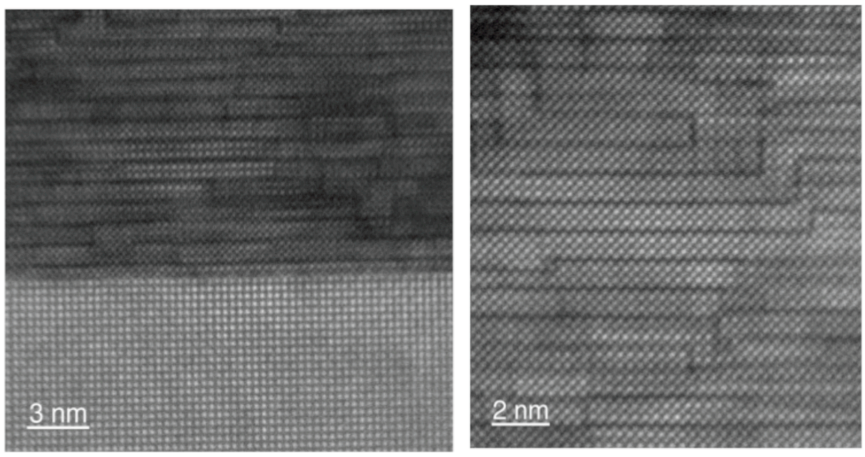

Fig. 3. Scanning transmission electron micrographs of the same $Ca_3Mn_2O_7$ epitaxial film studied in Fig. 2.

Having established a mechanism that can yield deterministic control of magnetic switching the next obvious question is whether this effect can be made to occur at higher temperatures. Once again, the materials by design element of our SISGR are leading the way in identifying systems where such behavior can be found. In collaboration with James Rondinelli of Argonne National Laboratory, we recently outlined the crystal-chemistry criteria guiding the rational design of octahedral rotation-induced ferroelectricity and demonstrated remarkable control of this behavior through changes in chemical compositions and rotation-patterns.[13] The breakthrough in this work is that our criteria are solely based on the properties of the centric octahedral building blocks, a dream of inorganic materials chemistry (as opposed to organic chemistry where such design concepts are the norm) that still proves incredibly challenging.

A promising type of artificial material identified by this work is superlattices of alternating unit-cell-thick layers of two different orthorhombic perovskites combined along the (001) pseudocubic direction. The targeted orthorhombic class of perovskites are those with space group *Pnma*—the most common space group among perovskites. Although such perovskites have a center of symmetry and thus cannot be ferroelectric, our first-principles calculations show that when such ABO_3 and $AB'O_3$ perovskites are combined in $(ABO_3)_1/(AB'O_3)_1$ superlattices, that the superlattice lacks a center of symmetry and can be a hybrid improper ferroelectric. As

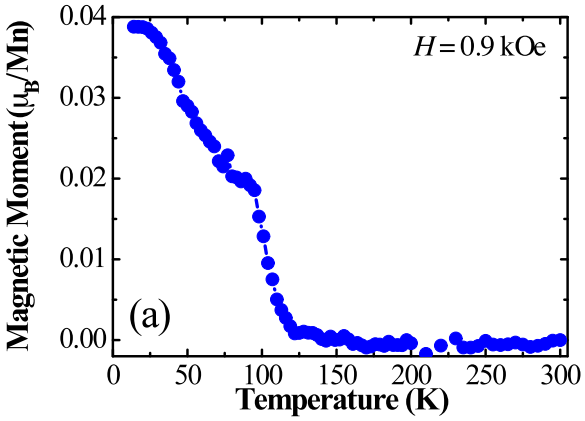

Fig. 4. In-plane magnetization vs. temperature of the same epitaxial $Ca_3Mn_2O_7$ film studied in Fig. 2.

there are many antiferromagnetic perovskites belonging to space group *Pnma*, this strategy is a promising approach to achieving deterministic switching of magnetization through the application of an electric field *at room temperature*.

III. FUTURE PLANS

As mentioned above, we have succeeded in synthesizing single-phase, epitaxial, unstrained $Ca_3Mn_2O_7$ films on (110) $YAlO_3$ substrates, which have the same properties as bulk $Ca_3Mn_2O_7$. We are now targeting the growth of $Ca_3Mn_2O_7$ strained sufficiently in biaxial compression where our SISGR calculations[1] indicate that an applied *electric field* will be able to globally and deterministically switch the magnetization by 180 degrees. We have also begun synthesizing epitaxial $(ABO_3)_1/(AB'O_3)_1$ superlattices following the design rules to achieve the desired phenomena, electrical control of magnetization, at elevated temperatures.[13]

IV. REFERENCES

1 N.A. Benedek and C.J. Fennie, "Hybrid Improper Ferroelectricity: A Mechanism for Controllable Polarization-Magnetization Coupling," *Phys. Rev. Lett.,* **106**, 107204 (2011).

2 G. Lawes, "Twisting and Turning Towards New Multiferroics," *Physics* **4**, 18 (2011).

3 P. Ghosez and J.-M. Triscone, "Multiferroics: Coupling of Three Lattice Instabilities," *Nature Mater.* **10**, 269-270 (2011).

4 E. Bousquet, M. Dawber, N. Stucki, C. Lichtensteiger, P. Hermet, S. Gariglio, J.-M. Triscone, and P. Ghosez, "Improper Ferroelectricity in Perovskite Oxide Artificial Superlattices," *Nature* **452**, 732-736 (2008).

5 D. Balz and K. Plieth, "Die Struktur des Kaliumnickelfluorids, K_2NiF_4," *Z. Elektrochem.* **59**, 545-551 (1955).

6 S.N. Ruddlesden and P. Popper, "New Compounds of the K_2NiF_4 Type," *Acta Cryst.* **10**, 538-539 (1957).

7 S.N. Ruddlesden and P. Popper, "The Compound $Sr_3Ti_2O_7$ and its Structure," *Acta Cryst.* **11**, 54-55 (1958).

8 K. Hawkins and T.J. White, "Defect Structure and Chemistry of $(Ca_xSr_{1-x})_{n+1}Ti_nO_{3n+1}$ Layer Perovskites," *Philos. Trans. R. Soc. London, Ser. A* **336**, 541-569 (1991).

9 T. Williams, F. Lichtenberg, A. Reller, and G. Bednorz, "New Layered Perovskites in the Sr-Ru-O System: A Transmission Electron Microscope Study," *Mater. Res. Bull.* **26**, 763-770 (1991).

10 R. Seshadri, M. Hervieu, C. Martin, A. Maignan, B. Domenges, B. Raveau, and A.N. Fitch, "Study of the Layered Magnetoresistive Perovskite $La_{1.2}Sr_{1.8}Mn_2O_7$ by High-Resolution Electron Microscopy and Synchrotron X-Ray Powder Diffraction," *Chem. Mater.* **9**, 1778-1787 (1997).

11 M.A. McCoy, R.W. Grimes, and W.E. Lee, "Phase Stability and Interfacial Structures in the SrO—$SrTiO_3$ System," *Philos. Mag. A* **75**, 833-846 (1997).

12 W. Tian, X.Q. Pan, J.H. Haeni, and D.G. Schlom, "Transmission Electron Microscopy Study of n = 1-5 $Sr_{n+1}Ti_nO_{3n+1}$ Epitaxial Thin Films," *J. Mater. Res.* **16**, 2013-2026 (2001).

13 J.M. Rondinelli and C.J. Fennie, "Ferroelectricity in Noncentrosymmetric Structures from Centric Polyhedral Building Blocks," submitted to *Nature Materials*.

V. PUBLICATIONS RESULTING FROM THIS WORK

1. Nicole A. Benedek and Craig J. Fennie, "Hybrid Improper Ferroelectricity: A Mechanism for Controllable Polarization-Magnetization Coupling," *Physical Review Letters,* **106**, 107204 (2011).
   DOE-SISGR supported CJF; NSF supported NAB.
2. James M. Rondinelli and Craig J. Fennie, "Ferroelectricity in Noncentrosymmetric Structures from Centric Polyhedral Building Blocks," submitted to *Nature Materials*.
   DOE-SISGR supported CJF; DOE supported JMR.

The fabrication and electrochemical properties of strained YSZ/GDC thin films

Weida Shen[1], Jun Jiang[2], and Joshua Hertz[1,2,3]
hertz@udel.edu
1 – Department of Mechanical Engineering
2 – Department of Materials Science and Engineering
3 – Center for Fuel Cell Research
University of Delaware, Newark, DE 19716

Program Scope

Solid electrolytes, found in batteries, fuel cells, and chemical sensors, are highly (and increasingly) important energy technology components. Nevertheless, the rigid atomic framework of solids provides for relatively few materials with high ionic conductivity, particularly at low temperatures. For example, solid oxide fuel cells typically must be operated at ≥ 800 °C in order to obtain sufficient oxygen ion conduction through the electrolyte. These temperatures necessitate the use of expensive components and limit device lifetimes, making them economically unfeasible at this time. Recently, the use of nanostructured multilayers has been proposed as a means to obtain vastly improved solid state ionic conduction. The presence of high mobility interfaces or lattice strain effects are suggested as possible causes, but the results remain controversial and difficult to repeat[1-3]. In the present grant, we are systematically varying the strain in epitaxial films of oxide solid electrolytes through growth of nanometric multilayers and measuring the effect on oxygen vacancy concentration and mobility. Complete control over the lattice parameter mismatch and the defect concentration is achieved through modulation of dopant and host atom compositions in the two alternating layers.

Recent Progress

Work on this grant has recently begun. The first step is to fabricate epitaxial thin films of the fluorite structured solid electrolytes yttria-stabilized zirconia (YSZ) and gadolinium doped ceria (GDC). They are the most commonly used in solid oxide fuel cells, due to their relative stability and moderately high ionic conductivity. We first calibrated deposition rates over a variety of conditions (especially RF sputtering powers) from single-element targets of Zr, Ce, Y, and Gd, using reactive sputtering with oxygen to create oxide films. Optical interferometry of shadow-masked samples later overcoated with a reflective layer was used to determine film thickness after deposition for a proscribed amount of time (Fig. 1). A few series of simultaneous co-sputtered depositions using more than one of these targets was then performed. Using both the total deposition rate and chemical analysis from x-ray energy dispersive spectroscopy, we verified that the films created are essentially linear combinations of the single-target films. From these measurements, we can now create any arbitrary composition within the space $(Zr_xCe_{1-x})D_yO_{2-d}$, where $0 \le \{x,y\} \le 1$ and $D=\{Y,Gd\}$. We believe this to be a unique capability that we now have, and will provide significant experimental flexibility relative to other researchers.

We next grew thin films of YSZ and GDC using a range of dopant concentrations. A few substrates were qualified for use in this study: Si, MgO, Al_2O_3, and $LiAlO_2$. The concerns are conductivity, lattice parameter and thermal expansion match with the films, and, what is ultimately perhaps most important, film quality. The lithium aluminate substrate has not, to our knowledge, been attempted before as a substrate for these materials despite an excellent lattice parameter match. Structural and electrochemical characterization of the film is ongoing and will

be presented, including impedance spectroscopy measurements of the films at high temperature and varied oxygen partial pressure.

Future Plans

We can now systematically vary the dopant concentration and lattice parameter of the films and can therefore make heterostructure multilayers of arbitrary compositions and complexity. The next goal of this work will be to make structures with systematic variations in lattice parameter mismatch in order to directly measure the effects of strain. In particular, we will first study multilayers that place a heavily doped ceria layers with large lattice parameter next to lightly doped zirconia layers with smaller lattice parameter. This configuration holds the promise of trapping vacancies in a high mobility layer. After building these multilayers, the nanostructures will be imaged via TEM and then they will be electrically characterized by impedance spectroscopy. Characterization of this series, including with variations in layer thicknesses, is expected to require all or most of the next year. Beyond this, the next series of multilayers to be examined will maintain constant lattice parameter mismatch but adjust the dopant concentrations in the two layers to ascertain where the defects are located and, specifically, whether they are spatially redistributing.

References

(1) Garcia-Barriocanal, J.; Rivera-Calzada, A.; Varela, M.; Sefrioui, Z.; Iborra, E.; Leon, C.; Pennycook, S. J.; Santamaria, J. Colossal ionic conductivity at interfaces of epitaxial ZrO2 : Y2O3/SrTiO3 heterostructures. *Science* **2008**, *321*, 676-680.

(2) Guo, X. Comment on "Colossal ionic conductivity at interfaces of epitaxial ZrO2:Y2O3/SrTiO3 heterostructures". *Science* **2009**, *324*, 465.

(3) Garcia-Barriocanal, J.; Rivera-Calzada, A.; Varela, M.; Sefrioui, Z.; Iborra, E.; Leon, C.; Pennycook, S. J.; Santamaria, J. Response to comment on "Colossal ionic conductivity at interfaces of epitaxial ZrO2:Y2O3/SrTiO3 heterostructures."*Science* **2009**, *324*, 465.

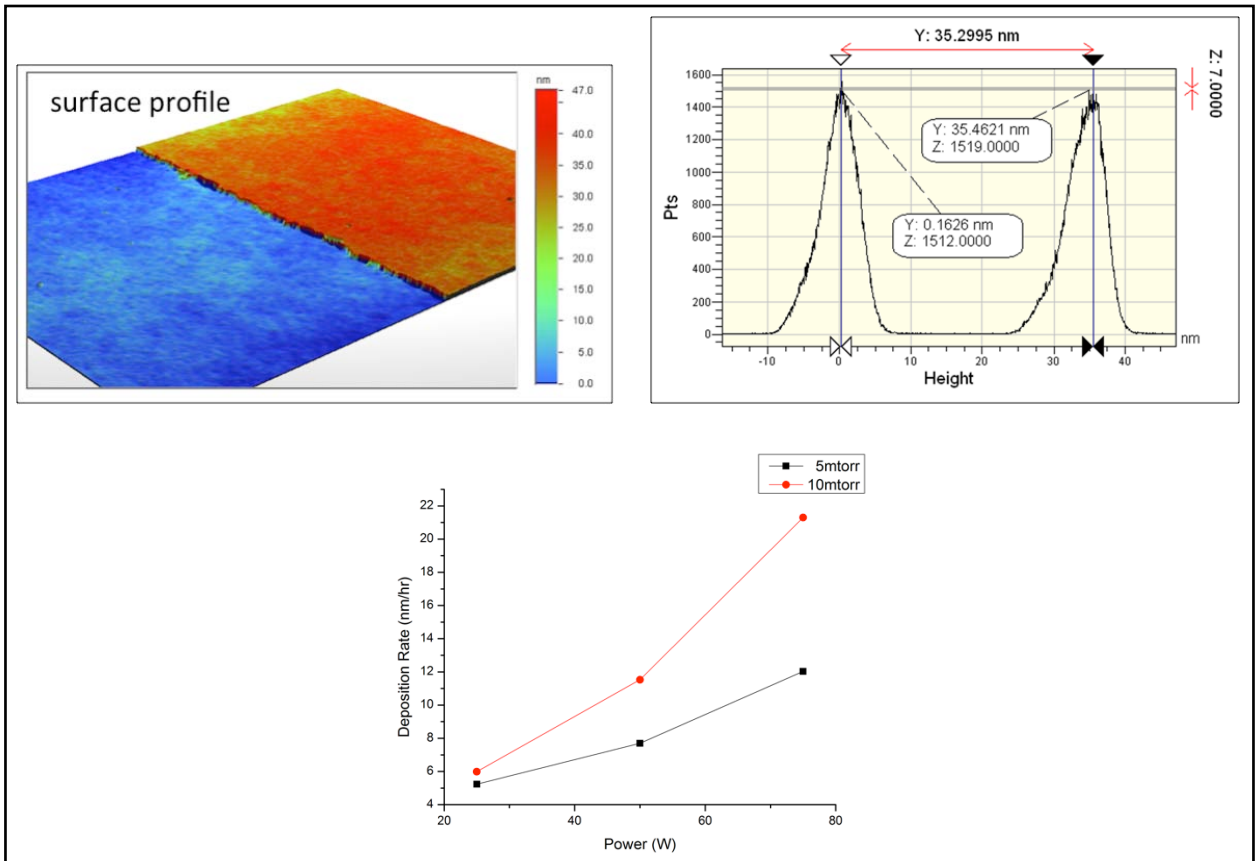

Figure 1. *Clockwise from top left*: white light interferogram of a shadow masked film step used to determine thickness and thereby deposition rate; histogram of height values from the interferogram, with the distance between the two maxima taken as the film thickness; the compiled growth rate of a pure Gd_2O_3 film using various sputtering powers and working pressures. The composition of the working gas for the data shown here was a constant 9:1::Ar:O_2. Working gases of 8:2::Ar:O_2 were also used, but the data is not shown.

Electric-Field Enhanced Kinetics in Oxide Ceramics: Pore Migration, Sintering and Grain Growth

I-Wei Chen

iweichen@seas.upenn.edu

Department of Materials Science and Engineering, University of Pennsylvania

Philadelphia, PA 19104-6272, USA

A New Program
This program will start in Summer 2011.

Summary of New Experimental Observations Motivating This Program
Recent studies at the University of Pennsylvania have discovered massive microstructure changes, including pore migration, electro-sintering and grain growth, in a yttria-stabilized zirconia (8YSZ) ceramic under an electric field/current. The findings are remarkable in three respects:

(a) *neutral* objects such as pores and bubbles can move in an uniform electric field without a direct thermodynamic force;
(b) pore migration and electro-sintering can occur at low temperatures without cation lattice/grain-boundary diffusion; and
(c) grain growth is position-biased even though the spatially uniform field is not.

These findings have direct bearings on the reliability of solid state electrochemical devices such as SOFC.

Further Background
Although oxide ceramics have been used in many solid state devices in which electric field is high and ion conduction is rapid, there has been little systematic study of the material stability under such conditions. Material stability is usually presumed after initial screening leading to the material selection, but long term operation and device miniaturization may pose new circumstances that challenge the presumption. Prominent solid state ionic devices that are pertinent to energy applications include solid oxide fuel cells and solid oxide electrolysis cells as well as solid state batteries. A large electric field is also utilized in extreme-condition processing such as spark plasma sintering.

We have observed dramatic electric effects on the sintering, grain growth and pore migration in yttria-stabilized zirconia (YSZ) ceramics—the electrolyte material of choice for solid oxide fuel

cells and solid oxide electrolysis cells. Neutral pore migration is found to be driven by an ion-wind effect and controlled by Zr/Y surface diffusion; it is also responsible for electro-sintering of thin sections. Both electro-migration and electro-sintering are active at surprisingly low temperatures (e.g., 800^{o}C) when grain boundary and lattice diffusion of Zr/Y are frozen—this also enables densification without grain growth. At higher temperatures (above 1150^{o}C), cation diffusivities are enhanced by orders of magnitude, giving rise to rapid grain growth on the cathode side. These results are indicative of the rich possibilities of solid state phenomena triggered by a high electric field, which are relevant not only to device applications but also to the harnessing of *electric* driving forces (as distinct from *thermal* driving forces, such as the one due to Joule heating) for materials processing.

Program Scope

This work will provide an in-depth understanding of these exotic phenomena and connect them to material applications and engineering predictions. By conducting model electric loading experiments in well defined systems including single crystals, ionomigration, electro-sintering and grain growth will be systematically studied to reveal the influence of ionic diffusivities, crystal structures and mixed conductivity. Our experimental and theoretical work will aim to elucidate the thermodynamic and kinetic principles of electric-field-induced microstructure evolutions in ion-conducting oxide ceramics, which have thus far received little scrutiny in the science community.

Thermochemistry of Anion Defect and Charge Coupled Substitutions in Fluorite and Perovskite Based Materials

Alexandra Navrotsky (P.I) and Sergey V. Ushakov
anavrotsky@ucdavis.edu
Peter A. Rock Thermochemistry Laboratory and NEAT ORU
University of California at Davis
Davis CA 95616

Program Scope

The project emphasizes the thermodynamics of ionic substitutions and order-disorder in materials with high ionic conductivity. Such materials find important applications in solid oxide fuel cells, gas separation membranes, catalysts, nuclear fuels, and nuclear waste ceramics. Fundamental and systematic thermodynamic data are essential for predicting possible new materials, for determining materials compatibility and longevity in use, for developing efficient synthesis and processing, and for assessing environmental impacts. Understanding the relations of thermodynamics, structure and bonding addresses the grand challenge of "how do we design and perfect atom- and energy-efficient synthesis of revolutionary new forms of matter with tailored properties?" The materials studied address basic research needs for solid oxide fuel cells, separation membranes, and catalysts.

The current project expands the range of materials studied to include some exciting new ceramics, different defect mechanisms leading to ionic conductivity, and mixed ionic/electronic conductors. It emphasizes the energetics of interactions at surfaces and interfaces. Specifically, work on fluorite-based solid electrolyte oxides include further exploration of the recently discovered strong linkage of thermodynamics of mixing and the ionic conductivity maximum and calorimetric study of nanopowders and dense nanocermaics to obtain surface and interfacial energies. The thermodynamics of apatite and melilite materials, two new groups of interstitial oxide ion conductors, are being investigated. Thin film and bulk transition metal perovskite solid solutions are studied. High temperature oxide melt solution calorimetry is the principal and unique technique utilized. In addition, thermal analysis, heat capacity measurements, and X-ray diffraction, infrared spectroscopy, and other analytical tools are used. New apparatus with capabilities for synthesis of anhydrous nanopowders by condensation from vapor produced by laser ablation, high temperature levitation and quenching of disordered and amorphous ceramics, and thermal analysis at high temperature (1500-3000 °C) are being constructed.

Recent Progress

Solid electrolyte thermochemistry

The performance of solid electrolytes, materials that are responsible for oxygen transport from cathode to anode in SOFCs, is determined by high oxygen and low electron mobility. Oxides of tetravalent ions with fluorite structure doped with trivalent rare earth cations are good candidates due to the presence of oxygen vacancies formed to charge-balance the doping. The number of vacancies is directly related to doping content but conductivity does not change linearly with the concentration of the doping cation. This phenomenon is associated with exothermic formation of defect clusters. Thermodynamic study of such systems sheds light on the vacancy association.

We have studied thermochemistry of CeO_2 doped with La^{3+}-, Gd^{3+}- and Y^{3+}- cations by high temperature oxide melt solution calorimetry [2]. In addition La^{3+}- and Y^{3+}- doped ThO_2 were examined, funded by the EFRC "Materials Science of Actinides". Enthalpies of formation from oxides (Fig. 1) for all systems were determined as a function of the doping content. At lower doping levels, the data support regular solution behavior and explain the partial solubility of rare earth oxides in fluorite systems as related both to the transformation energy of the rare earth oxide to the fluorite structure and to a positive enthalpy of mixing arising from size mismatch. At higher dopant levels, the enthalpy of mixing deviates from that of a regular solution and an exothermic contribution of vacancy association is observed. These competing effects lead to a point of maximum destabilization in the energetics which coincides with the composition of maximum ionic conductivity, confirming the generality of a trend now seen for both doped ceria and doped thoria systems. We have successfully estimated defect association enthalpy from calorimetric data for the first time. These experimental observations help validate DFT calculations being done under our EFRC and in other groups.

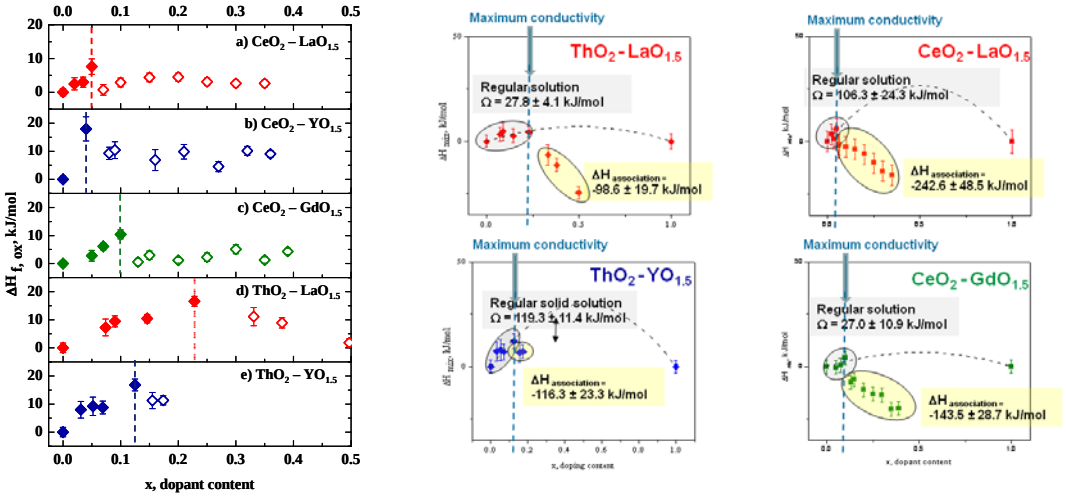

Fig. 1. Left: enthalpy of formation of fluorite solid solutions from oxides as a function of the doping content. Vertical lines show composition of maximum ionic conductivity [7]. Right: enthalpy of mixing showing regular solution fit at dopant levels below the conductivity maximum and clustering energetics above it [2].

Construction of laser synthesis and levitation apparatus and thermal analysis at high temperature

The laser synthesis system and aerodynamic levitator have been constructed and tested and are being used for synthesis of anhydrous nanomaterials and for production of small spheres of levitation, melted, and quenched materials. Our high temperature thermal analysis techniques have been greatly improved by the introduction of welded tungsten crucibles to minimize carbon contamination, as well as other technical improvements, including pyrometic temperature measurements. First experimental measurements of fusion and phase transition enthalpies of La_2O_3 were accomplished using laser-synthesis and high temperature thermal analysis (Fig. 2).

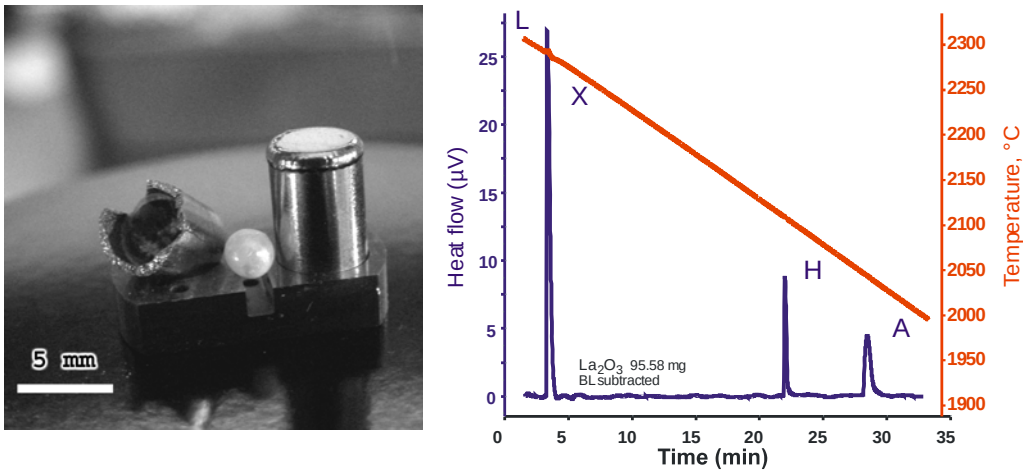

Fig. 2. Left: laser melted La_2O_3 sphere, welded tungsten crucible with La_2O_3 sample and transparent solidified La_2O_3 sample after melting in thermal analyzer and breaking the crucible. Photograph is taken through the glove box window. Right: heat flow trace on cooling of La_2O_3 melt. Peaks correspond to crystallization of cubic X phase from melt followed by reversible transformations to hexagonal H and A phases [10].

Surface and interfacial energy from solution and scanning calorimetry

Based on oxide melt solution calorimetric studies of dense nanoceramics [8] and of nanopowders [5] of yttria stabilized zirconia we found that the energy of interfaces is between that of hydrated and

anhydrous surfaces, confirming that there is no driving force for densification until water is removed. The surface energies of a number of fluorite structured materials (YSZ, ceria, thoria) are similar (near 1 J/m^2), which is low compared to many other oxides. We developed a differential scanning calorimetric method [13], complementary to oxide melt solution calorimetry, to study the surface and interface energies by energy release during grain growth during heating. Fig. 3 shows the DSC heat flow trace and characterization results of initial and final state. Surface energy directly measured by DSC for CeO_2 is 1.2 J/m^2 and agrees well with solution calorimetry data. Such cross-checked experimental surface energies are of paramount importance to benchmark theoretical calculations.

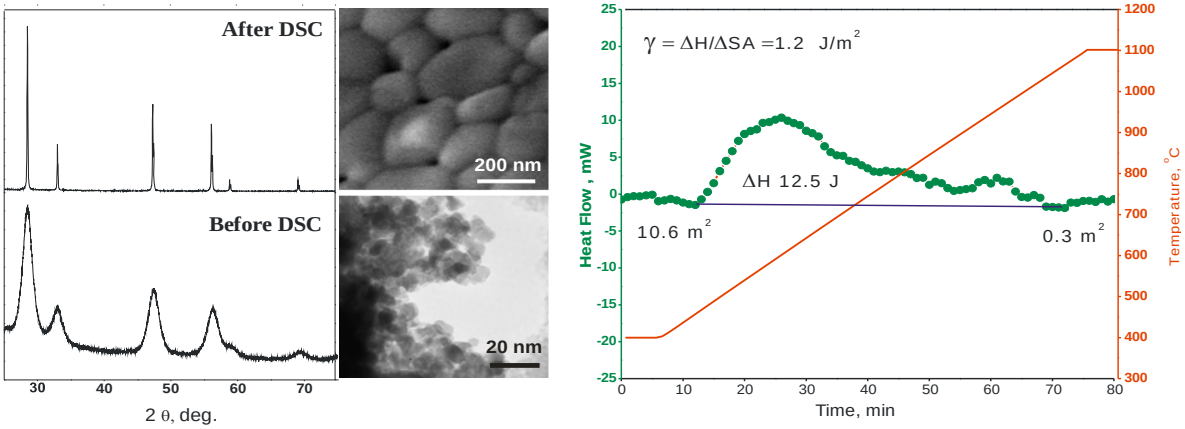

Fig. 3. Left: X-ray diffraction and electron microscopy characterization of CeO_2 sample before and after DSC. Right: calibrated heat flow trace from nanocrystalline CeO_2 measured in scanning calorimeter after subtraction of heat flow on second heating of the same sample. Linear baseline chosen for integration is represented by a blue line. Surface areas from nitrogen adsorption before and after heating and integration results are labeled under the curve [13].

Future Plans

We plan to complete studies of apatite and melilite materials and to continue work on surface and interface energies. We have completed calorimetry of bulk LSMO-LSFO perovskite solid solutions [11], and done some preliminary work on multilayers [4]. We have also been studying some alumina-YSZ multilayer systems [12]. The results are promising but calorimetric techniques still need further development.

The ultimate goal in the high temperature studies is development of drop calorimetry of oxides in an oxidizing atmosphere to measure fusion and phase transition enthalpies, for example of fluorite phases of ZrO_2, HfO_2 and their solid solutions with Y_2O_3. This work will be continued operating our levitator and laser system. In a quest to characterize structure and thermodynamics of oxides above 1700 °C in oxidizing environments, we performed diffraction experiments on levitated crystalline Y_2O_3 at beamline 11-ID-C at APS. It has an aerodynamic levitator, previously used exclusively for studying structure of melts. First data (Fig. 4) indicate great potential to identify high temperature phases in oxides and study thermal expansion and phase transformation. We plan to optimize this method for crystalline materials and use it in conjunction with high temperature enthalpy measurements.

We see a gradual shift in emphasis toward battery materials. There is a wealth of proposed new solids conducting via Li and also Na ions, yet their thermodynamic properties are largely unknown. We are collaborating with Jean-Marie Tarascon in France on calorimetric studies of new mixed iron manganese fluorophosphates (triflite and tavorite) We are also measuring surface energies and other changes in thermodynamic properties at the nanoscale for lithium cobalt oxides. This work will help define new directions for our renewal proposal.

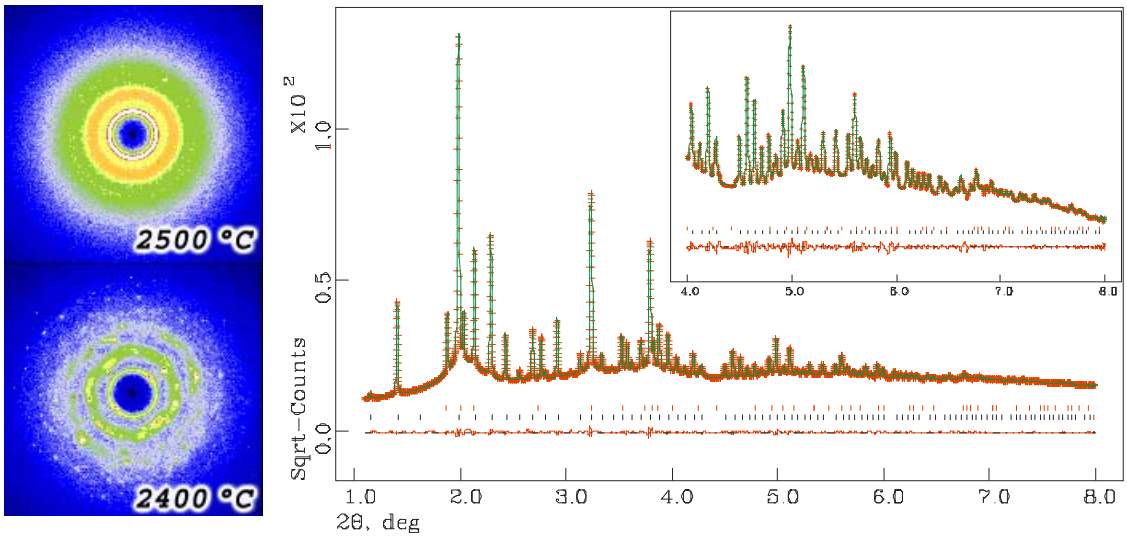

Figure 4. Left: 2D X-ray diffraction pattern of levitated Y_2O_3 sphere in Argon flow. Pyrometrically measured surface temperatures are labeled. Right: Le Bail fitting of integrated 1D X-ray diffraction profile of Y_2O_3 levitated in Oxygen flow at 2400° C surface temperature. Reflections for C-type Y_2O_3 are marked in red and for H-type Y_2O_3 are marked in black (11-ID-C beamline at APS at λ = 0.10798 Å).

DOE publications in last two years from the current grant

1. "Thermochemistry of lanthanum zirconate pyrochlore" A.V. Radha, S. V. Ushakov, and Alexandra Navrotsky, J. Mater. Res., Vol. 24, No. 11, 3350-3357 (2009)
2. "A correlation between the ionic conductivities and the formation enthalpies of trivalent-doped ceria at relatively low temperatures" H.J. Avila-Paredes, T. Shvareva, W. Chen, A. Navrotsky and S. Kim, Phys. Chem. Chem. Phys., 11, 8580–8585 (2009)
3. "Fluorite and pyrochlore phases in the HfO_2-La_2O_3 - Gd_2O_3 systems: characterization and calorimetricstudy of samples quenched from melts formed by laser heating and aerodynamic levitation", S. V.Ushakov, A. Navrotsky, and J.A. Tangeman, Mater. Res. Soc. Symp. Proc., 1122, 1122-O01-07 (2009)
4. "Synthesis and calorimetric studies of oxide multilayer systems: Solid oxide fuel cell cathode and electrolyte materials" Nihan Kemik, S.V. Ushakov, N. Schichtel, Y. Takamura, A. Navrotsky, J. Vac. Sci. Technol. B 28,4, C5A1-5 (2010)
5. "Calorimetric measurement of surface and interface enthalpies of yttria-stabilized zirconia (YSZ)", G.C. Costa, S.V. Ushakov, R.H.R. Castro, A. Navrotsky, R. Muccillo, Chem. Mater., Vol. 22, No. 9, 2937-2945 (2010)
6. "Modified polyol-mediated synthesis and consolidation of Gd-doped ceria nanoparticles", S. Wang, S.Chen, A. Navrotsky, M. Martin, S. Kim and Z. Munir, Solid State Ionics, 181, 372-378 (2010)
7. "Thermodynamics of solid electrolytes and related oxide ceramics based on the fluorite structure", A. Navrotsky, J. Mater. Chem., 20(47), 10577-10587 (2010)
8. "Grain boundary enthalpies of cubic yttria-stabilized zirconia", S. Chen, G. C. C. Costa, S. Wang, Z. A. Munir, S. Kim, and A. Navrotsky, J. Am. Ceram. Soc., 1-4, (2011)
9. "Nanoceria – energetics of surfaces, interfaces and water adsorption" S. Hayun, T.Y. Shvareva, and A. Navrotsky, J. Am. Ceram. Soc., 1–8 (2011)
10. "Direct measurements of fusion and phase transition enthalpies in lanthanum oxide", S.V. Ushakov, A. Navrotsky, J. Mater. Res., Vol. 26, No. 7, 845-847 (2011)
11. "Thermochemistry of $La_{0.7}Sr_{0.3}Mn_{1-x}Fe_xO_3$ Solid Solutions (0<x<1)", N. Kemik, Y. Takamura and A. Navrotsky, J. Solid State Chem., (in press)
12. "Yttria stabilized zirconia (YSZ) crystallization in Al_2O_3/YSZ Multilayers" N. Kemik, S.V. Ushakov, M. Gub, N. Schichtel, C. Korte, N. Browning, Y. Takamura, A. Navrotsky, J.Mater. Res., submitted (2011)
13. Direct measurement of surface energy of CeO_2 by differential scanning calorimetry, S. Hayun, S.V. Ushakov, A. Navrotsky, J. Eur. Cer. Soc., submitted (2011)

Developing Functionalized MMOFs for Enhanced and Selective CO_2 Adsorption

Jing Li (jingli@rutgers.edu), Chemistry and Chemical Biology, Rutgers University, Piscataway, NJ, **Yves J. Chabal**, Materials Science and Engineering, UT Dallas, Richardson, TX, and **David C. Langreth**, Physics, Rutgers University, Piscataway, NJ

Program Scope

The primary objective of this program is to develop functionalized microporous metal organic framework (MMOF) materials for enhanced and selective gas adsorption with a focus on CO_2 capture and separation. The structure design and characterizations are guided and assisted by first-principles theoretical calculations based on van der Waals density functional (vdW-DFT) and high-pressure and low-temperature infrared (IR) absorption and Raman spectroscopic methods. Modification and functionalization of MMOFs lead to significantly enhanced interactions between CO_2 (adsorbate) and framework (adsorbent), and thus substantially improved uptake capacity and adsorption selectivity. The selective adsorption of CO_2 is analyzed by experimental adsorption measurements as well as by molecular simulations. The outcome of this integrated program will contribute to a better understanding of the functionalization effect and molecular binding at the gas-solid interface, and provide useful information for future design and synthesis of porous MMOFs with enhanced properties for targeted applications.

Recent Progress:

a) Synthesis and adsorption study of functionalized MMOFs for enhanced CO_2 binding:

Functionalization of three-dimensional (3D) porous structure $Zn(bdc)(ted)_{0.5}$ (**1**) by hydroxyl and amino group leads to two new members of the $[Zn(bdc\text{-}R)(ted)_{0.5}]$ - family, $Zn(bdc\text{-}OH)(ted)_{0.5}$ (**2**) and $Zn(bdc\text{-}NH_2)(ted)_{0.5}$ (**3**) (bdc = terephthalate, ted = tryethylenediamine, bdc-OH = 2-hydroxylterephthalate, bdc-NH_2 = 2-aminoterephthalate).[1] A general decrease in surface area, pore volume and pore size is a consequence of space filling of the functional groups. Interestingly, however, both **2** and **3** show notable enhancement in CO_2 uptake at room temperature, along with higher isosteric heats of adsorption (in the order of **2** > **3** > **1**, see Fig. 1), suggesting stronger interactions between CO_2 and the functionalized structures. Such an enhancement can be attributed primarily to the strong electron donor-accepter interaction between the CO_2 molecule and the framework, where the O and N atoms containing lone pairs of electrons from hydroxyl and amino groups serve as the electron donor centers that are absent in the parent structure **1**. The higher CO_2 affinity through functionalization results in improved CO_2 selectivity to other small gases, such as N_2 and O_2. This study indicates that surface chemistry, rather than porosity, plays a more important role in the CO_2 adsorption of this type of structures.

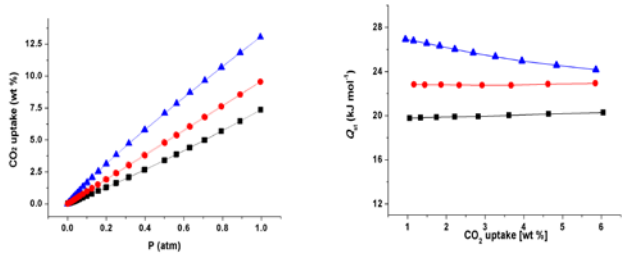

(a) (b)

Fig. 1. (a) Room temperature (25 °C) CO_2 adsorption isotherms for **1** (black), **2** (blue) and **3** (red). (b) Isosteric heats of CO_2 adsorption for **1** (black), **2** (blue) and **3** (red) calculated based on the adsorption isotherms taken at three temperatures (0, 15, and 25 °C).

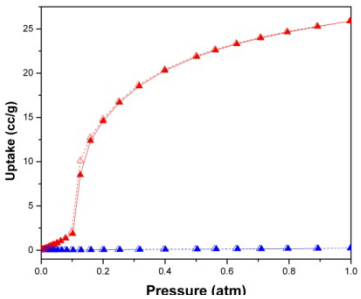

Fig. 2. Adsorption isotherms of CO_2 (red) and N_2 (blue) at 25 °C.

Our investigation on $[Zn_2(bpdc)_2(bpee)]$ (**4**) (bpdc = 4,4'-biphenyldicarboxylate, bpee = 1,2-bis(4-pyridyl) ethylene)[2]

demonstrates the structure effect on the selective CO_2 adsorption as a result of framework functionalization. Incorporation of a relatively long and flexible ligand bpee gives rise to a highly flexible one-dimensional (1D) pore structure. Single-component gas adsorption experiments show that this compound possesses high CO_2 adsorption enthalpy and the highest separation ratio of CO_2 over N_2 with respect to all MMOFs reported to date (Fig. 2). At 0.16 atm (a pressure similar to that of CO_2 in the post-combustion flue gas mixtures) and 25 °C, the value is 294, compared to 49 for MOF74-Mg (the best performing MMOF) at the same conditions, and 23 for **2** (at 1 atm).

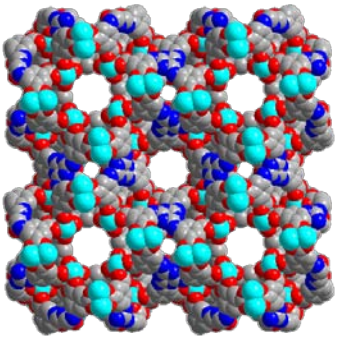

Fig. 3. The crystal structure of **5**. Color scheme: Cu (turquoise), O (red), N (blue), and C (gray).

While compound **4** is very attractive for its high CO_2 selectivity, its relatively low uptake capacity is not ideal for use in adsorption based CO_2 capture and separation applications. Our next approach is to introduce multifunctionality to the MMOF structures in order to achieve both high selectivity and capacity of CO_2 adsorption. One common way to increase gas-framework interactions is to create open metal sites (OMS). In addition, we have investigated the effect of Lewis basic sites (LBS) on the CO_2 adsorption. $[Cu_3(TDPAT)(H_2O)_3]$ (**5**) represents such an example that contains both OMS and LBS.[3] Compound **5** is made of a single hexacarboxylate ligand with imino triazine backbone (H_6TDPAT = 2,4,6-tris(3,5-dicarboxylphenyl amino)-1,3,5-triazine). It is a cage structure (Fig. 3) characterized by moderately high surface area (BET, 1938 m^2/g) and pore volume (0.93 cc/g). As the smallest member of all isoreticular *rht*-type structures which can also be described as (3, 24)-connected nets, it has the highest CO_2 uptake amount and binding affinity over all higher members, as well as the highest CO_2/N_2 selectivity under conditions that mimic flue gas mixtures. The compound adsorbs 6.2 wt% of CO_2 at room temperature and 0.1 atm, a condition similar to that of a flue gas mixture. The isosteric heat of CO_2 adsorption is calculated to be 42.2 kJ/mol at zero loading. Both values are considerably higher than other members of the *rht*-family which contain OMS only. These values also place **5** among a very small group of MMOFs with the highest CO_2/N_2 selectivity. Our adsorption and spectroscopic experiments, as well as theoretical and simulation calculations suggest that the high adsorption affinity and capacity of **5** can be attributed to the high density of both OMS ($1.76/nm^3$) and LBS ($3.52/nm^3$) unique to this compound. The smaller pore size in **5** compared to other members of the *rht* family is also likely a contributing factor to the stronger CO_2-framework interactions.

b) Spectroscopic studies, theoretical calculations and molecular simulations

The IR experiments show that the adsorption environment for CO_2 changes little upon functionalization of the pores going from structure **1** to **2** and **3**. A very small shift was observed in the hydroxyl functionalized structure **2**. The results confirm the earlier findings that IR shifts do not correlate with binding energies. The structure rearrangement in compound **4** during the CO_2 adsorption process was detected by Raman spectroscopy. Spectral changes that are associated with the changes in framework structure are observed and correlated to the preferential adsorption of CO_2 over N_2 with the assistance of DFT simulation of ligand reorientation.[2] Room temperature IR absorption

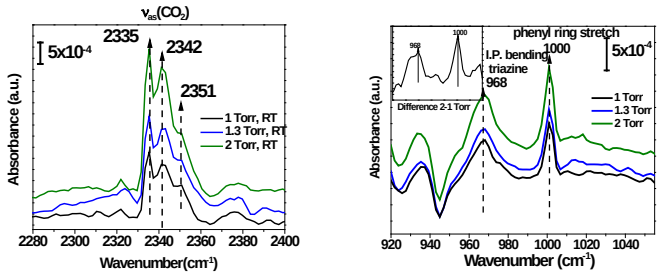

Fig. 4. RT IR absorption spectra of CO_2 adsorbed in **5** at low pressures. (a) The three absorption bands of CO_2, indicating three different CO_2 interactions (sites) within the framework. (b) Changes in the absorption bands of **5** upon CO_2 adsorption. The inset shows the difference of the spectra at 1 and 2 Torr, highlighting the intensity variation of the MOF bands as more CO_2 is loaded.

experiments were carried out on sample **5** to understand the nature of interactions between the CO_2 and the framework. Three distinct IR absorption bands of adsorbed CO_2 in **5** were identified, as shown in Fig. 4a.[3-4] The appearance of multiple CO_2 IR bands indicates that there are more than one strong adsorbing centers. The bands at 2335 and 2342 cm^{-1}, red shifted by ~-14 and -7 cm^{-1} from the unperturbed value of CO_2 asymmetric stretch (2349 cm^{-1}), are attributed to CO_2 adsorption sites at the LBS and phenyl rings, respectively.[5] The slightly blue shifted band at 2351 cm^{-1} (~+2 cm^{-1} shift) is attributed to CO_2 interacting through its oxygen with the unsaturated metal centers in a linear adsorption configuration.[6-7] The lower intensity of the band at 2351 cm^{-1} as compared to that of 2335 cm^{-1} indicates that less CO_2 is present for that specific site, consistent with the fact that **5** has a higher density of LBS (3.52/nm^3) than that of OMS (1.76 /nm^3). These assignments are consistent with observed changes in the vibrations of **5** upon CO_2 loading (See Fig. 4b).

The vdW-DFT2 calculations on benzene and trizine show that the highest CO_2 binding energies correspond to different structure configurations in the two cases. For benzene, it is achieved when CO_2 is located at the top of the aromatic ring, while for triazine, it is when CO_2 is placed at the edge of the ring with the carbon atom points to the nitrogen.

To mimic the separation behavior of **5** under a more real-world setting, we calculated its adsorption selectivity of CO_2 over N_2 in binary mixtures employing the ideal adsorbed solution theory (IAST) method[8] with the experimental single-component isotherms fitted by both dual-site Langmuir (DSL)[9] and dual-site Langmuir-Freundlich (DSLF) models. At a total pressure of 1 atm and CO_2 concentration of 15% and 20% (partial pressures of 0.15 and 0.2 atm), the IAST predicted selectivities are very high, 170 and 200, respectively (Fig. 5).

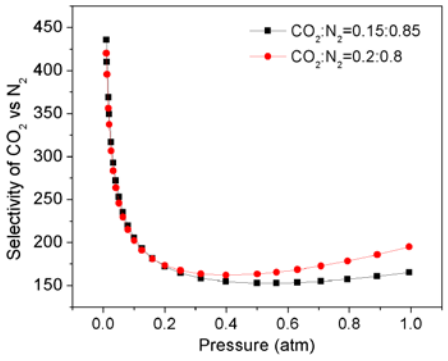

Fig. 5. Calculated IAST adsorption selectivities of CO_2 over N_2 in two binary mixtures. CO_2/N_2 (v/v): 0.15/0.85 (black) and 0.2/0.8 (red).

References:

(1) Y. Zhao, D. C. Langreth, Y. J. Chabal, J. Li. et al., *Chem. A. Euro. J.*, **2011**, *17*, 5101.
(2) H. H. Wu, R. S. Reali, D. A. Smith, M. C. Trachtenberg, J. Li, *Chem. A. Euro. J.* **2010**, *16*, 13951.
(3) B. Y. Li, Z. J. Zhang, Z. Shi, N. Nijem, Y. J. Chabal, J. Li, et. al. *Angew. Chem. Int. Ed.* Manuscript under review.
(4) N. Nijem, P. Thissen, Y. Yao, R. C. Longo, K. Roodenko, H. Wu, Y. Zhao, K. Cho, J. Li, D. C. Langreth, Y. J. Chabal, *J. Am. Chem. Soc.* **2011**, *133*, 12849.
(5) S. E. Siporin, B. C. McClaine, R. J. Davis, *Langmuir* **2003,** *19*, 4707.
(6) J. W. Ward and H. W. Habgood, *J. Phys. Chem.*, **1966**, *70*, 1178.
(7) T. Montanari, G. Busca, *Vibrational Spectroscopy*, **2008**, *46*, 45.
(8) (a) Myers, A.L.; Prausnitz, J.M. AIChE. J. **1965**, *11*, 121. (b) M. Heuchel, R. Q. Snurr, E. Buss, *Langmuir* **1997**, *13*, 6795.
(9) (a) S. Keskin, J. Liu, J. K. Johnson, D. S. Sholl, *Langmuir* **2008**, *24*, 8254. (b) P. Chowdhury, C. Bikkina, S. Gumma, *J. Phys. Chem. C* **2009,** *113*, 6616.
(10) (a) Y. S. Bae, K. L. Mulfort, H. Frost, P. Ryan, S. Punnathanam, L. J. Broadbelt, J. T. Hupp, R. Q. Snurr, *Langmuir* **2008,** *24*, 8592; (b) R. Babarao, Z. Hu, J. Jiang, S. Chempath, S. I. Sandler, *Langmuir* **2006,** *23*, 659.

Future Plans:

Our recent studies have shown that high CO_2 adsorption capacity and selectivity may be achieved by introducing multiple high binding sites in the porous structures, for example, open metal sites and Lewis basic sites. Our future efforts will center on a more systematic approach based on these preliminary findings. We will design and synthesize building units and ligands that carry targeted functionality and use them to construct multifunctionalized framework structures that have optimum pore size, and are also thermally and moisture stable. The combination and integration of experimental gas adsorption and spectroscopic (IR and Raman) methods, and molecular simulations and first-principle DFT calculations will serve as powerful tools to assist and guide us in understanding the properties and optimizing the performance of these adsorbent materials.

Publications in the past two years (acknowledging full DOE-DMSE support):

1. "Theoretical and experimental analysis of H_2 binding in a prototypical metal-organic framework material", L. Kong, V. R. C., N. Nijem, K. Li, J. Li, Y. J. Chabal, and D. C. Langreth, *Phys. Rev. B*, **2009**, *79*, 081407(R) .
2. "A Luminescent Microporous Metal Organic Framework for the Fast and Reversible Detection of High Explosives", A. J. Lan, J. Li et al., *Angew. Chem. Int. Ed.*, **2009**, *48*, 2334.
3. "RPM3: A Multifunctional Microporous MOF with Recyclable Framework and High H_2 Binding Energy", A. J. Lan, Y. J. Chabal, D. C. Langreth, J. Li et al., *Inorg. Chem.*, **2009**, *48*, 7165.
4. "Zeolitic Imadazolate Frameworks Capable of Kinetic Separation of Propane and Propene", K. H. Li, D. H. Olson, J. Seidel, T. J. Emge, H. W. Gong, H. P. Zeng; J. Li, *J. Am. Chem. Soc.*, **2009**, *131*, 10368.
5. "A Density Functional for Sparse Matter", D. C. Langreth et al., *J. Phys.: Condens. Matter*, **2009**, *21*, 084203.
6. "Highly Selective CO_2 Capture by A Flexible Microporous Metal Organic Framework (MMOF) Material", H. H. Wu, S. R. Randall, D. A. Smith, M. T. Trachtenberg, J. Li, *Chem. A. Euro. J.*, **2010**, *16*, 13951.
7. "Interaction of Molecular Hydrogen with Microporous Metal Organic Framework Materials at Room Temperature", N. Nijem, J. Li, D. C. Langreth, and Y. J. Chabal et al., *J. Am. Chem. Soc.*, **2010**, *132*, 1654.
8. "Molecular Hydrogen "Pairing" Interactions with the Unsaturated Metal Centers in MOF-74 System", N. Nijem, J. Li, D. C. Langreth, and Y. J. Chabal et al., *J. Am. Chem. Soc.*, **2010**, *132*, 14834.
9. "Higher-accuracy van der Waals Density Functional", Kyuho Lee, Éamonn D. Murray, Lingzhu Kong, Bengt I. Lundqvist and David C. Langreth, *Phys. Rev. B*, **2010**, *82*, 081101 (Rapid Communications) [partial support].
10. "Spectroscopic Evidence for the Influence of the Benzene Sites on Tightly Bound H_2 in Metal Organic Frameworks with Unsaturated Metal Centers", N. Nijem, Li, Langreth Chabal et al., *J. Am. Chem. Soc.*, **2011**, *133*, 4782.
11. "First-principles Approach to Rotational-vibrational Frequencies and infrared Intensity for H_2 Adsorbed in Nanoporous Materials", L. Kong, Y. J. Chabal, D. C. Langreth, *Phys. Rev. B*, **2011**, *83*, 121402.
12. "Enhancing Gas Adsorption and Separation Capacity through Ligand Functionalization of Metal Organic Framework Structures", Y. Zhao, D. C. Langreth, Y. J. Chabal, J. Li. et al., *Chem. A. Euro. J.*, **2011**, *17*, 5101.
13. "Commensurate Adsorption of Hydrocarbons in Microporous Metal-Organic Frameworks", K.H. Li, D.H. Olson, J. Li, *Trends in Inorg. Chem.*, **2011**, *12*, 13-24.

* Three manuscripts are currently under review in *Angew. Chem.*, *Adv. Func. Mater.* and *Inter. J. Hydrogen Energy*.

This page is intentionally blank.

Session 2

Soft Materials and Soft-Hard Interfaces

Session Chair: James Runt, The Pennsylvania State University

This page is intentionally blank.

Directed Assembly of Diblock Copolymers under Nano-Confinement

Qiang (David) Wang and David S. Dandy
q.wang@colostate.edu
Department of Chemical and Biological Engineering
Colorado State University, Fort Collins, CO 80523-1370

Program Scope

Our DOE project DE-FG02-07ER46448 is entitled "Achieving Three-Dimensional Well-Ordered Nanostructures in Block Copolymer Films by Combined External Fields". In this project, we use real-space parallel self-consistent field (SCF) calculations with high accuracy to study in detail the application of external fields, including surface fields due to the confinement and/or chemical/topological patterns of the surfaces and electric fields, to direct the self-assembled nanostructures formed in films of lamellae- and cylinder-forming diblock copolymers (DBC). The overall goal is to understand and predict the effects of graphoepitaxy, epitaxy, applied electric field, and their combinations on the self- and directed assembly of flexible DBC. This will allow knowledge-based rational design, instead of trial-and-error experiments in a large parameter space, to achieve perpendicular nanostructures (lamellae and cylinders) with long-range 3D order desirable for many applications of block copolymers in nanotechnology, including nanolithography, high-density storage devices, quantum dot or anti-dot arrays.

In this computational project, the stable structures are identified through free-energy comparisons, and our SCF predictions are compared with corresponding experiments in collaboration with other research groups. In particular, we find that nano-confinement strongly affects and can thus be used to control the self-assembled morphology of block copolymers. The confinement dimensions, geometries and patterns of the confining surfaces, and surface preferences all have significant effects on the self-assembled morphology under nano-confinement.[1] Much richer phase behaviors are found in our nano-confined systems, with complex morphologies that are very different from those found in the bulk.

Recent Progress

We have developed a FORTRAN 90 code ("PolySCF") that can be used for flexible DBC in either bulk or confined geometries and is parallelized using the message-passing interface for 3D, large-scale SCF calculations with high accuracy.[2] To demonstrate the capability and versatility of this code, we have used it to map out the phase diagrams of lamellae-forming symmetric DBC A-B confined between two parallel, flat and homogeneous surfaces.[E] By finely tuning the surface separation (confinement) and interactions with the two blocks, we found various complex morphologies shown in Fig. 1 that cannot be obtained in bulk. The free-energy data provided by our high-accuracy SCF calculations also reveal in detail the formation mechanism of these morphologies, which is due to the subtle balance among chain conformational entropy, surface preferences, and A-B repulsion. This demonstrates that understanding and predicting the self-assembled morphology of DBC under nano-confinement will help us obtain the desirable morphology for targeted applications, and real-space SCF

calculation is a powerful tool for this purpose. This work was featured on the inside front cover of *Soft Matter*.[E]

PolySCF was also used in our study of cylinder-forming asymmetric DBC thin films on chemically stripe-patterned substrates, in collaboration with an experimental group in Korea.[A] Here we demonstrated that, by controlling the substrate pattern (size, period, and interactions with the two blocks) and film thickness, directed assembly on *incommensurate* substrate patterns may induce well ordered complex nanostructures in block copolymer thin films. This is different from the idea of epitaxy[3] or density multiplication[4] where *commensurate* substrate patterns were used. Moreover, as shown in Fig. 2, our SCF calculations are in good agreement with experimental observations, and further provide detailed 3D structures inside thin films and their formation mechanism that are difficult to resolve in experiments. This work was featured on the frontispiece of *Advanced Materials*[A] and has been cited ~30 times since published in 2008.

Using PolySCF, we have further studied the bending of lamellae of flexible, symmetric DBC controlled by topographic guiding patterns; this work was in collaboration with the Almaden Research Center at IBM.[D] As shown in Fig. 3(a), symmetric DBC polystyrene-poly(methylmethacrylate) are confined between a pair of neutral, elbow-like side walls on a neutral substrate. By varying the elbow-pattern angle θ, the tilting angle φ of lamellae with respect to the side walls is measured and plotted in Fig. 3(b). Based on the experimental findings, we performed SCF calculations with all the input parameters taken directly from the experiments. The SCF results are in good agreement with the laboratory results, as shown in Fig. 3(b), and the free-energy information provided by our SCF calculations clearly explains the interesting φ-θ relation observed in the experiments. This work, published in *Macromolecules*,[D] definitively shows that high-accuracy SCF calculations can be used to understand and predict the directed assembly of block copolymers on topographically patterned substrates.

Future Plans

Our project DE-FG02-07ER46448 ends on Aug. 14th, 2011. A renewal project entitled "Directed Assembly of Rod-Coil Block Copolymers by Combined External Fields" is recently funded, so we will move on to this renewal project. This is also a computational study, where we will use 3D SCF calculations and the newly proposed fast off-lattice Monte Carlo simulations[C] with judiciously designed generic models to understand, predict, and ultimately control the self-assembled nanostructures of rod-coil block copolymers in bulk, under thin-film confinement and with applied magnetic field. This project will allow knowledge-based rational design of these nanomaterials, instead of trial-and-error experiments in a large parameter space, advancing their integration into a range of technologically important applications, including the fabrication of polymer-based photovoltaic cells, light-emitting diodes, field-effect transistors, and chemical and biological sensors.

References

1. *Q. Wang,* "Monte Carlo Simulations of Nano-Confined Block Copolymers", Chap. 16 in **Nanostructured Soft Matter: Experiment, Theory, Simulation and Perspectives**, 495-527, ed. A. V. Zvelindovsky, Springer, 2007.
2. *D. Meng and Q. Wang*, "Hard-Surface Effects in Polymer Self-Consistent Field Calculations", **J. Chem. Phys., 126**, 234902 (2007).

3. *S. O. Kim, H. H. Solak, M. P. Stoykovich, N. J. Ferrier, J. J. de Pablo, and P. F. Nealey*, "Epitaxial Self-Assembly of Block Copolymers on Lithographically Defined Nanopatterned Substrates", **Nature 424**, 411 (2003).
4. *R. Ruiz, H. Kang, F. A. Detcheverry, E. Dobisz, D. S. Kercher, T. R. Albrecht, J. J. de Pablo, P. F. Nealey*, "Density Multiplication and Improved Lithography by Directed Block Copolymer Assembly", **Science, 321**, 936 (2008).

Publications

A. *S. O. Kim, B. H. Kim, D. Meng, D. O. Shin, C. M. Koo, H. H. Solak, and Q. Wang*, "Novel Complex Nanostructure from Directed Assembly of Block Copolymers on Incommensurate Surface Pattern", **Adv. Mater., 19** (20), 3271-3275 (2007) [***Frontispiece***]; **20** (5), 866 (2008).
B. *Q. Wang*, "Effects of Interaction Range and Compressibility on Microphase Separation of Diblock Copolymers: Mean-Field Analysis", **J. Chem. Phys., 129**, 054904 (2008).
C. *Q. Wang and Y. Yin*, "Fast Off-Lattice Monte Carlo Simulations with 'Soft' Repulsive Potentials", **J. Chem. Phys., 130**, 104903 (2009).
D. *S.-M. Park, M. Dong, C. T. Rettner, D. S. Dandy, Q. Wang, and H.-C. Kim*, "Bending of Lamellar Microdomains of Block Copolymers on Nonselective Surfaces", **Macromolecules, 43**, 1665 (2010).
E. *D. Meng and Q. Wang*, "Complex Morphologies in Thin Films of Symmetric Diblock Copolymers as Stable and Unstable Phases", **Soft Matter, 6**, 5891 (2010) [***Inside Front Cover***].
F. *Q. Wang*, "Theory and Simulation of Self-Assembly of Rod-Coil Block Copolymer Melts: Recent Progress", **Soft Matter, 7**, 3711 (2011).
G. *D. Meng and Q. Wang*, "Stimuli-Response of Charged Diblock Copolymer Brushes", **J. Chem. Phys.**, submitted (2011).

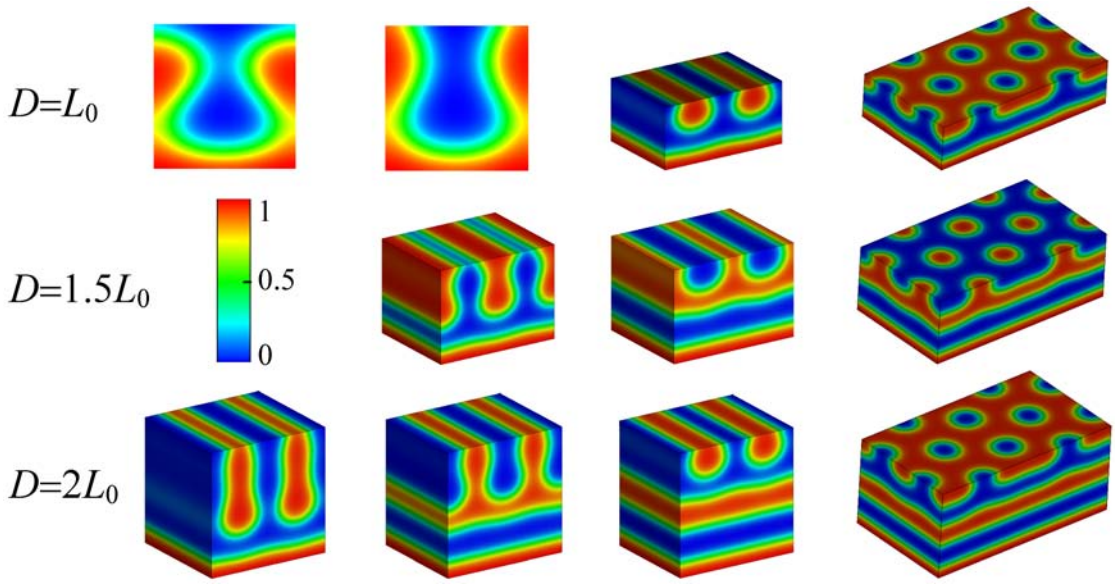

Fig. 1. Novel complex nanostructures formed by symmetric DBC A-B confined between two parallel, flat and homogeneous surfaces (placed at the top and bottom of each morphology, not shown for clarity), obtained from our SCF calculations. The red corresponds to A-rich regions and the blue for B-rich regions, and periodic boundary conditions are applied in the lateral directions. D denotes the film thickness and L_0 the bulk lamellar period. From Ref. [E].

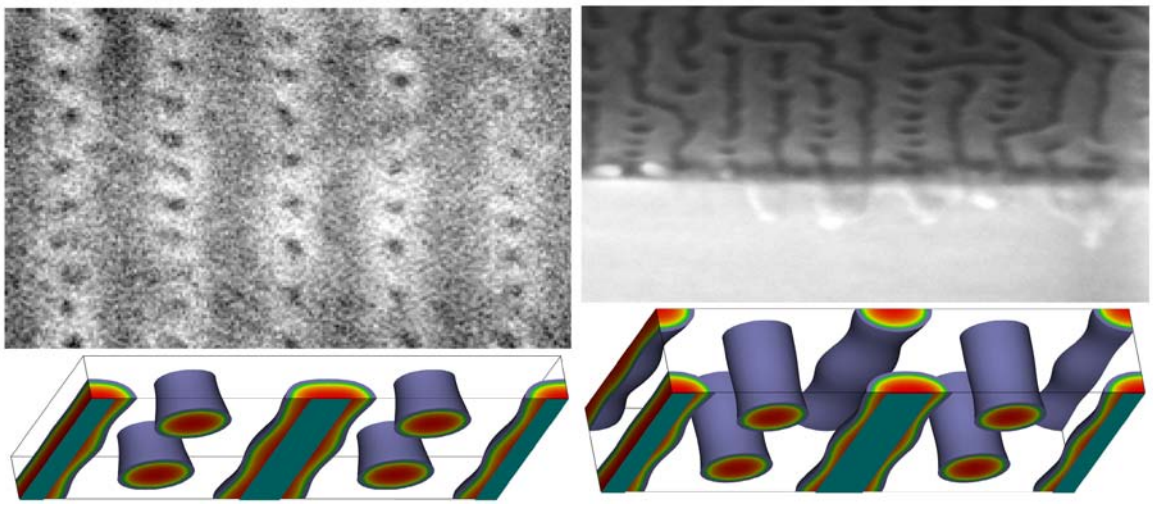

Fig. 2. Novel complex nanostructures of cylinder-forming diblock copolymers on incommensurate substrate pattern. The pre-patterned substrate consists of alternating neutral and preferential stripes and its pattern period is 100 nm, which is more than twice of the bulk inter-cylinder distance of 45 nm of the copolymer; the preferential stripes attract the minority (dark/red) block. **Left:** Plane-view SEM image (top) and SCF results (bottom) indicating well ordered arrays of parallel half-cylinders on preferential stripes (shown in teal) and perpendicular cylinders on neutral stripes (not shown for clarity) in a 20-nm-thick film. **Right:** Cross-sectional SEM image (top) and SCF results (bottom) indicating two layers of parallel half-cylinders on preferential stripes and perpendicular cylinders on neutral stripes in a 40-nm-thick film. From Ref. [A].

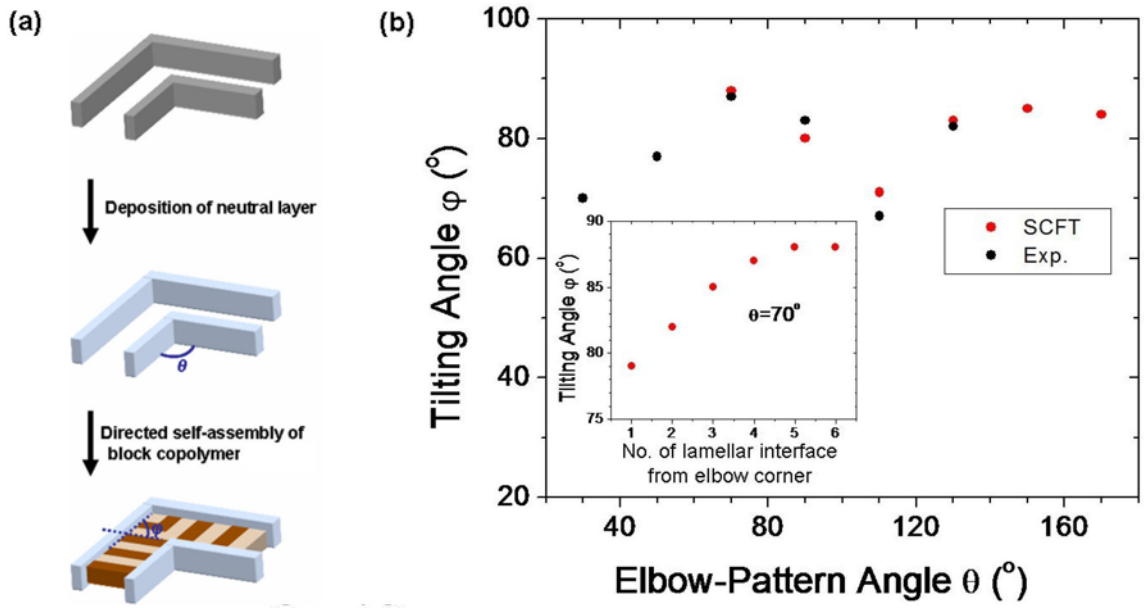

Fig. 3. Bending of lamellae of symmetric DBC A-B by topographic guiding patterns. The SCF results in the inset of part (b) can be used to explain the experimentally observed decrease of lamellae titling angle φ (with respect to the elbow-like sidewalls) as the elbow-pattern angle θ decreases from 70º. From Ref. [D].

AC Electrohydrodynamic Instabilities in Thin Liquid Films: A Route to Hydrodynamic Self-Assembly of Topographical Patterns on Soft Materials

Scott A. Roberts and Satish Kumar
kumar030@umn.edu
Department of Chemical Engineering and Materials Science
University of Minnesota, Minneapolis, MN 55455

Program Scope

Surface topography has a significant impact on the optical, adhesive, and wetting properties of materials [1]. For thin films of soft materials such as polymers, controlling surface topography in order to tailor associated properties to desired specifications is a crucial processing challenge. In this program, we are using theoretical tools to explore fundamentally new ways of creating and controlling the surface topography of thin films of soft materials that make use of principles from hydrodynamics and self-assembly. These methods are worthy of exploration because they have the potential to considerably advance state-of-the-art technologies as well as fundamental scientific understanding. Our principal focus to date has been on analyzing how AC electric fields lead to the formation of topographical patterns on the surfaces of thin liquid films through hydrodynamic instabilities.

Recent Progress

When DC electric fields are applied to a thin liquid film, the interface may become unstable and form a series of pillars [2], as shown in Figure 1.

Figure 1: The top panel shows a schematic of the problem setup. Layer 2 is a thin liquid film, typically a polymer, whereas Layer 1 could be another polymer, a low-molecular-weight fluid, or air. The bottom panel shows a series of pillars that form after the interface becomes unstable due to an applied electric field. The film thicknesses, pillar widths, and pillar spacings are ~100-1000 nm.

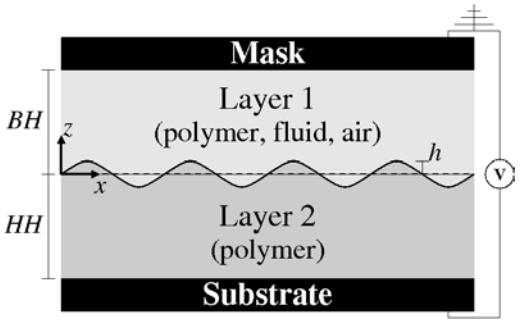

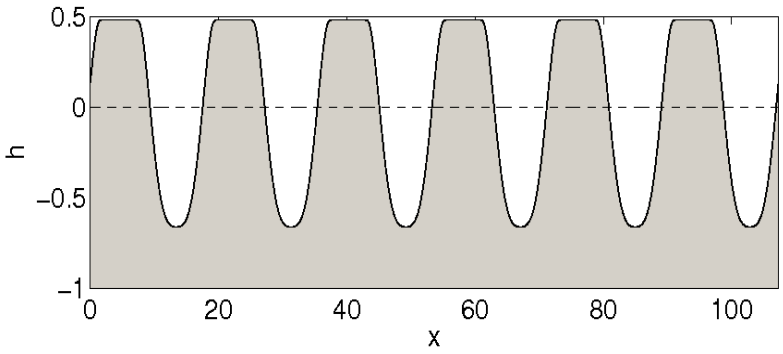

The formation of these pillars provides a route through which surface topography can be created on thin polymer films. Being able to precisely control surface topography is crucial to the advancement of technologies such as coatings, printed electronics, and biomaterials. Our work examines the possibility of using AC electric fields to exert further control over the size and shape of the pillars. The basic idea is that an AC field introduces two new parameters, the amplitude and the frequency of the voltage oscillation, which could potentially be manipulated to create new phenomena not seen when only DC fields are applied.

The mathematical model used in our study is based on well-established equations of electrohydrodynamics [3]. The model assumes that the fluids involved have (i) Newtonian rheological behavior, (ii) thicknesses much smaller than their characteristic lateral dimensions (thereby allowing the use of the well-known lubrication approximation, which yields great simplification of the governing equations), and (iii) the ability to accumulate charge at fluid-fluid interfaces (so-called leaky dielectric fluids). These assumptions lead to a model that consists of partial differential equations describing how the height of each fluid-fluid interface and the charge there evolve with space and time.

The principal accomplishment of the past year is publication of a study on AC electrohydrodynamic instabilities in systems with three thin liquid films. The geometry is similar to that shown in Figure 1, except that there are two polymer layers (Figure 2). This geometry is also extremely relevant to the applications mentioned above, but is much more difficult to investigate due to the presence of two fluid-fluid interfaces. Experiments show that novel pillar shapes can be generated from electrohydrodynamic instabilities at the interfaces of these thin polymer/polymer/air trilayer films [4]. However, until our work, it was unclear what role---if any---free charge plays in the instability process.

Figure 2: Schematic of trilayer system

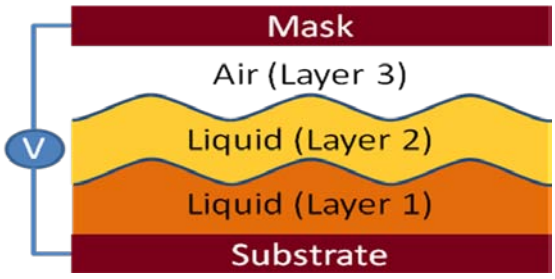

Motivated by our recent theoretical study [CG1] which demonstrates how AC electric fields can be used to increase control over the pillar formation process in thin liquid bilayer films, we applied linear stability analysis and nonlinear simulations to equations governing an analogous trilayer system. For perfect dielectric films, the effect of an AC electric field can be understood by considering an equivalent DC field. Leaky dielectric films yield pillar configurations that are drastically different from perfect dielectric films, and AC fields can be used to control the location of free charge within the trilayer system. This can alter the pillar instability modes and generate smaller diameter pillars when conductivities are mismatched due to a resonance between the oscillation frequency and the time scale for charge transport. This represents an entirely new physical mechanism for the creation of smaller topographical features, and may be of use for the fabrication of complex topographical patterns on polymer coatings and in microelectronics. Moreover, our results demonstrate that while free charge does not play an important role in the experiments noted above [4], its presence could lead to drastically different pillar morphologies (Figure 3). The results of this work are described in reference [CG2].

Figure 3: Sample results from nonlinear simulations in which free charge is neglected (left panel) and included (right panel). When free charge is neglected (left; perfect dielectric model), the lower layer forms a "shell" and the upper layer forms a "core". When free charge is included, the lower layer forms a "core" and the upper layer forms a "shell". The panel on the left more closely resembles what is seen in experiments [4], but the panel on the right suggests that free charge could be introduced in order to dramatically alter pillar morphology.

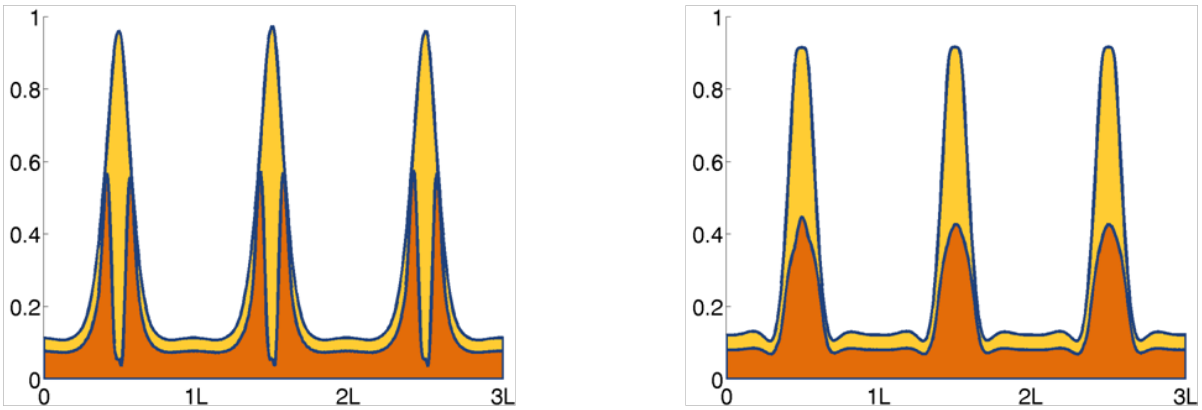

Future Plans

Currently we are examining the role of film viscoelasticity in order to determine whether a forcing frequency resonant with film relaxation times can produce novel pillar structures. We anticipate that this work will lead to strategies for tailoring the film rheology to produce a desired surface topography. In a related study, we are examining the effects of adventitious charge on the leveling of thin liquid films. Charge can inadvertently accumulate on fluid-fluid and fluid-solid interfaces and create effects that interfere with the types of electrohydrodynamic instabilities we are trying to examine. We expect that this work will provide insight into how to pattern surfaces to exert further control over surface topography. Some effort is being devoted to learning how to incorporate evaporation into our thin-film models, since evaporation is an

essential part of the drying and solidification of thin liquid films. We are also learning new theoretical methods that have been applied to analyze the stability of bulk flows of polymeric liquids [CG3, CG4] because of the potential of these methods to provide significant new insights into the stability of topographical patterns on thin polymer films (e.g., how stable the patterns are in the presence of external noise or thermal fluctuations). We expect that each of these efforts will advance the fundamental understanding needed to control the growth and self-assembly of nanoscale topographical features, which can ultimately be exploited in modern technologies involving thin films of soft materials.

References

[1] H. Assender, V. Bliznyuk, and K. Porfyrakis, How surface topography relates to materials' properties, Science 297 (2002) 973.

[2] S. Y. Chou, L. Zhuang, and L. Guo, Lithographically induced self-construction of polymer microstructures for resistless patterning, Appl. Phys. Lett. 75 (1999) 1004; E. Schäffer, T. Thurn-Albrecht, T. P. Russell, and U. Steiner, Electrically induced structure formation and pattern transfer, Nature 403 (2000) 874.

[3] D. A. Saville, Electrohydrodynamics: The Taylor-Melcher leaky dielectric model, Annu. Rev. Fluid Mech. 29 (1997) 27.

[4] M. D. Dickey, S. Gupta, K. A. Leach, E. Collister, C. G. Wilson, and T. P. Russell, Novel 3-D structures in polymer films by coupling external and internal fields, Langmuir 22 (2006) 4315; K. A. Leach, S. Gupta, M. D. Dickey, C. G. Wilson, and T. P. Russell, Electric field and dewetting induced hierarchical structure formation in polymer/polymer/air trilayers, Chaos 15 (2005) 047506; M. D. Morariu, N. E. Voicu, E. Schaffer, Z. Lin, T. P. Russell, and U. Steiner, Hierarchical structure formation and pattern replication induced by an electric field, Nature Mater. 2 (2003) 48.

DOE Sponsored Publications from Current Grant

[CG1] S. A. Roberts and S. Kumar, AC Electrohydrodynamic Instabilities in Thin Liquid Films, J. Fluid Mech. 631 (2009) 255-279.

[CG2] S. A. Roberts and S. Kumar, Electrohydrodynamic Instabilities in Thin Liquid Trilayer Films, Phys. Fluids. 22 (2010) 122102 (15 pages).

[CG3] M. R. Jovanović and S. Kumar, Transient Growth without Inertia, Phys. Fluids 22 (2010) 023101 (19 pages).

[CG4] M. R. Jovanović and S. Kumar, Nonmodal Amplification of Stochastic Disturbances in Strongly Elastic Channel Flows, J. Non-Newtonian Fluid Mech. 166 (2011) 755-778.

Brush-Coated Nanoparticle Polymer Thin Films

Peter F. Green (pfgreen@umich.edu)

Materials Science and Engineering, University of Michigan, Ann Arbor

Program scope

The technologically important class of materials, polymer nanocomposites (PNCs), which exhibits diverse functional properties, from optical and electronic, to biomedical and structural), is the focus of this research program.[1] The properties of PNCs are determined not only by the chemical composition of the polymer host and the functionality of the nanoparticle, but also on the nanoparticle size, dispersion, organizational order in some cases, inter-nanoparticle separation distances, and on the relative interactions between the nanoparticles and the host. One of the primary challenges in this field is associated with control of the nano and macro-scale structure. Because the properties of PNCs depend on the morphological structure, the development of reliable strategies to "tailor" structure of the PNC is essential. One effective strategy is to tether chains onto the surface of the nanoparticle, thereby enhancing the degree of compatibility. The proposed research is to discover and to develop an understanding of interrelations between the structure and specific properties (mechanical, glass transition, optical, dynamics) of thin film polymer nanocomposites (PNCs) containing brush-coated metallic nanoparticles. Our goal is to discover the basic principles that enable fabrication functional thin film PNC materials with tailored structures and properties. The first objective of our program is to develop an understanding of how interactions between the free chains and the brush layers on the nanoparticles, and the interfaces, determine the morphological structure of polymers. Specific systems include: (1) brush-coated metallic nanoparticle/homopolymer; (2) brush-coated metallic nanoparticle/polymer-A/polymer-B mixtures; (3) brush-coated metallic nanoparticle/diblock copolymer mixtures. Specific problems include, coarsening phenomena, dynamics of chains and of nanoparticles, surface mechanical properties, surface plasmon absorption.

Recent Progress

We showed that the interactions between the free chains and the brush layer may be "tuned" by controlling the chemistry, the grafting density, σ, the degrees of polymerization of the grafted chains, N, and of the polymer host, P, respectively, as well as the nanoparticle diameter, D.[*see papers published under this grant*] There are generally three basic situations of interest when considering miscibility in these brush coated nanoparticle/homopolymer mixtures. At very low grafting densities, Σ, a few chains per particle, the morphology is largely dictated by a competition between the attractive enthalpic interactions between the bare nanoparticle surfaces (cores), mediated by entropic interactions with the grafted polymer chains and host chain environment. At higher Σ, the grafted chains form a brush layer which would be intermixed with the P-mer chains, provided N/P>1; this is the so-called "wet brush" scenario. At much higher Σ, the free P-mer chains are largely excluded from the brush layer, resulting in a loss of translational entropy of the free chains. This is the so-called "dry brush" regime. Miscibility is generally high when the wet brush conditions are met. Miscibility is also enhanced with decreasing nanoparticle size (*Chen and Green, Soft Matter 2011*). The

behavior of the athermal system may be summarized using a morphological "phase" diagram where the structure of different regimes based on N and P are described (Kim and Green, Macromolecules, 2010).

There is a fundamental difference between bulk and thin film PNCs: the preferential attraction of grafted nanoparticles to interfaces renders thin film PNCs systems thermodynamically less stable than their bulk analogs (*Green, Soft Matter, 2011*). The nanoparticles exhibit a tendency to segregate to interfaces due to a number of effects: (i) the free host chains gain conformational entropy when they are displaced from the interfaces by the nanoparticles; (ii) van der Waals interactions; (iii) the N-mer chains, tethered to the nanoparticles, suffer a lower entropic loss at the substrate than the linear host chains. For cases where the brush thickness l>D and both N and P are large (where l>>R_c and $R_g(P)$>>$D/2$), the system exhibits a tendency to become thermodynamically unstable and phase separate, and the nanoparticles reside primarily at the interfaces. The effects of nanoparticle curvature are very important (*Chen and Green, Soft matter 2011*). Decreasing the nanoparticle size increases miscibility.

The situation in which the grafted chains are chemically different from the host chains was also examined. A "diagram of states" was proposed to identify the conditions under which the different regimes would be influenced by the enthalpic thermodynamic interactions (this is discussed further in section II). In short, the primary effect of a sufficiently negative interaction parameter is to shift the phase boundary toward enhanced miscibility. Entropic, effects, however can suppress this enhancement.

Progress of other projects

Role of defects on nanoparticle order in block copolymer thin films:

We showed, that nanoparticles would primarily reside at dislocation cores in thin diblock copolymer thin films (i.e.: boundaries of islands and holes), provided they are sufficiently large (Kim and Green, Macromolecules, 2011). Parenthetically, the distribution of spherical nanoparticles of diameter d, within a domain, is generally determined by the ratio d/L. Monodisperse particles of sufficiently small d/L, typically d/L<0.15, would reside throughout the copolymer domains, maximizing the translational entropy. Of practical interest here is that the domains act as scaffolds to direct the assembly of the nanoparticles. It turns out that if d/L is sufficiently large, the entropic cost for restricting the nanoparticles exclusively to the domains is too high. Consequently, thenanoparticles exhibit a strong tendency to reside at the boundaries of the islands in block copolymer thin films (cores of edge dislocations) to minimize the free energy. This is illustrated in Figure 1.

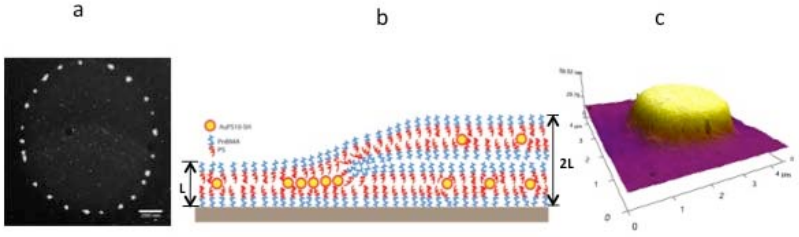

Figure 1: (a) nanoparticles at the boundary of an island; (b) Schematic of the NP location; (c) BCP island.

Coarsening in thin film PNCs

The phenomenon of coarsening is ubiquitous and occurs a diverse range of processes: aerosol aggregation, phase separation. [2] Ostwald ripening (OR) and coalescence are the primary mechanisms. Ostwald ripening is the process by which the larger particles grow at the expense of the smaller particles, through transfer of atoms; the driving force is to equalize the chemical potentials. The dynamic coalescence mechanism involves the center of mass, Brownian motion, of the particles (clusters of phases) that coalesce on coming in contact. The islands of pure BCPs and BCP/nanoparticle mixtures exhibit both phenomena (Figure 2) and the dynamics are well described by appropriate classical scaling exponents and distribution functions (not shown here).

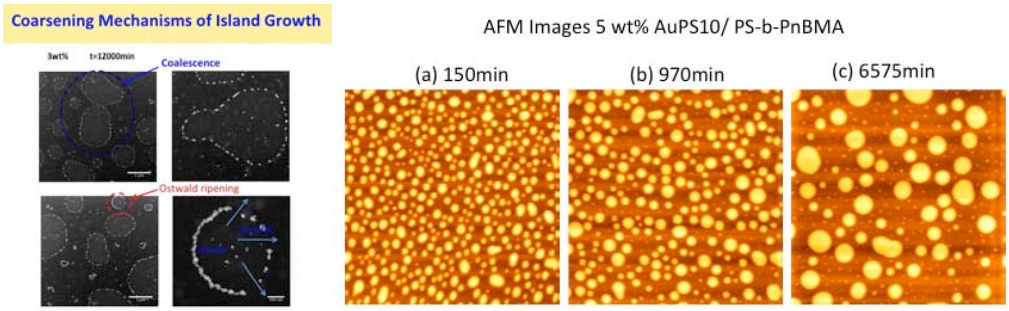

Figure 2: These islands undergo coarsening. Evidence of Ostwald ripening (decreasing particle sizes) and Coalescence (Islands coming together and coalescing) is shown here.

Tailoring the Optical Properties of thin film PNCs

In a third problem we examined the optical properties of these PNCs. Chain grafted Au nanoparticles were incorporated into a fluorescent polymer, poly[2-methoxy-5-(2-ethylhexyloxy)-1,4-phenylenevinylene] (MEH-PPV) host (Chen and Green, Langmuir). We showed that control of the Au nanoparticle distribution within the MEH-PPV is achieved by manipulating the enthalpic and entropic interactions between the grafted brush layers and the host chains. Additionally, we showed that the fluorescence of these Au/MEH-PPV nanocomposite thin films could be tailored by an order of magnitude, through changes only in the nanoparticle distribution, brush length and nanoparticle size; the fraction of Au remained constant.

Dynamics of homopolymer Chains in PNCs

Finally, we studied the dynamics of the host chains in the presence of the brush-coated nanoparticles (Oh and Green, Nature Materials, 2009). We examined ultra small particle regime 5 nm, where the effects on the chain relaxation times and the glass transition were quite remarkable. The bulk dynamics could be "tailored" to increase or decrease, by over an order of magnitude. Commensurate changes in the glass transition temperature were also documented.

Future Projects:
(1) 2 dimensional coarsening in BCP/brush coated nanoparticle systems; (2) dynamics of brush coated nanoparticles in homopolymer hosts; (3) structure of brush coated/polymer blend systems; (4) surface plasmon phenomena in model brush coated nanoparticle/polymer systems; (5) 2D coarsening of nanoparticles in polymer films; (6) glass transition of brush coated nanoparticle/homopolymer systems.

References:

[1] J.F. Douglas J. Jancar, F.W. Starr, S.K. Kumar, P. Cassagnau, A.J. Lesser, S.S. Sternstein and and M.J. Buehler, Polymer **51**, 3321 (2010); L. M. Hall, A. Jayaraman, and K. S. Schweizer, Current Opinion in Solid State and Materials Science **14** (2), 38 (2010); Jong-Young Lee Alfred J. Crosby, *Polymer Reviews* **47**, 217 (2007).

[2] E. D. Siggia, Phys Rev A **20** (2), 595 (1979); M. Zinke-Allmang, Thin Solid Films **346** (1-2), 1 (1999); D. J. Semin, A. Lo, S. E. Roark, R. T. Skodje, and K. L. Rowlen, J Chem Phys **105** (13), 5542 (1996); R. Limary and P. F. Green, Phys Rev E **66** (2) (2002);

DOE Sponsored publications 2009-2011 from current grant

1. Arceo, A., Meli, L., and Green, P.F. (2008). Glass transition of polymer-nanocrystal thin film mixtures: Role of entropically directed forces on nanocrystal distribution. Nano Letters *8*, 2271-2276.
2. J. Kim and P.F. Green, (2010). Directed Assembly of Nanoparticles in Block Copolymer Thin Films: Role of Defects. Macromolecules *43*, 10452.
4. Green, P.F. (2011). Tailoring the properties of brush coated nanoparticle homopolymer thin film mixtures. Soft Matter 2011 (ASAP).
5. X. Chelsea Chen and P.F. Green (2009). Control of Morphology and Its Effects on the Optical Properties of Polymer Nanocomposites. Langmuir *26*, 3659-3665.
6. X. Chelsea Chen and P.F. Green (2011). Structure of Thin Film polymer nanocomposites. Soft Matter *7*, 1192.
7. Kim, J., and Green, P.F. (2010). Phase Behavior of Thin Film Brush-Coated Nanoparticles/Homopolymer Mixtures. Macromolecules *43*, 1524-1529.
8. Meli, L., Arceo, A., and Green, P.F. (2009). Control of the entropic interactions and phase behavior of athermal nanoparticle/homopolymer thin film mixtures. Soft Matter *5*, 533-537.
9. Oh, H., and Green, P.F. (2009). Polymer chain dynamics and glass transition in athermal polymer/nanoparticle mixtures. Nature Materials *8*, 139-143, 2009.
10. P. F. Green, P. Akcora and S. K. Kumar P. F. Green, in *Series: "Neutron Scattering Applications and Techniques"*, edited by I. Anderson and A. Hurd Series Eds.: R. McGreevy (Springer, New York, 2011).

Nanoparticles Stabilize Thin Polymer Films: A Fundamental Study to Understand the Phenomenon

Michael E. Mackay,[1] Venkat Padmanabhan[1] Wenluan Zhang[1] and Amalie Frischknecht[2]
mem@udel.edu

[1]Department of Materials Science and Engineering
University of Delaware, Newark, DE 19716

[2]Center for Integrated Nanotechnologies
Sandia National Laboratories, Albuquerque, NM 87185

Program Scope

A new understanding of thermodynamics at the nanoscale resulted in a recently discovered first order phase transition that nanoparticles in a polymer film will all segregate to the supporting substrate. This is an unusual phase transition that was predicted using a modeling technique developed at Sandia National Laboratories and required the equivalent of many computational years on one computer. The original observation was made in this project through careful experimentation, however, it was the computational effort that demonstrated it was a phase transition which occurs only in a polymer film.

Presently the effect of polymer chain stiffness and the effect of other larger objects in the polymer film are being explored. Specifically, the phase transition is dictated by the entropy loss that a polymer chain experiences next to a solid substrate causing it to push the nanoparticle there and trapping it. A system entropy gain results as the polymer gains many degrees of freedom by sitting on a nanorough carpet of nanoparticles while the particle only loses three degrees of freedom. We wish to determine if a stiff polymer chain will not force the nanoparticles to substrate since it has less degrees of freedom to lose. A second aspect of the present study is to determine if larger particles will behave similarly to a solid substrate in creating nucleating sites throughout the film for nanoparticle assembly. Both these phenomena have applications in the manufacture of polymer-based solar cells.

Recent Progress

Simulations. We performed molecular dynamics (MD) simulations to study the effect of chain stiffness on this segregation since stiffness should affect the phenomenon. The nanoparticles are modeled as spheres and the polymers as semi-flexible bead-spring chains. Both purely repulsive and attractive forces are considered, while assuming non-selective Lennard-Jones interactions among all species. We find the nanoparticles are well-dispersed in the system having repulsive forces only and aggregate into clusters in the completely attractive system. For both kinds of interactions, however, the nanoparticles segregate to the substrate when the polymers are flexible. Yet, with increasing chain stiffness, the nanoparticle concentration at the substrate decreases substantially.

Simulations were performed on systems with different compositions for fully flexible chains with a bending constant $K = 0$ and for semi-flexible chains with $K = 5$ kT, and for both repulsive and attractive set of interaction parameters. Considering the purely repulsive system we find the results given in Figure 1. Here the excess absorption, made dimensionless with the polymer monomer diameter, is plotted as a function of nanoparticle bulk volume fraction in the film. The flexible system has less polymer next to the substrate while the stiffer system has a rather indifference as to whether the polymer or nanoparticle is present at the surface. This

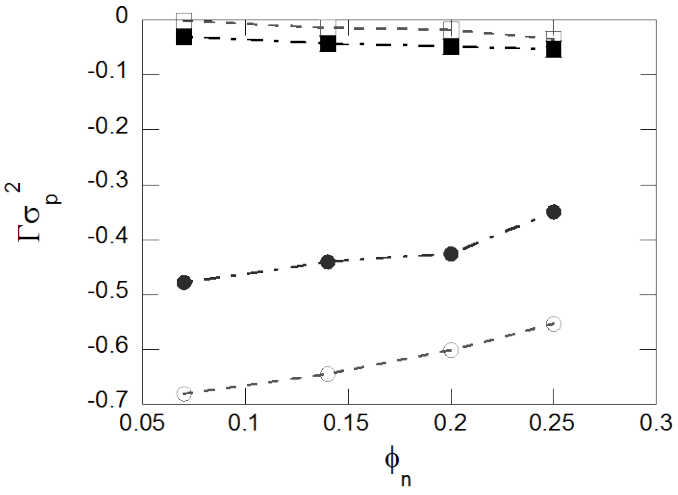

Figure 1. Excess adsorption of nanoparticles (closed symbols) and polymers (open symbols), as a function of nanoparticle volume fraction Φ_n for K = 0 (circles) and K = 5 (squares).

clearly demonstrates that entropic factors, dictated through chain stiffness, can change the excess component at a solid substrate.

Experiments. Organic photovoltaics have attracted substantial interest in scientific and industrial research because they can provide an enviromental friendly, portable and potential inexpensive energy source.[1,2] Although great improvement has been obtained to make energy conversion efficiency more than 8%,[3] it is still not feasible for commercialization compared to inorganic solar cells. The efficiency is simply not high enough to make a commercially relevant product.

The conjugated polymer acts as the electron donor and the fullerene is the electron acceptor which are blended together to form an interpenetrating structure at the nanoscale, to create the so called bulk-heterojunction (BHJ) solar cells. Because of the low polymer dielectric constant, strongly bound electron-hole pairs (excitons) are generated when light excites the active layer.[4] Due to the small exciton diffusion length, only 5-10 nm,[5] it is required that the excitons should be created near the interface of the polymer and fullerene rich domains to facilitate free charge carrier generation. Such a requirement suggests an optimum morphology of active layer consisting of long interpenetrating domains of order 10 nm in dimension.[6]

Much effort has been made to obtain high efficiency through controlling the morphology of the active layer, such as using thermal annealing and solvent annealing.[7,8] Due to the physical properties, there is a compromise between charge generation and charge transportation. The donor and acceptor should be well blended to increase the interfacial area to enhance charge generation. On the other hand, in order to enhance charge transportation, a certain degree of phase separation between donor and acceptor domains is needed to form bi-continuous pathway throughout the active layer.[9]

However, this compromise is not the only factor controlling morphology. Kiel et al. in our group recently demonstrated that the nanoparticle concentration profile also plays an important role on the performance of polymer based solar cells by using phase sensitive neutron reflectivity (PSNR) in NIST.[10,11] By thermal annealing, a higher concentration of PCBM was found near air and most likely contributed to a higher efficiency.

Based on our previous studies we hypothesize that adding larger particles to a polymer film containing smaller particles and polymer would cause the small nanoparticles to assemble around the larger. This could be a technique to promote a continuous network of small nanoparticles. This provides us a new prospective direction to control the morphology of polymer solar cells. Here we add Fe_3O_4, which has 10 nm diameter, to a 1:1 P3HT:PCBM blend as the active layer. Preliminary results show a slightly performance increase compared to pure P3HT:PCBM, see Figure 2.

The current – voltage relation for solar cells demonstrate that adding a nonconducting particle to the polymer-based solar cell slightly improves the operating efficiency and short circuit current. The magnetite particle has an oleic acid steric layer, which shields the oxide from the surroundings, to provide organic solvent solubility and significantly reduces the conducting characteristics. So, this addition should reduce the performance which it surely does not.

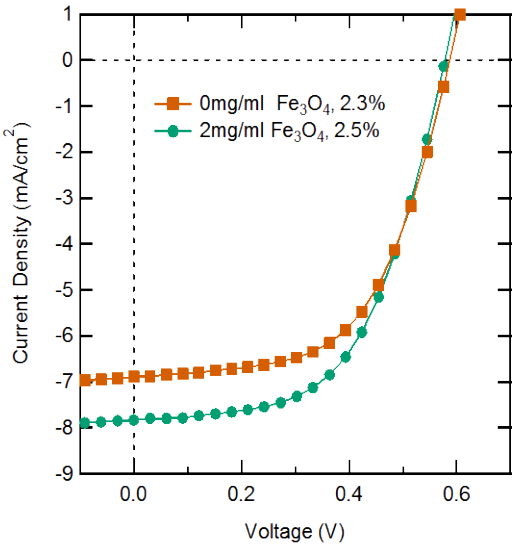

Figure 2. Adding approximately 1.5 wt% 10 nm diameter magnetite nanoparticles improves the short circuit current and the efficiency.

We believe the magnetite nanoparticles act as a nucleating agent to control the phase separation, similar to what a flat solid substrate would do. This has to be confirmed and is our future study.

References

1. Brabec, C. J.; Sariciftci, N. S.; Hummelen, J. C. Adv Func Materials 2001, 11, 15–26.
2. Dennler, G.; Scharber, M. C.; Brabec, C. J. Adv Materials 2009, 21, 1323–1338.
3. Green, M. A.; Emery, K.; Hishikawa, Y.; Warta, W. Prog Photovolt: Res App 2011, 19, 84–92.

4. B. C. Thompson, J. M. J. F. Angewandte Chemie Int Edi 2008, 47, 58–77.
5. Halls, J. J.M.;Walsh, C. A.; Greenham, N. C.; Marseglia, E. A.; Friend, R. H.; Moratti, S. C.; Holmes, A. B. Nature 1995, 376, 498–500.
6. Coakley, K. M.; McGehee, M. D. Chem Mater 2004, 16, 4533–4542.
7. Ma, W. L.; Yang, C. Y.; Gong, X.; Lee, K.; Heeger, A. J. Adv Func Materials 2005, 15, 1617–1622.
8. Li, G.; Yao, Y.; Yang, H.; Shrotriya, V.; Yang, G.; Yang, Y. Adv Func Materials 2007, 17, 1636–1644.
9. van Bavel, S.; Veenstra, S.; Loos, J.Macromolecular Rapid Communications 2010, 31, 1835–1845.
10. (Kiel, J.W.; Kirby, B. J.; Majkrzak, C. F.; Maranville, B. B.; Mackay, M. E. Soft Matter 2010, 6, 641–646.
11. Kiel, J. W.; Mackay, M. E.; Kirby, B. J.; Maranville, B. B.; Majkrzak, C. F. J Chem Phys 2010, 133, 074902–7.

Future Plans

The proposed activities will be conducted by the researchers to build on the above discoveries to develop a more fundamental understanding of the assembly process through development of new theoretical, as well as experimental, tools and to generalize the self assembly process from two-dimensions to one- and three-dimensions. Specifically we propose to:

1. Understand the phase separation as a function of polymer chain stiffness. This has direct application to polymer-based solar cells since these polymers are inherently stiffer than others due to the chemical conjugation.
2. Achieve controlled phase separation and a material by design using mixtures of different sizes of nanoparticles to make percolated networks of the smaller nanoparticles. Again, this has direct application to polymer-based solar cells as the smaller nanoparticles must form networks for improved charge conduction.
3. Create new three dimensional, polymer surfaces using nanoparticle assembly to stabilize the film. We seek to develop liquid polymer films that are three dimensional with predetermined thickness profiles that are optimized for photonic applications. After the liquid achieves its lowest energy configuration it will be solidified. This is a new direction for this project and builds on our previous discoveries, particular reference 1 below.

DOE Sponsored Publications in 2008 - 2010 from the Current Grant

1 Tseng, Tzu-Chia, McGarrity, Erin S., Kiel, Jonathan W., Duxbury, Phillip M., Mackay, Michael E., Frischknecht, Amalie L., Asokan, Subashini, and Wong, Michael S., Three-dimensional liquid surfaces through nanoparticle self-assembly. *Soft Matter* **7**, 1533 (2010).
2 Padmanabhan, V., Frischknecht, A. L., and Mackay, M. E., Binary fluid with attractions near a planar wall. *Physical Review E* **82** (2010).
3 Frischknecht, A. L., McGarrity, E. S., and Mackay, M. E., Expanded chain dimensions in polymer melts with nanoparticle fillers. *J Chem Phys* **132**, 204901 (2010).
4 Liu, J. W., Mackay, M. E., and Duxbury, P. M., Molecular Dynamics Simulation of Intramolecular Cross-Linking of BCB/Styrene Copolymers. *Macromolecules* **42**, 8534 (2009).
5 McGarrity, E. S., Frischknecht, A. L., and Mackay, M. E., Phase behavior of polymer/nanoparticle blends near a substrate. *J. Chem. Phys.* **128**, 154904 (2008).
6 McGarrity, E. S., Duxbury, P. M., Mackay, M. E., and Frischknecht, A. L., Calculation of entropic terms governing nanoparticle self-assembly in polymer films. *Macromolecules* **41**, 5952 (2008).

Conduction Mechanisms and Structure of Ionomeric Single-Ion Conductors
Part 1: PEO-Based Polymer Systems

Ralph H. Colby, Janna K. Maranas, Karl T. Mueller, James Runt
Materials Research Institute, Penn State University, University Park, PA 16803
and Karen I. Winey
Materials Science and Engineering, University of Pennsylvania, Philadelphia, PA 19104

Program Scope

Our group combines expertise in a variety of aspects of static and dynamic properties of ionomers to study the same set of materials: Low glass transition temperature ionomers that primarily comprise polyethers with sulfonated anions and either Li^+, Na^+ or Cs^+ counterions. The ether oxygens in these polymers play a vital role, solvating the ions and preventing the microphase separation of ions that occurs in conventional ionomers. We aim to thoroughly understand ion conduction mechanisms in this class of materials, with the ultimate goal of being able to design ionomer membranes for facile ion transport.

Recent Progress

Polyethylene oxide (PEO)-based polyester ionomers with variable ion content have been synthesized. A mixture of neutral dimethyl isophthalate and dimethyl 5-sulfo isophthalate sodium salt were used with M = 600 polyethylene glycol (PEG) to produce a range of ion contents with nomenclature PEO600-x%C (x% is the mole% of sulfonated phthalates 0%, 2.5%, 6%, 11%, 17%, 49%, 70%, 85%, 100%; C is the cation Li, Na, Cs).

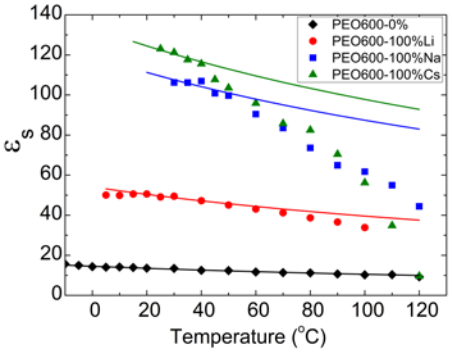

Morphology and Dielectric Spectroscopy of PEO-Ionomers The dielectric constant of all polar liquids decreases as temperature is raised due to thermal randomization of dipoles. The dielectric constant of our ionomers decreases as expected by Onsager's model (solid lines) near room temperature but when the dielectric constant becomes sufficiently small, the ion pairs start to aggregate, causing the dielectric constant to drop more rapidly, as shown at right.

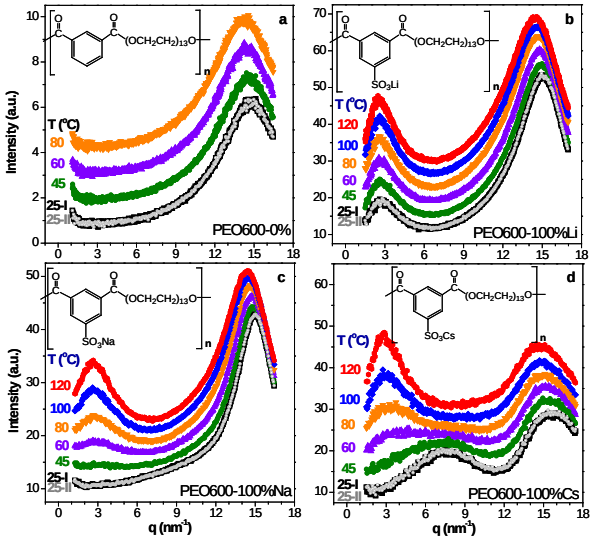

This aggregation is also evident in x-ray scattering, as ion aggregation peaks in the 2-4 nm^{-1} wavevector range. The plots at right show changes in x-ray scattering as temperature is raised. Plot (a) is the neutral nonionic polymer that shows no change. Plot (b) is the Li-ionomer that shows some aggregation at room T and more aggregation as T is raised. Plot (c) is the Na-ionomer showing even stronger aggregation as T is raised. Plot (d) is the

Cs-ionomer, showing a strong ion pair peak at room T in the 6-9 nm^{-1} range that transforms as T is raised to an ion aggregate peak in the 2-4 nm^{-1} range *(1, 2)*.

MD Simulations The techniques used in our collaboration (FTIR, DRS, SAXS) indicate that the cations in sodium based samples experience a large range of local configurations, including solvation by the polymer ("free"), ion pairs, and ion aggregates. We used MD simulations to investigate the sodium-based ionomers and the chart below shows the distribution of ion states at two temperatures *(3)*. We used MD to investigate issues that are hard to address experimentally.

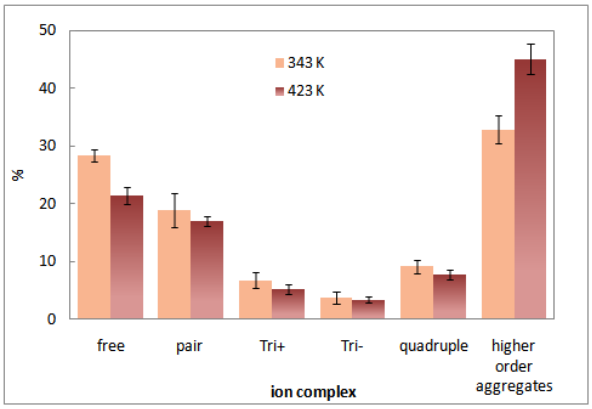

- **Correlation of ion state and mobility**. Surprisingly, the ions that are free are not the most mobile. Many of the slowest ions in the system are free ions. The fastest ions are those in pairs, and those on the edge of aggregates.
- **Shape of ionic aggregates**. Ion aggregates tend to be chain-like, with a range of sizes. It appears that transfer of charge may occur without equivalent movement of ions, as in the Grotthuss mechanism for proton movement. This observation, combined with the observation of more mobile ions near the edge of aggregates, suggests that aggregation is not entirely unwanted in single-ion conductors.
- **What makes an ion move quickly**? There is a wide range of ion mobilities in this system. While they all move by exploration of local cages, punctuated by hops to new cage locations, the number of cages explored during the simulation varies considerably. Ions that move the furthest do so not by the cage exploration, but by the nature of the hops to new cages. This occupies a small fraction of the simulation time (less than 1%) but the nature of this movement appears to control conductivity. Ions that are fast show more directed "inter-cage hops" than those that are slow.

Neutron scattering The ability of an ion to execute directed motion between hops depends on the mobility of the polymer chains. Even in the case of ion pairs or aggregates, polymer chain mobility remains important because the anions are attached to the polymer backbone. We used quasi-elastic neutron scattering (QENS) to investigate polymer mobility as a function of ion content, spacer length, and ion identity *(4)*.

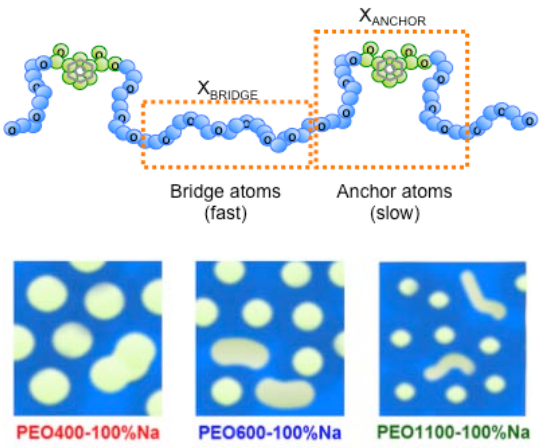

The mobility of the polymer spacer is divided into two classes: atoms near the ionic group (anchor atoms) and atoms in the mid-spacer regions (bridge atoms). The motion of bridge atoms is insensitive to ion content, spacer length, and identity, whereas the motion of anchor atoms depends strongly on these variables.

The mobilities of bridge and anchor atoms are separated by several orders of magnitude and spatially organized. This "dynamic separation" is a precursor to the ion aggregation observed at higher temperatures. When ion content is increased, the cations first saturate the bridge regions. Further increases involve the anchor regions, which slow polymer motion considerably via association of two or more polymer chains.

Nuclear Magnetic Resonance (NMR) Studies

^{7}Li pulsed-gradient spin-echo (PGSE) experiments were carried out to determine the self-diffusion coefficients of Li^{+} cations in PEO600-6%Li, -11%Li, and -17%Li as a function of temperature. Using the Nernst-Einstein equation, self-diffusion coefficients for Li^{+} were also calculated from the measured temperature dependence of conductivity from dielectric spectroscopy on the same ionomers and compared with the self-diffusion coefficients measured by ^{7}Li NMR in the figure to the right.

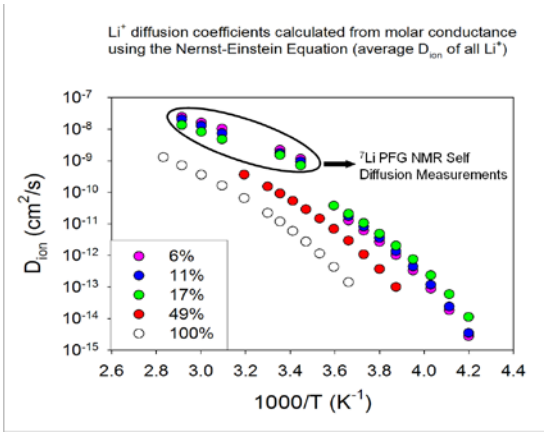

^{1}H and ^{7}Li spin-lattice relaxation times, T_1, of the bulk polymer and lithium ions were analyzed above T_g for PEO600-6%Li, -11%Li, -17%Li, and -100%Li to assess motion on the nanosecond timescale (*5*) and their temperature dependences are plotted at the right. Both ^{1}H and ^{7}Li correlation times become longer as lithium ion concentration increases, pointing to slower overall mobility of the polymer and cations. Although correlation times of the polymer backbone and lithium ions differ by about an order of magnitude, the similar activation energies for PEO600-6%Li, -11%Li, and -17%Li suggest the polymer segmental motions and lithium ion hopping motions are correlated. When T_g is taken into account the relative position of correlation times for PEO600-100%Li shifts significantly compared to the other samples. At lower temperatures this sample has the shortest correlation times, but as temperature increases correlation times eventually become longer than those measured for all other samples. This dissimilar trend in correlation times between the lower lithium concentration samples and PEO600-100%Li suggests lithium ion hopping and polymer segmental motions are controlled by either different mechanisms or occur in different phases. An explanation for these results could be related to results from X-ray scattering where an "ionomer peak" was detected in PEO600-100%Li, indicating the presence of microphase separated ionic aggregates. Thus, lithium ion hopping motions in this sample are being observed in both the polymer matrix and these ionic aggregates. The smaller activation energies for motions of the polymer in PEO600-100%Li along with the observed segmental motion suggest that there is less significant transient crosslinking due to lithium ions in this sample when compared to the other samples.

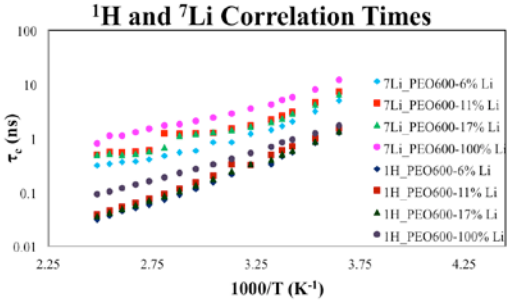

Future Plans

In the next year, we will study ionomers made from copolymers of PEG and polytetramethylene glycol (PTMG). These systems have interesting phase behavior compared to the PEG-only ionomers. In particular, there is greater ion association. If we can determine how to best utilize ion aggregation or ion strings for efficient conduction, this system presents the possibility of creating a surface for aggregation, and thus controlling the end structure. We have obtained deuterated monomers, which will be used to create materials to study microphase separation of PEG and PTMG domains using small angle neutron scattering, and dynamics of each domain using QENS. Compared with small angle x-ray scattering (which probes spatial organization of ions) and dielectric relaxation spectroscopy (which probes conductivity and ion pairing), these measurements will provide a comprehensive picture of this new system.

References (Each is a Result from Work Supported by this Project over the Last Two Years)

1) W. Wang, W. Liu, G.J. Tudryn, R.H. Colby and K.I. Winey, "Multi-scale Morphologies of Poly(ethylene oxide)-based Sulfonate Ionomers with Alkali Cations at Room Temperature", *Macromolecules* **43**, 4223 (2010).
2) W. Wang, G.J. Tudryn, R.H. Colby and K.I. Winey, "Thermally Driven Ion Aggregation in Poly(ethylene oxide)-based Sulfonate Ionomers", *J. Amer. Chem. Soc*, submitted for publication.
3) K.-J. Lin and J.K. Maranas, "A Molecular Dynamics Study of Cation Coordination and Motion in Poly(ethylene oxide)-based Ionomers", to be submitted for publication.
4) K. Sinha and J.K. Maranas, "Segmental Dynamics and Ion Association in Poly(ethylene oxide)-based Single-ion Conductors", *Macromolecules* **44**, 5381 (2011).
5) D.J. Roach, S. Dou, R.H. Colby and K.T. Mueller, "Nuclear Magnetic Resonance Investigation of Dynamics in Poly(ethylene oxide)-based Lithium Polyether-ester-sulfonate Ionomers", *J. Chem. Phys.*, submitted for publication.

Additional Publications Resulting from Work Supported by this Project over the Last Two Years

6) A. Castagna, W. Wang, K.I. Winey and J. Runt, "Influence of the Degree of Sulfonation on the Structure and Dynamics of Sulfonated Polystyrene Copolymers", *Macromolecules* **43**, 10498 (2010).
7) A. Castagna, W. Wang, K.I. Winey and J. Runt, "Structure and Dynamics of Zinc-Neutralized Sulfonated Polystyrene Ionomers", *Macromolecules* **44**, 2791 (2011).
8) A. Castagna, W. Wang, K.I. Winey and J. Runt, "Influence of Cation Type on Structure and Dynamics of Sulfonated Polystyrene Ionomers", *Macromolecules*, submitted for publication.
9) G.J. Tudryn, M.V. O'Reilly, S. Dou, D.R. King, K.I. Winey, J. Runt, and R.H. Colby, "Molecular Mobility and Cation Conduction in Polyether-ester-sulfonate Copolymer Ionomers", *Macromolecules,* submitted for publication.
10) S. Liang, U.H. Choi, W. Liu, M. O'Reilly, K.I Winey, J. Runt and R.H. Colby, "Synthesis and Lithium Ion Conduction of Polysiloxane-based Single-Ion Conductors Containing Novel Weak-Binding Borates", *J. Amer. Chem. Soc*., submitted for publication.

Giant Electrocaloric Effect at Room Temperature In Ferroelectric Polymers with Controlled Polar Nanostructures

Q. M. Zhang
qxz1@psu.edu
Materials Research Institute and Electrical Engineering Department
The Pennsylvania State University, University Park, PA 16802

Program Scope

Electrocaloric effect (ECE) is a result of direct coupling between the thermal properties such as entropy and electric properties such as electric field and polarization in a dielectric material, in which a change in the applied electric field induces a corresponding change in polarization, which in turn causes a change in the dipolar entropy S_p as measured by the isothermal entropy change ΔS and adiabatic temperature change ΔT in the dielectrics [1,2]. Although ECE has been investigated for many decades, the relatively small ECE demonstrated in bulk dielectrics was unimpressive for practical applications. The basic principle of ECE is the entropy change associated with the change of polarization ordering in a dielectric material, induced by an external electric field. Therefore, to realize large ECE, it is necessary that the dielectric material be able to support large polarization change and these polarization changes can be induced effectively by external field. Moreover, the ECE can be further enhanced by introducing defects to disrupt the long range polar-ordering and modify the local energy landscape to enhance the number of polar entities. Based on these considerations, we carried out a systematic study of the ECE in normal ferroelectric polymer at ferroelectric (polarization ordered)-paraelectric (polarization disordered) phase transition (FE-PE) and in the relaxor ferroelectric polymers with controlled polar-nanostructures and demonstrate that large ECE can be achieved [3,4]. Coupled with experimental results, thermodynamic model was also developed to address the fundamental questions of what are the key material parameters and desired nano-polar structures in order to achieve large ECE under low electric field.

Recent Progress

During this time period, a new calorimeter was developed which make it possible to characterize ECE in thin polymer films to high electric fields. Making use of this new set-up, the ECE in the normal ferroelectric polymers was directly characterized. Presented in figure 1 is the ECE in the normal ferroelectric P(VDF-TrFE) 55/45 mol% copolymer [5], which shows that ECE peaks at the FE-PE transition, where a $\Delta T \sim 12\ ^{o}C$ can be induced under a 120 MV/m field. The results here also show that ECE is weak for normal ferroelectric at temperatures away from the FE-PE transition. Although very large ECE can be obtained in normal ferroelectrics near FE-PE transition, a large reduction of ECE at temperatures away from the transition which also leads to weak ECE at room temperature is not desirable for most practical device applications.

In ferroelectric P(VDF-TrFE) polymers, introducing random defects to interrupt the long range polar-correlation can lead to the conversion of normal ferroelectric into a ferroelectric relaxor which displays a very broad dielectric peak around room temperature. We studied the ECE in the relaxor ferroelectric P(VDF-TrFE-CFE) terpolymer in which the bulky CFE termonomers behave as random defects. Presented in figure 2 is the ECE near room temperature for P(VDF-TrFE-CFE) 59.2/33.6/7.2 mol% terpolymer. The films were prepared using a solution cast method. The terpolymer film exhibits a very large ECE ($\Delta T > 15\ ^{o}C$ at 150 MV/m) [6]. What

is more interesting is that, the large ECE in the relaxor terpolymer is nearly temperature independent over a broad temperature range from 5 ^{o}C to 45 ^{o}C. This is in sharp contrast to the normal ferroelectrics (see figure 1) which have ECE peak at FE-PE transition and display strong temperature dependence.

On the other hand, for the same terpolymer composition, uniaxially stretching the terpolymer films to induce a preferred polymer chain orientation can cause a large change in the temperature dependence of ECE (see figure 3) although the ΔT at room temperature is nearly the same for unstrteched and uniaxially stretched films.

In order to understand what determines the ECE responses in polar-dielectrics, Pirc et al. at Jozef Stefan Institute of Slovenia worked with us to develop some fundamental understanding on ECE in polar-dielectrics [7]. In polar-dielectrics, as the electric field is increased from 0 to E, the isothermal entropy change ΔS and adiabatic temperature change ΔT can be expressed as,

$$\Delta S = S(E,T) - S(0,T) \text{ and } \Delta T = T\Delta S/c_E$$

where c_E is the specific heat and S(E,T) is the total entropy at a temperature T and electric field E. Since the lattice entropy is field independent, ΔS is determined by the dipolar entropy S_{dip}. In order to maximize ΔS, it is necessary to maximize the entropy $S_{dip}(0,T)$ at E=0 and minimize $S_{dip}(E,T)$, occurring in a field E sufficiently large to induce polarization saturation. As shown in a recent thermodynamic and statistical analysis, for a system of N dipolar entities, each having Ω discrete equilibrium orientations, the maximum entropy corresponds to the case where all directions i are equally populated or N_i=N/Ω, where N_i is the number of dipoles along symmetry direction i with the condition $\sum_i N_i = N$,

$$\Delta S = \frac{\ln \Omega}{3\varepsilon_0 \Theta} P^2 \qquad (1)$$

where Θ is the Curie constant in the asymptotic behavior of the linear dielectric susceptibility, $\chi=\Theta/(T-T_0)$, and T_0 the Curie-Weiss temperature for a ferroelectric, ε_0 is the vacuum permittivity. For normal ferroelectrics such as a tetragonal ferroelectric phase, Ω=6 due to 6 possible polarization directions (see schematic in Fig. 4). Therefore, a dipole system with a larger number of dipole entities Ω and small dipole correlation (small Θ) will have the potential to realize very large ECE.

Relaxor ferroelectrics, with short polar-correlation (due to random defects) and more possible local polar-states, may achieve large ECE compared with normal ferroelectric. Uniaxial stretching of terpolymer films causes preferred polymer chain orientation and hence reduces the number of possible polar states in the dipolar-disordered states and hence Ω. In addition, uniaxial stretching in general will favor all-trans molecular conformation and hence increase the polar-correlation which might be the reason for the faster reduction of ECE with reduced temperature below the broad dielectric maximum in the uniaxially stretched films [6].

Future Plans

Systematical study of ECE in the high energy irradiated P(VDF-TrFE) copolymers over a broad compositions (from normal ferroelectric to relaxor ferroelectric). P(VDF-TrFE) copolymers with higher VDF/TrFE ratio has promise to reach larger ECE under lower applied field. Irradiated copolymers of different compositions (from 80/20 mol% to 55/45 mol%) with different doses will be studied. High energy electron irradiation provides a very convenient means to vary the defects concentration (by varying the dosage) which will allow us to

systematically investigate how the defect concentration, the polar-correlation range, and local molecular structures influence the ECE.

Study of terpolymers of P(VDF-TrFE-CFE) and P(VDF-TrFE-CTFE) with different processing conditions. In ferroelectric polymers, processing conditions can also have significant effect on the materials responses. Here we plan to study how different processing conditions will influence the number of equivalent polar-state Ω (for example, by coupling to mechanical stresses) and polar-correlation and consequently the ECE.

References:

[1] F. Jona and G. Shirane, *Ferroelectric crystals* (Dover, New York, 1993).

[2] M. Lines, A. Glass, *Principles and Applications of Ferroelectrics and Related Materials* (Clarendon Press, Oxford, 1977)

[3] B. Neese, B. J. Chu, S. G. Lu, Y. Wang, E. Furman, and Q. M. Zhang, *Science* **321**, 821 (2008).

[4] S. G. Lu and Q. M. Zhang, *Adv. Mater.* **21**, 1983 (2009).

[5] S. G. Lu, B. Rožič Q. M. Zhang, Z. Kutnjak, and B. Neese, *Appl. Phys. Lett*., **98**, 122906 (2011).

[6] Xinyu Li, Xiao-shi Qian, S. G. Lu, Jiping Cheng, Zhao Fang and Q. M. Zhang, submitted to Appl. Phys. Lett. (2011).

[7] R. Pirc, Z. Kutnjak, R. Blinc, and Q. M. Zhang, *Appl. Phys. Lett.*, **98**, 021909 (2011).

DOE Sponsored Publications in 2009-2011 from Current Grant

- S. G. Lu, B. Rožič Q. M. Zhang, Z. Kutnjak, and B. Neese, "Enhanced Electrocaloric Effect in Ferroelectric Poly(vinylidene-fluoride/trifluoroethylene) 55/45 mol% Copolymer at Ferroelectric-Paraelectric Transition", ***Appl. Phys. Lett***., **98**, 122906 (2011).
- S. G. Lu**,** B. Rožič, Z. Kutnjak, and Q. M. Zhang, "Electrocaloric effect in ferroelectric P(VDF-TrFE) copolymers", ***Integrated Ferroelectrics***, **125**, 176 (2011).
- R. Pirc, Z. Kutnjak, R. Blinc, and Q. M. Zhang, "Upper bounds on the electrocaloric effect in polar solids." ***Appl. Phys. Lett.***, **98**, 021909 (2011).
- S. G. Lu, B. Rožič Q. M. Zhang, Z. Kutnjak, R. Pirc, Minren Lin, Xinyu Li, and Lee J. Gorny, "Comparison of directly and indirectly measured electrocaloric effect in the relaxor ferroelectric polymers". ***Appl. Phys. Lett.,* 97,** 202901 (2010).
- S. G. Lu, B. Rožič Q. M. Zhang, Z. Kutnjak, Xinyu Li, E. Furman, Lee J. Gorny, Minren Lin, B. Malič, M. Kosec, R. Blinc, and R. Pirc, "Organic and Inorganic Relaxor Ferroelectrics with Giant Electrocaloric Effect", ***Appl. Phys. Lett.***, **97**, 162904 (2010).
- S. G. Lu, Z. Fang, E. Furman, Y. Wang, Q. M. Zhang, Y. Mudryk, K. A. Gschneidner, Jr.,V. K. Pecharsky, and C. W. Nan. Thermally mediated multiferroic composites for the magnetoelectric materials. ***Appl. Phys. Lett***. 96, 102902 (2010).
- B. Rozic, Z. Kutnjak, B. Neese, S. G. Lu, and Q. M. Zhang, Electrocaloric effect in the relaxor ferroelectric polymer composition $P(VDF\text{-}TrFE\text{-}CFE)_{0.90}$ - $P(VDF\text{-}CTFE)_{0.10}$, ***Phase Transitions***, **83**, 819 (2010).
- B. Rozic, B. Malic, H. Ursic, J. Holc, M. Kosec, B. Neese, Q. M. Zhang, and Z. Kutnjak, Direct measurements of the giant electrocaloric effect in soft and solid ferroelectric materials. ***Ferroelectrics***, **405**, 26 (2010).
- Bret Neese, S. G. Lu, Baojin Chu, and Q. M. Zhang, Electrocaloric Effect of the Relaxor Ferroelectric P(VDF-TrFE-CFE) Terpolymer. ***Appl. Phys. Lett***. 94, 042910 (2009).
- S. G. Lu, Z. Kutniak, and Q. M. Zhang, "Chapter 44: Electrocaloric Effect (ECE) in Ferroelectric Polymer Films". Woodhead Publishers Ltd. United Kingdom (2011).
- S. G. Lu, B. Rozic, Z. Kutniak, and Q. M. Zhang, "Electrocaloric Effect (ECE) in Ferroelectric

Polymer Films". In *Ferroelectrics*, Indrani Coondoo (Ed.), Intech, Austria, Dec., 2011.

- Q. M. Zhang, S. G. Lu, X. Y. Li, L. Gorny, J. P. Cheng, B. Neese, and B. J. Chu, "Refrigeration devices based on polar polymers", US Patent, US2011/0016885.

Eleven publications and one patent in the past two years supported by the current grant

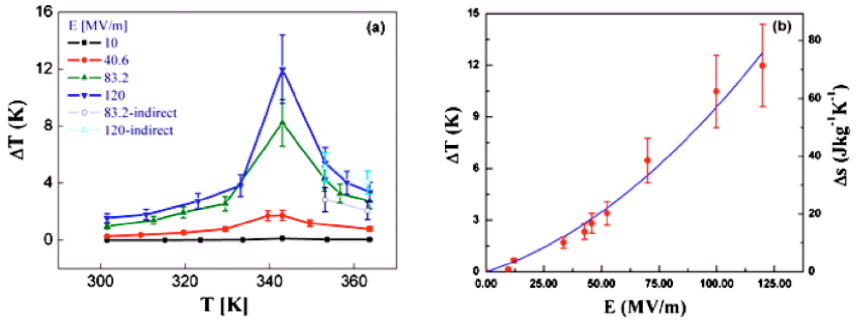

Fig. 1. (a) ECE ΔT versus sample temperature and (b) ΔT and ΔS versus applied electric field for P(VDF-TrFE) 55/45 mol% copolymer at FE-PE transition temperature (67 °C).

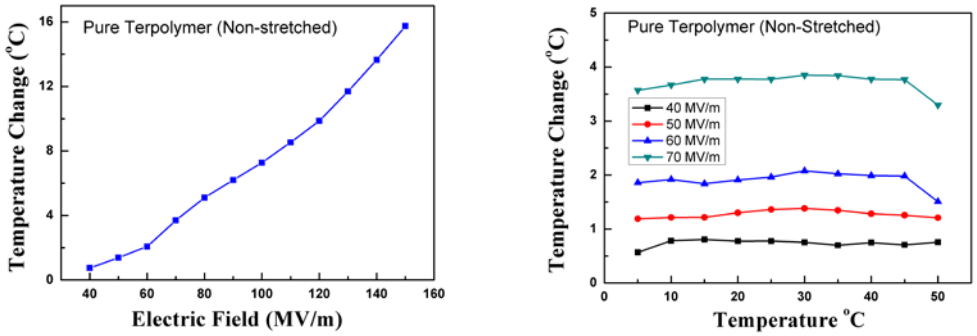

Fig. 2. (Left) ΔT versus applied field at 30 °C and (right) ΔT versus sample temperature under different applied field of the P(VDF-TrFE-CFE) 59.2/33.6/7.2 mol% terpolymer.

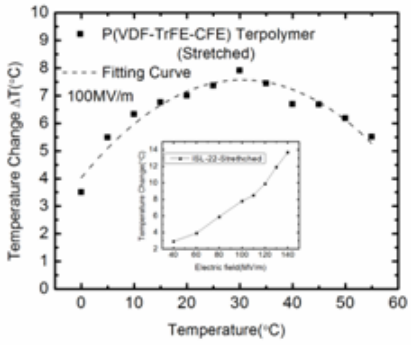

Figure 3. Adiabatic temperature change as a function of sample temperature in stretched P(VDF-TrFE-CFE) terpolymer under a constant electric field of 100 MV/m, while the inset shows the adiabatic temperature change as a function of applied electric field measured at 30 °C.

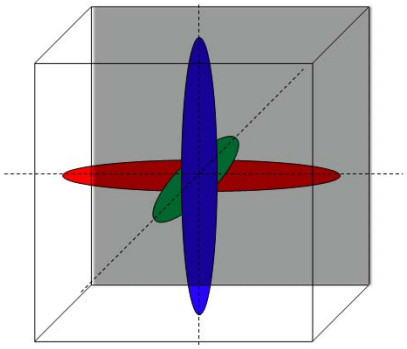

Fig. 4. Schematic of 6 possible polarization directions in a tetragonal ferroelectric phase.

This page is intentionally blank.

Session 3

Predictive Crystal Growth

Session Chairs: Hanchen Huang, University of Connecticut
Gyula Eres, Oak Ridge National Laboratory

This page is intentionally blank.

Boron Based Nanostructures: Stability and Synthetic Routes

Pulickel M. Ajayan and Boris I. Yakobson
biy@rice.edu
Department of Mechanical Engineering and Materials Science, Department of Chemistry,
Rice University, Houston, TX

Program Scope

Boron nanostructures, if systematically produced, would open variety of opportunities. B-fullerenes, similar to C_{60}, or the filled-solid clusters, must lead to a branch of chemistry with its own novelties; B-nanotubes (BT) should possess electronic properties beneficially more uniform than their carbon analogues. A systematic study of stability and investigation of possible ways of synthesis for boron nanostructures is critically timely. While theory has predicted some possibilities [1,2], the actual experimental evidence is so far rather sparse. The experimental report [3] on BT remains rather stimulating than conclusive. Theoretical models are being developed for the assessment of possible structures and properties, along with a series of experimental synthesis trials and characterization, including in our scope: hollow fullerene-type clusters, B-tubes, mono-atomic B-sheets—analog of graphene monolayer. Beyond the mono-elemental nanostructures, the chemical combinations of B with its neighbors in the periodic table (N, C) bring additional control in the synthesis and new rich functionality.

Recent Progress

Continued combined theoretical and experimental studies of B-rich nanostructures within B-C-N triangle, have yielded novel 2D-phase, an A-sheet of boron. It is more favorable-stable (or at least as stable) than the earlier known α-sheet, based on DFT generalized gradient approximation (GGA) calculations. Recent report suggested higher stability for volleyball-shaped [4] compared to buckyball B_{80} [1]. In this structure, 12 pentagons are filled and 12 hexagons are unfilled, rendering the structure tetrahedrally symmetric (Fig. 1). Similar to the α-sheet inspired by the B_{80} buckyball, we considered possible sheets obtained by unwrapping B_{80} volleyball. The result is called A-sheet (Fig. 1). Its unit cell consists of 21 atoms. The lattice constants are a_1=11.7 Å, a_2=5.1 Å. The hole density η=0.125 (compared to triangular sheet) is slightly higher than that of α-sheet (1/9). Its flat structure displays no buckling, its binding is slightly stronger than that of α-sheet (by 2 meV/atom, per GGA calculations). The close values of the cohesive energies and low interface energy between the α- and A-sheets (~0.066 eV/Å) compelled us to consider their coplanar combinations and study the role of entropy.

This finding has motivated us to further expand the investigation of boron sheets considered as a pseudo-alloy $B_{1-\eta}$ ⬣$_\eta$ system, where ⬣ is a vacancy in the parent triangular B lattice. This allows for an elegant combination of first-principles calculations with the cluster expansion (CE) method, a thorough exploration of the configurational space. A range of compositions η is found where the ground state energy is essentially independent of η, uncovering variety of new stable B-sheets, Fig. 2. This significant generalization has important implications for the search of pure B 2D-layera. This further suggests that they may emerge in form of mixed patches of nearly degenerate phases.

In experimental studies, we have worked systematically to synthesize pure boron nanostructures using different vapor phase deposition techniques. Preliminary results indicate that we have been able to successfully create boron nano-wires (BW) by a vapor transfer method on Si substrate with and without a thermal oxide layer. Before BW

growth, substrates were coated with a 2-10 nm thick gold film by sputtering. The source material was pellet of boron, boron oxide and Mg powder. The boron vapor was transferred via a high temperature vacuum annealing process at high temperature. Microscopy and electron spectroscopy were used for morphological and structural characterization of BW. The diameters of these BW were observed to be in the range of 50–400 nm. Fig. 3 shows a representative TEM (transmission electron microscopy) image of BW and EELS (electron energy loss spectroscopy) spectrum (inset). The EELS spectrum reveals the characteristic boron K-shell ionization edge (188 eV) and the nanowires contain mostly boron. Another approach to making boron nanostructures was to use template based synthesis to understand the effect the template has on the size and structure of boron. Anodized aluminum oxide (AAO), which contains channels of roughly 200 nm in diameter, was used as templates here. Initial observations indicate the growth of nanowires containing boron but the exact compositional analysis and structural characterization are under way.

Growth by CVD on metal substrates or MgB_2. By analogy with 2D-graphene, one can explore similar methods to synthesize B nano-sheets. Evaporation of Si from SiC leaves a graphene layer. Magnesium diboride (MgB_2) seems to be a good candidate for evaporation-growth method, since Mg has much lower melting point (~923 K) than B (~2573 K) and the lattice mismatch between MgB_2 (0001) surface and the B sheet is ~6%. Could this offer a feasible path for B-sheets synthesis? To this end, we have computed the structure and energy of B-sheets on Mg-terminated MgB_2 surface (DFT, PBE functional). We have calculated the key values for several types of sheets, with different B-vacancy densities, as shown in Fig. 4. Neither α- nor new A-sheet are most energetically favourable. Higher hole density is favoured, because MgB_2 is ionic and Mg provides electrons to the top B layer, to occupy part of the bonding states of B sheet, thus the system needs not as many B atoms. Another interesting finding is that the cleavage energy decreases with increasing B density. It suggests that after the growth, the B-sheet can be easily mechanically peeled off (so called scotch tape method).

Besides the pure B, and following the experimental discovery of the hybrid BCN layers within this team [5], we have developed a theory of edge energies, and morphology thermodynamics [6]. This revealed the possibility to control the shape of C inclusions in BN (or vice versa) and consequently to control important physical properties (band gap, optical, magnetic moment).

Future Plans

With the initial successes in experiments, we have plans to fine tune the growth condition/morphology relationship for more consistent growth and more uniform BMWs and explore growth of other boron nanostructures. We also plan on using other templates such as zeolites of various diameter channels and cages to understand the possibility of growing different sizes and structures of boron. As a neighbor of carbon, boron nanostructures are attractive candidates for nanoscale electronics, especially at high temperatures so we will test the above mentioned structures grown on Si substrate and AAO template for electrical, mechanical and optical properties for novel applications in electronics.

Theoretical studies will continue from now rather complete picture of free-standing 2D sheets towards effects of the substrate, and especially how this can suggest the growth methods. What is the nucleation barrier for the B-sheet growth in various substrates (e.g. metals, or diborides of Mg, Al, Y)? Is it energetically favored relative to nucleation of B_{12}-based bulk phases? These questions can be answered with modern computational methods and provide useful guidance to syhthetic efforts. A lot of useful

lessons can be taken from the traditional graphene methods. We will further continue investigation of B-rich compositions in $B_xC_yN_z$ triangle.

The work above is attributed to Arta Sadrzadeh, Evgeni Penev, Yuanyue Liu, Somnath Bhowmick, Li Song, Zheng Liu, Huma Jafry and Liehui Ge, all at Rice.

References

[1] N.G. Szwacki, A. Sadrzadeh, and B.I. Yakobson, Phys. Rev. Lett. **98**, 166804 (2007).
[2] H. Tang, and S. Ismail-Beigi, Phys. Rev. Lett. **99**, 115501 (2007).
[3] D. Ciuparu, R. F. Klie, Y. Zhu, and L. Pfefferle, J. Phys. Chem. B **108**, 3967 (2004).
[4] X.-Q. Wang, Phys. Rev. B **82**, 153409 (2010).
[5] L. Ci, P.M. Ajayan, et al. Nat. Mater. ***9***, 430–435 (2010).
[6] Y. Liu; S. Bhowmick; B. I. Yakobson, Nano Lett. DOI: 10.1021/nl2011142, (2011).

DOE Sponsored Publications in 2009-2011 from Current Grant

- K. Singh, A. Sadrzadeh, B.I. Yakobson, "Metallacarboranes: Toward Promising Hydrogen Storage Metal Organic Frameworks", J. Am. Chem. Soc. **132** (2010) 14126–14129.
- L. Song, L.J. Ci, H. Lu, P.B. Sorokin, C.H. Jin, J. Ni, A.G. Kvashnin, D.G. Kvashnin, J. Lou, B.I. Yakobson, P.M. Ajayan, "Large scale growth and characterization of atomic hexagonal boron nitride layers ", Nano Letters, **10** (2010) 3209-3215.
- Srivastava, C. Galande, L.J. Ci, L. Song, C. Rai, D. Jariwala, K.F. Kelly, P.M. Ajayan, "Novel liquid precursor-based facile synthesis of large-area continuous, single, and few-layer graphene films", Chemistry of Materials, **22** (2010) 3457-3461.
- N. Xiao, X.C. Dong, L. Song, D.Y. Liu, Y. Tay, S.X. Wu, L.J. Li, Y. Zhao, T. Yu, H. Zhang, W. Huang, H.H. Hng, P.M. Ajayan, Q.Y. Yan. "Enhanced thermopower of graphene films with oxygen plasma treatment" ACS Nano, DOI: 10.1021/nn2001849 (2011).
- Z. Liu, L. Song, S.Z. Zhao, J.Q. Huang, L.L. Ma, J.N. Zhang, J. Lou, P.M. Ajayan, "Direct growth of graphene/h-BN stacked layers", Nano Lett., ASAP article published online, April 2011.
- "Magnesium boride nanotubes: Relative stability, atomic and electronic structure", P.B. Sorokin, L.A. Chernozatonskii, P.V. Avramov, and B.I. Yakobson, J. Phys. Chem. C, **114** (2010) 4852.
- S. Bhowmick, A. K. Singh, and B. I. Yakobson, "Quantum dots and nanoroads of graphene embedded in hexagonal boron nitride", J. Phys. Chem. C, **115** (2011) 9889–9893.
- L. Song, Luis Balicas, Duncan J. Mowbray, Rodrigo B. Capaz, Kevin Storr, Lijie Ci, Deep Jariwala, Stefan Kurth, Steven G. Louie, Angel Rubio, Pulickel M. Ajayan, "Anomalous Insulator Metal Transition in BN-C Atomic Layers", PNAS, submitted (2011).
- P.B. Sorokin, H.K. Lee, L.Yu. Antipina, A.K. Singh, and B.I. Yakobson, "Calcium-decorated carbyne networks as hydrogen storage media", Nano Lett., **11** (2011) 2660–2665.
- Y. Liu; S. Bhowmick; B. I. Yakobson, "BN white graphene with 'colorful' edges: The energies and morphology" Nano Lett. DOI: 10.1021/nl2011142, (2011).

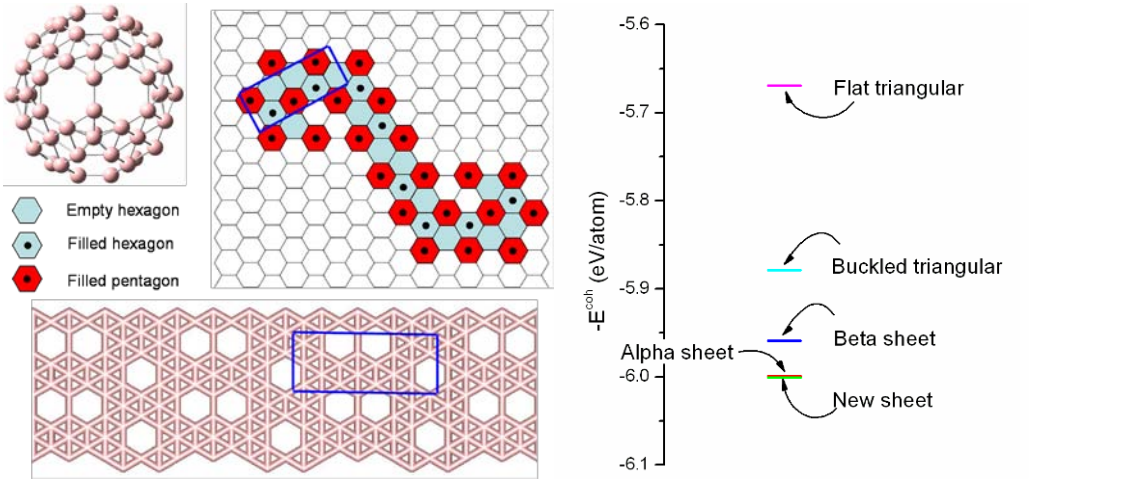

Figure 1. Top-left: the volleyball shaped B_{80}. Top-middle: Planar development of this B_{80} (blue hexagons) and (bottom-left) the structure of the new A-sheet, with unit cell highlighted. Right: Relative stability of different 2D layers.

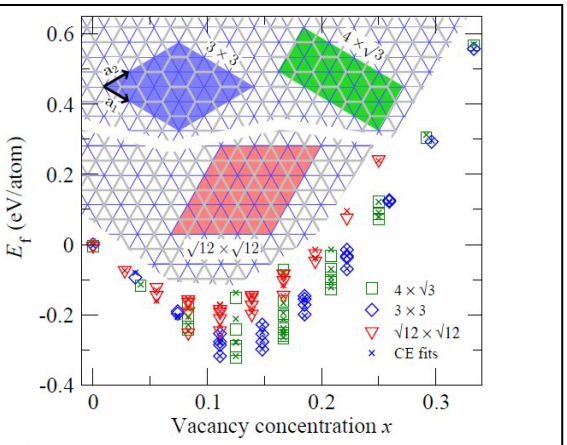

Figure 2. Computed formation energies E_f, for the $B_{1-\eta}\square_\eta$ sheets, as a function of vacancy concentration η (supercells are shown in the inset).

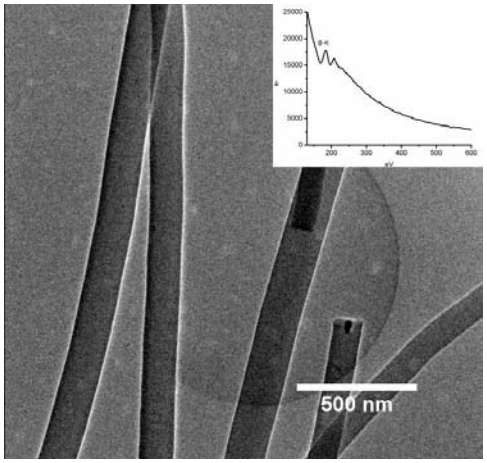

Figure 3. A representative TEM image of BNWs and EELS spectrum (inset). The EELS spectrum reveals the characteristic boron K-shell ionization edge (188 eV).

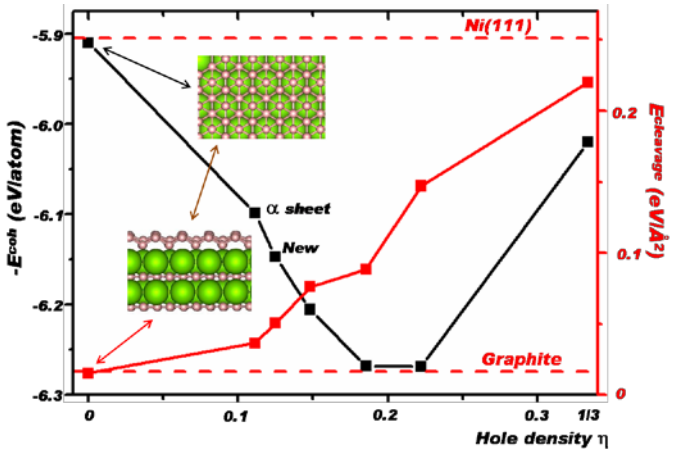

Figure 4. Calculated cohesive (black) and peel-off energies (red) of a B sheet on Mg-terminated MgB_2. For comparison, cleavage energies for Ni (111) (top) and graphite (bottom) are shown, dashed lines. Insets show triangular B sheet on MgB_2, top view and side view.

Non-Equilibrium Synthesis of Nanostructured Materials: Real-Time Studies of the Growth Kinetics and Product Distribution of Graphene (ERKCS81)

David B. Geohegan,[1] Alex Puretzky,[1] Christopher M. Rouleau,[1] Jason D. Readle,[2] Mina Yoon,[2] Gyula Eres,[2] Murari Regmi,[2] Karren L. More,[2] Matthew Chisholm,[2] and Gerd Duscher[2,3]
geohegandb@ornl.gov
[1]Center for Nanophase Materials Sciences and [2]Materials Science and Technology Division, Oak Ridge National Laboratory, Oak Ridge, TN 37831 and
the [3]Dept. of Materials Science and Engineering, Univ. of Tennessee, Knoxville, 37996

Program Scope

The goal of this program is to develop a fundamental understanding of the non-equilibrium aspects of nanomaterial synthesis by exploring the growth mechanisms and resulting structures of nanoscale materials formed in controlled environments. Pulsed, non-equilibrium growth and processing approaches, such as those involving lasers and supersonic molecular beams, are developed to supply the necessary kinetic energy required to explore the synthesis of nanostructures with metastable phases and structures that are inaccessible using traditional synthetic methods. A distinguishing feature of the program is the development and application of time-resolved, in situ diagnostics of nanomaterial growth kinetics and a corresponding development of models to understand the underlying kinetic and chemical pathways. Spatial confinement and reactive quenching approaches are developed to explore the synthesis mechanisms of rationally-designed nanostructures with enhanced intrinsic properties, targeting: (1) oxide, carbon, and alloy nanomaterials produced in metastable states by catalyst-free or catalyst-mediated processes, and (2) doped, decorated, and filled nanomaterial hybrids designed to induce permanent electric fields or distribute charge within nanostructures. Theoretical methods are used to understand fundamental mechanisms of synthesis in order to guide the formation of nanostructures tailored to enhance energy storage, catalysis, thermal management, and photovoltaics in support of DOE's energy mission.

Recent Progress

Here, non-equilibrium approaches are applied to explore the nucleation and growth kinetics of carbon nanostructures on thin metal films, including graphene and single-wall carbon nanotubes. Pulsed processing approaches (including pulsed laser deposition (PLD), and pulsed chemical vapor deposition (pulsed CVD)) are applied to deliver carbon feedstock and heat with sub-second time resolution while real-time optical reflectivity, imaging, and spectroscopy diagnostics are employed to measure the kinetics of nucleation and growth processes. Fundamental synthesis and processing questions are targeted, including the atomistic mechanisms by which carbon self-assembles into single- and multilayer-graphene in the absence of a metal catalyst, and the growth mechanisms of single- or multi-layer graphene and nanotubes under conditions of variable flux. Basic questions, such as the timescales for graphene nucleation and growth, and whether it grows at high temperatures or during cooldown are addressed.[1-6]

Recently, we developed time-resolved, *in situ* optical reflectivity and imaging techniques to understand the nucleation and growth kinetics of carbon nanostructures during CVD using fast (0.1 s) pulses of variable flux of acetylene to Fe or Ni films inside a standard tube furnace under actual growth conditions (Fig. 1(a)).[7] For single-wall carbon nanotubes grown on thin Fe films, we found that increasing the feedstock flux decreases nucleation times by three orders of magnitude, permitting aligned nanotube arrays to nucleate and grow to microns lengths at high (up to 7 micron/s) peak growth rates within single gas pulses and short ~ 0.5 s times. Low-frequency Raman scattering (> 10 cm^{-1}) and transmission electron microscopy measurements showed that increasing the feedstock flux in both continuous-CVD and pulsed-CVD shifts the product distribution to large single-wall carbon nanotube diameters > 2.5 nm. Sufficiently high fluxes in pulsed-CVD appear to temporarily terminate the growth of the fastest-growing, small-diameter nanotubes by overcoating the more catalytically-active, smaller catalyst nanoparticles within the ensemble with non-nanotube carbon in agreement with a growth model. The results indicate that subsets of catalyst nanoparticle ensembles nucleate, grow, and terminate growth within different flux ranges according to their catalytic activity.

To explore graphene nucleation and growth on Ni films, time resolved reflectivity is similarly used to detect the surface roughening and the deposition of carbon in situ at high temperatures (600-750°C)

resultingfrom single or successive sub-second pulses of acetylene in flowing argon and hydrogen at low pressure in standard growth furnaces. Figure 1(b) shows an example of the reflectivity intensity evolution during temperature ramp up of a Ni film to 700 °C, three C_2H_2 pulses at 0.1 Hz (rapid drop in reflectivity), and cool down to room temperature. Growth kinetics measured at different temperatures and peak fluxes reveal a variety of flux-dependent effects including incubation behavior at low fluxes and rapid, sub-second film growth at high fluxes (as in Fig. 1(b)). Under most conditions in this study, the diagnostics show that the majority of graphene growth occurs at high temperature before cooldown.

In situ microscopy and confocal micro Raman spectroscopy in a high temperature microscope stage confirm these growth kinetics. Using this approach we discovered that visible patches of graphene (nuclei) appeared only after ~ 0.5 s after release of C_2H_2 pulse, corresponding to the rapid drop in reflectivity in Fig. 2(a). Interestingly, from 0 to 0.5 s the reflectivity slightly increases, which indicates rapid changes in the Ni- surface structure upon exposure to C_2H_2. We also found that further growth of graphene occurs from the nuclei and develops very rapidly, during ~ 0.5 s. No other changes in the surface morphology were observed during cool down to the room temperature, however optical reflectivity and Raman spectroscopy cannot exclude some additional precipitation. Ex situ Raman spectroscopy confirmed patches of single and few layer graphene with a very low D-band intensity, as shown in Figs. 2(b) and 2(c). Therefore, it appears that the nonequilibrium conditions provided by brief, high flux gas pulses in pulsed CVD at low pressures alters the graphene growth dynamics to prefer surface growth in contrast to dissolution/precipitation as most commonly reported in other studies.

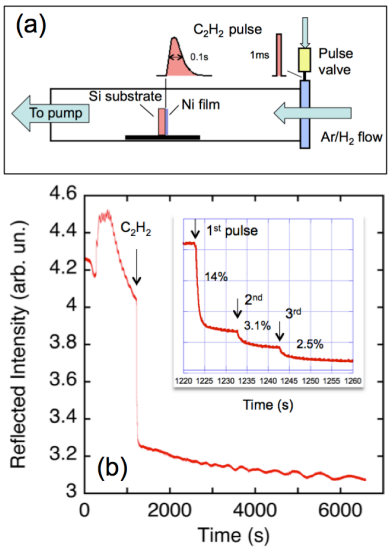

Fig.1. (a) Schematic of pulsed CVD setup: fast continuous flow of Ar (2000 sccm)/H_2 (200 sccm) at total pressure ~ 6 Torr and pulsed C_2H_2 injection (0.12s, FWHM gas pulse at the substrate). (b) Reflected laser intensity vs. time shows a rapid drop in reflected laser intensity within 1s on the 1st pulse, followed by growth or surface restructuring appears ~10s. Subsequent gas pulses show less effect.

Low-pressure CVD using continuous flows was found to grow continuous, large-area graphene free from double or multilayer flakes. Atomic resolution Z-STEM was used to image atomically resolved carbon atoms in the hexagonal networks of graphene. A molecular beam CVD technique for single layer graphene growth was then developed wherein a collisionless beam of hydrogen gas in 10^{-5} Torr background pressure controls the reaction to only the substrate surface. Using this technique a controlled reaction environment is created which can be used to terminate the growth at a single layer.

First-principles quantum mechanical (QM) calculations were performed to understand the CVD growth of graphene on metal substrates, focusing on the dissociation of hydrocarbons and generation of carbon adatoms on metal substrates. We found, in agreement with experimental observations, that at a very high temperature (T > 1500K) only a few hydrocarbons (such as methane) can produce carbon atoms that are energetically stable on Cu substrates. Our theoretical findings explain the importance of quantum and entropic effects which significantly lower the chemical potential of carbons on metal substrates at high temperatures in the CVD growth of graphene.

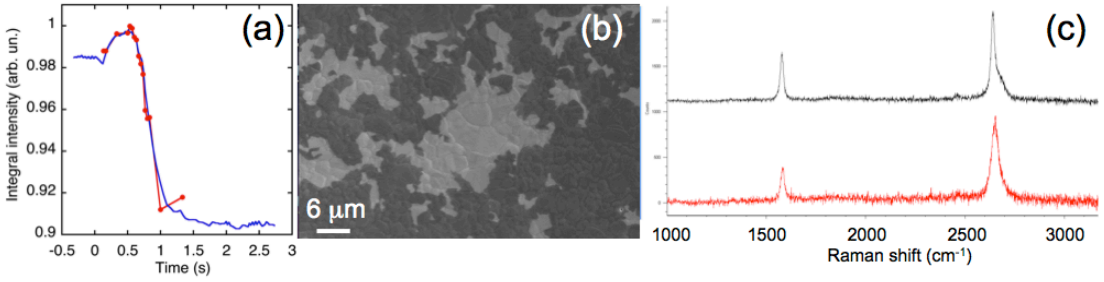

Fig. 2. (a) Kinetics of graphene growth using pulsed CVD of C_2H_2 on a Ni(500 nm) film on SiO2/Si in flowing Ar/H_2 at 686 °C comparing optical image integral intensity (red) and white light reflectivity (blue) analysis. (b) SEM and (c) Raman spectrum of graphene grown from a single gas pulse under these conditions.

To explore the possibility of graphene growth by pulsed fluxes of pure carbon atoms and molecules with high kinetic energy, a PLD approach was employed in vacuum (Fig. 3(a)). Ablation of pyrolytic graphite targets produce high-kinetic energy atoms and ions (~ 100 eV, plume shown in Fig. 3(b)) which can subplant to form tetragonally-coordinated amorphous carbon films with high sp^3 fractions at room temperature. This approach was used to incrementally deposit carbon in order to understand the threshold dose for graphene island nucleation and growth. As shown in Fig. 3(c), SEM analysis (and Raman spectroscopy) of Ni films exposed to different number of laser plumes showed a dose threshold for the number of laser pulses required to nucleate graphene. Using this PLD approach it was demonstrated that there is a clear threshold on the carbon feedstock flux to nucleate and grow graphene and that high quality single- and double-layer graphene can be grown by vacuum PLD.

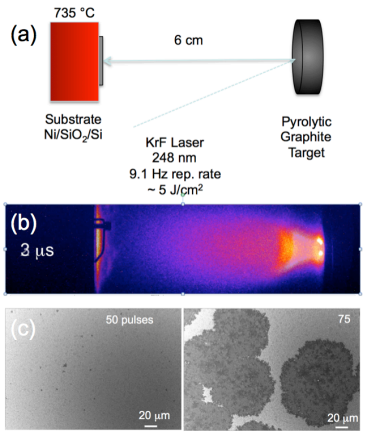

Fig. 3. (a) Schematic of PLD approach to graphene growth in vacuum. (b) Gated ICCD image of the carbon ablation plume measured at 3μs after ablation. The image shows rebound fluorescence near the heated substrate surface when the plume impinges the substrate. (c) SEM images of Ni film after PLD with 50 (left) and 75 (right) laser pulses.

Pulsed heating with the tunable pulse-widths of a high power Nd:YAG laser at 1064 nm was used with in situ optical pyrometry to fashion well-defined, transient temperature profiles (Fig. 4a) to explore the rapid growth of graphene by laser-CVD. Growth of graphene in several seconds, or as short as 0.1s at 1300 °C, was achieved on Ni films in acetylene/hydrogen/argon mixtures. Laser direct-write approaches of single- and few-layer graphenes have been developed on thick foils by Lu et al.[8] using a scanning laser, and it appears that laser processing combined with pulsed gas delivery may be a versatile method which could be developed to enable graphene growth on low-temperature substrates.

In summary, pulsed feedstock delivery and pulsed heating approaches with time resolved, in situ diagnostics are described to explore non-equilibrium growth of graphene (and nanotubes) by CVD and PLD. Low pressures are found to be essential for high-quality graphene in CVD. Using pulsed CVD to rapidly change the carbon feedstock partial pressure at low total pressures appears to alter the nucleation and growth kinetics in the competition between the mechanisms of dissolution and precipitation, and that of surface-driven growth. We find that graphene can grow very rapidly by pulsed CVD at high temperature, however with the inclusion of defects. This rapid growth of graphene on catalytic substrates is similar to the rapid "super-growth" of carbon nanotubes in aligned arrays under similar conditions where we find the catalytic activity of metal catalyst particles determines the diameter and defect levels of nanotubes through a flux-induced particle-overcoating mechanism. This surface carbon overcoating of nanoparticles in nanotube growth is analogous to the growth of graphene in the context of our growth model. Surprisingly, high quality graphene can be grown by in the highly energetic beam environment of PLD using pure carbon plumes.

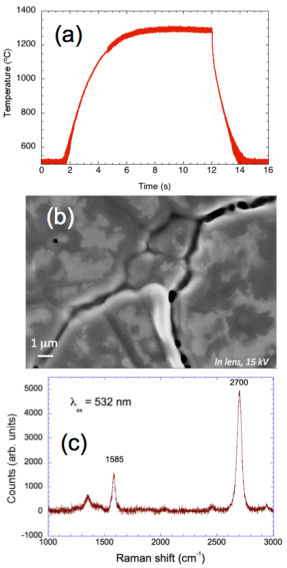

Fig. 4. Graphene growth by laser heating. (a) Fast pyrometer trace of the substrate temperature. (b) SEM image and (c) Raman spectrum of graphene patches.

Future plans

Through real-time diagnostics, including *in situ* Raman spectroscopy, optical reflectivity, and microscopy, we will utilize pulsed processing to understand the kinetics of graphene growth with attention to the inclusion of defects and opportunities for doping in order to obtain desirable architectures (e.g. predicted by first-principles QM calculations for enhanced hydrogen storage (Fig. 5(a), etc.). Obtaining clean graphene is a worldwide challenge, so efforts to produce, transfer, and clean graphene for investigation by atomic resolution Z-contrast STEM imaging will be pursued. Defects and dopants in graphene will be characterized by AC-Z-STEM as a function of our processing conditions and compared with theory. For example, dopants incorporated by dual beam PLD with a carbon target and a second (e.g. metals, boron, etc.) target will be investigated, and rapid laser processing of graphene on TEM grids will be used to induce oxidation and doping of existing graphene for direct imaging by AC-Z-STEM (e.g. as in Fig. 5(b).

References

1. S. Bhaviripudi, X. Jia, M.S. Dresselhaus, J. Kong, *Nano Lett.* **10**, 4128 (2010).
2. A. Grüneis, K. Kummer, D.V. Vyalikh, *New J. Phys.* **11**, 073050 (2009).
3. J. Lahiri, T. Miller, L. Adamska, I.I. Oleynik, M. Batzill, *Nano Lett.* **11**, 518 (2011).
4. X. Li, W. Cai, L. Colombo, R.S. Ruoff, *Nano Lett.* **9**, 4268 (2009).
5. F. Muller, H. Sachdev, S. Hufner, A.J. Pollard, E.W. Perkins, J.C. Russell, P.H. Beton, S. Gsell, M. Fischer, M. Schreck, and B. Stritzk, *Small* **5**, 2291 (2009).
6. P.W. Sutter, J. Flege, E.A. Sutter, *Nature Materials* **7**, 406 (2008).
7. J.J. Jackson, A.A. Puretzky, K. L. More, C.M. Rouleau, G. Eres, D.B. Geohegan, *ACS Nano* **4**, 7573 (2010).
8. J.B. Park, W. Xiong, Y. Gao, M. Qian, Z.Q. Xie, M. Mitchell, Y.S. Zhou, G.H. Han, L. Jiang, Y.F. Lu, *Appl. Phys. Lett.* **98**, 123109 (2011).

ERKCS81 Publications

1. Z. Gu, Y. Yang, K. Li, X. Tao, G. Eres, J. Y. Howe, L. Zhang, X. Li, and Z. Pan, "Aligned Carbon Nanotube-Reinforced Silicon Carbide Composites Produced by Chemical Vapor Infiltration," *Carbon* **49**(7), 2475–2482 (2011).
2. X. P. Huang, J. M. Wang, G. Eres, and X. W. Wang, "Thermophysical Properties of 2. Multi-Wall Carbon Nanotube Bundles at Elevated Temperatures up to 830 K," *Carbon* **49**(5), 1680 (2011).
3. M. Yoon, H. H. Weitering, and Z. Y. Zhang, "First-Principles Studies of Hydrogen Interaction with Ultrathin Mg and Mg-Based Alloy Films," *Phys. Rev. B* **83**, 045413 (2011).
4. M. Yoon, Y. Miyamoto, and M. Scheffler, "Enhanced Dipole Moments in Photo-Excited TTF-TCNQ Dimers", *New J. Phys.* **13**, 073039 (2011).
5. J. J. Jackson, A. A. Puretzky, K. More, C. M. Rouleau, G. Eres, D. B. Geohegan, "Pulsed Growth of Vertically Aligned Nanotube Arrays with Variable Density," *ACS Nano* **4**(12), 7573 (2010).
6. A. A. Puretzky, D. B. Geohegan, and C. M. Rouleau, "Narrow and Intense Resonances in Low Frequency Region of Surface Enhanced Raman Spectra of Single Wall Carbon Nanotubes," *Phys. Rev. B* B **82**, 245402 (2010).

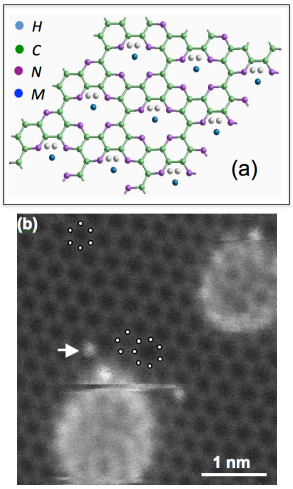

Fig. 5. (a) Nitrogen and metal-doped graphene for hydrogen storage (b) AC-Z-STEM image of graphene grown by CVD on Cu, and transferred to TEM grid with residual C and metal atoms (brighter atoms). One metal atom inserted in lattice,

7. M. Yoon and D. Tomanek, "Equilibrium Structure of Ferrofluid Aggregates," *J. Phys. Condens. Mater.* **22**, 455105 (2010).
8. N. A. Hatab, C.-H. Hsueh, A L. Gaddis, S. T. Retterer, J.-H. Li, G. Eres, Z. Zhang, and B. Gu, "Free-Standing Optical Gold Bowtie Nanoantenna with Variable Gap Size for Enhanced Raman Spectroscopy," *Nano Lett.* **10**, 4952 (2010).
9. H. Pan, B. Gu, G. Eres, and Z. Zhang, "Ab Initio Study on Noncompensated CrO Codoping of GaN for Enhanced Solar Energy Conversion," *J. Chem. Phys.* **132**, 104501 (2010).
10. G. Eres, D. B. Geohegan, A. A. Puretzky, and C. M. Rouleau, "All Carbon Nanotubes Are Not Created Equal," Book Chapter in *Nanotechnology for Electronics, Photonics, and Renewable Energy, Springer Series in Nanostructure Science and Technology,* 131-152 (2010). DOI: 10.1007/978-1-4419-7454-9_4.
11. D. B. Geohegan, A. A. Puretzky, C. M. Rouleau, J. J. Jackson, G. Eres, Z. Liu, D. Styers-Barnett, H. Hu, B. Zhao, K. Xiao, I. Ivanov, and K. More, "Laser Interactions in Nanomaterials Synthesis," Book Chapter in *Springer Series in Materials Science* **130**, 1 (2010).
12. H. Pan, X. Qiu, I. N. Ivanov, H. M. Meyer, W. Wang, W. Zhu, M. P. Paranthaman, Z. Zhang, G. Eres, B. Gu, *11.* "Fabrication and Characterization of Brookite-Rich, Visible Light-Active TiO_2 Films for Water Splitting," *Applied Catalysis B: Environmental* **93**, 90 (2009).
13. J. Zhang, J. Ge, M. D. Shultz, E. Chung, G. Singh, C. Shu, P. P. Fatouros, S. C. Henderson, F. D. Corwin, D. B. Geohegan, A. A. Puretzky, C. M. Rouleau, K. More, C. Rylander, M. N. Rylander, H. W. Gibson and H. C. Dorn, "In Vitro and In Vivo Studies of Single-Walled Carbon Nanohorns with Encapsulated Metallofullerenes and Exohedrally Functionalized Quantum Dots," *Nano Letters* **10**, 2843 (2010).
14. W. Zhu, X. Qiu, V. Iancu, X-Q. Chen, H. Pan, Wei Wang, M. Dimitrijevic, T. Rajh, H. M. Meyer III, M. P Paranthaman, G. M. Stocks, H. H. Weitering, B. Gu, G. Eres, and Z. Zhang, "Band Gap Narrowing of Titanium Oxide Semiconductors by Noncompensated Anion-Cation Codoping for Enhanced Visible-Light Photoactivity," *Phys. Rev. Lett.* **103**, 226401 (2009).
15. G. Eres, C.M. Rouleau, M. Yoon, A.A. Puretzky, D. B. Geohegan, "Model for self assembly of carbon nanotubes from acetylene based on real-time studies of Vertically Aligned Growth Kinetics," *J. Phys. Chem. C* **113**, 15484 (2009).
16. H. Pan, X. Qiu, I. N. Ivanov, H. M. Meyer, W. Wang, W. Zhu, M. P. Paranthaman, Z. Zhang, Gyula Eres, and B. Gu, "Fabrication and characterization of brookite-rich, visible light-active TiO_2 films for water splitting," *Applied Catalysis B* **93**, 90 (2009).
17. M. H. Upton, R. F. Klie, J. P. Hill, T. Gog, D. Casa, W. Ku, Y. Zhu, M.Y. Sfeir, J. Misewich, G. Eres, D. Lowndes, "Effect of number of walls on plasmon behavior in carbon nanotubes," *Carbon*, 47, 162 (2009).
18. Y.A. Yue, G. Eres, X. Wang, and L.Y. Guo, "Characterization of thermal transport in micro/nanoscale wires by steady-state electro-Raman-thermal technique," *Appl. Phys. A* **97**, 19 (2009).
19. Z. Zhou, G.Eres, R. Jin, A. Subedi, D. Mandrus, E.H. Kim, "The performance of in situ grown Schottky-barrier single wall carbon nanotube field-effect transistors," *Nanotechnology* **20**, 085709 (2009).
20. M. Yoon, S. Yang, and Z. Zhang, "Interaction between hydrogen molecules and metallofullerenes", *J. Chem. Phys.* **131**. 064707 (2009).

Multi-Scale Theory of the Growth and Assembly of Colloidal Nanoscale Materials

Kristen A. Fichthorn
fichthorn@psu.edu
Departments of Chemical Engineering and Physics
The Pennsylvania State University
University Park, PA 16802

Program Scope

A significant challenge in the development of functional nanomaterials is understanding the growth, transformations, and assembly of colloidal nanoparticles. From a practical perspective, this knowledge would benefit numerous applications in energy technology, including catalysis for energy conversions, optoelectronic devices, and solar cells. In these and many other applications, the sizes, shapes, phases, and assembly or dispersion of the nanoparticles significantly impacts their performance. Our research is aimed at addressing these factors using first-principles calculations based on density-functional theory (DFT), atomic-scale molecular dynamics (MD) simulations, and coarse-grained, meso-scale Monte Carlo (MC) simulations. We use first-principles DFT calculations to elucidate atomic-scale forces and interactions relevant for these systems. Although modeling the forces and assembly of nanometer-sized particles in the presence of solvent (and perhaps additives) is currently challenging for first-principles simulations, such problems fall within the capabilities of classical MD simulations. The interatomic potentials underlying such simulations can be parametrized and tested against DFT and/or experiment. With reliable coarse-grained simulations based on MC or MD methods, we can predict colloidal assembly and link it to underlying forces in the suspension. Below, we discuss some of our recent studies in this area.

Recent Progress

Shape-controlled synthesis of colloidal nanostructures

Achieving the controlled synthesis of colloidal nanomaterials with selected shapes and sizes is an important goal for a variety of applications that can exploit their unique properties. In the past decade, a number of promising solution-phase synthesis techniques have been developed to fabricate various nanostructures. A deep, fundamental understanding of the phenomena that promote selective growth and assembly in these syntheses would enable tight control of nanostructure morphologies in next-generation techniques. In these studies, we investigate two aspects that underlie the shape-controlled synthesis of nanomaterials: (1) The role of solvent in achieving the growth of one-dimensional (1D) nanostructures and; (2) Elucidating the interactions that govern surface-sensitive binding of solution-phase, structure-directing agents.

A. Role of solvent in the synthesis of 1D colloidal nanostructures

In this work, we focus on the role of solvent in facilitating the growth of 1D nanomaterials, such as nanowires, nanoribbons, and nanoplates, whose formation requires enhanced growth along certain directions and suppressed growth along others. There is evidence that solvent-mediated phenomena could facilitate the 1D growth of nanocrystals. For example, solvent most likely plays a role in the formation of "mesocrystals", or particles comprised of aligned crystallites with solvent and/or other solution-phase species in the space between the crystallites [1–3]. Mesocrystals have been proposed to be intermediates in the process of oriented attachment [1, 4], which is prevalent in the growth of 1D nanostructures [5–10]. In oriented attachment, nanocrystal aggregation occurs along specific crystal directions, such that the aggregate is a twinned or single-crystal structure [1, 11]. Yuwano *et al.* recently used cryogenic transmission electron microscopy to observe a correlation between the sizes and shapes of intermediate ferrihydrite mesocrystals and final 1D goethite nanocrystals grown by oriented attachment [3].

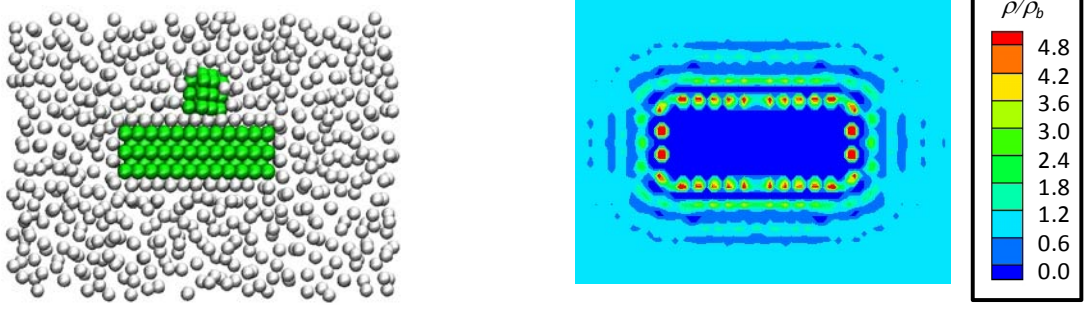

Figure 1: (a) A mesocrystal state with one layer of solvent between the small isotropic nanocrystal and the square plate. (b) Map of the projected solvent density surrounding the square plate.

We recently used MD simulations to study the role played by solvent in promoting 1D growth of colloidal nanostructures. Considering the growth of Ag nanowires and nanoplates in organic solvent, we study how solvent influences the aggregation of a small and relatively isotropic nanocrystal with a larger rectangular cuboid or a square plate. We observe that when the two nanocrystals approach one another, they almost always adopt a mesocrystal configuration, in which the two particles hover next to each other with their facets parallel and one or two layers of solvent between them - analogous to experimentally observed mesocrystal structures. An example of a mesocrystal state with one layer of solvent between the nanocrystals is shown in Fig. 1(a). Mesocrystal states are free-energy minima and the two particles must overcome a free-energy barrier for aggregation to occur. We observe that the height of the free-energy barrier, indicated by the frequency of aggregation, depends on the relative orientation of the two nanocrystals. Aggregation is the most facile on the smallest facets of the large nanocrystals: the ends of the rectangle and the thin sides of the square plate. In this way aggregation promotes anisotropic growth of the particles.

We can correlate the frequency of nanoparticle aggregation with solvent ordering around the nanoparticle surfaces. A map of the projected solvent density in a cut of the simulation box surrounding the square plate is shown in Fig. 1(b). The free-energy barrier for aggregation is the lowest on the end facets of the nanowire and the thin side facets of the square plate because solvent layering and ordering within the first layer is disrupted by the edges, making it easier to disrupt the positions of solvent atoms there. We observe instances of oriented attachment preferentially at the smallest facets – at the ends of the rectangle. These studies indicate that solvent can play a key role in promoting the 1D growth of colloidal nanostructures.

B. Surface-sensitive binding of polyvinylpyrrolidone to silver

Polyvinylpyrrolidone (PVP) is a stabilizer polymer that is often used in the shape-controlled synthesis of nanomaterials. In the synthesis of Ag nanostructures, for example, it is known that the final nanostructure morphology depends on the concentration of $AgNO_3$ salt, the ratio of $AgNO_3$ concentration to the concentration of PVP, and the molecular weight of PVP [12]. However, the exact role of PVP remains elusive. It has been hypothesized [13] that PVP binds more strongly to the (100) surface of Ag than to the (111) surface. This surface sensitivity would explain the formation of Ag nanowires [13], as well as that of nanocubes and nanobars [14]. However, other than this indirect evidence, there is no quantitative support for the surface-sensitive binding hypothesis.

In this work, we use first-principles calculations based on DFT to probe the binding of PVP to Ag(100) and Ag(111). These are challenging studies because (i) Full first-principles calculations of polymers are difficult and; (ii) The interaction of PVP with these surfaces involves both direct binding and van der Waals attraction. Inclusion of van der Waals interactions into DFT calculations is in its early stages and reliable protocols have not yet been firmly established. Regarding (i), we use a procedure first employed by Delle Site *et al.* [15], in which we break the repeat unit of PVP into a 2-pyrrolidone (2P) ring and ethane (cf., Fig. 2). We calculate the interaction of each of these molecules with the surfaces separately to gauge the total interaction. Regarding (ii), we employ the DFT GGA PBE exchange-correlation functional and we test two different methods for calculating the van der Waals interaction: Grimme's method (DFT-D2) [16] and the Tkatchenko-Scheffler (TS) method [17]. In both methods, van der Waals interactions are described as a sum of pair-wise additive dispersion terms between atoms in the system, whose magnitude is governed by C_6 coefficients. In DFT-D2, the C_6 coefficient is constant for a given atom, while in the TS method, C_6 depends on the local environment of the atom and it changes depending on the local electron density.

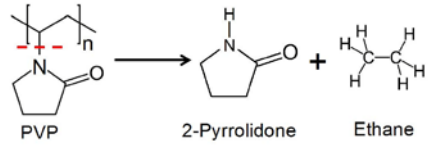

Figure 2: Breakdown of the PVP repeat unit into 2-pyrrolidone (2P) and ethane.

We find that DFT-D2 is not suitable for describing Ag surfaces, as it predicts that Ag(100) will undergo a hex reconstruction – contrary to what is seen experimentally. Several tests of the TS method reveal its suitability. Using the TS method, we find that 2P exhibits many different binding conformations on both of the surfaces. Two different binding conformations for 2P on Ag(100) are shown in Fig. 3. The binding of 2P is surface-sensitive and there are many conformations for 2P on Ag(100) that have stronger binding energies than we find on Ag(111). This finding is consistent with what has been proposed experimentally for PVP [13] on these surfaces. The surface sensitivity arises from a delicate balance between direct chemical bonding of 2P (via its oxygen or nitrogen) and van der Waals attraction: On Ag(100), 2P can adopt many different conformations where there is a synergy between these two types of interactions, while on Ag(111), van der Waals attraction outweighs chemical bonding. In the extreme case of this, van der Waals attraction can push the molecule into conformations where Pauli repulsion dominates over direct chemical bonding. The availability of large numbers of binding conformations with similar energies implies that 2P (and likely PVP) has high mobility over these surfaces and there are many ways for it to bind and facilitate nanostructure formation. We hypothesize that these characteristics are important for a successful structure-directing agent.

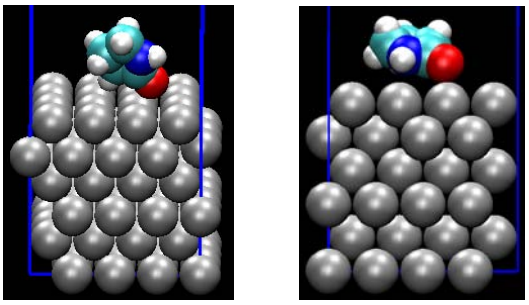

Figure 3: Two binding conformations for 2P on Ag(100). (a) A perpendicular conformation, with a binding energy of 0.6 eV and (b) a parallel conformation, with a binding energy of 0.78 eV. Carbon atoms are light blue, hydrogens are white, oxygen is red, nitrogen is blue, and Ag surface atoms are gray.

Future Plans

Work is continuing on projects (A) and (B) described above. Regarding (A), our current focus is on simulating TiO_2 nanoparticles in an aqueous environment to understand the role of hydroxyl groups and hy-

dration on nanoparticle alignment and aggregation, using our newly-developed force field to describe interactions between water and TiO_2 surfaces (reference 5 under Publications in the Past Two Years). These simulations will be directly relevant to the experimental studies of the crystallization of colloidal anatase [3], where oriented attachment was first discovered. We are interested not only in the initial contact of the nanoparticles, but also in their restructuring after aggregation and we are pursuing studies of the aggregation of anatase nanocrystals. In (B), we are currently using DFT to study the role of solvent (ethylene glycol) and its competitive adsorption with PVP to see if/how this interplay affects the structure-directing capabilities of PVP.

References

1. M. Niederberger and H. Coelfen, *Phys. Chem. Chem. Phys.* **8**, 3271 (2006).
2. D. Schwahn, Y. Ma, and H. Coelfen, *J. Phys. Chem. C* **111**, 3224 (2007).
3. V. M. Yuwano, N. D. Burrows, J. A. Soltis, and R. L. Penn, *J. Am. Chem. Soc.* **132**, 2163 (2010).
4. E. J. H. Lee, C. Ribeiro, E. Longo, and E. R. Leite, *J. Phys. Chem. B* **109**, 20842 (2005).
5. J. Zhang, Jianhui, H. Liu, Z. Wang, and N. Ming, *Appl. Phys. Lett.* **91**, 133112 (2007).
6. C. Schliehe, B. H. Juarez, M. Pelletier, S. Jander, D. Greshnykh, M. Nagel, A. Meyer, S. Foerster, A. Kornowski, C. Klinke, and H. Weller, *Science* **329**, 550 (2010).
7. A. Halder and N. Ravishankar, *Adv. Mater.* **19**, 1854 (2007).
8. K. S. Cho, D. V. Talapin, W. Gaschler, and C. B. Murray, *J. Am. Chem. Soc.* **127**, 7140 (2005).
9. G. Zhang, W. Wang, X. Lu, and X. Li, *Cryst. Growth Des.* **9**, 145 (2009).
10. T. J. Zhu, X. Chen, X. Y. Meng, X. B. Zhao, and J. He, *Cryst. Growth Des.* **10**, 3727 (2010).
11. R. L. Penn, and J. F. Banfield, *Geochim. Cosmochim. Acta* **63**, 1549 (1999).
12. B. Wiley, Y. G. Sun, B. Mayers, and Y. N. Xia, *Chem. Eur. J.* **11**, 454 (2005).
13. Y. G. Sun, B. Mayers, T. Herricks, and Y. N. Xia, *Nano Lett.* **3**, 955 (2003).
14. J. Zeng, Y. Zheng, M. Rycenga, J. Tao, Z.-Y. Li, Q. Zhang, Y. Zhu, and Y. Xia, *J. Am. Chem. Soc.* **132**, 8552 (2010).
15. L. Delle Site, C. F. Abrams, A. Alavi, and K. Kremer, *Phys. Rev. Lett.* **89**, 156103 (2002).
16. S. Grimme, *J. Comp. Chem.* **27**, 1787 (2006).
17. A. Tkatchenko and M. Scheffler, *Phys. Rev. Lett.* **102**, 073005 (2009).

Publications in the Past Two Years

1. M. Alimohammadi and K. A. Fichthorn, "Molecular Dynamics simulation of the aggregation of titanium dioxide nanocrystals: Preferential alignment", *Nano Letters* **9**, 4198 (2009).
2. D. A. Triplett, L. M. Dillenback, B. D. Smith, D. Hernandez Rodriguez, S. K. St. Angelo, P. Gonzalez, C. D. Keating, and K. A. Fichthorn, "Assembly of gold nanowires by sedimentation from suspension: Experiment and simulation", *J. Phys. Chem. C* **114**, 7346 (2010).
3. D. A. Triplett and K. A. Fichthorn "Entropic forces and directed alignment of hard squares in suspensions of rods and disks", *J. Chem. Phys*. **133**, 144910 (2010).
4. R. Sathiyanarayanan, M. Alimohammadi, Y. Zhou, and K. A. Fichthorn, "The role of solvent in the shape-controlled synthesis of one-dimensional colloidal nanostructures", (Submitted to *J. Phys. Chem. C*).
5. M. Alimohammadi and K. A. Fichthorn, "A force-Field for the Interaction of water with TiO_2 surfaces", (Submitted to *J. Phys. Chem. C*).
6. K. A. Fichthorn, W. Al-Saidi, H. Feng, and R. Sathiyanarayanan, "Adsorption of polyvinylpyrrolidone on Ag surfaces: Insight into the workings of a structure-directing agent" (Submitted to *Phys. Rev. Lett.)*

Four-Dimensional Analysis of the Evolution of Complex Dendritic Microstructures During Coarsening

J. Gibbs, C. Park*, P.W. Voorhees and K. Thornton*
Department of Materials Science and Engineering
Northwestern University, Evanston IL, 60208
Department of Materials Science and Engineering
University of Michigan, Ann Arbor MI,

Program Scope

Dendrites are tree-like structures that frequently form during solidification of castings. Dendrites possess secondary and, sometimes, even tertiary side branches. While the tip radius and tip velocity of the dendrite are set by the growth conditions, the side branches behind the tip undergo a coarsening process under nearly isothermal conditions. The resulting two-phase mixtures are morphologically complex. These dendritic two-phase mixtures are one example from a large class of morphologically complicated structures found in nature that undergo coarsening. Included in this class are the bicontinuous two-phase mixtures produced following phase separation. Understanding the coarsening process in these systems requires theory, simulation, and experiments that capture their three-dimensional morphology.

At the core of the investigation is a four-dimensional characterization and analysis approach, which follows the morphological evolution process in three dimensions and in time (an additional dimension). A combined theoretical and experimental program is employed to examine the nature of the coarsening process in these highly complex, dendritic microstructures. The experiments examine the time-dependent evolution of the dendritic mixtures in three dimensions *in situ* through X-ray microtomography. The results of these experiments are used both to provide insights into the coarsening process and to guide the development of theory. Simulations of coarsening in bicontinuous mixtures are used to develop a theory of coarsening in these systems that can elucidate the importance of the complicated morphology found in dendritic systems on the coarsening process.

Recent Progress

We have undertaken a combined experimental and theoretical program aimed at elucidating the manner in which these complex dendritic solid-liquid mixtures coarsen. We find that topological singularities in materials display a universal character. New data analysis methods have been developed that will be used to analyze both the experimental and simulation data. Using this data analysis technique we can now investigate the manner in which curvature evolves in bicontinuous two-phase mixtures.

Topological singularities during coarsening in dendritic structures can have major and sometimes deleterious impacts on the properties of castings, such as freckle formation in single-crystal turbine blades. In this case secondary dendrite arms detach from the

primary stem and float to other locations in the casting and nucleate new grains. One mechanism for the detachment of these arms is the Rayleigh instability, a topological singularity that is driven by interfacial curvature. Rayleigh instabilities are found in a wide range of two-phase mixtures, such as the bicontinuous two-phase mixtures, the roots of cells during cellular solidification, and rod eutectics. Using 4D microscopy at the TOMCAT beam line at the Swiss Light Source and the Al-Cu system, we examined the evolution of the morphology of both liquid and solid rod-like domains near a pinching instability; see Fig. 1 [1]. We searched for similarity solutions wherein the spatial coordinates and the inverse of concentration in the liquid become time-independent under the scaling $(t-t_s)^{\alpha}$, where $\alpha = 1/3$, yielding a free-boundary problem for the interface shape in the self-similar variables. Assuming an axisymmetric shape, the interface approaches a cone far from the pinching point and we find a discrete set of solutions, only one of which is observed experimentally. The self-similar interfacial shape is thus *universal*, depending only on whether the high diffusivity liquid phase is the rod or the matrix. The reason for this is that the divergence in the mean curvature of the interface at the pinching point makes the initial condition and interfacial morphology far from the pinching point irrelevant. The dynamics, however, depends on thermophysical parameters. Using the known materials parameters we find that the kinetics of the pinching process is well described by theory, with the disagreement between theory and experiment less than 5%, even far from the topological singularity. This behavior was observed for over 40 liquid rods and 19 solid rods [2]. Thus we can predict the dynamics of these topological singularities in any two-phase system in which interfacial motion occurs by bulk diffusion, including dendritic solid-liquid systems.

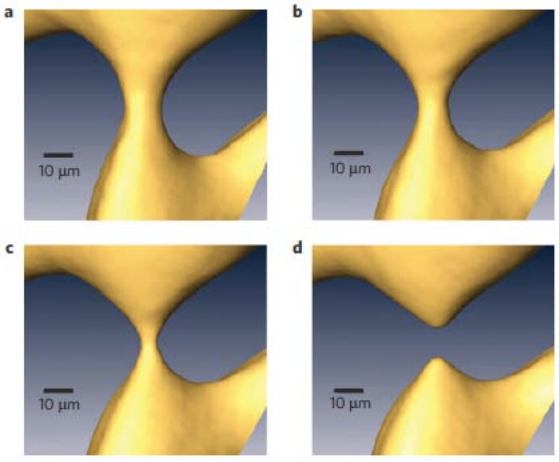

Figure 1. A liquid rod embedded in a solid pinching after (a) 142, (b) 155, (c) 165, and (d) 170 min..

The mathematical description of the evolution of the mean and Gaussian curvatures, which together define the interfacial morphology, can be derived from differential geometry for a given interfacial normal velocity [3], which are expressed as:

$$\frac{DH}{Dt} = -(2H^2 - K)v - \frac{1}{2}(v_{,11} + v_{,22}) \tag{1}$$

$$\frac{DK}{Dt} = -2HKv + \left\{-H(v_{,11} + v_{,22}) + \sqrt{H^2 - K}\,(v_{,11} - v_{,22})\right\}, \tag{2}$$

where D/Dt is the time derivative in the material frame (following a normal to the interface), v is the normal velocity, H is the mean curvature, K is the Gaussian curvature, and $v_{,11}$ and $v_{,22}$ are the second derivatives of the normal velocity with respect to the two principal directions of the interface. The first term in each equation represents the change in curvatures due to the normal motion of the interface. For a spherical particle, this is

the only term describing the dynamics as the other terms vanish and it represents the change in the curvatures due to uniform decrease of radii of particles. The remainder of the terms, which contain the second derivatives of the normal velocities, represents the interaction between nearby surface patches. We calculated various interfacial properties included in Eqs. (1) and (2) on a bicontinuous two-phase structure evolving via the Allen-Cahn dynamics. Even though the normal velocities are solely a function of the local property, H, under the Allen-Cahn dynamics studied, these terms lead to changes in the derivatives of H changes that are difficult to characterize. Fig. 2 illustrates that both of the two terms that constitute DH/Dt, the rate of the change of the mean curvature in the material frame are indeed important. The local term tends to be large in magnitude near protrusions where the interfacial shape is similar to those of spheres. On the other hand, the regions where nonlocal components dominate are less specific and more scattered. Since the local and nonlocal terms have similar maximum magnitudes, neither can be ignored in the formulation of a theory.

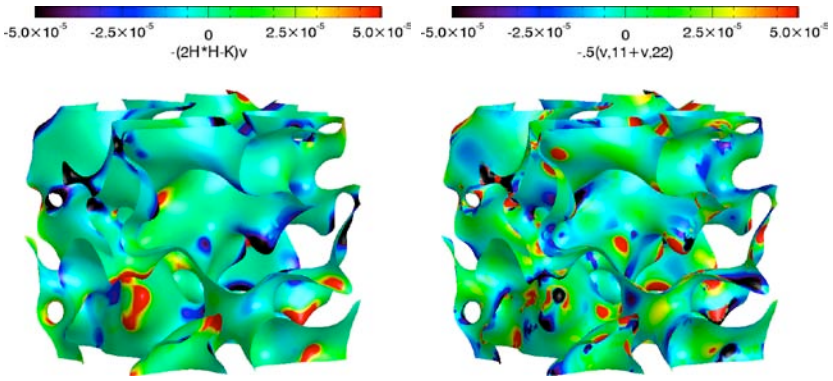

Figure 2. Two components of DH/Dt: local (left) and nonlocal (right) on the simulated microstructure obtained via the Allen-Cahn dynamics. All of them have similar maximum magnitude, but depending on the location, the dominant term varies. In addition, more rapid spatial variation is observed in the nonlocal term, which is expected because it has higher-order derivatives.

Future Plans

We plan on using 4D tomography to measure the dynamics of interfacial curvature in solid-liquid systems. Next year we will employ Al-Cu alloys with different volume fractions of solid, as well as samples that have been either directionally solidified or equiaxed solidified prior to coarsening. This will allow us to test the robustness of our conclusions on the evolution of curvature in these systems. Because the interfacial velocity depends only on the local mean curvature, the simpler Allen-Cahn dynamics is examined first in order to derive the evolution equations for the interface shape distribution, We will test our theory against the simulations of coarsening under Allen-Cahn dynamics.

References

1. L.K. Aagesen, A.E. Johnson, J.L. Fife, P.W. Voorhees, M.J. Miksis, S.O. Poulsen, E.M. Lauridsen, F. Marone and M. Stampanoni, Nature Physics, **6**, 796-800 (2010).

2. L.K Aagesen, A.E. Johnson, J.L. Fife, P.W. Voorhees, M.J. Miksis, S.O. Poulsen, E.M. Lauridsen, F. Marone and M. Stampanoni,, Acta Mater., **59** 4922-4932 (2011).
3. D.A. Drew, *SIAM J Appl Math* 1990; **50**:649-666.

DoE Sponsored Publications in the Last Two Years

1. L.K. Aagesen, A.E. Johnson, J.L. Fife, P.W. Voorhees, M.J. Miksis, S.O. Poulsen, E.M. Lauridsen, F. Marone and M. Stampanoni, "Pinch-Off of Rods by Bulk Diffusion", Acta Mater., 59 4922-4932 (2011).

2. L.K. Aagesen, A.E. Johnson, J.L. Fife, P.W. Voorhees, M.J. Miksis, S.O. Poulsen, E.M. Lauridsen, F. Marone and M. Stampanoni, "Universality and Self-Similarity in Pinch-Off of Rods by Bulk Diffusion", Nature Physics, **6**, 796-800 (2010).

3. L.K. Aagesen, J.L. Fife, P.W. Voorhees and E.M. Lauridsen, "The Evolution of Interfacial Morphology During Coarsening: A Comparison Between 4D Experiments and Theory", Scripta Materialia, **64** 394-397 (2011).

4. Y. Kwon, K. Thornton, and P.W. Voorhees, "Morphology and Topology in Coarsening of Domains via Nonconserved and Conserved Dynamics." Philosophical Magazine, **90**, 317 – 335 (2010).

5. A.L. Genau, P.W. Voorhees, and K. Thornton, "The Morphology of Topologically Complex Interfaces." Scripta Materialia, **60**, 301-304 (2009).

6. G. Spanos, D.J. Rowenhorst, M.V. Kral, P.W. Voorhees and D. Kammer, *Three-Dimensional Microstructure Representation*, ASM Metals Handbook, in press (2011).

7. Y. Kwon, K. Thornton, and P.W. Voorhees, "The Topology and Morphology of Bicontinuous Interfaces During Coarsening." Europhysics Letters (EPL), **86**, 46005 (2009).

Predicting Phase Selection in Systems driven Far from Equilibrium

M. J. Kramer,[*#] A.I. Goldman,[*@] R. E. Napolitano,[*#] M.I. Mendelev,[*] K.M. Ho,[*] R. T. Ott,[*]
X.Y. Song,[*%] R. Trivedi,[*#] C.Z. Wang,[*] N. Wang,[^] Y.E. Kalay,[*#] S.H. Zhou[*] and T. Wang[*]
mjkramer@ameslab.gov
[*]Materials Science and Engineering Division, Ames Labs DOE
[#]Department of Materials Science and Engineering, Iowa State University
[@]Department of Physics, Iowa State University
[%]Chemistry Department, Iowa State University
[^]Department of Applied Physics, Northwestern Polytechnical University, Xian 710072, China

1. Program Scope

Rapid solidification processes, such as melt spinning [1], are common means to produce non-equilibrium metal alloys, yet little is understood about the phase selection and nanoscale structural dynamics in such systems driven far from equilibrium. Effective exploitation of highly driven phase transformations for new materials with novel properties requires that we attain better understanding and control of the competitive mechanisms underlying the transition dynamics. The kinetic suppression of liquid dynamics during rapid cooling may give rise to phase transition pathways that involve departure from the equilibrium "equation of state" for the liquid before or during the formation of stable or metastable crystalline phases, which themselves may be far from equilibrium in terms of structure and chemistry [2-4]. These non-equilibrium liquid structures and glassy phase dynamics may contribute to or even dominate the structural transitions in systems driven far from equilibrium. In this way, noncrystalline forms of structural/chemical ordering may play an important role in establishing viable kinetic pathways which strongly influence transition dynamics [5;6]. Thus, the true challenge emerges. Specifically stated, if we are to extend the well-developed analytical framework of physical metallurgy into the realm of far-from-equilibrium phase transition dynamics involving noncrystalline materials as well as disordered or defected crystalline states, we must

(i) find effective strategies to describe the structural and chemical order in such phases and their interfaces in terms of a common basis set of fundamental elements of order;
(ii) formulate appropriate thermodynamic models to quantify the energetic landscapes with suitable "reduced sets" of order parameters that can be quantified through connection to measurable quantities but remain rich enough to characterize the structural-chemical coupling, and;
(iii) quantify the system dynamics and develop strategies to predict and control far-from-equilibrium phase selection and structural evolution.

In order to meet such ambitious goals, we have assembled a team with expertise in the critical areas of first-principles investigations of material behavior, classical potentials and molecular dynamics simulations, X-ray scattering and e-beam microanalysis, solution thermodynamics, solid-liquid interfaces, and solidification/transformation dynamics.

2. Recent Progress

While the stated goals above are quite ambitious, we have had significant success over the past two years in detailing the development of short to medium-range noncrystalline order in deeply undercooled metallic liquids and its relation to crystallization from the melt [3;7] or from the glass [4;8;9]. Here, we focus specifically on the Al- rare earth (RE is Sm or Tb) liquids [10;11]. /For the Al-Sm we have analyzed the thermodynamics of solidification at high undercooling [12;13], and we have investigated microstructure selection over a very wide range of undercooling under controlled conditions (Fig. 1). The eutectic spacing at the transition is characterized, and the results are analyzed by using a model of eutectic growth that incorporates

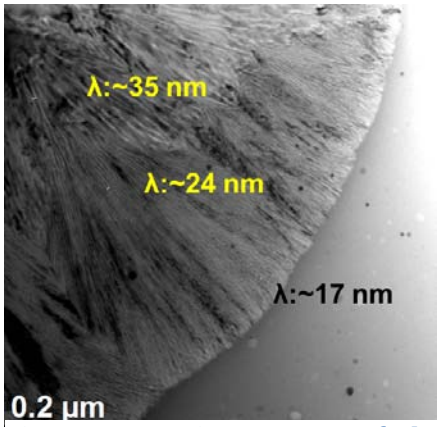

Figure 2 TEM microstructures of Al-10 at.% Sm hypereutectic melt-spun alloy showing the transition from eutectic to glass.

nonequilibrium effects at the interface [3;7]. We show that the very large undercooling at the interface required for glass formation is due to the combined effects of sharp decrease in the diffusion coefficient, or the sharp increase in viscosity of the liquid, coupled with nonequilibrium undercooling at the interface in this system. The undercooling for the experimentally measured eutectic spacing of about 15 nm is of the order of 300 K (Fig. 2).

Utilizing 3D atom probe tomography (APT), fluctuation microscopy and high-energy synchrotron X-ray diffraction (HEXRD), we were able to assemble a comprehensive 3D picture of the chemical and structural order of the nanometer scale in an amorphous Al-10 at% Sm and Tb (Fig. 1) and quantify the dominant MRO [4;8;9]. HEXRD and conventional TEM demonstrate that the sample is fully amorphous yet APT reveals a more complex chemical ordering with discrete regions ~ 1-2 nm in diameter which are nearly pure Al interspersed with regions close to the composition of the high temperature stable phases depending on the rare earth, (tetragonal phase $Al_{11}Sm_3$ or trigonal-like Al_3Tb). Upon heating, it is the Al-rich regions which are the locus for fcc-Al crystallization, which occurs before the intermetallic crystallization. Our model further suggests limited diffusion of the intermetallic network allows for the isolated Al-rich regions to form regions of high nuclei density ~10^{25} nuclei/m^3. The observed length scale of the chemical ordering (up to 10's of nm's) and the longer times these features have to develop in deeply undercooled liquids present challenges for atomistic simulations, which will be the focus of another talk in this session "Development of Order in Deeply Undercooled Liquid Metals".

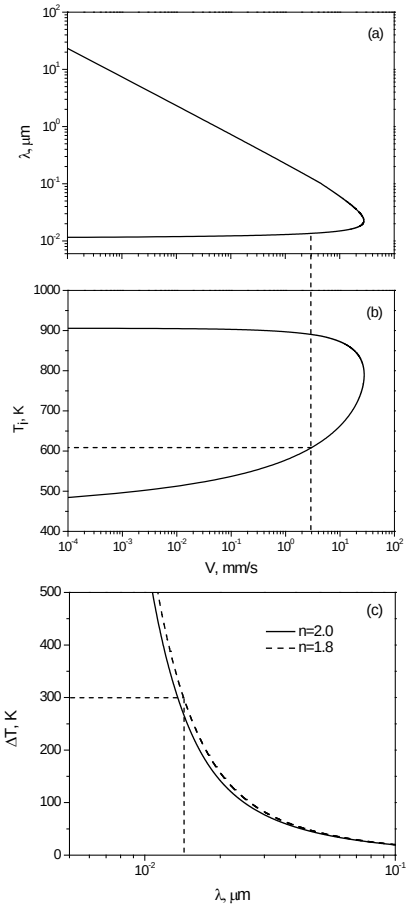

Figure 1. The variation in (a) eutectic spacing, and (b) interface temperature as a function of velocity. (c) The variation in interface undercooling with eutectic spacing. Al-10 at.% Sm.

3. Future Plans

We propose to study the various non-equilibrium liquid structures and glassy phase dynamics on structural transitions in systems driven far from equilibrium by comparing the same alloy chemistries prepared though very different processing routes. These methods will include directional solidification, electrostatic and magnetic levitation, injection casting, melt spinning and magnetron sputtering onto a liquid nitrogen-cooled substrate. These techniques cover cooling rates from 10^4 to 10^{10} K/s, respectively. The Al-RE alloys and alloy systems with good glass formability (e.g., Cu-Zr, Pd-Ni-P and Pd-Si-Cu) but with different SRO in the glassy state [14] [15] will be investigated. In all instances,

experiments and simulations are being performed in concert. Experiments will not only validate simulations but also expose unexplored realms of atomic-scale order in highly driven systems. Simulations on the other hand, provide a window into spatial and temporal scales not easily accessible experimentally. As a specific example, we have now synthesized thin films (from 70 nm to 5 μm) of the Al-10%Tb as shown in Fig. 1. We have been able to characterize these films with TEM, XRD and APT and perform thermal analysis which shows that the as-deposited structure and the devitrification pathways differ from the melt spun alloy. Relaxation studies are underway to measure how changes in the local ordering affect nucleation, phase selection and growth. Since even classical MD is frequently incapable of overcoming the space and time limitations associated with simulations of the glass structure, we are developing advanced methods to accelerate classical MD. We are developing thermodynamic models to quantify the energetic landscapes and using this as inputs for phase field modeling of phase selection and structural evolution.

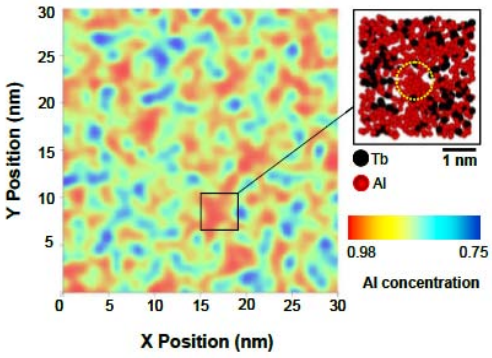

Figure 3. ***2D Al concentration map over 30x30x4 nm volume of data for as-quenched Al-10 at% Tb. Inset (right corner) shows APT results over a volume of 4x4x2 nm indicating cluster of pure Al (circled). The color bar (left corner) indicates the concentration limits.***

4. References

[1] M. J. Kramer, H. Mecco, K. W. Dennis, E. Vargonova, R. W. McCallum, and R. E. Napolitano, Journal of Non-Crystalline Solids **353** (2007), pp. 3633.

[2] M. J. Aziz, Journal of Applied Physics **53** (1982), pp. 1158.

[3] R. Trivedi, and N. Wang, Scripta Materialia **64** (2011), pp. 848.

[4] Y. E. Kalay, L. S. Chumbley, M. J. Kramer, and I. E. Anderson, Intermetallics **18** (2010), pp. 1676.

[5] S. G. Hao, C. Z. Wang, M. Z. Li, R. E. Napolitano, M. I. Mendelev, and K. M. Ho, Computational Materials Science **49** (2010), pp. 615.

[6] S. G. Hao, C. Z. Wang, M. Li , R. E. Napolitano, M. M. I., and K. M. Ho, Physical Review B (accepted)

[7] N. Wang, Y. E. Kalay, and R. Trivedi, Acta Materialia (2011)

[8] Y. E. Kalay, C. Yeager, L. S. Chumbley, M. J. Kramer, and I. E. Anderson, Journal of Non-Crystalline Solids **356** (2010), pp. 1416.

[9] Y. E. Kalay, I. Kalay, J. Hwang, P. M. Voyles, and M. J. Kramer, Acta Materialia (submitted)

[10] X. W. Fang, C. Z. Wang, Y. X. Yao, Z. J. Ding, and K. M. Ho, Journal of Physics-Condensed Matter **23** (2011)

[11] X. W. Fang, C. Z. Wang, Y. X. Yao, Z. J. Ding, and K. M. Ho, Physical Review B **83** (2011)

[12] S. H. Zhou, and R. E. Napolitano, Metallurgical And Materials Transactions A-Physical Metallurgy And Materials Science **39A** (2008), pp. 502.

[13] S. H. Zhou, and R. E. Napolitano, Physical Review B **78** (2008)

[14] H. W. Sheng, H. Z. Liu, Y. Q. Cheng, J. Wen, P. L. Lee, W. K. Luo, S. D. Shastri, and E. Ma, Nature materials **6** (2007), pp. 192.
[15] A. Anikeenko, and N. Medvedev, Physical Review Letters **98** (2007), pp. 1.

5. Select publications by this task within our DOE project over the last two years.

N. Wang, Y.E. Kalay and R. Trivedi, "Eutectic to Metallic Glass Transition in the Al-Sm System", Acta Materialia. accepted

N. Wang and R. Trivedi, "Limit of Steady-State Lamellar Eutectic Growth," *Scripta Materialia*, **64**, 848 (2011).

S. Liu, J.H. Lee, and R. Trivedi, "Dynamic Effects in the Lamellar-Rod Eutectic Transition," *Acta Materialia*, **59**, 3102 (2011).

X W Fang, C Z Wang, Y X Yao, Z J Ding and K M Ho, "Signature of $Al_{11}Sm_3$ fragments in undercooled $Al_{90}Sm_{10}$ liquid from ab initio molecular dynamics simulations", *J. Phys.: Condens. Matter* **23** 235104 (2011).

X. W. Fang, C. Z. Wang, Y. X. Yao, Z. J. Ding, and K. M. Ho, "Competition between fcc and icosahedral short-range orders in pure and samarium-doped liquid aluminum from first principles", Phys. Rev. B, **83**, 224203 (2011).

Y.E. Kalay, L.S. Chumbley, M.J. Kramer, and I.E. Anderson, "Local Structure in Marginal Glass Forming Al-Sm Alloy," *Intermetallics*, **18**, 1676 (2010).

Y.E. Kalay, C. Yeager, L.S. Chumbley, M.J. Kramer, and I.E. Anderson, "Initial Crystallization in a Nanostructured Al-Sm Rare Earth Alloy," *Journal of Non-Crystalline Solids*, **356**, 1416 (2010).

I. Kalay, M.J. Kramer, and R.E. Napolitano, "High-Accuracy X-Ray Diffraction Analysis of Phase Evolution Sequence During Devitrification of $Cu_{50}Zr_{50}$ Metallic Glass," *Metallurgical and Materials Transactions a-Physical Metallurgy and Materials Science*, **42A**, 1144 (2011).

P. Srirangam, M.J. Kramer, and S. Shankar, "Effect of Strontium on Liquid Structure of Al-Si Hypoeutectic Alloys Using High-Energy X-Ray Diffraction," *Acta Materialia*, **59**, 503 (2011).

S. G. Hao, C. Z. Wang, M. Z. Li, R. E. Napolitano, and K. M. Ho, "Dynamic arrest and glass formation induced by self-aggregation of icosahedral clusters in $Zr_{1-x}Cu_x$ alloys", Phys. Rev. B, accepted.

X. W. Fang, C. Z. Wang, S. G. Hao, M. J. Kramer, Y. X. Yao, M. I. Mendelev, Z. J. Ding, R. Napolitano, and K. M. Ho, "Development of Medium-Range Order in Metallic $Cu_{64.5}Zr_{35.5}$ Liquid and Glass", Scientific Report, submitted.

S.G. Hao, C.Z. Wang, M.J. Kramer, and K.M. Ho, "Microscopic Origin of Slow Dynamics at the Good Glass Forming Composition Range in $Zr_{1-x}Cu_x$ Metallic Liquids," *Journal of Applied Physics*, **107**, 053511 (2010).

M.I. Mendelev, M.J. Rahman, J.J. Hoyt, and M. Asta, "Molecular-Dynamics Study of Solid-Liquid Interface Migration in Fcc Metals," *Modelling and Simulation in Materials Science and Engineering*, **18**, 074002 (2010).

V.B. Warshavsky and X.Y. Song, "Perturbation Theory for Solid-Liquid Interfacial Free Energies," *Journal of Physics-Condensed Matter*, **22**, 364112 (2010).

S.H. Zhou and R.E. Napolitano, "Phase Stability for the Cu-Zr System: First-Principles, Experiments and Solution-Based Modeling," *Acta Materialia*, **58**, 2186 (2010).

M.J. Kramer, M.I. Mendelev, and R.E. Napolitano, "In Situ Observation of Antisite Defect Formation During Crystal Growth," *Physical Review Letters*, **105**, 245501 (2010).

Atomistic Structure, Strength, and Kinetic Properties of Intergranular Films in Ceramics

Stephen H. Garofalini
shg@rutgers.edu
Department of Materials Science and Engineering
Rutgers University

Program Scope

The thin glassy intergranular films (IGFs) present between the crystals in polycrystalline ceramics occupy only a small volume percent of the bulk ceramic but can significantly influence morphology and mechanical, chemical, and optical properties[1,2]. Because of their thin (~10^3 times smaller than the crystals they separate) nanoscale and amorphous nature, understanding the atomistic basis for how these IGFs affect material properties has been elusive, although advances in computer simulations[3-5] and recent electron microscopy[6,7] have provided information about the location of atoms at the IGF/crystal interface. Nonetheless, the specific role of these interfacial ions and, importantly, the effect of the interfaces on atoms within the IGF (away from the interfaces) and their effect on properties (e.g. fracture) have not been quantified from an atomistic perspective. It is our hypothesis that the adsorption of ions to the interface affects the structure and chemistry of the glassy IGF away from the interface that must play a pivotal role in fracture behavior of polycrystalline ceramics. Under the extremely important influence of the crystal interface, we must consider the three major features contributing to the material's properties: (1) the composition and structure of the glassy part of the IGF, (2) the role of the crystal on the effective composition and structure in the IGF as well as at the interface, extending from the crystal, and (3) the role of the interface acting as a sink for particular species from the IGF that affects segregation of those and other species to the interface as dictated by the combined effect of the bonding characteristics of the segregant in the glass versus the segregant in the interface. Understanding these features in these highly complex systems will provide a more fundamental basis for application to other nanoconfined amorphous phases in materials.

We address the detailed atomistic structure and behavior of these IGFs in oxide and nitride ceramics using molecular dynamics and atomic density functional (ADF) computer simulation techniques, with correlations to available and proposed experiments using HRTEM, AEM, and HAADF-STEM. The work will include the effect of compositional variations on interface structure as a function of crystal orientation, structure of the interior of the IGF (away from the IGF/crystal interface) as a function of IGF thickness, and the effect of these properties on fracture during tensile strain, with detailed analysis of the changes in local structure that would alter crack formation and paths. Our work is being done in conjunction with available experimental verification in collaboration with Dr. Pennycook at ORNL and Professors Phil Batson and Fred Cosandey at Rutgers, as well as interactions with Dr. Christoph Koch at Max-Planck Institut für Metallforschung, Stuttgart for initiating HAADF-STEM images from our simulation data for direct comparison to experimental HAADF-STEM images.

A major thrust of our work is quantifying the important role of *local* IGF composition and bounding crystal surface structures on properties.

Recent Progress

Overall, our results reproduce recent experimental data and show the extremely important role of *local* composition and structure of the IGF and the role of the bounding crystal interfaces on the properties of the material.

1. The MD simulations reproduce the locations of the first and second layers of La ions at the interfaces of the bounding crystals in the silicon nitride system, similar to HAADF-STEM by Pennycook (ORNL), Cockayne (Oxford), and Zeigler (LBNL) [8], as well as additional ordered sites for La extending farther from the prism interface into thick IGFs, similar to HAADF-STEM by the ORNL and Oxford groups of triple points (pockets), indicating an important role of IGF thickness on La ordering (see fig 1). These combined results enable us to extend our work to provide accurate descriptions of rare earth ions in the glassy interior of the IGF that is currently not readily amenable to definitive experimental analysis but which appears to play a dominant role in material properties.

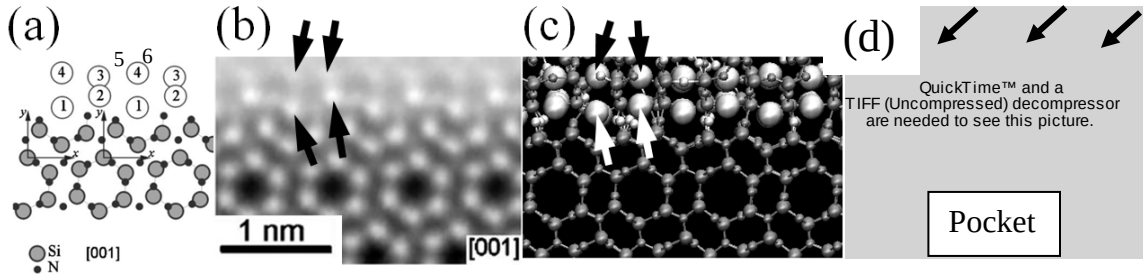

Figure 1. Four primary locations of La ions on the IGF/Prism interface viewed along the [001] direction, plus two sites slightly visible in the pocket. (a) Drawing of primary La sites from Winkelman *et al.* plus sites 5 and 6 from the pocket; (b) HAADF-STEM image of IGF from Winkelman *et al.*; (c) our IGF MD simulation results; (d) HAADF-STEM of pocket. Arrows show primary La sites from experiments in (b) and simulations in (c) showing exact same locations and in (d) sites 5 and 6 in pocket that are also seen in our thicker IGFs.

2. We see filling of these ordered sites that is dependent on both IGF composition and thickness, which modify poisoning of the surfaces that affects growth of the different crystal orientations consistent with anisotropic growth of the nitride, providing us with new information regarding growth mechanisms and the extremely important role of *local* composition on growth. The prism-oriented Si_3N_4 surface is preferentially poisoned; the basal-oriented surface has varying degrees of adsorption that depend on local composition that affects growth (see fig 2).

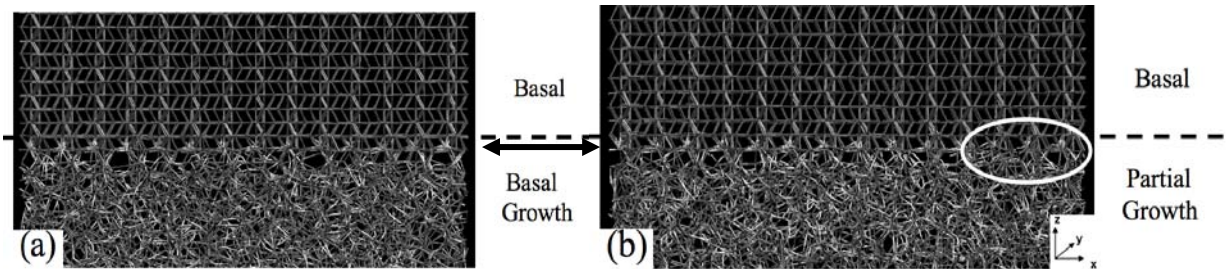

Figure 2. Snapshots of (a) basal growth (50N3La), and (b) partial basal growth (50N6La). Dashed lines are drawn to distinguish the original basal crystal and the new basal layer (at arrow). Ellipse is drawn in (b) to point out the region where basal growth is disrupted, allowing for growth of a curved surface similar to experiment as opposed to growth of a flat plane.

3. We quantify the driving forces (energetics) for adsorption and La ordering at the interfaces and in the IGF, providing the explanation for the different segregation behavior seen experimentally.

4. These driving forces change as a function of composition and thickness, which play an important role in varying the migration of La ions from a 'source' (the triple point) to the 'sink' (the IGF), which affects properties.

5. We show the **extremely important role of adsorption to specific interfaces on the variation of the composition remaining within the IGF and its affect on fracture**, again indicating the importance of detailed local compositions and interface structure on properties. That is, we show that IGF thickness affects La adsorption and ordering which affect strength and crack-path location; understanding this relationship is fundamental for engineering these materials.

Future work

Current results clearly indicate that the extent of La ordering into the IGF affects strength. Crack propagation is not seen within this ordered region, but rather remains in the glassy portion of the IGF. If RE ordering can be enhanced, then strength may be enhanced. Lu shows increased strength. We are incorporating Lu into the simulations to evaluate its structure in the IGF and see if ordering is greater than that seen in La-IGFs so as to determine if this is the mechanism by which Lu increases the strength of the IGF. Current theory on strength enhancement by Lu is lacking in that it resides only in the idea that Lu bond strength to N is stronger than La's. As such, our approach will be enlightening in that both the bonding idea and the ordering ideas can be tested.

1. Lu Additive in IGF: We have initiated development of the interatomic potentials for incorporation of Lu into the IGFs as a comparison to our results for La additives. Lu in the silicate IGF shows transgranular fracture, whereas La in the silicate IGF shows intergranular fracture. Our fracture results for the La case appear intergranular, in that the fracture occurs in the interior of the glassy IGF and away from the ordered interface. Since Lu additive creates different behavior, our intent is to evaluate the cause of this difference at the molecular level. Lu has been shown experimentally to sit at slightly different sites on the prism-oriented Si_3N_4 surface in comparison to La. We believe that affects not only interface behavior, but also the distribution of rare-earth ions in the interior of the IGF that affects strength. We will evaluate this in the future simulations.

2. The binding energies for La ions at different locations in the IGF vary as a function of composition and IGF thickness. Two effects, potentially competing, result from the evaluation of La binding energies: one is that after La segregation to the interface, additional La ions from the pocket would be less likely to migrate to a thin (0.6nm) IGF because of the lower cohesive energy of the La there in comparison to its binding energy in the pocket; the second is that a low N concentration in a thick IGF results in a low La binding energy, implying that if a triple point (making it synonymous with a very thick film) has a low N concentration, La ions from the pocket are more weakly bonded and would readily migrate into the IGF that has more N present, regardless of IGF thickness. We will evaluate this prediction with large scale simulations.

3. The School of Engineering has purchased a small GPU cluster for testing of GPU-codes. We hope to use this cluster to apply GPU computations to our problem, allowing for

larger scale and longer simulations to address item 2 above, which will require large numbers of atoms and long simulation runs.

References

(1) Becher, P. F.; Painter, G. S.; Sun, E. Y.; Hsueh, C. H.; Lance, M. J. *J. Am. Ceram. Soc.* **2000**, *48*, 4493.
(2) Becher, P. F.; Painter, G. S.; Shibata, N.; Waters, S. B.; Lin, H. *J. Am. Ceram. Soc.* **2008**, *91*, 2328.
(3) Garofalini, S. H.; Luo, W. *J. Am. Ceram. Soc.* **2003**, *86*, 1741.
(4) Zhang, S.; Garofalini, S. H. *J. Phys. Chem. B* **2006**, *110*, 2233.
(5) Painter, G. S.; Averill, F. W.; Becher, P. F.; Shibata, N.; Van Benthem, K.; Pennycook, S. J. *Phys. Rev. B* **2008**, *78*, 214206.
(6) Winkelman, G. B.; Dwyer, C.; Hudson, T. S.; Nguyen-Mahn, D.; Doblinger, M.; Satet, R. L.; Hoffmann, M. J.; Cockayne, D. J. H. *Appl. Phys. Lett.* **2005**, *87*, 061911.
(7) Shibata, N.; Painter, G. S.; Becher, P. F.; Pennycook, S. J. *Appl. Phys. Lett.* **2006**, *89*, 051908.
(8) Dwyer, C.; Ziegler, A.; Shibata, N.; Winkelman, G. B.; Satet, R. L.; Hoffmann, M. J.; Cinibulk, M. K.; Becher, P. F.; Painter, G. S.; Browning, N. D.; Cockayne, D. J. H.; Ritchie, R. O.; Pennycook, S. J. *J. Mater. Sci.* **2006**, *41*, 4405.

DOE Sponsored Publication from 2009-2011

1. "Effect of thickness and composition on the structure and ordering in La-doped intergranular films between Si_3N_4 crystals", Y. Jiang and S. H. Garofalini, Acta Mater. 59 (2011) 5368-5377 (exclusively acknowledge BES-MSE support)
2. "Order in nanometer thick intergranular films at Au-sapphire interfaces", M. Baram, S. H. Garofalini and W. D. Kaplan, Acta Mater. (Accepted, in press). (exclusively acknowledge BES-MSE support for SHG; the other two authors have support from the Israel Science Foundation)
3. INVITED PAPER in THEMED ISSUE: "Molecular dynamics simulations of La_2O_3-doped silicate intergranular films in Si_3N_4" Y. Jiang, S. H. Garofalini, J. Matl. Chem. 20 (2010) 10359-10365. (exclusively acknowledge BES-MSE support)
4. "Molecular dynamics simulations of the locations of La ions in La-Si-O-N intergranular films in silicon nitride" Y. Jiang and S. H. Garofalini, J. Am. Ceram. Soc. 93 (2010) 3886-3892. (exclusively acknowledge BES-MSE support)
5. "Molecular dynamics simulations of the effect of the composition of the intergranular film on fracture in Si_3N_4", S. H. Garofalini and S. Zhang, J. Am. Ceram. Soc. 93 (2010) 235-240. (exclusively acknowledge BES-MSE support).
6. "Effect of thickness of the intergranular film on fracture in Si_3N_4", S. Zhang, and S. H. Garofalini, J. Am. Ceram. Soc.92 (2009)147-151 (exclusively acknowledge BES-MSE support).

In Situ Visualization and Theoretical Modeling of Early-Stage Oxidation of Metal and Alloys

Guangwen Zhou
gzhou@binghamton.edu
Department of Mechanical Engineering, State University of New York, Binghamton, NY 13902

Program Scope

The surfaces of most materials in reactive or corrosive environments tend to restructure thereby adapting their geometrical and electronic structure to the environments [1-3]. A typical example is the oxidation of metal surfaces that results in profound changes in structures and materials properties. The challenge in the study of metal oxidation is to identify and then control the atomic processes governing the interfacial reactions of metal-oxygen, metal-oxide and oxide-oxygen at the different reaction regimes. The objective of this program is to address these issues by studying the reaction from the initial oxidation stage of oxygen surface chemisorption to bulk oxide formation. To achieve this goal, *in situ* microscopy and spectroscopy techniques have been utilized to monitor, in real time and at the atomic scale, the surface oxidation of a number of model systems of metals and alloys. Such atomic *in situ* experimental data feed into the density-functional theory (DFT) modeling for identifying the critical kinetic and thermodynamic factors controlling the interfacial processes of metal oxidation under the technological relevant reactive environments.

Recent Progress

Atomic structures of oxygen chemisorbed metal surfaces under realistic gas conditions

We used an aberration-corrected environmental transmission electron microscope (TEM) to visualize the surface structure of Cu(110). Fig. 1(a-c) depicts a sequence of *in situ* high-resolution TEM images of the Cu(110) surface, seen edge-on in the images, at an oxygen pressure (pO_2) of ~5×10^{-4} Torr and the temperature of 350°C. The topmost atomic layer of the (110) surface with a periodicity of 2.5 Å corresponds to a (1×1) oxygen chemisorbed layer. Fig. 1(b) is a time-lapsed TEM image from the same area showing the instantly formed lattice periodicity of 5.0 Å, which corresponds to a (2×1) oxygenated surface. This (2×1) structure is not a stable phase and changes back to the (1×1) surface in a few seconds. Our *in situ* TEM observations reveal that the (1×1) oxygen chemisorbed surface is a very stable phase over the time and inert to further oxidation even under pO_2 ~ 0.1 Torr. We have performed DFT calculations of the equilibrium structure (Fig. 1d and e) of these oxygenated surfaces and developed a kinetic model of the (1×1)↔(2×1) phase transitions based on desorption and adsorption of oxygen from long bridge Cu-Cu sites of alternative Cu[100] rows. Using the atomistic thermodynamics we have constructed a phase stability diagram delineating the preferred equilibrium oxygenated surface phase for a given oxidation temperature and oxygen gas pressure and compared with experimental observations (Fig. 1f).

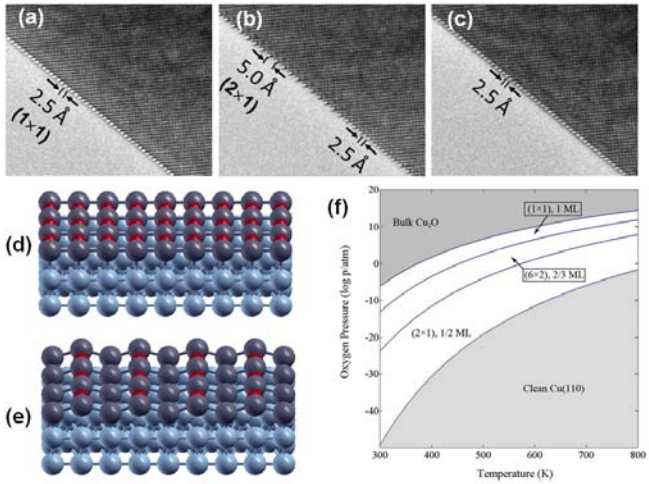

Fig. 1: (a-c) *In situ* TEM images of the (110) surface showing the instant (1×1) ↔ (2×1) transitions; (d, e) DFT result of the atomic structure of the oxygenated (1×1) and (2×1) surfaces; (f) DFT calculated surface phase diagram for the various phase as a function of oxygen pressure and temperature.

Oxygen chemisorption induced kinetic hindrance to bulk oxide formation

We use combined *in situ* x-ray photoelectron spectroscopy (XPS) and scanning tunneling microscopy (STM) to monitor the surface chemistry and surface structure during the oxidation of a Cu(110) surface under a wide range of $pO_2$and temperature T. We found that the formation of bulk oxide (Cu_2O) from the oxygen

chemisorbed surface requires a surprising significantly larger oxygen gas pressure than that predicted by first-principles atomistic thermodynamics (i.e., Fig. 1f). Fig. 2(a) shows the evolution of the amount of oxygen for Cu(110) oxidation at 100°C as a function of oxidation time for different pO_2. The oxidation experiment starts with a clean Cu surface which is oxidized first at $p(O_2) = 1\times10^{-8}$ Torr. The surface shows an initial fast oxygen uptake followed by reduction in the rate to the saturated oxygen coverage of a 0.5 monolayer (ML), which signals the onset and development of the (2×1) added-row reconstruction induced by oxygen surface chemisorption, as shown in the *in situ* STM image (Fig. 2b). This (2×1) surface was found quite stable and inert towards further oxygen uptake with the prolong exposure to oxygen gas with two orders of magnitude increase in oxygen pressure. The oxygen uptake was observed to take place again on the same surface only after the oxygen pressure was raised to 1×10^{-5} Torr, which corresponds to the phase transitions from (2×1) to the (6×2) and then to the (1×1), as shown in Fig. 2(c, d).

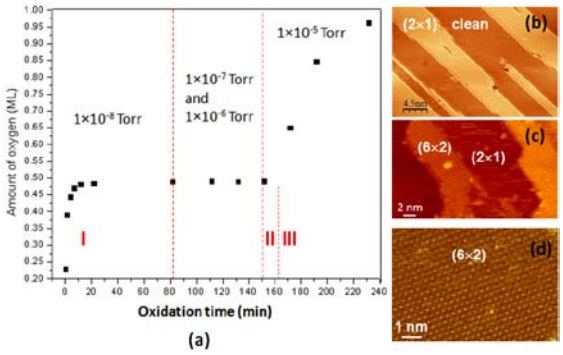

Fig. 2: (a) XPS measurements of the oxygen surface uptake as a function of time and pO_2. A stepwise increase in pO_2 is applied after reaching the saturated oxygen coverage. (b) STM image from region I, showing the nucleation/growth of (2x1) phase; (c) STM image from region II, showing (2×1) → (6×2) transition; (d) STM image from region III, showing the complete transition to (6×2).

The required significantly large oxygen pressure for the oxide formation is unexpected from the thermodynamics point of view. According to the well-known ASWS model [4, 5], the transition from a chemisorbed oxygen layer to the initial appearance of an oxide phase is controlled thermodynamically, i.e., the oxide growth should set in immediately as soon as it is thermodynamically possible. Bulk oxide formation on a flat surface is an activated process involving incorporation of oxygen into the subsurface region with massive restructuring of the oxygenated surface. Our results demonstrate that nucleation of a bulk oxide phase requires a critical oxygen pressure that can be many orders of magnitudes larger than the equilibrium oxygen pressure as predicted by the bulk or atomistic thermodynamics [6-8]. Such a kinetic hindrance to Cu_2O formation results in the enhanced stability of the oxygenated surface under the high oxygen pressure.

Step edge induced bulk oxide formation at thermodynamic equilibrium conditions

We found the kinetic hindrance to bulk oxide formation as described above vanishes when surface steps are present, leading to a completely different mechanism for the bulk oxide formation. Fig. 3(a) visualizes the growth of a monolayer of Cu_2O on the Cu(110)-(1x1) surface at T=350°C and $pO_2=5\times10^{-4}$ Torr, which is much closer to the Cu_2O /Cu(110)-(1×1) phase boundary of Fig. 1(f). Growth of the Cu_2O layer starts from the upper right corner and propagates rapidly along the Cu(110)-(1×1) surface. Rather than involving oxygen sub-surface penetration, the *in situ* TEM images show that the oxide grows via an adatom mechanism, i.e., Cu and O atoms are added onto the oxide growth front, where Cu adatoms are released from step edges and diffuse in by surface diffusion. Another evidence that the oxidation does not involve oxygen subsurface incorporation can be seen in Fig. 3(a), the oxygen-chemisorbed (1×1) structure remains intact after the Cu_2O layer covering, indicative of its non-participation in the oxide formation. Further evidence that the oxide growth occurs via adatom processes is provided by the retraction of steps upon the oxide growth, as shown in Fig. 3(b). We found that the oxide nucleates at the terrace-step corner and then propagates along the (100) terrace by incorporation of Cu adatoms detached from the step band. The *in situ* TEM observation reveals that the oxide forms directly on the (100) terrace and thickens via a layer-by-layer growth mode without oxygen subsurface incorporation, as evidenced by the immobile Cu_2O/Cu interface during the oxide growth.

We performed DFT calculation to understand why Cu atoms are not oxidized directly at step edges rather than being detached from the step edges and diffuse to the surface terrace for oxide growth. Our results indicate that oxygen atoms are bonded more strongly at surface terrace. We also found from our DFT results that the adsorption of oxygen atom on a step Cu atom results in significantly weakened bond strength of the Cu atom with its neighboring Cu, making Cu atoms more readily evaporating from step edges. Our results demonstrate that oxide formation for the presence of surface steps proceeds via precipitation of the solid oxide

phase from a fluid of mix phase consisting of O, Cu, and Cu-O precursors thermally diffusing across the surface, where Cu and Cu-O species evaporate from step edges. Such a process does not involve the surface restructuring for the bulk oxide formation and therefore brings the reaction to the thermodynamic conditions favored by the surrounding gas environments. The oxide growth by this mechanism deviates significantly from the long-held oxidation models of the solid-solid transformation via oxygen subsurface incorporation.

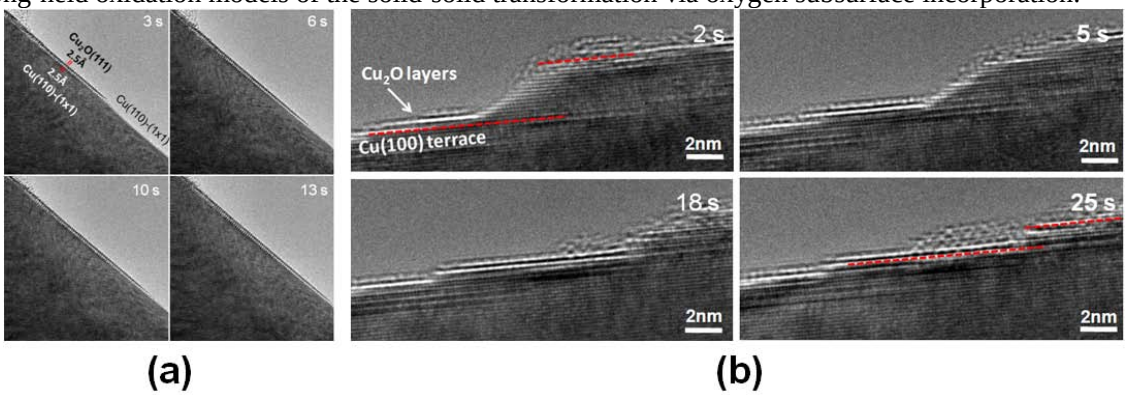

Figure 3: (a) *In situ* TEM observation of Cu_2O formation for the oxidation at 350°C and $pO_2=5\times10^{-4}$ Torr, (a) monolayer Cu_2O growth on the oxygen chemisorbed Cu(110)-(1×1) via an adatom mechanism, where adatoms of Cu and Cu-O species are supplied from step edges and diffuse in across the surface terrace, (b) layer-by-layer growth of Cu_2O on a Cu(100) terrace adjacent to a microfacet.

Dependence orientation of oxide nuclei on the oxygen pressure

The early stages of metal oxidation typically involve the nucleation and growth of oxide islands of bulk oxide phase, which are assumed to have thermodynamically controlled orientations. Using in situ TEM observations of the dependence of the degree of orientations of oxide nuclei on the oxygen pressure during the initial-stage oxidation of Cu(100) surfaces, we found that this is the case only if the metal surface is oxidized under a relatively low oxygen pressure, and increasing the oxygen pressure leads to nucleation of randomly oriented islands. As shown by the diffraction patterns in Fig. 4, our *in situ* TEM results demonstrates that the epitaxial nucleation of oxide islands cannot be maintained within the whole range of oxygen pressures, and a transition from nucleating epitaxial Cu_2O islands to randomly oriented oxide islands occurs with increasing pO_2 from 5×10^{-5} to 200 Torr. We developed a kinetic model, which shows that such a nucleation orientation transition is caused by the opposite effect (i.e., epitaxial vs. non epitiaxial) of oxygen pressure on the nucleation barrier and atom collision rates. Kinetically speaking, our results indicate that in order to obtain the epitaxial oxide film on the metal substrate by oxidation, the oxygen pressure should be relatively low. If the oxygen pressure is too high, the kinetics leads to a deviation of nucleating oxide islands from the orientation of the metal substrate and the epitaxial relation will be lost.

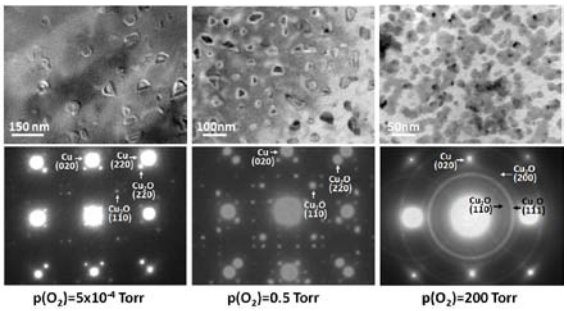

Fig. 4: Dependence of the orientation of Cu_2O nuclei on the oxygen pressure during the oxidation of Cu at 350°C. (Upper panel) Bright-field TEM images of Cu_2O islands formed on Cu(100) oxidized at 350° and different oxygen pressures for 10 min; (Lower panel) TEM diffraction patterns from the corresponding oxidized Cu(100) surfaces.

Future plans

We will continue to address a number of critical issues for controlling the oxide formation at the atomic level. A long-held assumption for oxide formation during metal oxidation is the solid-solid transformation, in which the nucleation of a bulk oxide phase requires a critical oxygen surface coverage followed by oxygen incorporation into the subsurface region. Such knowledge is obtained from surface science approaches that are mostly restricted to simple planar surfaces. However, both realistic surfaces and even

model single crystal surfaces are not completely perfect, but also exhibit with a certain amount of step edges or other low-coordinated surface sites. Thus, in order to gain a detailed understanding of the oxide formation under realistic conditions, one has to investigate the role of surface defects in the surface oxidation. Therefore, a major emphasis will be placed on bridging the materials gap by determining the mechanisms of surface defects including atomic defects such as steps, kinks, and vacancies and micro defects such as step bands and microfacets on the oxygen surface adosption, surface reconstruction, and bulk oxide formation.

Another area of work is to bridge the pressure gap for understanding the atomic mechanism of metal oxidation under realistic environmental condition. Over the past decades, surface science has gathered an unprecedented wealth of information about the oxygen-metal interactions from experiments of idealized conditions, i.e., ultrahigh vacuum (UHV). However, in many cases, the structure and reaction mechanisms of a surface in vacuum may differ from those under realistic conditions. For instance, increasing the oxygen pressure can not only result in new phases that do not exist at low pressure for thermodynamic reasons but may also promote reaction pathways that are insignificant at low pressures. Therefore, any extrapolation of UHV results to technological relevant pressures ranging from millitorr to atmospheres could naturally fail. We plan to employ *in situ* microscopy and spectroscopy techniques (e.g. high pressure TEM, STM and ambient XPS) to study surface oxidation from the initial oxidation stage of oxygen chemisorption to bulk oxide formation at the oxygen gas pressures that are many orders of magnitude higher than the conventional UHV experiments.

References

1 G. Ertl, H. Knozinger, F. Schuth, and J. Weitkamp, *Handbook of heterogeneous catalysis* (VCH-Wiley, Weinheim, Germany, 2008).
2 G. A. Somorjai and Y. Li, *Introduction to Surface Chemistry and Catalysis* (VCH-Wiley, Weinheim, Germany, 2010).
3 F. Tao and M. Salmeron, Science **331**, 171 (2011).
4 C. I. Carlisle, T. Fujimoto, W. S. Sim, and D. A. King, Surface Science **470**, 15 (2000).
5 W. A. Brown, R. Kose, and D. A. King, Chemical Reviews **98**, 797 (1998).
6 E. Lundgren, J. Gustafson, A. Mikkelsen, J. N. Andersen, A. Stierle, H. Dosch, M. Todorova, J. Rogal, K. Reuter, and M. Scheffler, Phys. Rev. Lett. **92**, 046101 (2004).
7 J. A. Eastman, P. H. Fuoss, L. E. Rehn, P. M. Baldo, G. W. Zhou, D. D. Fong, and L. J. Thompson, Appl. Phys. Lett. **87**, 051914 (2005).
8 G. W. Zhou, Phys. Rev. B **81**, 195440 (2010).

DOE Sponsored Publications from Current Grant

1 J.C. Yang, G.W. Zhou**,** "*In situ UHV TEM studies of early-stage oxidation of Cu and Cu Alloy thin films*", ***Micron*** (in press).
2 N. Cai, G.W. Zhou, K. Müller, D.E. Starr, "*Tuning the limiting-thickness of a thin oxide layer on Al (111) with oxygen gas pressure*", ***Physical Review Letters*** **107**, 035502 (2011)
3 L.L. Luo, Y.H. Kang, Z.Y. Liu, J.C. Yang, G.W. Zhou, "*A pressure gap in the nucleation orientations of oxide islands during the initial oxidation of metals*", ***Phys. Rev. B*** **83**, 155418 (2011)
4 L. Yuan, Y.Q. Wang, R. Mema, G.W. Zhou, "*The driving force and growth mechanism for spontaneous oxide nanowire formation during the thermal oxidation of metals*", ***Acta Materialia*** **59**, 2491 (2011)
5 L. Liang, G.W. Zhou, "*3D kinetic Monte Carlo simulations of crater growth during the reduction of oxide nanoislands on metal surfaces*", ***Surface Science*** **605**, 54 (2011)
6 G.W. Zhou, "*Nucleation induced kinetic hindrance to the oxide formation during the initial oxidation of metal surfaces*" ***Physical Review B*** 81, 195440 (2010)
7 L. Li, M. Xi, Y.F. Shi, G.W. Zhou, "*The precursor to the bulk oxide formation during the oxidation of Cu(100)*", **Physical Review Letters**, under final review
8 N. Cai, G.W. Zhou, K. Müller, D.E. Starr, "*Effect of oxygen gas pressure on the kinetics of alumina film growth during the oxidation of Al(111) at room temperature*", ***Phys. Rev. B*** (under review)
9 G.W. Zhou, L. Li, L.L. Luo, J. Ciston, E. Stach, J.C. Yang, "*Bridging the pressure and materials gaps of metal oxidation using in situ TEM atomic visualization*" (in preparation)
10 L.L. Luo, L. Li, J. Ciston, E. Stach, J.C. Yang, G.W. Zhou, "*Step edge induced oxide growth in the oxidation of Cu(100)*" (in preparation)

Atomic Layer Deposition (ALD) of Metal and Metal Oxide Films: A Surface Science Study

Francisco Zaera
zaera@ucr.edu
Department of Chemistry, University of California, Riverside, CA 92521

i) Program Scope

This project focuses on developing a molecular-level understanding of the thermal reactions that organometallic compounds used for atomic layer deposition (ALD) follow on surfaces. ALD is poised to become one of the dominant technologies for the growth of nanometer-sized conformal films in many industrial applications. In microelectronics in particular, the growth of diffusion, adhesion, and protection barriers and of metal interconnects is central to the buildup of diodes, transistors, and other elements within integrated circuits. All these processes require the deposition of isotropic films on complex topographies under mild conditions and with monolayer control. ALD is particularly suited to satisfy all those conditions, but many questions concerning the underlying surface chemistry need to be answer before it can find widespread use.

Our mechanistic studies of the ALD-related reactions is being pursued with the aid of a number of surface-sensitive techniques, including X-ray photoelectron (XPS), Auger electron (AES), low-energy ion scattering (LEIS), temperature programmed desorption (TPD), and infrared (IR) spectroscopies. Our initial focus has been on the study of processes for the deposition of metal interconnects and of metal nitride and metal oxide films, both central components in the microelectronics industry. Specific questions are being addressed in terms of the kinetics and mechanisms of the reactions involved, and also in connection with the composition and morphology of the resulting films. This knowledge will be directed to the design of ALD processes that operate under the mildest conditions possible and deposit stoichiometric and pure films with good density, low resistance, and smooth surfaces.

ii) Recent Progress

In the past year, we have made significant progress in developing an understanding on the surface reactions of both copper and tantalum nitride ALD processes. In terms of copper deposition, the thermal chemistry of copper(I)-*N,N'*-di-*sec*-butylacetamidinate on Ni(110) single-crystal and cobalt polycrystalline surfaces was characterized under ultrahigh vacuum (UHV) conditions by XPS and TPD [1]. A complex network of reactions were identified, starting with the dissociative adsorption of the precursor, from its dimeric form in its free state to a monomer once bonded to the nickel surface. The dissociation of a C–N bond in the acetamidinate ligand at ~200 K leads to the formation of adsorbed 2-butene and *N*-*sec*-butylacetamidinate. Some of the latter intermediate hydrogenate around 300 K to release *N*-*sec*-butylacetamidine into the gas phase, while the remaining adsorbed species dissociate further around 400 K, as the copper atoms become reduced to a metallic state, possibly to form acetonitrile and a *sec*-butylamido surface species that reacts further at 485 K to release 2-butene. By 800 K, only copper and a small amount of carbon can be seen on the surface by XPS. The essential steps of this mechanism are shown schematically in Figure 1.

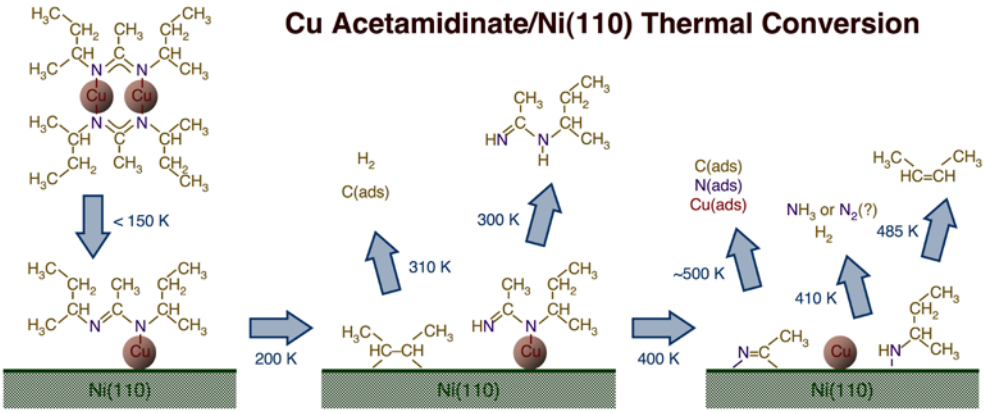

Figure 1. Schematic depiction of the main reactions proposed for the thermal chemistry of copper(I)-*N,N'*-di-*sec*-butylacetamidinate adsorbed on the nickel and cobalt surfaces.

The surface chemistry uncovered by our studies has some implications to the use of metal amidinates as precursors in thin film deposition by chemical means. Clearly, our results indicate that amidinate compounds are not as stable as desired when adsorbed on metal surfaces, and decompose at temperatures well below those used in ALD (typically between approximately 390 and 530 K). On the other hand, their initial decomposition, which starts at temperatures as low as 200 K, yields surface byproducts (*N*-*sec*-butylacetamidinate and 2-butene) that may still be eliminated cleanly upon subsequent reactions with molecular hydrogen, ammonia, water, or hydrogen sulfide (the second reactants used in these ALD processes). Moreover, since most of the organic matter may be eliminated in the form of *N*-*sec*-butylacetamidine in the first ALD half-cycle, the footprint of the adsorbed species should be greatly reduced, and deposition of more copper than what would be expected based on the surface area of the original precursor should be possible. We have shown by LEIS experiments that a significantly larger copper uptake can be reached upon dosing of copper(I)-*N,N'*-di-*sec*-butylacetamidinate at 350 K [2], a temperature above that require for *N*-*sec*-butylacetamidine desorption, than at 300 K.

Less clear is what may happen if the temperature used in ALD is high enough to promote the second set of reactions reported here. Our studies show that the copper atoms are reduced on the surface by 500 K. This observation brings into question the requirement of a reducing agent for the second half of the ALD cycles. It is our contention that the main role of the second ALD reactant may be to hydrogenate and/or desorb the organic fragments that may form on the surface during the precursor reactions in the first half of the ALD cycle, not to reduce the metal center, something that may have already taken place immediately upon adsorption. In connection with that, heating to ~400 K already results in the dissociation of the smaller *N*-*sec*-butylacetamidinate moiety formed at 200 K, possibly into nitrile and alkylamido surface species. It could still be possible to displace the nitrile from the surface by H_2 in the second half of the ALD process and also to hydrogenate the alkylamido species to the free alkylamine, but these reactions may be more difficult and may not occur to completion. However, by approximately 485 K, further dissociation of the alkylamido surface species occurs, releasing an olefin (butene in our case) and leaving NH_x species on the surface, adsorbates that would be quite difficult to remove. Finally, additional dehydrogenation occurs above ~500 K, and at that stage it would be certain that some carbon would be left behind on the growing metal film. By 480 K, the

deposition of copper films using the copper amidinate precursor along is no longer self-limiting, and continues indefinitely with increasing exposures [2]. That is a definitive threshold temperature to avoid the deposition of carbon impurities.

We have also made significant progress in our studies of metal nitride and oxide deposition. Two main accomplishes are worth reporting here. First, a novel G/MS approach was developed to characterize the thermal chemistry of key ALD precursors [3]. That approach was used to determine that tetrakis(dimethylamido) titanium (TDMAT) follows a number of competitive reactions, including not only the already known hydrogenation and β-hydride elimination steps, to produce dimethylamine and N-methylmethaneimine respectively, but also a new reductive elimination to yield tetramethylhydrazine and a more complex conversion to N,N,N'-tri-methyldiaminomethane and N,N,N',N'-tetra-methyldiaminomethane [4]. Typical data supporting these conclusions are shown in Figure 2. The latter reactions may account for the reduction of the metal when these compounds are used for the ALD of metal nitride films. Similar reactions take place with tetrakis(ethylmethylamido)titanium (TEMAT) and pentakis(dimethylamido)tantalum (PDMAT).

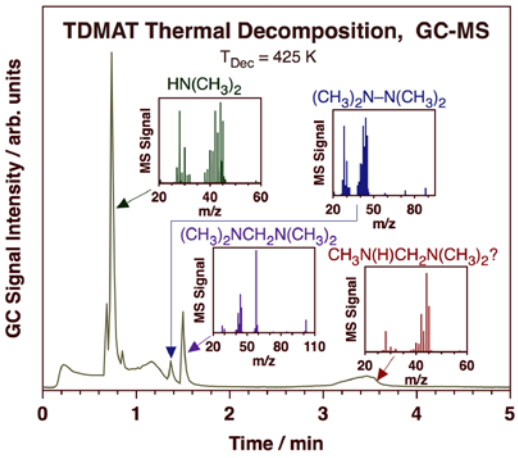

Figure 2. GC/MS characterization of the gas-phase products obtained from thermal activation of TDMAT at 425 K. The main frame reports the GC trace, whereas the insets correspond to the mass spectra of the products identified by each GC peak.

The second advance has been the incorporation of molecular beam techniques to follow the kinetics of these ALD reactions, specifically for the study of the surface chemistry of PDMAT on a Ta surface [5]. The results identified H_2, CH_4, C_2H_4, HCN, $HN(CH_3)_2$, and $H_2C{=}NCH_3$ as the main desorption species. Several reactions involving the amido ligands were observed on the Ta surface starting at about 450 K, including the expected hydrogenation to dimethylamine and β-hydride elimination to N-methyl methyleneimine as well as the decomposition to methane and hydrogen cyanide and a carbon-carbon forming step to yield ethylene. Addition of ammonia to the reaction mixture leads to an enhancement in hydrogenation to the amine at the expense of methane formation, but only at temperatures above approximately 550 K. Isotope labeling was used to establish that hydrogenation of the amido groups involves hydrogen atoms from the ammonia but methane formation occurs via intramolecular hydrogen transfer instead.

iii) Future Plans

In the next year, we plan to continue along the research directions already ongoing in this project. In terms of metal ALD, we intend to extend our initial studies on copper deposition to:

- Map out the surface chemistry of the copper amidinate precursors on the copper surfaces that are deposited by the ALD process. This chemistry is relevant to the build up of copper films beyond the first layer, irrespective of the initial surface used.

- Perform a comparative study with other precursors. An interesting candidate may be a Cu(I) precursor developed recently by Air Products known as Cu KI5. Another precursor of interest is $Cu(acac)_2$, to test the advantages and disadvantages of using Cu(I) vs. Cu(II) precursors.

In terms of the deposition of metal nitrides and metal oxides, some new directions include:

- The evaluation of the effect of (photon and electron) irradiation on the decomposition of adsorbed ALD precursors. We have seen some indication recently that this may be a significant factor, and, if so, it is worth evaluating in terms of its potential use in lithographic applications.
- The comparative study of the surface reactivity of amido precursors in terms of their metal center (Ti, Zr, Hf, Ta) and of the amido ligands (dimethyl, methyethyl, diethyl). Additional comparative studies will be carried out to establish the relative reactivity of those precursors with ammonia (for nitride deposition) versus water (for oxides).

In addition, we propose to develop our GC/MS approach to the study of the thermal chemistry of ALD precursors further. We plan to extend this experimental approach to other precursors and moieties, including compounds with the organic ligands often used for deposition of late transition metals.

iv) References

[1] Q. Ma, H. Guo, R. G. Gordon, F. Zaera, Chem. Mater. (2011) doi 10.1021/cm200432t.
[2] Q. Ma, H. Guo, R. G. Gordon, F. Zaera, Chem. Mater. 22 (2010) 352.
[3] M. Bouman, F. Zaera, ECS Trans. 33 (2010) 291.
[4] M. Bouman, F. Zaera, J. Electrochem. Soc. 158 (2011) D524.
[5] T. Kim, F. Zaera, J. Phys. Chem. C 115 (2011) 8240.

v) DOE-Sponsored Publications, This Grant, 2010-2011

1. Qiang Ma, Hansheng Guo, Roy G. Gordon, and Francisco Zaera, Uptake of Copper Acetamidinate ALD Precursors on Nickel Surfaces, *Chem. Mater.*, **22(2)**, 352–359 (2010).
2. Menno Bouman and Francisco Zaera, The Surface Chemistry of Atomic Layer Deposition (ALD) Processes for Metal Nitride and Metal Oxide Film Growth, *ECS Trans.*, **33(2)**, 291-305 (2010).
3. Tauseung Kim and Francisco Zaera, Surface Chemistry of Pentakis(dimethylamido)tanalum on Ta surfaces, *J. Phys. Chem. C*, **115(16)**, 8240–8247 (2011).
4. Menno Bouman and Francisco Zaera, Reductive Eliminations from Amido Complexes, *J. Electrochem. Soc.*, **158(8)**, D524-D526 (2011).
5. Qiang Ma, Roy G. Gordon, and Francisco Zaera, Surface Chemistry of Copper(I) Acetamidinates in Connection with Atomic Layer Deposition (ALD) Processes, *Chem. Mater.*, in press, doi 10.1021/cm200432t (2011).

Studies of Surface Reaction Mechanisms in Atomic Layer Deposition

Stacey F. Bent
sbent@stanford.edu
Department of Chemical Engineering
Stanford University, Stanford, CA 94305

i) Program Scope

Atomic layer deposition (ALD) promises to be an enabling technique for creating the innovative nanostructured materials needed for future applications, including those in solar energy and photoelectrocatalysis. However, molecular-level knowledge of ALD mechanisms is generally poorly known. In this project, we perform studies to uncover molecular level mechanisms and nucleation processes active during ALD. A combination of *in situ* and *ex situ* spectroscopies together with modeling studies are employed. The research examines both metal oxide and metal ALD systems, including TiO_2 and Pt. Studies of TiO_2 ALD have focused on elucidating the role of the substrate in controlling the ALD processes as a function of temperature. Studies of Pt ALD have examined the nucleation sites and nucleation mechanism for this system. The scope of the project is to develop the framework of governing principals for ALD nucleation and growth. Fundamental advances in the understanding of the surface chemistry and materials deposition will provide the scientific foundation important to a wide range of applications, including energy-relevant technologies.

ii) Recent Progress

Our initial *in situ* x-ray photoelectron spectroscopy (XPS) studies showed that the initial growth rate of TiO_2 ALD on hydroxyl-enriched silicon dioxide (SiO_2) is higher than on hydrogen-terminated silicon [1]. Moreover, the growth rate is accelerated during the first several ALD cycles on both surfaces. Chlorine incorporates into the TiO_2 films on both surfaces and is found to concentrate near the Si/TiO_2 interface.

To further understand the nature of the surface nucleation sites on silicon oxide for TiO_2 ALD, *in situ* XPS studies were carried out with different surface hydroxyl concentration by varying the substrate temperature. The results show that the initial adsorption of $TiCl_4$ on silicon oxide surfaces decreases with the pre-anneal temperature of the silicon wafer (Figure 1a). Furthermore, the sample annealed at higher temperature contains larger amount of chlorine contamination, possibly due to the reduction of hydroxyl group on the silicon surface after high temperature treatment (Figure 1b). Interestingly, raising the operating temperature of ALD process seems to reduce the amount of Cl impurities in the deposited TiO_2 film.

With Pt ALD, our studies have focused on understanding and ultimately controlling the nucleation process. Pt ALD is very sensitive to the underlying substrate, with nucleation being

sensitive to factors such as surface hydrophobicity and the presence of nucleation active sites. We have carried out a series of studies in which the Si substrate was intentionally deactivated toward Pt ALD using organic self assembled monolayers (SAM), as a means of leaving only discrete nucleation sites. Defects in the SAM resulting from incomplete formation time in solution were shown to act as nucleation sites for ALD [2]. The subsequent ALD process can lead to deposition of nanoparticles instead of a continuous film, as seen in Figure 2a. Post-ALD analysis, including XPS, scanning electron microscopy and scanning Auger electron spectroscopy, was used to determine nanoparticle density and size. We have shown that for a fixed number of Pt ALD cycles, nanoparticle aerial density decreases with increasing deactivation of the surface. For increasing numbers of Pt ALD cycles, average nanoparticle diameter increases together with the aerial density of the nanoparticles (Figure 2b), suggesting that new nucleation sites may appear during the process. The decrease in density and large increase in diameter after 200 cycles reflects coalescence of the Pt islands. The total number of Pt atoms per surface area has been calculated from the SEM data and the results are shown in Figure 2c. The data are suggestive of island growth within confined nucleation sites. Isothermal nucleation and growth models are being used to analyze the experimentally-measured nucleation behavior of Pt ALD.

iii) Future Plans

We are completing fabrication of an *in situ* infrared spectrsocopy/ALD system for mechanistic studies of atomic layer deposition. This system, together with our *in situ* XPS instrument will be used in conjunction with complementary *in situ* photoemission and x-ray scattering studies at the Stanford Synchrotron Radiation Lightsource (user proposal pending at SSRL) to carry out experimental studies of ALD nucleation and growth. In addition to continuing to explore the mechanism of TiO_2 and Pt ALD, we will carry out studies of Ru/RuO_2 ALD. The results of the TiO_2 studies will help to elucidate the ALD reaction intermediates and mechanisms during the initial cycles of ALD and allow us to find conditions to control the growth and impurity content of TiO_2 film. Nucleation and growth modeling of Pt ALD will be completed to provide insight into nucleation phenomena in metal ALD. The Ru/RuO_2 ALD studies will focus on a comparison between the growth mechanisms for different Ru precursors, which earlier have been shown to exhibit different nucleation behavior. We will explore the change of surface chemistries occurring during the nucleation process on different surface materials. The results from the Pt and Ru studies are intended to help us to discover strategies for enhancing the nucleation of metal ALD on non-metal surface for production of uniform ultra-thin films, which remains a key challenge in ALD.

iv) References

[1] R. Methaapanon and S. F. Bent, *J. Phys. Chem. C*, **114** (2010) 10498-10504.

[2] R. Chen and S. F. Bent, *Chem. Mater.*, **18** (2006) 3733-3741.

v) Publications resulting from work supported by the DOE project over the last two years

No publications to date.

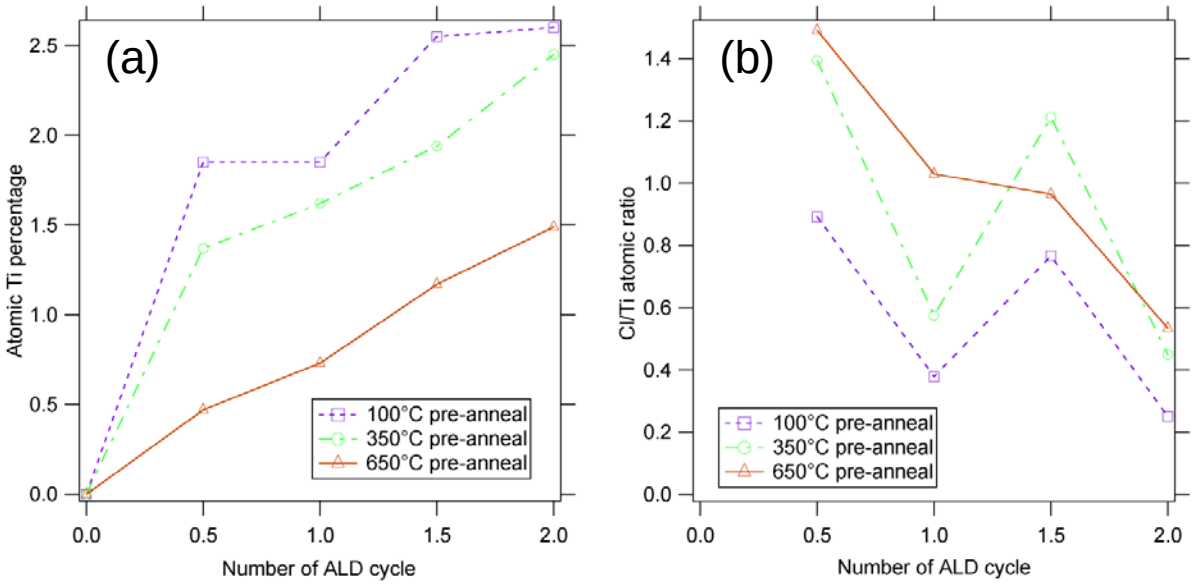

Figure 1. Results of *in situ* XPS studies as a function of ALD half-cycle during TiO_2 ALD on SiO_2-terminated Si substrates showing (a) atomic Ti percentage and (b) Cl/Ti atomic ratio. Data are shown for three different substrate pre-anneal temperatures.

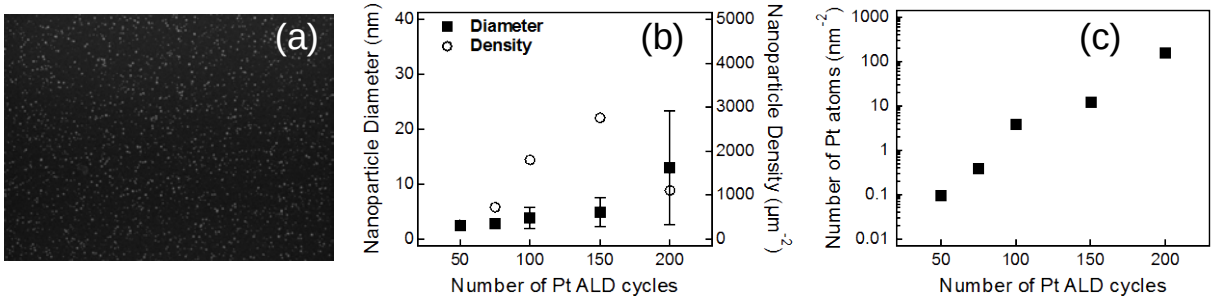

Figure 2. Results of nucleation studies of Pt ALD. (a) SEM image of Si substrate deactivated by a SAM after 100 cycles of Pt ALD; (b) Average diameter and aerial density of Pt nanoparticles versus number of Pt ALD cycles; (c) Calculated number of Pt atoms per area versus number of Pt ALD cycles.

This page is intentionally blank.

Poster Session II

This page is intentionally blank.

Utilizing Molecular Self-Assembly to Tailor Electrical Properties of Si Nanomembranes

Pengpeng Zhang
zhang@pa.msu.edu
Department of Physics and Astronomy
Michigan State University, East Lansing, MI 48824

Program Scope

The ability to control the synthesis of materials with nanometer precision has the potential to revolutionize technology. However, the utility of engineered nanomaterials for important applications such as photovoltaics, nanoscale electronic devices, and molecular/biological sensors has in many cases been severely limited by interfacial phenomena that emerge at the nanoscale. It is thus crucially important to develop a thorough physical understanding and a precise control of surfaces and interfaces, providing fundamental insights which may lead to the rational design of nanomaterials with desired properties via regulation of surfaces and interfaces. In this grant supported by the DOE Early Career Research Program, we will study the surface and interface chemical functionalization and its effects on the electronic structure and transport properties of silicon nanomembranes. We will as well address the critical issues of charge injection, distribution and separation at hetero-interfaces using scanning probe microscopy techniques in conjunction with electrical transport measurements.

Background

Si nanomembranes, a novel class of materials that combine many of the useful properties of semiconductors with the excellent mechanical properties of soft materials, find promising applications in flexible nanolectronic devices and solar cells.[1,2,3] Yet, the electronic properties of Si nanomembranes can not be effectively tuned by the bulk impurity dopants. In contrast to the conduction mechanisms in bulk Si, which is entangled between surface, space charge layer, and bulk,[4] the conductivity of Si nanomembranes is dominated by the surface and interface effects.[5]

We are interested in exploiting surface chemistry to tailor the electronic properties of Si nanomembranes via engineering the band structure or the distribution of charge. Since the carrier-density distribution in Si nanomembranes is sensitive to the surface boundary condition, e.g., electrical potential at the surface, membrane's transport characteristics will be influenced by the surface dipole layer. Meanwhile, changes in the net surface charge density due to the electronegativity of adsorbed molecules or the interaction between frontier molecular orbitals and the Si band edges may lead to a charge doping effect to Si nanomembranes. In addition, molecular adsorption on the Si nanomembrane surface might introduce local defects. If these

defects have density of energy levels inside the Si band gap, they can trap mobile carriers and influence the electrical conductivity of the membrane.

Future Plans

The specific aims are to 1) probe electronic structure of the hetero-interface and transport properties of Si nanomembranes by developing a comprehensive tool set in an UHV system, including scanning probe techniques and an *in-situ* back-gated van der Pauw setup at variable temperatures. Scanning tunneling microscopy and spectroscopy will be utilized to determine both the geometry of the molecular adsorption and the electronic structure of the molecule-substrate junction. QPlus tuning fork AFM and its Kelvin probe technique will help us understand charge transfer at the hetero-interface. To evaluate the effects of surface chemical functionalization on electronic properties of Si nanomembranes, we will conduct *in-situ* transport measurements. These experimental efforts will be complemented by density functional theory through collaborations with colleagues at Michigan State University, to establish the understanding of electrostatic interactions at the hetero-interface and to guide the development of self-assembly from individual molecules to multiple functionalizations.

2) Examine the mechanism of electronic interactions between molecular adsorbates and Si nanomembranes, and explore methodologies to modify Si nanomembrane's transport behaviors via engineering the band structure or distribution of charge. Our approaches for the surface chemical treatment will involve dipole interactions and charge doping effects by grafting molecules with strong dipole moments for the control of dipole interactions or molecules with the closely-lying molecular orbitals to the valence or conduction band edges of Si membrane to facilitate charge injection or charge transfer between the surface and the membrane. Particular emphasis will be devoted to the supramolecular assembly strategy, which has been recently demonstrated to be compatible with the Si surface after it is properly deactivated by incorporating subsurface boron atoms.[6]

3) Investigate the principles of supramolecular assembly on Si surfaces, in particular, how the mutual electronic interaction and charge transfer at the hetero-interface influence the molecular specific adsorption and diffusion on surfaces, and furthermore exploit hierarchy multifunctional supramolecular assembly schemes to control electronic properties of Si nanomembranes at the molecular scale. Supramolecular assembly is a versatile technique. We will explore the growth of periodic molecular structures on Si surfaces by means of controlling the delicate balance between molecule-molecule interactions and molecule-substrate interactions. In addition, through molecular design and synthesis, a robust and tunable nanoporous template may be fabricated to guide the deposition of "guest" molecules, thus creating diverse surface chemical functionalities with molecular scale precision.[7] The aforementioned features can be exploited to tailor the electronic properties of Si nanomembranes through the desired molecule-substrate interaction, e.g., dipole interaction or charge doping. The innovative techniques of

supramolecular assembly will likely lead to transformative approaches to control the molecular engineering of Si nanomembrane and its electrical properties to an unprecedented extent.

[1] M. M. Roberts, L. J. Klein, D. E. Savage, K. A. Slinker, M. Friesen, G. Celler, M. A. Eriksson, and M. G. Lagally. Elastically Relaxed Free-Standing Strained-Silicon Nanomembranes. *Nat. Mater.* **5**, 388 (2006).
[2] D. Y. Khang, H. Jiang, Y. Huang, and J. A. Rogers. Silicon for High-Performance Electronics on Rubber Substrates. *Science* **311**, 208 (2006).
[3] J. Yoon, A. J. Baca, S. Park, P. Elvikis, J. B. Geddes III, L. Li, R. H. Kim, J. Xiao, S. Wang, T. Kim, M. J. Motala, B. Y. Ahn, E. B. Duoss, J. A. Lewis, R. G. Nuzzo, P. M. Ferreira, Y. Huang, A. Rockett, and J. A. Rogers. Ultrathin Silicon Solar Microcells for Semitransparent, Mechanically Flexible and Microconcentrator Module Designs. *Nat. Mater.* **7**, 907 (2008).
[4] J. W. Wells, J. F. Kallehauge, T. M. Hansen, and Ph. Hofmann. Disentangling Surface, Bulk, and Space-Charge-Layer Conductivity in Si(111) – (7x7). *Phys. Rev. Lett*. **97**, 206803 (2006).
[5] P. P. Zhang, E. Tevaarwerk, B. N. Park, D. E. Savage, G. K. Celler, I. Knezevic, P. G. Evans, M. A. Eriksson, and M. G. Lagally. Electronic Transport in Nanometre-Scale Silicon-on-Insulator Membranes. *Nature* **439**, 703 (2006).
[6] Y. Makoudi, F. Palmino, M. Arab, E. Duverger, and F. Chérioux. Complete Supramolecular Self-Assembled Adlayer on a Silicon Surface at Room Temperature. *J. Am. Chem. Soc*. **130**, 6670 (2008).
[7] R. Madueno, M. T. Räisänen, C. Silien, and M. Buck. Functionalizing Hydrogen-Bonded Surface Networks with Self-Assembled Monolayers. *Nature* **454**, 618 (2008).

I. Group IV Semiconductor Nanomembranes: New Properties through Novel Synthesis and Strain Engineering

Max G. Lagally and Mark A. Eriksson
Lagally@engr.wisc.edu
University of Wisconsin-Madison, Madison WI 53706

Program scope

Semiconductor nanomembranes, very thin crystalline sheets with thicknesses ranging from less than 5 nm to ~500nm, represent a vehicle for both significant scientific discoveries and for energy related nanotechnologies. They are flexible, can be freestanding or transferred to other hosts, or can be layered to put crystalline materials next to each other that nature would not allow, yet with almost ideal interfaces. They can be strain engineered so that they contain localized periodic strain or roll into tubes or other shapes. They can be lithographically patterned into nanowires and hybrid structures.

With appropriate synthesis and processing, dramatically new or changed mechanical, electronic, and thermoelectric properties can be induced. Functionally new materials can be made. Surfaces now play a leading role, because of the high surface-to-volume ratio. Photonic, phononic, and electro-optic properties can be affected by appropriate strain engineering and patterning.

Our program addresses a broad spectrum of synthesis, processing, and characterization themes in Group IV semiconductors (specifically Si and Ge, although what is stated above should be generally true for other semiconductor nanomembranes). Specifically our interests have focused on 1) strain engineering and the use of strain to modify properties in very thin sheets or ribbons; 2) integration of membranes via transfer, bonding, and growth to create new properties; 3) novel characterization and development of tools and methods therefore, particularly structural and electronic transport; 4) theoretical interpretation and prediction via collaboration with Feng Liu (Utah) and theorists locally; and 5) exploring the use of nanomembranes to address grand challenges as envisioned by DOE-BES.

Recent Progress

We have expanded several directions listed in the summary 2 years ago, completed some others, and added new ones, focused on Si and Ge nanomembranes. They include development of new materials using nanomembrane technology; use of strain to modify properties; new charge transport characterization; new defect studies; and theoretical efforts to aid understanding of experiments. Since the last PI meeting, we have published or submitted 26 papers wholly or partially supported by this program. New directions include

- Use of thin membranes as a strain gauge in understanding stress evolution in growing films.
- UHV charge transport measurement system for new spectroscopy to investigate fundamental aspects of surface structure and chemistry and their influence on surface and interface electronic structure.
- Mechanical stress of Ge to make it direct-bandgap and thus possibly emit light.
- Processing periodically bent membranes for possible coherent light emission.
- New materials through membrane processing: structurally perfect SiGe as a growth substrate.

Below are brief descriptions of recent results:

1. **Use of SiNM as a strain gauge:** Deposition of a thin film onto a substrate in general produces stress in both the stressor and the substrate. The stresses are of the opposite sign to maintain equilibrium. Because na-

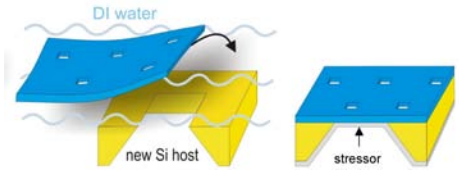

Figure 1. Geometry for NM strain gauge experiment. The NM is placed over a window etched into Si and a stressor layer is deposited underneath.

nomembranes (NMs) are so thin, they are flexible and sensitive to changes in strain at the surface. If one deposits a stressor film (essentially any Volmer-Weber or Stranski-Krastanov film) on a NM, its ability to accept strain means that the stress state in the growing film will change dynamically during growth. Mechanisms for how stress changes during deposition when the substrate is compliant are not understood. Figure 1 shows the experimental arrangement schematically. Because one can sensitively measure strain in Si with Raman spectroscopy, we will be able to measure stress as a function of NM thickness. Initial results show expected trends with thickness, but quite wrong magnitudes, implying that mechanical properties of the growing film are changing. The method is effectively a micro strain gauge with lateral resolution of the order of 100s of nanometers.

2. **Mechanical stress in Ge nanomembranes**: Strain influences band structure and, as we demonstrated on Si, a high degree of strain can be induced in NMs and therefore significant changes in band structure occur. Conduction band valleys move in energy differently with strain, and strain can in principle make Ge direct-band-gap because the relevant valley moves more rapidly in energy than the indirect valley. We have, we believe, stretched Ge NMs sufficiently to make then direct-gap. Figure 2 shows the experimental setup, the strain vs pressure curves for different Ge NM thicknesses, and the shifts in photoluminescence spectra with increasing strain.

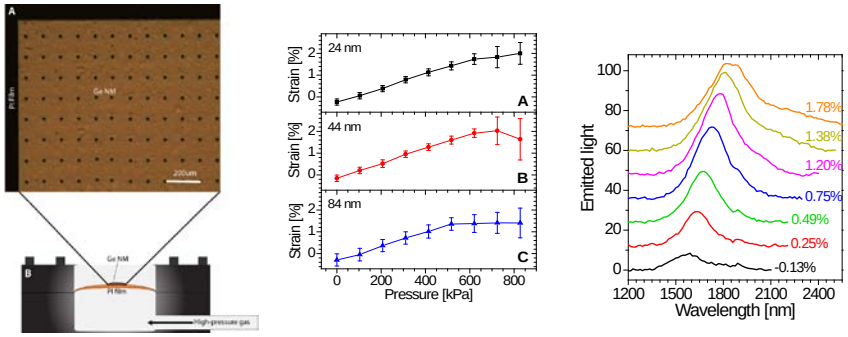

Figure 2. Device for mechanically stretching Ge. Data for straining Ge NMs of different thicknesses. Photoluminescence data for different strains.

3. **Surface modified electronic transport in SiNMs:** We have initial results for charge transport measurements using our UHV system. With very thin membranes, the surface begins to dominate the bulk. In UHV it is possible to produce the baseline conditions, a truly clean surface with the corresponding surface reconstruction (here Si(001) p2x1). Using van der Pauw measurements with a back gate one can effectively produce a spectroscopy of surface states; the bulk is relatively unim-

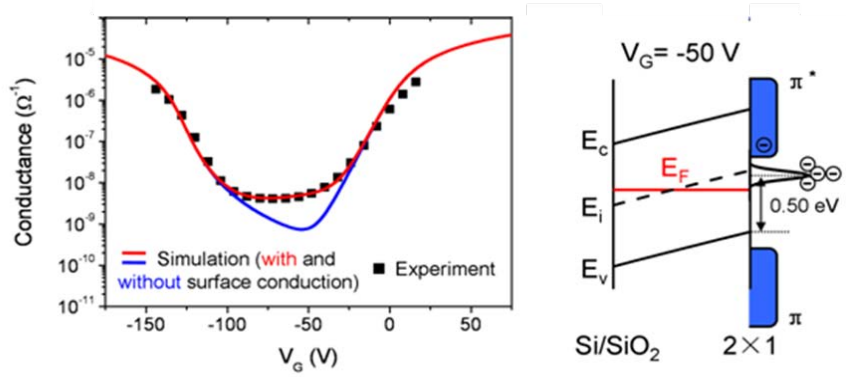

Figure 3. Conductance of a 120nm thick Si NM as a function of back gate voltage. The data demonstrate the influence of conductance through the dimer-row induced surface band on clean Si(001).

portant because the NM is so thin. We have been able to determine the conductance and mobility of electrons through the dimer row induced surface band in Si(001)

Future work

It should be evident that the opportunities for novel energy-related science are legion with nanomembranes. We finished a number of projects in the last year. We will continue to address NM layering and vertical transport, with an eye toward novel photovoltaic approaches. The projects described and listed here are all very new and will be continued. We will begin more complex growth schemes (via both CVD and MBE), in particular extending the design of novel crystals following on our success of making defect-free SiGe crystals, something not possible with bulk materials, but also growing multilayer structures by CVD to attempt to make structures that may be useful for light emission in SiGe systems. Our efforts in thermoelectrics are at a stage of measuring thermal conductivity in NMs. We expect to be able to make a significant contribution there in the future.

Selected publications supported by this grant in the last two years

1. "Relationships between Strain and Band Structure in Si(001) and Si(110) Nanomembranes", C. Euaruksakul, F. Chen, B. Tanto, C. S. Ritz, D. M. Paskiewicz, F. J. Himpsel, D. E. Savage, Zheng Liu, Yugui Yao, Feng Liu, and M. G. Lagally, Phys. Rev. B80, 115323 (2009).
2. "Nanostructure Formation in the Initial Roughening of a Thin Silicon Sheet", S. Seo, C. Euaruksakul, D. E. Savage, M. G. Lagally, and P. G. Evans, Phys. Rev. B81, 041302(R) (2010).
3. "New Strategy for Synthesis and Functionalization of Carbon Nanoparticles", H.Q. Jiang, F. Chen, M.G. Lagally, and F. S. Denes, Langmuir 26, 1991 (2010).
4. "Semiconductors Turn Soft: Inorganic Nanomembranes", Francesca Cavallo and M. G. Lagally, Soft Matter 6, 439 - 455 (2010) (invited).
5. "Effect of Surface Bonding on Semiconductor Nanoribbon Wiggling Structure", Y. Zhang, M. Yu, D. E. Savage, M. G. Lagally, R. H. Blick, and Feng Liu, Appl. Phys. Letters 96, 111904 (2010).
6. "Quantum Confinement, Surface Roughness, and the Conduction Band Structure of Ultrathin Silicon Membranes", Feng Chen, E. B. Ramayya, C. Euaruksakul, F. J. Himpsel, B.-J. Ding, I. Knezevic, and M. G. Lagally, ACS Nano 4, 2466 (2010).
7. "Electronic Phase Diagram of Silicon Single-Element Lateral 'Strain' Superlattice", Zheng Liu, Jian Wu, Wenhui Duan, M. G. Lagally, and Feng Liu, Phys. Rev. Letters 105, 016802 (2010).
8. "Nanoepitaxy in the Presence of Lattice Strain: Quantum Dots and Strain Engineering of Nanomembranes in the Silicon Model System", M.G. Lagally, AIP Proceedings of 14th International Summer School on Crystal Growth, Volume 1270, 316 (2010).
9. "Ordering of Nanostressors on Freestanding Silicon Nanomembranes and Nanoribbons", C. S. Ritz, H.J. Kim-Lee, D.M. Detert, M.M. Kelly, F.S. Flack, D.E. Savage, Z.H. Cai, P.G. Evans, K.T. Turner, and M.G. Lagally, New J. Phys. 12, 103011 (2010).
10. "Elastically Strain-Sharing Si(110) Nanomembranes", D. M. Paskiewicz, S. A. Scott, D. E. Savage, and M. G. Lagally, ECS Transactions 33, 813 (2010).
11. "Thermoelectric Power Factor Enhancement in Gated Silicon Nanostructures", Hyuk Ju Ryu, Zlaten Aksamija, D.M. Paskiewicz, S.A. Scott, M. G. Lagally, I. Knezevic, M. A. Eriksson, Phys.Rev. Letters 105, 256601 (2010).

12. “Nanomechanical Architecture of Semiconductor Nanomembranes”, M.H. Huang, F. Cavallo, Feng Liu, and M. G. Lagally, Nanoscale 3 (1), 96 – 120 (2011) (invited).
13. “Wafer-scale Integrated Freestanding Single-crystal Silicon Nanowires: Conductivity and Surface Treatment”, C-H Lee, C. S. Ritz, M.H. Huang, M. Ziwisky, R. Blise, and M. G. Lagally, Nanotechnology 22, 055704 (2011).
14. “Si/Ge Junctions Formed by Nanomembrane Bonding”, A.M. Kiefer, D. M. Paskiewicz, A.M. Clausen, W.R. Buchwald, R. A. Soref, and M. G. Lagally, ACS Nano 5, 1179 (2011).
15. “Si/SiGe Quantum Dot with Superconducting Single-Electron Transistor Charge Sensor”, Mingyun Yuan, Feng Pan, T. J. Gilheart, Zhen Yang, Fei Chen, D. E. Savage, M.G. Lagally, M. A. Eriksson, and A. J. Rimberg, Appl. Phys. Letters 98, 142104 (2011).
16. “Influence of Surface Properties on the Electrical Conductivity of Silicon Nanomembranes”, X-F. Zhao, S.A. Scott, M.H. Huang, W. Peng, A.M. Kiefer, F.S. Flack, D.E. Savage, and M.G. Lagally, Nanoscale Research Letters 6, 402 (2011) DOI: 10.1186/1556-276X-6-402.
17. “Semiconductor Nanomembranes: A Platform for New Science and Technology”, M. G. Lagally, A.M. Kiefer, D. M. Paskiewicz, F. Cavallo, S. A. Scott, Z.Q. Ma, and D. E. Savage. Proceedings of SPIE Vol. 8031 (2011) ISBN: 9780819486059. DOI: 10.1117/12.884810.
18. "Single-Shot Measurement and Tunnel-Rate Spectroscopy of a Si/SiGe Few-Electron Quantum Dot", M. Thalakulam, C. Simmons, B. Van Bael, B. Rosemeyer, D. E. Savage, M.G. Lagally, M. Friesen, S. Coppersmith, and M.A. Eriksson, Phys. Rev. B 84, 045307 (2011).
19. “Fabrication of Ultra-high Density Nanowires by Electrochemical Nanolithography”, Feng Chen, Hongquan Jiang, A.M. Kiefer, A.M. Clausen, Y.-H. Ting, A.E. Wendt, Bingjun Ding, and M.G. Lagally, Nanoscale Research Letters 6, 444 (2011).
20. “Symmetry in Strain Engineering of Nanomembranes: Making New Strained Materials”, D. M. Paskiewicz, S.A. Scott, D. E. Savage, G. K. Celler, and M.G. Lagally, ACS Nano 5, 5532 (2011).
21. “Defect-Free Single-Crystal SiGe: A New Material from Nanomembrane Strain Engineering”, D. M. Paskiewicz, B. Tanto, D. E. Savage, and M.G. Lagally, ACS Nano 5, 5814 (2011).
22. “Conduction Band Structure and Electron Mobility in Uniaxially Strained Si via Externally Applied Strain in Nanomembranes”, Feng Chen, Chanan Euaruksakul, Zheng Liu, Franz Himpsel, Feng Liu, and Max G. Lagally, J. Phys. D 44, 325107 (2011).
23. “Electron Tunneling Induced Periodic Nucleation and Growth of Nanoparticles: Physical Basis of Chemical Reduction”, Chen, Feng; You, Hongjun; Yang, Shengchun; Yang, Zhimao; Song, Xiaoping; Lagally, Max; Ding, Bingjun, Crystal Growth and Design, web published July 2011.
24. “Semiconductor Nanomembranes: Synthesis, Assembly, and Applications”, J.A. Rogers, M.G. Lagally, and R.G. Nuzzo, Nature, in press (invited review)
25. “Direct-bandgap infrared light emission from tensilely strained germanium nanomembranes”, F. Chen, C. Boztug, J. R. Sanchez-Perez, F. Sudradjat, D. M. Paskiewicz, R. B. Jacobson, R. Paiella, and M. G. Lagally, PNAS submitted.
26. “Stabilizing Graphitic Thin Films of Wurtzite Materials by Epitaxial Strain”, Dangxin Wu, M. G. Lagally, and Feng Liu, Phys. Rev. Letters submitted.

Integrated growth and ultra-low temperature transport study of the 2nd Landau level of the two-dimensional electron gas:

Principal Investigators: Gabor Csathy and Michael Manfra
Institution: Purdue University
Address: 525 Northwestern Ave., West Lafayette, IN 47907
E-mail of PIs: gcsathy@purdue.edu, mmanfra@purdue.edu

Program Scope

Our primary focus is the study of the fractional states of the second Landau level, corresponding to Landau level filling factors $2 \leq \nu \leq 4$. There is mounting theoretical and experimental evidence that several fractional Quantum Hall States in this region are not well described by the model of non-interacting composite fermions. For example, the even denominator state at $\nu=5/2$ may result from an unusual pairing mechanism of the composite fermions described by the Pfaffian wavefunction. Because the pairing is believed to be *p*-wave, the 5/2 state may resemble other condensed matter systems of current interest such as strontium ruthenate, certain fermionic atomic condensates, and the quantum liquid He-3.

The study of the 5/2 state has been reenergized with the prediction that its excitations obey exotic non-Abelian statistics. The $\nu=5/2$ and other novel states in the 2nd LL are not only of fundamental interest as they may manifest behavior not seen in any other physical system, but also may find technological utility in fault-tolerant schemes for quantum computation. These exotic states are, however, fragile and hence they develop only in the highest quality GaAs host crystals.

Historically advances in our understanding of the fractional quantum Hall effect proceed hand-in-hand with improvements in the fabrication of higher quality two-dimensional electron gases in GaAs. **Understanding and controlling disorder introduced in the growth process of GaAs heterostructures is a central theme of our planned work**. Indeed, it is becoming increasingly clear that we need understand in detail the different types of disorder introduced during by growth and their resulting impact on the formation of correlated electronic ground states if we are ever to make progress with solid-state quantum computation.

Building on a recently established combination of expertise and infrastructure at Purdue University, we will carry out an integrated growth and experimental study of the two-dimensional electron gas in GaAs in the 2nd LL. We plan to use incisive techniques that are expected to offer new insight into the nature of the exotic correlated states of the 2nd LL. We will focus on:

1) Growth of ultra-high quality GaAs/AlGaAs heterostructures specifically tailored to study the impact of various growth parameters on the stability of the fractional quantum Hall ground states in the 2nd LL.

2) Application of novel techniques together with transport measurements in the most interesting but technologically difficult ultra low temperature regime (T~5mK). As this regime is still largely unexplored, new and unanticipated results can be expected.

Recent Progress

This project builds on the ongoing collaboration at Purdue University established over the last two years. *Our team has recently developed a unique combination next generation growth and measurement capabilities needed to address several of the outstanding problems in the field of 2D electron physics.* Such a work calls for a highly focused and in house collaboration between sample design and growth specifically tailored to our experimental objectives and state-of-the-art ultra low temperature measurement capabilities.

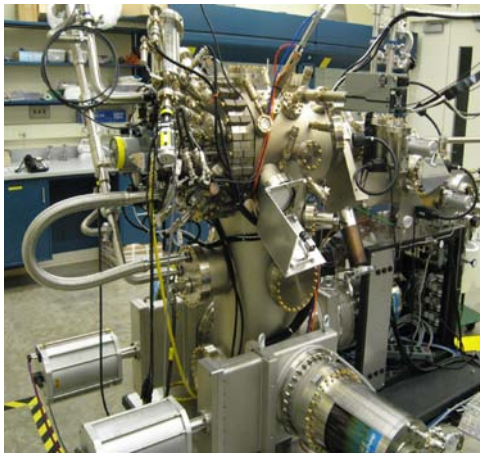

Fig.1. Manfra's custom-designed MBE installed at Purdue. Based on Manfra's 10+ years experience in high mobility semiconductor growth, this new machine will produce samples specifically tailored for our experiments.

Manfra has designed and built a highly customized MBE chamber designed for the growth of high mobility GaAs/AlGaAs heterostructures at the Birck Nanotechnology Center at Purdue University (see Figure 1). Highlights of his new machine include: 1) vastly increased pumping capacity as compared to standard commercial MBE systems, 2) modification of standard effusion cell design to increase thermal efficiency and minimize outgassing of undesirable impurities, 4) the addition of increased cyropaneling around the cells to trap impurities, 5) redesign of access ports to allow greater optical access and ease of machine maintenance, 6) built-in expandability – the new machine is designed to allow for the addition of new *in-situ* tools and pumping capabilities as experiments warrant. Our sample growth effort strives to ensure continuous progress in sample quality which has led to numerous discoveries in the past and will contribute to the vitality of this field in the future. Importantly, our preliminary growth studies indicate that quantifying disorder solely via a mobility measured in zero magnetic field transport is insufficient to capture the impact of various types of crystalline disorder on the formation of the fragile Quantum Hall States of the 2^{nd} LL.

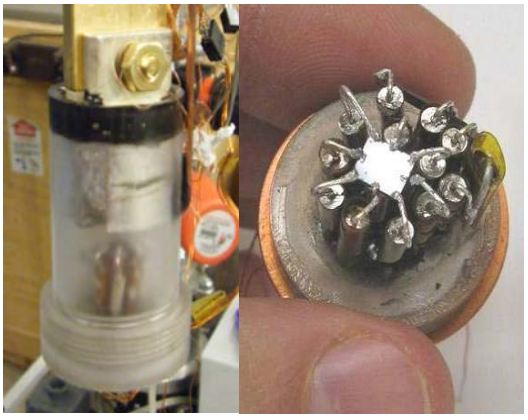

Fig.2. Csathy's He-3 immersion cell allows reaching temperatures of 5mK (left). A sample mounted on sintered Silver heat sinks (right). Reliable temperature measurement is achieved using a novel quartz He-3 viscometry.

Ultra-low temperature measurement has not yet been used to its full potential in the study of quantum Hall physics. Csathy's background in both Helium and fractional quantum Hall physics research has enabled him to build an ultra-low temperature refrigerator [1] capable of *cooling electrons in GaAs to 5mK* (see in Fig. 2). We emphasize that due to very weak electron-phonon coupling in GaAs in the mK regime, simply cooling the mixing chamber of a dilution refrigerator to T<10mK will not result in low electronic temperatures. One needs specialized heat sinking of the sample using sintered Silver heat exchangers which are immersed in a Helium-3 bath. This setup not only cools the electrons but also allows

for a reliable magnetic field independent temperature measurement of the local bath via He-3 viscometry [1]. Our close collaboration between growth and ultra-low temperature measurement will facilitate rapid progress.

Our collaboration has already produced exciting new physics. We have recently produced state-of-the-art magnetoresistance data in the second Landau level in both single layer two-dimensional electron [2] (see Figure 3) and hole samples [3]. Our progress is evident in the observation of new fractional Quantum Hall States [2, 3]. The observation of these states is already influencing our understanding of the second Landau level.

We are particularly encouraged by our recent progress in the growth of ultra-high quality GaAs two-dimensional electron systems. In particular our peak mobility has risen to $22 \times 10^6 cm^2/Vs$ and appears far from saturation. More importantly, we have had the opportunity to cool one of our samples grown at Purdue to T=7mK and found some quite astounding results. The sample under discussion has a density of $2.8 \times 10^{11}/cm^2$ and a mobility of $15 \times 10^6 cm^2/Vs$ and displays extraordinary fractional quantum Hall features in the 2nd Landau level.

What is most interesting about this sample is that it displays all fractional states ever observed in the highest mobility samples produced despite its significantly lower mobility. In fact the transport in this sample grown at Purdue compares favorably with any yet produced. The fine details of the transport features near ν=5/2 are also shown. In particular, we find a completely well-formed ν=2+2/5 state. This feature has only been reported in 2 samples during the past 6 years, yet it appears quite strong in our sample.

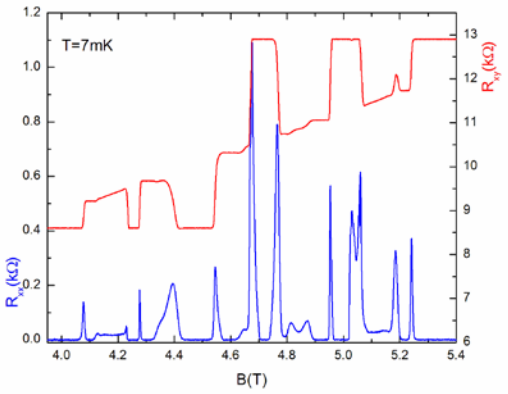

Fig.3. A recently measured magnetoresistance trace of a sample from Manfra's MBE measured at 7mK in Csathy's setup.

We have also measured the excitation gap of the ν=5/2 state in our sample. We extract an excitation gap of 520 mK, among the highest ever reported.

Our data emphatically punctuates the notion that zero magnetic-field mobility is neither a primary indicator of the visibility nor the strength of fragile quantum Hall states in the 2nd Landau level. While it has been know in the community that all high mobility samples are not created equal, and that some display better quantum Hall features than others, it has always been assumed that the path new fractional quantum Hall physics is through higher mobility. Our data calls this assumption into question. If a 15 million mobility sample can display all the features of a 30 million mobility sample, then how can we meaningfully state one sample is "better" than another with zero field mobility alone? We of course cannot fully answer this question at present, but we do want to emphasize that this is precisely one of the major focuses of our proposed work. We speculate that sample homogeneity is a particularly important property as any homogeneity will tend to smear out the narrow features in the 2nd Landau level.

Future Plans

The experiments we plan will attempt to answer several of the current outstanding questions in the physics of the 2nd LL. What is the spin polarization of the ν=5/2 state? How do several growth parameters influence the stability of the different fractional quantum Hall and insulating ground states in the 2nd LL? What other competing ground states will emerge as the purity of the GaAs host crystal is improved?

Such investigations call for a coordinated effort between growth and ultra-low temperature measurement and are part of our long term effort aimed at exploring unconventional collective behavior in low-dimensional systems. We think that progress with the experiments will uncover fundamental properties of the states in the 2nd LL and will also lead us in new and unanticipated research directions.

References

1. N. Samkharadze, A. Kumar, M.J. Manfra, L.N Pfeiffer, K.W. West, and G.A. Csathy, "Integrated Electronic Transport and Thermometry at milliKelvin Temperatures and in Strong Magnetic Fields", Review of Scientific Instruments **82**, 053902 (2011)
2. A. Kumar, G.A. Csathy, M.J. Manfra, L.N Pfeiffer, and K.W. West, "Nonconventional Odd Denominator Fractional Quantum Hall states in the Second Landau Level", Physical Review Letters **105**, 246808 (2010)
3. A. Kumar, N. Samkharadze, G.A. Csathy, M.J. Manfra, L.N Pfeiffer, and K.W. West, "Particle-Hole Asymmetry of Fractional Quantum Hall States in the Second Landau Level of a Two-Dimensional Hole System", Physical Review B **83**, 201305 (2011)

Epitaxial Electrodeposition/Reduction of Functional Metal Oxide Films

Jay A. Switzer
Department of Chemistry & Materials Research Center
Missouri University of Science and Technology
Rolla, MO 65409-1170
jswitzer@mst.edu

Program Scope

The emphasis of our research is the epitaxial electrodeposition of films and superlattices of metal oxide semiconductors (such as zinc oxide and cuprous oxide), spintronic materials (such as magnetite and zinc oxide), and solid-state memory materials (such as vanadium dioxide) at the solid/solution interface. This year we demonstrated that epitaxial films of Fe_3O_4 can be electrodeposited onto single-crystal Ni(111), and that epitaxial films of CuI and CuI/Cu nanocomposites can be electrodeposited onto the low-index faces of single-crystal Au. We also showed that epitaxial films of Fe_3O_4 can be electrochemically reduced at room temperature to epitaxial Fe films and to Fe/Fe_3O_4 heterojunctions. Another new result this year was the demonstration that VO_2 films can be electrodeposited by the electrochemical reduction of V(V) in aqueous solution, followed by a short anneal at 400 ^oC. The intensely blue material undergoes an ultrafast (~fs) phase transition at 68 ^oC, so it is of interest for room temperature solid-state memory (RRAM), memristors, neuromorphic computing, and electrochromic applications.

Recent Progress

This presentation will focus on two recent results from our lab: i) room-temperature electrochemical reduction of epitaxial magnetite (Fe_3O_4) films to epitaxial Fe films, and ii) resistance switching in electrodeposited vanadium dioxide (VO_2) thin films.

The electrochemical reduction of metal oxides to the corresponding metals has been studied for several decades as an alternative route to pyrometallurgical processes for the metallurgy industry because of its simplicity, environmental friendliness, and low cost.[1-9] Fray and Chen pioneered this field with their work on the direct electrochemical reduction of titanium dioxide to titanium in molten calcium chloride at 950 ºC.[3-6] Fray also showed that iron(III) oxide could be electrochemically reduced to iron in molten NaOH at 530 ºC by the same method.[7] In recent work, Allanore and co-workers electrochemically reduced porous iron ore (α-Fe_2O_3, hematite) particles to iron in 10 M KOH solution at 100 ºC. They proposed a dissolution/re-deposition mechanism with magnetite as the intermediate.[8,9] In addition to TiO_2 and Fe_2O_3, more insulating oxides such as SiO_2 and ZrO_2 can also be reduced to Si and Zr, respectively.[10-13] Kang and co-workers showed that nano-size Cu particles can be fabricated by electrochemically reducing CuO nano-particles in neutral solution at 300 K.[14] However, the previous work in this field was designed to achieve large scale and high rate of metal production as well as low CO_2 emissions, and were conducted on bulk polycrystalline metal oxides. Although single-crystal Bi_2S_3 and BiOCl were reported to be electrochemically reduced to Bi metal via an electron/proton transfer reaction at ambient temperature, there was no correlation between the initial orientation of the oxide crystals and the orientation of the metal crystallites after reduction.[15,16] That is, the order of the single crystals was lost after reduction. Here, we report that *epitaxial* Fe_3O_4 thin films on gold single-crystalline substrates can be electrochemically

reduced to *epitaxial* bcc-Fe thin films in 2 M NaOH solution at room temperature. This technique opens up new possibilities to produce special epitaxial metal/metal oxide heterojunctions and a wide range of epitaxial metallic alloys films from the corresponding mixed metal oxides. A cartoon of the reduction of epitaxial Fe_3O_4 to epitaxial Fe is shown in Fig. 1. Fig. 2 shows XRD evidence that the reduced Fe films have both in-plane and out-of-plane order.

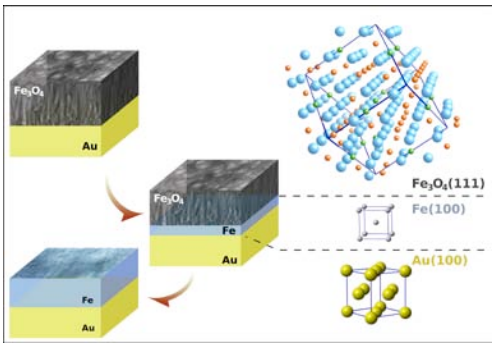

Figure 1- Scheme for the reduction of epitaxial Fe_3O_4 to Fe.

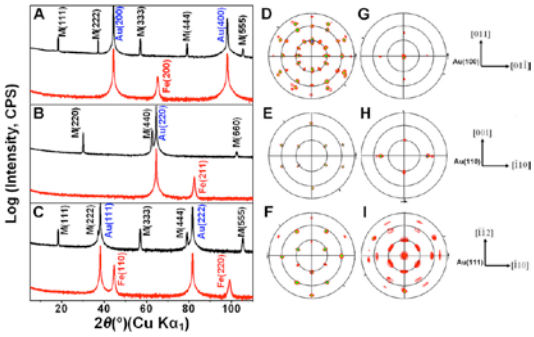

Figure 2- XRD characterization of electrodeposited epitaxial Fe_3O_4 films and the corresponding Fe films after reduction on single-crystal Au.

Vanadium dioxide (VO_2) is a compound that undergoes a sharp, first order metal-to-insulator transition (MIT) at a temperature of ~68 ^oC[17] accompanied by a structural change from an insulating, low temperature monoclinic form VO_2(M) to a high temperature, metallic rutile structure VO_2(R).[18-20] The MIT near room temperature and the ultrafast (~fs) phase transition[21] make this compound a very promising candidate for novel electronic applications, such as ultra-fast switches, Mott field effect transistors (MottFET), memristors, neuromorphic computing, and solid state memory.[20,22,23] Since the early discovery of the MIT in VO_2 by Morin in 1959[17] there has been a lot of effort to reveal the MIT mechanism, and to develop methods for deposition of VO_2 thin films and nanostructures.[20] To the best of our knowledge only one paper has been published on the preparation of VO_2 by electrodeposition.[24] However, this method can only produce VO_2 layers a few nm thick and the as-deposited xerogel has to be stored for 45 days prior to annealing in vacuum. Here, we report that ~150 nm thick VO_2 films can be produced by electrochemical reduction of V^{5+} ions complexed with triethanolamine (TEA), followed by an immediate, short anneal at 400 ^oC. The films were deposited at 80 ^oC from a solution of 0.4 M V(V) and 0.25 M TEA at a pH of 6.5. The VO_2 undergoes a metal-to-insulator transition (MIT) at 323 K, and exhibits sharp resistance switching at room temperature (see Fig. 3). The electrodeposition method opens up inexpensive possibilities for the fabrication of ultrafast switches, Mott field effect transitions, memristors, and solid-state memory.

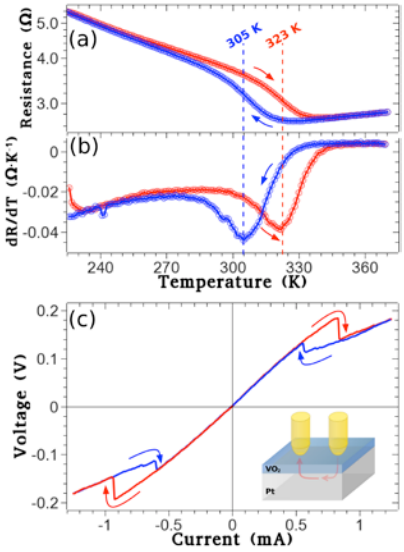

Figure 3- (a) Temperature dependence of the resistance of VO_2 showing the MIT temperatures upon heating (red) and cooling (blue). (b) Transition temperatures were determined by differentiating R-T curves. (c) I-V curves for VO_2 film showing reversible resistance switching at 300 K.

Future Plans

Our main emphasis will be on the electrochemical reduction of epitaxial metal oxide films to epitaxial metal films, the electrodeposition of vanadium and cobalt oxides, and the electrodeposition of CuI/Cu nanocomposites. These three research thrusts are outlined below.

Electrochemical reduction of epitaxial metal oxide films to epitaxial metal films. This year we showed that epitaxial Fe_3O_4 can be reduced to epitaxial Fe. In order to determine the generality of this method, we will reduce epitaxial films of Cu_2O, CuO, ZnO, and Bi_2O_3 to the corresponding metals. We also plan to study whether the reduction occurs by solid-state oxide ion transport, or by solution-phase dissolution/re-deposition. A grand challenge (i.e., very high risk but equally high payoff) that would be very relevant to DOE would be to produce epitaxial Si films by the electrochemical reduction of amorphous SiO_2 films. This, of course, would require nonaqueous solvents or molten salts, but it would be an inexpensive method to produce large-scale Si films for photovoltaic applications.

Electrodeposition of vanadium and cobalt oxides. This year we produced VO_2 by electrodeposition. Vanadium has very rich redox chemistry, because VO, V_2O_3, VO_2, and V_2O_5 are all stable oxides. V_2O_3 and VO undergo a MIT transition,[17] so they are of interest for solid-state memory. V_2O_5 is of interest for lithium ion batteries. These materials will all be electrodeposited from alkaline aqueous solution. We are also plan to electrodeposit epitaxial films of Co_3O_4. The material is an electrocatalyst for the oxidation of CO to CO_2. It is known that the [110] orientation is particularly active as a catalyst, so we will attempt to prepare epitaxial films of Co_3O_4 with a [110] orientation.

Electrodeposition of CuI/Cu nanocomposites. We have shown in unpublished work that we can electrodeposit epitaxial films of CuI and CuI/Cu nanocomposites. CuI is a p-type semiconductor that is of interest for solar cells. However, the bandgap of about 3.3 eV is too large to effectively absorb the solar spectrum. One approach to increase the visible absorption is to use nanometer-scale metal (e.g., Cu) particles to support surface plasmons. The surface plasmons act as an antenna or "inorganic sensitizer" to fold light into the thin layer.

References

(1) Oswin, H. G.; Cohen, M. *J. Electrochem. Soc.* **104**, 9 (1957).
(2) LeDuc, J. A. M.; Loftfield, R. E.; Vaaler, L. E. *J. Electrochem. Soc.* **106**, 659 (1959).
(3) Chen, G. Z.; Fray, D. J.; Farthing, T. W. *Nature* **407**, 361 (2000).
(4) Jiang, K.; Hu, X.; Ma, M.; Wang, D.; Qiu, G.; Jin, X.; Chen, G. Z. *Angew. Chem., Int. Ed.* **45**, 428 (2006).
(5) Li, W.; Jin, X.; Huang, F.; Chen, G. Z. *Angew. Chem., Int. Ed.* ***49***, 3203 (2010).
(6) Centeno-Sanchez, R. L.; Fray, D. J.; Chen, G. Z. *J. Mater. Sci.* **42**, 7494 (2007).
(7) Cox, A.; Fray, D. J. *J. Appl. Electrochem.* **38**, 1401 (2008).
(8) Allanore, A.; Lavelaine, H.; Valentin, G.; Birat, J. P.; Delcroix, P.; Lapicque, F. *Electrochim. Acta* **55**, 4007 (2010).
(9) Allanore, A.; Lavelaine, H.; Valentin, G.; Birat, J. P.; Lapicque, F. *J. Electrochem. Soc.* **155**, E125 (2008).

(10) Nohira, T.; Yasuda, K.; Ito, Y. *Nat. Mater.* **2**, 397 (2003).
(11) Jin, X.; Gao, P.; Wang, D.; Hu, X.; Chen, G. Z. *Angew. Chem., Int. Ed.* **43**, 733 (2004).
(12) Xiao, W.; Jin, X.; Deng, Y.; Wang, D.; Chen, G. Z. *J. Electroanal. Chem.* **639**, 130 (2010).
(13) Peng, J.; Jiang, K.; Xiao, W.; Wang, D.; Jin, X.; Chen, G. Z. *Chem. Mater.* **20**, 7274 (2008).
(14) Han, W.-K.; Choi, J.-W.; Hwang, G.-H.; Hong, S.-J.; Lee, J.-S.; Kang, S.-G. *Appl. Surf. Sci.* **252**, 2832 (2006).
(15) Pyper, O.; Hahn, B.; Schoellhorn, R. *J. Mater. Chem.* **7**, 465 (1997).
(16) Pfletschinger, G.; Hahn, B.; Schoellhorn, R. *Solid State Ionics* **84**, 151 (1996).
(17) Morin, F. J. *Phys. Rev. Lett.* **3**, 34 (1959).
(18) Jones, A. C.; Berweger, S.; Wei, J.; Cobden, D.; Raschke, M. B. *Nano Lett.* ***10***, 1574 (2010).
(19) Sohn, J. I.; Joo, H. J.; Ahn, D.; Lee, H. H.; Porter, A. E.; Kim, K.; Kang, D. J.; Welland, M. E. *Nano Lett.* **9**, 3392 (2009).
(20) Yang, Z.; Ko, C.; Ramanathan, S. *Annu. Rev. Mater. Res.* DOI: 10.1146/annurev-matsci-062910-100347 (2010).
(21) Baum, P.; Yang, D.-S.; Zewail, A. H. *Science* **318**, 788 (2007).
(22) Hyun-Tak, K.; Byung-Gyu, Ch; Doo-Hyeb, Y; Sung-Lyul, M; Gyungock, K; Kwang-Yong, K.; Yong-Sik, L. *New J. Phys.* **6**, 52 (2004).
(23) Driscoll, T.; Kim, H. T.; Chae, B. G.; Di Ventra, M.; Basov, D. N. *Appl. Phys. Lett.* **95**, 043503 (2009).
(24) Cezar, A. B.; Graff, I. L.; Rikers, Y.; Schreiner, W. H.; Mattoso, N. *Electrochem. Solid-State Lett.* **14**, D23 (2011).

Publications over the past two years resulting from work supported solely by the DOE project

(1) G. Mu, R. V. Gudavarthy, E. A. Kulp, and J. A. Switzer, "Tilted epitaxial ZnO nanospears on Si(001) by chemical bath deposition," *Chem. Mater.* **21**, 3960-3964 (2009).
(2) E. A. Kulp, H. M. Kothari, S. J. Limmer, J. Yang, R. V. Gudavarthy, E. W. Bohannan, and J. A. Switzer, "Electrodeposition of epitaxial magnetite films and ferrihydrite nanoribbons on single-crystal gold," *Chem. Mater.* **21**, 5022-5031 (2009).
(3) J. A. Switzer, R. V. Gudavarthy, E. A. Kulp, G. Mu, Z. He, and A. J. Wessel, "Resistance switching in electrodeposited magnetite superlattices," *J. Am. Chem. Soc.* **132**, 1258-1260 (2010).
(4) J. A. Switzer & G. Hodes, "Electrodeposition and chemical bath deposition of functional nanomaterials," *MRS Bulletin* **35**, 743-750 (2010).
(5) R. V. Gudavarthy, S. Gorantla, G. Mu, E. A. Kulp, T. Gemming, J. Eckert, and J. A. Switzer, "Epitaxial electrodeposition of Fe_3O_4 on single-crystal Ni(111)," *Chem. Mater.* **23**, 2017-2019 (2011).
(6) R. V. Gudavarthy, A. S. Miller, E. W. Bohannan, E. A. Kulp, Z. He, and J. A. Switzer, "Resistance switching in electrodeposited polycrystalline Fe_3O_4 films," *Electrochim. Acta.*, in press (2011), doi: 10.1016/j.electacta.2011.02.032. Available on-line.
(7) Z. He and J. A. Switzer, "Electrochemical reduction of epitaxial magnetite to epitaxial iron on single-crystal gold," *J. Am. Chem. Soc.*, manuscript #ja-2011-03975z, in press (2011).
(8) J. A. Koza, Z. He, A. S. Miller, and J. A. Switzer, "Resistance switching in electrodeposited VO_2 thin films," *Chem. Mater.*, manuscript #cm-2011-019394, submitted (2011).

In -Situ Micro Raman Detection of Reversible Basal Plane Hydrogenation in Pt-doped Activated Carbon

Xiao Ming Liu, Youjian Tang, En Shi Xu, Thomas C. Fitzgibbons, Humberto R. Gutierrez, John V. Badding, Vincent H Crespi, Angela D. Lueking (lueking@psu.edu),
The Pennsylvania State University
Departments of Energy and Mineral Engineering, Chemical Engineering, Chemistry, Physics
The EMS Energy Institute and the Materials Research Institute

Program Scope

Development of *in situ* spectroscopic measurement techniques capable of combined high-pressure and variable temperature measurements has allowed us to explore carbon-hydrogen interactions that are unresolved and debated in the literature. One such carbon-hydrogen interaction of particular interest is the binding mechanism between hydrogen and a carbonaceous support in the presence of a noble-metal dissociation catalyst, i.e. the hydrogen spillover mechanism. Incorporation of a catalyst into nanoporous materials has led to several reports of particularly high hydrogen uptake at room temperature and pressures less than 100 bar, but the results are contested, reproducible by only a fraction of laboratories, and the active sites on the nanoporous support that bind reversibly with spilled over atomic hydrogen remains unclear. We have investigated the local interaction between atomic H and the graphite basal plane adjacent to a Pt dissociation catalyst with *in-situ* Raman spectroscopy and complementary density functional theory (DFT) calculations. These results demonstrate spectroscopic evidence for hydrogenation of the carbon basal plane via the spillover mechanism; the feature is reversible for spillover to curved and defected activated carbon and irreversible to graphene. These results clarify whether H is chemisorbed or physisorbed, and how carbon structure and metal-carbon contact dictate the degree of reversibility.

Recent Progress

In-situ Raman spectroscopic measurements of Pt nanoparticles on graphene (Pt/G) were performed at hydrogen pressures of 100 bar in a 160 μm outer diameter (100 μm inner diameter) silica capillary high pressure vessel. Spectra were collected with a Renishaw inVia microRaman spectrometer with less than 1 mW of 514.5 nm. Graphene synthesized via a substrate-free gas-phase method (Electron Microscopy Sciences), and the resulting graphene was typically of 3 to 5 layers thick. Graphene was mixed with preformed Pt nanoparticles in benzene (2-20 nm Pt, STREM Chemicals Inc) and loaded into the silica fiber. The fiber was then sealed and the benzene removed via a ~100°C degas, after which either ~100 bar of He or ~100 bar of H_2 was introduced. Each subsequent introduction of a different gas was preceded by a 72 hr degas at room temperature. Elsewhere, EELS measurements of similarly prepared graphene sheets have shown essentially pure carbon with no detectable hydrogen or oxygen.[1]

The Raman spectra of Pt/G under 100 bar He pressure (Figure 1c) is characteristic of an sp^2-bonded carbonaceous solid, including a D-peak (~1350 cm^{-1}) and G-peak (~1590 cm^{-1}). When 100 bar H_2 is introduced into the capillary, sharp features at 817 cm^{-1} and 1037 cm^{-1} are seen, and are due to S2 and S3 rotational transitions of free hydrogen (latter shown in Figure 1d). A new mode at ~1160 cm^{-1} also arises, and is similar to a feature (at 1210 cm^{-1}) observed in HREELS of a H-covered graphite (0001) surface,[2] which provides corroborating evidence this

feature results from a carbon-hydrogen bond. When H_2 is removed from the capillary via vacuum degasing, the mode at 1160 cm^{-1} decreases, but does not vanish. Quantification of the magnitude of the reduction was difficult due to variations between spots. In a forthcoming publication,[†] we show when Pt/G is replaced with Pt-doped activated carbon the mode is reversible. The role of curvature, metal-carbon interface, metal mobility, and carbon structure on reversibility are currently being explored.

We have also performed multiple control studies to confirm that the 1160 cm^{-1} feature is associated with the catalytic activity of the Pt. We find that carbon materials with no Pt do not exhibit the ~1160 cm^{-1} Raman mode when subjected to the same cycle of ~100 bar H_2/He exposure, indicating that this feature does depend on the presence of catalytic Pt. Similarly, it is important to rule out Pt-H interactions as the source of this feature. Raman spectra of the preformed 2-20 Pt nanoparticles (benzene removed) in H_2 gas exhibit only the S3 band (1037 cm^{-1}) of H_2, with no feature near 1180 cm^{-1} (Figure 3a). Thus, the ~1160 cm^{-1} band cannot be attributed to a Pt-H vibrational mode. Finally, the ~1160 cm^{-1} mode cannot be attributed to the silica capillary. The Raman spectra of the silica fiber (Fig 2b) has broad features at ~1060 cm^{-1} (TO mode) and ~1190 cm^{-1} (LO+TO mode) [3], but the intensity ratio between the two peaks is always ~2:1. Thus from the absence of the more intense broad silica band at ~ 1060 cm^{-1} in the Pt/G Raman spectra, we can conclude that the silica capillary is not contributing to the observed Raman spectra.

To elucidate the origin of the 1060 – 1080 cm^{-1} mode, we performed a series of density function calculations of phonon vibrational spectra for hydrogen bound to planar sp^2 carbon. These calculations using the projector augmented wave (PAW) method in the local density (LDA) and generalized gradient (GGA) approximations. Frozen phonon calculations used a plane wave cutoff of 400 eV using the Vienna Ab-initio Simulation Package[4]. Linear response calculations[5] use a cutoff of 500 eV with a plane-wave basis within LDA using the CASTEP[6] code. Periodic boundary conditions were assumed in both cases, with relaxed in-plane lattice constants. First, we compare the structural energetics of a broad range of hydrogenation patterns, with results summarized elsewhere.[†] The simplest such geometry is an isolated H atom chemisorbed to a carbon atom within a 2×2 or 3×3 graphene supercell. These C_8H and $C_{18}H$ systems both yield a chemisorption binding energy of 1.04 eV, relative to a gas-phase H atom and bare graphene. Previous calculations for H bound to Pt on a graphene surface[7] suggest that this state is thermodynamically unfavorable compared to H bound to a Pt atom or a four-atom Pt cluster. However, higher H/C stoichiometries yield stronger binding: for example, C_8H_2 with the two H atoms located at the 1,4 positions of a graphene hexagonal ring (with C_{6V} symmetry) binds hydrogen at 2.07 eV per H, the highest hydrogen binding energy of all those studied. When two more H atoms are added to the 2×2 graphene cell to achieve C_8H_4, we arrive at C_{2V} symmetry and an adsorption energy of 1.90 eV per H. These favorable hydrogenation patterns can be rationalized in terms of the aromaticity of the remaining sp^2 portions of the structure. Overall, these results indicate that chemisorbed hydrogen atoms should tend to cluster, consistent with previous results[2,8,9].

Full vibrational spectra at the Γ point were calculated for each of these structures, with IR and Raman active modes identified and mode intensities calculated by linear response theory. These results consistently identify a C-H wagging mode whose frequency increases with increasing

hydrogen coverage, reaching the experimentally observed frequency range for the most energetically favorable patterns of hydrogen adsorption. The C_8H_2 state of C_{6V} symmetry discussed above yields two degenerate Raman-active wagging modes of E_2 symmetry at 1140 cm^{-1} for H and 890 cm^{-1} for D. In density functional perturbation theory, the intensity of this mode is about 1/12 that of the G band. For the higher hydrogen coverage C_4H_2, two non-degenerate A_1 wagging modes appear at 1250 cm^{-1} and 1140 cm^{-1} for hydrogen and 950 cm^{-1} and 840 cm^{-1} for deuterium, with an intensity about one seventh that of the G band. These DFT results are consistent with the assignment of the 1160/1180 cm^{-1} band to atomic hydrogen bound directly to the carbon basal plane.

References

(1) Dato, A.; Radmilovic, V.; Lee, Z.; Phillips, J.; Frenklach, M. *Nano Letters* **2008**, *8*, 2012-2016.

(2) Zecho, T.; Guttler, A.; Sha, X. W.; Jackson, B.; Kuppers, J. *Journal of Chemical Physics* **2002**, *117*, 8486-8492.

(3) Sharma, S. K.; Cooney, T. F.; Wang, Z. F.; vanderLaan, S. *Journal of Raman Spectroscopy* **1997**, *28*, 697-709.

(4) H. J. Monkhorst and J. D. Pack, Physical Review B 13, 5188 (1976); G. Kresse and J. Furthmuller, Physical Review B 54, 11169 (1996); G. Kresse and J. Furthmuller, Computational Materials Science 6, 15 (1996); G. Kresse and J. Hafner, Physical Review B 47, 558 (1993); P. E. Blochl, Physical Review B 50, 17953 (1994).

(5) K. Refson, P. R. Tulip, and S. J. Clark, Physical Review B 73, 155114 (2006).

(6) S. J. Clark, M. D. Segall, C. J. Pickard, P. J. Hasnip, M. J. Probert, K. Refson, and M. C. Payne, Z. Kristallogr. 220, 567 (2005).

(7) Psofogiannakis, G. M.; Froudakis, G. E. J*ournal of Physical Chemistry C* 2**009,** 1*13,* 14908-14915.

(8) Stojkovic, D.; Zhang, P.; Lammert, P. E.; Crespi, V. H. P*hysical Review B* 2**003,** 6*8,* 195406.

(9) Lin, Y.; Ding, F.; Yakobson, B. I. P*hysical Review B* 2**008,** 7*8,* -.

Future Work

The experimental results show shifts in the D and G peaks upon H_2 exposure that will be discussed in a subsequent paper, as well as observations associated with the second-order modes that will be discussed in the context of the DFT simulations. To help ascertain the differences that lead to irreversibility for Pt/G (described above) and Pt/AC (described in [†]), we are looking to systematically vary the carbon support to explore the role of carbon structure, basal plane length, curvature, and co-catalyst in the in situ experimental studies. Also, the methods developed herein are amenable to a number of other "spillover materials" including both carbon supports and microporous metal-organic frameworks. The latter should allow a systematic variation of surface chemistry, metal building unit, and coordination such that a role of these factors in binding with atomic hydrogen may be ascertained. In other on-going work, we have access to several MMOF-based spillover materials. The results of the first of these experiments are described in the second paper,[‡] and indicate an interaction between atomic hydrogen and the MMOF that will provide an alternative explanation to the one currently emerging in the literature.

DOE Sponsored Publications in 2010-2011

[†]Liu, XM; Tang, Y; Xu, ES; Fitzgibbons, TC; Gutierrez, HR; Tseng HH; Yu, MS; Tsao, CS; Badding, JV; Crespi, VH; Lueking, A.D. In-Situ Micro Raman Detection of Reversible Basal Plane Hydrogenation in Pt-doped Activated Carbon, Journal of American Chemical Society, Submitted 2011.

[‡]Liu, XM; Rather, S.U.; Li, Q.; Tang, Y; Lueking, A.D.; Zhao, Y.; Li, J. Hydrogenation of CuBTC framework with the introduction of a PtC hydrogen spillover catalyst. ACS Nano, Submitted 2011.

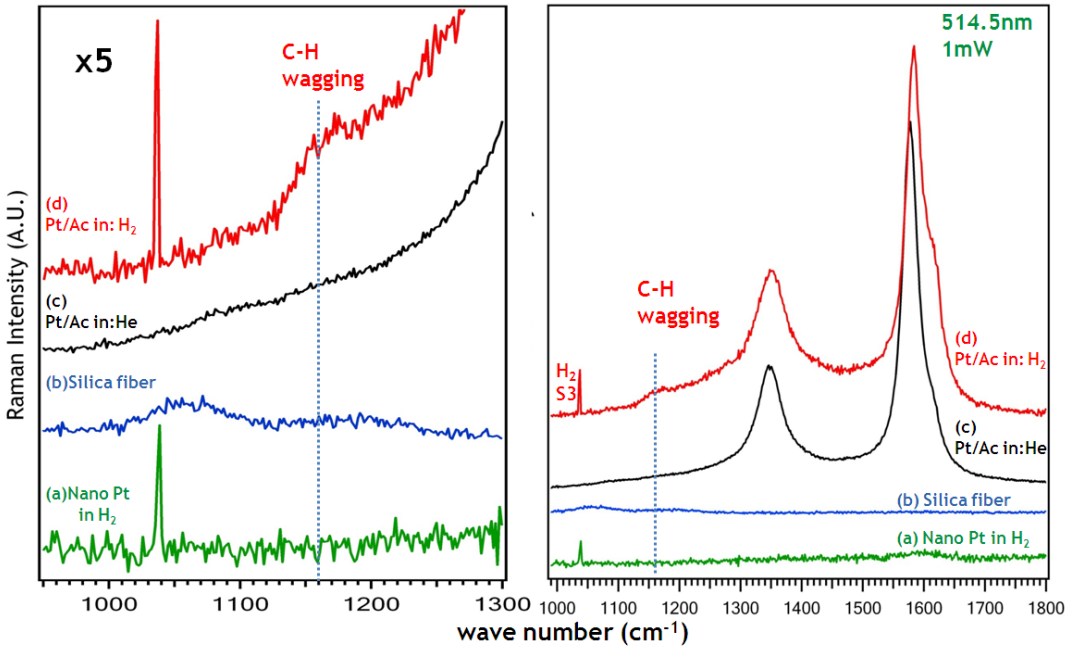

Figure 1. Raman spectra showing (a) nano Pt in 100 torr of H_2 gas, (b) silica fiber casing the sample and high pressure gas, and Graphene decorated with Pt nano particles at 298K showing the carbon D and G band, in (c) He and (d) H_2 at 298K. A feature at 1160 cm^{-1} is seen only in a hydrogen atmosphere.

In-situ neutron scattering studies of electrical energy storage materials

Ke An and Chengdu Liang
kean@ornl.gov and Liangcn@ornl.gov
Oak Ridge National Laboratory, Oak Ridge, TN 37831

Program scope

This program investigates the phase evolution and dynamics of materials for electrical energy storage. Transition metals and lithium are the key components for the function of lithium batteries. The high sensitivity of neutrons in the probing of light elements and differentiating transition metals imparts the unique capability of neutron scattering techniques to the study of lithium batteries. The intense neutron beam at SNS and the stroboscopic measurement technique allow ultrafast data collection for in-situ studies. Along with the high penetration capability of the neutron beam, neutron scattering provides nondestructive characterization of batteries with real-time monitoring of chemical and structural changes of materials during battery operations. Under this program we use neutron scattering to study the dynamics of lithium-ion batteries and the synthesis of battery materials. Particularly, we probe the transport of lithium-ions and phase changes of battery materials during electrochemical cycling of the batteries. In addition, we use neutron scattering to observe the crystal growth and the structure evolution during the synthesis of nanostructured cathode materials.

Recent progress

PART I: Probing Li-Ni Cation Disorder in Cathode Materials by Neutron Diffraction

Neutron powder diffraction measurements have been done on a series of nano-crystalline $Li_{1-x}Ni_{1+x-y}Al_yO_2$ made by different processes: near-stoichiometric $Li_{1-x}Ni_{1+x}O_2$, $Li_{1-x}Ni_{0.75+x}Al_{0.25}O_2$ from LiOH, $Li_{1-x}Ni_{0.75+x}Al_{0.25}O_2$ from Li_2O_2, and three lithium-deficient compounds $Li_{1-x}Ni_{0.75+x}Al_{0.25}O_2$. High resolution neutron powder diffraction measurements were performed using VULCAN, SNS, ORNL.

The crystal has a layered structure with a space group of *R-3m* and lattice parameters of $a \sim 2.8$ Å and $c \sim 14$ Å. Rietveld refinement of neutron powder diffraction data for near-stoichiometric $Li_{1-x}Ni_{0.75+x}Al_{0.25}O_2$ confirms Al^{3+} substitution of Ni^{3+} stabilizes the structure and reduces the formation of Ni^{2+}. The results of refined x indicate that the two different synthesis processes resulted in similar final products, although Li_2O_2 is a strong oxidant compared with LiOH. The decreased x values in Al-doped compounds compared with non-doped compounds confirm that the doping of Al^{3+} reduces the cationic disorder at Li *3b* site.

Both the lattice parameter a and the unit cell volume increases with decreasing lithium content (1-x), while the lattice parameter c first increases then decreases (Figure 1a). The increasing trend can be explained by the variation of average ionic radius of cations related to x. However, there is an abnormal decrease in the lattice parameter c from 1-x = 0.65 to 0.4. This is related to the appearance of secondary phase at 1-x = 0.65, as a series of unsymmetrical peaks were observed only at the high resolution diffraction pattern for $Li_{0.65}Ni_{1.1}Al_{0.25}O_2$. Phase identification suggests a cubic phase, possibly $Li_yNi_{1-y}O$. The secondary phase is expected to

have lithium content *y* around 0.1. The oxygen fractional coordinate *z* increases with increasing lithium content (Figure 1b). The thickness ratio of LiO_6 over MO_6 slabs increases with increasing *z*. It was found that *z* increases as the lithium content (1-*x*) increases; that is, the thickness ratio of LiO_6 over MO_6 slabs increases with decreasing *x*. The trend of *z* can be explained by both electrostatic interaction and ionic radius.

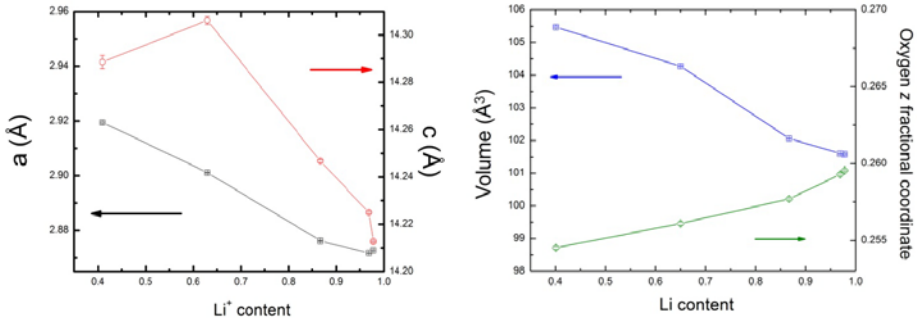

Figure 1 Left: a), Lattice parameters and right: b), Unit cell volume and oxygen fractional coordinate of $Li_{1-x}Ni_{0.75+x}Al_{0.25}O_2$.

PART II: In-situ Characterization of Lithium-ion Battery by Neutron Diffraction

In-situ neutron diffraction is used to monitor a lithium-ion battery during electrochemical cycling. Thanks to the deep penetration of neutrons, phase structural changes for both cathode and anode are observed simultaneously during real-time fast charge/discharge.

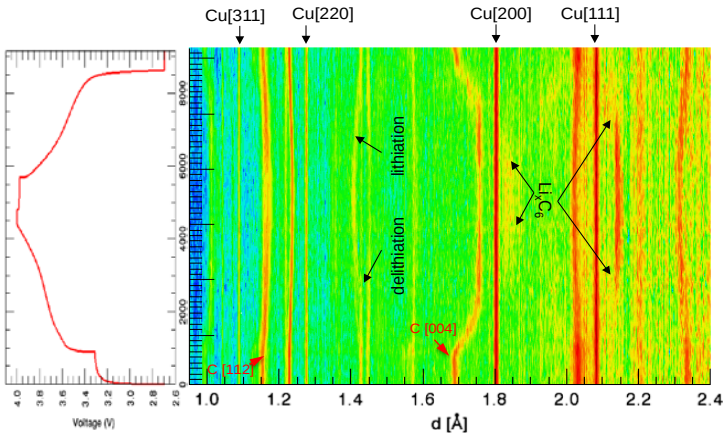

Figure 2, Neutron diffraction of battery under charge and discharge reveals the structural evolution of cathode and anode during lithiation and delithiation.

The investigated battery has $Li_xNi_{0.4}Mn_{0.3}Co_{0.3}O_2$ as the cathode, graphite as the anode and Cu, Al as current collectors. For in-situ experiments, the battery was charging and discharging at 1 C for several cycles while the neutron diffraction data were continuously collected. The data were then chopped into 62 diffraction patterns as shown in Figure 2. Each pattern corresponding to 2.5 minutes of data collection time in one cycle was summed over 7 cycles using the stroboscopic technique.

The evolution of the lattice and volume of the cathode is clearly observed by the in-situ diffraction measurement. The cathode material, $Li_xNi_{0.4}Mn_{0.3}Co_{0.3}O_2$ has a layered structure, with a space group of *R-3m* and lattice parameters of $a \sim 2.8$ Å and $c \sim 14$ Å. The changes in the d-spacing of the cathode signified directly the lithiation and delithiation process as shown in

Figure 2. The lattice parameter *c* increases with increasing capacity while *a* decreases with capacity. In $Li_xNi_{0.4}Mn_{0.3}Co_{0.3}O_2$, Li^+ is located between the oxygen layers. The removal of Li^+ causes an increase in the electrostatic repulsion of the oxygen layers, which in turn causes the expansion of *c*. The decrease in *a* with capacity is caused by the charge compensation in the valence of Ni ions during the removal of lithium ions.[1] The lattice parameters follow a reversible revolution back to the original value, with no hysteresis found. The unit cell volume decreases with the removal of lithium ions from the structure.

New staging dependence of charge rate was found for the graphite anode during fast electrochemical process. The lithium intercalation and deintercalation process in the graphite anode was evinced by the appearance of new peaks as well as significant changes in d-spacing. As shown in Figure 3 the d-spacing of (004) graphite at ~1.68 Å continuously increases during charging until it reaches ~1.75 Å, which is close to the reported (004) of LiC_{12}.[2-3] The arrival of (004) d-spacing at a constant value is accompanied by the appearance of a new peak at ~ 2.13 Å, which is the (110) of LiC_{12}. Upon deeper charging, an additional peak showing up at ~1.85 Å indicates the formation of LiC_6. The (110) of LiC_6 is greatly overlapped with (110) of LiC_{12} because of negligible difference in the lattice parameter *a* for each phase. The LiC_{12} phase is always present after the appearance of LiC_6. The LiC_6 first eliminates upon discharging. When the (110) peak at ~2.13 Å starts to disappear, the d-spacing of (004) does not follow the same route in the charging process but rather a hysteresis loop. It indicates there is a different structural path for the anode material. This subtle structure evolution and dynamic process can be only monitored by in-situ investigation.

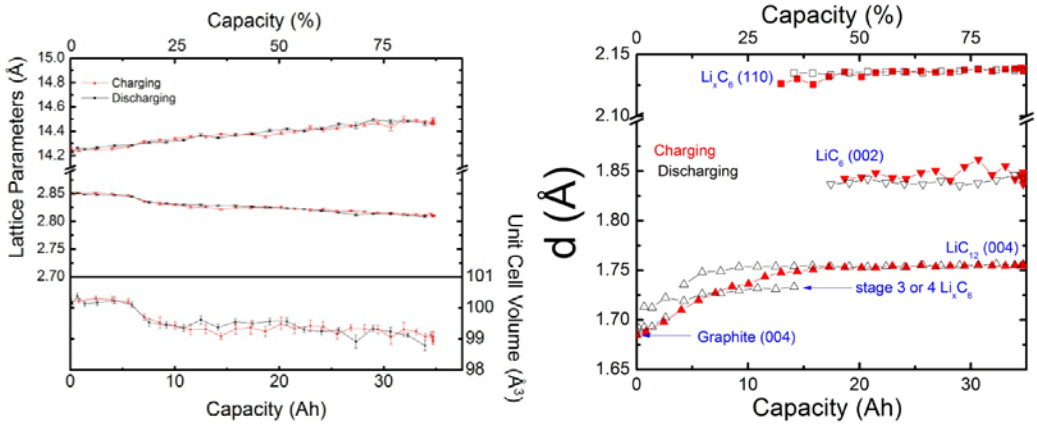

Figure 3, Lattice parameters and unit cell volume of the cathode material $Li_xNi_{0.4}Co_{0.3}Mn_{0.3}O_2$, and, the d-spacing change of the anode material as a function of charging capacity. The red solid spots are during charging and the black open ones are in discharging process.

PART III: In-situ Phase Formation Study of $LiMn_{1.5}Ni_{0.5}O_4$ by Neutron Diffraction

To provide understanding of the formation process and guidance on the development of this promising cathode material to meet the needs of lithium-ion batteries, in-situ neutron diffraction was performed to reveal phase formation of electrode materials from chemical precursors during heating. Phase transformation of $LiMn_{1.5}Ni_{0.5}O_4$ was observed by in-situ neutron diffraction. A pellet was made of a stoichiometric mixture of $Ni(COOCH_3)_2 \cdot 4H_2O$,

$LiCH_3COO{\cdot}2H_2O$, $Mn(CH_3COO)_2{\cdot}4H_2O$. In-situ diffraction patterns at elevated temperatures are shown in Figure 4, and phase transformations at different temperatures were successfully observed. At 450°C, high background observed is from the incoherent scattering of H in organic precursors. Between 700°C and 800°C where all the precursors decomposed or degassed, crystalline peaks showed up with considerable background, which indicates the formation of nanocrystalline and amorphous phases. The amorphous phases have been greatly depressed at 900°C. Surprisingly, even at 1000°C, no spinel $LiMn_{1.5}Ni_{0.5}O_4$ phase was detected. The spinel phase first appeared when annealing at 700°C after the 1000°C heat treatment as the strongest reflection (222) of the $LiMn_{1.5}Ni_{0.5}O_4$ phase showed up at ~ 2.4 Å.

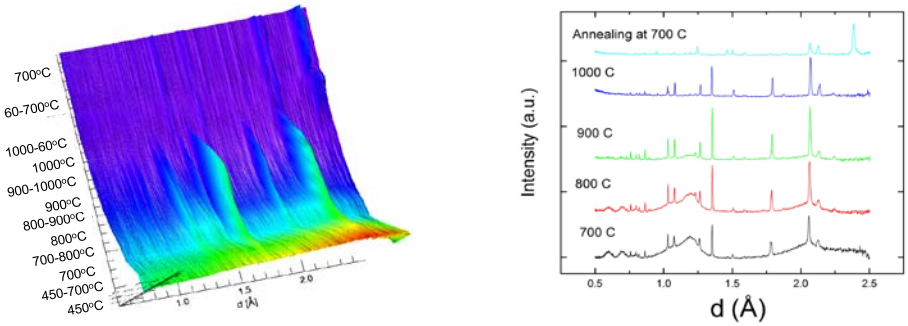

Figure 4. Left: 3-D plot of neutron diffraction in the $LiMn_{1.5}Ni_{0.5}O_4$ phase. Right: neutron diffraction patterns at different temperatures.

Future plans

Neutron scattering has been proven to be a powerful in-situ characterization tool for electrical energy storage materials. It offers rich structural information and state of charge kinetics. It will be used for other cathode material systems for studying material behavior under electrochemical process and material synthesis. To study battery performance dependency of charge rate, phase structural evolution of electrodes under charge/discharge will be investigated under different rates. Neutron scattering will also be used to probe degraded batteries to provide quantitative knowledge about battery deterioration over time.

Investigation of the order-disorder transition of $LiMn_{1.5}Ni_{0.5}O_4$ in controlled oxygen atmospheres by neutron diffraction is planned and scheduled with neutron beam time granted in POWGEN beamline at SNS.

References

1 Liao, P.Y., et al., *Electrochimica Acta*. **53**(4) 1850-1857 (2007).
2 Guerard, D. and A. Herold, *Carbon*. **13**(4) 337-345 (1975).
3 Dahn, J.R. *Physical Review B*. **44**(17) 9170-9177 (1991).

Publications Resulting from 2009-2011

In preparation: "Visualizing the Chemistry and Structure in Batteries at Work" Lu Cai, Ke An, Zhili Feng, Alexandru D. Stoica, Harley D Skorpenske, Xun-Li Wang, Chengdu Liang, Stephen E. Nagler, Claus Daniels, and Steve Harris.

In Preparation: "Probing Li-Ni Cation Disorder in $Li_{1-x}Ni_{1+x-y}Al_yO_2$ Cathode Materials by Neutron Diffraction" Lu Cai, Zengcai Liu, Ke An, and Chengdu Liang.

Novel Materials Preparation and Processing Methodologies

Controlled Nano-scale Architectures: Access to Beneficial Metastable States

I.E. Anderson, Qingfeng Xing and T. A. Lograsso
Ames Laboratory, Ames IA 50011

Program Scope

The growth, control and modification of novel materials in single crystal and polycrystalline form, represent a national core competency that is essential for scientific advancement within and across traditional disciplinary boundaries, and are critical components of the Basic Energy Sciences' mission. In support of this mission, the Novel Materials Preparation and Processing Methodologies strengthen the materials synthesis efforts of the Ames Laboratory. The objective of Novel Materials is to quantify and control processing-structure-property relationships: the basic science of how chemical inhomogeneities and structural defects affect properties of highly responsive materials; advance the ability to synthesize and characterize high purity, high quality materials, primarily in single crystal form; develop unique capabilities and processing knowledge in the preparation, purification, and fabrication of metallic elements and alloys. Single crystals are often required to achieve scientific understanding of the origin of various phenomena, whether from intrinsic or extrinsic origins, to elucidate its properties as well as to evaluate a material's full functionality. Our research objectives are: 1) developing synthesis and processing capabilities that support rapid materials discovery using bulk combinatorial approaches, 2) identifying synthesis protocols for specific novel materials through the rapid development and modification of methods to prepare high quality well-characterized single crystals, and 3) utilizing solidification processing to access metastable states in controlled nanoscale architectures. The research described herein is directed toward utilizing solidification based processing to access metastable states in controlled nanoscale architectures.

Preliminary Results and Future Work

Discovery and development of many of the materials that enable new and evolving technologies, including semiconductor electronics, solid state lasers, high strength permanent magnets, radiation detectors, compact disk storage, both cellular and optical communications, thermoelectrics, solar cells, fuel cells, high capacity batteries, and catalysts, rely on control of nano-scale architectures to achieve optimum performance. Often, such a nano-scale assemblage is in a metastable state or must be synthesized by route that involves large departures from equilibrium, e.g., vapor deposition/condensation or rapid solidification, that are capable of trapping or utilizing these transient configurations. As examples of these new materials, amorphous materials and highly disordered or nano-grained semiconductors and intermetallic compounds have been studied extensively. However, their practical applications are not common and are limited by the high costs of energy intensive production processes [1-4] and by usage of materials that are scarce/strategic [5], e.g., rare earth (RE) elements, or harmful to the environment, e.g., Pb or Cd. Thus, there is a critical need for a growing research effort in materials synthesis approaches with high efficiencies that involve alternative widely available or benign components to fully exploit these useful nano-scale architectures and metastable states.

Several types of solidification processing approaches are promising for use-inspired synthesis research on nano-scale architectures, controlled by purposeful composition modification to derive maximum advantage from elements that are earth abundant and non-toxic. In the new work that is planned, these approaches present significant potential if fully developed for photovoltaics (PV) and thermoelectrics (TE) or as high capacity anode materials for Li-ion batteries and non-RE high strength permanent magnets. The Si-Mg system is a prime example of one alloy system that holds promise for eventual use in

three of these applications. We believe that the eutectic morphology that is accessible during controlled solidification of Mg_2Si/Si (with substitutions of Sn and Ge) offers an opportunity to improve energy-conversion efficiency in PV and TE devices by optimizing the self-assembled nano-scale architecture in this system by directional solidification. Also, using the inherent electrical conductivity of the Mg_2Si phase can offer advantage for novel synthesis of nano-particulate for anode material in Li ion batteries. In the case of the Al-Ni-Fe system, a simplified version of "Alnico" magnet alloys, theoretical calculations show that significant improvements of the coercivity may be possible by control of the envelope, at the lower size limit, within which the spinodal transformation occurs.

While the many examples of metastable functional materials rely on architecture control at solidification rates within the range of conventional crystal growth, two other examples rely on the "ultra-rapid" quench (up to 10^9 ˚C /s) rate of spark erosion (SE) device that we have begun to utilize in this FWP. This little-studied nano-particulate processing approach involves dielectric liquid quenching of a mixed atomic vapor or superheated liquid that is derived from the pulsed plasma heating of consumable electrodes of any conducting material. Actually, judging by the wide-spread use of electro-discharge machining (EDM), SE processing may be a fully scalable manufacturing method for generating a broad range of nano-particulate. The eroded material from both electrodes is transformed upon quenching into nano-metric or larger particulate (from a few nm up to 10μm), where the size can be controlled by selection of the SE process mode through interdependent parameter selections [7]. For Li ion battery anode materials, SE processing must be tuned to produce only amorphous nano-particulate, preferably of a well controlled Si-rich off-eutectic (e.g. from Mg_2Si, Sn, Sb, etc./Si eutectic systems) composition, since nano-particles of pure Si are known to have the highest possible Li capacity and good potential for high cycle life only if they remain unfractured [8]. Current synthesis methods involve complex multi-step chemical precipitation and pyrolysis to produce C-coated Si nano-particulate, but SE processing has the potential for one-step preparation of essentially pure Si nano-particles with a direct C-coating and a dispersed conductive phase that can add strain tolerance (for Li ion lattice dilation) and internal particle conductivity. If this SE synthesis route can be developed successfully, substitution of these anode materials into the most advanced cell construction of Li-ion batteries could achieve up to 6 X typical capacities [8] with a lifetime that extends to thousands of charge cycles.

The SE approach to ultra-rapid quenching also enables us to explore the ultimate limits of nano-scale architecture control in the whole class of spinodal phase transformations [9], with a pioneering experimental examination of the influence of 3D system envelope confinement on spinodal decomposition patterns. This type of study has important implications for the development of Alnico non-RE permanent magnets (PM) that currently rely primarily on shape anisotropy of Fe-Co spinodal phase precipitates within a Ni-Al parent (matrix) phase to generate a (fairly weak) coercivity effect. If the free surface envelope size can be driven by the synthesis of nano-particles toward the lower theoretical limit [10] for operation of spinodal phase separation, polymer-based experiments (with increased viscosity) on 2D confinement show [11] that there can be an extreme refinement of the precipitate size and spacing, just before the spinodal reaction is completely suppressed. Such an extreme refinement could provide a huge increase in the interfacial area between the magnetically active Fe-Co phase and the non-magnetic Ni-Al matrix, beyond the most recent experimental observations on quenched and annealed samples [12]. Some very recent calculations [12] show that step increases in inter-phase boundary area could provide a major jump in coercivity that is sorely needed in these magnets, perhaps enabling the 3X increase in energy product that is important for vehicle drive motor applications.

What architecture provides the best efficiency and performance for Li ion anode materials, and non-RE magnets? Can the architecture be obtained via ultra-rapid solidification or is another synthesis approach required? These are open questions. Experimental work is essential to answer these questions, as current computation capability can neither make accurate predictions of the optimum structures nor tell us how to make the materials.

Preliminary results (see Fig. 1) on SE processing of electrodes from the Mg_2Si/Si eutectic composition, $Mg_{46.6}Si_{53.4}$, with $T_{eut.} = 944$ ˚C, showed a significant spread in particle size and in the resulting particulate composition, where both 0.5-1µm Si particles and 5-20 nm Si-80Mg (at.%) particles were observed. As mentioned above, past work that involved primarily pure metals or single phase alloys indicated that SE processing can result in a bimodal distribution of particles with the larger particles resulting from molten droplet ejection, while the finest particulate (<50 nm) results from atomic vapor evaporation and condensation into the dielectric fluid. However, in a 2-phase alloy electrode with a large difference in melting point between the phases, our initial studies on SE processing of Si-25Sn (at.%) revealed that composition segregation can occur in parallel with size segregation, where the yield contained crystalline Si-enriched micron-sized spherical particles and amorphous Sn-enriched nano-particles. Analysis of the post-SE electrode tip cross-sections indicated that the uniform chill cast (starting) microstructure was converted by the sparking process heating effect at the electrode surface into large Si islands that "floated" within a Sn-enriched sea. This suggested the origin of the observed composition and size segregation results, i.e., melting and solidification of the Si-enriched islands and extreme superheating/evaporation/condensation of the Sn-enriched phase regions, which was later verified by SE processing of Si-5Sn.

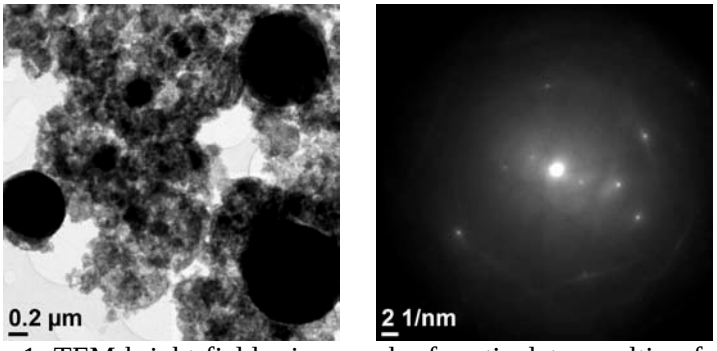

Fig. 1. TEM bright field micrograph of particulate resulting from SE of Mg_2Si/Si eutectic electrodes showing bi-modal size distribution and crystalline electron diffraction spots of Si particle.

Therefore, in addition to spark intensity parameter modifications, it was learned that the phase fraction of any low melting phase must be minimized to prevent this local surface segregation and rafting effect, even in the Mg_2Si/Si system with much closer melting points, i.e., Si (1414˚C) and eutectic (944˚C). Thus, one focus of future work will be on determining the minimum Mg content to provide sufficient electrical conductivity for effective spark erosion of the Mg_2Si/Si system. However, further modifications of the spark generator parameters (possibly adding a high frequency driver) for studies of the X/Si systems also will be performed to promote a strong preference for the evaporation mode to confine the yield to strictly nano-particulate that is preferred for the Li-ion anode material and for several other types of applications, including TE materials, as noted above. The Si-based nano-particulate produced by this process will be investigated by TEM and advanced spectroscopy, including Raman scattering, to explore these innovative anode materials for Li ion batteries with potential for high Li storage efficiency and cycling life. Experimental cell fabrication and electrochemical cycling exposure will also be performed (collaboration with S. Martin, Iowa State University) to investigate the capacity for reversible Li compound formation, as a method for ranking the results.

Complex "Alnico" permanent magnet alloys, e.g. Alnico 5-7, are a very mature commercial product and use a spinodal reaction to generate their beneficial magnetic properties, but there are fundamental aspects of the operation of spinodal transformations, especially near the lower size limit of the free surface envelope that remain and could be used to unlock a much higher regime of permanent magnet performance for this system. Extensions of the original theory of spinodal transformations [11] discuss the concept of a critical size or thickness (in 2D) called the bulk demixing length, below which the spontaneous periodic phase separation at high undercooling can be suppressed. However, some of the most interesting recent spinodal phase transformation work, also in the polymers field, involves the experimental study of 2D laminates that can experience an extremely refined population of dispersed "semi-crystalline" phases between the lower thickness limit, L_c, and a slightly higher thickness, L_c^*.

Since our initial studies of commercial Alnico microstructures with STEM (scanning transmission electron microscopy) recently confirmed that a typical spacing (center-to-center) of Fe-Co regions (in a cross-section that is transverse to the magnet axis) is about 50 nm (see Fig. 2), we are fairly confident that particle sizes smaller than about 50 nm will be needed to explore *for the first time* the 3D free surface envelop size needed to test the lower limit and, hopefully, the region between L_c and L_c^*.

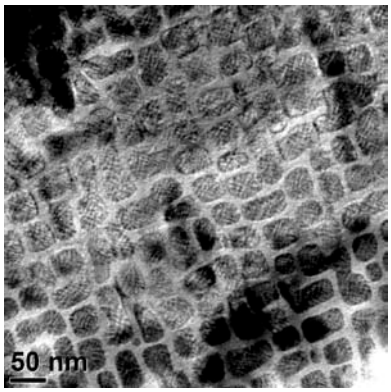

Fig. 2 TEM bright-field image showing the details of the spinodal structure in Alnico "5-7."

It is our intention to study the spinodal transformation in alloy particles in the approximate range of 1-100 nm of ternary Alnico-type alloys, Al-Ni-Fe, which was subject to detailed ternary phase diagram analysis, as well as more classic [110] anisotropic (Cu-Ni-Fe) and isotropic (Fe-Cr-Co) spinodal systems, among other, perhaps non-magnetic, systems. The Alnico-type alloy nano-particles will also be magnetically annealed to promote elongation of the precipitate phase along the magnet field axis. Because of the extremely small size of the precipitates, STEM characterization will be quite challenging and 3DAP (three dimensional atom probe) may also be required to gain sufficient information to make conclusions about attempts to access this type of nano-architecture in spinodal alloy systems. Of course, SQUID magnetometry will be used, as well, to investigate any effects on the magnetic properties that arise from such extreme precipitate refinement.

Refferences

1. V. Avrutin, N. Izyumskaya, and H. Morkoc, Superlattices Microst., **49**, 337 (2011).
2. A.J. Minich, M.S. Dresselhaus, Z.F. Ren, and G. Chen, Energy Environ. Sci., **2**, 466 (2009).
3. Y. Lan, A.J. Minnich, G. Chen, and Z. Ren, Adv. Funct. Mater., **20**, 357 (2010).
4. A.V. Dmitriev and I.P. Zvyagin, Physics-Uspekhi, **53**, 789 (2010).
5. Critical materials strategy, U.S. Department of Energy, December, 2010.
6. J. Tani and H. Kido, Intermetallics, **16**, 418 (2006).
7. J. Carrey, H.B. Radousky, and A.E. Berkowitz, J. Appl. Phys., **95**, 823-829 (2004).
8. J.R. Szczech and S. Jin, Energy Environ. Sci., **4**, 56-72 (2011).
9. J.W. Cahn, Acta Met. **9**, 795- 801(1961).
10. H.P. Fischer, P. Maass, and W. Dieterich, Europhys. Lett., **42**, 49-54 (1998).
11. X.Wang and N. Mashita, Polymer **45**, 2711-2719 (2004).
12. W.G. Chu, W.D. Fei, X.H. Li, D.Z. Yang, and J.L. Wang, Matls. Sci. and Tech., **16**, 1023-1028 (2000).

Conduction Mechanisms and Structure of Ionomeric Single-Ion Conductors
Part 2: Polysiloxane Ionomers

Ralph H. Colby, Janna K. Maranas, Karl T. Mueller, James Runt
Materials Research Institute, Penn State University, University Park, PA 16802
and Karen I. Winey
Materials Science and Engineering, University of Pennsylvania, Philadelphia, PA 19104

Program Scope

We are investigating low-T_g polysiloxane ionomers, which offer considerable versatility in polar groups, solvating groups and anions that can be attached as side groups. In particular, we have identified some large bulky borate anions with very diffuse charge, which offer substantially lower binding energy to small cations like Li^+. We aim to thoroughly understand ion conduction mechanisms of selected neat and plasticized members of this class of materials, toward our ultimate goal of designing ionomer membranes for facile ion transport.

Recent Progress Part 2: Polysiloxane Ionomers

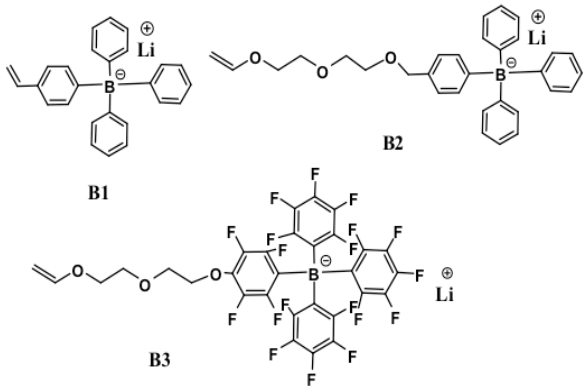

Three novel weak-binding borates: lithium triphenylstyryl borate (B1), lithium triphenyl (4-((2-(2-vinyloxy) ethoxy) ethoxy) methyl) phenyl) borate (B2) and lithium tris(perfluorophenyl) (2, 3, 5, 6 tetrafluoro-4-(2-(2-(vinyloxy) ethoxy) ethoxy)phenyl) borate (B3) were successfully synthesized and characterized by ^1H, ^{11}B and ^{19}F NMR spectroscopies. *Ab initio* calculations indicate that borates with the abovementioned structures have rather weak ion binding energies.

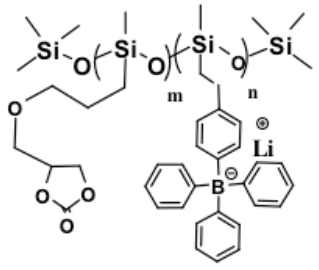

P-5(8, 10, 14)

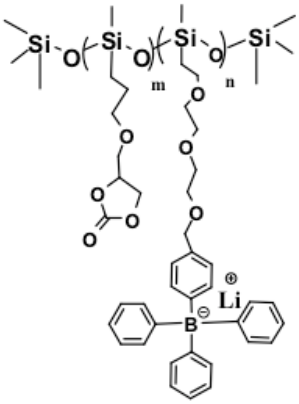

SP-2(5)

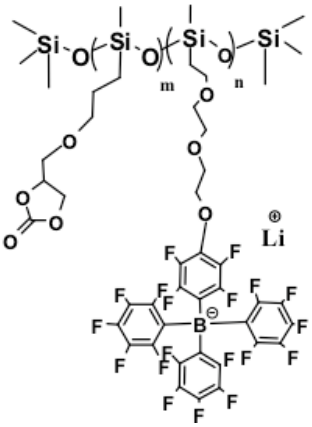

FSP-5

We successfully synthesized three groups of polysiloxane-based single-ion conductors with structures shown above, using a one-pot hydrosilylation reaction. The structures of these ionomers were confirmed by NMR spectroscopy. The borates are demonstrated to be intact after chemical reaction by ^{11}B NMR spectroscopy. The attached carbonate side chain groups are expected to increase the dielectric constant of the polymer matrix and facilitate ion solvation.

The conductivities of the ionomers as a function of temperature are displayed in the figures below. The relationship between ion concentration and conductivity at the same borate content indicates that, with increasing ion content, the ionomer T_g increases and the conductivity initially increases, then drops greatly. The conductivities normalized by T_g fall on nearly one curve, which demonstrates again the vital role of polymer segmental dynamics. At high ion content, a conductivity of 10^{-4} S/cm requires $T = 1.5\ T_g$, meaning that $T_g = -70$ ˚C is needed to achieve 10^{-4} S/cm at room temperature.

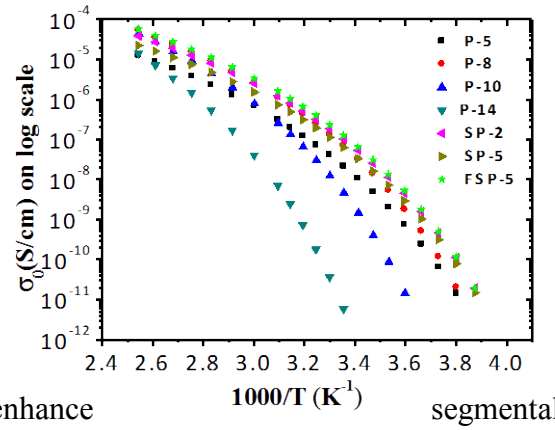

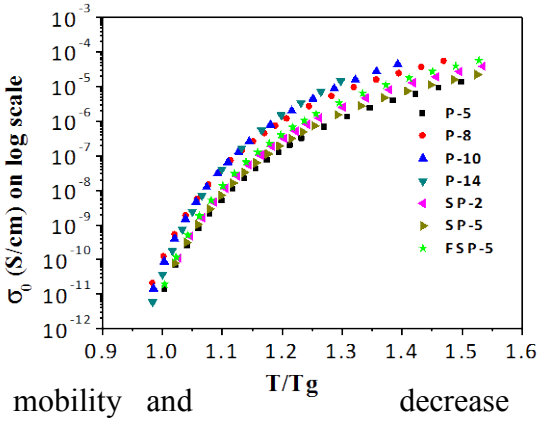

In order to enhance segmental mobility and decrease the tendency for ion aggregation, a typical polysiloxane single ion conductor, P5(10) in the schematic, was plasticized with polyethylene glycol (M_n = 600) to various extents (0, 13, 25, 34, 54, and 70 wt% PEG600).

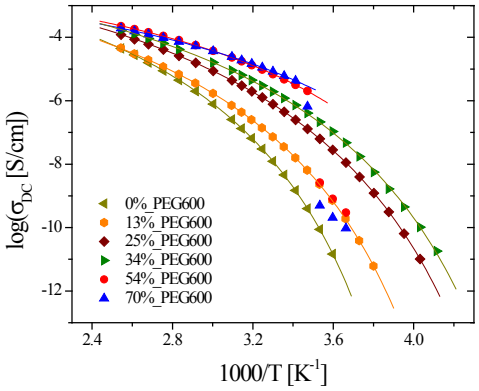

Ionic conductivities σ_{DC} for the neat polymer and the plasticized ones, shown in the figure at left, exhibit a Vogel-Fulcher-Tammann temperature dependence (solid lines). With increasing PEG600 content, the conductivity increases: the 54% and 70% PEG600 display the highest room temperature conductivity (10^{-5} S/cm). To better understand the conduction mechanism, a mean-field model of electrode polarization was used that allows separation of the conductivity $\sigma_{DC} = ep\mu$ into instantaneous conducting ion content p and mobility μ.[1,2] The fraction of ions participating in conduction (p/p_0 : p_0 is the total cation number density) is shown at below left. The temperature dependence of p/p_0 is well described by an Arrhenius equation (dashed lines), indicating that the conducting ions will be fully dissociated at infinite temperature. As PEG600 content increases, the fraction of conducting ions increases significantly by one to two orders magnitude. However, for the neat polymer approximately 90% of the ions are in aggregates. Shown below on the right is the temperature dependence of ion mobility, which follows VFT behavior (solid lines). The inset figure shows the dependence of T_g (DSC) (open symbols) and the T_g determined from dielectric spectroscopy (defined at $\omega_\alpha(T_g) = 10^{-2}$ rad/s , filled symbols), well described by the Fox equation (solid line). The mobility data demonstrates that adding PEG600 results in increasing ion mobility due to lowering T_g. The fact that adding PEG600 increases p and μ leads us to the proposal that PEG600 plays an important role in increasing ionic conductivity by solvating Li^+ so as to dissolve ionic aggregates as well as lower T_g.

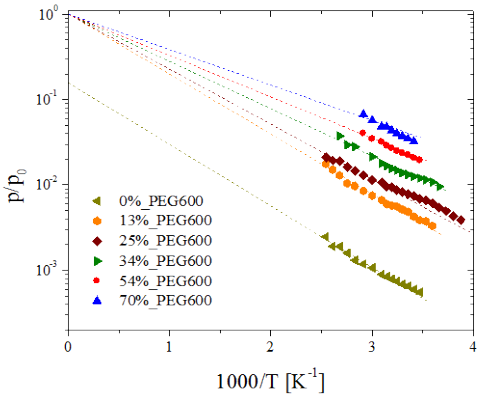

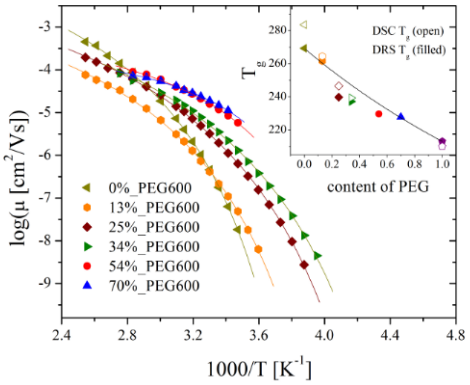

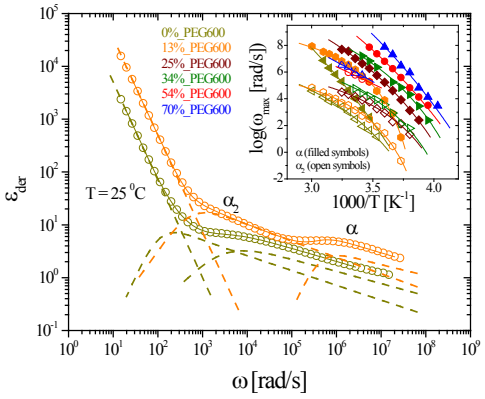

Derivative dielectric spectra ε_{der} reveal two relaxations. The usual segmental relaxation is denoted α and a second slower relaxation associated with ion motion is denoted α_2, shown in the figure at left. The inset figure shows the relaxation frequencies ω_{max} of the α (filled symbols) and α_2 (open symbols) processes, which follow VFT behavior (solid lines). It also demonstrates that the α and α_2 processes of 70% PEG600 (having the lowest T_g) are much faster than those for 0% PEG600. Increasing the PEG600 content from 0% to 13%, leads to an increase in strength of the α_2 relaxation and the static dielectric constant ε_s, shown in the figure at right, significantly increases. Adding a relatively small amount of PEG600 results in ion pairs become solvent-separated as opposed to contact pairs, leading to the rapid increase in ε_s. Adding further PEG600 reduces ε_s due to dilution with lower dielectric constant PEG600.

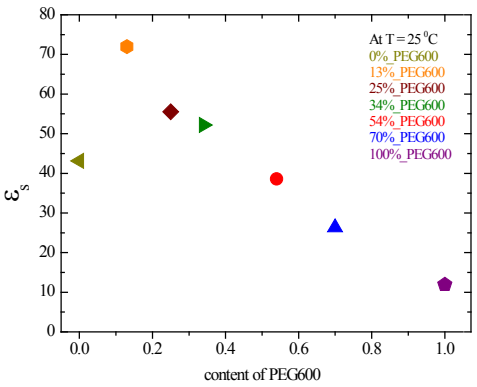

Future Plans

We are currently working on replacing the carbonate side groups of the polysiloxane ionomers with PEG side chains. Our preliminary results indicate that by incorporating such side groups, the T_g of the ionomer can be lowered to -70 ˚C. We are also synthesizing new plasticizers with both carbonate and ether oxygen groups and will be adding them to single-ion conductors to further improve the ionic conductivity and better understand the conduction mechanism. Polycationic ionomers based-on polysiloxane are being synthesized and characterized as a third generation of single-ion conductor by our research team. ^{7}Li, ^{11}B, ^{29}Si, and ^{1}H-^{13}C cross polarization magic angle spinning NMR experiments are being undertaken to elucidate both the structure and dynamics of the cation and anion in these novel ionomers, as well as the polymer backbone. Nanoscale structure and polymer/ion dynamics of the new

materials will be further characterized using multi-angle X-ray scattering and dielectric spectroscopy, respectively.

References

1. D. Fragiadakis, S. Dou, R.H. Colby and J. Runt, *J. Chem. Phys.* 130, 064907 (2009).
2. D. Fragiadakis, S. Dou, R.H. Colby, and J. Runt, *Macromolecules* 41, 5723 (2008).

DOE Sponsored Publications in 2010-2011

- W. Wang, G. Tudryn, R.H. Colby, K.I. Winey, "Thermally Driven Ionic Aggregation in Poly(ethylene oxide)-based Sulfonate Ionomers." *J. Amer. Chem. Soc.* 133, 10826 (2011).
- A. Castagna, W. Wang, K.I. Winey, J. Runt, Influence of Cation Type on Structure and Dynamics of Sulfonated Polystyrene Ionomers, *Macromolecules.* 44, 5420 (2011).
- K. Sinha and J.K. Maranas, Segmental Dynamics and Ion Association in Poly(ethylene oxide)-based Single-ion Conductors, *Macromolecules* 44, 5381 (2011).
- A. Castagna, W. Wang, K.I. Winey, J. Runt, Structure and Dynamics of Zinc Neutralized Sulfonated Polystyrene Ionomers, *Macromolecules.* 44, 2791 (2011).
- W. Wang, W. Liu, G.J. Tudryn, R.H. Colby and K.I. Winey, Multi-scale Morphologies of Poly(ethylene oxide)-based Sulfonate Ionomers with Alkali Cations at Room Temperature, *Macromolecules* 43, 4223 (2010).
- A. Castagna, W. Wang, K.I. Winey, J. Runt, Sulfonation Effects on the Structure and Dynamics of Sulfonated Polystyrene Copolymers, *Macromolecules* 43, 10498 (2010).
- D.J. Roach, S. Dou, R.H. Colby and K.T. Mueller, Nuclear Magnetic Resonance Investigation of Dynamics in Poly(ethylene oxide)-based Lithium Polyether-ester-sulfonate Ionomers, *J. Chem. Phys.*, Submitted for publication.
- S. Liang, U.H. Choi, W. Liu, M. O'Reilly, K.I Winey, J. Runt and R.H. Colby, Synthesis and Lithium Ion Conduction of Polysiloxane-based Single-Ion Conductors Containing Novel Weak-Binding Borates, *J Amer Chem Soc,* Submitted for publication.
- G.J. Tudryn, M.V. O'Reilly, S. Dou, D.R. King, K.I. Winey, J. Runt, and R.H. Colby, "Molecular Mobility and Cation Conduction in Polyether-ester-sulfonate Copolymer Ionomers", *Macromolecules,* Submitted for publication.

Characteristic Length Scales of Growing Nanorods

– Atomistic Simulations, Analytical Formulations, and Experiments

Longguang Zhou, Soohwan Lee, Ruoxin Zhang, Stephen Stagon, and Hanchen Huang
hanchen@uconn.edu
Department of Mechanical Engineering
University of Connecticut, Storrs, CT 06269

Program Scope

Growth of nanorods has been a common practice using physical vapor deposition [1, 2], but the scientific original of their dimension has not been known for a long time. The dimension of nanorods is on the order of 100 nm, and this dimension should be a characteristic length scale of materials and growth processes [3]. Without chemical catalysis such as in chemical vapor deposition, this length scale is likely the result of competition between diffusion kinetics and thermodynamics. This DoE/BES project focuses on the origin of the length scale in pure materials and its control using surfactants in the previous period (before March 31, 2011), and focuses on the identification of related characteristic length scales and the interplay of these length scales and nanorod dimension during nanorod growth in the current period (after April 1, 2011).

Recent Progresses

We focus on four related advancements in the basic science of nanorod growth.

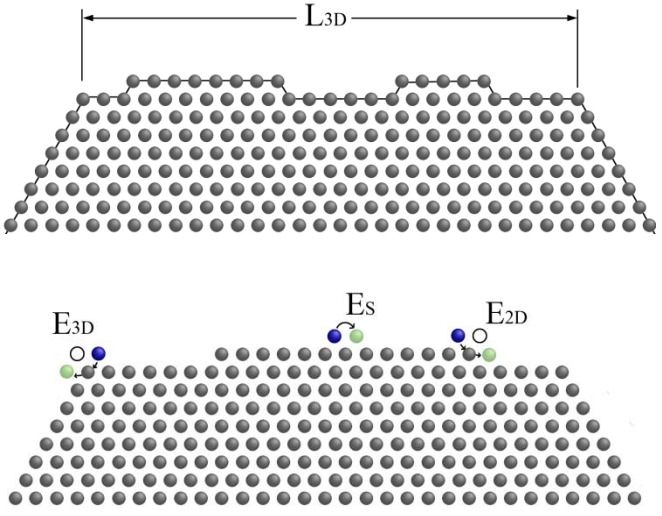

Figure 1: Concept of new characteristic length scale (top) and competing diffusion kinetics (bottom).

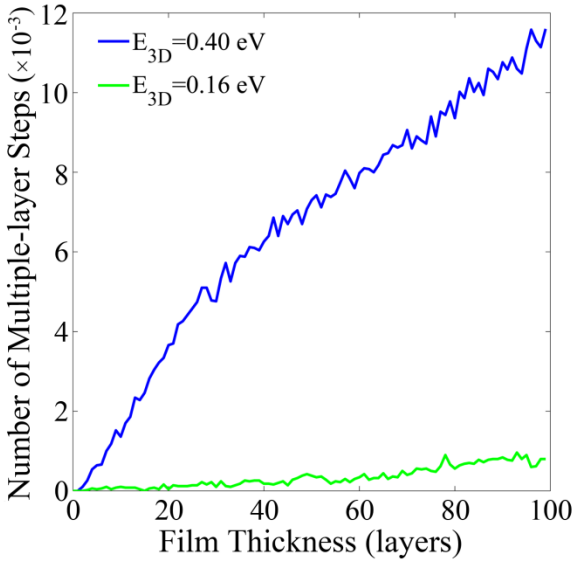

Figure 2: Stabilization of multiple-layer steps by 3D ES barrier.

First, we have proposed the concept of a new characteristic length scale (Figure 1) and identified the origin of nanorod dimension [3]. Using both atomistic simulations and analytical formulation, we show that the nanorod dimension is the result of three-dimensional Ehrlich-Schwoebel (3D ES) barriers and other diffusion barriers. The operation of 3D ES barrier relies on the availability of multiple-layer surface steps.

Second, we have identified a mechanism of stabilizing multiple-layer steps (Figure 2), which are necessary for the operation of 3D ES barriers and the development of nanorod dimension. Even starting from a flat substrate, multiple-layer surface steps can nucleate through random collision of monolayer steps. However, the multiple-layer surface steps can stabilize only if 3D ES barriers are sufficiently large. That is, large 3D ES barriers stabilize multiple-layer steps, and multiple-layer steps in turn facilitate the operation of 3D ES barriers. This positive feedback allows the eventual nanorod growth even from flat substrates [4].

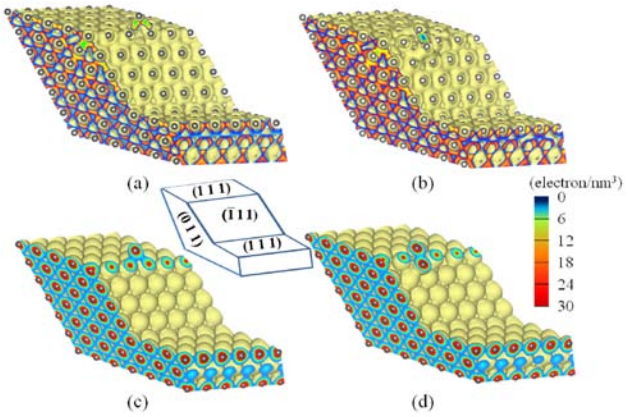

Figure 3: Electron density distribution of Al (top) and Cu (bottom), showing the different degrees of covalence.

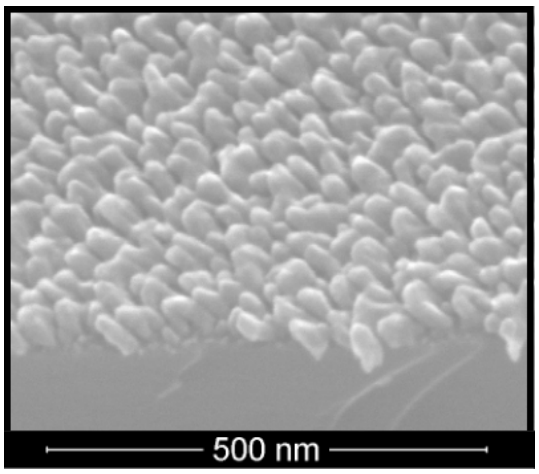

Figure 4: Scanning electron microscopy image of ultrasmall Cu nanorods.

Third, we have identified a correlation between covalence in metals and the magnitude of 3D ES barriers (Figure 3); reference [5]. In particular, Al and Cu have comparable melting temperatures and sublimation energies, but they have very different 3D ES barriers (0.13 eV versus 0.40 eV). The much smaller 3D ES barrier of Al is the result of covalence. This result has three other implications: (1) it can now be understood why numerous papers have described Cu nanorods but none have reported Al nanorods (to our best knowledge), (2) surfactant can work through a new mechanism – one can use surfactant to control the local covalence so as to control the 3D ES barrier and the characteristic length scales, and (3) it may be possible to realize Al nanorods using surfactant to reduce local covalence (and similar to realize Cu films more easily by enhancing local covalence).

Finally, we have realized nanorods of ***extrinsic*** characteristic length scale, somewhat accidentally. Through CINT user project in collaboration with Amit Misra of Los Alamos National Laboratory, we experimentally explored the application of surfactants. Using physical vapor deposition, we have obtained Cu nanorods of about 30 nm in diameter (Figure 4), which is almost an order of magnitude smaller than the intrinsic characteristic length scale; reference [6]. In connection with the second advancement on the stability of multiple-layer steps, it is understandable that the ultrasmall Cu nanorods can result from higher stability of multiple-layer steps and the higher stability can result from smaller separation of nanorod nuclei. On the other hand, this experimental work also shows that the eventual dimension of nanorods also depends on other length scales, such as the separation of nanorod nuclei. What are the origins of all these length scales and how do they interplay during nanorod growth? Answering these questions is the focus in the current period of this DoE/BES project (after April 1, 2011).

Future Plans

The overall goal is to identify the origins of relevant characteristic length scales and their interplay during nanorod growth. The plan is to first conceptualize the relevant characteristic length scales, including the dimension of nanorod nuclei, the dimension of surface islands bounded by monolayer steps, the dimension of surface islands bounded by multiple-layer steps, and the dimension of surface islands bounded by a dynamic mixture of monolayer and multiple-layer steps. Next, we use atomistic simulations to guide theoretical formulations of models that describe these characteristic length scales. In parallel, we will carry out selected experiments for validation and also for stimulation of new concepts. The newly approved CINT user project (U2011A1012) will enable the continued collaboration with Amit Misra in the experimental studies.

References

1. J. Wang, H. C. Huang, S. V. Kesapragada, and Daniel Gall, “Growth of Y-shaped Nanorods through Physical Vapor Deposition”, **Nano Letters** *5*, 2505-2508 (2005).
2. F. Tang, C. Gaire, D.-X. Ye, T. Karabacak, T.-M. Lu, and G.-C. Wang, “AFM, SEM and in situ RHEED study of Cu texture evolution on amorphous carbon by oblique angle vapor deposition”, **Physical Review B** *72*, 035430 (2005).
3. L. G. Zhou and H. C. Huang, “A Characteristic Length Scale of Nanorods Diameter during Growth”, **Physical Review Letters** *101*, 266102-1-4 (2008).
4. R. X. Zhang and H. C. Huang, “Another Kinetic Mechanism of Stabilizing Multiple-layer Surface Steps”, **Applied Physics Letters** *98*, 221903 (2011).

5. S. W. Lee and H. C. Huang, “Control of Diffusion Barriers via Covalence in Metals”, **Applied Physics Letters** (2011) submitted.
6. S. Stagon, Hanchen Huang, J. K. Baldwin and A. Misra, “Physical Vapor Deposition of Ultrasmall Cu Nanorods”, in preparation.

Publications Resulted from DoE/BES Sponsored Project

1. S. W. Lee and H. C. Huang, “Control of Diffusion Barriers via Covalence in Metals”, **Applied Physics Letters** (2011) submitted.
2. S. Stagon, H. C. Huang, J. K. Baldwin and A. Misra, “Physical Vapor Deposition of Ultrasmall Cu Nanorods”, in preparation.
3. H. C. Huang, “Twin Boundaries in Nanowires – Controllable Introduction”, **JOM** (2011) in press – to appear in Sept 2011.
4. R. X. Zhang and H. C. Huang, “Another Kinetic Mechanism of Stabilizing Multiple-layer Surface Steps”, **Applied Physics Letters** *98*, 221903 (2011).
5. Y. F. Zhang and H. C. Huang, "Controllable Introduction of Twin Boundaries into Nanowires", **Journal of Applied Physics** *108*, 103507 (2010).
6. Y. Yang, H. C. Huang, S. K. Xiang, and E. Chason, "Another Mechanism of Stress Control in Thin Films: Use of Surfactants", **Applied Physics Letters** *96*, 211903 (2010).
7. S. K. Xiang and H. C. Huang, "Binding of In and Pb Surfactants on Cu{111} Surfaces", **Surface Science** *604*, 868-871 (2010).
8. C. G. Johansen, H. C. Huang, and T. M. Lu, “Diffusion and Formation Energies of Adatoms and Vacancies on Magnesium Surfaces”, **Computational Materials Science** *47*, 121-127 (2009).
9. D. Aidhy, P. C. Millett, S. R. Phillpot, D. Wolf, and H. C. Huang, “Kinetically-driven Point-defect Clustering in Irradiated MgO by Molecular-dynamics Simulation”, **Scripta Materialia** *60*, 691-694 (2009).
10. H. C. Huang and H. van Swygenhoven, “Atomistic Simulations of Mechanics of Nanostructures”, **MRS Bulletin** *34*, 160-163 (2009).
11. H. S. Park, W. Cai, H. D. Espinosa, and H. C. Huang, “Mechanics of Crystalline Nanowires”, **MRS Bulletin** *34*, 178-183 (2009).
12. H. W. Shim, J. D. Kuppers, and H. C. Huang, “Strong Friction of Silicon Carbide Nanowire Films”, **Nanotechnology** *20*, 25704-1-4 (2009); highlighted in news report **http://nanotechweb.org/cws/article/lab/37263**.

Understanding and Controlling Nanoscale Crystal Growth Using Mechanical Forces

Mostafa Bedewy, Justin D. Beroz, and A. John Hart
Department of Mechanical Engineering
University of Michigan, Ann Arbor, MI

1. Program Scope

Growth of one-dimensional nanostructures such as carbon nanotubes (CNTs) and silicon nanowires (SiNWs) is analogous to bulk crystal growth, where a solid is formed by precipitation due to a thermodynamic driving force at an interface. While it is well-known that mechanical stress affects crystal growth, diffusion, and defect migration [1-3], the mechanisms and roles of these phenomena at the nanoscale are not comprehensively understood, and have not been studied with respect to growth of nanostructures. In this program, we will explore how mechanical stimulation may be used to control the formation rate, geometry, and perfection of one-dimensional nanostructures; and thereby aim to understand how mechanical stress affects the growth of crystals at the nanoscale. Specifically, we will study growth of CNTs and SiNWs because their basic growth processes are well-known, yet there is important need to more precisely control the structure and properties of CNTs and SiNWs for many applications. For this purpose, we are constructing micromanipulation systems for application of controlled forces to one-dimensional nanostructures during growth. We will employ comprehensive *in situ* and *ex situ* characterization to relate the measured growth kinetics and structural transformations of the nanostructures to the imposed mechanical stimuli.

2. Recent Progress

Since the program began in September 2010, we have focused on two main tasks: (1) design and fabrication of a new CVD growth chamber that will enable *in situ* manipulation of nanostructure growth; (2) analysis of the population dynamics of CNT ensembles (forests), enabled by high-resolution mapping using X-ray scattering. Key findings are described below.

(1) CVD reactor with in situ micromanipulators

We have designed (Fig. 1a), and are currently fabricating, a "cold-wall" CVD reactor chamber with two *in situ* manipulators. The first manipulator is contained within the tower above the substrate, and comprises a linear motion system, coupled to a flat probe electrode via a linear motion system. The flat tip will be used to grab CNT pillars using electric fields and/or capillary action. A catalyst substrate will be placed on a on a feedback-controlled heater platform connected to a four degree-of-freedom (X-Y-Z-θ) alignment stage. After heating the stage, growth gases will then be introduced through the inlet, causing CNTs to grow from the lithographically-patterned patches on the substrate.

The manipulator comprises an electrode mounted to a linear motion system via a series load cell connection. The motion system consists of a central shaft which is actuated vertically by a voice coil motor and constrained by a pair of flexure bearings (Fig 1b). Position and velocity of the shaft are controlled via a closed loop feedback control based on readings from the optical encoder. This design allows frictionless translation of the shaft, which enables very smooth motion with 20nm resolution.

The two linear flexure bearings (Fig. 1c) have been designed to be compliant only in the vertical direction and stiff along the other 5 degrees of freedom. Principles of symmetry have been employed to allow vertical displacement without parasitic rotation. Flexure beam dimensions have been optimized to provide a force-displacement curve tailored to our voice-coil actuator and to the strain limits of the flexure bearing material. Bearing deflection characteristics were numerically calculated using finite element simulations in ANSYS. Following clockwise, Fig. 1c shows the bearing finite element mesh, undeformed bearing, and deformed bearing due to Z-direction force.

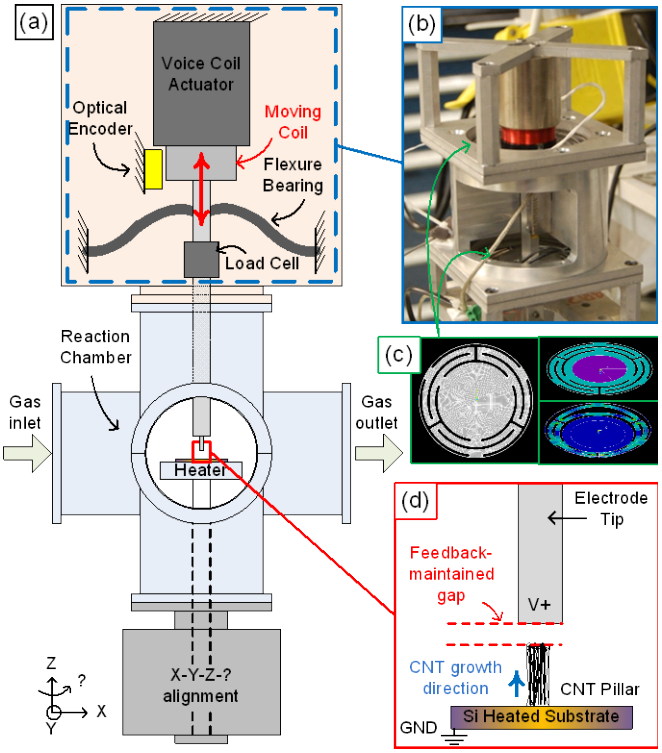

Figure 1: CVD system for growth manipulation: (A) Schematic of CVD chamber and integrated manipulators; (B) Assembled vertical motion system in the lab; (C) Finite Element Analysis of flexure bearing; (D) Schematic of electrostatic gripping configuration.

(2) CNT population analysis

In preparation for analysis of CNT growth under applied mechanical and electrical stimulation, we have developed a precise and nondestructive technique for the spatial mapping of CNT characteristics within a vertically aligned forest. This is a significant step beyond our previous work, because now using a focused X-ray beam we can obtain high-resolution (10-20 μm beamspot) maps of the internal structure of the forest, in a beamline configuration where X-ray scattering and absorption data are acquired simultaneously (Fig. 2a). Each data point represents a differential slice of the sample. X-ray scattering was performed as an external user at the G1 beamline of the Cornell High Energy Synchrotron Source (CHESS).

By combining X-ray scattering images, X-ray absorption data, and in situ measurements of CNT forest height versus time (taken during growth), we have

Initial experimentation with this setup has shown that vertical attractive forces develop between CNTs and the electrode tip under the influence of an applied electric potential. These forces will be measured by the load cell. Load cell measurements will be monitored as part of a closed-loop control algorithm which will apply constant or time-varying forces to a CNT pillar *in situ* and record the growth kinetics (Fig. 1d). In parallel with this effort and with separate funding from ONR, we have designed a compliant microgripper. This will provide another option for grasping the CNTs.

We have also designed the heater system, the X-Y-Z-θ manipulation stage and the tilt stage, and are currently in the process of manufacturing parts to be assembled with the off-the-shelf components. While this system is designed for experiments on CNT ensembles, we also plan to try growing individual CNTs by mounting a sharp tip as the vertical moving electrode, and growing the CNT downward toward the stage.

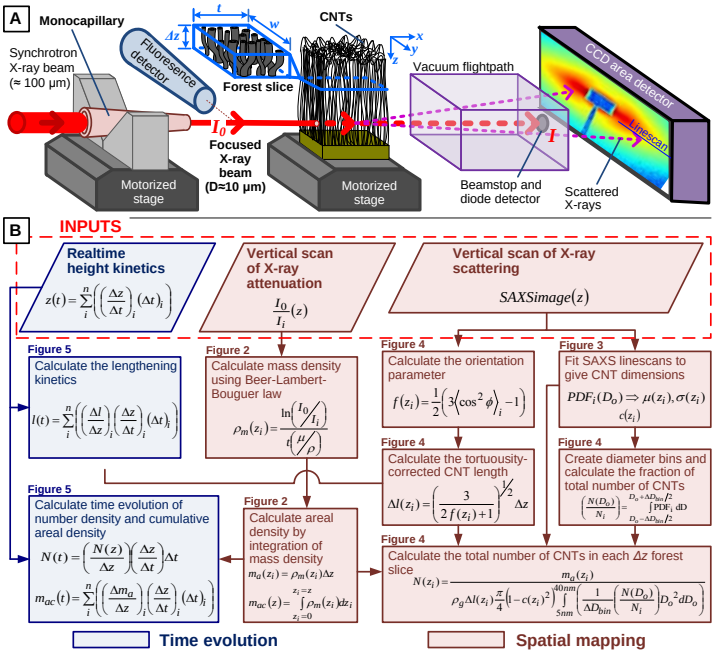

Figure 2: Method of X-ray mapping and analysis of CNT populations: (A) Schematic of experimental setup for simultaneous spatially-resolved synchrotron X-ray absorption and scattering measurements; (B) Quantitative analysis procedure incorporating real-time CNT height measurements with X-ray data to give mass and number density kinetics.

developed a comprehensive methodology (Fig. 2b) to obtain the "true" kinetics of CNT forest growth. To understand the population evolution of CNTs, we use the small angle X-ray scattering (SAXS) patterns in order to obtain diameter distribution and alignment information of CNTs within each CNT slice. We can map the evolution of CNT outer diameter (CNT OD) through the forest (modeling the CNTs as a lognormally distributed population of hollow cylinders), and find that the diameter decreases gradually while the coefficient of variation first decreases then increases (Fig. 3a). This data, in turn enables mapping of the number density of CNTs, which increases rapidly at the initial stage of growth, then decreases gradually, leading to eventual collective self-termination [4] (Fig 3b).

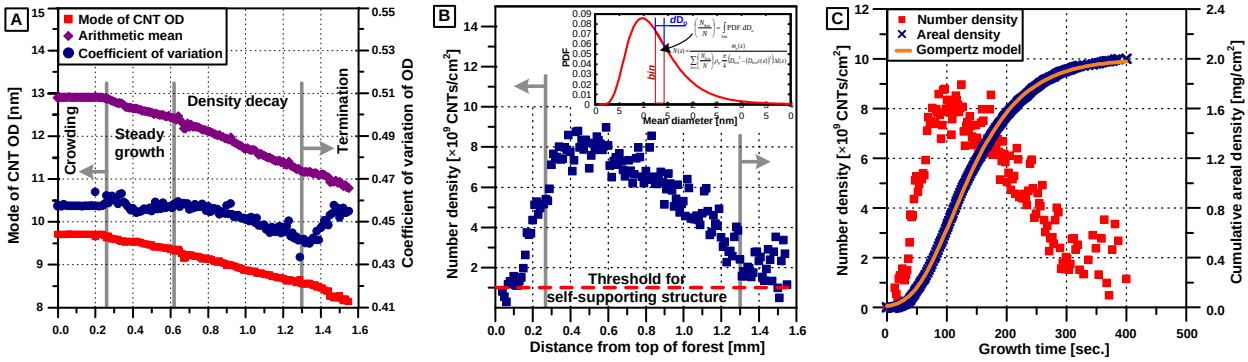

Figure 3: Population evolution of CNTs: (A) Mode, arithmetic mean, and coefficient of variation of outer CNT diameter (OD), calculated for each beam position ("slice") of the forest; (B) Spatial map of CNT number density, calculated using the CNT diameter distribution and the tortuosity-corrected average CNT length for each slice. Inset to (B) describes calculation of the total number of CNTs from PDF of CNT OD distributions. (C) Time evolution of both the number density and areal density of CNTs during growth

Using real-time height kinetic measurements, the time evolution of mass per unit area (areal density) and the number density can be calculated. Fig. 3c shows that a Gompertz model of population growth [5] perfectly fits all stages of growth. These results suggest that CNT self-organization may be limited by both mechanical and chemical effects due to autocatalysis within the reaction atmosphere. Analysis of diameter-dependent CNT growth kinetics is ongoing. Data from this study will be used to inform a model of mechanically coupled CNT growth which will be developed during the next year.

3. Future Plans

First experiments will investigate the effect of electrostatically and/or mechanically applied forces on the growth kinetics of individual micron sized CNT pillars using the CVD reactor manipulation system described above. The applied voltage and electrode-pillar separation gap may be temporally varied in response to applied force and pillar growth kinetics.

To understand the effects on the CNT morphology and crystal structure, we will first perform *ex situ* SAXS mapping of the grown CNT pillars, and will later perform *in situ* SAXS by mounting the reactor directly in the beamline. The sample will be aligned to the focal length of the optics, and by illuminating only a small portion of the capillary, the divergence at the sample position will be limited. For *in situ* measurements we will use GI-SAXS to interrogate the CNTs within several microns of the substrate and obtain <0.1s time resolution of the scattering.

We plan to construct a MEMS device for exerting one-dimensional mechanical forces on individual nanostructures. This device will enable precise investigation of how the growth rate and structure of CNTs and SiNWs respond to applied forces, and will be capable of mounting in a custom TEM sample holder for direct imaging of the structures during and after tension and compression. Forces will be applied using a silicon flexure mechanism that will have an integrated actuator. The specifications of this mechanism (i.e., stiffness, force resolution, displacement resolution, and stroke) will be chosen based on the characteristics of the nanostructures, and different mechanism specifications will likely be chosen for

CNTs and SiNWs. The design will be guided by recent work on directed CNT growth within MEMS devices, and in situ mechanical testing of CNTs using microfabricated mechanisms [6, 7]. Actuation of SWNT growth will likely be the most stringent requirement, as we will aim for a displacement resolution of 1 nm with travel of 10 μm to allow for profiling of the SWNT by Raman spectroscopy.

4. References

1. Aziz, M.J., et al., *CRYSTAL-GROWTH KINETICS OF BORON-OXIDE UNDER PRESSURE.* Journal of Applied Physics, 1985. **57**(6): p. 2233-2242.
2. Aziz, M.J., *Thermodynamics of diffusion under pressure and stress: Relation to point defect mechanisms.* Applied Physics Letters, 1997. **70**(21): p. 2810-2812.
3. Nygren, E., et al., *PRESSURE-DEPENDENCE OF ARSENIC DIFFUSIVITY IN SILICON.* Applied Physics Letters, 1985. **47**(2): p. 105-107.
4. Bedewy, M., et al., *Collective Mechanism for the Evolution and Self-Termination of Vertically Aligned Carbon Nanotube Growth.* Journal of Physical Chemistry C, 2009. **113**(48): p. 20576-20582.
5. Frenklach, M. and D. Clary, *ASPECTS OF AUTOCATALYTIC REACTION-KINETICS.* Industrial & Engineering Chemistry Fundamentals, 1983. **22**(4): p. 433-436.
6. Stampfer, C., et al., *Fabrication of single-walled carbon-nanotube-based pressure sensors.* Nano Letters, 2006. **6**(2): p. 233-237.
7. Stampfer, C., et al., *Nano-electromechanical displacement sensing based on single-walled carbon nanotubes.* Nano Letters, 2006. **6**(7): p. 1449-1453.

5. Program Publications Supported by DOE Funds

1. M. Bedewy, M.J. Reinker, E.R. Meshot, A.R. Woll, A.J. Hart. Population dynamics of carbon nanotube forest growth. Submitted for publication, 2011.
2. J. Beroz, S. Awtar, M. Bedewy, A.J. Hart. Compliant microgripper with straight-line jaw trajectory. To appear in Proceedings of the Annual Meeting of the American Society of Precision Engineering, 2011.

Non-Equilibrium Synthesis of Nanostructured Materials: Laser Vaporization Synthesis of Nanoparticle Building Blocks (ERKCS81)

Alex Puretzky,[1] David B. Geohegan,[1] Christopher M. Rouleau,[1] Jason D. Readle,[2] Mina Yoon,[2] Gyula Eres,[2] Murari Regmi,[2] Karren L. More[2] and Gerd Duscher[2,3]
puretzkya@ornl.gov
[1]Center for Nanophase Materials Sciences and [2]Materials Science and Technology Division, Oak Ridge National Laboratory, Oak Ridge, TN 37831 and the [3]Dept. of Materials Science and Engineering, Univ. of Tennessee, Knoxville, 37996

Program Scope

The goal of this program is to develop a fundamental understanding of the non-equilibrium aspects of nanomaterial synthesis by exploring the growth mechanisms and resulting structures of nanoscale materials formed in controlled environments. Pulsed, non-equilibrium growth and processing approaches, such as those involving lasers and supersonic molecular beams, are developed to supply the necessary kinetic energy required to explore the synthesis of nanostructures with metastable phases and structures that are inaccessible using traditional synthetic methods. A distinguishing feature of the program is the development and application of time-resolved, in situ diagnostics of nanomaterial growth kinetics and a corresponding development of models to understand the underlying kinetic and chemical pathways. Spatial confinement and reactive quenching approaches are developed to explore the synthesis mechanisms of rationally-designed nanostructures with enhanced intrinsic properties, targeting: (1) oxide, carbon, and alloy nanomaterials produced in metastable states by catalyst-free or catalyst-mediated processes, and (2) doped, decorated, and filled nanomaterial hybrids designed to induce permanent electric fields or distribute charge within nanostructures. Theoretical methods are used to understand fundamental mechanisms of synthesis in order to guide the formation of nanostructures tailored to enhance energy storage, catalysis, thermal management, and photovoltaics in support of DOE's energy mission.

Recent Progress

Here, time-resolved in situ diagnostics are used to understand the formation of nanoparticles by laser ablation, and develop new processing approaches for their integration as building blocks in the processing of new architectures. Nanoparticles may be directly ejected from laser-vaporized targets, especially in the case of ultrafast laser ablation, however clusters and nanoparticles are principally formed by the condensation of laser-vaporized atoms and molecules when confined by a background gas or liquid. These clusters can serve to change the growth morphology of thin films grown by pulsed laser deposition, or provide the feedstock for the growth of a great variety of nanoparticles, nanowires and nanotubes either by self-assembly or by directed growth from metal catalyst nanoparticles. These processes, coupled with the additional synthesis opportunity provided by metal catalyst nanoparticles, offer unique opportunities for non-equilibrium growth of nanoparticles, nanowires, and nanostructured films.

To understand the growth kinetics and transport of nanoparticles resulting from laser vaporization processes we have developed combined *in situ* diagnostics incorporating gated-intensified CCD imaging and spectroscopy in conjunction with time-delayed, tunable laser excitation in three growth environments: (i) pulsed laser deposition (PLD), (ii) laser vaporization (LV) at high temperatures in a tube furnace, and (iii) femtosecond laser ablation of thin films. In addition, a scanning mobility particle sizing system (SMPS) is being adapted to provide particle size distributions of gas-suspended nanoparticles formed in these different pressure environments. In PLD, it is well-known that background gas pressures for smooth films are limited by the formation of clusters and nanoparticles in the thermalizing plume at higher pressures. This has recently been developed to grow oxide nanoparticle architectures and nanorods by intentionally using nanoparticles as the feedstock in NAPLD (nanoparticle assisted PLD).[1]

LAND - Laser Ablated Nanoparticle Deposition - Figure 1 illustrates an approach to explore the synthesis of nanowires by catalyst-assisted growth from nanoparticle feedstocks (LAND - laser ablated nanoparticle deposition). As shown in Fig. 1(a), KrF-laser ablation of a target (e.g. SnO_2) in flowing gas is used to generate nanoparticles which are carried to metal catalyst nanoparticles on a substrate, here Au on Si or $SrTiO_3$. This technique is carried out in a tube furnace and is similar to chemical vapor deposition, except that clusters and nanoparticles of materials otherwise difficult to supply as growth gases can be used as stoichiometric aerosols instead of gas molecules which must be catalytically decomposed. We are exploring how nanowires grow by condensed phase conversion of laser-synthesized clusters and nanoparticles of different sizes.

Alternatively, aggregates of nanoparticles can be photodissociated to provide sufficient feedstock for nanowire growth. Fig. 1(b) shows visible photoluminescence from the KrF-laser interaction with separated clouds of nanoparticles produced from previous laser pulses. As shown in Fig. 1(c), by firing a second laser (355 nm) delayed from either the 1st or 2nd KrF-laser pulse we can examine the plasma (Fig. 1(d), its evolution into nanoparticles (by imaging of nanoparticle clouds by Rayleigh scattering), the interaction with the subsequent KrF laser pulse (Fig. 1(e)), and the remnants of the nanoparticle cloud (Fig 1(f)).

The most effective nanowire growth is found to occur at the position corresponding to the photodissociated products, indicating that smaller clusters or molecules are preferred to large nanoparticles under these growth conditions. Figures 2(a) and 2(b) show SEM and Z-STEM images of SnO_2 nanowires grown by LAND on Si substrates at 700°C in 150 Torr Ar. EDX confirms that the nanowires are rutile (tetragonal) SnO_2 and the nanoparticles are AuSn alloys. This approach appears to be a versatile system to explore the growth of a variety of nanowires using clusters and nanoparticles formed from laser vaporization as stable, transportable feedstocks for growth.

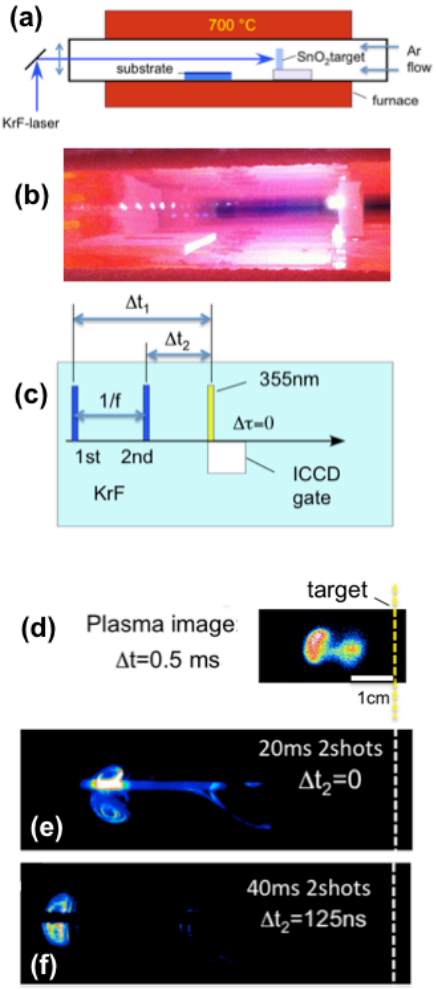

Fig. 1. (a),(b) KrF-laser ablation of SnO_2 inside a hot oven grows SnO_2 nanowires on a Au-coated Si substrate at 700°C in Ar (150 Torr). Optimal growth is obtained at the position of visible luminescence from KrF-dissociated clusters. (c) ICCD imaging using a 2nd laser delayed at Δt_1 records (d) plasma luminescence and Rayleigh scattering from forming nanoparticles, (e) the KrF-laser dissociation of the nanoparticles on subsequent pulses and (f) subsequent nanoparticle propagation.

Femtosecond Generation of Nanoparticles in Vacuum - Ultrashort laser pulses provide highly non-equilibrium conditions for the synthesis and processing of materials. When laser pulse widths become shorter than a few picoseconds (~ electron-phonon relaxation time) irradiated material is excited so rapidly to a plasma that it does not boil and vaporize in the conventional sense, but undergoes phase explosion or Coulomb explosion.[2] Experimentally, nanoparticles have been reported as the principal ejecta observed from femtosecond laser ablation of various targets,[3-6] in contrast to that for nanosecond laser vaporization where atoms and molecules are the desired principal ejecta, and micron-sized particulates are undesirable byproducts formed from spallation of residual molten material on the target surface.

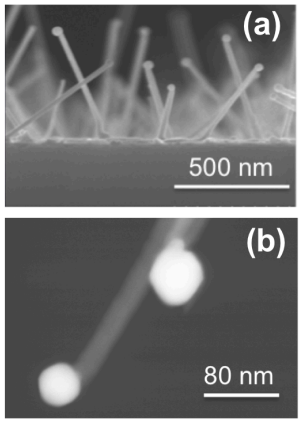

Fig. 2. (a) SEM and (b) STEM images of SnO_2 nanowires grown from transported nanoparticles as shown in Fig. 1.

We have recently explored the femtosecond laser vaporization of thin metallic films (single-layer and multilayer) for the synthesis of metastable alloy nanoparticles. In situ diagnostics were employed to understand whether nanoparticles are indeed formed as the principal ejecta under such nonequilibrium vaporization conditions, and if so, how they form and propagate. A Ti:Sapphire fs-laser (40-fs pulse width, λ = 800 nm, ~ 2 μJ/pulse) is used to ablate thin (~ 20 nm) films deposited onto the backside of transparent substrates as illustrated in Fig.

3(a). The extremely thin films limit the possibility of the formation of micron-sized particulates, and provide opportunities to explore the formation of core-shell and multicomponent nanoparticle stoichiometries through variation of the order and layer spacing of the different materials. Gated intensified CCD imaging is used to directly image the blackbody emission from hot nanoparticulates in vacuum, as shown in Figure 3(b), or fluorescence from atoms and molecules. The particle size distributions were measured both by HRTEM and scanning mobility particle sizing system.

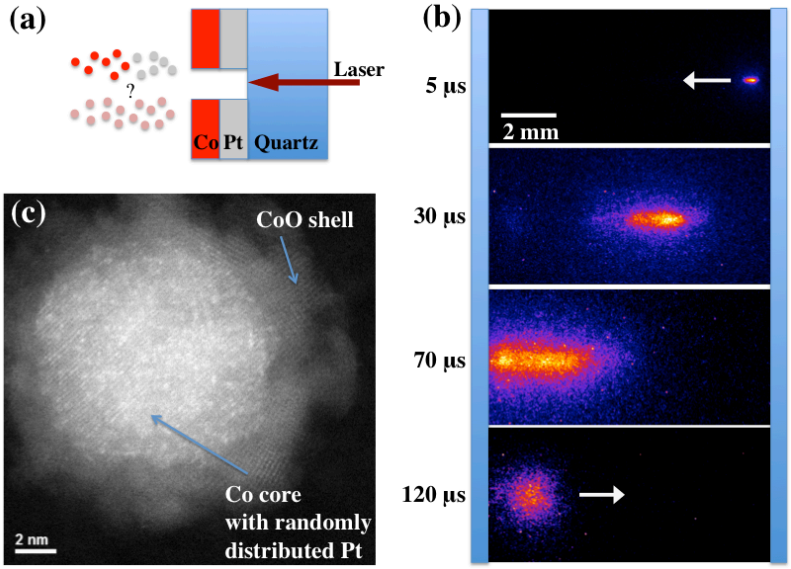

Fig. 3. (a) Experimental setup for backside fs-laser ablation of (10nm Co)/ (10 nm Pt) films deposited on a quartz substrate (not to scale). (b) ICCD imaging of the resultant plume at different time delays after ablation reveal a highly-forward directed plume of hot nanoparticles traveling at 70-140 m/s to a quartz plate 1cm away that partially rebounds at ~ 1/3 the incoming velocity (c) Dark-filed STEM image of a collected CoPt nanoparticle with Pt cluster inclusions in a Co core, surrounded by a CoO shell.

These measurements confirm that femtosecond vaporization just above ablation threshold produces plumes primarily consisting of hot nanoparticulates that travel in highly forward-directed packets at center of mass velocities ~ 100 m/s. These velocities are ~100 times slower than typical velocities of atoms and ions which comprise plumes used for pulsed laser deposition of thin films. Such plumes offer the potential to directly produce and pattern nanoparticles into thin films onto substrates, both in vacuum and in background gases. The interactions of the particles with substrates and background gases have also been explored. As shown in Fig. 3(b), a significant fraction of material rebounds with a coefficient of restitution of ~ 0.3 from the quartz receptor substrate, a behavior that is not well understood.[7] Atomistic modeling is addressing the mechanisms governing the sticking of the particles to different surfaces, both to understand the possibilities for a new processing technique and the fundamental understanding of nanoparticle dynamics afforded by these unique measurements. Rapid quenching of nanoparticles induced by substrate cooling is being explored. HRTEM of the nanoparticles deposited directly onto TEM grids in vacuum (as in Fig. 3(c)) reveals highly intermixed metals from the two layers, indicating a rapid quenching of Pt clusters within the Co core for the CoPt nanoparticle shown. The segregation of sub-nm metal catalyst clusters within host metals is being investigated as a function of the nonequilibrium vaporization and quenching conditions, and may have important implications for the catalytic activity of nanoparticles.

Future Plans

Determining how nm-sized crystallites are stabilized into nanowires and metastable nanoparticles is central to understanding the growth of nanowires, nanoparticle assemblies, and nanoparticles from laser-synthesized clusters. Modeling will be performed to quantify the energetics involved in stabilizing cluster dopants in the fs-laser generated metal nanoparticles, and in doped oxides. Experimentally, laser-induced fluorescence measurements will be performed to understand the role of photodissociated clusters in the LAND growth of nanowires. Atomic-resolution Z-STEM will be used to investigate the stoichiometry of very small clusters observed on the larger nanoparticles to understand the fundamental particle sizes inherent to fs-laser generation of nanoparticles. In situ diagnostics of the ns-laser NAPLD of high surface area nanoparticle assemblies for dye-sensitized solar cells and doped variants for photocatalytic water splitting will be performed for TiO_2 nanoparticles. Scanning mobility particle sizing will be developed for use at low pressures to measure particle size distributions.

References

1. T. Okada, R. Q. Guo, J. Nishimura, M. Matsumoto, and D. Nakamura, Appl Phys A **93**, 843 (2008).
2. L. V. Zhigilei, Z. B. Lin, and D. S. Ivanov, J Phys Chem C **113**, 11892 (2009).
3. S. Amoruso, R. Bruzzese, N. Spinelli, R. Velotta, M. Vitiello, X. Wang, G. Ausanio, V. Iannotti, and L. Lanotte, *Appl Phys Lett* **84**, 4502 (2004).
4. S. Amoruso, G. Ausanio, R. Bruzzese, M. Vitiello, and X. Wang, *Phys Rev B* **71** 033406-1, (2005).
5. C. Boulmer-Leborgne, J. Perriere, R. Benzerga, and S. Tricot, *J Phys D Appl Phys* **40**, 7069 (2007).
6. T. E. Glover, et al., *Phys Rev Lett* **90**, 236102-1 (2003).
7. A. I. Ayesh, S. A. Brown, A. Awasthi, S. C. Hendy, P. Y. Convers, and K. Nichol, *Phys Rev* B **81** (2010).

ERKCS81 Publications

1. Z. Gu, Y. Yang, K. Li, X. Tao, G. Eres, J. Y. Howe, L. Zhang, X. Li, and Z. Pan, "Aligned Carbon Nanotube-Reinforced Silicon Carbide Composites Produced by Chemical Vapor Infiltration," *Carbon* **49**(7), 2475–2482 (2011).
2. X. P. Huang, J. M. Wang, G. Eres, and X. W. Wang, "Thermophysical Properties of Multi-Wall Carbon Nanotube Bundles at Elevated Temperatures up to 830 K," *Carbon* **49**(5), 1680 (2011).
3. M. Yoon, H. H. Weitering, and Z. Y. Zhang, "First-Principles Studies of Hydrogen Interaction with Ultrathin Mg and Mg-Based Alloy Films," *Phys. Rev. B* **83**, 045413 (2011).
4. M. Yoon, Y. Miyamoto, and M. Scheffler, "Enhanced Dipole Moments in Photo-Excited TTF-TCNQ Dimers", *New J. Phys.* **13**, 073039 (2011).
5. J. J. Jackson, A. A. Puretzky, K. More, C. M. Rouleau, G. Eres, D. B. Geohegan, "Pulsed Growth of Vertically Aligned Nanotube Arrays with Variable Density," *ACS Nano* **4**(12), 7573 (2010).
6. A. A. Puretzky, D. B. Geohegan, and C. M. Rouleau, "Narrow and Intense Resonances in Low Frequency Region of Surface Enhanced Raman Spectra of Single Wall Carbon Nanotubes," *Phys. Rev. B* B **82**, 245402 (2010).
7. M. Yoon and D. Tomanek, "Equilibrium Structure of Ferrofluid Aggregates," *J. Phys. Condens. Mater.* **22**, 455105 (2010).
8. N. A. Hatab, C.-H. Hsueh, A L. Gaddis, S. T. Retterer, J.-H. Li, G. Eres, Z. Zhang, and B. Gu, "Free-Standing Optical Gold Bowtie Nanoantenna with Variable Gap Size for Enhanced Raman Spectroscopy," *Nano Lett.* **10**, 4952 (2010).
9. H. Pan, B. Gu, G. Eres, and Z. Zhang, "Ab Initio Study on Noncompensated CrO Codoping of GaN for Enhanced Solar Energy Conversion," *J. Chem. Phys.* **132**, 104501 (2010).
10. G. Eres, D. B. Geohegan, A. A. Puretzky, and C. M. Rouleau, "All Carbon Nanotubes Are Not Created Equal," Book Chapter in *Nanotechnology for Electronics, Photonics, and Renewable Energy, Springer Series in Nanostructure Science and Technology,* 131-152 (2010). DOI: 10.1007/978-1-4419-7454-9_4.
11. D. B. Geohegan, A. A. Puretzky, C. M. Rouleau, J. J. Jackson, G. Eres, Z. Liu, D. Styers-Barnett, H. Hu, B. Zhao, K. Xiao, I. Ivanov, and K. More, "Laser Interactions in Nanomaterials Synthesis," Book Chapter in *Springer Series in Materials Science* **130***,* 1 (2010).
12. H. Pan, X. Qiu, I. N. Ivanov, H. M. Meyer, W. Wang, W. Zhu, M. P. Paranthaman, Z. Zhang, G. Eres, B. Gu, *11. "*Fabrication and Characterization of Brookite-Rich, Visible Light-Active TiO_2 Films for Water Splitting," *Applied Catalysis B: Environmental* **93**, 90 (2009).
13. J. Zhang, J. Ge, M. D. Shultz, E. Chung, G. Singh, C. Shu, P. P. Fatouros, S. C. Henderson, F. D. Corwin, D. B. Geohegan, A. A. Puretzky, C. M. Rouleau, K. More, C. Rylander, M. N. Rylander, H. W. Gibson and H. C. Dorn, "In Vitro and In Vivo Studies of Single-Walled Carbon Nanohorns with Encapsulated Metallofullerenes and Exohedrally Functionalized Quantum Dots," *Nano Letters* **10**, 2843 (2010).
14. W. Zhu, X. Qiu, V. Iancu, X-Q. Chen, H. Pan, Wei Wang, M. Dimitrijevic, T. Rajh, H. M. Meyer III, M. P Paranthaman, G. M. Stocks, H. H. Weitering, B. Gu, G. Eres, and Z. Zhang, "Band Gap Narrowing of Titanium Oxide Semiconductors by Noncompensated Anion-Cation Codoping for Enhanced Visible-Light Photoactivity," *Phys. Rev. Lett.* **103**, 226401 (2009).
15. G. Eres, C.M. Rouleau, M. Yoon, A.A. Puretzky, D. B. Geohegan, "Model for self assembly of carbon nanotubes from acetylene based on real-time studies of Vertically Aligned Growth Kinetics," *J. Phys. Chem. C* **113**, 15484 (2009).
16. H. Pan, X. Qiu, I. N. Ivanov, H. M. Meyer, W. Wang, W. Zhu, M. P. Paranthaman, Z. Zhang, Gyula Eres, and B. Gu, "Fabrication and characterization of brookite-rich, visible light-active TiO_2 films for water splitting," *Applied Catalysis B* **93**, 90 (2009).
17. M. H. Upton, R. F. Klie, J. P. Hill, T. Gog, D. Casa, W. Ku, Y. Zhu, M.Y. Sfeir, J. Misewich, G. Eres, D. Lowndes, "Effect of number of walls on plasmon behavior in carbon nanotubes," *Carbon*, 47, 162 (2009).
18. Y.A. Yue, G. Eres, X. Wang, and L.Y. Guo, "Characterization of thermal transport in micro/nanoscale wires by steady-state electro-Raman-thermal technique," *Appl. Phys. A* **97**, 19 (2009).
19. Z. Zhou, G.Eres, R. Jin, A. Subedi, D. Mandrus, E.H. Kim, "The performance of in situ grown Schottky-barrier single wall carbon nanotube field-effect transistors," *Nanotechnology* **20**, 085709 (2009).
20. M. Yoon, S. Yang, and Z. Zhang, "Interaction between hydrogen molecules and metallofullerenes", *J. Chem. Phys.* **131**. 064707 (2009).

Non-Equilibrium Synthesis of Nanostructured Materials: Real Time Monitoring of Non-Equilibrium Doping of TiO_2 in Pulsed Laser Deposition for Energy Applications (ERKCS81)

Gyula Eres[1], David Geohegan[1,2], Alex Puretzky[1,2], Christopher Rouleau[1,2], Mina Yoon[1], Jason D. Readle[1,2], Murari Regmi[1], Zhenyu Zhang[3], Hanno Weitering[3], Norman Mannella[3] and Gerd Duscher[4]
eresg@ornl.gov
[1]Materials Science and Technology Divison and [2]Center for Nanophase Materials Sciences Oak Ridge National Laboratory, Oak Ridge, TN 37831
the [3]Dept. of Physics and Astronomy, and the [4]Dep. of Materials Science and Engineering, University of Tennessee, Knoxville, 37996

Program Scope

The goal of this program is to develop a fundamental understanding of the non-equilibrium aspects of nanomaterial synthesis by exploring the growth mechanisms and resulting structures of nanoscale materials formed in controlled environments. Pulsed, non-equilibrium growth and processing approaches, such as those involving lasers and supersonic molecular beams, are developed to supply the necessary kinetic energy required to explore the synthesis of nanostructures with metastable phases and structures that are inaccessible using traditional synthetic methods. A distinguishing feature of the program is the development and application of time-resolved, in situ diagnostics of nanomaterial growth kinetics and a corresponding development of models to understand the underlying kinetic and chemical pathways. Spatial confinement and reactive quenching approaches are developed to explore the synthesis mechanisms of rationally-designed nanostructures with enhanced intrinsic properties, targeting: (1) oxide, carbon, and alloy nanomaterials produced in metastable states by catalyst-free or catalyst-mediated processes, and (2) doped, decorated, and filled nanomaterial hybrids designed to induce permanent electric fields or distribute charge within nanostructures. Theoretical methods are used to understand fundamental mechanisms of synthesis in order to guide the formation of nanostructures tailored to enhance energy storage, catalysis, thermal management, and photovoltaics in support of DOE's energy mission.

With the seminal discovery of water splitting by Fujishima and Honda in the early 1970s, titanium dioxide (TiO_2) emerged as the premier photocatalysts for solar energy utilization [1]. However, TiO_2 has a wide intrinsic band gap and absorbs light only in the ultraviolet region resulting in less than 3% solar energy conversion efficiency. Reducing the band gap of TiO_2 is the main avenue for increasing photocatalytic efficiency. This work describes a conceptually new approach for bandgap narrowing of TiO_2 and other wide bandgap photocatalysts using non-compensated codoping [2,3]. Non-compensated codoping consists of simultaneous doping using two dopants with opposite but unequal oxidation states illustrated in Fig. 1a. The electrostatic

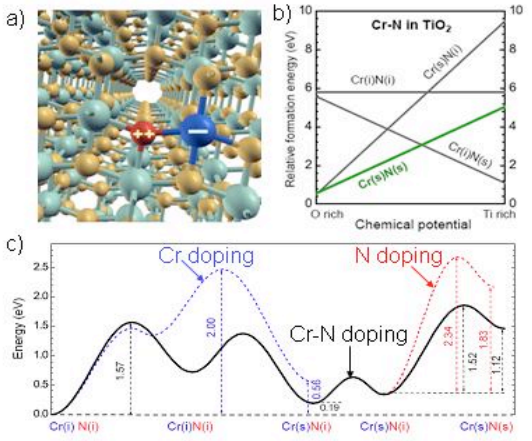

Fig. 1 a) Schematic illustration of non-compensated codoping of anatase. b) The thermodynamic solubility plot showing that the desired substitutional doping, Cr(s)N(s) is most favorable at oxygen rich conditions. c) The kinetic solubility plot showing that codoping reduces the barrier for incorporation of Cr-N compared to single element doping.

attraction within the anion-cation dopant pair enhances both the thermodynamic (Fig. 1b) and kinetic solubility (Fig. 1c) and the non-compensated nature ensures the creation of tunable intermediate bands that effectively narrow the bandgap. The key features of the concept are demonstrated using first-principles calculations. The codoping of TiO_2 with the non-compensated Cr-N pair in a form of nanoclusters synthesized by sol-gel methods confirmed the bandgap narrowing predicted by theory [2]. However several fundamental questions, notably what is the oxidation state, the location of the dopants and the electronic structure of the codoped TiO_2 cannot be answered unambiguously because the nanoclusters are not a well defined system in term of phase, composition and lattice defects.

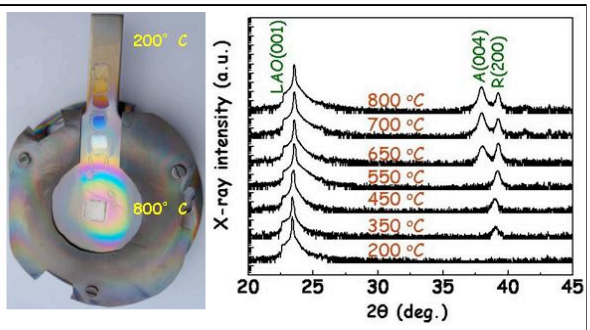

Fig. 2 a) The temperature gradient sample holder allows growth of up to 8 samples in a single run. b) The XRD data show that rutile (R(200)), the high temperature phase is obtained with Cr-N codoping at low temperatures where anatase (A(004)) is typically observed.

Recent Progress

Here we describe the use of pulsed laser deposition (PLD) for controlling the important parameters in non-equilibrium codoping of TiO_2 in a form of thin films on $LaAlO_3$ (LAO) and $SrTiO_3$ (STO) substrates. The first intriguing observation in thin film growth is that Cr-N codoping alters the phase of the TiO_2. Although it is the thermodynamically stable phase at high temperature, in Cr-N codoped growth Fig. 2 shows that the rutile phase appears first at low temperature, followed by the appearance of anatase with increasing temperature resulting in mixed phase samples. In addition to the growth temperature the phase can be controlled by changing the laser repetition rate, which amounts to changing the growth rate. Anatase is stabilized at 5 Hz, and rutile forms at 10 Hz repetition rate, and both films grow phase pure at this temperature. The phase change is observed only for Cr-N codoped samples and not for undoped or Cr only or N only doped samples. This behavior is explained by the Ostwald step rule according to which crystallization goes through successive metastable phases before a final stable phase is formed [4]. The critical parameter that regulates the sequence of the phase formation is the surface free energy. The presence of mixed phase is also reported in oxygen plasma assisted molecular beam epitaxy (OPA-MBE) of TiO_2 films. However, here the phase change is observed with undoped material and occurs as a rutile nanoparticle inclusion in majority anatase [5]. The TEM images in Fig. 3 and EELS data show that unlike in MBE the mixed phase samples consist of distinct anatase and rutile layers. EELS data from boxes 1 and 2 show that TiO_2 growth starts as anatase and after about 2 nm it changes to rutile. The phase change is important because it is thought to result in increased photocatalytic activity. The key behind the proposed mechanism for photocatalytic enhancement is the longer carrier lifetime resulting from the spatial separation of carriers across the rutile/anatase interface [6]. X-ray

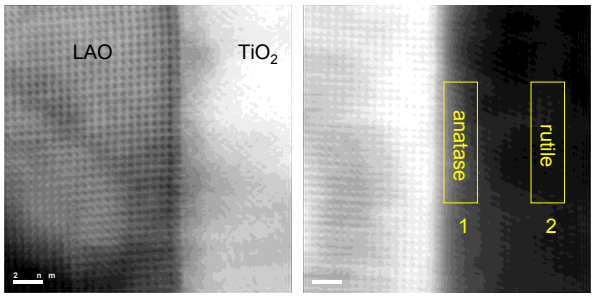

Fig. 3 Bright field (left) and Z-contrast images of the LAO TiO_2 interface region. EELS shows that area 1 corresponds to anatase and area 2 is rutile.

diffraction (XRD) measurements of the films show that the doping levels of both Cr and N decrease with increasing growth temperature. Comparison of the XRD measurements shows that the increase in the doping level is accompanied by broadening of the XRD line width. This broadening is caused by mosaic spread and the incorporation of crystalline defects with decreasing growth temperatures.

The electronic structure of the Cr-N, Cr only, N only and undoped TiO_2 was studied with STM, STS, and soft x-ray spectroscopies using high quality epitaxial thin films grown by PLD on LAO. The results using soft x-ray spectroscopies that will be reported in a future publication confirm independently the bandgap narrowing in Cr-N codoped samples observed in both nanocluster and thin film samples by STS. In addition, these measurements reveal some unexpected behavior concerning dopant incorporation and dopant localization depending on the phase of the TiO_2. The N doping in rutile is both interstitial and substitutional. However, only weak interstitial N doping of anatase was observed. The most interesting piece of data concerns the location of the electronic states associated with N doping. It is widely reported that N doping introduces localized states in the vicinity of the top of the valance band. Using a combination of soft x-ray spectroscopies we show that the electronic states introduced by N in Cr-N codoping are delocalized at the top of the valance band. Future measurements will be used to determine whether this behavior is unique to Cr-N codoping or it is also present in N only doped rutile. The EELS data reveal strong non-uniformities in the distribution of N in the epitaxial TiO_2. A much higher concentration of N is observed near grain boundaries and near the top surface suggesting strong dopant segregation out of the TiO_2 lattice.

Future Plans

The deposition and characterization of the PLD codoped TiO_2 films has narrowed down the origin of the enhanced photocatalytic activity to segregation of the dopants to the near surface region. The photocatalytic activity can also be enhanced by the proximity of an interface that can play a role in enhancing charge separation. These factors steer future work in this project toward synthesis of nanoparticles with well defined phase and composition. PLD is the ideal tool for controlling nanoparticle synthesis because real time optical spectroscopic data can be used to characterize the timing and the composition of the plume from which the nanoparticles condense. These characterization methods will be used to monitor the emission spectra from dopant species such as Cr and N to assess the dopant incorporation efficiency by comparison with post growth characterization of the phase and the composition of the particles. Increasing dopant incorporation will be explored by using a second ablation plume. By crossing the two plumes and using timing to delay the arrival of the dopant plume with respect to the host plume new nanoparticle configurations ranging from homogeneous alloy particles to particles with only a thin dopant shell can be formed in the PLD plume.

References

1. A. Fujishima and K. Honda, Nature **238**, (1972) 37.
2. W. Zhu, X. Qiu, V. Iancu, X. Chen, H. Pan, W. Wang, N. Dimitrijevic, T. Rajh, H. M. Meyer III, M. P. Paranthaman, M. Stocks, H. Weitering, B. Gu, Gyula Eres, and Z. Zhang, Phys. Rev. Lett. **103,** (2009) 226401.
3. H. Pan, B. Gu, Gyula Eres, and Z. Zhang, J. Chem. Phys. **132,** (2010) 104501.
4. M.R. Ranade, A. Navrotsky, H.Z. Zhang, J.F. Banfield, S.H. Elder, A. Zaban, P.H. Borsel, S.K. Kulkarni, G.S. Doran and H.J. Whitfield, Proc. Natl. Acad. Sci. **99**, (2002) 6476.
5. R. Shao, C. Wang. D.E. McCready, T.C. Droubay, and S.A. Chambers, Surf. Sci. **601** (2007) 1582.
6. T. Ohno, K. Sarukawa, K. Tokieda, and M. Matsumura, J. Catal. **203** (2001) 82.

ERKCS81 publications

1. Z. Gu, Y. Yang, K. Li, X. Tao, G. Eres, J. Y. Howe, L. Zhang, X. Li, and Z. Pan, "Aligned Carbon Nanotube-Reinforced Silicon Carbide Composites Produced by Chemical Vapor Infiltration," *Carbon* **49**(7), 2475–2482 (2011).
2. X. P. Huang, J. M. Wang, G. Eres, and X. W. Wang, "Thermophysical Properties of 2. Multi-Wall Carbon Nanotube Bundles at Elevated Temperatures up to 830 K," *Carbon* **49**(5), 1680 (2011).
3. M. Yoon, H. H. Weitering, and Z. Y. Zhang, "First-Principles Studies of Hydrogen Interaction with Ultrathin Mg and Mg-Based Alloy Films," *Phys. Rev. B* **83**, 045413 (2011).
4. J. J. Jackson, A. A. Puretzky, K. More, C. M. Rouleau, G. Eres, D. B. Geohegan, "Pulsed Growth of Vertically Aligned Nanotube Arrays with Variable Density," *ACS Nano* **4**(12), 7573 (2010).
5. A. A. Puretzky, D. B. Geohegan, and C. M. Rouleau, "Narrow and Intense Resonances in Low Frequency Region of Surface Enhanced Raman Spectra of Single Wall Carbon Nanotubes," *Phys. Rev. B* B **82**, 245402 (2010).
6. M. Yoon and D. Tomanek, "Equilibrium Structure of Ferrofluid Aggregates," *J. Phys. Condens. Mater.* **22**, 455105 (2010).
7. N. A. Hatab, C.-H. Hsueh, A L. Gaddis, S. T. Retterer, J.-H. Li, G. Eres, Z. Zhang, and B. Gu, "Free-Standing Optical Gold Bowtie Nanoantenna with Variable Gap Size for Enhanced Raman Spectroscopy," *Nano Lett.* **10**, 4952 (2010).
8. H. Pan, B. Gu, G. Eres, and Z. Zhang, "Ab Initio Study on Noncompensated CrO Codoping of GaN for Enhanced Solar Energy Conversion," *J. Chem. Phys.* **132**, 104501 (2010).
9. G. Eres, D. B. Geohegan, A. A. Puretzky, and C. M. Rouleau, "All Carbon Nanotubes Are Not Created Equal," Book Chapter in *Nanotechnology for Electronics, Photonics, and Renewable Energy, Springer Series in Nanostructure Science and Technology,* 131-152 (2010). DOI: 10.1007/978-1-4419-7454-9_4.
10. D. B. Geohegan, A. A. Puretzky, C. M. Rouleau, J. J. Jackson, G. Eres, Z. Liu, D. Styers-Barnett, H. Hu, B. Zhao, K. Xiao, I. Ivanov, and K. More, "Laser Interactions in Nanomaterials Synthesis," Book Chapter in *Springer Series in Materials Science* **130***,* 1 (2010).
11. H. Pan, X. Qiu, I. N. Ivanov, H. M. Meyer, W. Wang, W. Zhu, M. P. Paranthaman, Z. Zhang, G. Eres, B. Gu, *11. "*Fabrication and Characterization of Brookite-Rich, Visible Light-Active TiO_2 Films for Water Splitting," *Applied Catalysis B: Environmental* **93**, 90 (2009).
12. J. Zhang, J. Ge, M. D. Shultz, E. Chung, G. Singh, C. Shu, P. P. Fatouros, S. C. Henderson, F. D. Corwin, D. B. Geohegan, A. A. Puretzky, C. M. Rouleau, K. More, C. Rylander, M. N. Rylander, H. W. Gibson and H. C. Dorn, "In Vitro and In Vivo Studies of Single-Walled Carbon Nanohorns with Encapsulated Metallofullerenes and Exohedrally Functionalized Quantum Dots," *Nano Letters* **10**, 2843 (2010).
13. W. Zhu, X. Qiu, V. Iancu, X-Q. Chen, H. Pan, Wei Wang, M. Dimitrijevic, T. Rajh, H. M. Meyer III, M. P Paranthaman, G. M. Stocks, H. H. Weitering, B. Gu, G. Eres, and Z. Zhang*,* "Band Gap Narrowing of Titanium Oxide Semiconductors by Noncompensated Anion-Cation Codoping for Enhanced Visible-Light Photoactivity," *Phys. Rev. Lett.* **103**, 226401 (2009).
14. G. Eres, C.M. Rouleau, M. Yoon, A.A. Puretzky, D. B. Geohegan, "Model for self assembly of carbon nanotubes from acetylene based on real-time studies of Vertically Aligned Growth Kinetics," *J. Phys. Chem. C* **113**, 15484 (2009).
15. H. Pan, X. Qiu, I. N. Ivanov, H. M. Meyer, W. Wang, W. Zhu, M. P. Paranthaman, Z. Zhang, Gyula Eres, and B. Gu, "Fabrication and characterization of brookite-rich, visible light-active TiO_2 films for water splitting," *Applied Catalysis B* **93**, 90 (2009).
16. M. H. Upton, R. F. Klie, J. P. Hill, T. Gog, D. Casa, W. Ku, Y. Zhu, M.Y. Sfeir, J. Misewich, G. Eres, D. Lowndes, "Effect of number of walls on plasmon behavior in carbon nanotubes," *Carbon*, 47, 162 (2009).
17. Y.A. Yue, G. Eres, X. Wang, and L.Y. Guo, "Characterization of thermal transport in micro/nanoscale wires by steady-state electro-Raman-thermal technique," *Appl. Phys. A* **97**, 19 (2009).
18. Z. Zhou, G.Eres, R. Jin, A. Subedi, D. Mandrus, E.H. Kim, "The performance of in situ grown Schottky-barrier single wall carbon nanotube field-effect transistors," *Nanotechnology* **20**, 085709 (2009).
19. M. Yoon, S. Yang, and Z. Zhang, "Interaction between hydrogen molecules and metallofullerenes", *J. Chem. Phys.* **131**. 064707 (2009).
20. M. Yoon, Y. Miyamoto, and M. Scheffler, "Enhanced Dipole Moments in Photo-Excited TTF-TCNQ Dimers", *New J. Phys.* **13**, 073039 (2011).

Simulation and Theory of Solid-Liquid Interface Migration

M.I. Mendelev, M.J. Kramer, R.E. Napolitano, V.B. Warshavsky and X. Song
mendelev@ameslab.gov
Materials Science and Engineering Division, Ames Laboratory USDOE, Ames, IA, 50011

Program Scope

The fundamental nature of structural selection during phase transitions in an undercooled liquid involves the simultaneous action of numerous physical forces, collectively governing the natural evolution of multiscale morphological hierarchy. Considered in concert, the prediction and control of phase selection and morphological dynamics, particularly far from equilibrium, is indeed a formidable task, but recent advances have lead to quantitatively accurate predictive modeling methods that can be used to simulate many of the relevant structural and chemical features that evolve upon solidification. These methods, however, rely on accurate parameterization of fundamental thermodynamic and kinetic properties. The present subtask addresses these issues through integrating fundamental thermodynamic measurements[1], new approaches in bulk thermodynamic modeling[2], *ab initio* calculations[3], investigation of bulk and solid-liquid interface (SLI) behavior with molecular dynamics (MD) simulations [4, 5] and investigation of microstructural dynamics through experiments[6]. In this work we combine MD simulations of SLIs with *in situ* X-ray scattering experiments to quantify the SLI kinetics and identify the governing mechanisms. This work represents a significant advancement in our understanding of the fundamental nature of structural dynamics in solid-liquid phase transitions.

Recent Progress

Crystallization of an undercooled liquid or glass is largely controlled by interfacial mechanisms between the growing crystals and the liquid that operate to accommodate the changes in both structure and composition across the boundary. To alleviate the kinetic burden of long range transport, the pathways of highly driven (fast) crystallization processes may involve forming nonequilibrium structures and compositions that arise from the trapping of defects such as excess solute atoms or atomic-scale packing anomalies, such as vacancies, site-occupancy defects, stacking faults, *etc*. Although direct observation of the formation of anti-site defects is not possible at the present time, the investigation presented here demonstrates that indirect quantification of defect incorporation during crystallization can be achieved through a combination of in-situ high energy X-ray diffraction (HEXRD) and Rietveld analysis with MD simulations[6]. We choose, as a test material, the Zr_2Cu alloy that crystallizes congruently to the *C11b* phase[7] from the liquid or from the glass[8] with no requirement for chemical partitioning or associated diffusion.

The experimental data shown in Fig.1 reveal six stages of devitrification. There are two principal experimental observations. First, we observe a significant change in both the unit cell volume and the individual lattice parameters for the C11b phase from the start of stage III to the completion of stage IV, indicating that the change in unit cell volume and the relative lattice response are more than transient elastic effects of the transition. Rapid crystal growth occurs after a substantial fraction of the original glass has crystallized (Fig. 2a and 2b), and is accompanied by a jump in the lattice parameters where the a-axis lengthens and the c-axis shortens (see Δa and Δc in Figs. 1b and 1c; for the rest of the abstract, we will use the Δ symbol only for the jump in the lattice parameters during rapid crystal growth.). Moreover, Fig 2c shows

that the magnitude of this lattice distortion increases with maximum in crystallization rate, as determined from the time dependence of the crystallized fraction (Fig. 1a). A roughly constant crystallite number density observed through TEM analysis of quench-interrupted annealing specimens indicates that the rapid crystallization rate can primarily be attributed to growth, rather than nucleation. Second, while the unit cell volume exhibits nearly linear thermal expansion from ~675 to 775 K, the individual axes have an unusual response, a decreasing a-axis (inset Fig. 1b) and accelerated increasing c-axis with increasing temperature over the same temperature range (inset Fig. 1c).

To examine in detail the effect of point defects on lattice distortion we used MD simulation. For all MD simulations, we utilized a semi-empirical potential of the Finnis-Sinclair type [9], developed specifically for the Cu-Zr system [10]. MD simulation results are summarized in Fig.3. We found that in the case of C11b lattice, only introducing anti-site defects lead to increasing the a-axis and decreasing the c-axis owing to the smaller atomic radius for the Cu atom. Thus our experimental observation of the lattice distortion, (a-axis expansion and c-axes contraction) during rapid growth (see Figs. 1b and 1c) is explained by incorporation of 1% to 2% of anti-site defects. These defects annihilated by atomic transport at higher temperatures which explains anomalous thermal expansion from ~675 to 775 K.

Thus, we propose a new approach for quantifying anti-site defect formation during fast crystal growth, where in situ time resolved x-ray diffraction can provide high quality data on the change in lattice parameter during the crystal growth, while MD simulation provides an accurate means to quantify the anti-site defect concentration.

Recent Progress on Other Projects

In order to establish a link between various structural and kinetic properties of metals and the crystal-melt interfacial mobility, free solidification molecular dynamics simulations have been performed for a total of nine embedded atom method interatomic potentials describing pure Al, Cu and Ni[5]. To fully explore the space of materials properties three new potentials have been developed. The new potentials are based on a previous description of Al, but in each case the liquid structure, the melting point and/or the latent heat is varied considerably. The kinetic coefficient, μ, for all systems has been compared to several theoretical predictions. It is found that at temperatures close to the melting point the magnitude of μ correlates well with the value of the diffusion coefficient in the liquid (see Fig. 4).

A perturbation theory is developed to calculate solid–liquid interfacial free energies, including anisotropy[11]. The method is applied to systems with inverse-power and Lennard-Jones pair potentials as well as to metal systems with embedded-atom model potentials. The results are in reasonable agreement with the corresponding ones obtained from molecular dynamics simulations.

Future Plans

We will perform MD simulations to obtain the interface velocity for congruently melting compounds in the Cu-Ni-Zr alloys. Special attention will be paid to the dependence of the interface velocity on the crystallographic orientation of growing crystalline phases. The kinetic characteristics of the liquid phase (diffusivity, typical relaxation times, etc.) will also be determined from MD simulations in order to develop empirical correlations between the liquid properties and interface velocity as well as an analytical model for the interface migration. In order to explore how the liquid structure affects the SLI we will alter the semi-empirical

potentials to produce more or less ordered liquid structure while trying to keep all other materials properties unchanged like it was done in [5]. We will also use template-assisted MD to promote special cluster structures in the liquid to see how it affects the SLI mobility. This can provide unprecedented insight on the atomic mechanism of the SLI migration if it is indeed cooperative in nature as was assumed in the Mikveev-Chernov theory[12]. Finally, beyond the classical MD simulations, we will develop a dynamical density functional theory for computing the SLI mobility.

References:

1 S. H. Zhou and R. E. Napolitano, Acta Mater. **58**, 2186 (2010).
2 S. H. Zhou and R. E. Napolitano, Metall. Mater. Trans. A-Phys. Metall. Mater. Sci. **39A**, 502 (2008).
3 L. Huang, C. Z. Wang, S. G. Hao, M. J. Kramer, and K. M. Ho, Physical Review B **81**, 014108 (2010).
4 J. Monk, Y. Yang, M. I. Mendelev, M. Asta, J. J. Hoyt, and D. Y. Sun, Model. Simul. Mater. Sci. Eng. **18**, 18 (2010).
5 M. I. Mendelev, M. J. Rahman, J. J. Hoyt, and M. Asta, Model. Simul. Mater. Sci. Eng. **18**, 074002 (2010).
6 M. J. Kramer, M. I. Mendelev, and R. E. Napolitano, Phys. Rev. Lett. **105**, 245501 (2010).
7 D. Arias and J. P. Abriata, Bulletin of Alloy Phase Diagrams **11**, 452 (1990).
8 M. J. Kramer, M. Xu, Y. Y. Ye, D. J. Sordelet, and J. R. Morris, Metallurgical and Materials Transactions a-Physical Metallurgy and Materials Science **39A**, 1847 (2008).
9 M. W. Finnis and J. E. Sinclair, Philos Mag A **50**, 45 (1984).
10 M. I. Mendelev, M. J. Kramer, R. T. Ott, D. J. Sordelet, D. Yagodin, and P. Popel, Philos Mag **89**, 967 (2009).
11 V. B. Warshavsky and X. Y. Song, J. Phys.-Condes. Matter **22**, 7.
12 L. V. Mikheev and A. A. Chernov, J. Cryst. Growth **112**, 591 (1991).

Selected DOE Sponsored Publications in 2010-2011 from Current Project

1. M.J. Kramer, M.I. Mendelev and R.E. Napolitano, *In situ observation of anti-site defect formation during crystal growth*, Phys. Rev. Lett. **105**, 245501 (2010).
2. J. Monk, Y. Yang, M.I. Mendelev, M. Asta, J.J. Hoyt and D.Y. Sun, *Determination of the crystal-melt interface kinetic coefficient from molecular dynamics simulations*, Modelling Simul. Mater. Sci. Eng., **18**, 015004 (2010)
3. M.I. Mendelev, M.J. Rahman, J.J. Hoyt and M Asta, *Molecular-dynamics study of solid-liquid interface migration in fcc metals*, Modelling Simul. Mater. Sci. Eng. **18**, 074002 (2010).
4. V.B. Warshavsky and X.Y. Song, *Perturbation Theory for Solid-Liquid Interfacial Free Energies*, *Journal of Physics-Condensed Matter*, **22**, 364112 (2010).
5. Y.X. Yao, R. Napolitano, C.Z. Wang, and K.M. Ho, *Thermodynamic Limits of Crystallization and the Prediction of Glass Formation Tendency*, Physical Review B, **81**, 212202 (2010).
6. M.I. Mendelev, M.J. Kramer, R.T. Ott, D.J. Sordelet, M.F. Besser, A. Kreyssig, A.I. Goldman, V. Wessels, K.K. Sahu, K.F. Kelton, R.W. Hyers, S. Canepari and J.R. Rogers, *Experimental and computer simulation determination of the structural changes occurring through the liquid-glass transition in Cu-Zr alloys*, Phil. Mag. **90**, 3795-3815 (2010).

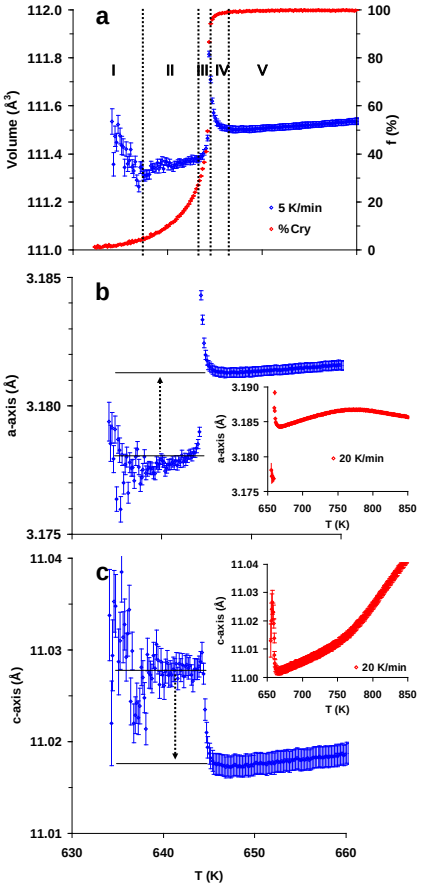

Figure 1. Unit cell volume (a) and lattice parameters a-axis (b) and c-axis (c) as function of temperature for the heating rate of 5 K/min. The insets show the temperature dependences of the lattice parameters for the heating rate of 20 K/min.

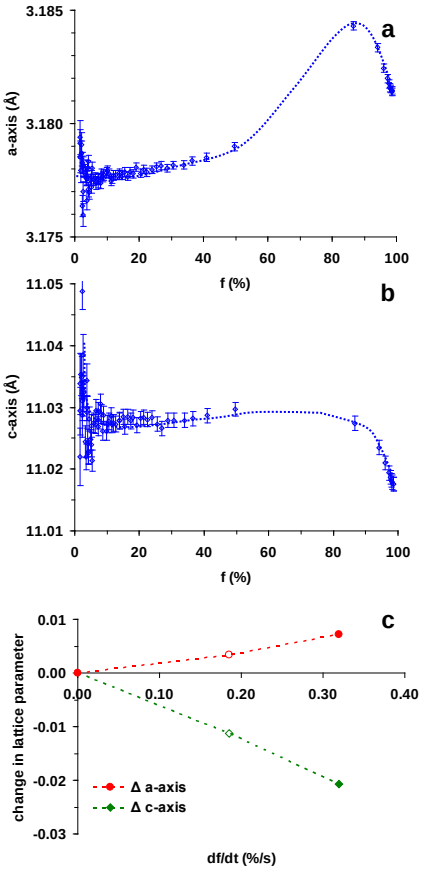

Figure 2. The change in the a- and c-axes lattice parameters ((a) and (b)) as function of the fraction crystallized (f) for the 5 K/min data set. The anisotropic changes in lattice as a function of the maximum in the growth rate.

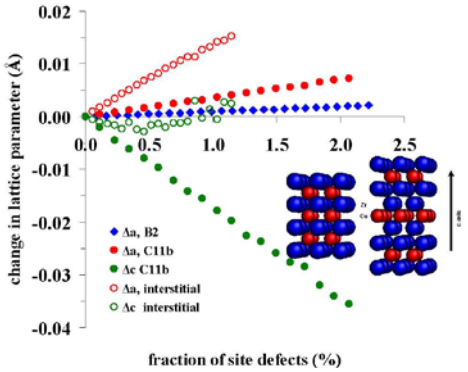

Figure 3. Changes in the lattice parameters as function of site defects concentration from MD simulation. Inset is a cartoon of the *B2* and *C11b* structures.

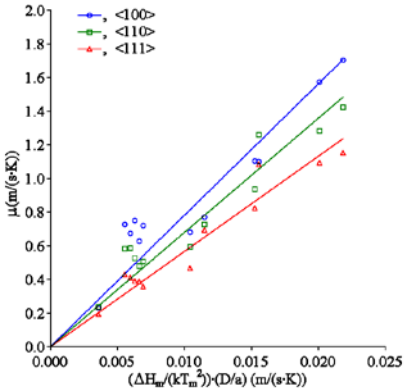

Figure 4. Comparison between MD simulation data on the SLI kinetic coefficient and the Wilson-Frenkel theory.

Development of Order in Deeply Undercooled Liquid Metals

X. W. Fang, C. Z. Wang, M. J. Kramer, S. G. Hao, L. Huang, Y. X. Yao, M. I. Mendelev,
R. E. Napolitano, R. T. Ott, and K. M. Ho
wangcz@ameslab.gov
Ames Laboratory, Iowa State University, Ames, IA 50011

1. Program Scope

While an overwhelming body of evidence, reported by us and others [1-6], shows that non-crystalline metallic phases (i.e. liquids and glasses) have clear elements of short- and medium-range order, this order is not easily defined. From an energetic standpoint, this lack of uniqueness in the description of structural order (and its coupling with chemical order) in non-crystalline metallic phases severely limits our ability to extend the traditional models of Gibbs free energy and associated analyses to understand and predict phase transformations. An accurate description of order parameters for non-crystalline systems would enable predicting the dynamics of phase selection and glass formation in undercooled liquid materials. The thrust of this subtask is a combined experimental and modeling approach to move beyond traditional descriptions of the short-range order (SRO) and to develop new ways of characterizing and quantifying the medium-range order (MRO) that develops from the undercooled liquid and glasses. Some of the key questions which need to be addressed are: (1) What are the prevailing forms of non-crystalline order in liquids and glasses? (2) What is the spatial extent of these more energetically stable interconnected regions within the undercooled liquid? (3) How stable are these features, i.e., do they form and then dissolve over some lifetime? (4) How do these features change in size, temporal stability and chemistry with under cooling? (5) How does the undercooling rate affect these structures? (6) How sensitive are these stable cluster structures to changes in chemistry, including major and minor constituents? and (7) What role do these stable networks play in nucleation and phase selection during solidification?

2. Recent Progress

Although several methods (e.g. Bond-Orientation order [7], Honeycutt-Anderson index [8] and Voronoi tessellation [9]) have been widely used in analysis of atomistic structures of liquid and glass, they do not provide a statistically robust description of how individual clusters correspond to, or deviate from, the average SRO. Most

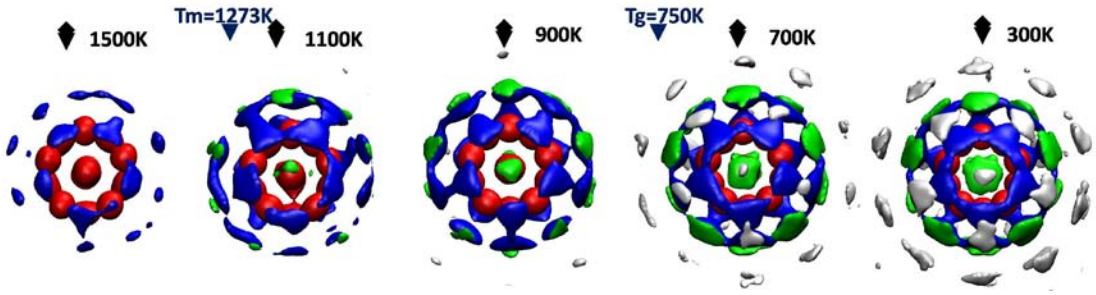

Fig. 1 Development of Bergman triacontahedron MRO around Cu in $Cu_{64.5}Zr_{35.5}$ alloy upon cooling from the liquid state. T_m and T_g are the melting point and the glass transition temperatures, respectively. Different colors are used here to indicate different coordination shells: red (first shell, icosahedron), blue (second shell, dodecahedraon), green (third shell, icosahedron), and white (fourth shell, rhombic triacontrahedron).

conspicuously, these methods only address structural arrangements in the first coordination shell, and thus, the characterization beyond the first shell is not straightforward or, in many cases, non-existent. To address this *critical* need, we have developed a robust cluster alignment tool that corrects all of the above deficiencies in existing methods [10]. Our method provides a visual picture of the structural motif as well as a scheme for defining an order parameter to measure the strength of any structural motif at a given locality in the system. The definition of this quantitative order parameter treats all different structural motifs on an equal footing and can be incorporated into modified MD schemes to manipulate the tendencies of the system towards various competing structural motifs. Applying this alignment method to the well-studied $Cu_{64.5}Zr_{35.5}$ alloy with a well validated interatomic potential [6,11], we demonstrate that the average structure extends multiple-shells during cooling from the liquid forming a Bergman triacontahedron in the glassy state [12]. Through a sequence of simulations from 1500 to 300K, we show that the MRO is a network of Bergman-type clusters with increasing interconnections as the system approaches the glass transition as shown in Fig. 1 and Fig. 2. The discovery of Bergman-type MRO from our order-mining technique provides unique insights into the nature of the glass transition and the relationship between metallic glasses and quasicrystals.

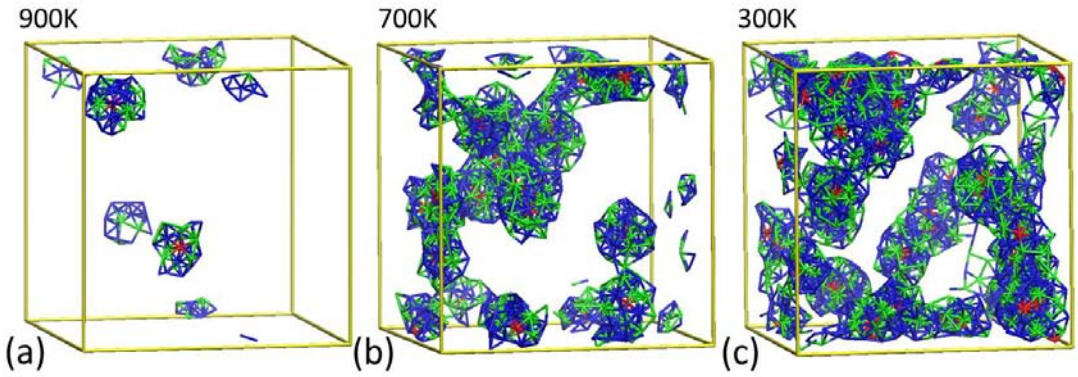

Fig, 2 The network of Bergman triacontahedral clusters in the $Cu_{64.5}Zr_{35.5}$ sample. (a) 900K, 3 Bergman triacontahedral clusters which contain 2.7% atoms; (b) 700K, 28 Bergman triacontahedral clusters which contain 19.0% atoms. (c) 300K, 31% of the atoms are in 57 Bergman triacontahedral clusters. The Cu atoms are in blue, Zr in green and the center atoms of the Bergman triacontahedral clusters are in red.

Our "order mining" method is generic and can be used to uncover hidden order in any form of disordered systems including metallic liquids and glasses. For example, using the cluster alignment approach, we have examined the SRO and MRO in Zr_2Pd metallic glass [3]. We have also examined the competition between icosahedral and FCC SRO orders in liquid Al [13] and $Cu_{80}Si_{20}$ [14], as well as the fluctuation between icosahedral and BCC orders in liquid Zr [15]. The cluster alignment approach has also been used to identify the non-icosahedral SRO in $Pd_{82}Si_{18}$ liquid [16].

3. Future Plans

Based on the order parameters determined from the cluster alignment method discussed above, we will develop a template-assisted MD (TAMD) method to overcome

the cooling-rate gap between atomistic simulations and experiments (computer simulations can treat quench rates ~10^{14}K/s to 10^{9}K/s whereas experimental quench rates are typically ~10^{5}K/s to 10^{2}K/s). In the TAMD approach, the order parameters (e.g., icosahedral clusters for the Zr-Cu systems) obtained from cluster alignment analysis will serve as a template and extra forces can be applied on each atom to steer the system to align the local order with a selected template when the system is cooled down from high temperature liquid. This procedure is similar to the dynamics of the atoms in metadynamics [17,18] using the order parameter (i.e., template) as the collective variable. However, instead of sampling the whole configuration space in metadynamics, the TAMD quickly drives the system toward the basin representing the template. This guidance could effectively assist the system to achieve processes that can take unreasonably long simulation times in conventional MD methods. An accurate definition of order parameter is the key to the success of this approach.

Identification of the structural motifs in non-crystalline phases by the cluster alignment method also allow us to examine the influence of changing stoichiometry on the free energy competition between non-crystalline and various crystalline motifs and hopefully understand the chemical influence on glass formation tendency. Using the structure motifs obtained from our order mining techniques and various stable and metastable structures from the phase diagram, we will investigate the relative stability and free energy landscape of these structures as a function of chemical compositions to understand the interconnection between the chemistry and the stability and competition of various structures. Genetic algorithms [19] will generate a set of lower-energy structures for a given structure motif and chemical compositions allowing configuration free energy calculations to be performed using first-principles or accurate atomistic potential calculations. These tools will allow us to quantitatively describe the free energy landscapes of disordered systems to enable thermodynamically robust predictions of phase selection and transformation pathway during rapid solidification or devitrification.

4. References

1. D. R. Nelson and F. Spaepen, *Solid State Physics*, edited by H. Ehrenreich, F. Seitz and D. Turnbull (academic New York, 1989), Vol **42**, p. 1.
2. Li Huang, C.Z. Wang, S.G. Hao, M.J. Kramer, and K.M. Ho, *Phys. Rev. B* 81, 014108 (2010).
3. Li Huang, X.W. Fang, C.Z. Wang, M.J. Kramer, Z.J. Ding, and K.M. Ho, Appl. Phys. Lett., 98, 231906 (2011).
4. M. Li, C. Z. Wang, S. G. Hao, M. J. Kramer, and K. M. Ho, Phys. Rev. B, 80, 184201 (2009).
5. H. W. Sheng, W. K. Luo, F. M. Alamgir, J. M. Bai, and E. Ma, Nature 439 419, (2006).
6. Y. Q. Cheng, H. W. Sheng, and E. Ma, Physical Review B 78, 014207 (2008)
7. P. J. Steinhardt, D. R.Nelson, M. Ronchetti, Phys. Rev. B **28**, 784 (1983)
8. J. D. Honeycutt and H. C. Andersen, J. Phys. Chem. **91**, 4950 (1987).
9. J. L. Finney, Nature **266**, 309 (1977); Proc. R. Soc. A **319**,479(1970)
10. X. W. Fang, C. Z. Wang, Y. X. Yao, Z. J. Ding, & K. M. Ho, Phys. Rev. B **82**, 184204(2010)
11. M. I. Mendelev *et al.* Philos. Mag. **90,** 3795-3815 (2010)
12. X. W. Fang, C. Z. Wang, S. G. Hao, M. J. Kramer, Y. X. Yao, M. I. Mendelev, Z. J. Ding, R. Napolitano, and K. M. Ho, Scientific Report, submitted.
13. X. W. Fang, C. Z. Wang, Y. X. Yao, Z. J. Ding, and K. M. Ho, Phys. Rev. B, **83**, 224203 (2011).

14. S. Wu, M. J. Kramer, X. W. Fang, S. Y. Wang, C. Z. Wang, K. M. Ho, Z. J. Ding, and L. Y. Chen, Phys. Rev. B, submitted.
15. S. Wu, X. W. Fang, S. Y. Wang, C.Z. Wang, Y. X. Yao, K. M. Ho, Z. J. Ding and L. Y. Chen, J. Appl. Phys. submitted.
16. X. W. Fang, C. Z. Wang, Z. J. Ding, and K. M. Ho, Phys. Rev. B, to be submitted.
17. A. Laio and M. Parrinello, PNAS, **99**, 12562 (2002).
18. A. Laio and F. L. Gervasio, Rep. Prog. Phys. **71** 126601 (2008).
19. M. Ji, C. Z. Wang, and K. M. Ho, Phys. Chem. Chem. Phys. **12**, 11617 (2010).

5. Select publications by this task within our DOE project over the last two years.

1. "Development of Medium-Range Order in Metallic $Cu_{64.5}Zr_{35.5}$ Liquid and Glass", X. W. Fang, C. Z. Wang, S. G. Hao, M. J. Kramer, Y. X. Yao, M. I. Mendelev, Z. J. Ding, R. Napolitano, and K. M. Ho, Scientific Report, submitted.
2. "Dynamic arrest and glass formation induced by self-aggregation of icosahedral clusters in $Zr_{1-x}Cu_x$ alloys", S. G. Hao, C. Z. Wang, M. Z. Li, R. E. Napolitano, and K. M. Ho, Phys. Rev. B, Accepted.
3. "Competition between fcc and icosahedral short-range orders in pure and samarium-doped liquid aluminum from first principles", X. W. Fang, C. Z. Wang, Y. X. Yao, Z. J. Ding, and K. M. Ho, Phys. Rev. B, 83, 224203 (2011).
4. "Medium-range icosahedral order in quasicrystal-forming Zr_2Pd binary metallic glass", Li Huang, X.W. Fang, C.Z. Wang, M.J. Kramer, Z.J. Ding, and K.M. Ho, Appl. Phys. Lett., 98, 231906 (2011).
5. "Structure and dynamics of liquid $Ni_{36}Zr_{64}$ by ab initio molecular dynamics", Li Huang, C. Z. Wang, and K. M. Ho, Phys. Rev. B, 83, 184103 (2011).
6. "Signature of $Al_{11}Sm_3$ fragments in undercooled $Al_{90}Sm_{10}$ liquid from ab initio molecular dynamics simulations", X W Fang, C Z Wang, Y X Yao, Z J Ding and K M Ho, J. Phys.: Condens. Matter 23 235104 (2011).
7. "Atomistic cluster alignment method for local order mining in liquids and glasses", X. W. Fang, C. Z. Wang, Y. X. Yao, Z. J. Ding, and K. M. Ho, Phys. Rev. B, 82, 184204 (2010).
8. "Prediction of cooling rate dependent ordering in metallic glass transition using a two-state model", S. G. Hao, C. Z. Wang, Maozhi Li , R. E. Napolitano, M. I. Mendelev and K. M. Ho, Comp. Mat. Sci. 49, 615 (2010).
9. "Energetics of local clusters in $Cu_{64.5}Zr_{35.5}$ metallic liquid and glass", S. Q. Wu, C. Z. Wang, S. G. Hao, Z. Z. Zhu, and K. M. Ho, *Appl. Phys. Lett*., 97, 021901 (2010).
10. "Short- and Medium-Range Order in Amorphous Zr_2Ni Metallic Alloys", Li Huang, C.Z. Wang, S.G. Hao, M.J. Kramer, and K.M. Ho, *Phys. Rev. B* 81, 094118 (2010).
11. "Structure of $Zr_{1-x}Cu_x$ Metallic Liquids and Origin of Slow Diffusion at the Good-Glass-Forming Composition Range", Shaogang Hao, C. Z. Wang, Maozhi Li, M. J. Kramer, and Kai-Ming Ho, J. Appl. Phys. 107, 053511 (2010).
12. "Atomic Size and Chemical Effects on the Local Order of Zr2M (M= Co, Ni, Cu, Ag) Binary Liquids", Li Huang, C.Z. Wang, S.G. Hao, M.J. Kramer, and K.M. Ho, *Phys. Rev. B* 81, 014108 (2010).
13. "Effect of local structures and atomic packing on glass forming ability in Cu_xZr_{100-x} metallic glasses", H. L. Peng, M. Z. Li, W. H. Wang, C.-Z. Wang, and K. M. Ho, *Appl. Phys. Lett*., 96, 021901 (2010).

Designing Graphene Nanoarchitectures for a New Paradigm of Nanoelectronics

Feng Liu (fliu@eng.utah.edu)
Department of Materials Science & Engineering
University of Utah, Salt Lake City, UT 84112

Program Scope

This program explores the opportunity of employing solid-state semiconductor nanomembranes as a two-dimensional (2D) platform for designing next-generation nanoelectronics materials and technology. In addition to Si, SiGe and III-V membranes, our recent theoretical efforts have geared towards graphene, which represents the thinnest possible solid membrane consisting of single atomic layer of carbon atoms in a honeycomb structure. Graphene has not only exhibited a wealth of fascinating properties of fundamental interest, but also shown many useful properties for potential applications in electronics, such as extreme flexibility and stability, high carrier mobility, and long spin relaxation time. Nanopatterning of graphene provides an attractive route towards large scale device integration, and its planar structure affords an ideal 2D platform to pattern the whole device architecture in one sheet, compatible with the existing electronics [1]. By performing extensive studies of function-design relationships, we have carried out function driven structural designs for several unique graphene nanoarchitectures to realize some targeted functionalities, as demonstrated below.

Topic I: Manipulation of Electron Beam by Hetero-Dimensional Graphene Junction.

Dexterous manipulation of light beams underpins the two definitive technologies of our times of information age: telecommunication and the Internet. Information is processed and transferred through carefully controlled light as information carriers. In an analogy, manipulation of electron beams is expected to form the foundation for quantum information processing and quantum computing in the future. Recently, we have proposed a new mechanism for the energy-selective manipulation of electron beam by nanostructured hetero-dimensional graphene junctions (HDGJs) [2]. Beam splitting, collimation, and beam guide can all be realized by designing HDGJs of different dimensionality, size and orientation. The basic concept of a HDGJ device is illustrated in Fig. 1 for the case of electron beam splitting. It consists of a HDGJ made of 1D graphene nanoribbon (GNR) and 2D graphene sheet with zigzag interface. As an electron beam is injected into the 1D GNR, it splits into two beams at 60° angle in the 2D graphene sheet upon passing through the 1D-2D junction. The electron beam splitting (or complete electron propagation path) is mapped out by measuring the conductance of the HDGJs while scanning using a scanning probe microscopy (SPM). One important advantage of our proposed HDGJ electron beam manipulator is that individual functions of beam manipulation

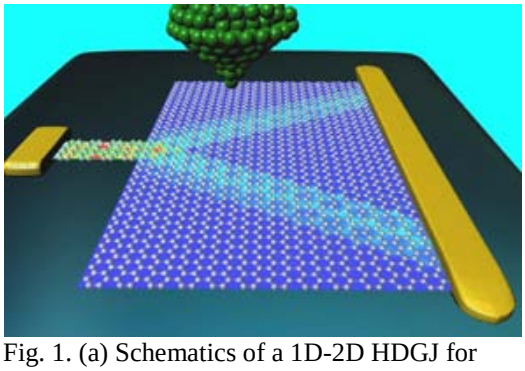

Fig. 1. (a) Schematics of a 1D-2D HDGJ for electron beam splitting and SPM mapping of electron propagation paths.

can be integrated together by patterning different HDGJs in one structural setting, affording opportunities for the realization of novel device functionalities.

Topic II: Quantum Cellular Automata Operated by Graphene Quantum Dots

Quantum cellular automata (QCA) [3] is an innovative approach that incorporates quantum entities into classical computation processes. Binary information is encoded in different charge states of the QCA cells and transmitted by the inter-cell Coulomb interaction. However, it remains a challenge to identify suitable building blocks for the construction of QCA. Recently, we proposed a new QCA architecture built upon graphene quantum dots (GQDs) [4]. Using the tight-binding model, we determine the phenomenological cell parameters and cell-cell response functions of the GQD-QCA to characterize its performance. A GQD-QCA architecture is also designed to demonstrate the functionalities of fundamental (NOR and NAND) logic gates, with four QCA cells arranged in a T-shape nanoarchitecture (Fig. 2). The polarization of the central cell is assigned as the output (Out), the left and right cell is assigned as operands B and C, respectively, and the top cell A is a programming bit. If A is programmed as "1", the logic is $Out = \overline{B \cap C}$, a NAND gate; if A is "0", the logic is $Out = \overline{B \cup C}$, a NOR gate. From these two fundamental gates, all digital logic operations can be designed. Our results show great promise for constructing high-density ultrafast GQD-QCA devices from a single nanopatterned graphene sheet.

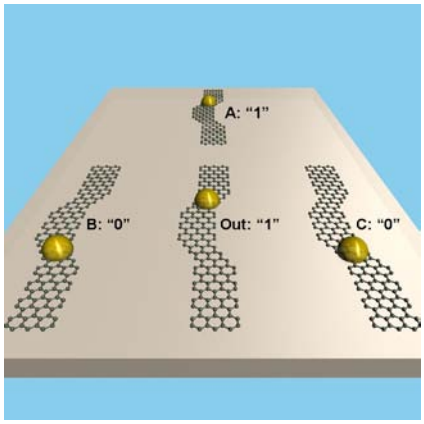

Fig. 2. Schematic of four QCA cells in a T-shape arrangement as a logic gate. A, B and C are the input bits, Out is the output bit. The ball in the GQD denotes the occupation of electron; "1" and "0" label the bit information.

Topic III: Band Gap Engineering by Hydrogenated Graphene Nanoripple

Nanostructuring affords an effective means to convert the semimetal graphene into semiconducting graphene based nanostructures, which is desirable for many nanoelectronics applications. A number of theoretical proposals and experimental attempts have been

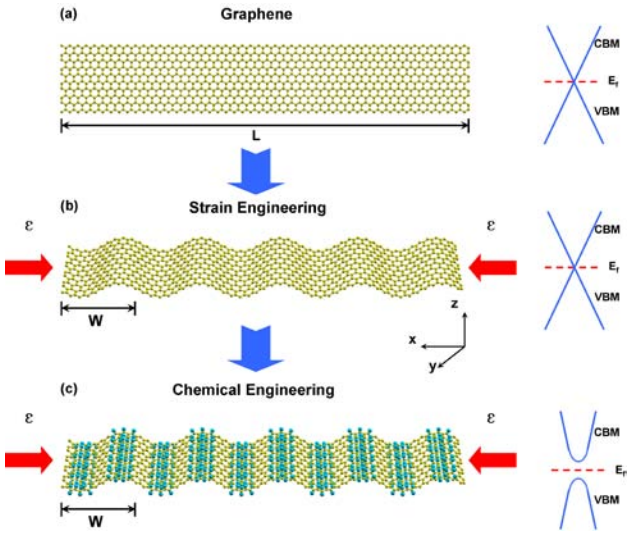

Fig. 3. Schematic illustration of a combinatorial approach of straining graphene and directing H adsorption to form HGNR. (a) Pristine graphene with zero band gap. (b) Graphene nanoripple with zero band gap. (c) HGNR with nonzero band gap.

made to create graphene-based nanostructures, such as GNRs, nanohole superlattices, hydrogenated graphene nanostripes, and graphane. However, our current success is still far below our expectations. Although the physical principles for opening the graphene band gap are well established, it remains challenging to synthesize the semiconducting graphene-based nanostructures with desirable precision and control. We proposed a strain-engineered self-assembly process to synthesize a new class of semiconducting graphene-based nanostructures, the hydrogenated graphene nanoripples (HGNRs) [5]. It is a combinatorial two-step strain engineering plus chemical engineering process: first strain engineering graphene into periodic nanoripple patterns, followed by a directed self-assembly of H adsorption onto the nanoripple template, as illustrated in Fig. 3. The combination of the strain engineering and the directed H surface self-assembly offers a high level of control of the dimensions of the HGNRs and hence of their band gaps. The combination of strain-engineered nanoripple formation and the curvature-directed surface self-assembly can be generally applied beyond graphene to other nanomembranes.

Recent progress on other projects:

1. Stabilizing graphitic thin films of wurtzite materials by epitaxial strain: (0001) ultrathin films of wurtzite materials have been shown to surprisingly transform into a stable graphite-like structure; but the stability is limited to thickness of only a few atomic layers. Using first-principles calculations, we predict that the thickness range of stable graphitic films depends sensitively on strain and can be substantially extended to much thicker films by epitaxial tensile strain. Moreover, the band gap of the graphitic films can be tuned over a wide range either above or below that of the bulk wurtzite phase.
2. Electron Phase Diagram of Single-Element Silicon "Strain" Superlattice: Superlattices (SLs) are conventionally made of two semiconductor materials with different band gaps. Recently, a new type of "strain" SL has been demonstrated, made of a single semiconductor material whose band gap is periodically modulated by strain. Using first-principles calculations, we have mapped out the electronic phase diagram of a silicon strain SL to differentiate the SL phase from the alloy phase as a function of strain magnitude and period.

Future Plans

(1) Continue with "function driven materials design" on the solid-state nanomembrane platform, in particular focusing on the system of bi-layer and multilayer graphene.
(2) Extend the study of "graphitic thin films of wurtzite materials" to defects.
(3) Calculation of XAS spectra of Si nanomembranes in correlation with experiments.
(4) Study of electronic and electric transport properties of some membranes-based nanoarchitectures, e.g. silicene. A special focus will be on "strain engineering" of electronic and transport structures, as all the nanoarchitectures are inherently strained in novel geometries accommodating high level of strains.

References

1. Q. Yan et al., Nano Lett. 7, 1469 (2007).
2. Z. F. Wang and Feng Liu, ACS Nano, 4, 2459 (2010).
3. C. S. Lent, P. D. Tougaw, W. Porod and G. H. Bernstein, Nanotech. 4, 49 (1993).
4. Z. F. Wang and Feng Liu, Nanoscale, (submitted).
5. Z. F. Wang , Y. Zhang and Feng Liu, Phys. Rev. B, 83, 041403(R), (2011).

The DOE funded publications (2009-2010)

1. "Manipulation of Electron Beam Propagation by Hetero-Dimensional Graphene Junctions", Z. F. Wang and Feng Liu, *ACS Nano.* **4**, 2459 (2010).
2. "Electron Phase Diagram of Single-Element Silicon "Strain" Superlattice", Z. Liu, J. Wu, W. Duan, M.G. Lagally and Feng Liu, *Phys. Rev. Lett*. **105,** 016802 (2010).
3. "Atomic Layers of Hybridized Boron Nitride and Graphene Domains", L. Ci, L. Song, C. Jin, D. Jariwala, D. Wu, Y. Li, A. Srivastava, Z. F. Wang, K. Storr, L. Balicas, Feng Liu, P. M. Ajayan, *Nature Mat*. **9**, 430 (2010).
4. "Tunable interfacial properties of epitaxial graphene on metal substrates", M. Gao, Y. Pan, C. Zhang, H. Hu, R. Yang, H. Lu, J. Cai, S. Du, Feng Liu, and H.-J. Gao, *Appl. Phys. Lett*. **96**, 053109 (2010).
5. "Effect of Surface Bonding on Semiconductor Nanoribbon Wiggling Structure", Y. Zhang, M. Yu, D. E. Savage, Max G. Lagally, R. H. Blick, and Feng Liu , *Appl. Phys. Lett*. **96**, 111904 (2010).
6. "Nanomechanical Architecture --- A Mechanics-Driven Nanofabrication Approach", Feng Liu, M. G. Lagally and J. Zang, *MRS Bulletin* **34**, 190 (2009). (**Invited review**).
7. "Strain – band structure relationships in Si(001) and Si(110) nanomembranes", C. Euaruksakul, F. Chen, B. Tanto, C. S. Ritz, D. M. Paskiewicz, F. J. Himpsel, D. E. Savage, Z. Liu, Y. Yao, Feng Liu, and M. G. Lagally, *Phys. Rev. B* **80**, 115323 (2009).
8. "The effect of next nearest neighbor coupling on the optical spectra in bilayer graphene", A. R. Wright, Feng Liu and C Zhang, *Nanotechnology* **20**, 405203 (2009).
9. "Effects of Ge Adsorption on Dewetting and Thermal Agglomeration of Thin Silicon-on-Insulator", P.P. Zhang, B. Yang, P. Rugheimer, M. Roberts, D.E. Savage, F. Liu, and M. G. Lagally, *J. Phys. D: Appl. Phys*. **42**, 175309 (2009).
10. "Quantum Manifestations of Graphene Edge Stress and Edge Instability: A First-Principles Study", B. Huang, M. Liu, N. Su, J. Wu, W. Duan, B. Gu and Feng Liu, *Phys. Rev. Lett*. **102,** 166404 (2009).
11. "Mechano-electronic Superlattices in Silicon Nanomembranes", M. Huang, C. S. Ritz, B. Novakovic, D. Yu, Y. Zhang, F. Flack, D. E. Savage1, P. G. Evans1, I. Knezevic, Feng Liu, and M. G. Lagally, *ACS Nano*, **3**, 721 (2009).
12. "Band Gap Scaling of Graphene Nanohole Superlattices", W. Liu, Z. F. Wang, Q. W. Shi, J. Yang, and Feng Liu, *Phys. Rev. B* **80**, 233405 (2009).
13. "Nanopumping molecules via a carbon nanotube", M. Chen, J. Zang, D. Xiao, C. Zhang and Feng Liu, *Nano Res.* **2**, 938 (2009).
14. "Directed self-assembly of monodispersed platinum nanoclusters on graphene Moiré template", Y. Pan, M. Gao, L. Huang, Feng Liu, and H.-J. Gao, *Appl. Phys. Lett*. **95**, 093106 (2009).
15. "Vacancy trapping mechanism for hydrogen bubble formation in metal", Y.-L. Liu, Y. Zhang, H.-B. Zhou, G.-H. Lu, Feng Liu, and G. -N. Luo, *Phys. Rev. B* **79**, 172103 (2009).
16. "Mechanical Wave Propagation in Carbon Nanotubes Driven by an Oscillating Tip Actuator", M. Chen, J. Zang, D. Xiao and Feng Liu, *J. Appl. Phys.* **105**, 026102 (2009).
17. "Highly Ordered, Millimeter-Scale, Continuous, Single-Crystalline Graphene Monolayer Formed on Ru (0001)", Y. Pan, H. Zhang, D. Shi, J. Sun, S. Du, Feng Liu, H.-J. Gao, *Adv. Mat*. **21**, 2777 (2009).

Templated Bottom-Up Synthesis of Semiconducting and Nanostructured Graphene Materials

Michael S. Arnold
msarnold@wisc.edu
Department of Materials Science and Engineering
University of Wisconsin, Madison, WI 53706

Program Scope

Graphene has received tremendous attention because of its exceptional properties such as its ultrafast charge transport characteristics[1, 2]; excellent mechanical strength, flexibility, and resilience[3]; outstanding thermal conductivity[4]; and its ultrahigh surface area / volume ratio. The nanostructuring of graphene further enhances its properties by altering its electronic structure, opening an energy gap resulting in semiconducting behavior[5-7], and increasing the accessibility of the surfaces and the edge density. The exceptional properties of nanostructured graphene materials have the potential to lead to advances in next-generation photovoltaic energy harvesting, energy storage, and semiconductor-based logic and sensing. These technological advances will be possible, however, only if the synthesis of planar nanostructured graphene materials can be realized with high quality and by rationally controllable means.

Traditionally, planar nanostructured graphene materials have been fabricated by growing continuous sheets of graphene and then etching the sheets into nanostructures, from the top-down. However, the top-down nanopatterning of graphene is severely limited by the etching tools that are available, which induce substantial defects, oxidation, and disorder. These defects *degrade* materials performance: for example, the electron mobility in sub-20 nm graphene nanoribbons patterned using reactive ion etching has been shown to be ~1/10,000 of unpatterned graphene due to disorder.[5, 8, 9] Therefore, while the properties of unpatterned graphene materials are exceptional, the properties of nanostructured graphene materials have, thus far, not been exceptional, by most measures.

The overarching objective of the present grant (which just began in July 2011) is to overcome this challenge and to learn how to synthesize both monolayered and multilayered nanostructured graphene materials without highly detrimental etch-induced disorder and with exceptional properties – from the bottom-up via chemical vapor deposition.

Recent Progress

Along these lines, we have developed a new strategy for the rational synthesis of patterned graphene from the bottom-up, called barrier-guided chemical vapor deposition (BG-CVD). In BG-CVD, graphene growth is laterally restricted on planar Cu surfaces by selectively passivating the catalytic activity of the Cu with patterned barrier templates designed to (i) locally limit the generation of atomic C species and (ii) confine their migration. We have successfully implemented BG-CVD using oxide barriers on Cu foils to fabricate highly crystalline, single-layered structures including channels, nanoribbons, and nanoperforated membranes, over large-areas without etching. The barriers restrict the nucleation of graphene to the exposed Cu and then guide its growth, remarkably, with 1 nm lateral precision and are expected to enable the direct synthesis of rationally-designed micro- and nanostructured graphene materials with superior performance.

The BG-CVD process is schematically depicted in Fig. 1 for atmospheric pressure methane CVD on an oxide barrier / Cu system. During growth, methane decomposes selectively on the exposed regions of Cu to produce atomic C (Fig. 1(i)), which does not appreciably dissolve into the bulk Cu due to its extremely low solubility[10]. The C instead laterally diffuses and preferentially accumulates on the exposed regions of the Cu surface until a supersaturation is reached and graphene nucleates (Fig. 1(ii)). The preferential deposition and accumulation of C on the exposed Cu is driven by the relative inertness of the oxide and the strong Cu-C bonding energy ~ 5 eV[11].

Following nucleation, the graphene crystallites grow up to the Cu/barrier edge-interface (Fig. 1(iii)). At this stage, the supply of atomic C becomes locally depleted due to the passivation of the underlying Cu by both the graphene and the barrier, and after the entire Cu surface is passivated the catalytic decomposition of methane ceases, terminating growth (Fig. 1(iv)). Following BG-CVD, the structured graphene is transferred to arbitrary substrates via a temporary polymer support membrane and etching of the Cu and oxide.

We have successfully implemented BG-CVD to create a variety of graphene structures at different scales including micron-scale boxes (Fig. 2a-c), arbitrary patterns (Fig. 2e-g), nanoribbons (Fig. 2h), and nanoperforated graphene, showing the versatility and scalability of the method. To explore the resolution limits of the BG-CVD method on the nanoscale, we have explored growth through channels as narrow as 15 nm. The oxide barriers are able to terminate the growth of graphene with nearly atomic exactness at the Cu/oxide edge-interface. Our data suggests that the BG-CVD strategy could be used to template nanostructured graphene materials with sub-5 nm features and < 1 nm resolution. The BG-CVD graphene is highly crystalline with low interior defect-density, evidenced by a Raman spectroscopy, relatively high charge transport mobility, and the observation of edge faceting. Ultimately, because BG-CVD avoids chemical etchants and instead relies on self-limiting growth processes to abruptly define edges, we expect that this method will lead to micro- and nanostructured graphene materials with superior performance.

Future Plans

While these preliminary approaches have been highly successful, the mechanisms that control the bottom-up growth of nanostructured graphene have not yet been elucidated and their ultimate capabilities are not yet clear. Both aspects will be the focus of the present grant. Our future objectives will be to: (1) Understand the nucleation, kinetics, and energetics of graphene growth in confined patterns or channels; (2) Learn how to halt the growth of graphene with atomic abruptness; (3) Discover how to confine the surface-driven growth of monolayered graphene; (4) Investigate how to confine the precipitation-driven growth of multilayered graphene; (5) Characterize the atomic ordering at the edges and learn the growth conditions and mechanisms that can control the edge ordering; and (6) Demonstrate enhanced materials performance.

References

1. J. H. Chen, C. Jang, S. D. Xiao, M. Ishigami, M. S. Fuhrer, *Intrinsic and extrinsic performance limits of graphene devices on SiO2*, Nature Nanotechnology **3**, 206-209 (2008).
2. X. Du, I. Skachko, A. Barker, E. Y. Andrei, *Approaching ballistic transport in suspended graphene*, Nature Nanotechnology **3**, 491-495 (2008).
3. C. Lee, X. D. Wei, J. W. Kysar, J. Hone, *Measurement of the elastic properties and intrinsic strength of monolayer graphene*, Science **321**, 385-388 (2008).
4. W. W. Cai, A. L. Moore, Y. W. Zhu, X. S. Li, S. S. Chen, L. Shi, R. S. Ruoff, *Thermal Transport in Suspended and Supported Monolayer Graphene Grown by Chemical Vapor Deposition*, Nano Letters **10**, 1645-1651 (2010).
5. M. Kim, N. S. Safron, E. Han, M. S. Arnold, P. Gopalan, *Fabrication and Characterization of Large-Area, Semiconducting Nanoperforated Graphene Materials*, Nano Letters **10**, 1125-1131 (2010).
6. C. Stampfer, J. Gutttinger, S. Hellmueller, F. Molitor, K. Ensslin, T. Ihn, *Energy Gaps in Etched Graphene Nanoribbons*, Physical Review Letters **102**, (2009).
7. L. Yang, C. H. Park, Y. W. Son, M. L. Cohen, S. G. Louie, *Quasiparticle energies and band gaps in graphene nanoribbons*, Physical Review Letters **99**, (2007).
8. N. S. Safron, M. S. Arnold, *Characterization of conduction mechanisms relevant to device performance in nanoperforated graphene*, Submitted, (2010).
9. N. S. Safron, A. S. Brewer, M. S. Arnold, *Semiconducting Two-Dimensional Graphene Nanoconstriction Arrays Fabricated Using Nanosphere Lithography*, Small **7**, 492-498 (2011).
10. X. S. Li, W. W. Cai, L. Colombo, R. S. Ruoff, *Evolution of Graphene Growth on Ni and Cu by Carbon Isotope Labeling*, Nano Letters **9**, 4268-4272 (2009).
11. H. Chen, W. Zhu, Z. Zhang, *Contrasting Behavior of Carbon Nucleation in the Initial Stages of Graphene Epitaxial Growth on Stepped Metal Surfaces*, Physical Review Letters **104**, 186101 (2010).

DOE Sponsored Publications from Current Grant (which just began July 2011)

N. S. Safron, M. Kim, P. Gopalan, M. S. Arnold, *Barrier-Guided Growth of Micro- and Nano-Structured Graphene*, Submitted, (2011).

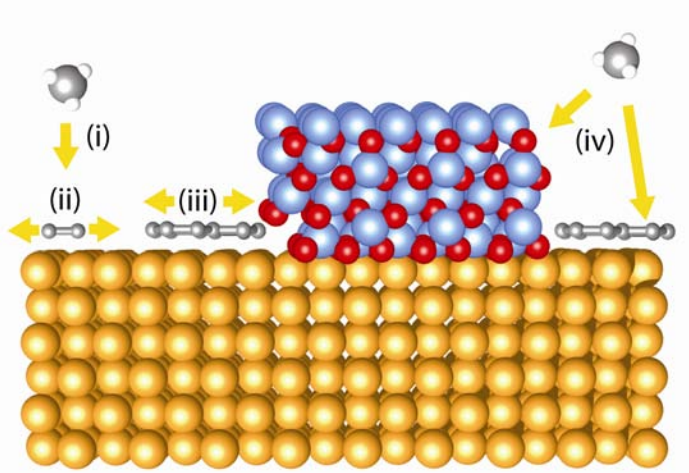

Figure 1. Schematic of BG-CVD: (i) methane decomposes on the Cu surface into atomic C, which (ii) diffuses and nucleates graphene, (iii) growing to cover the entire unmasked Cu surface until (iv) the entire surface is covered by graphene or oxide and methane can no longer decompose, terminating growth.

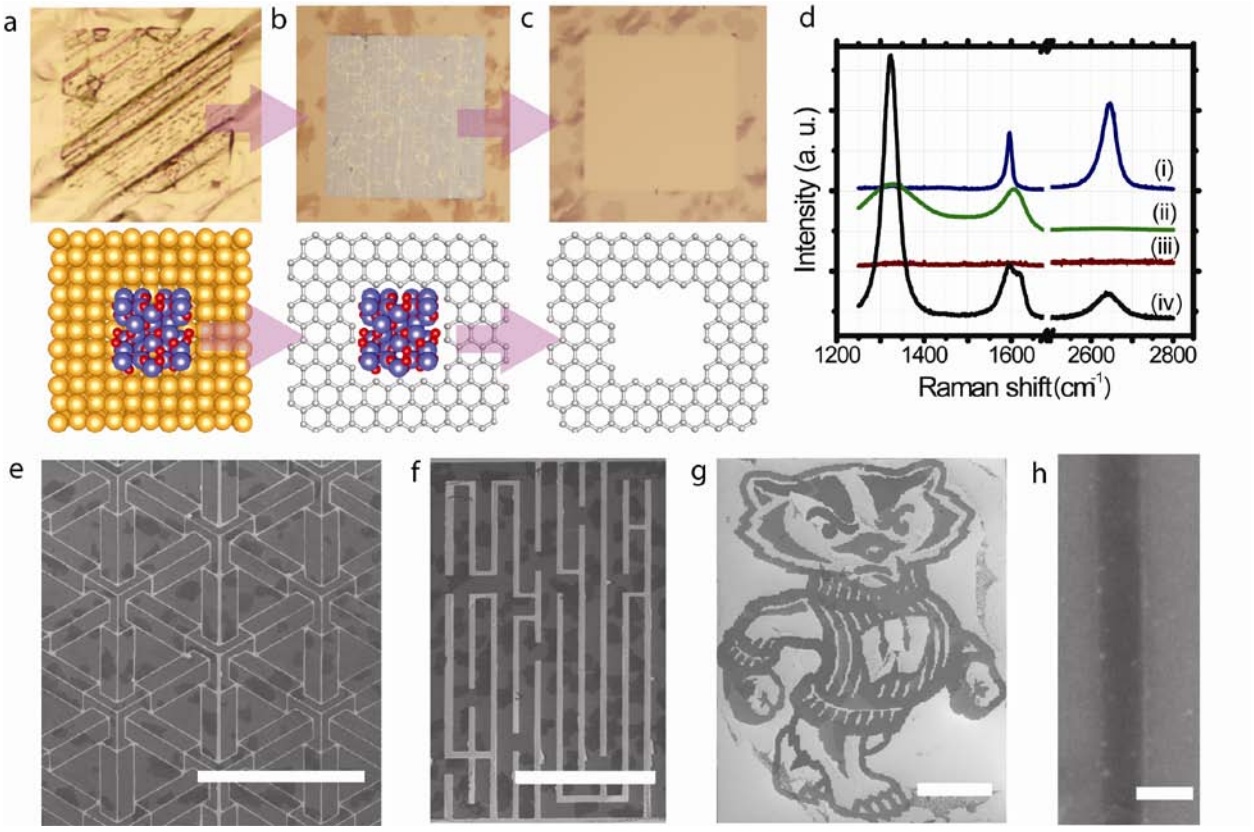

Figure 2. Demonstration of BG-CVD: a-c) optical micrograph (top) and schematics (bottom) of BG-CVD with a 60 μm barrier. d) Raman spectroscopy of (i) graphene on the exposed Cu, (ii) carbon clusters on the barrier, (iii) the masked region after barrier etching, and (iv) BG-CVD nanoperforated graphene (not shown). SEM of BG-CVD e) M. C. Escher pattern, f) Simple maze, g) Bucky the Badger, mascot of the University of Wisconsin, Madison, and h) graphene nanoribbon of width 40 nm. The graphene is seen as darker grey, Si/SiO_2 substrate as white, scale bar = 20 μm, 20 μm, 10 μm, 50 nm, respectively.

Nanoscale Morphology Evolution Under Ion Irradiation

Michael J. Aziz, Harvard School of Engineering and Applied Sciences, Cambridge MA 02138

PROGRAM SCOPE

The use of ion beams has great promise for morphology control in materials synthesis and processing at sub-lithographic length scales. We are studying experimentally and theoretically the fundamental physical principles governing nanoscale surface morphology evolution during ion irradiation at energies low enough that the principal phenomena are observed at the surface rather than in the bulk. Self-organized one- and two-dimensional arrays of nanoscale surface features ("ripples" and "dots") sometimes form spontaneously on initially flat surfaces. If the medium-range order exhibited by the spontaneous patterns could be guided predictably by fundamental understanding combined with known templating methods, then useful periodic structures as small as 7 nm could be generated in high-throughput settings.

RECENT PROGRESS

Since its discovery nearly half a century ago, it has been suspected that this "sputter pattern" formation is caused by sputter erosion effects. The erosion-based paradigm was established firmly 23 years ago when the destabilizing effect of the surface curvature-dependent sputter yield (atoms removed per incident ion) was incorporated into the linear stability theory of Bradley and Harper (BH) [1]. In BH theory the characteristic length scale of the pattern originates from differing wavenumber dependences of two competing effects: the destabilizing effect of a sputter yield that increases with increasing concave curvature, and the stabilizing effect of capillarity-driven surface diffusion. Although BH theory explains several experimental observations, its prediction that an initially flat surface will display a pattern-forming instability at all incidence angles is contradicted by our experimental studies on amorphous silicon surfaces, for which there are no potentially confounding effects of singular crystallographic surface energetics and kinetics. We observe rippled surfaces at high angles θ of deviation from normal incidence, *with a transition to a stable flat surface* with decreasing θ. We and others [2] have analyzed an impact-induced prompt mass redistribution effect as potentially a small modification of the BH model, sufficient to rescue stability at low angle and perhaps moderating the erosion-driven instability at high angle. We have now discovered that, as far as the stability/instability transition is concerned, *the redistribution effect is essentially the whole story – not only the cause of stability at low angle, but also the cause of instability at high angle – and that the erosive effect is essentially irrelevant.* We have arrived at this conclusion from two independent lines of reasoning - one experimental [DOE09], and one theoretical [DOE08]. These papers spell the end of the erosion-based paradigm that has dominated the field for half a century and propose its replacement with a paradigm based on the redistribution of atoms that are displaced, but not removed, by the impact.

Experimental work: Impact-induced redistribution explains everything

In a collaboration with Karl Ludwig of Boston University to measure the linear dispersion relation *in situ* in real time using Grazing Incidence Small Angle X-Ray Scattering (GISAXS) at the National Synchrotron Light Source at Brookhaven National Laboratory, we measure the real-time diffusely scattered intensity corresponding to topographic correlations at the sample surface. The objective is to measure the effective curvature coefficient for destabilization of a flat surface, S. Positive values of S stabilize the surface and negative values cause instability.

For each Fourier mode with wavenumber q we fit the evolution of the structure factor to the appropriate theoretical form to determine the amplification rate $R(q)$. The effective curvature

coefficient for destabilization for the parallel mode (wave vector in the *x* direction, parallel to the projected ion beam on the sample surface) instability, $S_{x,effective}$, is extracted from a fit of the quadratic plus quartic functional form,

$$R(q) = - Sq^2 - Bq^4, \quad (1)$$

to the data. The Bradley-Harper prediction for the erosive contribution ($S_{x,erosive}(\theta)$) is not only of the wrong sign but also is of such a small magnitude as to be essentially irrelevant, except possibly at the most grazing angles of incidence. The data are well fit by our synthesis of some phenomenological models with a single free parameter. The finding of profound significance is that the experimental data for the $S_{x,effective}$ coefficient show that the Bradley-Harper effect is negligible. This strongly suggests that erosive effects are negligible, although the possibility remains that the Bradley-Harper model is merely a vast underestimate of the magnitude of the erosive effect. In the theoretical work we confirm the former option: erosive effects are negligible.

Theoretical Work: From crater functions to phase diagrams

We have developed a new theoretical methodology for deriving the governing partial differential equation for surface evolution from the accumulation of topographic responses to individual ion impacts. The local response (the "crater function" $\Delta h(x - x')$, with x' the impact point) can be obtained by experiment (e.g. STM images) or simulation (e.g., Molecular Dynamics (MD)). Although no two craters are completely identical, it's only the average over many craters that matters. The theory exploits a separation in length scale between the topographic changes due to a single ion impact and the emerging pattern. It also exploits a separation in time scale between the "prompt regime", in which kinetic energy-induced sputter erosion and bombardment-induced surface mass transport go to completion, and the "gradual regime" in which thermally-activated morphological relaxation processes occur. The theory derives for the prompt regime, *without any free parameters*, the *S* coefficients (there is one for each independent spatial dimension, *x* and *y*) in Eq. (1), from the crater functions. A flat surface is stable if both S_x and S_y are positive; if either is negative the surface is unstable. Prior to this work, the best models for the *S* coefficients contained adjustable parameters, and in many cases there was no way to reliably estimate the magnitude of those parameters.

The final term in Eq. (1), $-Bq^4$, is the phenomenological relaxation term that comes from the simplest classical relaxation models in the gradual regime; it doesn't affect the absence or presence of instability but in combination with the value of the appropriate *S* coefficient it sets the length scale. We obtain the value of *B* from the published MD work of others in a nearly identical system.

The theoretical framework starts with an expression for the net result of accumulated responses to single ion impacts:

$$\frac{\partial h(x,t)}{\partial t} = \int_{-\infty}^{\infty} I(x')\Delta h(x - x')dx', \quad (2)$$

in terms of the single-impact crater function $\Delta h(x - x')$ and the ion flux over the surface *I*. The complete description of the evolution of an initially-flat interface in the "prompt regime" (including the values of the *S* coefficients) then follows from some complex but rigorous math:

$$\frac{\partial h(x,y,t)}{\partial t} = \left(I\tilde{M}^{(0)}\right) + \varepsilon\nabla\bullet\left(I\tilde{M}^{(1)}\right) + \frac{1}{2}\varepsilon^2\nabla\bullet\nabla\bullet\left(I\tilde{M}^{(2)}\right) + O\left(\varepsilon^3\right) \quad (3)$$

where ε is the amplitude of the modulation and the $\tilde{M}^{(n)}$'s are simply combinations of moments of the average crater function. For linear stability the terms of order ε^2 and higher are insignificant and the $\tilde{M}^{(1)}$ term determines whether a flat surface is stable.

To obtain converged crater functions from MD simulations, we have been collaborating with Kai Nordlund of the University of Helsinki. They have obtained results from a large number of impact simulations over a range of incidence angles. When we compute the moments from their results we obtain the predictions for stability vs. instability. The predictions for the angle of the transition between smooth stable surfaces and a parallel mode instability, and for the angle-dependence of the instability wavelength agree remarkably well with experiment.

This result is significant for several reasons:

1. Of general scientific interest, it is a methodological milestone. We have successfully predicted a very large, continuum-scale phenomenon observed in materials systems using only the inter-atomic interaction potentials as input. These potentials, although they are classical and have been optimized by others for other phenomena, are found to be widely useful in silicon simulations and we did not tinker with them in any way. In essence, we have started with molecular dynamics simulations lasting < 10 ps and extending < 5 nm, derived rigorously from them a PDE for the prompt regime, and appended to it a phenomenological term with no free parameters to account for the gradual regime. The result is a completely parameter-free prediction of the morphology evolution, which agrees to a remarkable extent with experimental observations conducted over time scales of hours and length scales of microns.
2. For the first time in the morphology evolution field, a theory predicts the existence of a transition to stable flat surfaces with zero free parameters;
3. The predicted divergence of the wavelength with decreasing angle is qualitatively consistent with the experiments for parallel-mode ripples and the small degree of quantitative disagreement is of the magnitude one might expect from the classical potential used in the MD;
4. Even the nonlinear terms in the morphology evolution are captured by Eq. (3), which means that, in principle, crater function theory can predict not only the initial pattern formation instability, but also the entire evolution of complex morphologies;
5. In the broader context, our research provides new insight toward the design of plasma-facing fusion reactor walls. Here, a long-standing design consideration has been the need for wall materials that are as stable as possible under sustained exposure to He ions with average energies of about 60 eV. With a threshold energy of 100 eV for sputter removal of target atoms by He ions, tungsten has been the material of choice due to the assumption that suppressing the sputter yield suppresses the ion bombardment induced morphological stability. Although under some conditions the surface appears morphologically stable, and degradation mechanisms are understood to involve helium bubble nucleation and growth beneath the surface, in certain environments a mysterious “foamy tungsten” morphology develops under fusion-relevant plasma conditions. As we have shown, the suppression of erosion is not sufficient to guarantee stability, and we conjecture that atom redistributive effects may be important contributors to the origin of these mysterious morphologies. There was no way to test such conjectures before, but now that our crater-function approach has been introduced, it is plausible to apply it to He impacts on W. Ultimately, if our conjecture proves correct, it may lead to crater function engineering

considerations providing a more refined materials design criterion than simply a low sputter yield for solid surfaces that must withstand energetic particle irradiation.

PLANS

Our plans include (1) investigating the orthogonal (*y*) in-plane direction; (2) investigating other materials and ion species in order to understand the limits of applicability of our conclusions; (3) investigating the effects of non-local effects such as impact-induced stress using a new custom-made system currently under construction; (4) investigating nonlinear amplification effects with a new high-flux ion gun and a theoretical investigation of the nonlinear regime of Eq. (3).

LITERATURE CITED

[1] R.M. Bradley and J.M. Harper, *J. Vac. Sci. Technol. A* **6**, 2390 (1988)

[2] G. Carter and V. Vishnyakov, " *Phys. Rev. B* **54**, 17647 (1996)

PUBLICATIONS ACKNOWLEDGING DOE SUPPORT

[DOE01] B. Davidovitch, M.J. Aziz, and M.P. Brenner, "Linear Dynamics of Ion Sputtered Surfaces: Instability, Stability and Bifurcations", *J. Phys. Cond. Mat.* **21**, 224019 (2009)

[DOE02] S.A. Norris, M.P. Brenner, and M.J. Aziz, "From Crater Functions to PDEs: A New Approach to Ion Bombardment Induced Nonequilibrium Pattern Formation", *J. Phys. Cond. Mat.* **21**, 224017 (2009).

[DOE03] C.S. Madi, H.B. George, and M.J. Aziz, "Linear Stability and Instability Patterns in Ion- Sputtered Silicon", *J. Phys. Cond. Mat.* **21**, 224010 (2009)

[DOE04] K.Z. House, C.H. House, D.P. Schrag, and M.J. Aziz, "Electrochemical Acceleration of Chemical Weathering for Carbon Capture and Sequestration", Proceedings of Ninth International Conference on Greenhouse Gas Control Technologies, Washington DC, November 16-20, 2008. *Energy Procedia* **1**, 4953 (2009).

[DOE05] R. Asmatulu, A. Karthikeyan, D.C. Bell, S. Ramanathan, and M.J. Aziz, "Synthesis and variable temperature electrical conductivity studies of highly ordered TiO_2 nanotubes", *J. Mater. Sci.* **44**, 4613 (2009).

[DOE06] H.B. George, Y. Tang, X. Chen, J. Li, J.W. Hutchinson, J.A. Golovchenko and M.J. Aziz, "Nanopore fabrication in amorphous Si: viscous flow model and comparison to experiment", *J. Appl. Phys.* **108**, 014310 (2010).

[DOE07] H.B. George, D.P. Hoogerheide, C.S. Madi, D.C. Bell, J.A. Golovchenko and M.J. Aziz, "Ion Sculpting of Nanopores in Amorphous Metals, Semiconductors, and Insulators", *Appl. Phys. Lett.*, **96**, 263111 (2010).

[DOE08] S.A. Norris, J. Samela, C.S. Madi, K. Nordlund, M.P. Brenner and M.J. Aziz, "Molecular Dynamics of Single-Particle Impacts Predicts Phase Diagrams for Large Scale Pattern Formation", *Nature Communications* **2**, 276 (2011).

[DOE09] C.S. Madi, E. Anzenberg, K.F. Ludwig, and M.J. Aziz, "Mass Redistribution Causes the Structural Richness of Ion-Irradiated Surfaces", *Phys. Rev. Lett.* **106**, 066101 (2011) .

[DOE10] D.P. Hoogerheide, H.B. George, J.A. Golovchenko, and M.J. Aziz, "Thermal Activation and Saturation of Ion Beam Sculpting", *J. Appl. Phys.* **109**, 074312 (2011).

[DOE11] J. Samela, S.A. Norris, K. Nordlund, and M.J. Aziz, "Optimization of Large Amorphous Silicon and Silica Structures for Molecular Dynamics Simulations of Energetic Impacts", *Nucl. Instr. Meth. Phys. Res. B* **269**, 1568 (2011).

Molecular Dynamics simulations and experimentation on the liquid-phase assembly of thin metallic film nanostructures

Miguel Fuentes-Cabrera, Jason D. Fowlkes, Philip D. Rack and Michael L. Simpson
fuentescabma@ornl.gov; prack@utk.edu

Center for Nanophase Materials Sciences, Oak Ridge National Laboratory, Oak Ridge, 37831, TN

Program Scope

Thin film dewetting can be exploited to self-assemble and organize nanoparticles. To control self-assembly and organization, it is crucial to understand the nanoscale liquid phase dynamics. In this respect, Molecular Dynamics simulations (MD) using a Lennard-Jones (LJ) potential is a powerful tool. Huang *et al.*[1] have used MD simulations with a LJ potential to investigate the dynamics of metals clusters on a static graphite surface. They described the metal-metal interactions using the Sutton-Chen potential and the metal-C interactions using the LJ potential; although their study did not focus on wetting *per se*, they did observe a correlation between wetting and the strength of the metal-C interaction. This observation is important because it suggested to us that MD simulations with LJ potentials can be used to describe the wetting of metals on graphite -provided that one stays within the limitations imposed by that LJ potential.

Employing a LJ potential to investigate the de-wetting of metallic liquids on graphite carries with it several limitations. One cannot use this potential to describe situations in which the metals are incorporated in the graphitic layer. Employing a LJ potential has, on the other hand, one important advantage: one can change its depth and describe different wetting situations. The work of Bertrand, Blake and De Coninck[2] is a good example of how one can describe situations ranging from complete wetting to non-wetting by simply changing the parameters of the LJ potential. Inspired by this work, in the past two years we have carried out a research program in which we have investigated the de-wetting of liquid metals on graphite using MD simulations with a LJ potential whose strength and depth varies.

Recent Progress

**** We have developed a methodology to generate LJ potentials that describe accurately the liquid metal/grahite interactions.*** We have initially focused on the Cu-C systems and, to gauge the accuracy of the LJ potential used in our simulations, we developed a routine in which we fit the potential to reproduce the experimental wetting contact angle of Cu on graphite and the *ab initio* binding energy of the graphene/Cu(111) interface. In doing so, we found that a previously published Cu-graphite LJ potential[1] (termed as LJ2 from now on) resulted in a contact angle smaller than what is known experimentally, and a binding energy 6 times larger than the *ab initio* value. On other hand, our fitting routine produced a potential, LJ1, that reproduced very well the equilibrium contact angle while overestimating (about three times) the Cu(111)/graphene binding energy. Nonetheless, we have used LJ1 and two more other LJ potentials (LJ2 and LJ3) to study different regimes of wetting.

**** We have shown that MD simulations with LJ potentials can be used to study the de-wetting of metallic liquids on graphite while accessing different wetting regimes.*** The MD simulations done with LJ1-3 span a significant transition in the self–assembly dynamics. Thus, it was found that relatively stronger liquid–substrate cohesion, LJ2-3, is required to initiate self–assembly confined to the original substrate surface plane. In contrast, relatively weaker liquid–solid cohesion, LJ1, leads to the ejection of nanodroplets (see Fig. 1).

**** Our results suggest that nanosecond laser pulses can be used to control the velocity of jumping nanodroplets*** MD simulations done with LJ1 revealed that a nanostructure in the shape of a circle dewets and coalescence into a droplet that is ejected from the graphitic substrate with a velocity of about 100 m/s. [3] This result mimicked very well previous experimental studies on Au triangles deposited on silica or graphite[4]. This fact encouraged us to explore the possibility of using de-wetting induced directed assembly to control the magnitude of the velocity of jumping nanodroplets. We have recently demonstrated that such a control is possible: theoretical calculations based on molecular dynamics simulations showed that nanostructures deposited on a graphitic substrate dewet and coalesced into nanodroplets that are ejected with velocities that depend on their initial shape and temperature. The dependence of the ejected velocity on shape is due to the temporal asymmetry of the mass coalescence during the droplet formation: the more symmetric is a nanostructure the faster it is ejected from the graphitic substrate.[5]

Our results suggest that nanosecond laser pulses can be used to control the velocity of ejected nanoparticles, opening up a realm of possibilities towards using de-wetting phenomena to control and guide the movement of nanoscale objects.

**** The time and length scales of the assembly of bi-metallic nanoparticles formed via pulsed laser induced dewetting were examined.*** Pulsed-laser-induced dewetting (PLiD) was used to assemble patterned, nanoscale metallic thin film features into bimetallic nanoparticles (Figure 2). The liquid-phase flow is related to a conventional droplet impact test and, in appropriate dimensions, have inertial and viscoinertial flow characteristics. The final size, morphology, composition, and interdiffusion of the nanoparticles is governed by the interplay of capillary, inertial, and viscous forces and an appropriate dimensional regime defined by competing Rayleigh-Plateau and spinodal instabilities.

Future work

The fitting routine that we used to generate an accurate LJ for the Cu-C system can be used to investigate other metal-C system as well. Thus, we plan to expand our fitting routine to other metal-C systems of interest. We have already started to fit an Au-C LJ potential and, as it happened before for the Cu-C system, we have also found that a previous published potential for Au-C, which was used to investigate "hot" Au cluster on graphite, is not appropriate for investigating the de-wetting of Au liquids on graphite. This underlines the usefulness of our approach: it corrects previous potentials and provides better potentials to the community.

With all these potentials we will explore further the possibility of using de-wetting for controlling the movement of nanoscale objects. For example, we have currently found that nanotubes can be ejected by using de-wetting: a portion of a capped nanotube was coated with a liquid Cu; when the liquid dewets, it is propelled in one direction whereas the nanotube is propelled in the opposite direction. Similar ideas are currently being explored by us.

References

1. Huang, S. P.; Mainardi, D. S.; Balbuena, P. B., Structure and dynamics of graphite-supported bimetallic nanoclusters. *Surf Sci* **2003,** *545* (3), 163-179.
2. Bertrand, E.; Blake, T. D.; Ledauphin, V.; Ogonowski, G.; De Coninck, J.; Fornasiero, D.; Ralston, J., Dynamics of dewetting at the nanoscale using molecular dynamics. *Langmuir* **2007,** *23* (7), 3774-3785.
3. Fuentes-Cabrera, M.; Rhodes, B. H.; Fowlkes, J. D.; Lopez-Benzanilla, A.; Terrones, H.; Simpson, M. L.; Rack, P. D., Molecular dynamics study of the dewetting of copper on graphite and graphene: Implications for nanoscale self-assembly. *Phys Rev E* **2011,** *83* (4), -.

4. Habenicht, A.; Olapinski, M.; Burmeister, F.; Leiderer, P.; Boneberg, J., Jumping, nanodroplets. *Science* **2005,** *309* (5743), 2043-2045.
5. Fuentes-Cabrera, M. R., B. R.; Baskes, M. I.; Terrones, H.; Fowlkes, J. D.; Simpson, M. L.; Rack, P. D., Controlling the velocity of jumping nanodroplets via their initial shape and temperature. *Acs Nano* **(Accepted for Publication)**.

DOE Sponsored Publications in 2009-2011 from Current Grant

1. M. Fuentes-Cabrera, B. H. Rhodes, M. I. Baskes, H. Terrones, J. D. Fowlkes, M. L. Simpson, P. D. Rack, "Controlling the velocity of jumping nanodroplets via their initial shape and temperature", *ACS Nano (accepted for publication)*
2. J. D. Fowlkes, L. Kondic, J. Diez, Y. Wu and P. D. Rack, "Self–Assembly versus Directed Assembly of Nanoparticles via Pulsed Laser Induced Dewetting of Patterned Metal Films", *Nano Letters* 11, 2478 (2011)
3. M. Fuentes–Cabrera, B. H. Rhodes, J. D. Fowlkes, A. Lopez–Benzanilla, H. Terrones, M. L. Simpson and P. D. Rack, "Molecular dynamics study of the dewetting of copper on graphite and graphene: Implications for nanoscale self – assembly", *Physical Review E* 83, 041603 (2011)
4. A. V. Melechk, R. C. Pearce, D. K. Hensley, M. L. Simpson T. E. McKnight, "Challenges in process integration of catalytic DC plasma synthesis of vertically aligned carbon nanofibres", *Journal of Physics D-Applied Physics* 44, 174008 (2011)
5. Y. Wu, J. D. Fowlkes and P. D. Rack, "The optical properties of Cu–Ni nanoparticles produced via pulsed laser dewetting of ultrathin films: The effect of nanoparticle size and composition on the Plasmon response", *Journal of Materials Research* 26, 277 (2011)
6. M. F. Sarac, R. M. Wilson, A. C. Johnston-Peck, J. Wang, R. Pearce, K. L. Klein, A. V. Melechko, J. B. Tracy, "Effects of Ligand Monolayers on Catalytic Nickel Nanoparticles for Synthsizing Vertically Aligned Carbon Nanofibers", *ACS Applied Materials & Interfaces* 3, 946 (2011)
7. R. Clearfield, J. G. Railsback, R. C. Pearce, D. K. Hensley, J. D. Fowlkes, M. Fuentes–Cabrera, M. L. Simpson, P. D. Rack and A. V. Melechko, "Reactive solid–state dewetting of Cu–Ni films on silicon", *Applied Physics Letters* 97, 253101 (2010)
8. J. D. Fowlkes, Y. Wu and P. Rack, "Directed Assembly of Bi–Metallic Nanoparticles by Pulsed Laser Induced Dewetting: a Unique Time and Length Scale Regime", *ACS Applied Materials & Interfaces* 2, 2153 (2010)
9. E.C. Landis, K.L. Klein, A. Liao, E. Pop, D.K. Hensley, A.V. Melechko, and R.J. Hamers, "Covalent Functionalization and Electron-Transfer Properties of Vertically Aligned Carbon Nanofibers: The Importance of Edge-Plane Sites", *Chemistry of Materials* 22, 2357 (2010)
10. Y. Wu, J. D. Fowlkes, P. D. Rack, J. A. Diez and L. Kondic, "On the Breakup of Patterned Nanoscale Copper Rings into Nanoparticles: Competing Instability and Transport Mechanisms", *Langmuir* 26, 11972 (2010)
11. B. L. Fletcher, J. T. Fern, K. Rhodes, T. E. McKnight, J. D. Fowlkes, S. T. Retterer, D. J. Keffer, M. L. Simpson and M. J. Doktycz, "Effects of ultramicroelectrode dimensions on the electropolymerization of polypyrrole", *Journal of Applied Physics* 105, 124312 (2009)
12. L. Kondic, J. A. Diez, P. D. Rack, Y. Guan and J. D. Fowlkes, "Nanoparticle assembly via the dewetting of patterned thin metal lines: Understanding the instability mechanisms", *Physical Review E* 79, 026302 (2009)
13. Melechko, A.V., R. Desikan, T.E. McKnight, K.L. Klein, and P.D. Rack, "Synthesis of vertically aligned carbon nanofibres for interfacing with live systems", *Journal of Physics D: Applied Physics* 42, 193001 (2009)

Figures

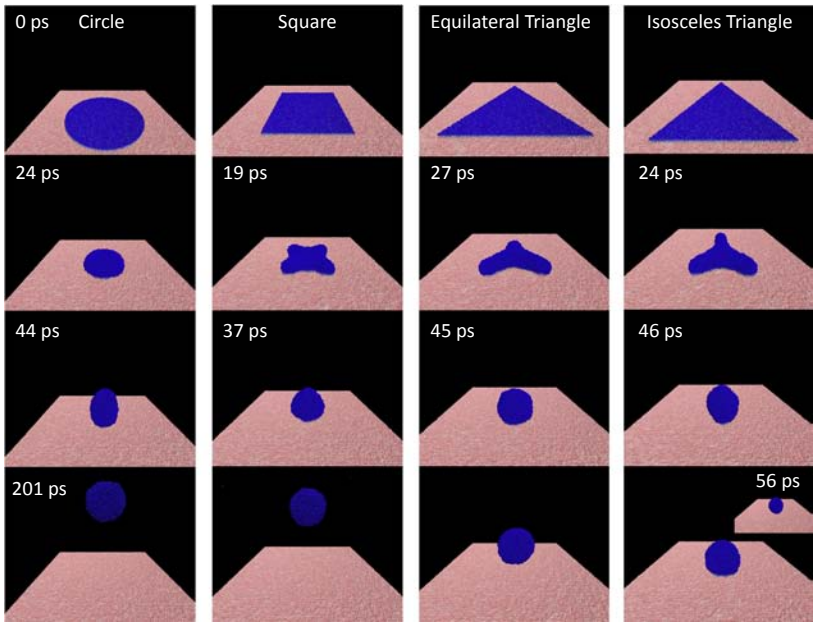

Figure 1 Snapshots of the different shapes simulated at 1900 K (tilted at 70°). The top row is the original liquid Cu nanostructures (blue atoms) on the graphitic substrate (pink atoms). All the areas are equal to ~45239 Å^2. Column 4 shows the snapshots at 201 ps and they illustrate the position of the droplet above the substrate for all shapes except for the isosceles triangle, in which case the droplet does not jump but remains in equilibrium with the substrate.

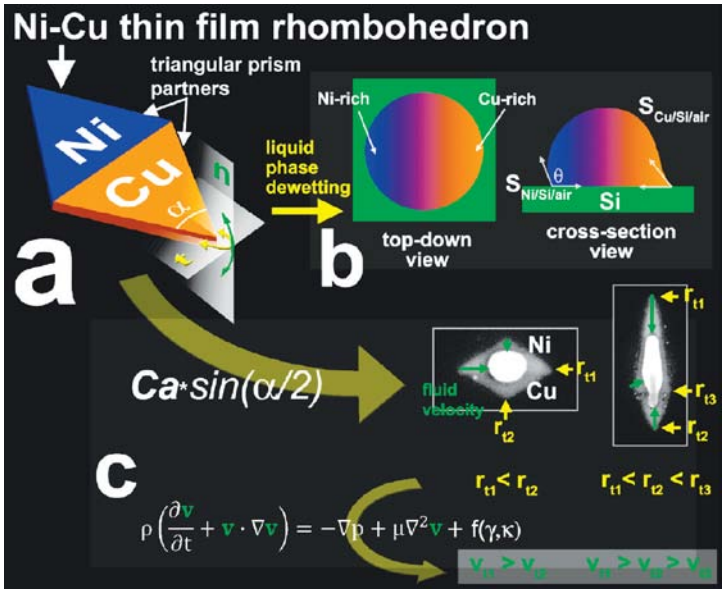

Figure 2 Schematic illustrating the bi-metallic nanoparticle self assembly process in which the in-plane curvature enhances the velocity of the small angle vertices of the patterned nanostructures. A thorough study of the transport and competing instabilities revealed the unique nanoscale time and length regimes that bimetallic nanoparticle formation is possible.

Molecularly Organized Nanostructural Materials
Subtask: Theoretical Modeling of Nanostructural Materials Synthesis Using Self-Assembly Process

Maria Sushko and Jun Liu
jun.liu@pnnl.gov
Pacific Northwest National Laboratory, Richland, WA 99352

Subtask Scope

Developing synthesis pathways, which utilize directed growth and self-assembly processes, would open a new avenue in developing environmentally benign scalable synthesis methods. It is also equally important to gain a fundamental understanding of structure / property relations in complex nanocomposite materials. The solution of these two problems will allow synthesis of materials "by design" tailored to perform specific task with optimum efficiency.

We focus on developing novel multiscale computational methods for designing the architecture and synthesis methods for energy storage nanocomposite materials with optimized performance. We apply these models to gain a detailed fundamental understanding of ion and electron transport in nanocomposite electrode materials and of the factors determining their templated growth and three-dimensional self-assembly.

Recent Progress

1. Theoretical modeling of surfactant layers at surfaces.

We have made progress towards elucidating the main factors that determine the structure and stability of surfactant templates by elucidating the effects of electrolyte and geometrical confinement, which underpin the essential physics of surfactant self-assembly at surfaces.[1,2] For this purpose we have developed novel multiscale computational software, based on one-dimensional classical Density Functional Theory (cDFT) for surfactant/solvent/surface (or slit pore) systems. Our theoretical approach allows deconvoluting the components of the free energy corresponding to excluded volume and ion correlation effects, surfactant interactions with the surface and the solvent. Based on the analysis of the evolution of the individual components of the free energy in response to the changes in external parameters we were able to formulate a general model for structural rearrangements in surfactant layers revealing the major role of the normal to the surface interactions. We have shown that the balance of normal to the surface interactions between surfactant molecules, the surface and solution can be quantified by a single interaction parameter χ. In particular, negative values of χ correspond to prevailing surfactant/surface interactions and a hemicylindrical configuration of the surfactant layer, while positive χ correspond to a tilted monolayer configuration. For example, in a 2:1 electrolyte $\chi < 0$ and the surfactant layer remains in a hemicylindrical configuration at all confinements studied, while the change in the sign of χ induces the transition in the structure of surfactant layers in 1:1 and 2:2 electrolytes (**Figure 1**). This model provides a simple tool for choosing the optimum surfactant chemistry and solvent composition for controlled self-assembly of surfactant templates with the desired structure and stability. This model can be directly used to control the properties of surfactant templates for hierarchical self-assembly of functional materials.

Based on these results we will choose solvent composition and surfactant chemistry to form surfactant layers with hemicylindrical and tilted monolayer configurations on graphite substrate.

The performance of the novel software was tested against atomistic molecular dynamics[3] and Monte Carlo simulations[4] and experimental data for surfactants at surfaces[1] and for supported self-assembled monolayers.[5,6] Therefore, the software can be directly used for similar systems and further developed for modeling more complex three-dimensional self-assembly processes.

2. Simulations of templated growth of oxide nanoparticles.

Using the data on template stability we have investigated how do growing oxide nanoparticles influence the template structure. In particular we considered TiO_2 nanoparticles on CTAB/graphene templates in NaCl and $CaCl_2$. Using cDFT simulations we have shown that nanoparticles are confined in the gaps between surfactant hemicylindrical micelles until they reach critical size (**Figure 2**). Subsequent growth induces partial rearrangement of surfactant template to a monolayer configuration with the nanoparticles residing on top of the monolayer. In agreement with surfactant stability study, we have shown that in 1:1 electrolyte this transition occurs when TiO_2 nanoparticles exceed 2.0 nm in diameter, while in 2:1 electrolyte, which stabilizes the hemicylindrical configuration of the template, the critical size increase to 5.5 nm. These results demonstrate that nanoparticle growth mechanism can be controlled by surfactant templates and solvent composition. Indeed, nanoparticles grown confined between hemicylindrical micelles are expected to grow mainly via thermodynamic pathway, which produces very uniform nanoparticles. On the other hand, on the monolayer template nanoparticles are free to move and coalesce, which results in higher polydispersity in their sizes.

Recent Progress on Other Projects

Multiscale modeling of charge transport in nanocomposite energy storage materials

We have developed novel hierarchical hybrid multiscale simulation technique for modeling coupled ion and electron transport in nanostructured energy storage materials (**Figure 3**). The model uses multiphysics approach, in which instead of formal consecutive upscaling we introduce novel types of collective long-range interactions along with short-range effects of the finer scale models. The fine scale model take advantage of high accuracy embedded cluster quantum mechanical simulations of elementary charge transport as well as the state-of-the-art molecular dynamics free energy simulations of coupled ion and electron diffusion. The collective long-range electrostatic and excluded volume interactions are introduced on the mesoscale (10-300 nm) via classical Density Functional theory coupled with Poisson-Nernst-Planck formalism for dynamic effects. The mesoscopic free energy, which includes contribution from short-range activation dynamics of ions and electrons, derived in the atomistic models, is then used in a larger scale (microns) phase field model to simulate charge transport in a network of nano-sized grains. As a demonstration of the application of the model for elucidating the basic principles of charge transport in nanostructured energy materials, the fundamental physics of Li^+ and electron transport in nanostructured TiO_2 has been studied. We have shown that the conductivity in TiO_2 nanoparticles strongly

depends on the titania polymorph, the crystallographic direction for the conductivity and the nanoparticle size. These effects reflect the competition between constant ion and electron fluxes and redistribution of mobile charges towards nanoparticle boundaries to form the space-charge zone (**Figure 4**).[7,8] These results on charge transport in metal oxide nanoparticles and interfaces will guide the choice of experimental conditions for controlled self-assembly of nanocomposite materials with enhanced electric properties for energy storage applications.

Future Plans

More complex molecules, such as DNA and proteins, allow for much wider diversity of template structures compared to ionic surfactant architectures at surfaces. We will investigate self-assembly of DNA and peptide molecules on graphene surface to enhance the level of control over template architecture.

Another important question, that will be addressed using long time scale atomistic simulations and in-situ experiments, is the control over metal oxide nucleation and growth by template chemistry, structure and stability. We will systematically study the morphology and orientation of the growing oxide nanoparticles on simple surfactant templates with various functional groups and more complex biomolecular architectures to elucidate the mechanism for controlling the templated mineralization process.

To make the transition from two-dimensional organic/inorganic interfaces to a three-dimensional nanostructural material the existing models of the self-assembly process will be further developed. Based on these data and the data for structure/performance relation for nanostructural energy storage materials we will be able to develop synthesis pathways for new materials with significantly enhanced properties for energy applications.

References

(1) Sushko, M. L.; Liu, J. *J. Phys. Chem. B* **2010**, *114*, 3847-3854.
(2) Sushko, M. L.; Liu, J. *J. Phys. Chem. B* **2011**, *115*, 4322-4328.
(3) Srinivas, G.; Nielsen, S. O.; Moore, P. B.; Klein, M. L. *J. Am. Chem. Soc.* **2006**, *128*, 848-853.
(4) Cao, D. P.; Wu, J. Z. *Macromolecules* **2005**, *38*, 971-978.
(5) Sushko, M. L. *Faraday Discuss.* **2009**, *143*, 63-80.
(6) Sushko, M. L.; Harding, J. H.; Shluger, A. L.; McKendry, R. A.; Watari, M. *Adv. Mater.* **2008**, *20*, 3848-3853.
(7) Sushko, M. L.; Rosso, K. M.; Liu, J. *J. Phys. Chem. Lett.* **2010**, *1*, 1967-1972.
(8) Sushko, M. L.; Rosso, K. M.; Liu, J. *J. Phys. Chem. C* **2010**, *114*, 20277-20283.

DOE Sponsored Publications in 2010-2011 from Current Subtask

* *Surfactant Two-Dimensional Self-Assembly under Confinement.* ML Sushko, and J Liu. J. Phys. Chem. B **115** (2011) 4322.
* *Structural Rearrangements in Self-Assembled Surfactant Layers at Surfaces* ML. Sushko, and J Liu. J. Phys. Chem. B **114** (2010) 3847.
* *Mechanism of Li^+/Electron Conductivity in Rutile and Anatase TiO_2 Nanoparticles.* ML Sushko, KM Rosso, and J Liu. J. Phys. Chem. C **114** (2010) 20277.
* *Size Effects on Li^+/Electron Conductivity in TiO_2 Nanoparticles.* ML Sushko, KM Rosso, and J Liu. J. Phys. Chem. Lett. **1** (2010) 1967.

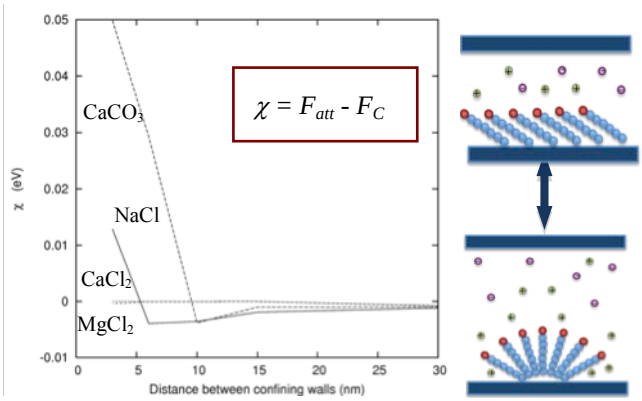

Figure 1. *Dependence of the interaction parameter χ on the distance between the confining walls for anionic surfactants in aqueous salt solutions. Parameter χ reflects the difference between the attraction free energy between surfactant segments and the wall (F_{att}) and electrostatic free energy between surfactant charged groups and ions in solution (F_C).*

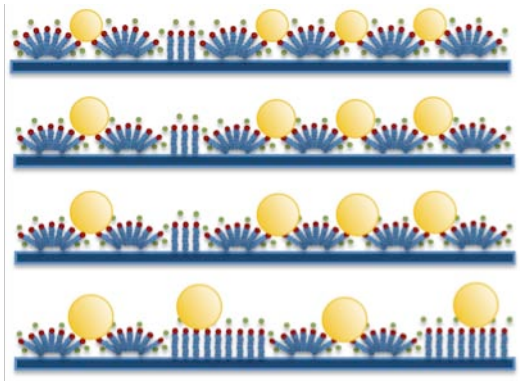

Figure 2. *Schematics of nanoparticle growth on surfactant templates.*

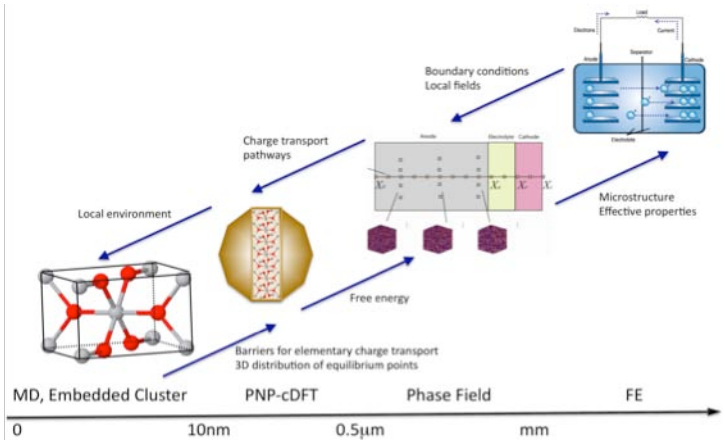

Figure 3. *Hierarchical multiscale model for charge transport in energy storage materials and devices.*

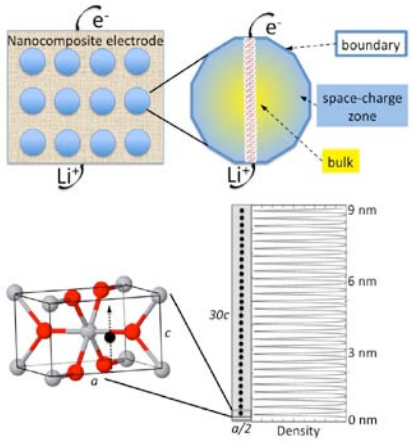

Figure 4. *Mesoscopic modeling of ion and electron transport in metal oxide nanoparticles.*

Molecularly Organized Nanostructural Materials

Subtask: Nanostructural Materials Synthesis and Guest Induced Structural Transformation

Praveen K. Thallapally, Jun Liu and Gregory J. Exarhos
jun.liu@pnnl.gov
Pacific Northwest National Laboratory, Richland, WA 99352.

Subtask Scope: Self-assembled nanostructured materials with controlled pore channels have great potential for energy storage, carbon capture and catalysis.[1-4] Fundamental understanding of the formation of such materials and the phase transitions induced by the chemical environments will provide important knowledge regarding the mechanistics of the self-assembly process and the driving force for the structural change.[4] The overall goal of this project is to investigate a combination of self-assembly and controlled nucleation and growth approaches for synthesizing nanostructured materials with controlled three-dimensional architectures and desired stable crystalline phases of metal organic frameworks.

Recent Progress on Nanostructured MOFs (nMOFs):

For the first time, we reported the shape selective (Hexagonally shaped nZIF-8) synthesis of well or mono dispersed nanoparticles of metal organic frameworks by simple mixing of zinc nitrate hexahydrate with 2-methyl imidazole at room temperature in the presence of methanol and 1 % high molecular weight poly(diallyldimethylammonium chloride) solution (average M_w 400,000-500,000) upon continuous stirring of the reaction mixture for 24 hrs. Figure 1 illustrates the TEM and SEM images of the hexagonally shaped nZIF-8 at different magnifications. Low magnification TEM and SEM images clearly demonstrate the formation of uniform nanoparticles with narrow size distribution. Absence of polymer results in the formation of non uniform agglomerates. Similarly, changing the polymer to polycationic electrolyte solutions such as a mixture of methanol and chitosan (1%), poly(ethyleneimine) PEI (1%), poly(allylamine hydrochloride) PAH and low molecular weight (poly(diallyldimethylammonium chloride) average M_w <100,000) and 2 % polyvinly pyrrolidine (PVP) did not result in the formation of hexagonally shaped nanoparticles. Therefore, the poly-diallyl-dimethyl-ammonium chloride has played a critical role in controlling the morphology of the nanoparticles during the reaction.

Recent Progress on Guest Induced Phase Transformations in Porous MOFs

Fluorinated Metal Organic Framework (FMOF-2)

Metal organic frameworks built with flexible ligands have shown to provide some intriguing properties such as breathing phenomena in other words large pore (*lp*) to narrow pore (*np*) transformation. Understanding what causes these materials to respond to external stimuli can have applications in the development of smart materials. We successfully synthesized and reported the breathing behavior when exposed to gases and solvent vapors in two flexible metal organic frameworks

(FMOF-2 and TetZB). In addition, we study the thermodynamics of FMOF-2 during gas sorption and the energetics involved during the phase transitions compared to hypothetical rigid FMOF-2 framework. In brief, FMOF-2 is built from the coordination of flexible V-shaped organic building block [2, 20-bis(4-carboxyphenyl)hexafluoropropane, **1**] and Zn_2 clusters to generate a 2-fold interpenetrated framework filled with coordinated DMF and ethanol molecules (Figure 2). When tested the activated FMOF-2 at higher pressures of CO_2, shows a step in the adsorption at approximately 15 bar (Figure 3). The same behavior was observed with SO_2, H_2S at 1 bar. The guest induced transformations in FMOF-2 were explained (Figure 3) based on the difference in free energy of the hypothetical phases involved in the transition.

Recent Progress on Other Projects

Flexible Metal Organic Framework (TetZB)

TetZB was obtained by heating a DMF solution containing tectonic acid, zinc nitrate hexahydrate, and bipyridine at 110°C resulted in a doubly interpenetrated PtS network topology. The pores are partially filled with 4,4 -bipyridine molecules connected to paddle-wheel SBUs of the framework while the remaining channels are filled with solvent DMF and water molecules. Once the sample was activated, the behaviour of **TetZB** during the adsorption of gases including CO_2, polar and non-polar solvents was tested using gas analyzer and *in-situ* PXRD. As seen from the variable-temperature PXRD, upon removing the solvent a slight change in the PXRD pattern was observed at lower angles (Figure 4). The original phase cannot be generated by simply returning to the original temperature; however when exposed to 200 psi of CO_2 at room temperature the sample was found to transform back to the original pattern suggesting the expansion of the framework due to the CO_2 inclusion (Figure 5). Pore expansion and contraction was not observed when bipyridine was replaced with pyrazine and dabco. Similar sorption experiments were carried out with shorter and longer alkyl chain hydrocarbons to understand the role of chain length.

Future Plans: Further studies will be focused on the role of surfactants on the formation of hexagonal shaped nanoparticles and the effect of polymer concentration in the process of nucleation and crystal growth will be investigated using state of the spectroscopic techniques and theory. Simialrly role of functional groups, secondary building blocks and metal centers played in pore expansion and contraction of metal organic frameworks will be investigated in greater detail. For example, by incorporating photo and electro responsive functional groups, can we able to control the porosity of the metal organic frameworks by applied light and potential will be investigated.

Refereneces:

(1) Liu, J.; Cao, G. Z.; Yang, Z. G.; Wang, D. H.; Dubois, D.; Zhou, X. D.; Graff, G. L.; Pederson, L. R.; Zhang, J. G. *Chemsuschem* **2008**, *1*, 676.

(2) Eddaoudi, M.; Kim, J.; Rosi, N.; Vodak, D.; Wachter, J.; O'Keeffe, M.; Yaghi, O. M. *Science* **2002**, *295*, 469.

(3) Thallapally, P. K.; McGrail, B. P.; Dalgarno, S. J.; Schaef, H. T.; Tian, J.; Atwood, J. L. *Nat Mater* **2008**, *7*, 146.

(4) Thallapally, P. K.; Tian, J.; Kishan, M. R.; Fernandez, C. A.; Dalgarno, S. J.; McGrail, P. B.; Warren, J. E.; Atwood, J. L. *J Am Chem Soc* **2008**, *130*, 16842.

DOE Sponsored Publications in 2010 - 2011 from current subtask

18 publications, 5 cover arts and 1 book chapter

- Thallapally, P. K.; Motkuri, R. K.; Nune, S. K.; Fernandez, C. A.; McGrail, B. P.; Atwood, J. L., Role of hydrocarbons in pore expansion and contraction of a flexible metal-organic framework. *Chem Commun* **2011,** *47* (25), 7077-7079;
- Thallapally, P. K.; Tian, J. A.; Liu, J.; Exarhos, G. J.; Atwood, J. L. *Chem Commun* **2011**, *47*, 701.
- Thallapally, P. K.; Tian, J.; Ma, S. Q.; Fowler, D.; McGrail, B. P.; Atwood, J. L. *Chem Commun* **2011**, *47*, 7626
- Thallapally, P. K.; Nune, S. K.; Dohnalkova, A.; Wang, C. M.; Liu, J.; Exarhos, G. J., Synthesis and properties of nano zeolitic imidazolate frameworks. *Chem Commun* **2010,** *46* (27), 4878-4880.
- Thallapally, P. K.; Fernandez, C. A.; Nune, S. K.; Motkuri, R. K.; Wang, C. M.; Liu, J.; Exarhos, G. J.; McGrail, B. P., Synthesis, Characterization, and Application of Metal Organic Framework Nanostructures. *Langmuir* **2010,** *26* (24), 18591-18594;
- Thallapally, P. K.; Fernandez, C. A.; Motkuri, R. K.; Nune, S. K.; Sumrak, J. C.; Tian, J.; Liu, J., Gas-Induced Expansion and Contraction of a Fluorinated Metal-Organic Framework. *Cryst Growth Des* **2010,** *10* (3), 1037-1039;
- Thallapally, P. K.; Kishan, M. R.; Tian, J. A.; Fernandez, C. A.; Dalgarno, S. J.; Warren, J. E.; McGrail, B. P.; Atwood, J. L.; Teat, S. J. *Chem Commun* **2010**, *46*, 9259.
- Thallapally, P. K.; Fernandez, C. A.; Motkuri, R. K.; Nune, S. K.; Liu, J.; Peden, C. H. F. *Dalton T* **2010**, *39*, 1692.
- Thallapally, P. K.; Nune, S. K.; McGrail, B. P. *J Mater Chem* **2010**, *20*, 7623.

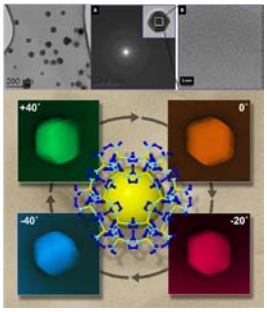

Figure 1. From molecular self-assembly to controlled nanocrystals

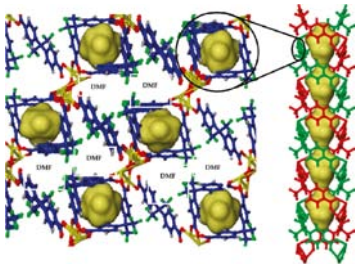

Figure 2. Two-fold interpenetrated molecular box with helical channels.

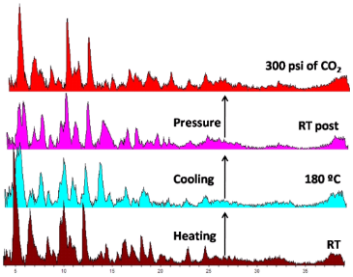

Figure 3. *In-situ* PXRD of TetZB at high temperature and pressure.

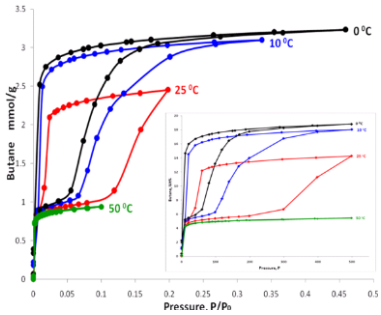

Figure 4. Pore Expansion and contraction up on gas pressure.

Atomic layer Controlled Growth of Ferro Pnictide Thin Films

Chang-Beom Eom
eom@engr.wisc.edu
Department of Materials Science and Engineering
University of Wisconsin-Madison, Madison, WI 53706

Program Scope

The discovery of superconductivity with transition temperatures of 20K-50K in iron-based materials has initiated a flurry of activity to understand and apply these novel materials. The superconducting mechanism, structural transitions, magnetic behavior above and below T_c, doping dependence, and critical current and flux-pinning behavior have all been recognized as critical to progress toward understanding the pnictides. A fundamental key to both basic understanding and applications is the growth and control of high-quality epitaxial thin films and multilayer heterostructures. The ability to control the orientation, the strain state, defect and pinning site incorporation, the surface and interfaces, and potentially the layering at the atomic scale, are crucial in the study and manipulation of superconducting properties. Our main tasks are to control pnictide thin film and oxide templates at the atomic level, to understand the relation between structure and superconducting properties, and to design and grow novel crystalline pnictide heterostructures tuned to take advantage of the superconducting structure/property relationships possible in this unique new superconductor.

Recent Progress

We have developed a novel template engineering making use of single-crystal intermediate layers of (001) $SrTiO_3$ and $BaTiO_3$ grown on various perovskite substrates to enable for the first time genuinely epitaxial films of Co-doped $BaFe_2As_2$ with high transition temperature (T_c, ρ =0 of 21.5K), small transition widths (ΔT_c = 1.3K), superior J_c of 4.5 MA/cm^2 (4.2K) and strong *c*-axis flux pinning [1]. Prior to this advance, high-quality epitaxial pnictide thin films had been difficult to produce. Alkaline earth (AE) 122 phases have been grown directly on (001) oriented (La,Sr)(Al,Ta)O_3 (LSAT) and $LaAlO_3$ (LAO) single-crystal substrates by us and other groups [2,3]. However, the quality of the films reported had not been satisfactory ($T_{c,\rho=0}$ and ΔT_c are 14~17K and 2~4K, respectively, values which are much lower and broader than those of bulk single crystals [2]). Furthermore, the 5K self-field J_c of these films is only ~10kA/cm^2, one to two orders of magnitude lower than in bulk single crystals [2]. Films typically had a poorly connected superconducting phase whose grains are separated by high-angle grain boundaries, wetting GB phases such as FeAs, and/or off-stoichiometric grains [3].

We believed that the low quality of many films was due to not appreciating a fundamental growth issue – that the 112 pnictide is a metallic system that does not bond well with oxide substrates. Our technique, developed through extensive experimentation, implements thin epitaxial template layers with divalent cations, such as $SrTiO_3$ or $BaTiO_3$, that promote interfacial matching with the metallic Ba-122 system. This has opened new avenues for epitaxial growth of ferropnictides, as well as providing a framework for heteroeptiaxial growth of other intermetallic compounds by matching interfacial layers between templates and thin film overlayers.

Figure 1 shows the azimuthal ϕ scans of films on bare LSAT and 100 unit cell thick STO template LSAT substrate. The orientational epitaxy is dramatically improved by templating. The

high crystalline quality of our templated films is indicated by the 004 reflection rocking curve of the film on STO/LSAT - it is as narrow as 0.55^{o}, which is the narrowest ever reported for 122 thin films. Remarkably, the FWHM of the film on BTO/LSAT is as narrow as 0.17° similar to that of a Ba-122 bulk single crystal. Figure 2 shows a high-resolution TEM image of Co-doped Ba-122 grown on a 20 u.c. STO template layer on an LSAT substrate. Although there is some localized atomic disorder at the STO/Ba-122 interface, perhaps due either to interface reaction or to the ion beam damage during TEM sample preparation, the high-quality of the Ba-122 layer is evident.

These films show high $T_{c,\rho=0}$ and narrow ΔT_c. In particular, $T_{c,\rho=0}$ of the film on 100 u.c. STO/LSAT is as high as 21.5K and ΔT_c is as narrow as 1.3K, which are the highest and narrowest values ever reported for 122 thin films. The templated films showed high J_c, over 1 MA/cm^2 (4.2K, SF), which are the highest values ever reported for 122 thin films. Remarkably, the J_c of the film on BTO/LSAT is as high as ~4.5 MA/cm^2. Furthermore, the J_c of the templated films have only have a weak field dependence, indicative of little or no suppression of the J_c by strong fields as indicated by the STO/LSAT film which had J_c = ~0.4 MA/cm^2 even at 14 T (see Figure 3).

Our advance in pnictide single-crystal film growth for the first time allows the design and control of pnictide superconducting films and heterostructures to probe the fundamental superconducting mechanisms of this unique class of materials. We believe that the templating technique will lead to growth of films and superlattices that have up to now not been possible.

Future Plan

Our main tasks are to control pnictide thin film and oxide templates at the atomic level, to understand the relation between structure and superconducting properties, and to design and grow novel crystalline pnictide multilayered heterostructures tuned to take advantage of the superconducting structure/property relationships possible in this unique new superconductor. We will use thin-film crystal growth techniques with template interfacial engineering as our means to accomplish these goals.

We are guided to these goals by our understanding developed over the last year in relating pnictide structural and superconducting properties. The new film growth methods we developed enables us to not only resolve these uncertainties, but also to design and synthesize new pnictide atomic layered structures that explore the limits of this material's superconducting properties. We plan to grow artificial layered superlattice of ferro-pnictide on oxide templates by pulsed laser deposition to investigate fundamental superconducting properties of pnictides including flux pinning, proximity effect and dimensional crossover. We also plan to study the grain boundary properties of doped ferronictide thin films on bicrystal substrates.

References

1. S. Lee, J. Jiang, C. T. Nelson, C. W. Bark, J. D. Weiss, C. Tarantini, H. W. Jang, C. M. Folkman, S. H. Baek, A. Polyanskii, D. Abraimov, A. Yamamoto, Y. Zhang, X. Q. Pan, E. E. Hellstrom, D. C. Larbalestier, C. B. Eom, *Nature Materials,* **9**, 397 (2010)
2. X. F Wang, T Wu, G Wu, H Chen, Y. L Xie, J. J Ying, Y. J Yan, R. H Liu, X. H Chen, Phys. Rev. Lett. **102,** 117005 (2009).
3. F. Kametani, P. Li, D. Abraimov, A. A. Polyanskii, A. Yamamoto, J. Jiang, E. E. Hellstrom, A. Gurevich, D. C. Larbalestier, Z. A. Ren, J. Yang, X. L. Dong, W. Lu, and Z. X. Zhao, Appl. Phys. Lett. 95, 142502 (2009)

DOE Sponsored Publications in 2009-2011 from Current Grant

1. "Coexistence of superconductivity and ferromagnetism at the interface between $LaAlO_3$ and $SrTiO_3$" D.A. Dikin, M. Mehta, C.W. Bark, C.M. Folkman, C.B. Eom and V. Chandrasekhar, *Phys. Rev. Lett.*, **107**, 056802 (2011)
2. "Superfluid density measurements of $Ba(Co_xFe_{1-x})_2As_2$ films near optimal doping" Jie Yong, S. Lee, J. Jiang, C. W. Bark, J. D. Weiss, E. E. Hellstrom, D. C. Larbalestier, C. B. Eom, and T. R. Lemberger, *Phys. Rev. B,* **83**, 104510 (2011)
3. "Dependence of epitaxial $Ba(Fe_{1-x}Co_x)_2As_2$ thin films properties on $SrTiO_3$ template thickness", S. Lee, J. Jiang, J. D. Weiss, C. W. Bark, C. Tarantini, M. D. Biegalski, A. Polyanskii, Y. Zhang, C. T. Nelson, X.Q. Pan, E. E. Hellstrom, D. C. Larbalestier, and C. B. Eom, *IEEE Trans on Applied Superconductivity,* **21**, 2882 (2011)
4. "Self-Assembled Oxide Nanopillars in Epitaxial Co-doped $BaFe_2As_2$ Thin Films for Vortex Pinning" Yi Zhang, Christopher T. Nelson, Sanghan Lee, Jianyi Jiang, Chung Wung Bark, Jeremy Weiss, Chiara Tarantini, Chad M. Folkman, Seung-Hyub Baek, Eric E. Hellstrom, David C. Larbalestier, Chang-Beom Eom, Xiaoqing Pan, *Appl. Phys. Letts.*, **98**, 042509 (2011)
5. "Pair-breaking effects and coherence peak in the terahertz conductivity of superconducting $BaFe_{2-2x}Co_2xAs_2$ thin films", R. Vald´es Aguilar, L.S. Bilbro, S. Lee, C.W. Bark, J. Jiang, J.D. Weiss, E.E. Hellstrom, D.C. Larbalestier, C.B. Eom, and N. P. Armitage, *Phys. Rev. B. Rapid Communications*, **82**,180514 (2010)
6. "Phase-Incoherent Superconducting Pairs in the Normal State of $Ba(Fe_{1-x}Co_x)_2As$" G. Sheet, M. Mehta, D. A. Dikin, S. Lee, C.W. Bark, J. Jiang, J. D. Weiss, E. E. Hellstrom, M.S. Rzchowski, C.B. Eom and V. Chandrasekhar, *Phys. Rev. Lett.,* **105**, 167003 (2010)
7. **"**Conductance asymmetry in point-contacts on epitaxial thin films of $Ba(Fe_{0.92}Co_{0.08})_2As_2$" Mehta, G. Sheet, D. A. Dikin, S. Lee, C.W. Bark, J. Jiang, J. D. Weiss, E. E. Hellstrom, M. S. Rzchowski, C.B. Eom and V. Chandrasekhar, *Appl. Phys. Lett.* **97**, 012503 (2010)
8. "Multi-gap superconductivity in a $BaFe_{1.84}Co_{0.16}As_2$ film from optical measurements at terahertz frequencies" A. Perucchi, L. Baldassarre, C. Marini, S. Lupi, J. Jiang, M. Putti, I. Pallecchi, J.D. Weiss, E. E. Hellstrom, S. Lee, C.W. Bark, C. B. Eom, and P. Dore, *Eur. Phys. J.,* B **77**, 25 (2010)
9. "Template Engineering of Co-doped $BaFe_2As_2$ single-crystal thin films" S. Lee, J. Jiang, C. T. Nelson, C. W. Bark, J. D. Weiss, C. Tarantini, H. W. Jang, C. M. Folkman, S. H. Baek, A. Polyanskii, D. Abraimov, A. Yamamoto, Y. Zhang, X. Q. Pan, E. E. Hellstrom, D. C. Larbalestier, C. B. Eom, *Nature Materials,* **9**, 397 (2010)
10. "Strong vortex pinning in Co-doped BaFe2As2 single crystal thin films" A rewritable nanoscale oxide photodetector" C. Tarantini, S. Lee, Y. Zhang, J. Jiang, C. W. Bark, J. D. Weiss, C. T. Nelson, H. W. Jang, C. M. Folkman, S. H. Baek, J.W. Park, X. Q. Pan, A. Gurevich, E. E. Hellstrom, C. B. Eom, D. C. Larbalestier, *Appl. Phys. Lett.* **96**, 142510, (2010)
11. "New Fe-based superconductors: properties relevant for applications", M. Putti, I. Pallecchi, E. Bellingeri, M.Tropeano, C. Ferdeghini, A. Palenzona, C. Tarantini, A. Yamamoto, J. Jiang, J. Jaroszynski , F. Kametani, D. Abraimov, A. Polyanskii, J.D. Weiss, E.E. Hellstrom, A. Gurevich, D.C. Larbalestier, R. Jin, B.C. Sales, S.A. Sefat,

M.A. McGuire, D. Mandrus, P. Cheng, Y. Jia, H.H. Wen, S. Lee, C.B. Eom, SUST, 23, 034003 (2010)
12. "Impact of substitutional and interstitial carbon defects on lattice parameters in MgB_2" Amelia K. Bengtson , Chung Wung Bark , Jonathan Giencke , Wenqing Dai , Xiaoxing Xi, Chang-Beom Eom, accepted for publication in *J. Appl. Phys.* **107**, 023902 (2010)
13. "Weak link behavior of grain boundaries in Co-doped $BaFe_2As_2$ pnictide superconductors", S. Lee, J. Jiang, J. Weiss, C.M Folkman, C.W. Bark, C. Tarantini, A Xu, D. Abraimov, A. Polyanskii, C. T. Nelson, Y. Zhang, S.H. Baek, H.W. Jang, A. Yamamoto, F, Kametani, X. Pan, E. Hellstrom, A. Gurevich, C. B. Eom, D. C. Larbalestier, *Appl. Phys. Lett.*, **95**, 212505 (2009)

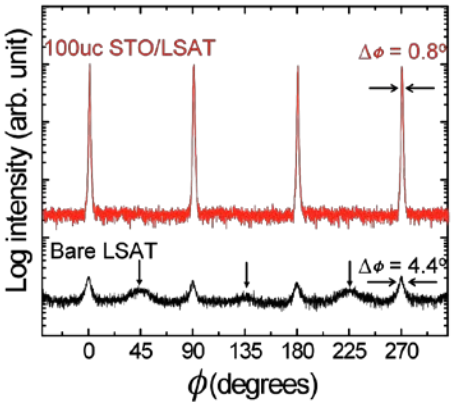

Figure 1. Azimuthal ϕ scan and $\Delta\phi$ of the off-axis 112 reflection of Ba-122 on STO templated LSAT compared to bare LSAT substrate

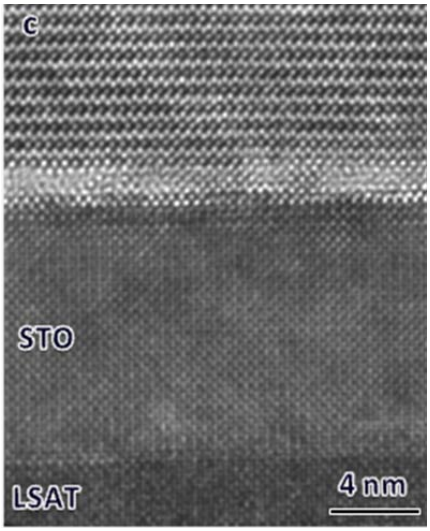

Figure 2 High-resolution TEM of Ba-122 grown on a 20uc STO template layer on an LSAT substrate.

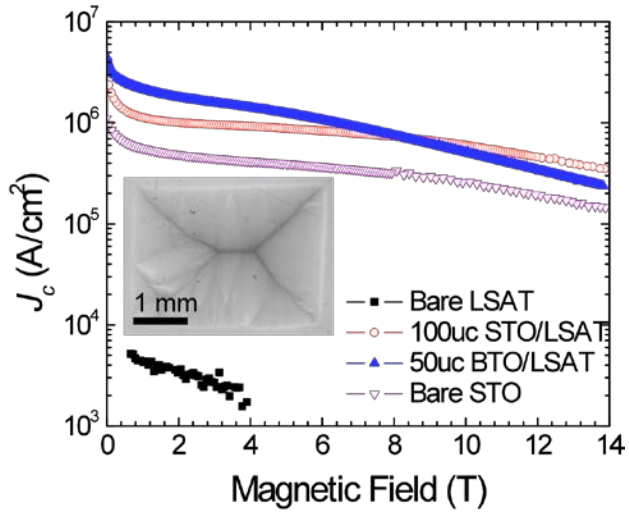

Figure 3: Field-dependent critical current density for Ba-122 films grown on various template layers and substrates.

Session 4

Large Scale Assembly

Session Chair: Michael Aziz, Harvard University

This page is intentionally blank.

III-Nitride Nanowires: From the Bottom-Up to the Top-Down

George T. Wang
gtwang@sandia.gov
Advanced Materials Sciences Department
Sandia National Laboratories, Albuquerque, NM 87185

1D nanostructures, such as nanowires and nanorods, based on the III nitride (AlGaInN) materials system have attracted attention as potential nanoscale building blocks in LEDs, lasers, sensors, photovoltaics, and high power and high speed electronics. Compared to planar films, III-nitride semiconductor nanowires have several potential advantages including higher crystalline quality and reduced strain, which enables growth on arbitrary substrates as well as allowing for a greater range of alloy compositions and hence energies to be achieved. However, before their promise can be fully realized, several challenges must be addressed in the areas of 1) controlled nanowire synthesis; 2) understanding and controlling the nanowire structural, electrical, thermal, and optical properties; and 3) nanowire device integration. Our work seeks to address these areas to lay the scientific and technological foundation for nanowire-based lighting and other energy-related applications.

III-nitride nanowires can be fabricated by a variety of techniques, including "bottom-up" approaches and "top-down" lithographic approaches. Bottom-up techniques have been the dominant method and typically involve a nanoscale metal catalyst particle to direct the 1D growth or anisotropic growth conditions. Advantages of using this approach include nanowires free of detrimental crystal defects known as dislocations, and the ability to grow on inexpensive, lattice mismatched substrates, including glass and metal foil, which we have demonstrated in our lab. I will discuss recent results involving the aligned, bottom-up growth[1] of Ni-catalyzed GaN and III-nitride core-shell nanowires, along with extensive results providing insights into the nanowire properties obtained using cutting-edge structural, electrical (Fig. 1b), and optical nanocharacterization techniques. Some topics I will cover include: *in-situ* TEM studies of nanowire electrical breakdown and nanomechanics[2,3], spatially-resolved cathodoluminescence studies of band-edge and defect luminescence in NWs[4]; and strain-related spatial variation of In incorporation in InGaN shells (Fig. 1a)[5]. I will also discuss the development of an inexpensive, lithography-free technique employing nanowire templates for the growth of high-quality GaN[6], which could enable more efficient and longer-lifetime visible LEDs.

Bottom-up nanowire growth methods do however have the disadvantage of requiring highly specific growth conditions to increase the on-axis growth rate while minimizing lateral growth, which can lead to non-optimal material quality and less flexibility in material design, such as doping and heterostructures. I will describe a new "top-down" approach for fabricating ordered arrays of high quality GaN-based nanorods with controllable height, pitch and diameter (Fig. 1c). This top-down method allows fabrication of nanorods from high quality, arbitrarily doped films grown by metal-organic chemical vapor deposition using standard, optimized conditions. The fabrication, structure, optical properties, lasing characteristics, and device performance of the nanorods and nanorod LEDs will be discussed.

Sandia National Laboratories is a multi-program laboratory managed and operated by Sandia Corporation, a wholly owned subsidiary of Lockheed Martin Corporation, for the U.S. Department of Energy's National Nuclear Security Administration under contract DE-AC04-94AL85000.

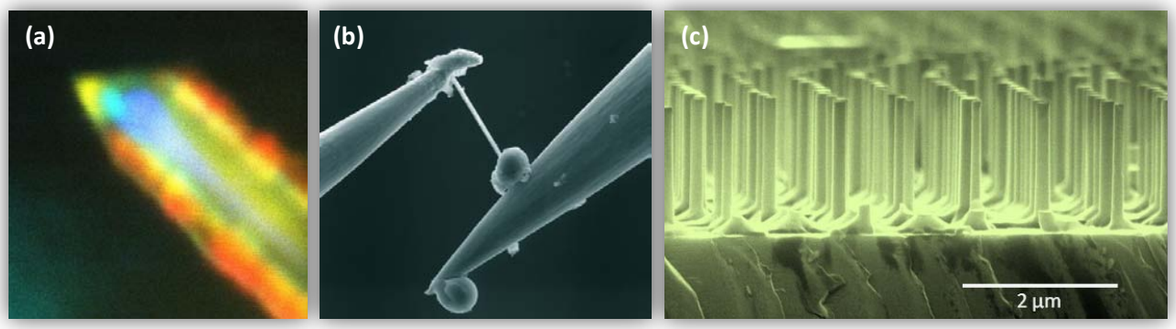

Figure 1. (a) Composite CL image showing multicolor emission from a triangular GaN/InGaN core-shell nanowire; (b) *in-situ* SEM GaN nanowire diode measurement using Ga droplet to form an Ohmic contact; (c) periodic array of GaN nanorods formed by two-step top-down etching process.

References

1. G.T. Wang, A.A. Talin, D.J. Werder, J.R. Creighton, E. Lai, R.J. Anderson, and I. Arslan, *Nanotechnology* **17** (23), 5773 (2006).
2. J.Y. Huang, H. Zheng, S.X. Mao, Q.M. Li, and G.T. Wang, *Nano Lett.* **11** (4), 1618 (2011).
3. T. Westover, R. Jones, J.Y. Huang, G. Wang, E. Lai, and A.A. Talin, *Nano Lett.* **9** (1), 257 (2009).
4. Q.M. Li and G.T. Wang, *Nano Lett.* **10** (5), 1554 (2010).
5. Q.M. Li and G.T. Wang, *Appl. Phys. Lett.* **97** (18), 181107 (2010).
6. Q. Li, Y. Lin, J.R. Creighton, J.J. Figiel, and G.T. Wang, *Adv. Mater.* **21** (23), 2416 (2009).

DOE BES Sponsored Publications (Last 2 years)

[1] B.M. Wong, F. Leonard, Q. Li, G.T. Wang, "Nanoscale Effects on Heterojunction Electron Gases in GaN/AlGaN Core/Shell Nanowires" *Nano Lett,* dx.doi.org/10.1021/nl200981 (2011)

[2] J. Y. Huang, H. Zheng, S. X. Mao, Q. Li, and G. T. Wang, "In Situ Nanomechanics of GaN Nanowires," *Nano Lett.*, **11(4)**, 1618, **2011**. http://pubs.acs.org/doi/pdfplus/10.1021/nl200002x

[3] L. Baird, Cp. P. Ong, R. A. Cole, N. M. Haegel, A. A. Talin, Q. Li, G. T. Wang, "Transport imaging for contact-free measurements of minority carrier diffusion in GaN, GaN/AlGaN, and GaN/InGaN core-shell nanowires," *Appl. Phys. Lett.*, **98**, 132104, **2011**. http://apl.aip.org/resource/1/applab/v98/i13/p132104_s1

[4] Q. M. Li, G. T. Wang, "Strain influenced indium composition distribution in GaN/InGaN core-shell nanowires", *Appl. Phys. Lett.*, ***97***, 181107, **2010**. http://apl.aip.org/resource/1/applab/v97/i18/p181107_s1

[5] G. T. Wang, "III-Nitride Semiconductor Nanowires – Novel Materials for Optoelectronic & Energy Applications", *A to Z of Nanotechnology - Nanotechnology Thought Leaders Series*, **2010**. http://www.azonano.com/details.asp?ArticleId=2655

[6] A. Armstrong, Q. Li, Y. Lin, A. A. Talin, G. T. Wang, "GaN nanowire surface state observed using deep level optical spectroscopy", *Appl. Phys. Lett.*, ***96***, **2010**. http://apl.aip.org/resource/1/applab/v96/i16/p163106_s1

[7] Q. M. Li, G. T. Wang, "Spatial Distribution of Defect Luminescence in GaN Nanowires", *Nano Lett.*, ***10***, 1554 **2010**. http://pubs.acs.org/doi/abs/10.1021/nl903517t

[8] P. C. Upadhya, Q. M. Li, G. T. Wang, A. J. Fischer, A. J. Taylor, R. P. Prasankumar, "The influence of defect states on non-equilibrium carrier dynamics in GaN nanowires", *Semicon. Sci. Tech.*, ***25***, **2010**. http://iopscience.iop.org/0268-1242/25/2/024017/

[9] A. Armstrong, Q. Li, K. H. A. Bogart, Y. Lin, G. T. Wang, "Deep level optical spectroscopy of GaN nanorods", *J. Appl. Phys.*, ***106***, 053712 **2009**. http://jap.aip.org/resource/1/japiau/v106/i5/p053712_s1

[10] Q. Li, Y. Lin, J. R. Creighton, J. J. Figiel, G. T. Wang, "Nanowire-templated lateral epitaxial growth of low-dislocation density nonpolar a-plane GaN on r-plane sapphire", *Adv. Mat.*, ***21***, 2416 **2009**.

Design and Synthesis of Nanomaterials

Jason D. Fowlkes, Miguel Fuentes-Cabrera, Anatoli V. Melechko, Philip D. Rack, G. Malcolm Stocks, and Michael L. Simpson
fowlkesjd@ornl.gov
Oak Ridge National Laboratory, Oak Ridge, TN

Program Scope: The synthesis and assembly of functional nanomaterials with unique properties is critical for realizing many of the overarching goals of nanoscience and nanotechnology. Due to increasing complexity, the future of nanomaterials synthesis will likely require the confluence of both top-down and bottom up self-assembly techniques. The objective of this program is to perform basic research that provides a new level of understanding of the mechanisms that control the organization of nanostructured materials. The approach is to understand and elucidate intrinsic material properties that govern the assembly dynamics and determine extrinsic parameters that can influence and guide the assembly pathways for improved control. The primary focus of the program is the self and directed assembly of elemental and multi-component nanoparticles on surfaces by the destabilization of spatially defined, thin solid films. Thin solid films inherently contain stored energy which can be exploited for the self- and directed-assembly of organized nanoparticle ensembles via dewetting/destabilization enabled by plasma, pulsed laser heating or annealing. We are currently investigating how the initial thin film size, geometry, substrate and dimensionality, as well as thermodynamic properties, affect the evolution of the solid/liquid phase instabilities and nucleation events that ultimately dictate materials assembly. A fundamental understanding of the underlying instabilities and assembly dynamics taking place during thin-film destabilization is evolving making it possible to direct the assembly of metal alloy nanoparticles with designed composition, morphology, orientation and spatial arrangement.

Recent Progress:

The Directed Assembly of Linear Nanoparticle Arrays by engaging and harnessing the Liquid Phase, Rayleigh–Plateau Instability

Materials assembly predicated on easily defined initial conditions constitutes a groundbreaking demonstration of advanced materials synthesis. We have demonstrated a materials assembly method, based on nanoscale synthesis, where a simple input geometry (a metal thin film strip) was designed to produce a more complex output (a precise, linear array of nanoparticles) by making use of a naturally occurring instability, present in cylindrical fluid rivulets. Specifically, pulsed laser induced dewetting (PLiD) was used to transform thin metal strips (figure 1a), with and without sinusoidal perturbations imposed on the boundaries into linear nanoparticle arrays by directing the natural evolution of a Rayleigh–Plateau (RP) liquid instability modified by the solid substrate–liquid thin film strip interaction.

Materials assembly took place in the liquid phase. Capillary forces drove the assembly through the large surface–to–volume ratio present in the thin film strip that transforms into a substrate supported fluid jet, or rivulet. Unstable surface oscillations grew exponentially on the rivulet surface ultimately forming droplets at the positions of maximum amplitude (figure 1b). For the case of a straight edged thin film strip, nanoparticle arrays formed according to the (RP) liquid instability, yet nanoparticle diameter and pitch were poorly controlled and disperse (figure 1c). However, by patterning a nanoscale sinusoid onto the original strip edge, a precise nanoparticle diameter and pitch emerged superseding the naturally evolving RP instability (figure 1d).

Such a coupled chain of assembly events required both an experimental and computation thrust. A simulation considering both hydrodynamic transport and evolving instabilities proved crucial to interpret and unravel experimental results. Linear stability analysis provided a modified Rayleigh–Plateau model considering the substrate interaction with the liquid rivulet and nonlinear hydrodynamic simulations reproduced the nanoscale spatial/temporal features observed in the assembly process.

Simulations of Nanoparticle Formation revealed the Crossover between Substrate and Liquid Dictated Assembly

In order to successfully achieve "directed" assembly requires characterizing the various instabilities and dynamical processes that intersect/propagate over the time scale of interest. For the pulsed laser induced self- and directed-assembly, *nanosecond timescales are relevant*. The thin film instability, caused by nucleation or the so–called spinodal dewetting, which is driven by the repulsion between the liquid–vapor and solid–liquid interfaces, becomes significant at the nanosecond time scale for ultra (<10nm) thin films.

Experimental, computational and theoretical studies during the PLiD of lithographically patterned thin film annuli (Cu on Si/SiO_2) revealed a smooth transition in nanoparticle morphology dependent on the initial pattern geometry. The transition was attributed to the thin film instability in cases where both the starting film thickness (h) is small (< 13nm) and the initial height–to–width ratio of the annuli is relatively small (< 0.05). The disjoining pressure $\Pi(h)$ described the net repulsive force between interfaces in the study and hinged critically on the determination of the Hamaker constant (A). Significantly, the Hamaker constant derived from real experiments, when included in non–linear hydrodynamic simulations, predicted final nanoparticle morphologies and the transition from a RP instability to a thin film instability driven assembly. In addition, this work demonstrated the impact that the coupling between hydrodynamic transport and competing instabilities have on the final morphology: account must be made for liquid phase transport during directed assembly which effectively "blurs" the morphology transition from abrupt to smooth (figure 2). This work provided more validation of the disjoining pressure treatment of the thin film instability than unraveling its true nature. Thus, we have also explored molecular dynamics (MD) treatments of dewetting to further explore these critical interface interactions. MD simulations have been found to reproduce various experimental observations during dewetting including dewetting retraction velocities, substrate ejection velocities in the event of large capillary energies and extreme patterning conditions (*such a sharp vertices in lithographically patterned thin film features*).

Molecular Dynamics Investigations of Thin Film Dewetting

MD simulations utilizing a Lennard–Jones (LJ) interface potential were effectively used to study various wetting regimes on nanoscale Cu features supported on a graphite substrate. It was found that the dewetting velocity and the equilibrium contact angle, during and after dewetting, respectively, increase with a decrease in the Cu–C potential. Inertial and capillary forces were found to dictate the retraction velocity. Wetting angle determination via MD simulations facilitates the aforementioned nonlinear hydrodynamic, continuum model which describes instability and transport behavior. In addition, MD has proved an ideal platform to understand the competition between thin film edge retraction and instability propagation; initial results have suggested the ability to shift an RP-like instability to longer wavelengths, and ultimately nanoparticle spacing, by controlling the retraction velocity for pseudo 1D thin film strips.

Future Plans: Directed assembly via the Rayleigh–Plateau instability will be further explored to create more ordered and/or complex patterns. *Multiple* synthetic oscillations superimposed along the thin film strip edges will be investigated to modulate pitch and nanoparticle size within a single film strip, i.e., parallel materials assembly. Recently, it was shown that *stable* oscillations promote the decay of imposed edge perturbations on thin films strips. This result implies that, during a brief time window, it may be possible to produce nanoparticle arrays separated by pseudo–1D wires which would also constitute a significant step towards relevant parallel assembly. An intriguing question that has naturally resulted from this research work is, "what is the smallest perturbation that can be applied to a thin film strip to precisely direct assembly?" Toward answering this question it has been found that edge imposed sinusoids with an amplitude as small as 20nm leads to directed assembly. In the future, the extent of the imposed waveform will be reduced further to determine the minimum amount of energy required to direct assembly.

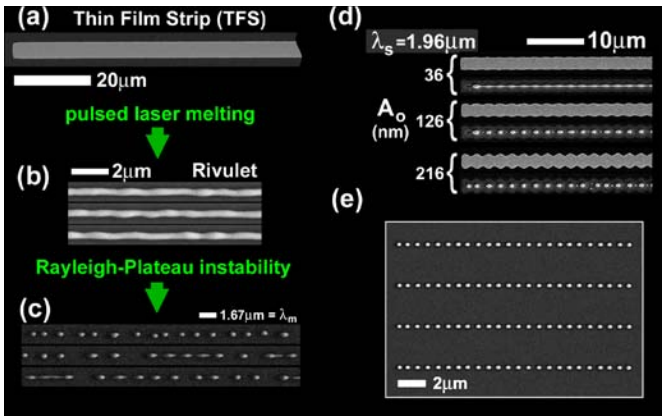

Figure 1 (a) The initial thin film strip. (b) The rivulet morphology forms in response to KrF 248nm pulsed (18ns) laser induced melting (~300 mJ/cm^2). Multiple rivulets are shown to indicate the various surface waves that propagate on the rivulet. (c) Unstable surface oscillations, according to the Rayleigh–Plateau (RP) theory, propagate on the rivulet surface ultimately breaking the rivulet up into droplets. The droplets resolidify as nanoparticles. (d) Directed assembly is achieved by defining RP predicted unstable, sinusoidal oscillations, of amplitude (A_o), along the thin film strip edges. Larger amplitudes lead to more rapid nanoparticle evolution. (e) A precisely defined nanoparticle array produced by the directed assembly approach.

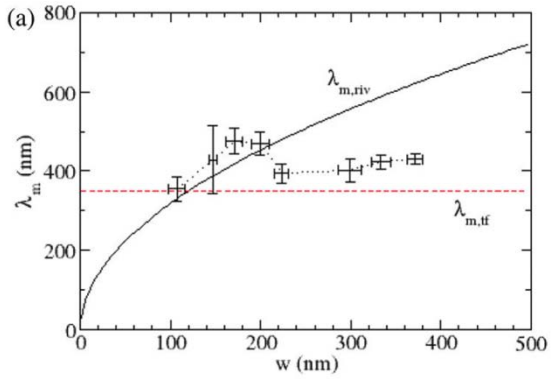

Figure 2 Nanoparticle spacing versus the width of the initial thin film annuli. Each thin film annuli consisted of 13nm thick Cu supported on a Si wafer substrate with an annuli radius of >5μm. Superimposed are the characteristic length scales for the Rayleigh-Plateau instability ($\lambda_{m,riv}$) and the thin film instability ($\lambda_{m,tf}$). The nanoparticle spacing seems to correlate with the RP length scale for widths < 200nm and correlates with the thin film instability at widths >200nm.

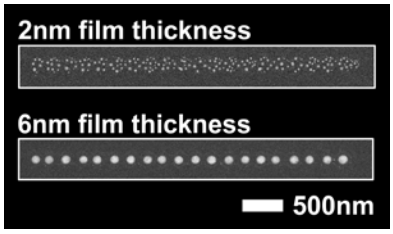

Figure 3 Dewetted Ni strips supported on a SiO_2 substrate. An unstable wavelength of 200nm was patterned along the thin films strip edge which, according to the Rayleigh-Plateau theory, should lead to the formation of droplets. However, for a film thickness of ~2nm, the thin film instability time scale is less than the RP time scale. As a result, the thin film instability

dictates break-up leading to a quasi–2D pattern which has no correlation with the original edge sinusoid. However, at a Ni thickness of ~6nm the RP time scale is relatively shorter and leads the formation of a well–defined nanoparticle array.

Publications (2009-2011)

1. M. Fuentes-Cabrera, B. H. Rhodes, M. I. Baskes, H. Terrones, J. D. Fowlkes, M. L. Simpson, P. D. Rack, "Controlling the velocity of jumping nanodroplets via their initial shape and temperature", *ACS Nano (accepted for publication)*
2. J. D. Fowlkes, L. Kondic, J. Diez, Y. Wu and P. D. Rack, "Self–Assembly versus Directed Assembly of Nanoparticles via Pulsed Laser Induced Dewetting of Patterned Metal Films", *Nano Letters* 11, 2478 (2011)
3. M. Fuentes–Cabrera, B. H. Rhodes, J. D. Fowlkes, A. Lopez–Benzanilla, H. Terrones, M. L. Simpson and P. D. Rack, "Molecular dynamics study of the dewetting of copper on graphite and graphene: Implications for nanoscale self – assembly", *Physical Review E* 83, 041603 (2011)
4. A. V. Melechk, R. C. Pearce, D. K. Hensley, M. L. Simpson T. E. McKnight, "Challenges in process integration of catalytic DC plasma synthesis of vertically aligned carbon nanofibres", *Journal of Physics D-Applied Physics* 44, 174008 (2011)
5. Y. Wu, J. D. Fowlkes and P. D. Rack, "The optical properties of Cu–Ni nanoparticles produced via pulsed laser dewetting of ultrathin films: The effect of nanoparticle size and composition on the Plasmon response", *Journal of Materials Research* 26, 277 (2011)
6. M. F. Sarac, R. M. Wilson, A. C. Johnston-Peck, J. Wang, R. Pearce, K. L. Klein, A. V. Melechko, J. B. Tracy, "Effects of Ligand Monolayers on Catalytic Nickel Nanoparticles for Synthsizing Vertically Aligned Carbon Nanofibers", *ACS Applied Materials & Interfaces* 3, 946 (2011)
7. R. Clearfield, J. G. Railsback, R. C. Pearce, D. K. Hensley, J. D. Fowlkes, M. Fuentes–Cabrera, M. L. Simpson, P. D. Rack and A. V. Melechko, "Reactive solid–state dewetting of Cu–Ni films on silicon", *Applied Physics Letters* 97, 253101 (2010)
8. J. D. Fowlkes, Y. Wu and P. Rack, "Directed Assembly of Bi–Metallic Nanoparticles by Pulsed Laser Induced Dewetting: a Unique Time and Length Scale Regime", *ACS Applied Materials & Interfaces* 2, 2153 (2010)
9. E.C. Landis, K.L. Klein, A. Liao, E. Pop, D.K. Hensley, A.V. Melechko, and R.J. Hamers, "Covalent Functionalization and Electron-Transfer Properties of Vertically Aligned Carbon Nanofibers: The Importance of Edge-Plane Sites", *Chemistry of Materials* 22, 2357 (2010)
10. Y. Wu, J. D. Fowlkes, P. D. Rack, J. A. Diez and L. Kondic, "On the Breakup of Patterned Nanoscale Copper Rings into Nanoparticles: Competing Instability and Transport Mechanisms", *Langmuir* 26, 11972 (2010)
11. B. L. Fletcher, J. T. Fern, K. Rhodes, T. E. McKnight, J. D. Fowlkes, S. T. Retterer, D. J. Keffer, M. L. Simpson and M. J. Doktycz, "Effects of ultramicroelectrode dimensions on the electropolymerization of polypyrrole", *Journal of Applied Physics* 105, 124312 (2009)
12. L. Kondic, J. A. Diez, P. D. Rack, Y. Guan and J. D. Fowlkes, "Nanoparticle assembly via the dewetting of patterned thin metal lines: Understanding the instability mechanisms", *Physical Review E* 79, 026302 (2009)
13. Melechko, A.V., R. Desikan, T.E. McKnight, K.L. Klein, and P.D. Rack, "Synthesis of vertically aligned carbon nanofibres for interfacing with live systems", *Journal of Physics D: Applied Physics* 42, 193001 (2009)

Inverse Optimization Techniques for Targeted Self-Assembly

Salvatore Torquato
Department of Chemistry, Princeton Institute for the Science and Technology of Materials,
and the Princeton Center for Theoretical Science
Princeton University, Princeton, N.J. 08544 USA
torquato@princeton.edu
http://cherrypit.princeton.edu

Abstract

Program Scope

The term "self-assembly" typically describes processes in which entities (atoms, molecules, aggregates of molecules, etc.) spontaneously arrange themselves into a larger ordered and functioning structure. Biology offers wonderful examples, including the spontaneous formation of the DNA double helix from two complementary oligonucleotide chains, the formation of lipid bilayers to produce membranes, and the folding of proteins into a biologically active state. On the synthetic side, molecular self-assembly is a potentially powerful method to fabricate nanostructures as an alternative to nanolithography. For example, it has been demonstrated that intricate two-dimensional structures can emerge by the placement of organic molecules onto inorganic surfaces [1]. Block copolymers can self-assemble into ordered arrays that have possible use as photonic band-gap materials [2]. Highly robust self-assembly of unique, small clusters of microspheres that can themselves be used for self-assembly of more complex architectures has been demonstrated [3]. DNA-mediated assembly of micrometer-size polystyrene particles in solution could enable one to build complex structures starting from a mesoscale template or seed followed by self-assembly [4]. These examples offer glimpses into the materials science of the future – devising building blocks with specific interactions that can self-organize on a larger set of length scales.

This is an emerging field with a wealth of experimental data that has been supported theoretically and computationally using the "forward" approach of statistical mechanics. Such an approach has generated a long and insightful tradition. The forward approach identifies a known material system that possesses scientific and/or technological interest, creates a manage- able approximation to the interparticle interactions that operate in that material, and exploits simulation and analytical methods to predict non-obvious details concerning structural, thermodynamic and kinetic features of the system.

Several years ago, we proposed that inverse statistical-mechanical methods could be employed to find optimized interactions that most robustly and spontaneously lead to a targeted many-particle configuration of the system for a wide range of conditions [5, 6]. We will discuss these nascent developments in this connection as well as other closely related inverse realizability problems that we have introduced, all of which are solved using various

optimization techniques. Results produced by these inverse approaches have already led to a deeper fundamental understanding of the mathematical relationship between the collective structural behavior of many-body systems and the interactions: a basic problem in materials science and condensed matter theory. As will be shown, such methodologies hold great promise to control self-assembly in many-particle systems to a degree that surpasses the less-than-optimal path that nature has provided. Indeed, employing such inverse optimization methods, we envision being able to "tailor" potentials that produce varying degrees of disorder, thus extending the traditional idea of self-assembly to incorporate both amorphous and crystalline structures as well as quasicrystals.

The idea of *tailoring* potentials to generate targeted structures is motivated by the rich array of fundamental issues and questions offered by this fascinating inverse statistical-mechanical problem as well as our recent ability to identify the structures that have optimal bulk properties or desirable performance characteristics. The latter includes novel crystal and quasicrystal structures for photonic band-gap applications, materials with negative or vanishing thermal expansion coefficients, with negative Poisson ratios, materials with optimal or novel transport and mechanical properties, mesoporous solids for applications in catalysis, separations, sensors and electronics, and systems characterized by entropically driven inverse freezing, to mention a few examples.

Output from these optimization techniques could then be applied to create de novo colloidal particles or polymer systems with interactions that yield these structures at the nanoscopic and microscopic length scales. Colloidal particles suspended in solution provide an ideal experimental testbed to realize the optimized potentials, since both repulsive and attractive interactions can be tuned (e.g., via particle surface modification or the addition of electrolytes) [7] and therefore offer a panoply of possible potentials that far extends the range offered by molecular systems.

Recent Progress

The research program has been aimed at first devising completely new inverse statistical-mechanical methods and then applying them for novel material design. The following is a list of the highlights of our accomplishments during last two years:

- Development of inverse methods for novel ground states [8–10];
- Optimized isotropic pair interactions for novel crystal ground states [9–11];
- Designing isotropic pair interactions for negative Poisson's ratio behavior [12];
- Collective-coordinate inverse methods for disordered ground states [13–15];
- Characterization of hyperuniform materials [16];
- Duality relations for classical ground states [17];
- Reformulation of the covering and quantizer problems as many-particle ground states [18];
- Inverse techniques for material microstructure reconstructions [19–21]; and
- Thermodynamic and transport properties of soft-matter systems [22–24].

Figure 1 illustrates some of the novel target many-particle configurations that we have devised using our inverse statistical-mechanical techniques. Both structure and bulk properties can be optimized.

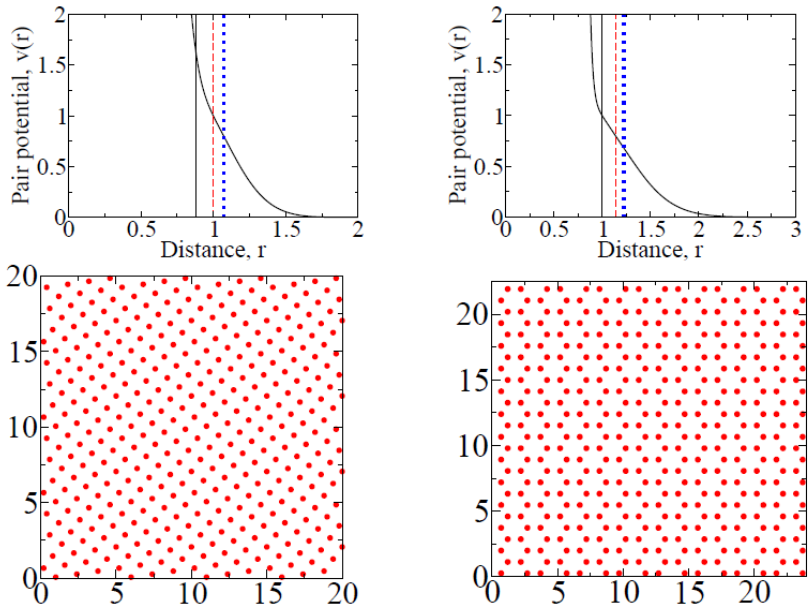

Figure 1: Monotonic convex pair potentials whose ground states are the square (top left) and honeycomb (top right) crystal structures, as shown in the corresponding bottom panels [9,10]. Note that both potentials have a short-distance cut-off.

Future Plans

Our interest in future work will be in finding the interaction potential, not necessarily pair-wise additive or spherically symmetric, that optimally stabilizes a targeted many-body system, which may be a crystal, disordered or quasicrystal structure, by incorporating structural information that is not limited to the pair correlation function and generally accounts for complete configurational information. Our primary interest is in the possible many-body structures that may be generated, some of which may include interesting but known structures, while others may represent entirely new structural motifs. We plan on extending our inverse methods to multicomponent systems. Moreover, the inverse methods described here can be employed to find targeted structures for metastable states as well as nonequilibrium configurations. Finally, an important component of future research will be the development of robust potentials (even if not optimal) for targeted structures and bulk properties that can be synthesized experimentally with colloids or other soft matter systems.

References

[1] G. M. Whitesides and P. E. Laibinis. Wet chemical approaches to the characterization of organic-surfaces - self-assembled monolayers, wetting, and the physical organic-chemistry of the solid liquid interface. *Langmuir*, 6:87–96, 1990.

[2] S. A. Jenekhe and X. L. Chen. Self-assembly of ordered microporous materials from rod-coil block copolymers. *Science*, 283:372–375, 1999.

[3] V. N. Manoharan, M. T. Elsesser, and D. J. Pine. Dense packing and symmetry in small clusters of microspheres. *Science*, 301:483–487, 2003.

[4] M. P. Valignat, O. Theodoly, J. C. Crocker, W. B. Russel, and P. M. Chaikin. Reversible self-assembly and directed assembly of DNA-linked micrometer-sized colloids. *Proc. Nat. Acad. Sci.*, 102:4225–4229, 2005.

[5] M. C. Rechtsman, F. H. Stillinger, and S. Torquato. Optimized interactions for targeted self-assembly: Application to honeycomb lattice. *Phys. Rev. Lett.*, 95:228301:1–4, 2005.
[6] M. Rechtsman, F. H. Stillinger, and S. Torquato. Synthetic diamond and wurtzite structures self-assemble with isotropic pair interactions. *Phys. Rev. E*, 75:031403, 2007.
[7] W. B. Russel, D. A. Saville, and W. R. Schowalter. *Colloidal Dispersions*. Cambridge University Press, Cambridge, England, 1989.

Publications Over the Past Two Years Acknowledging DOE-BES Support on This Grant

[8] S. Torquato. Inverse optimization techniques for targeted self-assembly. *Soft Matter*, 5:1157–1173, 2009.
[9] ´E. Marcotte, F. H. Stillinger, and S. Torquato. Optimized monotonic convex pair potentials stabilize low-coordinated crystals. *Soft Matter*, 7:2332–2335, 2011.
[10] ´E. Marcotte, F. H. Stillinger, and S. Torquato. Unusual ground states via monotonic convex pair potentials. *J. Chem. Phys.*, 134:164105, 2011.
[11] R. B. Batten, D. A. Huse, F. H. Stillinger, and S. Torquato. Novel ground-state crystals with controlled vacancy concentrations: From kagom´e to honeycomb to stripes. *Soft Matter*, 7: 6194,2011.
[12] M. C. Rechtsman, F. H. Stillinger, and S. Torquato. Negative Poisson's ratio materials via isotropic interactions. *Phys. Rev. Lett.*, 101:085501, 2008.
[13] R. D. Batten, F. H. Stillinger, and S. Torquato. Novel low-temperature behavior in classical many-particle systems. *Phys. Rev. Lett.*, 103:050602, 2009.
[14] R. D. Batten, F. H. Stillinger, and S. Torquato. Interactions leading to disordered ground states and unusual low-temperature behavior. *Phys. Rev. E*, 80:031105, 2009.
[15] C. E. Zachary and S. Torquato. Anomalous local coordination, density fluctuations, and void statistics in disordered hyperuniform many-particle ground states. *Phys. Rev. E*, 83:051133, 2011.
[16] C. E. Zachary and S. Torquato. Hyperuniformity in point patterns and two-phase heterogeneous media. *J. Stat. Mech.: Theory & Exp.*, page P12015, 2009.
[17] S. Torquato and F. H. Stillinger. Duality relations for the classical ground states of soft-matter systems. *Soft Matter*, 7:3780–3793, 2011.
[18] S. Torquato. Reformulation of the covering and quantizer problems as ground states of interacting particles. *Phys. Rev. E*, 82:056109, 2010.
[19] Y. Jiao, F. H. Stillinger, and S. Torquato. A superior descriptor of random textures and its predictive capacity. *Proc. Nat. Acad. Sci.*, 106:17634–17639, 2009.
[20] Y. Jiao, F. H. Stillinger, and S. Torquato. Geometrical Ambiguity of Pair Statistics. II. Heterogeneous Media, Physical Review E, 82, 011106 (2010).
[21] Y. Jiao, F. H. Stillinger, and S. Torquato. Distinctive features arising in maximally random jammed packings of superballs. *PRE*, 81:041304, 2010.
[22] J. L. Gevertz and S. Torquato. Mean survivial times of absorbing triply periodic minimal surfaces. *Phys. Rev. E*, 80:011102, 2009.
[23] R. D. Batten, F. H. Stillinger, and S. Torquato. Phase behavior of colloidal superballs: Shape interpolation from spheres to cubes. *Phys. Rev. E*, 81:061105, 2010.
[24] W. T Gilleland, S. Torquato, and W. B. Russel. New bounds on the sedimentation velocity for hard, charged, and adhesive hard sphere colloids. *J. Fluid Mech.*, 667:403–425, 2011.

Mesoscopic Simulations of the Self-Assembly of Non-Spherical Colloids

Fernando A. Escobedo
School of Chemical & Biomolecular Engineering, Cornell University, Ithaca, NY 14853

i) Program Scope

Colloidal particles of non-spherical shapes can form ordered solid and liquid phases that possess unique optical, rheological, and mechanical properties, making them attractive components in the preparation of novel fibers, liquid armor, nanocomposites, photonic and photovoltaic materials. Overall, the joint experimental-theoretical work in this project has addressed aspects related to the synthesis of particles of non-spherical shapes (with minimal polydispersity), the processing and modeling of self-assembled morphologies, and their use as photonic-gap materials for light control. The goal of this paper is to describe recent results obtained in our group on the use of molecular simulations to map out thermophysical properties of suspensions of particles with polyhedral, multilobed, and spherical-cap shapes. Our results provide both a basis to existing experimental observations and predictions of novel phases yet to be seen in the lab.

ii) Recent Progress

2.1 Polyhedral Particles. Since the six known convex space-filling polyhedrons have known crystal close-packing structure, they are ideal to probe the questions: How does particle shape

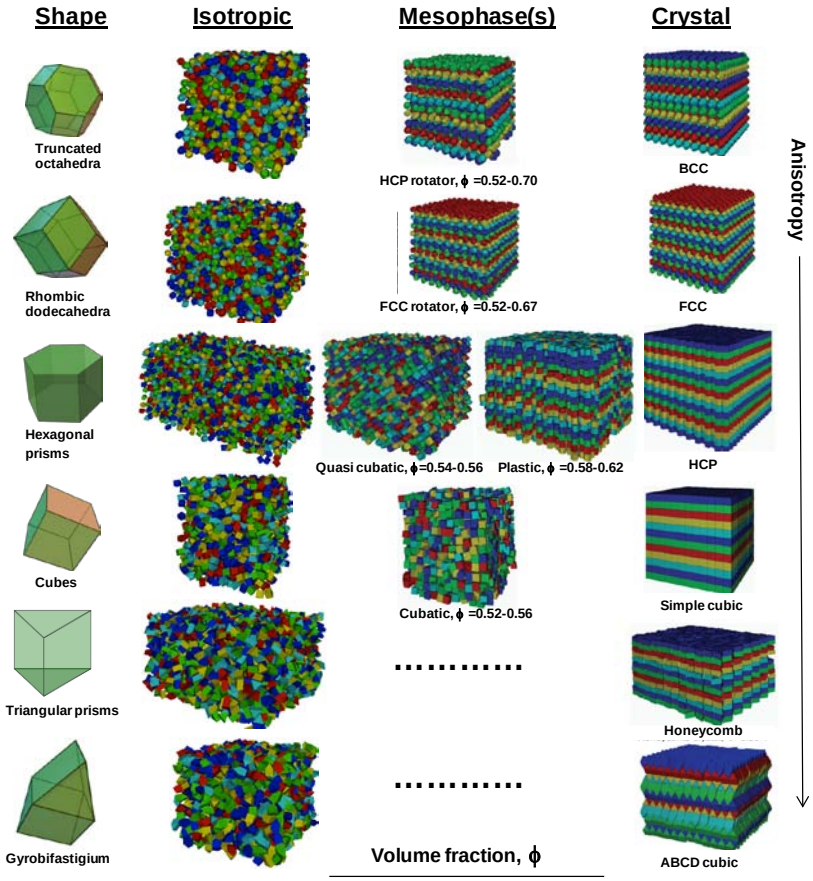

Fig. 1. Snapshots of the phases observed for polyhedra in order of increasing shape anisotropy (from top to bottom). Particle colors are used for visual effect and to detect mixing of the initial crystal layers.[1]

influence the way crystalline order is lost upon dilution? Can partial disordering give rise to mesophases? (a mesophase is a phase with order intermediate between that of a liquid and a solid like plastic solids and liquid crystals). Monte Carlo Simulations (Fig. 1) indeed predict the formation of various novel entropy-driven liquid-crystalline and plastic-crystalline phases at intermediate volume fractions. It was found that polyhedral shapes with high rotational symmetry are in general prone to mesophase formation, with shapes of low anisotropy favoring plastic-solid behavior and intermediate anisotropy favoring liquid crystalline behavior. It was also found that dynamic disorder is crucial in defining mesophase behavior, and that the apparent kinetic barrier for the liquid-mesophase transition is much lower for liquid crystals (orientational order) than for plastic solids (translational order).

2.2 Molecular Simulation of Spherical Caps: Confinement-Induced Self-Assembly Control

Compared to spheres, anisotropic particles possess extra orientational degrees of freedom that enrich the phase behavior of colloidal particles. Additionally, confinement also affects the phase behavior of the colloidal particles in a non-trivial fashion, and has been a topic of intensive research over the last years. A case in point are mushroom-like [2-5] and bowl-like colloidal particles [6-7] whose phase behavior and the mechanism of phase formation are still not completely understood.

Via molecular simulation, we have been studying spherical-cap shaped colloidal particles under confinement between hard walls separated by a distance *H*. The geometry of the particle is obtained by taking the region of a sphere, which lies above a given plane (c.f. Fig. 2(a)). The crystal structures have been obtained by using Monte Carlo simulation in the N-H-$P_{||}$-T ensemble, in which the number of particles N, the walls separation H, the temperature T, and the tangential (to the wall) pressure $P_{||}$, are kept constant. The structures presented in Fig. 2(b) and 2(c), corresponding to small confinements are similar to the buckled and hexagonal phases observed in the experiments reported by Prof. Liddell group [2] (the project PI), which indicates that the geometry of the model used in this work is able to reproduce the cascade of phases observed in experiments. In addition we also have identified some other phases for large confinement not observed in experiments. This crystal structures are presented in Fig. 2(d) and (e). The methodology employed in this work [8] is very efficient and allows predicting crystal structures using small number of particles during the simulation, which *per se* improves the computational time.

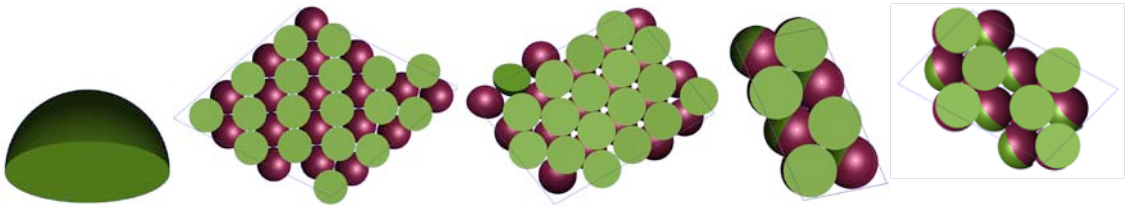

Fig 2. (a) Geometry of the spherical cap (hemisphere) used in this work. The diameter of the hemisphere has been set to the value of 1. (b-e) crystal structures obtained using Monte Carlo simulations for different confinements: b) H=0.6, buckled phase; c) H=0.85, hexagonal bilayer; d) H=1.125 and e) H=1.5 novel phases with square symmetry.

2.3 Monomers and dimers under 2D confinement

Our investigations have also centered on understanding defect dynamics in colloidal solids formed by dimers. Confined to 2D, dimer lobes occupy triangular lattice sites, but the particles are randomly oriented along the three underlying lattice directions. Experimentally, it was found that mechanical perturbation of degenerate crystals indicated that dislocations are caged by particles in the glide-blocking orientations and may hop between cages through multi-defect mechanisms. The processes are reminiscent of the motion of particles within colloidal glass [9]. To complement experimental observations based on tracking defect motions after local deformations, extensive non-equilibrium molecular dynamics simulations of homogenous shear flow were performed for monolayer crystals of pure dimers, pure spheres, and mixtures of monomers and spheres. The dynamic relaxation of dislocations in these systems was characterized and observations (from single-particle dragging-relaxation experiments) were confirmed that suggested a glassy behavior in the dimer crystals. Our simulations allowed for comparison of crystals of dimers, spheres, and their mixtures under steady state conditions and without grain boundaries or particle polydispersity (ideal conditions not accessible to the experiments). Uniform shear was applied at both small strain rates to detect yield stress behavior and high strain rates to induce melt the crystal. The simulations confirmed the strikingly different defect transport mechanisms in crystals of spheres and of dimers.

iii) Future Plans

3.1 Simulation of the kinetics and mechanism of selected ordering transitions. To engineer processes that produce phases having particles arranged in a particular type of structural order, it is necessary to not only know what the equilibrium phases are, but also the mechanisms by which such phases are accessed from other phases and whether metastable phases exist. This information is needed to evaluate the kinetics of phase transformations, how to circumvent undesirable metastable states and defects, how to access desired metastable states, and to identify conditions that would catalyze slow transformations.

While mapping out free-energy landscapes and quantifying thermodynamic barriers (which can be probed via umbrella sampling) is an important step toward understanding the basis of the dynamic behavior of a system, to truly characterize the mechanism and kinetics of key steps during an order-to-disorder transition, ensembles of transition paths need to be produced. This would be inaccessible via straightforward simulations because of the long waiting time at dynamic bottlenecks. To overcome this, we will employ 'forward flux sampling' (FFS) [10], a transition path sampling method that uses a divide-and-conquer strategy to create complete paths from partial, shorter paths between successive interfaces along a chosen order parameter. We have advanced several fronts of the FFS methodology, [11] including a way to extract reaction coordinates that best describe the dynamic evolution of a system (crucial for any ensuing attempt to engineer the process). Current work is aimed at applying FFS to the melting of dimers in 2D and the isotropic-cubatic transition in bulk suspensions of cubes.

3.2 Rheology of colloidal ordered phases. Building on the knowledge of thermodynamic phase diagrams for a variety of particles shapes (such as dimers and hemispheres as planned above), we will examine the effect of shear on the structure of diverse stable phases, and as well investigate whether homogeneous shear may help disordered phases (in a metastable glassy state) to achieve a target ordered state. Different types of non-equilibrium dynamics simulations (NEMD) will be

used to probe the flow behavior and measure the shear viscosity of a system and allow comparisons with experimental results in Prof. Cohen's group (a co-PI). We will simulate the suspensions near the order-disorder transition where shear could either promote or hamper structural order. Polybead models (rather than perfect shapes) will be used for computational convenience for particles of non-trivial geometry (like hemispheres or polyhedrons) as these are more readily handled by conventional NEMD methods and allow the incorporation of explicit solvent (to account for hydrodynamic interactions). These studies are expected to yield important insights into the mechanical properties of confined suspensions having significant structural order and hence highly non-Newtonian behavior.

iv) References

1. U. Agarwal and F. Escobedo, *Nature Materials* **10**, 230-235 (2011).
2. E. K. Riley, and C. M. Liddell, *Langmuir* **26**, 11648 (2010).
3. J. A. Weiss, D. W. Oxtoby, D. G. Grier, and C. A. Murray, J. Chem. Phys. 103, 1180 (1995).
4. A. Fortini, and M. Dijkstra, *J. Phys.: Condens. Matter* **18**, L371 (2006).
5. I. D. Hosein, and C. M. Liddel, *Langmuir* **23**, 8810 (2007).
6. M. Marechal, R. J. Kortschot, A. F. Demirors, A. Imhof, and M. Dijkstra, *Nano Lett.* **10**, 1907 (2010).
7. M. Marechal, and M. Dijkstra, *Phys. Rev. E* **82**, 031405 (2010).
8. L. Filion, M. Marechal, B. van Oorschot, D. Pelt, F. Smallenburg, and M. Dijkstra, *Phys. Rev. Lett.* **103**, 188302 (2009).
9. S. J. Gerbode, D. C. Ong, U. Agarwal, C. M. Liddell, F. Escobedo, I. Cohen. *Physical Review Letters, 105* (2010): 078301-1 - 078301-4.
10. Allen, R. J.; Frenkel, D.; ten Wolde, P. R. *J. Chem. Phys.* **2006**, *124*, 024102-1 – 024102-16.
11. Escobedo, F. A.; Borrero, E.; Araque, J. C. Transition Path Sampling and Forward Flux Sampling. Applications To Biological Systems. *Journal of Physics - Condensed Matter* **2009**, *21*, 333101-1 – 33101-23.

v) Publications resulting from DOE support in last two years

PR1. U. Agarwal and F. Escobedo, "Mesophase behavior of polyhedral particles" *Nature Materials* **10**, 230-235 (2011).

PR2. S. J. Gerbode, D. C. Ong, C. M. Liddell, I. Cohen. "Dislocations and Vacancies in 2-D Mixed Crystals of Spheres and Dimers." *Physical Review E, 82* (2010): 041404.

PR3. E. K. Riley and C. M. Liddell. "Confinement-Controlled Self Assembly of Colloids with Simultaneous Isotropic & Anisotropic Cross-Section." *Langmuir, 26* (2010): 11648-11656.

PR4. S. J. Gerbode, D. C. Ong, U. Agarwal, C. M. Liddell, F. Escobedo, I. Cohen. "Glassy Dislocation Dynamics in Colloidal Dimer Crystals." *Physical Review Letters, 105* (2010): 078301-1 - 078301-4.

PR5. S. H. Lee, E. Y. Fung, E. Riley and C. M. Liddell. "Asymmetric Colloidal Dimers Under Quasi-2D Confinement." *Langmuir*, 25 (2009): 7193-7195.

Shear induced assembly of anisotropic colloidal particles

Itai Cohen
ic64@cornell.edu
Department of Physics
Cornell University, Ithaca, NY 14853

Program Scope

Colloid-based materials offer the ability to dramatically alter dispersion relations and enhance light-matter interactions for solar energy conversion; light localization (high quality factor microcavities and waveguides); spontaneous emission control for lasing and solid state lighting; slow-light media to enhance nonlinearity for miniaturization, low power consumption, optical network switching, and signal regeneration; and effective negative refraction for flat lens and subwavelength imaging.[1-3] In addition, hypersonic crystals with phononic band gaps have been cited for application in thermal management and shear thickening particle suspensions have been explored for their promise in anti-ballistic textiles.[1] Colloidal systems also offer fundamental models for understanding phase behavior in ionic and molecular solids.[4]

Colloidal self-assembly specifically incorporating anisotropic motifs is developing as a viable solution to the fabrication challenge of achieving complexity from relatively simple building blocks, since unconventional nonspherical colloidal particles— boomerrangs, square crosses, hexagonal prisms, pentagons, UFO-shapes, red blood cell-shapes, w-motifs, ellipsoids, cylinders, spherocylinders, asymmetric dimers— have been prepared recently with low size dispersity.[5-13] A number of groups including ours are pursuing such routs towards complex assemblies. As an additional tuning parameter, hydrodynamic interactions between colloidal particles under shear can be used to drive a suspension out of equilibrium thereby enabling exploration of an even richer phase behavior.[14-18] Anisotropic particles are particularly attractive systems for exploring this method of assembly since their anisotropic shape leads to orbits and trajectories that substantially bias the orientation of the particles within the flows and therefore affect the long time diffusive behavior of the particles. Here we report on recent progress that we have made in understanding how an imposed shear flow leads to the assembly of spherical particles into string like structures. We then describe our plans to extend this work to the anisotropic particles relevant for a sub-project of the DOE award, 'Self-Assembly of Non-Spherical Colloids: New reduced symmetry crystals and mesophases for templating functional materials at fine scales'.

Recent Progress

Our colloidal suspension consists of d = 0.96 μm silica particles suspended in an index-matched glycerol/water mixture (see Methods). We apply a plane sinusoidal shear in the suspensions with a fixed shear strain γ = 3.51±0.16 and controllable shear angular frequencies ω. The structure of particles in the flow (x) – vorticity (z) plane is imaged at different locations along the shear gradient direction (y). With the hard-sphere particles under shear, the relevant dimensionless parameters are the volume fraction of suspensions, ϕ, and the Péclet number $\mathrm{Pe} \equiv \eta_0 \dot{\gamma} d^3 / (8 k_B T)$, which is the ratio of the diffusion and advection time scales. Here, η_0 is the viscosity of the solvent and $\dot{\gamma} = \omega\gamma$ is the shear rate.

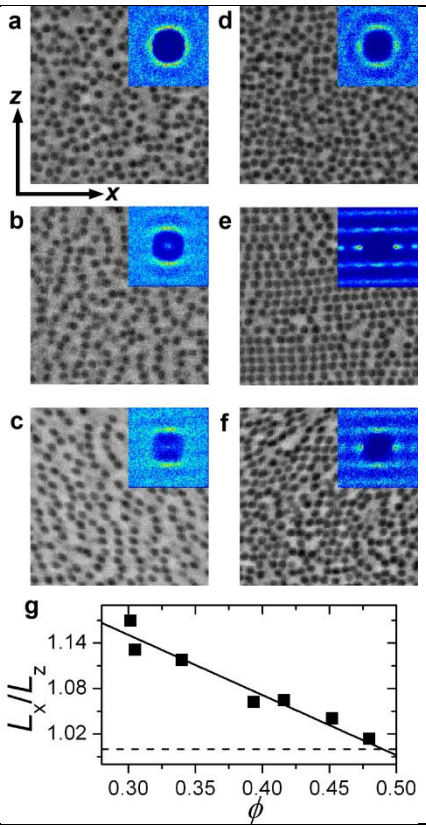

Figure 1 | String phase in sheared colloidal suspensions. a-c, The real-space structure of particles in an *x*-*z* layer are shown for a suspension of $\phi = 0.34$ under confinement $h = 7.0d$ at Pe = 0.72 (**a**), Pe = 72 (**b**) and Pe = 337 (**c**). The corresponding pair correlation function $g(x, z)$ is shown in the inset of each plot. $g(x, z)$ is defined as the probability of finding a particle at position (x, z) with respect to the center of each particle. **d-f** show the structure and $g(x, z)$ for the $\phi = 0.46$ sample under otherwise same experimental conditions of **a-c**. **g** shows the ratio of the distances between neighboring particles along the *x* and *z* directions, L_x/L_z, versus ϕ at Pe = 70. $L_x/L_z = 1$ is indicated by the dashed line. The solid line is a linear fit of the data. All these measurements are for the 2nd particle layer in *x*-*z* plane counted from the top plate.

We explore particle configurations at different Pe in a sample of $\phi = 0.34$, well below the crystallization threshold, $\phi = 0.49$, for hard-sphere colloidal suspensions. The sample is confined between the two shear plates at a separation $h = 7.0d$. At this gap size, the particles form weak layers parallel to the flat shear plates (*x*-*z* layers) in equilibrium. These layers enhance strongly with increasing shear[6]. We image the particle structure in these *x*-*z* layers. Without shear or at low Pe, particles have nearly isotropic structure (Fig. 1a). The corresponding pair correlation function, $g(x, z)$, shows a uniform ring indicating the first shell of neighboring particles (Fig. 1a inset). However, at intermediate Pe, the suspension develops a string structure, where chains of particles align predominately along the vorticity direction (Fig. 1b). This trend is also shown in the change of $g(x, z)$. Here, the ring at low Pe breaks into two crescents along the *z* direction indicating the 1D symmetry of the string phase (Fig. 1b inset). Although the existence of a string phase is consistent with some simulations, the orientation of the strings is unexpected: it is normal to the numerically predicted flow direction[7-13]. As Pe is increased further, the vorticity-aligned string structure becomes more pronounced (Fig. 1c).

When samples with higher ϕ are sheared, we find the vorticity-aligned strings in *x*-*z* layers are pushed closer along the *x* direction. Finally, at $\phi = 0.46$ near the crystallization threshold, we observe that strings locally collapse into crystalline islands with four-fold symmetry (Fig. 1d,e). These square crystalline islands melt gradually at an even higher Pe above 40 (Fig. 1f). To quantify the smooth transition between the string phase and the shear-induced crystalline phase at intermediate Pe, we measure the average distance between neighboring particles along the *x* and *z* direction, L_x, L_z, over a range of ϕ (Fig.

1g). L_x/L_z starts at 1.15 for the string phase at low ϕ and approaches to 1.0 for the square crystalline phase at high ϕ. L_x/L_z extrapolates to 1.0 at ϕ = 0.50±0.03, which is consistent with the fluid-crystal transition for hard sphere suspensions in 3D.

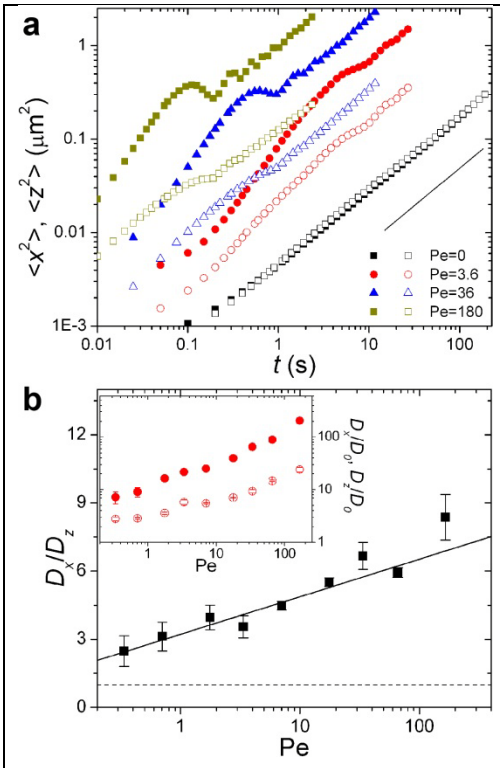

Figure 3 | Effective particle diffusion in *x*-*z* plane. a shows the mean squared displacement of particles along *x* direction, $\langle x^2 \rangle$, (solid symbols) and along *z* direction, $\langle z^2 \rangle$, (empty symbols) in the reference frame of the oscillatory shear. To obtain particle motions in the shear frame, the global shear motion, measured with Particle Image Velocimetry, is subtracted from the motion of individual particles. A residual oscillatory shear motion can still be identified at a short time scale. The solid line has an exponent of 0.81. Particles show sub-diffusive behavior even in equilibrium, which may result from the formation of rough particle layers due to confinement. Particle motions are measured in the 2nd layer of the suspension with $\phi = 0.34$ and $h = 7.3d$. The diffusion constant D_x and D_z are obtained by fitting the slope of $\langle x^2 \rangle$ and $\langle z^2 \rangle$ versus time *t* in the log-log scale at later time. **b** shows D_x/D_z and the inset of **b** shows D_x/D_0 and D_z/D_0 versus Pe respectively, where D_0 is the diffusion constant of particles without shear.

To gain further insights into the symmetry breaking mechanisms that lead to string formation, we experimentally investigate the microscopic dynamics of individual particles. Specifically, we measure the effective particle diffusion in the *x*-*z* plane in the reference frame of the oscillating shear flows (Fig. 2a). By comparing the effective diffusion constant in the *x* and *z* directions, D_x/D_z, we find a broken symmetry in the particle dynamics: with increasing Pe the enhancement of particle diffusion under shear along the *x* direction is much stronger than enhancement along *z* (Fig. 2b). Since the experiments are conducted at constant $\dot{\gamma}$, the increase of D_x/D_z cannot be due to Taylor dispersion[25], which suggests a different mechanism for the observed trends. Due to the anisotropic particle diffusion, particle density along *z* has to increase relative to that along *x* to maintain a uniform osmotic pressure within the layer. Consequently, close-packed strings along the vorticity direction gradually emerge with increasing Pe.

Future Plans

These results demonstrate that anisotropy in the diffusion constant can be used as a mechanism for assembling particles into structures that are not observed under equilibrium conditions. Anisotropic

particles naturally display anisotropic diffusive behavior due to their shape. In particular a rod like particle, for example, can diffuse more readily along its long axis since the area presented to the oncoming fluid is small compared with that presented when the rod moves in a direction perpendicular to this axis. As such, rods have anisotropic diffusion constants associated with the axial and radial directions. Under equilibrium conditions, an isolated rod will also display rotational diffusion so that on average its diffusive properties within the lab frame end up being isotropic in the lab reference frame. However, under shear, rods can display distinct Jeffreys orbits that bias the amount of time a particle is oriented in a particular configuration relative to the apparatus. Consequently, in addition to the anisotropic diffusive properties exhibited by the spherical particles, we anticipate being able to enhance the diffusive anisotropy by taking advantage of the anisotropy associated with the shape of the colloidal particles we are able to synthesize. Such experiments will point the way towards new routes towards self-assembly of particles into structures difficult to obtain under equilibrium conditions.

References

1. Glotzer, S. C.; Solomon M. J. *Nat. Mater.* **2007**, *6*, 557-562.
2. Yang, S. M.; Kim, S. H.; Lim, J. M.; Yi, G. R. *J. Mater. Chem.* **2008**, 18, 2177-2190.
3. Lu, Y.; Yin, Y.; Xia Y. *Adv. Mater.* **2001**, 13, 415-420.
4. Lu, Y.; Yin, Y.; Li, Z.-Y.; Xia Y. *Langmuir* **2002**, 18, 7722-7727.
5. Sun, Z. Q.; Chen, X.; Zhang, J. H.; Chen, Z. M.; Zhang, K.; Yan, X.; Wang, Y. F.; Yu, W. Z.; Yang, B. *Langmuir* **2005**, 21, 8987-8991.
6. Mock, E. B.; Zukoski, C. F. *Langmuir* **2007**, 23, 8760-8771.
7. Hosein, I. D.; Liddell, C. M. *Langmuir* **2007**, 23, 8810-8814.
8. Ding,T.; Song, K.; Clays, K.; Tung, C.-H. *Adv. Mater.* **2009**, 21, 1936–1940.
9. Marechal M.; Dijkstra, M. *Phys. Rev. E*, **2008** 77, 061405-1 – 061405-10.
10. Branka A. C.; Wojciechowski, K. W. *Phys. Rev. Lett.* **1983** 50, 846-849.
11. Bolhuis P.; Frenkel, D. *J. Chem. Phys.* **1997** 106, 666-687.
12. Wojciechowski, K. W. *Phys. Lett. A* **1987** 122, 377-380.
13. Lee, S. H.; Fung, E. Y.; Riley E.; Liddell C. M. *Langmuir*, **2009** 25, 7193-7195.
14. Clark, N. A., Hurd, A. J. & Ackerson, B. J. *Nature* 281, 57-60 (1979).
15. Haw, M. D., Poon, W.C. K. & Pusey, P. N. *Phys. Rev. E* 57, 6859-6864 (1998).
16. Cohen, I., Mason, T. G. & Weitz, D. A. *Phys. Rev. Lett.* 93, 046001 (2004).
17. Vermant, J. & Solomon, M. J. *J. Phys.: Condens. Matter* 17, R187-R216 (2005).
18. Wu, Y. L., Derks, D., van Blaaderen, A. & Imhof, A. *Proc. Natl Acad. Sci.* USA 106, 10564-10569 (2009).
19. Erpenbeck, J. J. *Phys. Rev. Lett.* **52**, 1333-1335 (1984).
20. Xue, W. & Grest, G. S. *Phys. Rev. Lett.* **64**, 419-422 (1990).
21. Yamada, T. & Nosé, S. *Phys. Rev. A* **42**, 6282-6284 (1990).
22. Padilla, P., Toxvaerd, S. & Stecki, J. *J. Chem. Phys.* **103**, 716-724 (1995).
23. Bagchi, K., Balasubramanian, S., Mundy, C. J. & Klein, M. L. P *J. Chem. Phys.* **105**, 11183(1996).
24. Phung, T. N., Brady, J. F. & Bossis, G. *J. Fluid Mech.* **313**, 181-207 (1996).
25. Gray, R. A., Chynoweth, S., Michopoulos, Y. & Pawley, G. S. *Europhys. Lett.* **43**, 491-496 (1998).

DOE sponsored publications since Sept. 2009

1. Sharon J. Gerbode, Desmond C. Ong, Chekesha M. Liddell, and Itai Cohen "Dislocations and vacancies in two-dimensional mixed crystals of spheres and dimers." *PHYSICAL REVIEW E* **82**, 041404 (Oct 2010)
2. S.J. Gerbode, U. Agarwal, D.C. Ong, C.M. Liddell, F. Escobedo, and I. Cohen "Glassy Dislocation Dynamics in 2D Colloidal Dimer Crystals." *PHYS. REV. LETT.* **105**, 078301 (Aug 2010)

Directed Self-Assembly of Nanodispersions

Eric M. Furst
Department of Chemical Engineering and Center for Molecular and Engineering Thermodynamics, University of Delaware, Newark, DE 19716

I. Project Scope

The structure of many materials arises spontaneously through specific, local interactions between individual molecules, macromolecules, proteins or particles. This kind of spontaneous organization is called *self-assembly*. It occurs when, for instance, molecules reduce their free energy through arrangements of like-interacting chemical domains. A classic example is the formation of micelles in a surfactant solution, in which the oily, hydrophobic tail groups cluster together, with the hydrophilic polar groups pointing outward towards the aqueous solvent. Self-assembly is the basis of many sophisticated functional nanostructures in biology. With a rapidly expanding library of nanoparticles available with different shapes, chemistries, and properties (catalytic, photonic, *et cetera*), we have the opportunity to direct the assembly of functional nanomaterials from these building blocks for man-made applications. Indeed, the spontaneous, bottom-up process of self-assembly is likely to become a key approach in manufacturing new functional nanomaterials and nanodevices.

Self-assembly, though, has a significant shortcoming: equilibrium thermodynamics may favor a desired nanostructure, but frequently the structure that forms is limited by the kinetics of the assembly process. For instance, during the deposition of anisotropic particles, such as the titania ellipsoids or latex dicolloids in figure 1, these high aspect ratio particles favor aligned structures when they are above a certain concentration. However, suspensions often lack the necessary time to reach this state due to their slow relaxation dynamics; the result is a disordered or partially ordered film. To overcome this limitation, *directed* self-assembly, in which self-assembly is enhanced or guided by an external force, has become essential for attaining the potential of bottom-up nanofabrication.[1] For instance, using elongational flows or electric fields, anisotropic nanoparticles can be preconditioned in an oriented state that then pack efficiently. Examples of highly ordered structures are shown in figure 1. Furthermore, the degree of order can be finely tuned, enabling us to control the properties of these films, as well as create gradients, alternating structures, and so on.

II. Recent Progress

Using an increasingly large library of nanoparticles, we've developed methods to direct nanoparticle suspension assembly to create advanced materials with applications in energy production, transport and storage, and optics.[1] Two examples are shown in figure 1. Using knife blade flow coating, we deposit anisotropic titania nanoparticles into thin films with controlled nanostructure and thickness.[2] Depending on the coating speed, blade angle and particle concentration, the deposited film can vary in structure from randomly oriented nanoparticles to highly aligned and densely packed films. With collaborators at Sandia National Laboratories, we've demonstrated that these films have novel tunable, ultra-low thermal conductivities (figure 2). Similarly, it is difficult to grow photonic crystals from dicolloid nanoparticles, (which resemble two fused spheres); for such anisotropic particles, both the translational and orientational order must be controlled. Electric-field assisted assembly enables us to orient the dicolloids as they are deposited, thus directing the kinetic pathway to self-assembly.[3]

Field-directed assembly has tremendous potential, and provides many novel control capabilities as well. For instance, the orientation of nanoparticles in an alternating current (ac) electric field is dependent both on the field direction and frequency. [4] As shown in figure 3, this frequency dependent alignment enables real-time control over the structure during deposition.

Electric field assembly is also sensitive to particle shape. Disks, ellipsoids and dumbbell particles form different ordered structures.[5,4,6,3] This raises the interesting possibility of creating *programmable* particles that are designed to couple to fields in ways that lead to novel structures. If such programmability is to be realized, however, the physical design rules for particles need to be established. Along these lines, we have studied the interactions between particles in electric fields and established a phase diagram for the disorder-to-order transition of spherical particles as a function of field strength and frequency.[7] Shown in figure 4 this phase diagram collapses data taken from several studies for particles ranging in diameter from 200-3000nm. The basis of our phase diagram is the induced dipole-dipole interaction between particles. The maximum dipole interaction energy between particles is the dipole strength, $\lambda = \pi\varepsilon\varepsilon_0 C^2 E^2 a^3 / kT$, where C is the dipole coefficient (related to the polarizability of the particle). Taking the square root of λ gives us a scaled field strength that depends on temperature and particle size. The field frequency is scaled by a characteristic timescale for ion diffusion around the particles. This identifies double layer polarization as the underlying mechanism.

The dominant presence of dipoles and the dipole-dipole interaction leads us to identify heuristics for electric field directed assembly. The fact that anisotropic particles have two characteristic relaxation times associated with the polarization explains the frequency dependence of the orientation that we exploited in the assembly of titania films shown in figure 1 while disk shapes will tend to orient to minimize the distortion of the electric field, and thus with the disk face orthogonal to the field. Indeed, we observed this form of assembly using zeolite nanoparticles, which have a disk-like shape.

III. Future Plans

Over the project period, we have significantly advanced externally controlled directed assembly, both in the fundamental understanding of electric-field driven assembly and in the applications towards the fabrication of novel structured materials from anisotropic nanoparticles. In particular, we found that electric fields are powerful tools for directing other forms of self-assembly, such as convective deposition. The novel thermal properties of titania nanoparticle films demonstrate the potential for creating novel materials for a wide variety of engineering applications. In our current and future work, we are measuring the polarization of particles using dielectric spectroscopy. Second, we are experimenting with other particle shapes to further develop directed assembly of nanoparticles.

IV. References

(1) Grzelczak, M.; Vermant, J.; Furst, E. M.; Liz-Marzan, L. M. *ACS Nano* **2010**, *4*, 3591–3605.
(2) Mittal, M.; Niles, R. K.; Furst, E. M. *Nanoscale* **2010**, *2*, 2237–2243.
(3) Forster, J. D.; Park, J.-G.; Mittal, M.; Noh, H.; Schreck, C. F.; O'Hern, C. S.; Cao, H.; Furst, E. M.; Dufresne, E. R. *ACS Nano* **2011**, 1–18.
(4) Mittal, M.; Furst, E. M. *Adv. Funct. Mater.* **2009**, *19*, 3271–3278.
(5) Singh, J. P. B.; Nettesheim, F.; Wagner, N. J.; Furst, E. M. *Phys Rev E* **2009**, *79*, 050401(R).
(6) Mittal, M.; Furst, E. M. *J. Mater. Res.* **2011**, 26, 215-222.
(7) Mittal, M.; Lele, P. P.; Kaler, E. W.; Furst, E. M. *J Chem Phys* **2008**, *129*, 064513.

V. Publications resulting from work supported by the DOE project over the last two years

1. M. Grzelczak, J. Vermant, E. M. Furst and L. M. Liz-Marzan, ``Directed self-assembly of nanoparticles," ACS Nano 4, 3591-3605 (2010).
2. Patrick E. Hopkins, Manish Mittal, Leslie M. Phinney, Anne M. Grillet and Eric M. Furst, ``Tunable thermal conductivity of TiO$_2$ nanoparticle close-packed films," Proceedings of the ASME/JSME 8th Thermal Engineering Joint Conference, AJTEC2011, Honolulu, HI, March 13 - 17, 2011.

3. J. D. Forster, J.-G. Park, M. Mittal, H. Noh, C. F. Schreck, C. S. O'Hern, H. Cao, E. M. Furst, and E. R. Dufresne, ``Assembly of optical scale dumbbells into dense photonic crystals," ACS Nano, accepted.
4. P. E. Hopkins, M. Mittal, A. M. Grillet and E. M. Furst, ``Nanostructured oxide films with ultra-low thermal conductivity," submitted to Physical Review Letters.
5. P. Beltramo and E. M. Furst, ``Dielectric spectroscopy of bidisperse colloidal suspensions," in preparation.
6. P. Beltramo and E. M. Furst, `` Dielectric spectroscopy of colloidal suspensions through the order-disorder transition," in preparation.

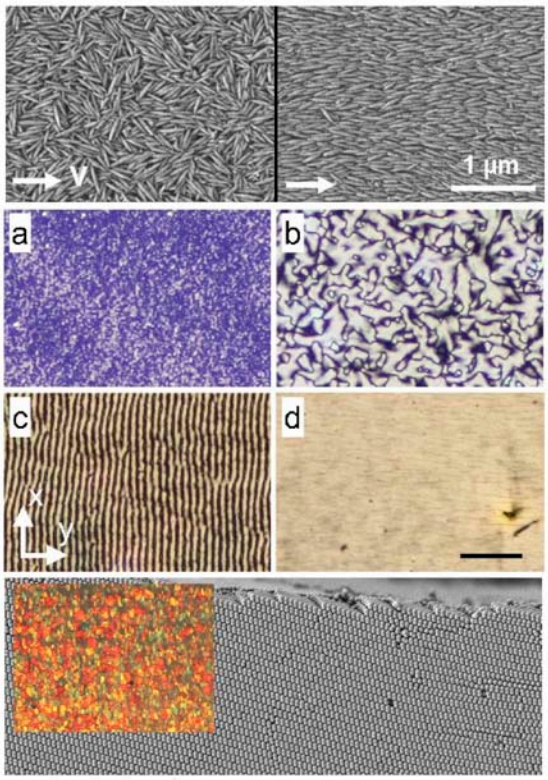

Figure 1. (Top) Anisotropic titania nanoparticles form thin films of random or aligned orientations. The optical and thermal transport properties can be controlled. The nanoscale structure of the films is apparent by the colorful patterns when viewed using polarized light microscopy. (Bottom) Optical scale nanoparticle dicolloids with a dumbbell-like shape, are deposited by field-directed convective assembly into photonic crystals.

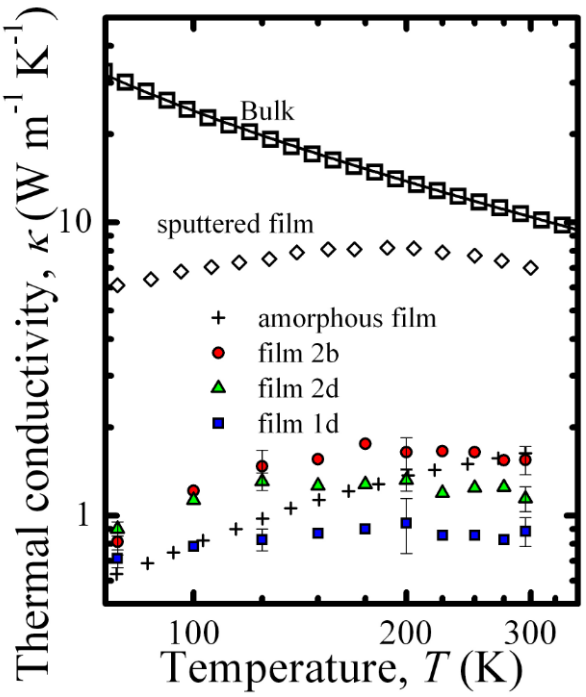

Figure 2. Thin films formed by the directed assembly of anisotropic titania nanoparticles have tunable, ultra-low thermal conductivities. Data courtesy of Patrick Hopkins, Sandia National Laboratories.

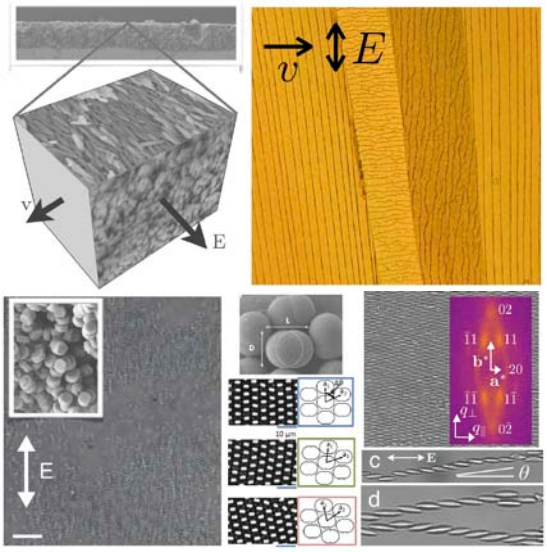

Figure 3. Examples of electric field directed assembly. (Left) The deposition of anisotropic titania nanoparticles in electric fields is controlled by both the field direction and frequency. Frequency changes during deposition, lead to different nanoparticle alignments, as evidenced by the cracking pattern. (Right) Different particle shapes, including ellipsoids, disks and dumbbells lead to different equilibrium structures in ac electric fields.

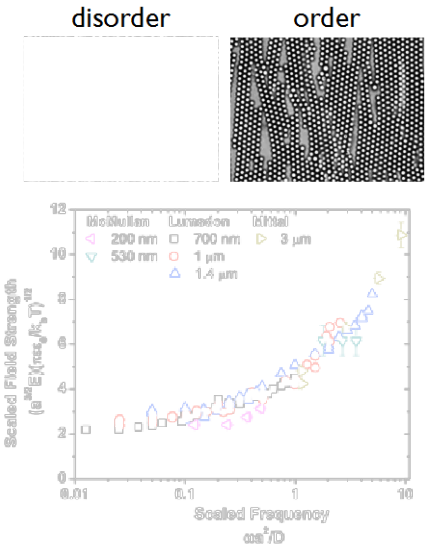

Figure 4. A master phase diagram collapses the order-disorder transition of spherical particles in ac electric fields as a function of field strength and frequency. The particles range in diameter from 200-3000nm.

Molecularly Organized Nanostructural Materials

Jun Liu, Gregory J. Exarhos, Maria Sushko, Praveen Thallapally,
Yongsoon Shin, Yun Jung Lee, Birgit Schwenzer, Xiaolin Li
Jun.liu@pnl.gov
Pacific Northwest National Laboratory
Richland, WA 99352

Program Scope: The overall goal of this project is to investigate a combination of self-assembly and controlled nucleation and growth approaches for synthesizing nanostructured materials with controlled three-dimensional architectures and desired stable crystalline phases of conductive or semiconducting metal oxides suitable for energy applications. Of importance is the understanding of crystallization in self-assembled materials in order to control both resident porosity and pore interconnectivity in these materials because these traits impart certain properties to the material that are underpinning for energy technologies including conversion and storage. The project contains the following components:

- Manipulation of the kinetics of competing self-assembly and precipitation reactions
- Use of molecular ligands and interfaces to control nucleation and growth
- Multiscale modeling of the self-assembly process in solution
- *S*tructure-property relationships for energy applications

Recent Progress: Nanomaterials with controlled micro- and nanoporosities, crystalline phases and structural ordering are important for energy storage, catalysis, and many other energy related applications. In this project, we investigate two fundamental approaches to synthesize such materials. The first approach is molecularly directed assembly and crystallization, and the second approach is interfacially controlled nucleation and self-assembly. One class of material, metal-organic frameworks (MOFs) have come to the forefront during the last decade as a new type of well-controlled microporous materials. However, there have been few reports on their crystallization process. For example, we studied the nucleation and crystallization of nanocrystalline MOFs and for the first time reported shape selective (Hexagonally shaped nZIF-8) synthesis of mono dispersed nanoparticles of metal organic frameworks by simple mixing of zinc nitrate hexahydrate with 2-methyl imidazole at room temperature in the presence of methanol and 1 % high molecular weight poly(diallyldimethylammonium chloride) solution (average M_w 400,000-500,000) (Figure 1 (1) to (2). We found that the crystallization is controlled by the polymer additive, without which disordered aggregates are observed.

Interfacial chemistry can also plays a critical role in the synthesis of complex materials. In the past, we and many other groups have performed extensive study of controlled nucleation and growth on functionalized substrates. In this project, we are developing a new strategy to take advantages of the interfacial reactions using nanoscale building blocks to construct complex three-dimensional structures. We can use molecularly dispersed graphene sheets as the template and nanoscale building block. Depending on the surface chemistry of the graphene sheets and the interactions with other constituents, a wide range of complex nanostructures are developed. First, we take advantage of the defect chemistry and the associated functional groups on graphene surfaces. These functionalized graphene sheets are synthesized through thermal oxidation and expansion, and the density of the defects can be systematically controlled. Through extensive computer modeling and electron microscopy study, we found that the defect chemistry controls

the nucleation and growth of metal oxides and metals on the graphene surface. The surface chemistry also determines which crystalline phases are stabilized. Graphene-metal-metal oxide nanocomposite can be constructed using this approach with the metal nanoparticles stabilized in the triple junction points between graphene and metal oxides (Figure 1 (3)). Furthermore, the functional graphene sheets can be assembled into 3D hierarchical porous electrode for high performance Li-air batteries with the defect structure controlling the nucleation of the reaction products (Figure 1(4)).

The graphene sheets can be also dispersed in the hydrophobic domains of surfactant molecules or polymers. Extensive computer modeling, small angle scattering and dispersion experiments show that two conditions have to be met to optimize surfactant efficiency in stabilizing graphene in aqueous solutions with ionic surfactants: i) surfactant hydrophobic regions should be sufficiently long to achieve stable dense surfactant layers on graphene; ii) surfactant hydrophilic regions should either carry sufficient charge density to provide strong double-layer repulsion or be sufficiently long to provide strong hydration and/or steric repulsion between functionalized graphene sheets. For short chain nonionic surfactant, the main stabilization mechanism is the hydration force and the dispersion depends on the hydrophilic chain length. For long chain nonionic polymers, the main mechanism is the steric repulsion and the dispersion depends on the hydrophobic chain length (Figure 1(5)). The surfactant dispersed graphene sheets can further self-assemble with metal oxides to form ordered graphene-metal oxide composites for energy storage with enhanced capacity and stability (Figure 1(6)).

Recently, we demonstrated that the graphene template self-assembly approach can be used to synthesize ordered nanoporous materials such as highly crystalline mesoporous TiO_2. This is a good example of using 2D chemistry to form 3D nanostructures that are otherwise very difficult to synthesize under normal experimental conditions.

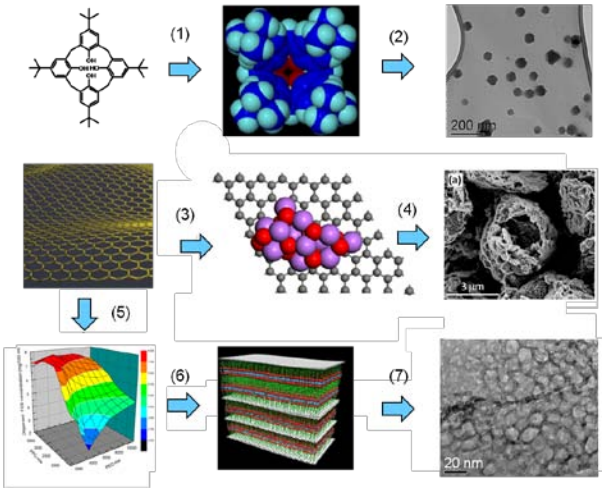

Figure 1. Molecularly directed and interfacially controlled synthesis and assembly. (1) Molecular ligand directed formation of MOFs. (2) Controlled crystallization of MOFs to form monodispersed nanocrystals. (3) Defect controlled nucleation and growth to form metal-metal oxide-graphene nanocomposites. (4) 3D hierarchical porous electrode for high performance Li-air batteries. (5) Systematic investigation of dispersion of graphene in surfactants. (6) Surfactant assisted self-assembly of ordered metal oxide-graphene nanocmposites. (7) Graphene template self-assembly of nanoporous TiO_2.

Significance: The recent progress on this project has the potential to bridge the gap of two-dimensional crystallization and three-dimensional self-assembly, and the gap between microporous and nanoporous materials. First, we have proven that the surface chemistry (defects and functional groups) on the graphene surfaces controls nucleation and crystallization, as well the crystalline phases. We have further demonstrated that the 2d structures can be used as the building blocks to build complex 3D structures. In the past, self-assembled oxide materials are mostly limited to single phase materials and nanoparticle based systems. Our study points to a new direction for self-assembly using multiple phases and multilength building blocks. The materials developed under this project already demonstrated superior kinetics and stability for

electrocatalysis in fuel cells, good performance in Li-ion and Na-ion batteries, and in Li-sulfur and Li-air batteries.

Future Plan: Our future plan will pursue further fundamental understanding of the molecular level interactions by developing and using state-of-the-art characterization and simulation tools. Specifically, we will use molecular simulation and surface sensitive spectroscopy techniques to investigate the molecular interaction of complex polymers and biomolecules such as DNA and protein molecules on graphene surfaces. The use of more complex molecules will provide more flexibility in synthesizing complex materials. Second, we will use DFT computer modeling and expand our recently developed in-situ transmission electron microscopy technique to investigate the nucleation mechanism of metal oxide, zeolite and nanoporous materials on graphene and other well-defined surfaces. Finally, we will greatly expand the range of complex materials that can be synthesized using our approach. Currently many other building blocks are available besides graphene sheets, such as carbon nanotubes, nanowires and nanorods, and ceramic nanoplates. Similar principles should apply for such nanoscale building blocks and will lead to truly multifunctional composite materials with controlled architectures.

Selected Publications:

1. J Tian, PK Thallapally, J Liu, GJ Exarhos, and JL Atwood. 2011. "Gas-Induced Solid State Transformation of an Organic Lattice: From Nonporous to Nanoporous." Chemical Communications 47(2):701-703.
2. Y Cao, L Xiao, W Wang, D Choi, Z Nie, J Yu, LV Saraf, Z Yang, J Liu, 2011, Reversible Sodium Ion Insertion in Single Crystalline Manganese Oxide Nanowires with Long Cycle Life, Advanced Materials, 23 (28) 3155-3160.
3. CM Wang, W Xu, J Liu, JG Zhang, LV Saraf, BW Arey, D Choi, ZG Yang, J Xiao, S Thevuthasan, DR Baer 2011. "In Situ Transmission Electron Microscopy Observation of Microstructure and Phase Evolution in a SnO_2 Nanowire during Lithium Intercalation." Nano Letters, 11 (5) 1874-1880.
4. Y Cao, X Li, IA Aksay, JP Lemmon, Z Nie, Z Yang, and J Liu. 2011. "Sandwich-Type Functionalized Graphene Sheet-Sulfur Nanocomposite for Rechargeable Lithium Batteries." Physical Chemistry Chemical Physics. PCCP, 13 (17) 7660-7665.
5. ML Sushko and J Liu. 2011. "Surfactant Two-Dimensional Self-Assembly under Confinement." Journal of Physical Chemistry B., 115 (15) 4322-4328.
6. DH Wang, R Kou, D Choi, ZG Yang, ZM Nie, J Li, LV Saraf, DH Hu, JG Zhang, GL Graff, J Liu, MA Pope and IA Aksay 2010. "Ternary Self-Assembly of Ordered Metal Oxide-Graphene Nanocomposites for Electrochemical Energy Storage." ACS Nano 4(3): 1587-1595.
7. SK Nune, PK Thallapally, A Dohnalkova, CM Wang, J Liu and GJ Exarhos 2010. "Synthesis and Properties of Nano Zeolitic Imidazolate Frameworks." Chemical Communications 46(27): 4878-4880.
8. ML Sushko and J Liu 2010. "Structural Rearrangements in Self-Assembled Surfactant Layers at Surfaces." Journal of Physical Chemistry B 114(11): 3847-3854.

This page is intentionally blank.

Session 1b

Function-Driven Materials Design: Exploratory Caged Materials

Session Chairs: Raymond Schaak, The Pennsylvania State University

This page is intentionally blank.

Novel theoretical and experimental approaches for understanding and optimizing molecule-sorbent interactions in metal organic framework materials

Y.J. Chabal (chabal@utdallas.edu**),** Materials Science and Engineering, UT Dallas, Richardson, TX
Jing Li and David Langreth, Chemistry and Physics, Rutgers University, Piscataway, NJ

Program Scope

The aim of this program is to develop a *fundamental mechanistic understanding of the interaction guest molecules (e.g. H_2, CO_2, N_2, CH_4)* in porous metal organic framework (MOF) materials, using a combination of novel synthesis, theoretical analysis and characterization. In particular, we combine *high-pressure and low-temperature infrared (IR) absorption and Raman measurements, adsorption isotherms and isosteric heat of adsorption measurements* with first-principles calculations based on *van der Waals density functional* (vdW-DF), to study a number of different MOF materials. One of the goals is to provide insight for the role of unsaturated metal centers in enhancing molecular uptake, selective adsorption and diffusion. The short term impact of the proposed work will result from the control and the understanding of common MOF systems, making it possible to determine the theoretical loading limits and stability of a specific class of materials. The long term impact will involve the development of 1) theoretical/experimental methods to gain a fundamental understanding of molecular interactions in these systems, and 2) new classes of microporous MOFs with enhanced molecular binding and selectivity.

Recent Progress:

a) Synthesis of new MOFs for gas adsorption and separation: Our recent effort in the development of new MOFs for small gas separation (with a focus on CO_2 capture and separation from power-plant flue gas mixtures) has been primarily on the structures that (a) exhibit high CO_2 adsorption enthalpy, (b) have high CO_2 adsorption capacity, and (c) demonstrate both high selectivity and uptake of CO_2 over other small gases. $Zn_2(bpdc)_2(bpee)$ (bpdc = 4,4'-biphenyl di carboxylate, bpee = 1,2-bis(4-pyridyl) ethylene) has a very flexible framework structure. Single-component gas adsorption experiments show that this compound possesses the highest separation ratios of CO_2 vs. several other small gases, including N_2, H_2, CO, O_2, CH_4, and H_2. At 0.16 atm and 25 °C, they are 294, 190, 257 and 441 (v/v) for CO_2/N_2, CO_2/H_2, CO_2/CH_4 and CO_2/CO, respectively, and 768 (v/v) for CO_2/O_2 at 0.2 atm. Ligand functionalization of $[Zn(bdc)(ted)_{0.5}]$ (bdc = terephthalate, ted = tryethylenediamine) yields $[Zn(bdc\text{-}R)(ted)_{0.5}]$ (R = -OH, -NH_2) that take up a significantly enhanced CO_2 amount and have increased CO_2-MOF binding energy at ambient conditions. Imposing dual functionality (metal open sites and Lewis basic sites) to MOF structures produces Cu-TDPAT that exhibits both high isosteric heat of adsorption and uptake level of CO_2. With Q*st* = 42.2 kJ/mol at zero loading, the compound adsorbs 6.2 wt% of CO_2 at room temperature and 0.1 atm, a condition that mimics a flue gas mixture. These values place Cu-TDPAT among a very small group of MOFs with the highest selectivity for CO_2/N_2.

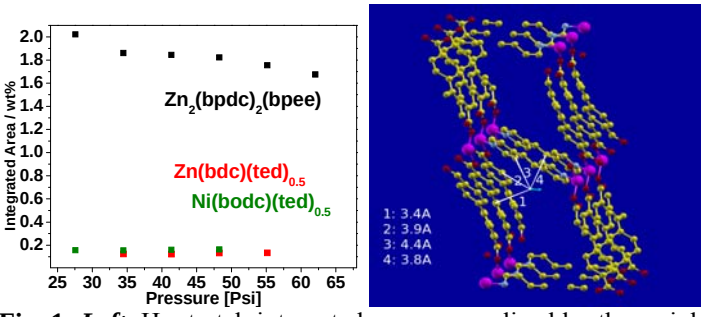

Fig. 1: ***Left***: H_2 stretch integrated areas normalized by the weight percent of adsorbed hydrogen (isotherm measurements). Higher (~×10) intensities are observed for $Zn_2(bpdc)_2(bpee)$;
Right: H_2 adsorption sites in $Zn_2(bpdc)_2(bpee)$. The interaction lines between one of the H atoms with C atoms in four different ligands are shown, responsible for higher binding energy.

b) Identification and properties of H_2 adsorption sites in MOFs with saturated metal centers:[1] We have studied MOFs with 3-D pore structures such as $M(bdc)(ted)_{0.5}$ and $Ni(bodc)(ted)_{0.5}$ [where M=Zn,Ni and Cu, bdc=1,4-benzenedicarboxylate;ted=triethylenediamine and bodc=bicycle[2.2.2]octane-1,4-dicarboxylate] and investigated the effect of aromatic (bdc) versus aliphatic ligand (bodc) exchange and the effect of metal center exchange. There is no dependence of the adsorbed H_2 vibrational frequency on

the nature of the metal center. However, larger shifts are observed for aromatic ligands (~-38 cm^{-1}). Although previous studies have assumed a dependence of the IR frequency shifts on binding energies and a relation between the integrated areas of the H_2 vibrational band and the amount of adsorbed H_2,[2-4] we find no evidence of a dependence of the IR shifts or intensities on the binding energies. Instead, the integrated area of adsorbed H_2 (the dipole moment of H_2) is found to be strongly influenced by parameters such as the symmetry of adsorption sites and the local interactions between H_2 and the organic ligand, as illustrated in Fig. 1 for $Zn_2(bpdc)_2(bpee)$ [where bpdc= 4,4'-biphenyldicarboxylate and bpee=1,2-bipyridylethethe]. The left panel shows the normalized integrated area of adsorbed H_2 in $Zn(bdc)(ted)_{0.5}$, $Ni(bodc)(ted)_{0.5}$ and $Zn_2(bpdc)_2(bpee)$. $Zn_2(bpdc)_2(bpee)$ exhibits much larger absorption (i.e. dynamic dipole moment) than the other two systems. However, isotherms show a larger adsorption of H_2 in $Zn(bdc)(ted)_{0.5}$ than in $Zn_2(bpdc)_2(bpee)$. VdW-DF calculations clearly show that the larger dipole moment arises from the adsorption site asymmetry and the large interaction with several aromatic ligands.

c) Identification of H_2-H_2 interactions in MOF-74 using IR and vdW-DFT calculations:[5] Combing IR spectroscopy and vdW-DFT calculations we have observed and explain a distinct vibrational response of H_2 in the higher-binding-energy site "unsaturated metal" site caused by H_2 occupation of the second "oxygen" binding site. The effects are manifested by an increase in IR shift (~-30 cm^{-1}) and a decrease in dipole moment of H_2 adsorbed at the metal site. IR studies at low temperature (~40K) confirm such changes, illustrated in Fig. 2 as substantial variations in the IR frequencies and integrated areas of the band at 4133 cm^{-1}, attributed to isolated H_2 adsorbed at the metal site, and at 4091 cm^{-1}, attributed to H_2 adsorbed at the metal site after the "oxygen" site is occupied.

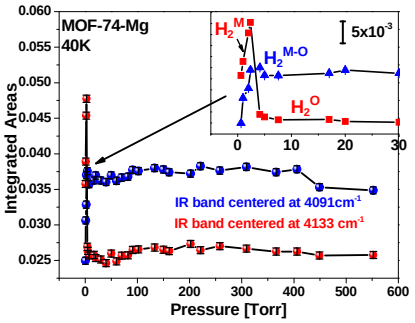

Fig. 2: Integrated areas of adsorbed H_2 as a function of pressure at 40 K in MOF-74-Mg. A shift of the IR band at 4133 cm^{-1} is observed as the oxygen site is occupied, a decrease in dipole moment.

We have also observed effects caused by H_2 adsorption at next nearest neighboring "benzene" sites in MOF-74-Co,[6] including a decrease in dipole moment of H_2 adsorbed at the metal site when the benzene sites are partially occupied (Fig. 3). At full occupation (highest loading), an additional ~-10 cm^{-1} red shift of H_2 adsorbed at the metal site is observed. These results underscore the sensitivity of H_2 vibrational frequencies on long range interactions, even for H_2 adsorbed at low binding energy sites (benzene sites), thus providing precious information for such complex systems.

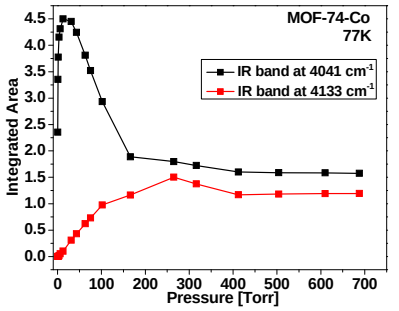

Fig. 3: Integrated areas of H_2 adsorbed in MOF-74-Co as a function of pressure. The integrated area of H_2 at the metal site decreases as the benzene sites are occupied.

d) Study of structural changes induced by CO_2 adsorption in a flexible MMOF system ($Zn_2(bpdc)_2(bpee)$) using Raman spectroscopy: We have investigated the isotherms of CO_2 and N_2 in the $Zn_2(bpdc)_2(bpee)$ system (where bpdc= 4,4'- biphenyl dicarboxylate, bpee = 1,2-bis(4-pyridyl)ethylene). We find that there is a preferential adsorption of CO_2 over N_2.[7] Furthermore, the isotherms reveal a breathing behavior, characterized by a pore opening upon CO_2 adsorption at 0.1 atm, but not upon N_2 adsorption under similar conditions. Using Raman spectroscopy, we are able to detect important spectral changes (Figure 4), associated with structural rearrangement occurring during pore opening (only for CO_2), that are correlated to the preferential adsorption of CO_2 over N_2. Using DFT simulations of ligand reorientation (e.g. twisting), the observed Raman shifts could be related to a rotation of the bpdc ligand, consistent with a pore opening mechanism. The interaction of the CO_2 carbon center with the inter-ring C-C bond of this ligand is believed to be the origin of this twisting, which is possible because the special connectivity of the bpdc ligand (unidentate bonding) to the metal center is favorable for a rotation around this point. The bpee ligand can accommodate the changes because the C=C bond of the ethylene can change length to accommodate accommodates these changes.

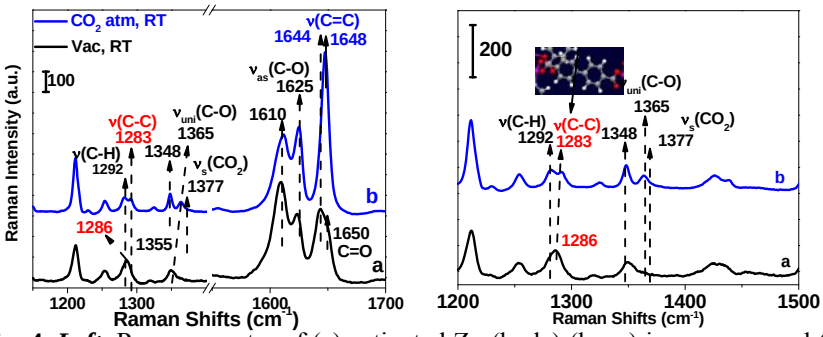

Fig. 4. ***Left***: Raman spectra of (a) activated $Zn_2(bpdc)_2(bpee)$ in vacuum, and (b) after introducing 1 atm of CO_2 at room temperature; ***Right***: zoom of the 1200-1500 cm^{-1} region. A twisting of the bpdc ligand is evidenced by: i) a red shift of the band at 1286 cm^{-1} attributed to the inter-ring C-C, and ii) a blue shift of the band at 1355 cm^{-1} attributed to the ν(C-O). The c-axes decreases as evidenced by the blue shift of the ν(C=C) at 1644 cm^{-1} of the bpee ligand.

Spectral changes associated with the C=C bond of the bpee ligand are consistent with interaction with CO_2, only possible because of its larger quadruple moment compared N_2: $4.3x10^{26}$/esu cm^2 vs $1.52x10^{26}$/esu cm^2.

Using a modified vdW-DFT2 method, we are able to identify the adsorption sites of CO_2 (Fig. 5). The energy map shows that there can be 16 CO_2 mol /unit cell. Moreover, sites 1 and 4 are the most energetically favorable adsorption sites. Contrary to expectations, the energies of sites on top of the benzene and pyridine rings are ~10kJ/mol larger than site 1 and 4. CO_2 at the lowest energy adsorption sites interact with both the C-C interring in the bpdc ligand and the C=C in the bpee ligand.

e) Fundamental understanding of the IR and Raman shifts of CO_2 adsorbed in MOF-74 with Mg and Zn metal centers: We have already shown above that there is no clear correlation between the frequency shifts of the adsorbed molecules and the binding energy or the adsorption sites inside the MOF structure, which makes it difficult to interpret the observed results. To fully understand these observations for CO_2 molecules, we have theoretically examined CO_2 adsorption in MOF74-Zn and MOF74-Mg. While the two MOFs are expected to be rather similar, we find that while the shift of the asymmetric stretch mode is ~-10cm^{-1} for MOF74-Zn, it is close to zero for MOF74-Mg, in agreement with our IR measurements. We find that the CO_2 molecule adsorbed in MOF74-Mg is closer to the open Mg atom, and has a larger binding energy, indicating a stronger binding within MOF74-Mg, which makes the IR shifts of the CO_2 asymmetric stretch even more puzzling. Using first-principles vdw DF2 calculations, we are able to understand the competing contributions of several different factors affecting the frequency shift by artificially freezing different flexibilities of the system. When adsorbed within the MOF, the CO_2 molecule is distorted, featuring a changed overall length as well as an off-center asymmetric distortion of the carbon atom. The simulations show that the asymmetric stretch of CO_2 molecule is strongly affected by the overall length of the molecule: a longer molecule has a larger redshift than a free CO2 molecule. The asymmetric distortion of the CO_2, on the other hand, causes a small blue shift of the asymmetric stretch. The effect of the metal site only can be inferred by freezing the CO_2 molecule in its free CO_2 geometry (fixing the molecule length and symmetry), and changing the metal. We find that the open Zn site in MOF74-Zn causing a ~-4cm^{-1} redshift of the asymmetric stretch. In contrast, the open Mg site in MOF74-Mg has no effect. Thus, the overall frequency shifts of the CO_2 adsorbed in MOF74 are clearly attributed to three distinct contributions: the open metal site, the length of the adsorbed CO_2 molecule, and the asymmetric distortion of the adsorbed CO_2 molecule.

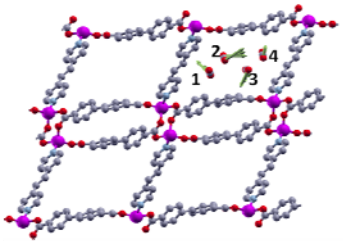

Fig. 5: Adsorption sites of CO_2 in complete occupation in $Zn_2(bpdc)_2(bpee)$ determined by vdW-DFT2. Sites 1 and 4 are the lowest energy adsorption positions. The arrows show the change in position as the unit cell is loaded.

This new method to identify the physical origins of the vibrational shifts of molecules in MOFs makes it possible to study the frequency shifts, and thus the interactions of weakly adsorbed molecules in a variety of systems, and to provide a new guide for designing MOF structures with better adsorption and selection properties.

References:

(1) Nijem, N.; Veyan, J.-F.; Kong, L.; Li, K.; Pramanik, S.; Zhao, Y.; Li, J.; Langreth, D.; Chabal, Y. J. *Journal of the American Chemical Society* **2010**, *132*, 1654-1664.
(2) Bordiga, S.; Regli, L.; Bonino, F.; Groppo, E.; Lamberti, C.; Xiao, B.; Wheatley, P. S.; Morris, R. E.; Zecchina, A. *Physical Chemistry Chemical Physics* **2007**, *9*, 2676-2685.
(3) Bordiga, S.; Vitillo, J. G.; Ricchiardi, G.; Regli, L.; Cocina, D.; Zecchina, A.; Arstad, B.; Bjorgen, M.; Hafizovic, J.; Lillerud, K. P. *Journal of Physical Chemistry B* **2005**, *109*, 18237-18242.
(4) FitzGerald, S. A.; Allen, K.; Landerman, P.; Hopkins, J.; Matters, J.; Myers, R.; Rowsell, J. L. C. *Physical Review B* **2008**, *77*, 224301.
(5) Nijem, N.; Veyan, J.-F. o.; Kong, L.; Wu, H.; Zhao, Y.; Li, J.; Langreth, D. C.; Chabal, Y. J. *Journal of the American Chemical Society* **2010**, *132*, 14834-14848.
(6) Nijem, N.; Kong, L.; Zhao, Y.; Wu, H.; Li, J.; Langreth, D. C.; Chabal, Y. J. *Journal of the American Chemical Society* **2011**, *133*, 4782-4784.
(7) Wu, H.; Reali, R. S.; Smith, D. A.; Trachtenberg, M. C.; Li, J. *Chemistry – A European Jour.* **2010**, *16*, 13951.

Future plans:

Previous studies have demonstrated that open metal sites (OMS) in MOF compounds are the most active sites for small molecules (e.g. CO_2 and H_2). Very recent studies also show that Lewis basic sites (LBS) interact strongly with CO_2. Based on these considerations and our preliminary findings, future synthesis will be focused on the incorporation of high density of both MOS and LBS into MOF structures that have optimum pore size, and are thermally and moisture stable. We will also test the stability of these new structures in water vapor and other environments by performing spectroscopic studies (IR and Raman) of H_2O as a function of both pressure and temperature. Finally, we will continue the characterization of CO_2, CO, CH_4 and H_2 adsorption and interaction within MOFs combining IR and Raman spectroscopy with adsorption isotherms to examine the specific interactions of each molecule in the MOFs and refine the theoretical first principle calculations. The development of vdW-DFT2 will help us look at interactions of molecules to isolate the physical effects influencing the specific properties of these materials.

Publications in past two years (acknowledging full DOE-DMSE support):

1. "A Luminescent Microporous Metal Organic Framework for the Fast and Reversible Detection of High Explosives", A. J. Lan, J. Li *et al*., **Angew. Chem. Int. Ed. 2009, 48, 2334**.
2. "Theoretical and experimental analysis of H_2 binding in a prototypical metal-organic framework material", L. Kong, V. R. C., N. Nijem, K. Li, J. Li, Y. J. Chabal, and D. C. Langreth, **Phys. Rev. B, 2009, 79, 081407(R)** .
3. "A Density Functional for Sparse Matter", D. C. Langreth *et al.*, **J. Phys.: Condens. Matter, 2009 21,084203.**
4. "RPM3: A Multifunctional Microporous MOF with Recyclable Framework and High H_2 Binding Energy", A. J. Lan, Y. J. Chabal, D. C. Langreth, J. Li *et al.*, **Inorg. Chem., 2009, 48, 7165**.
5. "Zeolitic Imadazolate Frameworks Capable of Kinetic Separation of Propane and Propene", K. H. Li, D. H. Olson, J. Seidel, T. J. Emge, H. W. Gong, H. P. Zeng; J. Li**, J. Am. Chem. Soc., 2009, 131, 10368**.
6. "Highly Selective CO_2 Capture by A Flexible Microporous Metal Organic Framework (MMOF) Material", H. H. Wu, S. R. Randall, D. A. Smith, M. T. Trachtenberg, J. Li, **Chem. A. Euro. J., 2010, 16, 13951.**
7. "Interaction of Molecular Hydrogen with Microporous Metal Organic Framework Materials at Room Temperature", N. Nijem, J. Li, D. C. Langreth, and Y. J. Chabal *et al*., **J. Am. Chem. Soc. 2010, 132, 1654.**
8. "Molecular hydrogen "pairing" interactions with the unsaturated metal centers in MOF-74 system", N. Nijem, J. Li, D. C. Langreth, and Y. J. Chabal *et al*., **J. Am. Chem. Soc. 2010, 132, 14834.**
*9. "Higher-accuracy van der Waals density functional"***,** Kyuho Lee, Éamonn D. Murray, Lingzhu Kong, Bengt I. Lundqvist and David C. Langreth, **Phys. Rev. B 82**, 081101 (**Rapid Communications**) (2010) [**partial support**]
10."Spectroscopic evidence for the Influence of the benzene sites on tightly bound H_2 in Metal Organic Frameworks with Unsaturated Metal Centers",N. Nijem, (Li, Langreth Chabal *et al*.), **J. Am. Chem. Soc., 2011, 133, 4782.**
11."First-principles approach to rotational-vibrational frequencies and infrared intensity for H_2 adsorbed in nanoporous materials", L. Kong, Y. J. Chabal, D. C. Langreth, **Phys. Rev. B, 2011, 83**, **121402.**
12."Enhancing Gas Adsorption and Separation Capacity through Ligand Functionalization of Metal Organic Framework Structures", Y. Zhao, D. C. Langreth, Y. J. Chabal, J. Li. *et al.*, **Chem. A. Euro. J., 2011, 17, 5101**.
13."Commensurate Adsorption of Hydrocarbons in Microporous Metal-Organic Frameworks", K.H. Li, D.H. Olson, J. Li, **Trends in Inorg. Chem., 2011, in press.**
+ two other papers under review in *Inter. J. Hydrogen Energy* and ***Adv. Func. Mater.***

DOE-BES Award DE-FG02-05ER46242

Metastability of Clathrate Hydrates for Energy Storage

PIs: Carolyn A. Koh and Amadeu K. Sum
Center for Hydrate Research, Chemical Engineering Department, Colorado School of Mines

Current Program Scope:

The present award has three key objectives that are vital towards realizing the potential of this new class of H_2 storage materials.

- To design, synthesize, and develop novel clathrate materials for H_2 storage.
- To investigate the structural properties of novel H_2 clathrate materials that will efficiently store and release molecular hydrogen at near-ambient temperatures and pressures.
- To obtain a fundamental understanding of the structure and molecular-level dynamics, and H_2 formation/release rates and mechanisms in these novel crystalline compounds.

Recent Progress:

(I) First synthesis of H_2 - tetrabutylphosphonium bromide (TBPB) semiclathrate hydrate *(Yasuda et al., 2011)[1].*

The TBPB semi-clathrate was investigated as a potential H_2 storage medium and new semi-clathrate structure. The effect of pressure, concentration and formation pathways on the H_2 capacity was studied. Raman analysis confirmed the enclathration of H_2 in these new structures at 60 MPa due to the presence of TBPB. The H_2 pressure was found to have a significant effect on H_2 capacity, reaching a maximum at 60 MPa. The concentration of TBPB used did not have a significant effect on the H_2 capacity. The other variable investigated was the effect of synthesis pathway on the H_2 enclathration (Fig. 1). The H_2 capacity did not appear to be severely affected by any of these synthesis techniques. On average the H_2 enclathration was about 0.38 wt% for the TBPB semi-clathrate (at stoichiometric concentration).

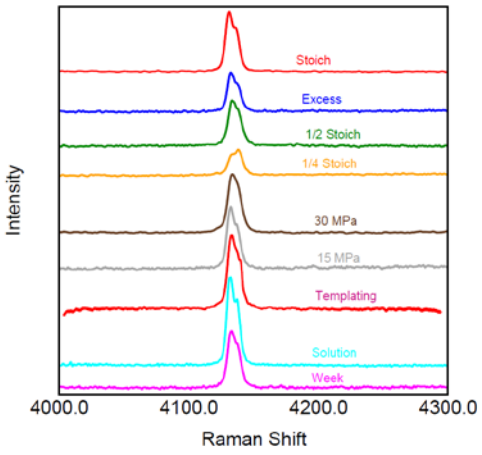

Fig. 1. Raman vibron spectra of different synthesis methods of TBPB semi-clathrate. H_2 vibron peaks at 4130 and 4136 cm^{-1}, are very similar to the H_2 peaks of H_2 in the small cages of the THF binary hydrate, therefore confirming enclathration of H_2 in each case.

(II) Discovery of key clathrate hydrate building blocks: Identified seven common cages in hydrate nucleation and quantified hydrate formation (Walsh et al., submitted to Phys. Chem. Chem. Phys., 2011) [2]. Direct molecular dynamics (MD) simulations of the spontaneous nucleation and growth of sI methane hydrate were performed for the first time. Fig. 2 shows snapshots of the progression from the initial clustering of water and methane molecules to a fluctuating network that grows to a clathrate hydrate structure at the end. These results were the first to provide a molecular level description of a hydrate nucleation process. Our simulation efforts on CH_4 and CO_2 clathrate hydrates have also identified seven elementary cage types, which comprise 95% of all cages present in the nucleating trajectories. The cages identified

have been observed experimentally in either hydrogen-bonded clathrate hydrates or as defects in covalently-bonded clathrate structures.

(III) Structure-synthesis relations: Recent efforts are focussed on investigating the behavior of preformed hydrate (seed-hydrate) + ice + H_2 gas mixtures at low temperatures for the effect of tuning and templating. Binary H_2-THF hydrate samples were prepared by mixing 5.6 mol% solid THF with hexagonal ice (particle size: < 180 μm) under a liquid nitrogen (LN_2) environment. The solid mixture (1.0 – 1.5 grams) was loaded into a high pressure cell (internal volume 4.0 mL) precooled to LN_2 temperature. The cell was pressurized with H_2 gas to 60± 2MPa and subsequently placed in a glycol bath at 255±1K for 3 days. Subsequently, hydrate sample was recovered at LN_2 temperature and analyzed with *ex-situ* cryogenic Raman spectroscopy to examine the initial composition of the hydrate and to confirm H_2 occupancy in only the small cavities of the sII hydrate. The remaining part of the hydrate sample was mixed with additional powdered hexagonal ice grains (<180 μm) at 10% and 40% of the stoichiometric ratio (X_{THF} = 0.00556 and 0.0224). The resultant mixture (1.0 – 1.5 grams) was loaded into another LN_2 cooled high pressure cell and subsequently pressurized with H_2 gas up to 60± 2MPa and placed in the coolant bath at 255±1K for ~1 hour to equilibrate the internal sample temperature with the bath. The cell was later isolated from the system and quenched for 20 minutes in a LN_2 bath. Raman spectroscopy measurements were performed on the post quench sample.

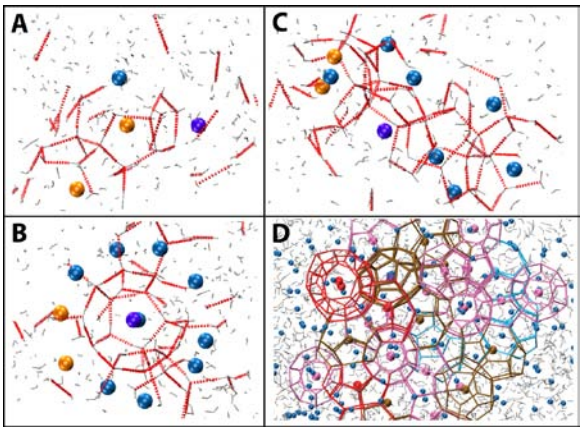

Fig. 2. Fluctuating nature of the first cages involved in clathrate hydrate nucleation. The sequence in the panel shows the evolution from the initial clustering of water and methane molecules (A) to a crystalline-like state with sI and sII domains (D).

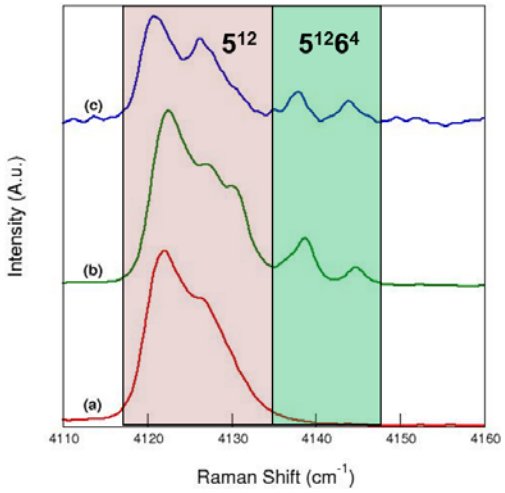

Fig. 3. Raman spectra of the H-H vibron region for the different hydrate samples formed showing similarities in H_2 occupancy between the tuning and seeding method. (a) 'Pre-Mix' sample baseline, (b) 'Tuned' sample with X_{THF} = 0.00556, (c) Seeding-Mix sample with effective THF concentration of X_{THF} = 0.00556.

Effect of quenching on seed-hydrate + ice + H_2 gas mixture. Fig. 3 compares the results from the seeding synthesis pathway outlined above with the tuning method described by Sugahara et al. [3,4]. Raman spectra of THF-H_2 binary seed-hydrate **(e.g. Fig. 3 a)** show no presence of peaks that can be attributed to the large cage occupancy of H_2 (4135 – 4155 cm^{-1}). This is due to a stoichiometric mixture of THF-ice that results in sII hydrate with THF occupying virtually all of the large cages of sII (Florusse et al., 2004; Strobel et al., 2008) [5,6]. However 0.00556 mol% of THF-ice mixture under H_2 pressure when quenched

to LN_2 temperature (~70 K) for 20 min. resulted in a small amount of H_2 occupancy in the large cages of sII **(e.g. Fig. 3 b).** This is consistent with results reported by Sugahara et al. [3] as a tuning effect where H_2 molecules stabilize large cages of sII hydrate that grow from binary THF-H_2 hydrate. We evaluated this behavior by mixing pre-formed THF-H_2 binary hydrate and ice at similar H_2 pressure, THF concentration and quench time. Raman spectra of the resultant 'mix' sample also show evidence of large cage H_2 occupancy **(e.g. Fig. 3 c)**. Since Raman spectra of the 'pre-mix' seed hydrate does not show H_2 occupancy in the large cages, the H_2 occupancy in the large cages observed from our seeding method may be attributed to pure H_2 hydrate (sII) formed during the 20 minute quenching under LN_2 (~70 K) which is consistent with Lokshin et al. [7] where the fast formation of pure H_2 hydrate was observed at PT conditions within the sII H_2 hydrate formation region.

Impact of Current Work

Recent work shows the potential implications of quenching high pressure clathrate systems. We have demonstrated rapid growth of pure H_2 hydrate when mixtures of hydrate seed and ice under H_2 pressure were quenched to LN_2 temperature for 20 minutes. 'Tuning' systems, systems with concentrations of hydrate promoters lower than their stoichiometric concentrations, will normally contain unconverted ice along with hydrate. These results show that in these situations the formation of pure H_2 hydrate from seed hydrate, ice, and H_2 can occur during quenching. This implies that pure H_2 hydrate growth during quenching could be attributed to the large cage H_2 occupancy observed in tuning experiments. It is also important to note that during the periods of quenching within pure H_2 hydrate stability conditions, no pure H_2 hydrates were nucleated from bulk ice even after 60 minutes. Every case where seed hydrates were present resulted in pure H_2 hydrate growth. These results imply that a seed hydrate framework provides a kinetic effect which promotes further hydrate growth. This could lead to templating or propagation of a desired clathrate structure from seed hydrate-ice mixtures. The rapid templating behavior of clathrates may allow for the formation of H_2 hydrate structures other than sII, which could have implications for higher storage capacity of H_2 in clathrates.

Future Research Plans

The current research builds upon our knowledge of the fundamental science of key processes controlling the synthesis and structures of clathrate hydrates containing H_2 and other guest molecules for energy storage. The current research focuses on the molecular level interactions between guest and host molecules in clathrate hydrates. This research promises a transformative understanding of clathrate hydrate metastability that is central to the broader energy applications of clathrate hydrates, including energy storage, energy transportation, and energy recovery. The key objectives of this current study on clathrate hydrate metastability are to investigate:

1. Self-preservation metastability – hydrates preserved outside equilibrium conditions.
2. Structure/phase metastability - coexistence/transitions of metastable phases.
3. Metastable cage composition/occupancy – variable cage occupancy and dynamics.

Highlights of DOE Sponsored Publications in 2008-2011 from Current Grant:

A number of important breakthrough discoveries have been achieved from the current project (DE-FG02-05ER46242), resulting in high impact publications. The notable highlights are listed below.

- **Breakthrough synthesis method** for tuning of binary hydrogen hydrates, achieving increased storage capacity of ~3.6 wt% with H_2 recyclability in host clathrate hydrate structure (Sugahara et al., *J. Am. Chem. Soc*., 2009 & *J. Chem. Phys. C.,* 2010) [3,4]. Prior to this breakthrough the maximum storage capacity was ~1 wt% (following on from our paper by Florusse et al., *Science*, 2004) [5].
- **Synthesis – structure effects** of hydrate seed crystals on H_2 occupancy and kinetics *(Grim et al., Proc. ACS Meeting, 2011, in preparation).*
- **First synthesis of H_2 - tetrabutylphosphonium bromide (TBPB) semiclathrate hydrate** *(Yasuda et al., 2011)[1]*.
- **New molecular guest – hydrogen-bonded water frameworks,** semi-clathrates of t*etra-n-butylammonium borohydride (TBABh) for H_2 storage (Shin et al., J. Phys. Chem. A,* 2009) [8]
- **Hybrid hydrogen clathrate structures** synthesized with potential for an order of magnitude storage increase (Strobel et al., *J. Am. Chem. Soc.*, 2008 [6]; Shin et al., *J. Phys. Chem. A*, 2009 [8])
- **Key paper on hydrogen clathrate storage** (Strobel et al*., Chem. Phys. Lett*., 2009; cover article) [9]
- **First microsecond-scale MD simulation** on clathrate hydrate nucleation (Walsh et al., *Science,* 2009) [10].
- **Discovery of key clathrate hydrate building blocks** during nucleation. Hydrate nucleation studied using molecular dynamics (MD) simulations, showing formation of multiple adjacent crystalline unit cells of sI methane hydrate from a fully-disordered system. Identified seven common cages in hydrate nucleation and quantified hydrate formation (Walsh et al., submitted to Phys. Chem. Chem. Phys., 2011) [2].
- **First use of microsecond MD simulations** to calculate methane hydrate nucleation rates which increase with dissolved methane concentration, consistent with experimental results (Walsh et al., submitted to J. Phys. Chem. C, 2011) [11].

References Cited

1. Yasuda, K., Braniff, M., Sloan, E.D. et al., *Designing Clathrate Hydrate Material for Hydrogen Storage*. in *7th International Conference on Gas Hydrates*. 2011. Edinburgh, UK.
2. Walsh, M.R., Rainey, J.D., Lafond, P. et.al., *Elementary cages of clathrates and their transformations.* submitted to Phys. Chem. Chem. Phys. 2011.
3. Sugahara, T., Haag, J.C., Prasad P.S. et al., *Increasing Hydrogen Storage Capacity Using Tetrahydrofuran.* Journal of the American Chemical Society, 2009. **131**(41): p. 14616-14617.
4. Sugahara, T., Haag, J.C., Warntjes, A.A. et al., *Large-Cage Occupancies of Hydrogen in Binary Clathrate Hydrates Dependent on Pressures and Guest Concentrations.* The Journal of Physical Chemistry C, 2010. **114**(35): p. 15218-15222.
5. Florusse, L.J., Peters, C.J., Joop, S. et al., *Stable Low-Pressure Hydrogen Clusters Stored in a Binary Clathrate Hydrate.* Science, 2004. **306**(5695): p. 469-471.
6. Strobel, T.A., Kim, Y., Andrews, G.S. et al., *Chemical−Clathrate Hybrid Hydrogen Storage: Storage in Both Guest and Host.* Journal of the American Chemical Society, 2008. **130**(45): p. 14975-14977.
7. Lokshin, K.A., Zhao, Y., He, D. et al., *Structure and Dynamics of Hydrogen Molecules in the Novel Clathrate Hydrate by High Pressure Neutron Diffraction.* Physical Review Letters, 2004. **93**(12): p. 125503.
8. Shin, K., Kim, Y., Strobel T.A. et al., *Tetra-n-butylammonium Borohydride Semiclathrate: A Hybrid Material for Hydrogen Storage.* The Journal of Physical Chemistry A, 2009. **113**(23): p. 6415-6418.
9. Strobel, T.A., Hester, K.C., Koh, C.A. et al., *Properties of the clathrates of hydrogen and developments in their applicability for hydrogen storage.* Chemical Physics Letters, 2009. **478**(4-6): p. 97-109.
10. Walsh, M.R., Koh, C.A., Sloan, E.D. et al., *Microsecond Simulations of Spontaneous Methane Hydrate Nucleation and Growth.* Science, 2009. **326**(5956): p. 1095-1098.
11. Walsh, M.R., Beckham, G.T., Koh, C.A. et.al., Submitted to J. Phys. Chem. C, 2011.

Hydrogen Caged in Carbon—
Exploration of Novel Carbon-Hydrogen Interactions

Angela Lueking, John Badding, Vincent Crespi, Xiao Ming Liu, En Shi Xu,
Thomas C. Fitzgibbons, Paramita Ray
The Pennsylvania State University
Departments of Energy and Mineral Engineering, Chemical Engineering, Chemistry, Physics
The EMS Energy Institute and the Materials Research Institute

Program Scope

Hydrogen trapped in a carbon cage, captured through *repulsive* interactions, is a novel concept in hydrogen storage. Trapping hydrogen via repulsive interactions borrows an idea from macroscale hydrogen storage (i.e. compressed gas storage tanks) and reapplies these concepts on the nanoscale in specially designed molecular containers. Under extreme conditions of pressure, hydrogen solubility in carbon materials is expected to increase and carbon is expected to restructure to minimize volume via a mixed sp^2/sp^3 hydrogenated state. Our approach to form hydrogen caged in carbon relies on unique chemical reaction conditions provided by mechanochemistry, including dynamic shearing/compression via mechanical milling and static high-pressure chemistry in a diamond anvil cell. Materials are currently being characterized via multiwavelength *in situ* Raman spectroscopy to probe carbon-hydrogen interactions and structural changes in the carbon backbone. Complementary first-principles materials theory is being used to examine candidate carbon-cage structures to predict the characteristic Raman signatures of hydrogen held in place by either repulsive interactions (caged hydrogen) or attachment to the carbon backbone in mixed sp^2/sp^3 states.

Recent Progress

Aromatic and polyaromatic ring systems polymerize to form extended amorphous carbon networks under high-pressure, thereby providing a means to trap H_2. Compression of benzene to high-pressure in a diamond anvil cell (DAC) shows loss of features characteristic of benzene (Fig. 1a) and an increase in the background fluorescence as the material is monitored with visible (514 nm) Raman (Fig. 1, left). These observations provide evidence for the formation of a metastable polymer network. Indeed, analysis of the recovered polymerized benzene with deep ultraviolet Raman excitation at 244 nm (Fig. 1, right) shows features characteristic of a solid carbonaceous network that includes both sp^2 (a broad D peak at ~1350 cm^{-1} and G peak at ~1600 cm^{-1}) and sp^3 bonding (a small broad T-peak at 1060 cm^{-1}). Additional studies with anthracene and pentacene are on-going, such that the role of aromatic ring structure on polymerization can be determined. Subsequently, the compression will be completed in the presence of gaseous H_2 using a newly developed gas-loading apparatus.

Graphite ball milled in hydrogen (GBMH) has a similar stoichiometry to benzene ($1:0.95^1$ vs. 1:1), yet its amorphous, highly defected, combined sp^2 and sp^3 structure should lead to significantly increased reactivity. Compression of GBMH in the DAC under non hydrostatic conditions led to significant shifts in the G peak ~1560 cm-1 (arrow, Fig 2). Upon decompression there is a complete disappearance of the G peak (Fig 2, inset). UV Raman analysis of the depressurized material is on-going.

Formation of 3-D carbon networks via cycloaddition reactions (e.g. 4+2 Diels Alder) provides an alternative strategy to trap molecular H_2, and the 4+2 Diels Alder reaction is both kinetically and thermodynamically favored at high pressure due to its negative activation volume and negative volume of reaction. Reaction between anthracene and 1,4-benzoquinone in xylene solvent serves as the first model high-pressure cycloaddition reaction, as the product is expected to be a 3D paddlewheel structure which has been theoretically shown to adsorb H_2.[2-4] Raman spectra at 514 nm (Fig. 3) show distinct differences after application of 440 MPa relative to the starting material, suggesting reaction. Additional analysis is on-going.

Thermodynamics dictate that pre-formed C-H structures will rearrange with increased pressure, yet the final carbon-hydrogen interactions may be dependent upon the mechanism by which hydrogen is introduced. Molecular dynamics with reactive force fields (ReaxFF) have been implemented in modeling compressed hydrocarbons and hydrogenated C_{60} (mainly $C_{60}H_{36}$ and $C_{60}H_{18}$, systems also being investigated experimentally). The cage structure of C_{60} and the interplay between inter-ball polymerization into sp^3 geometries and on-ball sp^3 sites of H attachment could be beneficial for loading hydrogen into local traps. Compression of two initial crystal structures of $C_{60}H_{36}$ was simulated by ReaxFF under a series of high pressures around 20GPa. The results show polymerization of C_{60} and release of molecular hydrogen. A simple theoretical model for understanding the propensity for H release during compression of various hydrocarbon systems has been designed in which a volume is associated with each bond type (C-H, etc.). The model shows consistency with simple alkane molecules. The model will be extended further to apply to complex hydrocarbons with the support of ReaxFF calculations. Experimental validation of these studies is underway using synthesis techniques that have been modified to reduce oxidation of the product. Using a combination of solid state ^{13}C NMR and FTIR, we have verified synthesis of $C_{60}H_{18}$ and $C_{60}H_{28}$. These materials will be used to validate the theoretical predictions.

References

1. Orimo, S.; Majer, G.; Fukunaga, T.; Zuttel, A.; Schlapbach, L.; Fujii, H., Hydrogen in the mechanically prepared nanostructured graphite. *Appl Phys Lett* **1999,** *75* (20), 3093-3095.
2. Ghanem, B. S.; Hashem, M.; Harris, K. D. M.; Msayib, K. J.; Xu, M. C.; Budd, P. M.; Chaukura, N.; Book, D.; Tedds, S.; Walton, A.; McKeown, N. B., Triptycene-Based Polymers of Intrinsic Microporosity: Organic Materials That Can Be Tailored for Gas Adsorption. *Macromolecules* **2010,** *43* (12), 5287-5294.
3. McKeown, N. B.; Budd, P. M.; Book, D., Microporous polymers as potential hydrogen storage materials. *Macromolecular Rapid Communications* **2007,** *28* (9), 995-1002.
4. Wong, M.; Van Kuiken, B. E.; Buda, C.; Dunietz, B. D., Multiadsorption and Coadsorption of Hydrogen on Model Conjugated Systems. *Journal of Physical Chemistry C* **2009,** *113* (28), 12571-12579.

Future Plans

Future work will include a full analysis of the Raman spectra gathered for both linear (anthracene and pentacene) and staggered (phenanthrene and picene) polyaromatic ring systems, as well as those expecting to undergo cycloaddition reaction. This analysis will lead us to determine the bonded hydrogen content of the polymer and can allow us to develop a tool to determine the hydrogen content of many amorphous carbons. Potential hydrogen evolution/trapping will be evaluated by monitoring the appearance of the hydrogen Q-band at ~4200 cm^{-1}. Experiments will be

done both with and without the presence of hydrogen gas to examine if these amorphous carbons can trap hydrogen within their polymer structures. The reactivity of the precursor in the formation of trapped H_2 will be determined. Hydrogenated C_{60} will be compressed in the diamond anvil cell to validate the theoretical predictions. The hydrogenated amorphous carbon prepared via hydrogenating graphite in the ball mill will be further studied to determine if the carbon transformations are reproducible and to ascertain the structural changes occurring for this system (relative to benzene).

DOE Sponsored Publications in 2010-2011

Liu, XM; Tang, Y; Xu, ES; Fitzgibbons, TC; Gutierrez, HR; Tseng HH; Yu, MS; Tsao, CS; Badding, JV; Crespi, VH; Lueking, A.D. In-Situ Micro Raman Detection of Reversible Basal Plane Hydrogenation in Pt-doped Activated Carbon, Journal of American Chemical Society, Submitted 2011.

Liu, XM; Rather, S.U.; Li, Q.; Tang, Y; Lueking, A.D.; Zhao, Y.; Li, J. Hydrogenation of CuBTC framework with the introduction of a PtC hydrogen spillover catalyst. ACS Nano, Submitted 2011.

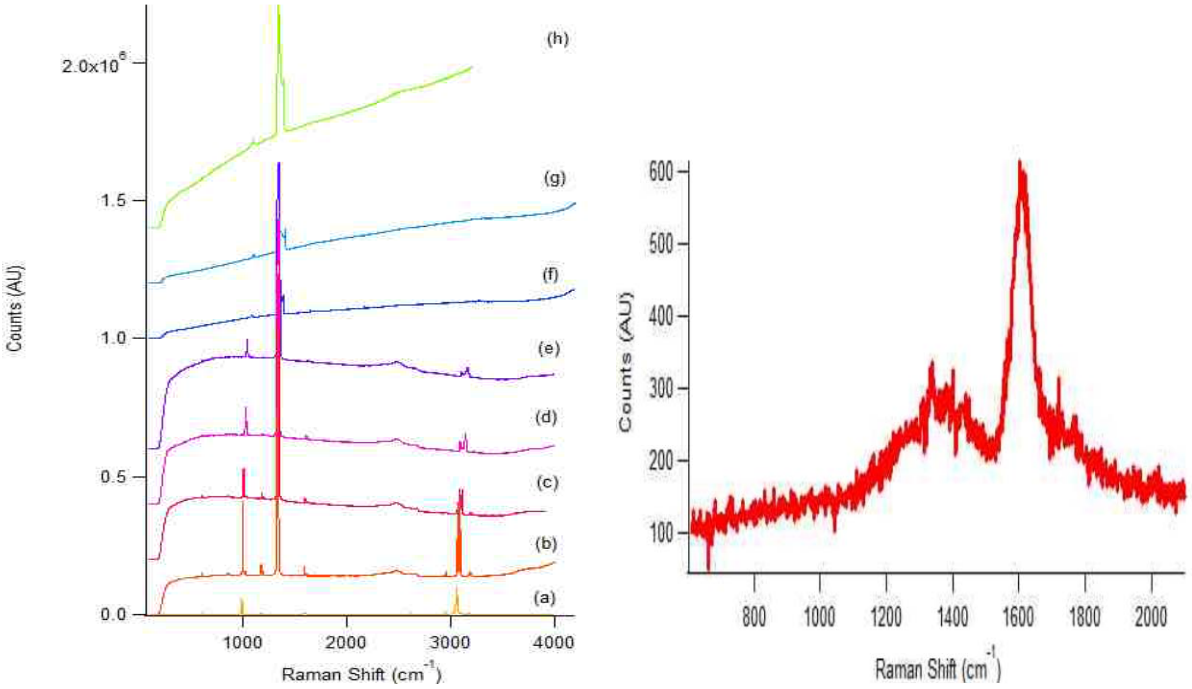

Figure 1: Left: Raman of Benzene at different pressures at 514 nm excitation: (a) ambient liquid benzene, (b-g) are benzene at 2.23, 3.84, 7.81, 10.32, 26.69, and 33.22 GPa, respectively, and (h) is quenched polymer. The intense peak seen in spectra (b-h) at 1333 cm^{-1} is signal from the diamond anvil cell, and the broad peak between 2200 and 2700 cm^{-1} is due to the second order diamond signal. Right: After pressure reduction the polymerized benzene from (h) is measured in the Deep UV at 244 nm, and shows features characteristic of solid carbon.

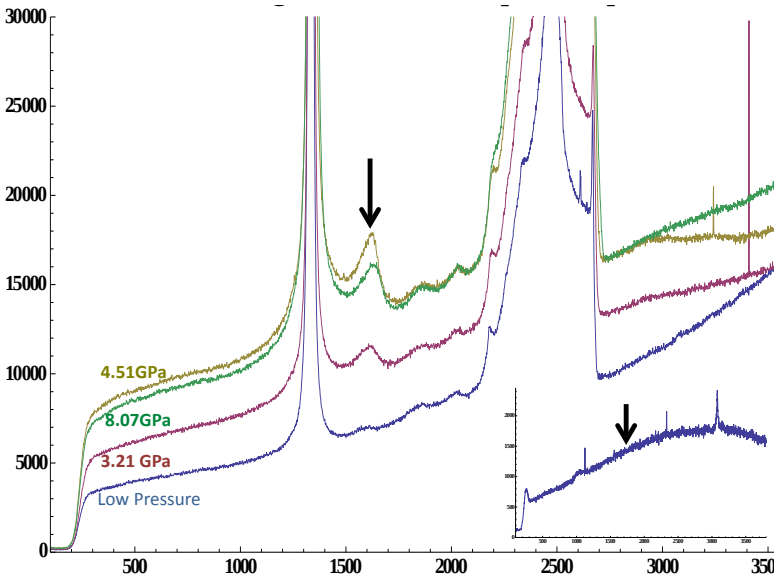

Figure 2: Compression of amorphous CH material in the diamond anvil cell to (from bottom): loading, 3.21 GPa, 8.07GPa, 4.51 GPa. Inset shows the recovered material after decompression.

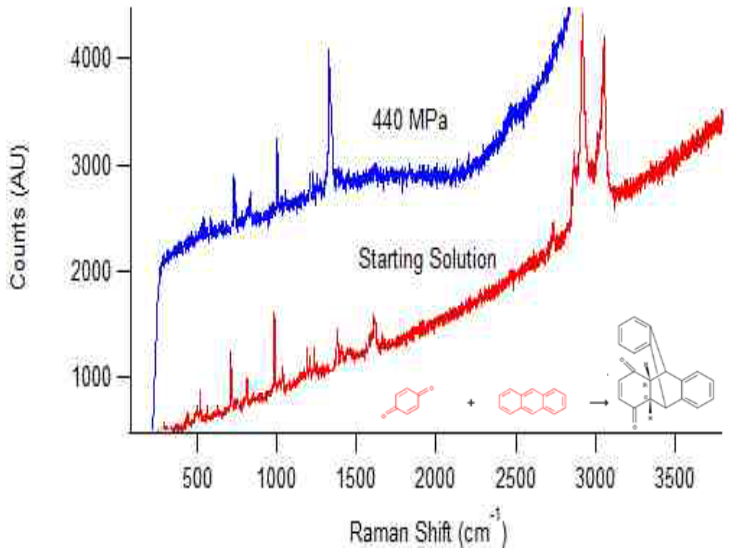

Figure 3: Anthracene and 1,4-benzoquinone in the presence of xylenes before and after application of 440 MPa, in which a 4+2 Diels Alder cyloaddition reaction (inset) is expected. 514 nm excitation.

A Fundamental Study of Inorganic Clathrates and other Open-Framework Materials

George S. Nolas (gnolas@usf.edu)
Department of Physics, University of South Florida, Tampa, 33620

Program Scope

For many materials the preparation of high-quality single crystals by traditional techniques is especially challenging. Examples include cases where the elemental constituents have greatly differing melting points and/or vapor pressures, when the desired compound is thermodynamically metastable, or where growth with participation of the melt is generally not possible. A variety of synthetic techniques have been successfully employed in the preparation of intermetallic compounds however these approaches are typically not possible for the majority of new or metastable phases. As such, conventional crystal growth techniques are here generally inapplicable. New crystal growth techniques and apparatus are therefore essential in investigating the intrinsic and fundamental properties of new and novel materials. In this project we successfully initiated new approaches for the crystal-growth of intermetalic clathrate-II materials and their subsequent intrinsic properties measurements. The rich variety of compositional variations in intermetallic clathrate-II materials represents an ideal material system to investigate new crystal growth techniques as well as the fundamental properties of group 14 elements in novel crystal structures and bonding schemes. The intellectual merit of investigating this material system is very closely tied with its novel structure and the corresponding physical properties it exhibits, and aims to develop important fundamental research towards potential applications in power-conversion and energy storage technologies.

Recent Progress

The synthesis of single-crystal type II clathrates is perhaps the most conspicuous aspect of this DOE project. Initially, these materials were prepared *via* the thermal decomposition of the Zintl compound Na_4Si_4 under vacuum. This approach was optimized under this DOE project to produce large-yield relatively high-purity microcrystalline powders of Na_xSi_{136}, and thus continues to be employed in our research. Accurate measurements of electrical and thermal transport on clathrates are, however, highly challenging due to difficulties in the preparation of dense specimens free from detrimental grain boundary affects.[1] We have therefore developed two separate synthetic approaches for single-crystal growth of clathrates of different composition and types.

The use of SPS for the crystal growth of $Na_{24}Si_{136}$ is depicted in Figure 1. A pulsed DC electrical current was sourced through the Na_4Si_4 precursor and graphite die which simultaneously acted for application of uniaxial pressure to the precursor. This approach resulted in single-phase crystals of $Na_{24}Si_{136}$ at 600 °C and 100 MPa. $Na_{24}Si_{136}$ forms by oxidation of Si_4^{4-} at the anode, whereas sodium is reduced at the cathode. Upon oxidation of the Si_4^{4-} cluster anions, the clathrate framework is formed, while simultaneously encapsulating sodium in the resulting Si_{20} and Si_{28} cages of the silicon framework. The process is driven by the electric field and the evaporation of Na formed at the cathode. This approach allowed for intrinsic transport properties characterization of $Na_{24}Si_{136}$ for the first time.

In a separate and different approach, selective single crystal growth of both Na_8Si_{46} and $Na_{24}Si_{136}$ was achieved. In this approach, alkali metal is removed from the Na_4Si_4 precursor by reaction of the vapor phase with spatially separated graphite in an effectively closed volume under uniaxial pressure (Figure 2). A customized reaction vessel comprising a simple graphite punch and die design was constructed such that uniaxial pressure was applied to the specimen while heated in a tube furnace. To prevent the adhesion between graphite and clathrate crystals, a 1 mm thick layer of dry NaCl powder is introduced between the Na_4Si_4 precursor and graphite. The NaCl layer serves as an effective passive physical barrier to direct reaction between graphite and Na_4Si_4, but allows diffusive exchange of Na *via* the vapor phase. This C-NaCl-Na_4Si_4-NaCl-C "sandwich" is encapsulated on all sides by graphite foil to impede the escape of Na vapor. The Na vapor, released from the Na_4Si_4 precursor, reacts with the spatially separated graphite,

forming intercalation compounds Na_xC. This approach allows for selectivity in crystal growth of Na_8Si_{46} or $Na_{24}Si_{136}$ by merely changing the reaction temperature (Figure 2).

It is noteworthy that direct synthesis and crystal growth of these phases from the elements is unsuccessful, and the available Na-Si equilibrium diagram describes only a eutectic between Na_4Si_4 and Si and the absence of the clathrate phases.[2] Single-crystal XRD studies and transport properties measurements on several different crystals of Na_8Si_{46} and $Na_{24}Si_{136}$ resulted in the detailed investigation of the structure and bonding of these materials, their intrinsic low temperature transport properties, as well as an indication of the reproducibility of our two crystal-growth techniques. The intrinsic structural and transport properties of both clathrate compositions were revealed for the first time through these two synthetic techniques.

The synthesis of "partially-filled" Na_xSi_{136} specimens in microcrystalline form via thermal decomposition of Na_4Si_4, under this DOE project, allowed for a thorough investigation of the relative "cage" occupancy, unit cell contraction with increased Na concentration for $x < 8$, and dynamic disorder increase with decreasing Na concentration.[3] Our systematic investigation on a whole range of "guest" occupancies allowed for a comprehensive and fundamental structural analysis of Na_xSi_{136} that will serve as a reference for our work on single crystals, as well as for other research groups. This synthesis approach continues to prove important in investigating intermetallic clathrates.

Employing a combination of two approaches described above, namely crystal-growth followed by thermal decomposition, Na_xSi_{136} clathrate-II crystals were synthesized. Preliminary examination of the framework inter-atomic distances and bond angles from our single-crystal XRD analyses reveal interesting trends. The average Si-Si and Na(2)-Si bond lengths, where Na(2) represents $Na@Si_{28}$, increase with increasing Na concentration, although the Na(2)-Si2 distance decreases. This results in a larger isotropic thermal parameter at Na(2) with decreasing Na content. This would presumably result in a lower thermal conductivity, κ, at lower Na concentrations. These preliminary results demonstrate the opportunity to better understand the complex structure-property relationships that define these materials, as well as the suitability of this material system for energy-related applications. Our new approach for the preparation of Na_xSi_{136} also resulted in tightly packed, dense clusters of the crystals that allow for an investigation into the transport properties of polycrystalline Na_xSi_{136} as a function of x without the necessity for consolidation of fine powders, as previously attempted (Figure3).[1] This data is very revealing in light of the anticipated metal-insulator transition at $x \sim 8$,[4] in addition to the unit cell decrease with increasing x up to $x = 8$ followed by a unit cell increase with x above this point.[3]

Future Plans

The intrinsic transport properties measured on single-crystals of $Na_{24}Si_{136}$ grown by SPS and from the slow controlled removal of Na *via* Na vapor phase intercalation of graphite serve to illustrate some of the capabilities now available through the use of these two synthetic approaches for the preparation, crystal growth and physical properties characterization of intermetallic clathrates. We can now apply these synthetic approaches to other alkali metal tetrelide precursors. Single crystals of the ternary clathrate-II $Na_{16}Cs_8Ge_{136}$ of significantly larger size than those typically obtained from direct reaction of a stoichiometric mixture of the elements [5] can also prepared from the ternary precursor $NaCsGe_2$. We expect these crystal growth techniques to be generally applicable to a variety of precursors; further investigation of the mechanisms behind the growth process and the application to other material systems will be one aspect of our future work plan.

The key aspect of this work, however, is not in overcoming the extrinsic effects that were previously unavoidable when consolidating microcrystalline specimens of these compositions, but in the fact that these synthetic approaches affords us the ability to explore key physical concepts associated with the structure-property relationships in intermetallic clathrate materials of differing compositions and "guest" concentrations. The availability of single crystals allows for such exploratory research. In addition, other new and novel materials can by prepared by one or both of these approaches, allowing for the further investigation into new materials with potentially unique properties. For example, structures with host frameworks composed solely of Group 14 elements in which the guest species are not entirely

encapsulated in closed cages, such as intermetallic clathrates, but rather in tunnel or channel frameworks are far less common.[6] One such example is $Na_{1-x}Ge_{3+z}$, a new binary framework phase in the Na–Ge system that constitutes a rare example in which an exclusively Group 14 framework crystallizes in a tunnel configuration reminiscent of those found in the microporous zeolites.[7] This composition represents a new crystalline binary phase in the Na–Ge system that has not previously been synthesized nor its crystal structure determined.

References

1. M. Beekman and G.S. Nolas, Physica B **38**3, 111 (2006).
2. H. Morito, T. Yamada, T. Ikeda, H. Yamane, J. Alloys Comp**. 480**, 723 (2009).
3. M. Beekman, E.N. Nenghabi, K. Biswas, C.W. Myles, M. Baitinger, Y. Grin and G.S. Nolas, Inorg. Chem. **49**, 5338 (2010).
4. V.I. Smelyansky and J.S. Tse, Chem. Phys. Lett. **264**, 459 (1997).
5. S. Bobev and S.C. Sevov, J. Am. Chem. Soc**. 121**, 3796 (1999).
6. A. K. Cheetham, G. Fe´rey and T. Loiseau, Angew. Chem., Int. Ed. **38**, 3268 (1999).
7. M. Beekman, S. Stefanoski, W. Wong-Ng, J.A. Kaduk, Q. Huang, C. Reeg, C.R. Bowers, G.S. Nolas, J. Solid State Chem. **183**, 1272 (2010).

DOE Sponsored Publications in 2009 – 2011 for Current Grant (one patent and 13 publications)

[M. Beekman and G.S. Nolas, "Novel Methods for Solid State Crystal Growth", Patent Pending, Serial No. 12/859,534, filed August 19, 2010]
1. S. Stefanoski, M. Beekman, W. Wong-Ng, P. Zavalij and G.S. Nolas, 'A simple approach for selective crystal growth of intermetallic clathrates', Chem. Mater. **23**, 1491 (2011).
2. S. Stefanoski, J. Martin and G.S. Nolas, 'Low temperature transport properties and heat capacity of single-crystal Na_8Si_{46}', J. Phys.: Condens. Mater **22**, 485404 (2010).
3. A.D. Ritchie, M.A. MacDonald, P. Zhang, M.A. White, M. Beekman, J. Gryko and G.S. Nolas, 'X-ray absorption spectroscopy studies of local structure and electronic properties of Na_xSi_{136} ($0<x<24$) clathrates', Phys. Rev. B **82**, 155207 (2010).
4. M.Beekman, R.P. Hermann, A. Mochel, F. Juranyi and G.S. Nolas, 'Low-energy Na phonon modes in silicon clathrate-II', J. Phys.: Cond. Matter **22**, 355401 (2010).
5. M. Beekman, E.N. Nenghabi, K. Biswas, C.W. Myles, M. Baitinger, Y. Grin and G.S. Nolas, 'Framework contraction in Na-stuffed Si(*cF*136)', Inorg. Chem. **49**, 5338 (2010).
6. M. Beekman, S. Stefanoski, W. Wong-Ng, J.A. Kaduk, Q. Huang, C. Reeg, C.R. Bowers and G.S. Nolas, 'Structure and thermal conductivity of Na1-xGe3+z', J. Solid State Chem. **183**, 1272 (2010).
7. M. Beekman, W. Schnelle, H. Borrmann, M. Baitinger, Yu. Grin and G.S. Nolas, 'Intrinsic electrical and thermal properties from single crystals of $Na_{24}Si_{136}$', Phys. Rev. Letter **104**, 018301 (2010).
8. M. Beekman, M. Baitinger, H. Borrmann, W. Schnelle, K. Meier, G.S. Nolas, Y. Grin, 'Preparation and crystal growth of $Na_{24}Si_{136}$: An electrochemical solid state route', J. Amer. Chem. Soc. **131**, 9642 (2009).
9. M. Beekman, J.A. Kaduk, J. Gryko, W. Wong-Ng, A. Shapiro and G.S. Nolas, 'Synthesis and characterization of framework-substituted $Cs_8Na_{16}Cu_5Ge_{131}$', J. Alloy Comp. **470**, 365 (2009).
10. A.N. Mansour, M. Beekman, W. Wong-Ng, and G.S. Nolas, 'Local structure of Cu in $Cs_8Na_{16}Cu_5Ge_{131}$ type II clathrate', J. Solid State Chem, J. Solid State Chem. **182**, 107 (2009).
11. M. Beekman, C.P. Sebastian, Y. Grin and G.S. Nolas, 'Synthesis, Crystal Structure, and Transport Properties of $Na_{22}Si_{136}$', J. Electronic Materials **38**, 1136 (2009)
12. G.S. Nolas, X. Lin, J. Martin, M. Beekman and H. Wang, 'Open-structured Materials: Skutterudites and Clathrates', J. Electronic Materials **38**, 1052 (2009).
13. S. Stefanoski, L.N. Reshetova, A.V. Shevelokov, and G.S. Nolas, 'Low-Temperature Transport Properties of $Sn_{24}P_{19.3}Br_8$ and $Sn_{17}Zn_7P_{22}Br_8$', J. Electronic Materials **38**, 985 (2009).

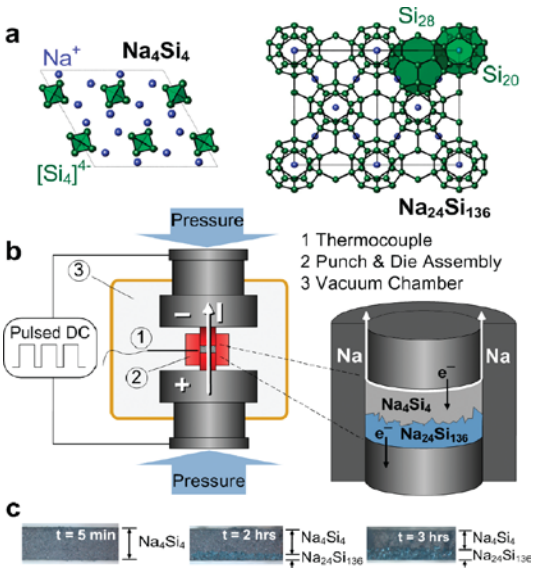

Figure 1. (a) Crystal structures of Na_4Si_4 and $Na_{24}Si_{136}$ with Si_{20} and Si_{28} cages and Si_4 tetrahedrons highlighted. (b) SPS setup. (c) Cross sections of SPS-treated specimens at 600 °C and 100 MPa.

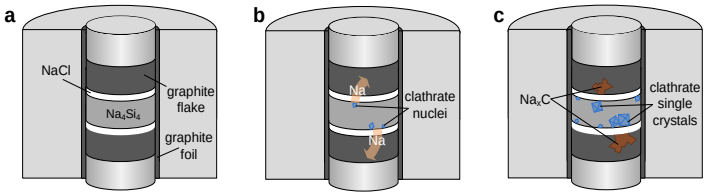

Figure 2. Simple schematic illustrating the Na_8Si_{46} and $Na_{24}Si_{136}$ crystal growth processes. (a) The initial precursor configuration, under uniaxial pressure in the punch and die. (b) Local composition change and nucleation of the clathrate phase. (c) Formation of intercalated graphite and clathrate crystal growth.

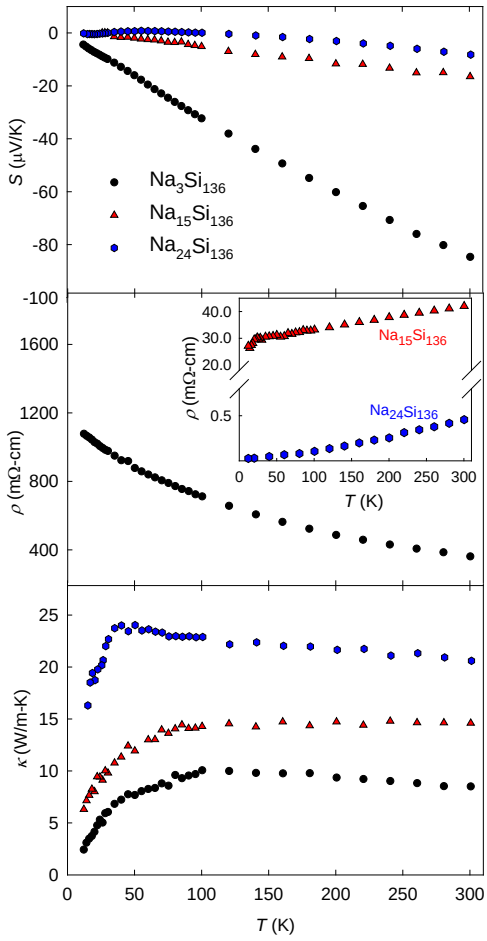

Figure 3. Low temperature resistivity, thermopower and thermal conductivity of single-crystal $Na_{24}Si_{136}$ as well as polycrystalline Na_3Si_{136} and $Na_{15}Si_{136}$.

Enhanced Hydrogen Storage in Boron-Doped Carbon Nanospaces

Peter Pfeifer,[1] Carlos Wexler,[1] M. Frederick Hawthorne,[1,2,3] Mark W. Lee,[2,3] Satish S. Jalisatgi[3]
Departments of [1]Physics, [2]Chemistry, and [3]Radiology
University of Missouri, Columbia, MO 65211

Project Scope

This project is an integrated synthesis/characterization/computational effort to develop novel materials—monolithic boron-doped carbon made from polymeric precursors, crisscrossed by networks of nanopores—expected to have superior hydrogen storage capacities not available in other materials. The aim is to develop a fundamental understanding of the mechanisms by which boron, through its electron-deficient electronic structure and long-range effect on distant carbon atoms, combined with appropriate pore geometries, creates deep potential wells which can hold films of physisorbed molecular hydrogen at densities much higher than undoped carbon. Such high-density films and their understanding at the molecular, statistical mechanical, and macroscopic thermodynamic level are critical for the rational design of high-performance materials with controlled reversible storage characteristics at low pressure and room temperature. The program supports one of the high-priority research directions of the National Hydrogen Storage Project.

Recent Progress

Since the start of this project we built an extensive "library" of nanoporous carbons, this library includes samples which have achieved record-breaking H_2 storage: gravimetric excess adsorption of 0.073 ± 0.003 kg H_2/kg carbon (7.3 wt%), gravimetric storage capacity of 0.106 ± 0.005 kg H_2/kg carbon (11 wt%), and volumetric storage capacity of 0.040 ± 0.003 kg H_2/liter carbon, at $T = 80$ K and $p = 50$ bar. This library of carbons was the result of a broader research effort by our collaboration, with partial support from DOE/EERE and US Navy, in which high-surface-area activated carbons, made from corncob in a multistep process ("biocarbon"), are investigated. A significant effort went into classifying the members of the library according to their structure and their potential to store hydrogen [1]. At present the library consists of over 100 different carbons, including undoped activated biocarbon, boron doped activated biocarbons, and carbons based on synthetic polymers (mostly poly-vinylidene chloride-*co*-vinyl chloride), PVDC, with and without boron copolymerization). Typical BET surface areas for biocarbons are in the $\Sigma = 2{,}000$–$3{,}100$ m^2/g range. Synthetic carbons currently have $\Sigma = 500$–$1{,}000$ m^2/g. Figure 1 shows a comparison of the gravimetric excess adsorption (80 K, 303K) of polymer-based materials HS;0B (no boron) and HS;2B (1.7% B) and several biocarbons. PVDC samples HS;0B and HS;2B have much lower surface areas, 600-700 m^2/g; yet their gravimetric excess adsorption, especially HS;0B at 303 K, competes with, or outperforms, that of the high-surface carbons. Sample HS;2B shows significant enhancement in the *low pressure* region, indicating the presence of high-binding energy sites, consistent with our theoretical predictions that boron enhances H_2 binding [2]. The large capacities of the PVDC samples can be explained from their relatively large number of small pores (Fig. 1), which are most favorable for H_2 adsorption[1,2]. This preponderance of small pores should produce large binding energies and thus result in high adsorption, particularly at room temperature.

Our understanding on how boron enhances the interaction energy of H_2 with carbon hinges on the presence of an empty p_z orbital in a boron atom that substitutes a carbon in an sp^2 structure like graphene/graphite. Our early boron-doped carbons had failed to show promising H_2 sorption characteristics; this was due to the fact that our samples were exposed to oxygen at some point during the manufacture/processing/characterization/ measurement. During 2010, upgrades to the laboratory equipment allowed us to keep samples under oxygen-free conditions at all times. Our first

batch of samples processed in the new facilities show significant promise: we observed a 30% enhancement of the excess adsorption per unit area at room temperature and high pressures. This increase in areal excess adsorption at high T & P indicates an increase in *average* binding energy, not solely highest binding energy. In addition, we performed FTIR spectra and observed a peak at 1022cm^{-1} consistent with the presence of B-C bonds.

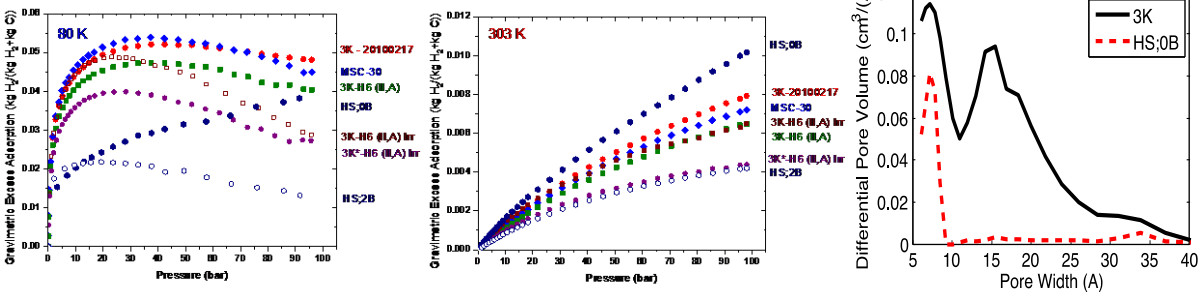

Fig. 1. Gravimetric excess adsorption of H_2 on PVDC and biocarbons at T = 80 K and 303 K, and representative pore size distributions.

The isosteric heat of adsorption, ΔH, equals the heat released when a molecule is adsorbed at constant coverage (absolute adsorption). It can be computed from two adsorption isotherms via the Clausius-Clapeyron (CC) equation, $\Delta H = RT_1T_2/(T_2 - T_1)\ln(p_2/p_1)$, where p_i, T_i, are two pressures and temperatures for the same *absolute* adsorption. This requires conversion of experimental *excess* adsorption isotherm, G_{ex}, into *absolute* adsorption, $G_{abs} = G_{ex} + \Sigma \times t_{film} \times \rho_{gas}$, where Σ, t_{film}, and ρ_{gas} are the specific surface area of the adsorbent, thickness of the adsorbed film, and density of bulk gas. Incorrectly using the excess adsorption leads to an unphysical rise in ΔH with coverage, the smallest value of Σt_{film} which results in a decreasing ΔH is an experimental determination of a lower bound for the adsorbed film volume (Fig. 2). Direct experimental determination (microcalorimetry) of ΔH of hydrogen at 77 K give comparable results.

Inelastic neutron scattering from hydrogen adsorbed in carbon: IINS is capable of probing both energy levels and quantum states of adsorbed H_2 directly. We completed and published the theoretical analysis [3] (Fig. 3), and have recently conducted Q-resolved experiments at ORNL, where we observed the 1st rotational transition ($E_1 - E_0$) at 14.7 meV and a roto-vibrational peak at 29.5 meV (Fig. 3). The method currently shows potential for characterization of sub-nm pores. Broadening of the peaks yields information about the recoil of the H_2 molecules and coupling to phonon modes.

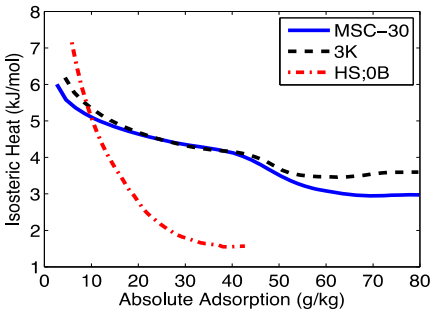

sample	type	l (Å)	m_e/Σ (μg/m^2)	Δh (kJ/mol)
MSC-30	AC	5.4	19.6	6.0-3.0
3K	AC	5.1	21.0	6.2-3.6
HS;0B	PVDC	5.3	52.8	7.2-1.6
Li+Wu(2009)	Zeolite NaX		29.3	4.1-?
Saha (2008)	MOF-177		33.6	4.0-0.5
Saha (2009)	MOF-5		28.1	2.6-2.1

Fig. 2. Isosteric heats of adsorption for 3 carbons. Table of ΔH and t_{film} for various samples.

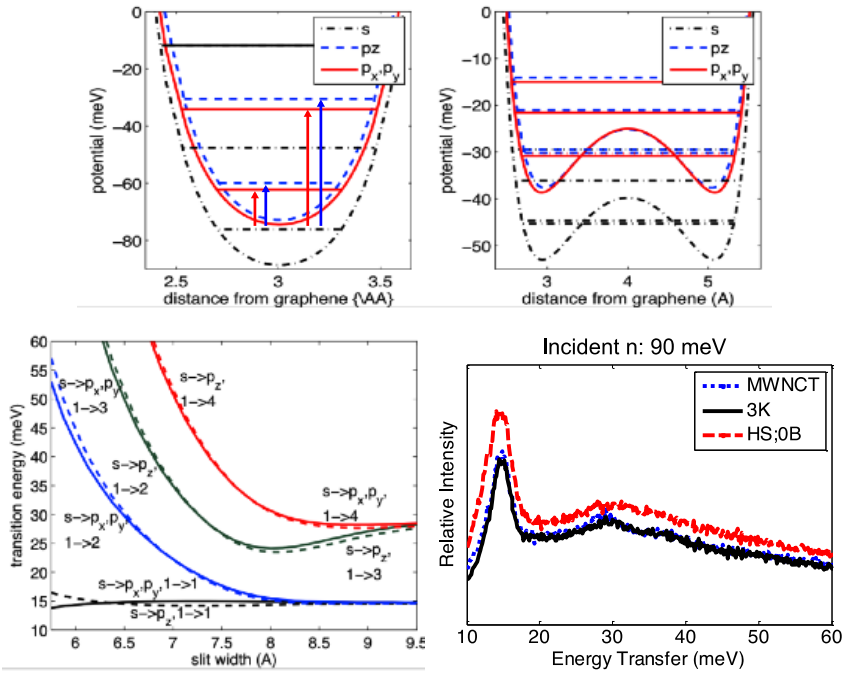

Fig. 3. Top: quantum energy levels for roto-vibrational states of H_2 in a 6 Å and 8 Å slit-shaped pore. Left: IINS peak locations vs. pore width. Right: Q-averaged IINS spectra.

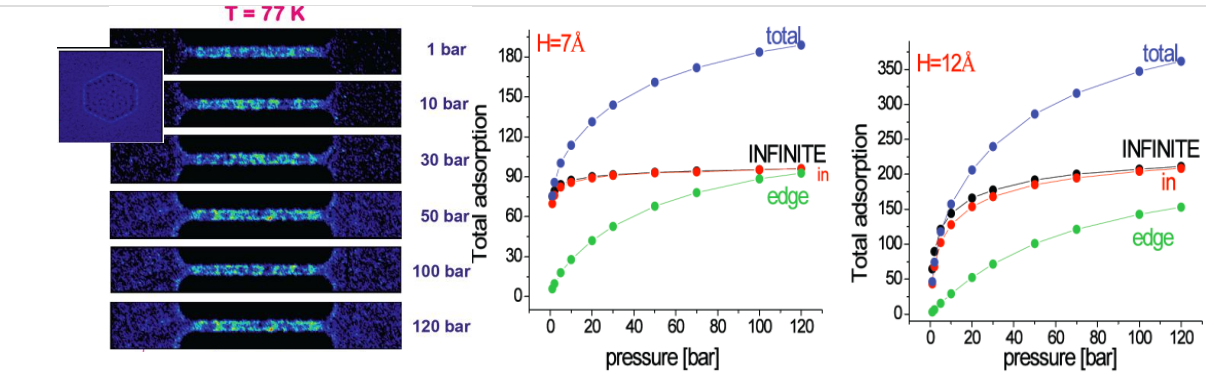

Fig. 3. Left: Simulation cells. Right: total adsorption for two pore widths.

Improved models for hydrogen adsorption in heterogeneous materials. We are in the process of completing extensive Grand canonical Monte Carlo simulations in non-traditional geometries (beyond slit- and strip-shaped pores, Fig. 4). We observe significant adsorption at the *edges* of the pores (30-50%) and adsorption isotherms that keep rising significantly even as pressure is increased. These weak adsorption sites may explain some of the experiments where a maximum of the excess adsorption is not seen.

Future Plans

For the next year we plan to continue fabrication, optimization and characterization of PVDC-derived samples, with and without boron under oxygen-free conditions. Characterization methods will include: N_2 subcritical adsorption isotherms, H_2 adsorption at room and cryogenic temperatures, USAXS/SAXS characterization of pore structures, IINS experiments (and theory), characterization by NMR and FTIR, and SEM/TEM imaging. We will also continue our effort to build an extensive library of carbon samples, to continue our GCMC simulations to build a library of "simulated carbons" for comparison, and to improve our ab initio potentials of interaction of hydrogen and boron-doped carbon. We will also theoretically and computationally consider changes

in the adsorbants due to the presence of high densities of H_2 (e.g., "pore bending"), which we have hypothesized (not shown in this report) may explain the discrepancy between the high sorption capacity of PVDC samples and the low isosteric heats of adsorption derived from CC equation.

UNDERSTAND HS;0B
Show presence of BC bonds in PVDC samples.
More IINS experiments are scheduled at ORNL and theoretical analysis of the recoil interactions is underway.

References

1. J. Burress, M. Kraus, M. Beckner, R. Cepel, G. Suppes, C. Wexler, and P. Pfeifer, *Nanotechnology* **20**, 204026 (2009).
2. P. Pfeifer, M.F. Hawthorne, and C. Wexler. In: *DOE Hydrogen Program, 2009 Annual Progress Report*, ed. S. Satyapal (U.S. Department of Energy, Washington, DC, 2009; DOE/GO-102009-2950), p. 824.
3. L. Firlej, Sz. Roszak, B. Kuchta, P. Pfeifer, and C. Wexler, *J. Chem. Phys.* **131**, 164702 (2009).
4. R. Olsen, L. Firlej, B. Kuchta, H. Taub, P. Pfeifer, and C. Wexler, *Carbon* **49**, 1663- (2011).

DOE Sponsored Publications in 2009-11 from Current Grant

5. R. Olsen, M. Beckner, J. Romanos, P. Pfeifer, and C. Wexler, "Best Methods for Determining the Coverage-Dependent Isosteric Heat of Adsorption for Hydrogen," *Langmuir* (under review).
6. C. Hou, S. Gheorghiu, V.H. Huxley, and P. Pfeifer, "Reverse Engineering of Oxygen Transport in the Lung: Adaptive Control from Fractal Networks." *PLoS Comput. Biol.* **6** (8), e1000902 (2010).
7. R. Olsen, "Investigations of Novel Hydrogen Phenomena," Ph.D. Dissertation, University of Missouri, 2011.
8. M. Kraus, "Fundamental building blocks of nanoporous networks from ultra-small-angle x-ray scattering (USAXS) and small-angle x-ray scattering (SAXS) experiments," Ph.D. Dissertation, University of Missouri, 2010.
9. S. Kjelstrup, M.-O. Coppens, J. Pharoah, and P. Pfeifer, "Nature-Inspired Energy and Material Efficient Design of a Polymer Electrolyte Fuel Cell." *Energy Fuels* **24**, 5097-5108 (2010).
10. R. Olsen, L. Firlej, B. Kuchta, H. Taub, P. Pfeifer, and C. Wexler, "Sub-nanometer characterization of activated carbon by inelastic neutron scattering," *Carbon* **49**, 1663-1671 (2011).
11. L. Firlej, B. Kuchta, M. Roth, and C. Wexler, "Molecular simulations of intermediate and long alkanes adsorbed on graphite: Tuning of non-bond interactions," *J. Mol. Model.* **17**, 811 (2011).
12. B. Kuchta, L. Firlej, Sz. Roszak, P. Pfeifer, and C. Wexler, "Influence of structural heterogeneity of nanoporous sorbent walls on hydrogen storage," *Appl. Surf. Sc.* **256**, 5270 (2010).
13. B. Kuchta, L. Firlej, P. Pfeifer, and C. Wexler, "Numerical estimation of hydrogen storage limits in carbon based nanospaces," *Carbon* **48**, 223 (2010).
14. B. Kuchta, L. Firlej, R. Cepel, P. Pfeifer, and C. Wexler, "Structural and energetic factors in designing a nanoporous sorbent for hydrogen storage," *Coll. Surf. A: Physicochem. Eng. Apsects* **357**, 61 (2010).
15. C. Wexler, R. Olsen, P. Pfeifer, B. Kuchta, L. Firlej, and Sz. Roszak, "Numerical analysis of hydrogen storage in carbon nanopores," *Int. J. Mod. Phys. B* **24**, 5152 (2010).
16. M. Roth, M. Kaspar, C. Wexler, L. Firlej, and B. Kuchta, "Molecular dynamics simulations of submonolayer hexane and pentane films on graphite," *Mol. Simul.* **36**, 326 (2010).
17. L. Firlej, Sz. Roszak, B. Kuchta, P. Pfeifer, and C. Wexler, "Enhanced hydrogen adsorption in boron substituted carbon nanospaces," *J. Chem. Phys.* **131**, 164702 (2009).
18. C. Wexler, L. Firlej, B. Kuchta, and M. Roth, "Melting of Hexane Monolayers Adsorbed on Graphite: The Role of Domains and Defect Formation," *Langmuir* 25, 6596 (2009).

Session 1c

Function-Driven Materials Design: Use-Inspired Science

Session Chairs: Michael Coltrin, Sandia National Laboratories

This page is intentionally blank.

Solid Electrolyte and Solid Electrolyte Interphase (SEI) on Nanostructured Cathode Materials

Yoongu Kim, Zengcai Liu, Wujun Fu, Nancy Dudney, and Chengdu Liang
dudneynj@ornl.gov and liangcn@ornl.gov
Oak Ridge National Laboratory, Oak Ridge, TN 37831

Program Scope:

The program focuses on the structure and dynamics of SEIs on high surface area and high voltage cathode materials. The use of nanostructured materials and the high voltage operation of lithium-ion batteries has led to increased awareness of the formation, structure, and function of SEIs on the cathode due to the high surface-to- bulk ratio of nanomaterials that cause a high ratio of the SEI to the bulk material.[1-2] The SEI on the cathode is a phase which forms spontaneously from the reaction of the solid cathode material with the liquid electrolytes.[1] The uncontrolled spontaneous reactions pose uncertainties of the structure and therefore the properties of SEIs. The instability of the SEI eventually leads to the failure of materials and safety issues of the batteries. A well-defined SEI with optimized properties on the cathode is highly desirable for the pursuit of high performance materials for electric energy storage. This program investigates the formation, structure, and function of the SEI on the cathode by using advanced synthesis techniques that create well-defined structures of SEI, unraveling the mystery of spontaneously formed SEI. Instead of the spontaneous growth of SEI, we create a pre-formed SEI on the cathode with a known structure and electrochemical properties. Solid electrolytes of lithium phosphorous sulfides (LiPS) and lithium phosphorus oxynitride (LiPON) have been developed as the model compounds to correlate ionic conductivity, electrochemical stability, and chemical compatibility to chemical and crystal structures.

Recent Progress:

Novel synthesis approach for lithium phosphorous sulfides (LiPS) as potential SEI compounds: We have developed a solution-based approach that allows the synthesis of LiPS as potential model compounds for SEI. LiPS are solid electrolytes with superior ionic conductivities at room temperature. In particular, the binary Li_2S-P_2S_5 glass system, which exhibits high lithium ionic conductivity up to 10^{-3} S/cm and wide electrochemical window over 5 V, has attracted much attention in the research field.[3] The binary Li_2S-P_2S_5 electrolytes are generally synthesized via conventional solid-state synthesis at extremely high temperatures (up to 900) under vacuum or through long -period mechanical milling by using a ball mill apparatus. In some cases, materials of high ionic conductivity are metastable phases. The harsh synthesis conditions of high temperature exclude the solid-state synthesis of these metastable phases. Most importantly, the solid-state approaches are inapplicable to coating the nanostructured cathode materials. To enable the LiPS as a pre-formed SEI for cathode materials, we developed a facile, solution-based synthesis method by using organic solvents as the template to guide the formation of the pure, metastable Li_2S-P_2S_5 crystalline phase. We found that Li_2S reacts with P_2S_5 in acetonitrile (ACN) at room temperature. Elemental analysis reveals that the product is a crystalline, 2:1 stoichiometric compound of $Li_4P_2S_7$ with two ACN

molecules trapped in the crystal structure. X-ray diffraction (XRD) shows that the compound is a new compound of the Li_2S-P_2S_5 family of solid electrolytes. ACN molecules leave at 140 °C under vacuum. The crystalline structure is retained when ACN is partially removed, however the complete removal of ACN leads to the collapse of the crystalline structure. Upon further heating at 200 °C, the material evolves as a complex crystalline phase that needs further identification. Shown in Figure 1 is the powder XRD of the $Li_4P_2S_7$ treated under different conditions. Raman spectra of the products treated at different temperatures reveal that ACN does not chemically bond to $Li_4P_2S_7$, rather it acts as a template that stabilizes the crystal structure. The ionic conductivity of the new compound after the removal of ACN is 1.68×10^{-5} S/cm at room temperature, as determined by electrochemical impedance measurements. The activation energy of lithium-ion conduction is significantly influenced by the residual ACN molecules. The activation energy increased from 0.42 eV of the as-synthesized sample to 0.62 eV after the complete removal of ACN. Although the specific role of ACN on the conductivity is as yet unknown, it is clear that this facile solution-based synthesis method allows for the synthesis of novel solid lithium superionic conductors that could be applied as coatings to cathode materials as model compounds of SEI with well-defined chemical and crystalline structures.

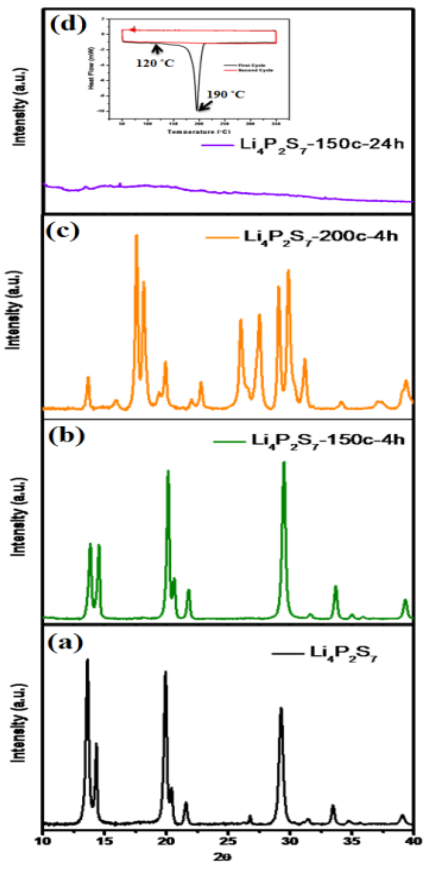

Figure 1. Powder X-ray diffraction patterns of the (a) as-synthesize $Li_4P_2S_7$; (b) heated at 150 °C for 4h under vacuum; (c) heated at 200 °C for 4h under vacuum; (d) heated at 150 °C for 24h under vacuum and the insert is the DSC of the as-synthesized compound.

Nano-scale LiPON coating for high voltage stability of $LiCoO_2$, and $LiMn_{1.5}Ni_{0.5}O_4$ cathodes: In spite of a high lithium content equivalent to 274 mAh·g^{-1}, the practical capacity of $LiCoO_2$ is limited to only 140 mAh·g^{-1} and a cut-off voltage of 4.2V versus Li in order to maintain a reasonable cycling stability. Charging to higher voltage leads to higher specific capacity, but this is offset by a more rapid capacity fade with cycling [4]. On the other hand, for solid state batteries the cycling to 4.4V is quite stable with 170 mAh·g^{-1} and a capacity fade below 0.1%/cycle [5]. Only at 4.5-5V does the cycling of a solid $LiCoO_2$ battery begin to degrade rapidly. Here the capacity loss is associated with phase transitions due to Li extraction [6] and the irreversible rearrangement of Co atoms forming defects and secondary phases, notably a spinel phase. Unless these irreversible defects are concentrated at the surface, it is unlikely that such lattice degradation processes above 4.5V will be impacted by modification of the particle interface with the electrolyte. So the focus of this study is to understand the impact of the solid electrolyte coating in a liquid electrolyte cell at voltages of 4.2 to 4.5V. An effective barrier coating will enhance the specific capacity of

the $LiCoO_2$ and enhance the tolerance for high voltage excursions. A combination of RF-magnetron sputtering with mechanical agitation of cathode powders was successful in coating $LiCoO_2$ particles with a 1nm thick amorphous LiPON film. Similar to reports of metal oxide coatings, the LiPON layer enables $LiCoO_2$ particles to deliver much better performance and capacity retention than the bare $LiCoO_2$ particles when cycled to at least 4.4V. After many cycles, the bare $LiCoO_2$ particles were badly cracked (Figure 2a) and the resistance attributed to the interface reactions increased dramatically. Degradation of the LiPON-coated $LiCoO_2$ particles, however, was far less (Figure 2b). A LiPON film, only 1 nm thick, is surprisingly effective for slowing interfacial chemical reactions between the electrolyte and the $LiCoO_2$ particles and may impede crack initiation or growth. This is an ideal system for fundamental study because the coating is formed at low temperature without exposure to precursors and solvents. For practical application, a very thin LiPON coating will limit damage to the cathode in the event of accidental or repeated voltage excursions above 4.2V; however, LiPON also impedes electron transport and reduces high power performance, particularly as the film thickness is increased.

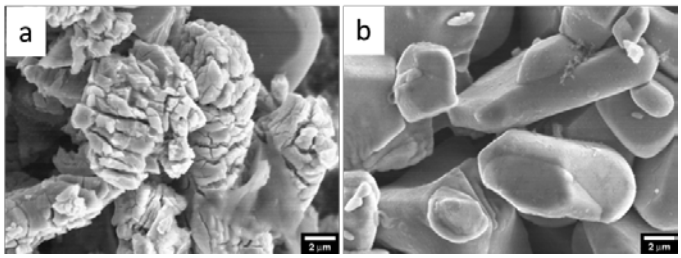

Figure 2. Morphologies of LiCoO2 without (a) and with (b) LiPON coating after cycled at 4.4 V.

$LiMn_{1.5}Ni_{0.5}O_4$ is a high voltage cathode material that cycles at 4.9V, which is only 0.1 V lower than the oxidation voltage of the electrolyte. The stability of electrolyte could be a problem for long-term cycling. Differing from the layered $LiCoO_2$ the degradation of the spinel $LiMn_{1.5}Ni_{0.5}O_4$ results from the dissolution of Mn in organic electrolytes and the intensified side reactions between the cathode and the electrolyte at high voltage.[7] When $LiMn_{1.5}Ni_{0.5}O_4$ is coated with LiPON, we find that the solid electrolyte effectively prevents the dissolution of Mn and retards the side reactions with the organic electrolytes. The cycling of LiPON coated electrode is more stable than the pristine electrode (Figure 3). Striking contrast was observed when the materials were cycled at 60 °C, a temperature that aggravates the Mn dissolution and accelerates side reactions. In cycles of 50 times, $LiMn_{1.5}Ni_{0.5}O_4$ cathode cells retained capacities at room temperature and 60°C when coated with a subnanometer LiPON layer. Thicker LiPON coatings led to highly restricted Li-ion and electron transports into $LiMn_{1.5}Ni_{0.5}O_4$ particles resulting in much lower than the expected capacities. The thinner LiPON coatings provided comparable capacities to uncoated $LiMn_{1.5}Ni_{0.5}O_4$ particles because they

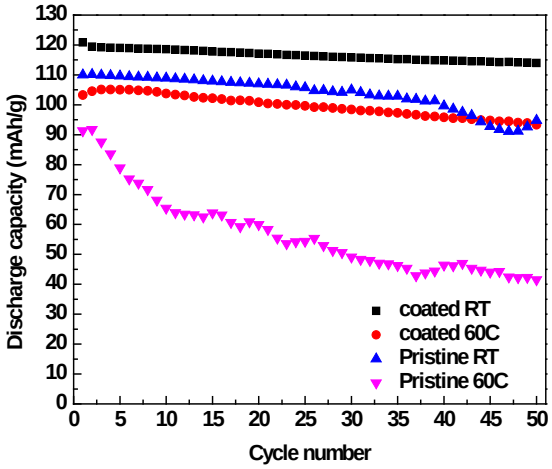

Figure 3. Cycling performance of $LiMn_{1.5}Ni_{0.5}O_4$ with and without LiPON coated at room temperature and 60 °C.

allowed sufficient Li-ion and electron transports.

Future Plans:

The LiPON coating on $LiCoO_2$ and $LiMn_{1.5}Ni_{0.5}O_4$ significantly promotes the cycling performance of cathode materials. These results show that a pre-formed SEI with known structure and ionic conductivity is superior to the spontaneously formed SEI. The properties of the SEI could be fine-tuned if a known structure of SEI is grown on the surface of the cathode. Therefore, we will seek to deepen the understanding of the function of solid electrolyte coatings. Key questions are the following: (a) Is there any additional SEI formed on top of the LiPON coating? (b) Can other solid electrolyte coatings on the cathode function in a manner similar to the LiPON coating? The lithium conductivity of LiPS is a few magnitudes higher than that of LiPON. However, a coating of LiPS on the cathode is often limited by the harsh synthesis conditions. The wet-chemistry synthesis approach developed in our lab provides the avenue for coating the cathode with LiPS through a simple solution-based route. This approach allows the synthesis and coating of a broad range of solid electrolytes on the cathode. We will apply the new synthesis approach to the formation of SEIs with various chemical compositions of phosphate and thiophosphate solid electrolytes. With a thorough characterization of the crystal and chemical structures of the solid electrolyte coating, we expect to derive a fundamental understanding of the SEI on cathode and guide the research of advanced materials for electrical energy storage.

References:

1, Edström, K.; Gustafsson, T.; Thomas, J.O., *Electrochim. Acta*, 50, 397 (2004).

2, Bruce, P.G.; Scrosati, B.; Tarascon, J.M., *Angew. Chem.-Int. Edit.*, 47, 2930 (2008).

3, Hayashi, A.; Minami, K.; Tatsumisago, M., *J. Solid State Electrochem. 14*, 1761-1767 (2010).

4, Y. Takahashi, S. Tode, A. Kinoshita, H. Fujimoto, I. Nakane, S. Fujitani, J. Electrochem. Soc. 155 A537 (2008).

5, Y. I. Jang, N. J. Dudney, D. A. Blom, L. F. Allard, J. Electrochem. Soc. 149 A1442 (2002).

6, G. G. Amatucci, J. M. Tarascon, L. C. Klein, Solid State Ionics 83 167 (1996).

7, D. H. Jang, Y. J. Shin, S. M. Oh, *J. Electrochem. Soc. 143*, 2204 (1996).

Publications Resulting from 2009-2011

In Press: Electrochmica Acta. doi:10.1016/j.electacta.2011.03.070 "High voltage stability of $LiCoO_2$ particles with a nano-scale LiPON coating", Yoongu Kim, Gabriel M. Veith, Jagjit Nanda, Raymond R. Unocic, Miaofang Chi, Nancy J. Dudney.

In preparation:

1, "Subnanometer thick Li-ion electrolyte coating towards capacity stabilization of 5V spinel $LiMn_{1.5}Ni_{0.5}O_4$," Yoongu Kim, Miaofang Chi, Chengdu Liang, Surendra K. Martha, Jagjit Nanda, Gabriel M. Veith and Nancy J. Dudney

2, "Low-temperature wet chemistry synthesis of superionic lithium conductor $Li_4P_2S_7$" Wujun Fu, Zengcai Liu, Zhan Lin, Zili Wu, Xiang Yu, Andrew E. Payzant, Nancy J. Dudney, Jim Kiggans, Jane Y. Howe, Kunlun Hong, and Chengdu Liang*

SISGR-Fundamental Experimental and Theoretical Studies on a Novel Family of Oxide Catalyst Supports for Water Electrolysis

Moni Kanchan Datta[1], O.I. Velikokhatnyi[1], Karan Kadakia[2] and Prashant.N. Kumta[1,2,3]

mkd16@pitt.edu, olv3@pitt.edu, pkumta@pitt.edu
[1]Department of Bioengineering
[2]Department of Chemical and Petroleum Engineering
[3]Department of Mechanical Engineering and Materials Science
University of Pittsburgh, Pittsburgh, PA 15261

Program Scope

Noble metals and their oxides (e.g. IrO_2 and RuO_2) are known for their excellent electro-catalytic activity for use in proton exchange membrane (PEM) based water electrolyzers to generate hydrogen without any pollutants or toxic byproducts when the electric current is generated using renewable energy (wind, solar, geothermal and hydropower) [1,2]. The cost of noble metals makes it imperative to search for stable catalyst supports to minimize the noble metal oxide loading while also enhancing the electro-catalytic activity and durability. Generation of acidic protons at almost zero pH, and the high electrochemical potentials during electrolysis conditions require that the catalysts and supports remain stable under these extremely corrosive environments which is a very daunting task. It is desirable therefore that these catalyst supports or diluents exhibit high electronic conductivity, excellent chemical and electrochemical stability at the operating potentials of water electrolysis. Consequently, it is also desirable to generate high specific surface area (HSA) supports to minimize the catalyst loading while exhibiting enhanced electro-catalytic activity. Identification of a new family of ternary oxides encompassing the electrochemically stable oxides, SnO_2, Nb_2O_5, Ta_2O_5 and their solid solutions with other bivalent ion containing oxides selected from transition metals (TM) and alkaline earth metals series; Ca, Mg, Ba, Sr, Zn, and Cd, combined with various metal, M^{2+} and TM site dopants using first principle theoretical methods will lay the foundation for the generation of nano-structured high HSA oxides using innovative wet chemical, complexation, sol-gel, solvothermal, hydrothermal and surfactant template based experimental approaches.

Recent Progress

A convenient approach to reduce the relative amount of expensive noble metal catalyst loading, such as in the case of IrO_2 is to generate a solid solution of this oxide with SnO_2 and transition metal oxides such as Nb_2O_5 or Ta_2O_5. The current density at ~1.75V (vs. NHE) of a solid solution of IrO_2, SnO_2 and Nb_2O_5, denoted as $(Ir,Sn,Nb)O_2$, of different compositions with a total loading ~0.3mg/cm^2 is plotted in Figure 1. It has been identified that $(Ir,Sn,Nb)O_2$ of composition up to $(Ir_{0.40}Sn_{0.30}Nb_{0.30})O_2$ shows similar electrochemical activity compared to pure IrO_2 as shown in Figure 1. On the other hand, $(Ir_{0.20}Sn_{0.40}Nb_{0.40})O_2$ shows only 20% lower electrochemical activity than that of pure IrO_2 though the noble IrO_2 loading is reduced by 80 mol. %. However, addition of only 10wt.% F to $(Ir_{0.20}Sn_{0.40}Nb_{0.40})O_2$ shows electrochemical activity comparable to IrO_2 (Figure 2). The accelerated life test of the anode electrocatalyst followed by elemental analysis of the electrolyte shows that $(Ir,Sn,Nb)O_2$ improves the stability of the electrode in comparison to pure IrO_2 electrocatalyst under oxygen reduction processes. This indicates the promising nature of introducing SnO_2 and transition metal oxides, Nb_2O_5 and Ta_2O_5, which have the ability to exhibit multiple oxidation states thus offering the opportunity to

improve the electronic conductivity while also maintaining the chemical stability as shown by the initial and continued theoretical studies conducted in the research project.

Accordingly, in the present study executed in Year 2, $Ir_{1-2x}Sn_xNb_xO_2$ with x=0-0.5 with rutile crystal structure has been chosen for investigation of the electronic properties of its most stable surface (110). Figure 3 demonstrates the Ir d-band density of the electronic states at the surface (110) for x=0, 0.125, 0.25, 0.375. Arrows denote the d-band center position for each concentration. It is clearly seen that from x=0 up to x=0.25 (Figure 3, a-c) the Ir d-band center is almost fixed near -1.32 eV, and it is only at higher concentration of the inactive material the position is shifted toward the Fermi level (-0.49 eV). This behavior of the d-band center may contribute to the fundamental understanding of the catalytic activity of this ternary oxide containing various amounts of inactive components.

Also, one can see that all the compounds demonstrate metallic behavior although to different extents. In general, metallic conductivity is proportional to the density of states at the Fermi level $n(E_F)$, so that it provides a qualitative evaluation of the electronic conductivity of the material as a function of the residual amount of Ir in the ternary compounds. Figure 4 shows the dependence of $n(E_F)$ vs. composition of $(Ir\text{-}Sn\text{-}Nb)O_2$. For comparison, the values of $n(E_F)$ are normalized to electrons per one $(Ir_{1-2x}Sn_xNb_x)O_2$ formula unit. The graph shows that the conductivity decreases with decrease in Ir-content up to 0.25 atoms per formula unit and then keeps the value almost the same at zero content of Ir. Poor electronic conductivity is one of the factors known to impair the overall catalytic activity of the material, however the reduction in electronic conductivity with decrease in IrO_2 concentration up to 50 at% most likely is not sufficient to significantly deteriorate the catalytic properties of the material.

The cohesive energy, E_{coh} considered as a qualitative measure of the structural and chemical stability of all the materials studied here demonstrates an increase in the absolute value (becomes more negative) with decrease in Ir concentration in the compounds. It therefore reflects an improvement in the overall structural and chemical stability of the oxide primarily due to the presence of much stronger Nb-O bonds in comparison to the Ir-O bonds. Thus, the fundamental aspects of improved an overall stability with no significant compromise in the electronic conductivity determined by the first principles theoretical studies combined with the excellent catalytic activity validated by the experimental studies indicates that this novel family of materials is potentially, a very prospective candidate as a catalyst for water electrolysis and hydrogen generation. Additionally, the incorporation of Group IV oxides, SnO_2, and transition metal oxides, Nb_2O_5 provides the added value of potentially rendering the Ir-Sn-Nb-O system a cost effective alternative to the noble metal analog.

Future Plans

The theoretical component of the research will consist of conducting an *ab-initio* study of the electronic structure, bulk and surface properties of pure Nb_2O_5, and Ta_2O_5 combined with doped structures containing small amounts of F, Nb, Ta, As, Sb, Bi, Cr, Mo, W. Particular attention will be given to the investigation of the surface stability in the presence of sulfuric acid, which is the preferred electrolyte and the catalytic reaction mechanisms providing key answers to the scientific questions pertaining to the potentially promising electrochemical performance of these novel materials. Also, based on the results obtained on doped tin, niobium and tantalum oxides, pure ternary oxides of the Me-Nb-O and Me-Ta-O systems (Me = Mg, Sr, Ba, Zn, Cd, Pb) will also be evaluated for their desirable catalyst support properties. In addition, doped ternary oxides with a small amount of the additional elements, such as F, Sc, Y, As, Sb, Bi, Cr, Mo, W, will be studied for their chemical stability and electronic conductivity.

The experimental component of the study will be directed towards meeting the near term goal for realizing hydrogen production using PEM based water electrolysis. In this regard, work will be focused on the fundamental science of development of new materials and the synthesis pathways to achieve these systems comprising of reduced noble metal catalyst loading. These fundamental studies will be conducted with the primary aim of understanding the correlation of the synthesis procedures with the theoretical studies to study the improved catalytic activity for the compositions containing reduced noble metal contents. The scientific underpinning of the experimental study while validating the theoretical studies will certainly have a bearing on identification of novel materials compositions comprising non-noble metal contents contributing to the added value proposition of reduced noble metal content systems offering significant improvements in the efficiency. Synthesis of high surface area suitable supports combined with the generation of high surface area nanocrystalline electro-catalysts in powder form will therefore be the primary efforts to understand the increase in the efficiency with reduced over-potentials of these novel electro-catalyst systems containing reduced noble metal contents. Materials durability will also be tested under the harsh electrolysis conditions which will provide indications of the effect of the materials system and the synthesis procedure on attaining microstructural aspects contributing to increased system efficiency. For the mid and long term objectives therefore, the work will be directed towards understanding the effect of the synthesis procedures and the resultant materials structure, surface and bulk composition, and microstructure (particle size, shape, nanoscale architecture) on the performance of the cell stack and integration of the water electrolyzer with renewable energy sources (solar energy). Such a fundamental study will provide the strong correlation of the synthesis procedures, structure and microstructure of the catalysts on the electrocatalytic performance while validating the on-going theoretical studies.

References

[1] Hydrogen production road map: Technology pathways to the future. FreedomCAR & Fuel partnership. Hydrogen production technical team. 2009.
[2] Crabtree GW, Dresselhaus MS, Buchanan MV. The hydrogen economy. Phys. Today 2004; 57: 39-44.

DOE Sponsored Publications in 2010-2011 from Current Grant

1. O. I. Velikokhatnyi and P. N. Kumta, "Ab-initio study of fluorine-doped tin dioxide: A prospective catalyst support for water electrolysis", Physica B: Condensed Matter (Amsterdam, Netherlands) 406(3), 471-477 (2011).
2. O. I. Velikokhatnyi and P. N. Kumta, "Ab-initio study of doped calcium niobates and tantalates as prospective catalyst supports for water electrolysis", Journal of the Electrochemical Society (submitted).
3. K. Kadakia, M. K. Datta, O. Velikhokhatnyi and P. N. Kumta, "Experimental and theoretical studies on the electrochemical performance of $(Ir,Sn,Nb)_{O2}$ thin film anode electrocatalyst for PEM based water electrolysis", International Journal of Hydrogen Energy (submitted).
4. M. K. Datta, K. Kadakia, O. Velikhokhatnyi and P. N. Kumta, "Electrochemical performance of IrO_2-SnO_2:F anode electrocatalysts for water electrolysis", Advanced Materials, (submitted).
5. K. Kadakia, M. K. Datta and P. N. Kumta, "High surface area nanocrystalline IrO_2-SnO_2:F anode electro-catalysts for water electrolysis", J. Power Sources (in preparation).

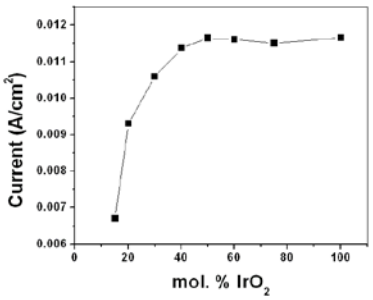

Figure 1: Variation of current density at ~1.75V (vs. NHE) with (Ir,Sn,Nb)O_2 anode electrocatalyst compositions.

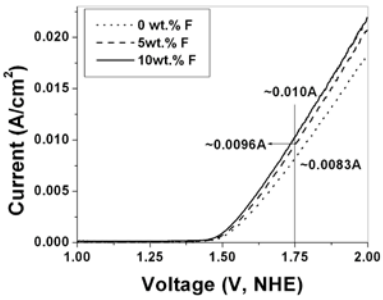

Figure 2: Electrochemical performance of ($Ir_{0.20}Sn_{0.40}Nb_{0.40}$)$O_2$ with F content (0-10wt.%).

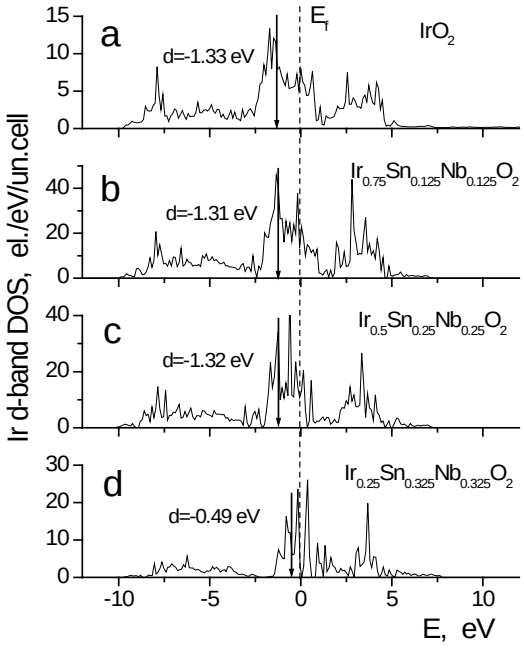

Figure 3: Ir d-DOS at (110) surface for $Ir_{1-2x}Sn_xNb_xO_2$ with x=0, 0.125, 0.25, and 0.375. Dashed lines denote Fermi level.

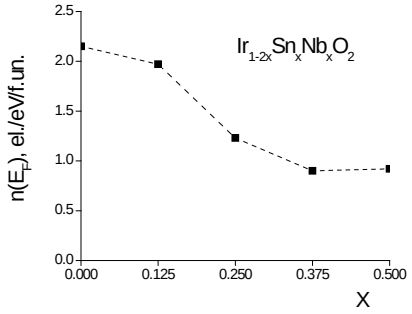

Figure 4: Total DOS at the E_f for $Ir_{1-2x}Sn_xNb_xO_2$.

Doping Cuprous Oxide (Cu_2O) in Electrolyte Solution: Dopant Incorporation, Atomic Structures and Electrical Properties

Meng Tao and Qiming Zhang
mtao@uta.edu
Departments of Electrical Engineering and Physics
University of Texas at Arlington, Arlington, TX 76019

Program Scope

Doping is a common practice in the semiconductor industry to control the conduction type (n-type or p-type) and resistivity of a semiconductor for optimum device performance. Conventional doping techniques are usually vacuum based, including diffusion and ion implantation. Vacuum-based doping by co-deposition is also practiced, such as chemical vapor deposition of a semiconductor with a dopant. Solution-based doping is better suited for low-cost, large-area, and high-throughput applications. Such applications include some of the most important solar energy conversion devices: photovoltaic and photoelectrochemical cells. Efforts on solution-based doping have been rare and scattered. The overall objective of this project is to develop a fundamental understanding of doping mechanisms in the solution phase, thus laying down one of the foundations for solution-fabricated low-cost high-efficiency energy devices.

This project focuses on electrodeposited Cu_2O as a model system and investigates solution-based doping by co-deposition. The recipes for electrodeposition of Cu_2O and CuO are well established [1]. Cu_2O is naturally p-type. We demonstrated n-type Cu_2O, without any external dopant, by reducing the pH of the deposition solution, leading to a solution-prepared p-n homogeneous junction by sequential deposition of n-type and p-type Cu_2O [2]. However, a solar cell made on a Cu_2O p-n homojunction showed little improvement in efficiency [3]. A more detailed study found that the resistivity of the n-type and p-type Cu_2O changes with solution pH, but only in the range of 50 kΩ-cm – 200 MΩ-cm. Therefore, doping both n-type and p-type Cu_2O to reduce their resistivity is necessary for a higher-efficiency solar cell. This project involves both experimental and theoretical studies to understand and control dopants in Cu_2O and related materials.

Recent Progress

All the previous theoretical studies predicted Cu_2O as intrinsically p-type, no matter it is grown in a Cu-rich or O-rich environment. They assumed that the chemical potential of Cu is capped by that of metallic Cu, which is correct for vacuum-based deposition of Cu_2O. To understand n-type Cu_2O by electrodeposition, we assume that the chemical potential of Cu is related to solution pH [4]. The first step is to determine the chemical potential of OH^- ions. It is bounded by the energy of OH^-, in an extreme basic case, and the energy of H_2O, in an extreme acidic environment. A linear scale over pH is assumed. The chemical potential of Cu is thus obtained through its equilibrium in the hydrolysis reaction for a given pH value. The formation energies of native point defects and their charged states are calculated as a function of the Fermi level. It is found that an antisite defect (Cu on O site) is dominant under acidic conditions and responsible for the n-

Table 1. Potential n-type and p-type dopants for Cu_2O and ZnO.

	n-Type		p-Type	
	Cation site	Anion site	Cation site	Anion site
Cu_2O	Group II	Group VII	None	Group V
ZnO	Group III	Group VII	Group I	Group V

type conduction at low solution pH, while p-type Cu_2O is obtained at higher solution pH [4].

Doping in solution-prepared Cu_2O has also been studied by first-principles calculations. n-type dopants including F, Cl and Br have been considered at solution pH of 4. Energetically, they are found more stable on the substitutional O site, not interstitial sites. All of the three halogens show n-type behavior. The donor levels are shallow, with the Cl donor level just 0.17 eV below the minimum of the conduction band, which is dominated by the s-state of O atoms [5]. n-type dopants of Ca, Mg and Zn on the substitutional Cu site have also been studied. Unlike halogens where the formation energies of substitutional dopants on the O site are always several electron volts lower than that of the lowest interstitial site, the formation energies of interstitial dopants compete with substitutional dopants in formation energy, making them less promising than the halogens.

Experimentally, we have demonstrated n-type doping in Cu_2O by anion substitution and in ZnO by cation substitution. Dopants in metal oxides can substitute either the cation or anion site, so there are in principle two types of n-type dopants and two types of p-type dopants based on the valence argument (Table 1). n-type dopants for Cu_2O include Cl and Br for the O site and Ca and Zn for the Cu site, and p-type As and P for the O site and none for the Cu site. For ZnO, n-type dopants include Al and Y for the Zn site and F for the O site, and p-type dopants are Na and K for the Zn site and As and P for the O site. We have also learned various constraints to solution-based doping in Cu_2O and ZnO. For example, the dopant precursor has to be soluble in the deposition solution and the resultant compound has to be insoluble in the deposition solution. For example, group I Na and K are not suitable n-type dopants in solution-prepared ZnO. As they are soluble in water, they will not incorporate into ZnO in an aqueous solution. In addition, the doping mechanism has to be compatible with the deposition mechanism. We will describe several examples of successful and unsuccessful mechanisms in doping metal oxides.

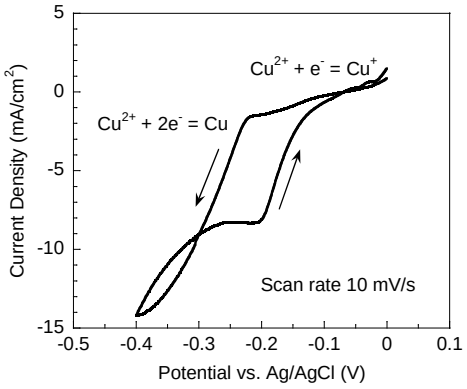

Fig. 1. Voltammetry of a solution containing 0.3 M $CuSO_4$, 0.1 M $CuCl_2$ and 4 M $NaC_3H_5O_3$. The solution temperature is 60°C and pH 7.5.

n-Type Doping in Cu_2O by Anion Substitution: We have successfully doped electrodeposited Cu_2O n-type with Cl and Br, which substitute O atoms in Cu_2O [6,7]. This is particularly interesting as a universal n-type doping technique for all chalcogenides. The doping mechanism is co-precipitation of Cu_2O with CuCl or CuBr. Cyclic voltammetry in a solution containing 0.3 M $CuSO_4$, 0.1 M $CuCl_2$ and 4 M $NaC_3H_5O_3$ reveals that the reduction potential for the following reaction is between –0.05 V and –0.15 V (Fig. 1):

$$Cu^{2+} + e^- \rightarrow Cu^+ \quad \text{(R1)}$$

We choose –0.1 V as the deposition potential for Cu_2O. The Cu^+ ions react with OH^- and Cl^- (or Br^-) ions:

$$2Cu^+ + 2OH^- \rightarrow Cu_2O\downarrow + H_2O \quad \text{(R2)}$$

$$Cu^+ + Cl^- \rightarrow CuCl\downarrow \quad \text{(R3)}$$

CuCl (or CuBr) co-precipitates with Cu_2O, leading Cl-doped Cu_2O.

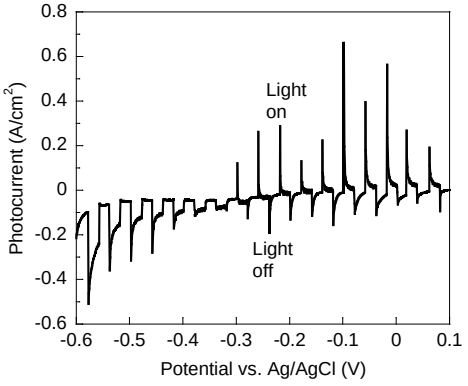

Fig. 2. Photocurrent from Cl-doped Cu_2O. The photocurrent turns from negative to positive at –0.3 V, indicating an n-type semiconductor.

Fig. 2 shows photocurrent from Cl-doped Cu_2O. At –0.3 V, there is a direction change in photocurrent from cathodic to anodic, indicating an n-type semiconductor by Cl doping. For p-type Cu_2O, the photocurrent should be always cathodic. Fig. 3 shows the resistivity of Cl-doped Cu_2O as a function of Cl concentration in the solution. Without doping, the resistivity of electrodeposited Cu_2O is 40 MΩ-cm. With 0.1 M Cl in the solution, the resistivity of Cu_2O is reduced to 75 Ω-cm. When the Cl concentration increases from 0.01 to 0.15 M, the resistivity of Cu_2O is reduced from 157 Ω-cm to 48 Ω-cm (insert in Fig. 3). The lowest resistivity we have achieved so far in Cl-doped Cu_2O is 7 Ω-cm.

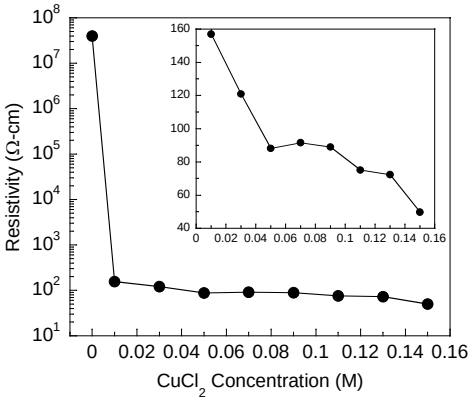

Fig. 3. Resistivity of Cl-doped Cu_2O as a function of Cl concentration in the solution. The plot is semi-logarithmic and the insert is linear.

Br has also been successfully doped into Cu_2O during electrodeposition. The most noticeable feature of Br-doped Cu_2O is the large grains, up to 30 μm (data not shown). For comparison, the grain size in Cl-doped Cu_2O is ~1 μm. Large grains typically provide higher minority carrier lifetime, thus better cell efficiency.

n-type doping in Cu_2O by cation substitution is difficult. A Ca or Zn salt added to the basic solution results in precipitation of oxide or hydroxide. p-type doping in Cu_2O by cation substitution is not feasible. The valence of Cu in Cu_2O is +1, and p-type dopant would be group VIII, which does not chemically bond to O. p-type doping in Cu_2O by As or P has also failed. In a basic solution, As or P does not appear in an elemental form such as As^{3+}, but in a compound form such as AsO_3^{3-}. It requires an acidic solution to obtain elemental As^{3+}:

$$H_3AsO_3 \rightarrow As^{3+} + 3OH^- \quad \text{(R4)}$$

This is not compatible with Cu_2O deposition in a basic solution.

n-Type Doping in ZnO by Cation Substitution: We have demonstrated a record-low resistivity in Y-doped ZnO by electrodeposition [8], where n-type doping is accomplished by cation substitution. This is intended as a low-cost high-performance transparent conducting oxide for photovoltaic devices. The doping mechanism is co-precipitation of Y_2O_3 with ZnO. The cyclic voltammetry in Fig. 4 reveals that the reduction potential for the following reaction is around –0.65 V in a solution containing 0.1 M $Zn(NO_3)_2$ and 0.16 mM $Y(NO_3)_3$:

$$NO_3^- + H_2O + 2e^- \rightarrow NO_2^- + 2OH^- \quad \text{(R5)}$$

The OH^- ions react with Zn^{2+} and Y^{3+} ions in the solution:

$$Zn^{2+} + 2OH^- \rightarrow ZnO\downarrow + H_2O \quad \text{(R6)}$$

$$2Y^{3+} + 6OH^- \rightarrow Y_2O_3\downarrow + 3H_2O \quad \text{(R7)}$$

Y_2O_3 co-precipitates with ZnO, leading to Y-doped ZnO.

Fig. 5 shows the sheet resistance of Y-doped ZnO as a function of Y^{3+}/Zn^{2+} ratio in the solution, where the samples are annealed in 1 atm N_2 at 300°C for 3 hours. The minimum sheet resistance of 1.5 Ω/□ is obtained at Y^{3+}/Zn^{2+} ratio of 0.1, corresponding to a resistivity of 6.3×10^{-5} Ω-cm for Y-doped ZnO. This is the lowest resistivity reported for any solution-prepared ZnO.

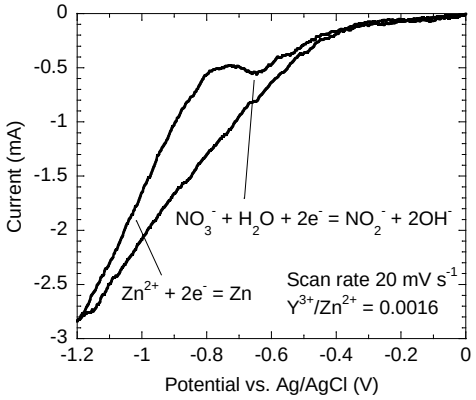

Fig. 4. Voltammetry of a solution containing 0.1 M $Zn(NO_3)_2$ and 0.16 mM $Y(NO_3)_3$. The solution temperature is 70°C and pH 5.5.

Transmittance and reflectance measurements confirm high transmittance of ~80% and low absorbance of 5 – 10% for a 400-nm Y-doped ZnO film (data not shown).

n-type doping in ZnO by anion substitution is difficult. Addition of F into the solution leads to precipitation of ZnF_2. Addition of Cl will not incorporate Cl into ZnO, as $ZnCl_2$ is soluble in water. p-type doping in ZnO by anion substitution such as As is not feasible. The acidic solution can produce As^{3+} ions, but Zn^{2+} and As^{3+} ions will precipitate as Zn_3As_2. p-type doping in ZnO by cation substitution is possible with Ag. Ag has a valence of +1. p-type doping in ZnO by Ag will be investigated.

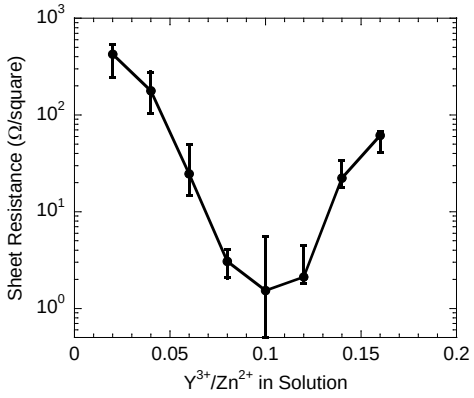

Fig. 5. Sheet resistance of Y-doped ZnO as a function of Y^{3+}/Zn^{2+} ratio in the solution after post-deposition annealing in N_2 at 300°C for 3 hours.

Future Plans

One focus for next year is p-type doping in ZnO by Ag during electrodeposition. In addition, we will investigate doping in metal sulfides for two reasons. It is believed that next-generation terawatt-scale photovoltaic material will be likely a metal sulfide [9]. Second, the acidic conditions for metal sulfide deposition allow various metals to be added to the solution, and both n-type and p-type doping by cation substitution is thus possible in solution-prepared metal sulfides, leading to a solution-prepared metal sulfide p-n homojunction.

References

1. P. Poizot, C.-J. Hung, M.P. Nikiforov, E.W. Bohannan, and J.A. Switzer, Electrochem. Solid-State Lett. **6** (2003) C21.
2. L. Wang and M. Tao, Electrochem. Solid-State Lett. **10** (2007) H248.
3. K. Han and M. Tao, Solar Energy Mater. Solar Cells **93** (2009) 153.
4. W. Wang, D. Wu, Q.-M. Zhang, L. Wang, and M. Tao, J. Appl. Phys. 107 (2010) 123717.
5. Q. Bai, W. Wang, Q.-M. Zhang, and M. Tao, submitted to Sol. Energy Mater. Sol. Cells.
6. X. Han, K. Han, and M. Tao, Electrochem. Solid State Lett. **12** (2009) H89.
7. X. Han, K. Han, and M. Tao, Thin Solid Films **518** (2010) 5363.
8. X. Han, K. Han, and M. Tao, J. Electrochem. Soc. **157** (2010) H593.
9. C. Wadia, A. P. Alivisatos and D. M. Kammen, Environ. Sci. Techno. **43** (2009) 2072.

DOE Sponsored Publications in 2009 – 2011

1. W. Wang, D. Wu, Q.-M. Zhang, L. Wang, and M. Tao, "pH-Dependence of Conduction Type in Cuprous Oxide Synthesized from Solution", J. Appl. Phys. **107** (2010) 123717.
2. Q. Bai, W. Wang, Q.-M. Zhang, and M. Tao, "n-Type Doping in Cu_2O with F, Cl and Br: A First-Principles Study", Sol. Energy Mater. Sol. Cells, submitted.
3. X. Han, K. Han, and M. Tao, "Characterization of Cl-Doped n-Type Cu_2O Prepared by Electrodeposition", Thin Solid Films **518** (2010) 5363.
4. C. S. Tao, J. Jiang, and M. Tao, "Natural Resource Limitations to Terawatt-Scale Photovoltaic Solar Cells", Sol. Energy Mater. Sol. Cells, in press.
5. K. Han, F. Kang, X. Han, and M. Tao, "Enhanced Crystal Grain Size by Bromine Doping in Electrodeposited Cu_2O, J. Cryst. Growth, submitted.

Poster Sessions

This page is intentionally blank.

Synthesis and Processing Science
Principal Investigators' Meeting

Poster Session I

1. Depolarized Light Scattering from Plasmonic Structures
George Chumanov, *Clemson University*

2. Metal Oxide Core Shell Nanostructures as Building Blocks for Efficient Light Emission
James A. Dorman and ***Jane P. Chang***, *University of California- Los Angeles*

3. Synthesis of ZTO Nanowires and Physical Deposition of Quantum Dots
Jiajun Chen, Qilin Dai, Liyou Lu, Jinke Tang, and ***Wenyong Wang***, *University of Wyoming*

4. Synthesis and Engineering of Submonolayer Type-II Quantum Dots to Enhance Material Properties of Wide Bandgap Semiconductors
Maria Tamargo, *Igor Kuskovsky, Gertrude Neumark, Carlos Meriles, and Cevdet Noyan, The City College of New York*

5. Plasmonic Nanostructures Integrated with Semiconductor Light Emitting Materials for Enhanced Efficiency and Functionality
Roberto Paiella *and Ted D. Moustakas, Boston University*

6. Heteroepitaxial Science of Polar, Semipolar and Nanopolar (In)GaN
B. Leung, C. Yerino, Y. Zhang, ***Jung Han***, *and Michael E. Coltrin[b], Yale University and [b]Sandia National Laboratories*

7. Solid-State Lighting Science Energy Frontier Research Center
Mike Coltrin (Invited), *Sandia National Laboratories*

8. Synthesis, Characterization, and Investigation of Charge Separation and Recombination in Carbon Nanotube-Quantum Dot Nanoscale Heterostructures
Xiaohui Peng, Matthew Y. Sfeir, James A. Misewich, and ***Stanislaus S. Wong***, *Brookhaven National Laboratory*

9. Synthesis and Characterization of RFeAsO Based Single Crystals at Ambient Pressures
R. W. McCallum *and T.A. Lograsso, Ames Laboratory*

10. Chemical Routes to Intermetallic, Carbide, and Chalcogenide Nanomaterials
Raymond E. Schaak, *The Pennsylvania State University*

11. Superconductors in Confined Geometries
Zhili Xiao, *Northern Illinois University*

12. Molecular Beam Epitaxy and Nano-Structuring of Perovskite Oxide Materials toward Understanding of Strongly Correlated Systems
Ivan Bozovic, *Brookhaven National Laboratory*

13. Structure-Property Relationships at Polar/Nonpolar Perovskite Interfaces
Scott A. Chambers, *L. Qiao, T.C. Droubay, T.C. Kaspar, M.E. Engelhard, M.E. Bowden, V. Shutthanandan, P. Sushko,[b] T. Feng[c], H. D. Lee[c], T. Gustafsson[c], E. Garfunkel[c], A.B. Shah[d], J.-M. Zuo[d], and Q.M. Ramasse[e], Pacific Northwest National Laboratory, Richland, WA [b]University College, London, UK, [c]Rutgers University, Piscataway, NJ, [d]University of Illinois at Urbana-Champaign [e]SuperSTEM Laboratory, STFC Daresbury, UK*

14. Magnetic and Electronic Properties of Doped Oxide Semiconductors
S.A. Chambers (PI), ***Tiffany C. Kaspar****, T.C. Droubay, S.J.S. McCloy, J.V. Ryan, A. Ney[b], T. Kammermeier[b], K. Ollefs[b], S. Ye[b], V. Ney[b], F. Wilhelm[c], A. Rogalev[c], C.A. Johnson[d], K.R. Kittilstved[d], D.R. Gamelin[d], and D.C. Look[e], Pacific Northwest National Laboratory, Richland, WA [b]Universität Duisburg-Essen, Duisburg, Germany [c]European Synchrotron Radiation Facility, Grenoble, France [d]University of Washington, Seattle, WA [e]Wright State University, Dayton, OH*

15. Digital Synthesis: A Pathway to New Materials at Interfaces of Complex Oxides
Anand Bhattacharya*, Argonne National Laboratory*

16. Development and Understanding of Multifunctional Nanostructured Magnetoelectric and Spintronic Materials
Ram S. Katiyar, *M. Gomez, G. Morell, L. Fonseca, W. Otano, O. Perales, M. S. Tomar, Y. Ishikawa, R. Palai, R. Thomas, A. Kumar, J. Velev, and V. Makrov, University of Puerto Rico*

17. $Ca_3Mn_2O_7$ and $Ca_3Ti_2O_7$—An Example of Multiferroic Matter by Design
Craig J. Fennie, David A. Muller, Peter Schiffer[b], and ***Darrell G. Schlom****, Cornell University and [b]The Pennsylvania State University*

18. The Fabrication and Electrochemical Properties of Strained YSZ/GDC Thin Films
Joshua Hertz*, Weida Shen, and Jun Jiang, University of Delaware*

19. Electric-Field Enhanced Kinetics in Oxide Ceramics: Pore Migration, Sintering and Grain Growth
I-Wei Chen*, University of Pennsylvania*

20. Thermochemistry of Anion Defect and Charge Coupled Substitutions in Fluorite and Perovskite Based Materials
Alexandra Navrotsky *and* ***Sergey V. Ushakov****, University of California at Davis*

21. Developing MMOFs for Enhanced and Selective CO_2 Adsorption
Jing Li*, Rutgers University*

Synthesis and Processing Science
Principal Investigators' Meeting

Poster Session II

1. Utilizing Molecular Self-Assembly to Tailor Electrical Properties of Si Nanomembranes
Pengpeng Zhang, *Michigan State University*

2. Group IV Semiconductor Nanomembranes: New Properties through Novel Synthesis and Strain Engineering
Max G. Lagally *and Mark A. Eriksson, University of Wisconsin–Madison*

3. Integrated Growth and Ultra-Low Temperature Transport Study of the 2nd Landau Level of the Two-Dimensional Electron Gas
Gabor Csathy *and* ***Michael Manfra***, *Purdue University*

4. Epitaxial Electrodeposition/Reduction of Functional Metal Oxide Films
Jay Switzer, *Missouri University of Science and Technology*

5. In-Situ Micro Raman Detection of Reversible Basal Plane Hydrogenation in Pt-Doped Activated Carbon
Xiao Ming Liu, Youjian Tang, En Shi Xu, Thomas C. Fitzgibbons, Humberto R. Gutierrez, John V. Badding, Vincent H. Crespi, and ***Angela D. Lueking***, *The Pennsylvania State University*

6. In-Situ Neutron Scattering Studies of Electrical Energy Storage Materials
Ke An *and* ***Chengdu Liang***, *Oak Ridge National Laboratory*

7. Controlled Nano-Scale Architectures: Access to Beneficial Metastable States
Iver E. Anderson, *Qingfeng Xing and T.A. Lograsso, Ames Laboratory*

8. Conduction Mechanisms and Structure of Ionomeric Single-Ion Conductors – Part 2: Polysiloxane Ionomers
Ralph H. Colby, Janna K. Maranas, Karl T. Mueller, ***James Runt***, *and Karen I. Winey[b], The Pennsylvania State University and [b]University of Pennsylvania*

9. Characteristic Length Scales of Growing Nanorods – Atomistic Simulations, Analytical Formulations, and Experiments
Longguang Zhou, Soohwan Lee, Ruoxin Zhang, Stephen Stagon, and ***Hanchen Huang***, *University of Connecticut*

10. Understanding and Controlling Nanoscale Crystal Growth using Mechanical Forces
Mostafa Bedewy, Justin D. Beroz, and ***A. John Hart***, *University of Michigan*

11. Non-Equilibrium Synthesis of Nanostructured Materials: Laser Vaporization Synthesis of Nanoparticle Building Blocks
Alex Puretzky, *David B. Geohegan, Christopher M. Rouleau, Jason D. Readle, Mina Yoon, Gyula Eres, Murari Regmi, Karren L. More, and Gerd Duscher, Oak Ridge National Laboratory*

12. Non-Equilibrium Synthesis of Nanostructured Materials: Real Time Monitoring of Non-Equilibrium Doping of TiO_2 in Pulsed Laser Deposition for Energy Applications
Gyula Eres, *D.B. Geohegan, A.A. Puretzky, C.M. Rouleau, M. Yoon, J.D. Readle, M. Regmi, Z. Zhang[b], H. Weitering[b], N. Mannella[b], and G. Duscher[b], Oak Ridge National Laboratory and [b]University of Tennessee*

13. Simulation and Theory of Solid-Liquid Interface Migration
M. I. Mendelev, *M.J. Kramer, R.E. Napolitano, V.B. Warshavsky, and X. Song, Ames Laboratory*

14. Development of Order in Deeply Undercooled Liquid Metals
X.W. Fang, C.Z. Wang, M.J. Kramer, S. G. Hao, L. Huang, Y. X. Yao, M. I. Mendelev,
R. E. *Napolitano,* *R.T. Ott, and K. M. Ho, Ames Laboratory*

15. Designing Graphene Nanoarchitectures for a New Paradigm of Nanoelectronics
Feng Liu, *University of Utah*

16. Templated Bottom-Up Synthesis of Semiconducting and Nanostructured Graphene Materials
Michael S. Arnold, *University of Wisconsin–Madison*

17. Nanoscale Morphology Evolution under Ion Irradiation
Michael J. Aziz, *Harvard University*

18. Molecular Dynamics Simulations and Experimentation on the Liquid-Phase Assembly of Thin Metallic Film Nanostructures
Miguel Fuentes-Cabrera, *Jason D. Fowlkes,* ***Philip D. Rack***, *and Michael L. Simpson, Oak Ridge National Laboratory*

19. Molecularly Organized Nanostructural Materials – Subtask: Theoretical Modeling of Nanostructural Materials Synthesis using Self-Assembly Process
Maria Sushko *and Jun Liu, Pacific Northwest National Laboratory*

20. Molecularly Organized Nanostructural Materials – Subtask: Nanostructural Materials Synthesis and Guest Induced Structural Transformation
Praveen K. Thallapally, *Jun Liu, and Gregory J. Exarhos, Pacific Northwest National Laboratory*

21. Atomic Layer Controlled Growth of Ferro Pnictide Thin Films
Chang-Beom Eom, *University of Wisconsin–Madison*

Author Index

This page is intentionally blank.

Author Index

This page is intentionally blank.

Participant Listing

This page is intentionally blank.

Participant Listing

Last Name	First Name	Organization	E-Mail Address
Ajayan	P. M.	Rice University	ajayan@rice.edu
An	Ke	Spallation Neutron Source, ORNL	kean@ornl.gov
Anderson	Iver	Ames Laboratory	andersoni@ameslab.gov
Arnold	Mike	University of Wisconsin-Madison	msarnold@wisc.edu
Aziz	Mike	Harvard University	maziz@harvard.edu
Bent	Stacey	Stanford University	sbent@stanford.edu
Bhattacharya	Anand	Argonne National Laboratory	anand@anl.gov
Bozovic	Ivan	Brookhaven National Laboratory	bozovic@bnl.gov
Chabal	Yves	University of Texas at Dallas	chabal@utdallas.edu
Chambers	Scott	Pacific Northwest National Laboratory	sa.chambers@pnl.gov
Chang	Jane	University of California, Los Angeles	jpchang@seas.ucla.edu
Chen	I-Wei	University of Pennsylvania	iweichen@seas.upenn.edu
Christen	Hans	Oak Ridge National Laboratory	christenhm@ornl.gov
Chumanov	George	Clemson University	gchumak@clemson.edu
Cohen	Itai	Cornell University	ic64@cornell.edu
Coltrin	Mike	Sandia National Laboratories	mecoltr@sandia.gov
Crockett	Teresa	DOE, Basic Energy Sciences	teresa.crockett@science.doe.gov
Dandy	David	Colorado State University	ddandy@mac.com
Datta	Moni	University of Pittsburgh	mkd16@pitt.edu
Eom	Chang-Beom	University of Wisconsin-Madison	eom@engr.wisc.edu
Eres	Gyula	Oak Ridge National Laboratory	eresg@ornl.gov
Eriksson	Mark	University of Wisconsin-Madison	maeriksson@wisc.edu
Escobedo	Fernando	Cornell University	fe13@cornell.edu
Exarhos	Greg	Pacific Northwest National Laboratory	greg.exarhos@pnnl.gov
Fichthorn	Kristen	The Pennsylvania State University	fichthorn@psu.edu
Fowlkes	Jason	Oak Ridge National Laboratory	fowlkesjd@ornl.gov
Fuentes-Cabrera	Miguel	Oak Ridge National Laboratory	fuentescabma@ornl.gov
Furst	Eric	University of Delaware	furst@udel.edu
Garofalini	Steve	Rutgers University	shg@rutgers.edu
Geohegan	Dave	Oak Ridge National Laboratory	geohegandb@ornl.gov
Gersten	Bonnie	DOE, Basic Energy Sciences	Bonnie.Gersten@science.doe.gov
Green	Peter	University of Michigan	pfgreen@umich.edu
Grim	Gary	Colorado School of Mines	rgrim@mines.edu
Han	Jung	Yale University	jung.han@yale.edu
Hart	John	University of Michigan	ajohnh@umich.edu
Hertz	Josh	University of Delaware	hertz@udel.edu
Horton	Linda	DOE, Basic Energy Sciences	linda.horton@science.doe.gov
Horwitz	Jim	DOE, Basic Energy Sciences	james.horwitz@science.doe.gov

Last Name	First Name	Organization	E-Mail Address
Huang	Hanchen	University of Connecticut	hanchen@uconn.edu
Jain	Himanshu	Lehigh University	h.jain@lehigh.edu
Johnson	Duane	Ames Laboratory	feller@ameslab.gov
Kaspar	Tiffany	Pacific Northwest National Laboratory	tiffany.kaspar@pnl.gov
Katiyar	Ram	University of Puerto Rico	rkatiyar@uprrp.edu
Kerkar	Prasad	Colorado School of Mines	kerkarpb@gmail.com
Kini	Arvind	DOE, Basic Energy Sciences	a.kini@science.doe.gov
Koh	Carolyn	Colorado School of Mines	ckoh@mines.edu
Kramer	Matt	Ames Laboratory	mjkramer@ameslab.gov
Kumar	Satish	University of Minnesota	kumar030@umn.edu
Kumta	Prashant	University of Pittsburgh	pkumta@pitt.edu
Lagally	Max	University of Wisconsin-Madison	lagally@engr.wisc.edu
Li	Jing	Rutgers University	jingli@rutgers.edu
Liang	Chengdu	Oak Ridge National Laboratory	liangcn@ornl.gov
Liddell Watson	Chekesha	Cornell University	cliddell@ccmr.cornell.edu
Liu	Feng	University of Utah	fliu@eng.utah.edu
Liu	Jun	Pacific Northwest National Laboratory	jun.liu@pnnl.gov
Liu	Xiaoming	The Pennsylvania State University	xul106@psu.edu
Lograsso	Tom	Ames Laboratory	lograsso@ameslab.gov
Lueking	Angela	The Pennsylvania State University	adl11@psu.edu
Mackay	Michael	University of Delaware	mem@udel.edu
Manfra	Michael	Purdue University	mmanfra@purdue.edu
Markowitz	Mike	DOE, Basic Energy Sciences	mike.markowitz@science.doe.gov
McCallum	Bill	Ames Laboratory	mccallum@ameslab.gov
Mendelev	Mikhail	Ames Laboratory	mendelev@ameslab.gov
Moustakas	Ted	Boston University	moustakas@bu.edu
Mueller	Karl	The Pennsylvania State University	ktm2@psu.edu
Napolitano	Ralph	Ames Laboratory / Iowa State University	ralphn@iastate.edu
Nolas	George	University of South Florida	gnolas@usf.edu
Ott	Ryan	Ames Laboratory	rtott@ameslab.gov
Paiella	Roberto	Boston University	rpaiella@bu.edu
Park	Chal	University of Michigan	challan@umich.edu
Petrovic	Cedomir	Brookhaven National Laboratory	petrovic@bnl.gov
Pfeifer	Peter	University of Missouri	pfeiferp@missouri.edu
Puretzky	Alex	Oak Ridge National Laboratory	puretzkya@ornl.gov
Rack	Philip	University of Tennessee / ORNL	prack@utk.edu
Raj	Rishi	University of Colorado	rishi.raj@colorado.edu
Runt	Jim	The Pennsylvania State University	runt@matse.psu.edu
Schaak	Ray	The Pennsylvania State University	res20@psu.edu
Schlom	Darrell	Cornell University	schlom@cornell.edu
Schwartz	Andrew	DOE, Basic Energy Sciences	andrew.schwartz@science.doe.gov

Last Name	First Name	Organization	E-Mail Address
Sennett	Michael	DOE, Basic Energy Sciences	michael.sennett@science.doe.gov
Stagon	Stephen	University of Connecticut	stephen.stagon@uconn.edu
Sushko	Maria	Pacific Northwest National Laboratory	maria.sushko@pnnl.gov
Switzer	Jay	Missouri University of Science and Technology	jswitzer@mst.edu
Talley	Lee-Ann	Oak Ridge Institute for Science and Education	lee-ann.talley@orise.orau.gov
Tamargo	Maria	City College of New York	mtamargo@ccny.cuny.edu
Tao	Meng	University of Texas at Arlington	mtao@uta.edu
Thallapally	Praveen	Pacific Northwest National Laboratory	praveen.thallapally@pnnl.gov
Thornton	Katsuyo	University of Michigan	kthorn@umich.edu
Torquato	Sal	Princeton University	torquato@princeton.edu
Ushakov	Sergey	University of California, Davis	svushakov@ucdavis.edu
Velikokhatnyi	Oleg	University of Pittsburgh	olv3@pitt.edu
Voorhees	Peter	Northwestern University	p-voorhees@northwestern.edu
Wang	C. Z.	Ames Laboratory / Iowa State University	wangcz@ameslab.gov
Wang	George	Sandia National Laboratories	gtwang@sandia.gov
Wang	David	Colorado State University	q.wang@colostate.edu
Wang	Wenyong	University of Wyoming	wwang5@uwyo.edu
Wong	Stanislaus	Brookhaven National Laboratory	sswong@bnl.gov
Xiao	Zhili	Northern Illinois University	zxiao@niu.edu
Xing	Sam	Ames Laboratory	qxing@ameslab.gov
Yacobson	Boris	Rice University	biy@rice.edu
Zaera	Francisco	University of California, Riverside	zaera@ucr.edu
Zhang	Pengpeng	Michigan State University	zhang@pa.msu.edu
Zhang	Qiming	The Pennsylvania State University	qxz1@psu.edu
Zhou	Guangwen	State University of New York at Binghamton	gzhou@binghamton.edu
Zhou	Longuang	University of Connecticut	lgzhou@engr.uconn.edu
Zinin	Pavel	University of Hawaii	zinin@soest.hawaii.edu